LBL-10301
SLAC-PUB-2575
UC-28
CONF-7910122

PROCEEDINGS OF THE HEAVY ION FUSION WORKSHOP

CLAREMONT HOTEL, BERKELEY, CALIFORNIA
HELD
OCTOBER 29 – NOVEMBER 9, 1979

September 1980

Lawrence Berkeley Laboratory
University of California

Stanford Linear Accelerator Center

Prepared for the U.S. Department of Energy
under Contract No. W-7405-ENG-48
and
Contract DE-AC03-76SFOO515

Printed in the United States of America
Available from
National Technical Information Service
U.S. Department of Commerce
5285 Port Royal Road
Springfield, VA 22161
Price Code: A22

LBL-10301
SLAC-PUB-2575

PROCEEDINGS OF THE HEAVY ION FUSION WORKSHOP

HELD AT
CLAREMONT HOTEL, BERKELEY, CALIFORNIA

OCTOBER 29 – NOVEMBER 9, 1979

FINAL REPORT
SEPTEMBER 1980

Proceedings Editor
W. B. Herrmannsfeldt

LAWRENCE BERKELEY LABORATORY
UNIVERSITY OF CALIFORNIA
BERKELEY, CALIFORNIA 94720
and
STANFORD LINEAR ACCELERATOR CENTER
PALO ALTO, CALIFORNIA 94305

TABLE OF CONTENTS

PREFACE

It is customary for the proceedings of a workshop such as this one to include a summary of the conclusions. In this case, a letter from the chairman, Burton Richter, was sent to Dr. Greg Canavan a few weeks after the conference ended. This letter was the cover for a summary based on the preliminary reports of the subsection chairmen, which, owing to the press of time, I put together without consulting the other members of the organizing committee. These documents became the real record of the conference and thus are reproduced here as the summary reports. To reduce redundancy, the preliminary reports of the subsection chairmen have been replaced by their final reports.

Many people contributed to the success of the workshop, but special recognition is due for the cooperation of the subsection chairmen, and for the support provided by Judy Zelver and the rest of the secretarial staff of the Accelerator and Fusion Research Division of LBL. Also, thanks are due to those who attended from accelerator laboratories outside the US. Their participation was essential to fulfilling the goals of the conference. My cochairman, Terry Godlove, joins me in expressing our appreciation to all of the above, and to everyone else who participated in the study session.

Bill Herrmannsfeldt

STANFORD UNIVERSITY

STANFORD LINEAR ACCELERATOR CENTER

Mail Address
SLAC, P. O. Box 4349
Stanford, California 94305

27 November 1979

Dr. G. Canavan
Office of Inertial Fusion
Department of Energy
Washington, D.C. 20545

Dear Greg:

I am enclosing a summary of the work of the Heavy Ion Accelerator Study Session which was held under the auspices of your office October 29, to November 9, in Berkeley. This summary was prepared by W.B. Herrmannsfeldt, who was chairman of the Organizing Committee of the Conference, from the reports of the heads of the various working groups at the Conference. This meeting was organized to bring together members of the world community of accelerator physicists to examine potential problem areas in the design of heavy ion drivers for inertial fusion. It is gratifying to note that these experts found no fatal flaws in the heavy ion drivers but, as you might expect, they did find some matters which needed further theoretical as well as experimental work.

After the formal end of this study session, I convened a meeting of some of the participants to discuss what they thought needed doing in the light of the work in the study session. Their first conclusion was that the pellet designers had gone too far in lowering the beam energy for heavy ion drivers to 5 GeV. This low energy makes space charge problems in these drivers much more severe than the old 20 GeV case. A good compromise for both the pellet design and the driver design will probably be about 10 GeV. The pellet designers should specify the energy, peak power, and beam radius required for a 10 GeV driver and the accelerator designers should then carry out new reference designs for the required systems. The next workshop in this series should concentrate on the review of these reference designs.

Four areas which needed more work were identified in this study. These are 1) final transport in vacuum with space charge; 2) longitudinal stability in induction linacs with emphasis on wave form tolerances; 3) longitudinal stability in storage rings; 4) longitudinal-transverse coupling in induction linacs which operate in an unusual mode with many transverse and few longitudinal oscillations during acceleration.

It was emphasized that the theoretical calculations are difficult and some estimate should be made of the possibility of scaled experiments using existing low and medium energy accelerators.

I think that this study session was very useful to the program and it gave me increased confidence that the work of the past few years had not overlooked any major problem areas.

Sincerely,

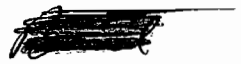

Burton Richter
Professor

BR:skd

HEAVY ION ACCELERATOR STUDY SESSION

W.B. Herrmannsfeldt
Stanford Linear Accelerator Center

Objective

To study the physics of high-intensity heavy-ion accelerators to assess their promise as ignitor systems for inertially confined fusion.

Participation

Approximately one hundred accelerator scientists participated in the study session held at the Claremont Hotel, Oakland, California for two weeks during the period October 29 to November 9, 1979.

Organization

The study session was jointly sponsored by the Office of Inertial Fusion, (OIF) U.S. Department of Energy and the Lawrence Berkeley Laboratory, (LBL). The chairman of the conference was Professor Burton Richter, Stanford Linear Accelerator Center (SLAC). The organizing committee was chaired by W.B. Herrmannsfeldt, SLAC, and T. Godlove, OIF. Other members of the organizing committee were: A. Maschke and E. Courant, BNL, R. Martin and T. Khoe, ANL, and D. Keefe and L. Smith, LBL.

The study was divided into five working groups with attendees participating in one or more of these according to their specific interests and areas of specialization. Chairmen for these groups were chosen from among the attendees who were not part of one of the funded OIF heavy-ion fusion (HIF) programs. (More than half of the attendees were from programs other than HIF, including universities, foreign countries, high-energy physics, etc.) The working groups and their cochairmen were:

Low-beta Accelerators: R. Jameson, LASL and P. Lapostolle, France.

(Beta refers to the velocity in units of the velocity of light, v/c.)

Linear Accelerators: S. Penner and M. Wilson, both NBS.

Storage Rings: L. Teng, FNAL, E. Courant, BNL, and N. M. King, Great Britain.

Final Transport in Vacuum: A. Garren, LBL and I. Hofmann, West Germany.

Final Transport in Gas: C. Olson, SLA.

Background

This was the fourth in the series of annual workshops held to study the subject of heavy ion accelerator drivers for inertial fusion. Since the status of the field has changed rapidly during this period, the purpose and style of each of these sessions has also changed.

The first Claremont meeting, held in the same hotel in 1976, actually preceded formal funding for accelerator laboratories for HIF. This study was held to test the validity of early claims by proponents that HIF was in fact feasible, and to identify the most promising techniques and most critical questions.

The second workshop, held at BNL in 1977, saw a multitude of proposed systems and subsystems being sorted out to enable the community to better concentrate on comparable approaches. Some of the theoretical studies, such as the space charge limits for beam transport, began to show some progress.

The third workshop, held at ANL in 1978, resulted in over 400 pages of technical proceedings complete with a comparative evaluation of the complete driver systems proposed by each of the three major centers; ANL, BNL and LBL. During this workshop, one of the systems, that using synchrotrons as the principal element for increasing the total energy in the beam, was more or less dropped leaving two main line approaches: 1) a conventional rf accelerator with a system of storage rings for current multiplication, and 2) a single-pass linear induction accelerator

propelling a single high intensity bunch of ions using waveform shaping to compress the bunch and increase the current. Both approaches require the use of a system of pulsed induction modules followed by a system of tranport magnets extending over a distance sufficient to allow the beam to ballistically compress longitudinally to achieve the peak pulse power needed to ignite a fusion pellet.

It should be noted that the synchrotron approach, which was dropped at least partially because of the limited funding and manpower available to study it, has continued to be studied by two Japanese laboratories which were represented by three attendees at this year's workshop.

Finally, the 1979 study was convened with the express purpose of looking carefully at the physics questions (as opposed to questions of systems, pellets, economics, etc.) posed by the two main-line approaches. These questions were to be formulated and examined particularly in the light of recent experiences with other new accelerator systems such as storage rings for high-energy physics and induction accelerators for weapons-related activities. The majority of attendees, and all of the chairmen of the working groups, were from such outside groups, and many had not attended any of the previous workshops. A brief discussion of target parameters and the results of recent theoretical work in pellet design was presented by way of an introduction for new workers. A significant change in beam requirements was identified by R. Bangerter, LLL, who presented the following table of target beam parameters:

Case	A	B	C
Beam energy	1 MJ	3 MJ	10 MJ
Peak power	100 TW	150 TW	300 TW
Kinetic energy	5 GeV	10 GeV	10 GeV
Spot radius	1 mm	2.5 mm	3 mm
Pulse length (total)	20 ns	40 ns	70 ns
Pulse length (peak)	6 ns	16 ns	20 ns

Ions at or above A = 200 atomic mass are assumed. Comparison with data given to previous workshops shows that, while the multimegajoule cases continue to be favored as higher confidence for achieving useful gain, the kinetic energy allowed for the ion beams has decreased. This requires a corresponding increase in beam intensity, although some growth (about a factor of two) has occured in spot radius and peak pulse length. Qualitatively, of course, increased intensity adds to the difficulty of achieving the necessary beam parameters while increasing the spot size and the peak pulse length increases the permitted six-dimensional beam emittance, thus easing the requirements. Paradoxically, increases in beam energy and kinetic energy tend to make the accelerator parameters somewhat less stringent. This is because it is easier to contain and transport a higher energy beam in which overcoming collective (space charge) forces requires a relatively smaller fraction of the total force needed for confinement.

Technical questions

A representative list of specific technical questions was defined by the organizing committee:

(1) For low-beta and rf linacs:
   a) Preservation of emittance during combining of beamlets.
   b) Coherent instabilities in the main accelerator.

(2) For induction linacs:
   a) High current injector systems.
   b) Coherent instabilities, both transverse and longitudinal.
   c) Waveform tolerances and jitter.

(3) For storage rings:
   a) Injection requiring debunching and stacking.
   b) Rebunching in the ring.
   c) Coherent effects, both transverse and longitudinal.

d) Vacuum requirements.
e) Charge exchange.
f) Extraction.
g) Cooling techniques, if useful.

(4) Final Transport, vacuum:
a) Longitudinal pulse compression.
b) Geometric aberrations.
c) Chromatic aberrations.
d) Beam splitting.
e) Coherent effects.

(5) Final transport, gas (may be required in a power reactor):
a) Charge and current neutralization.
b) Two-stream instability.
c) Availability of "windows" for beam transport, i.e., ranges of pressure in which beam transport and reactor first-wall protection are compatible.

Test Beds

The two largest DOE laboratory programs in HIF, ANL and LBL, have each developed proposals to design and construct accelerator systems, called Test Beds, to demonstrate the principal parameters and components needed to construct a full-scale prototype driver. The test beds would be far too small and too low in energy to be useful as pellet drivers, but should serve to provide for the testing of components and verification of theoretical stability calculations. The study session did not have time to assess adquately the degreee to which the proposed test beds would fulfill these requirements, but did establish some specific questions which the test beds should be designed to answer.

Working Group Summaries

At the end of the study session the meeting site was shifted to the LBL auditorium to allow unlimited attendance by interested scientists who had not been able to participate in the workshop. The reports began with a summary of the target parameters described above. Then the working groups reported their findings starting with the final transport groups and working backwards.

(1) Final transport in gas: The group considered possible reactor scenarios to test the compatibility of the reactor environment (diameter and kind and pressure of gas) with the problem of transporting the beam to the target. The presently favored design concept, using either a lithium fall or a lithium wetted wall operating at about 375°C, would have a pressure in the range 10^{-4} to 10^{-3} Torr. (This temperature is about the same as the operating temperature for light water reactors.) The group found that transport at pressures up to about 10^{-3} Torr for a reactor radius of five meters would be suffciently unaffected by the two-stream instability to be effectively stable. The 0.1 to 1.0 Torr "window" that had been defined earlier (assuming a noble gas to provide reactor front wall protection) appears to be closing off with the lower kinetic energies called for (5-10 GeV). A practical problem with this scenario is the difficulty of pumping a noble gas well enough to avoid beam loss due to stripping in the last focusing magnet. The pinch mode, similar to that required for light ion beam fusion, still appears to be a possible transport mode. The most promising conclusion, however, is that the newly found window, coinciding with the parameters of the liquid lithium reactor scenario, provides a final beam transport scenario consistent with the favored reactor system.

(2) Final transport in vacuum: The transport line from the accelerator and/or storage ring to the reactor is evacuated. The problem of stable transport in this system is complicated by the fact that the beam is rapidly compressing longitudinally, thus causing the current to be continuously increasing. The approach used by the working group was to design the best possible system without space charge and then to modify the solution assuming uniform

charge density in both the transverse and longitudinal directions. The designs resulting from this approach would then be tested using the numercial simulation methods developed for the space charge limited transport studies by Haber, Penner, Laslett, etc. These simulations, which were beyond the capabilities of the workshop during the limited time available, would account for the nonuniform space charge distribution. An example beam line was designed by K. Brown and J. Peterson during the study. It consists of three one-half wave modules and includes sextupole magnets for chromatic correction. Second order calculations yielded 85% transmission onto a 4 mm diameter target with 3% momentum spread. The relatively large momentum spread permits higher currents to be transported below instability thresholds, and is a significant parameter for all the preceding parts of an accelerator system. The principal effect of including space charge was to increase the maximum beam radius from 25 to 36 cm. In spite of the promising result given above, there was concern expressed in the summary that chromatic correction schemes may in practice do more harm than good, and that momentum spreads should be limited to ± 1%. The final transport group also issued a call for an intensified program of numerical calculation for the full simulation of these transport system.

(3) Storage Rings: The working group on the storage rings developed parameter sets for each of the three target cases. The special situations considered include:

a) Stacking at injection, with resulting emittance dilution,
b) Bunch compression in the ring prior to extraction,
c) Losses due to charge exchange collisions,
d) Current limitations imposed by coherent longitudinal effects.

Among the more significant conclusions was the finding that injection and ejection elements must be carefully protected against significant beam loss. The workshop resulted in a more intensified look at problems of coherent longitudinal instabilities. The thresholds for such instabilities were used to define the maximum currents to be stored. The limitations are acceptable if the coupling impedance can be limited to ~ 25 ohms per mode. Even if this should be difficult, the growth times for the instabilities may be longer than the necessary storage time. The spokesman for the working group called for intensified efforts to determine charge exchange cross sections of ions suitable for the HIF application. One rather high cross section for cesium was reported from the University of Belfast by the delegates from Great Britain. There was also a call for intensified studies of the coherent longitudinal effects and the structure impedances that can drive longitudinal instabilities. The summary concluded that there are important and fascinating problems but "no insuperable obstacles" were found.

(4) Linacs: The linac working group considered both rf linacs and induction linacs.

RF linacs: The problem of merging beams by frequency multiplying, and the resultant emittance dilution, attracted the most attention. Numerical methods exist to treat these problems and need to be applied. Impedance effects and possible resulting instabilities need further study. The working group reported their concensus that transverse blowup is not to be expected and longitudinal blowup is unlikely but need to be calculated.

The induction linac presents a very different, and in some ways, a simpler case than the rf linac. However, because there is so little relevant experience, there are more questions remaining than for the rf case. Most of these questions deal with longitudinal stability; the use of feedback control, waveform tolerances, behavior of the bunch ends, etc. Transverse dynamics, at least in the absence of transverse-longitudinal coupling, appears to be in good theoretical shape.

The recommendations of the linac working group include development of numerical methods of treating the problems described above and careful diagnostics to ensure useful measurements when beams are available from the proposed test bed systems. The conclusions were that "no fatal flaws were found and the concensus is that there probably aren't any."

(5) Low-beta accelerators: There are now several candidate systems for the low-beta accelerator for injection into the rf linac. These include, a) conventional high voltage injection into a low frequency Wideroe linac. b) the rf quadrupole accelerators first developed in Russia and now being tested at LASL, and c) the arrays of small electrostatic quadrupoles, called MEQALAC by A. Maschke of BNL. The low-beta working group considered many of the same problems faced by the linac group, and emerged with essentially the same conclusions described above. They ran some comparisons of the three systems defined above to check the scaling laws reported. They concluded that adequate safety margins exist for all parameters, although the necessary intensity could require some beam scraping. Scraping at low energy is quite tolerable and, in the worst case, simply requires more branches to the linac trees at slight overall increased cost.

European and Japanese Programs

The foreign delegates were asked to describe their HIF programs during the summary session. S. Kawasaki of Kanasawa University gave a brief discussion of the synchrotron program in Japan and discussed energy balance accounting in fusion. Since a fusion power plant of the same size is expected to be somewhat more expensive than a similar fission plant, it was not surprising that the energy balance payoff period is similarly longer. D. Bohne of GSI described the German effort. It is presently split between GSI, Frankfurt and Garching and is only just beginning to be funded. N.M. King described the program in Great Britain. Some funds that are available are earmarked for university programs. This permits starting such work as the charge exchange cross section work described earlier, but makes it difficult to begin serious work in a laboratory such as Rutherford which could act as a focus of the university efforts. John Lawson discussed broader international collaborations, either among the European states or with independent alliances with the U.S. DOE programs. Since the classification problems do not directly affect the accelerator systems, the heavy ion drivers would be the ideal vehicle for such collaborations.

SUMMARY OF LOW-β LINAC WORKING GROUP

R. A. Jameson

Los Alamos Scientific Laboratory

and

P. Lapostolle

GANIL

Requirements

The linac is required to deliver a certain current within a prescribed 6-D phase space volume to the storage ring(s). Ion sources exist with brightness greater than can be handled by linacs. Adequate brightness for the storage rings can be preserved through the linacs if the current is shared by multiple linacs at the low-β end, with funneling to a single linac as beta increases.

Assumptions

Quite adequate safety margins can be insured, perhaps at the expense of a few extra low-β linac branches, (1) by requiring that the ratio of space charge to restoring force be ≤ 0.5 in transverse and longitudinal phase space, implying a tune shift $\sigma/\sigma_0 \geq 0.7$; (2) by keeping the beam loading on the rf system ≤50% (probably over-restrictive); and (3) by realizing that beam scraping can be tolerated to any degree in the low-β linac, since no radioactivity is induced.

Scaling Laws

Scaling laws for current limits work very well within the range of the assumptions. At the Workshop some scalings pertinent to phase-space density and emittance growth under various conditions were compared to simulation and experimental results. Further work in this area would be useful to clarify design issues and relative merits of various structures.

Problem Areas

There appear to be no fundamental problem areas in meeting the low-β linac requirements.

Emittance dilution must be controlled. The assumptions above essentially assure this, at the expense of a linac tree to split up the current at the low-β end. Two modes of operation were proposed by the various participants: one where the emittance always remains smaller than the machine acceptance even if growth occurs, and another where the acceptance is filled and some particles are lost. Further work is needed to clarify the trade-offs involved.

Combining the branches of the linac tree can be done in a variety of ways by stacking, funneling and interlacing the beams transversely and/or longitudinally. Schemes are possible which keep the emittance within the requirements. Nominal allowances for growth should be made for some tuning error during operation. Rf deflectors would be required for longitudinal interlacing; detailed design and simulation work is needed, particularly at the final highest-β combination sections.

A detailed simulation combining all elements of a linac tree has not been done - this is easily within the capability of existing codes and would quickly answer questions about emittance dilution for proposed designs.

Some further experimental work in determining voltage breakdown limits at various frequencies with actual beams would be most helpful in eventual performance optimization.

Wall effects, structure impedance interactions, beam loading and coherent effects do not appear to be problems within the range of the assumptions - at least for conventional structures. New types such as the RFQ require scrutiny. The induction linac is a rather independent line of approach and much more experimental evidence is needed to arrive at level of confidence similar to rf linacs.

Machine Studies

Test programs under way at ANL (Dynamitron + independently-phased-cavities + Wideröes), LBL (long drift-tubes), BNL (multiple-beam-electrostatic-focusing linac (MEQALAC)), and LASL (radio-frequency-quadrupole (RFQ) structure) seem adequate to provide beam to subsequent stages where the problems are harder, and provide options for eventual optimization.

Studies on the low-β accelerators will be very useful in pushing the performance to the ultimate levels and understanding effects in detail.

Computer Simulation

As stated above, detailed simulation of complete systems should resolve most remaining questions for conservative designs where the assumptions are applied. Existing codes have good accuracy and have been experimentally verified in terms of what happens to the main 95% or so of the beam.

Simulations can help develop guidelines or formulas for predicting emittance growth.

We used simulation tools at the Workshop to partially test a new code against the PARMILA standard, and to simulate the ANL Wideröe and the BNL MEQALAC to check scaling.

Design of the low-β sections will benefit from code development (e.g. 3-D space-charge) when it becomes necessary to optimize system efficiency and performance.

Finally, comparison of simulations with experiments on the linacs will push hardest the development of the experimental techniques.

Further Remarks

We expand the summary above, prepared immediately after the Workshop, with the following remarks.

Requirements and Assumptions

The assumptions above are very conservative. Even though the economic impact of the low-beta section is small in terms of total facility cost, there has been and will be interest in optimizing this section. This would involve operating with tune shifts ≤ 0.7, closer to (or even near) the space-charge limit. It must be strongly emphasized, however, that the HIF requirement is on six-dimensional brightness, and the requirement is reasonably stringent. Few of the designs presented so far have adequately considered the overall brightness requirement. Little is known about emittance behavior, except at the limits of zero or saturated current. Also, "current limits" mean different things to different authors, and the definition being used in a particular case is often not stated.

Saturated vs. Unsaturated Operation

Two asymptotic regions are commonly used in discussions of linac operation: a low-current region where things are essentially linear and a high-current region where the linac is saturated. We must carefully separate these two extrema from each other and also from the region where we usually operate a linac, which usually turns out to be in neither asymptotic region. The scaling laws for each of these regions are very different from each other, a point that needs to be emphasized.

Direct comparison between designs running in these two very different operating modes, and "scaling" inferences drawn from these comparisons are rather too common in the HIF literature to date.* We argue with this method of inferring general properties and deciding "best approaches," rather than with the results of the particular cases. In other words, such comparisons should not be called "scaling."

In the low-current region, single-particle dynamics essentially holds, the particle loss is low or zero, and the tune depression is small. Since the particle loss is negligible, it is meaningful to talk about a ratio of exit to entrance emittance (dilution factor). The brightness of the output beam is linear with input current if the input emittance is constant, or conversely, if the input brightness is constant, so is the output brightness if the machine always operates in the very-low-current mode. Few real linacs operate in this region (but the SuperHILAC may be one of them).

In the intermediate region, tune shift is significant and emittance blow-up is not negligible. Scaling equations which account for emittance behavior do not exist yet, but particular cases can be investigated quite well with computer simulation codes. It is essential that emittance as well as current be considered in system designs.

Scaling Laws

"Scaling laws" presented without proper explanation can be confusing, if not outright misleading.

Using linearized equations of motion and assuming ellipsoidal beam bunches with uniform charge distribution and no emittance growth, general equations result for the transverse and longitudinal beam envelope behavior

*Including these proceedings. Let the reader beware.

in periodic focusing systems with acceleration. These equations, written in terms of the forces acting on the particles, are the same for all rf linacs.

The equations may then be rewritten in forms specific to a particular type of linac. For example, the rf-quadrupole linac has continuous focusing and may be formulated in that manner, or may be represented by an equivalent hard-edged quad system. The number of $\beta\lambda$'s per focusing period has a particularly strong influence.

Certain criteria may then be placed on the linac performance, for example on the phase advance per period at zero current, σ_0, or on the phase advance with current, σ, or on both σ_0 and σ.

Further, physical constraints appropriate to a particular type of structure or focusing method (e.g. electrostatic or electromagnetic) may then be added. Cost constraints, for instance from rf power requirements, can also be folded in.

The resulting equations, and numbers from them, can be extremely confusing to someone else, unless the derivation is made very clear. That is why we want to emphasize that the basic equations are the same, but performance and physical constraints can change the effect of a parameter drastically. Further, direct comparisons of examples using two different sets of assumptions are likely to be misleading. A particularly good elucidation of this point is given by Reiser[1] for transport systems. For application to linacs, the longitudinal properties must be taken into account simultaneously, but the concepts are the same.

It was very apparent at the Workshop that a consistent comparison of various low-beta linac types has not been made. By systematically deriving relations for different sets of constraints, in the manner of Reiser, rather than imposing the constraints a priori and instantly jumping to conclusions and specific designs, we would at least clarify the issues and might even find more attractive systems.

We did check various specific designs currently under consideration, and found that the calculated current limits agreed well with computer code simulations in which the input current was raised until the output current saturated. We also found that the envelope equations, used with a tune shift $\sigma/\sigma_0 = 0.4$, give a value for the saturated transverse output emittance which agrees very well with computer simulations. The limit formulas must

be applied on the basis of experience gained from the simulations as to the point in the machine where the "bottleneck" occurs. For example, in the LASL RFQ, the current limit bottleneck occurs at the end of the gentle buncher, where the bunches are well-formed and the rapid acceleration begins. In machines where bunched beams are injected, the current is limited at the injection end.

Having gained this confidence in the agreement between computer codes and the formulae at the current limit, we could, and should, now proceed as suggested above to refine our estimates of performance bounds, including saturated emittance and current loss.

The scaling relationships also are quite accurate and useful at lower currents, except that they do not account for emittance growth. Some systematic numerical experiments have been done[2] which provide some insight into emittance growth, but there are no useful formulas yet. However, meaningful system comparisons could be made by assuming reasonable growth factors. In this regime we must also be aware of the ion source brightness and how it varies as the current is changed, either by changing the ion source parameters or by various types of scraping.

Funneling

Some of the important requirements on funneling schemes were reemphasized at the Workshop, in particular the desirability of filling every accelerating bucket in each stage. The geometries of the RFQ and Wideröe structures are particularly suited to accomplishing this,[3] while other multi-channel configurations may not be.

Computer simulation work is needed on the funneling regions to design suitable transport lines and deflectors and look at possible emittance growth. With proper design, it is expected that the funneling sections will not degrade the emittance significantly. Accelerator arrays having close-packed beam channels and intrinsic longitudinal phasing (thus avoiding flight-path differences in the funneling transport) are clearly preferable.

At the lowest energy end of the system, there may be some advantage in running in a current-saturated mode, with the consequent beam loss and geometry defined emittance. This might, for example, avoid another level in the tree while not compromising the emittance required downstream

by an excessive amount. At the funneling points in the tree, the degree to which the space charge limit is approached can easily be controlled by choosing the appropriate velocity for the transition point. Consideration of longitudinal matching will also be important in the funneling region.

Computer Simulation

We wish to reemphasize our belief that existing rf linac simulation codes are quite adequate to proceed with more detailed designs and system comparisons. Simulation of induction linacs is less advanced; the problem is complicated by the extreme aspect ratio of the beam bunch.

Experiment vs. Simulation

It was mentioned in the initial summary above that existing codes for rf linacs have been experimentally verified for the main part of the beam. It must be said that a spectrum of opinion could be found on this point. The above statement is considered reasonable if the modeling is done with extreme care, and if physics clearly not in the present simulations, like neutralization effects, is also clearly not a factor in the experiment. The main particle-tracing codes for rf linacs are six-dimensional and include non-linear effects; thus there is general confidence in the physical description for the bulk of the beam. A whole host of detailed considerations come into any discussion of the entire beam, including fringe particles. The main point is there is not a wide body of experimental verification, and research accelerators will be very helpful. Development of diagnostic techniques is necessary, and the work involved in an overall verification program is far from trivial. An area which will be particularly hard to measure experimentally, and to simulate properly, is the initial injection and beam bunching region, where neutralization and longitudinal-transverse coupling effects will complicate the situation.

Acknowledgment

We greatly appreciated the assistance of J. Staples, LBL, in expanding the Workshop results and preparing this summary.

References

1. M. Reiser, Particle Accel. 8, 167 (1978).
2. R. A. Jameson, contributed paper to this working group.
3. D. Swenson, contributed paper to this working group.

Low-β Linac Working Group Participants -

D. Boehne - GSI, R. Burke - ANL, W. Hermannsfeldt - SLAC, R. Jameson - LASL (Co-Chairman), S. Jorna - PD, T. Khoe - ANL, C. Kim - LBL, E. Knapp - LASL, P. Lapostolle - GANIL (Co-Chairman), R. Martin - ANL, A. Maschke - BNL, R. Mobley - BNL, S. Ohnuma - FNAL, J. Shiloh - LBL, J. Staples - LBL, R. Stokes - LASL, D. Swenson - LASL, T. Wangler - LASL, J. Watson - ANL.

ANL LOW BETA DEVELOPMENT (PHASE 0)

J. M. Watson
Argonne National Laboratory

Introduction

The HIF group at Argonne National Laboratory is currently developing the initial Accelerator Demonstration Facility (ADF) for the rf linac reference concepts. This has been dubbed Phase 0 since it is a preliminary step before our two proposed ADF's which could deposit 10 kJ (Phase I) and 500 kJ (Phase II) on target. Phase 0 is a $25 million project over a three-year period. Unfortunately, much of the funding expected for this project was withdrawn from the FY 1980 budget, thereby delaying its completion by a year.

The basic configuration of Phase 0 is shown in Fig. 1. The low-beta front end consists of a high voltage preaccelerator followed by an array of 12.5 MHz independently-phased linac resonators and Wideröe linacs to accelerate 25 mA of Xe^{+1} to 20 MeV. The beam is then stripped to charge state +8 and accelerated in a 25 MHz Wideröe to 220 MeV. It will be injected into a ring (using the Princeton-Penn accelerator magnets) housed in the ZGS tunnel. The extracted beam will be compressed, split into four beams and focussed onto target foils.

Phase 0 could demonstrate adequate beam quality and intensity through many stages common to a HIF driver:

Ion source
Low-beta acceleration
Charge stripping
Frequency jump with simulated funneling
Multi-turn injection into a storage ring
Storage ring vacuum and instabilities
Extraction
Compression
Beam splitting
Final focus
Energy deposition

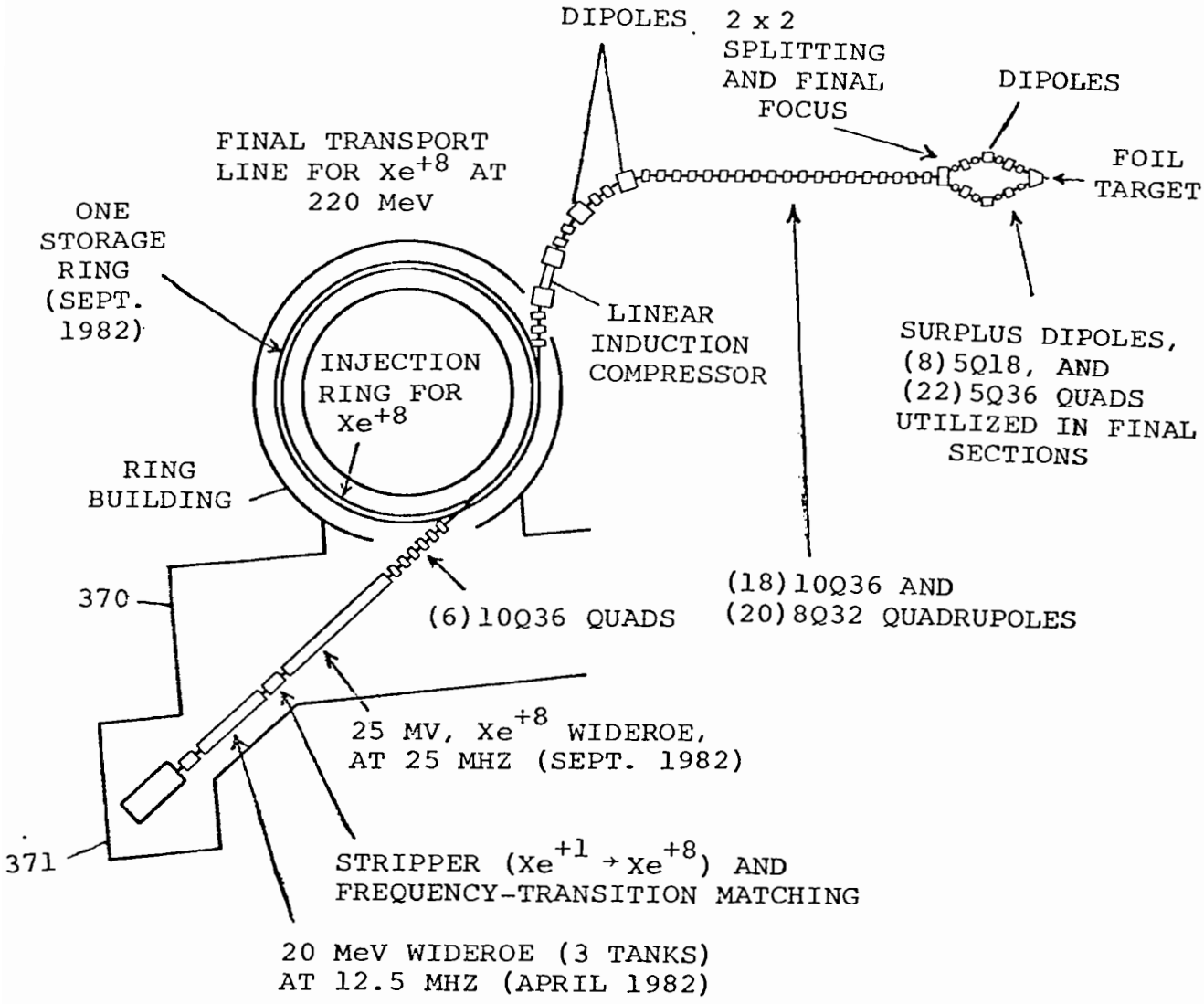

Fig. 1 ANL Phase 0

Because we are trying to demonstrate accelerator technology at many stages in a short time, it is important that we develop and extend upon the techniques which have a reasonable probability of early success. To do the storage ring and final focus studies we will need a front end which can perform reliably over long periods. This has been among our considerations in determining the configuration of the accelerator. Even so, the HIF requirements are a considerable extrapolation from any existing heavy ion accelerators. The development of an ADF will require more extensive computer simulations during

its design than has been typical for HEP accelerators. They will also require a new generation of diagnostics for the evaluation of the beam characteristics in six-dimensional phase space as it passes through each stage of the facility.

Preaccelerator

There are several advantages to operating the preaccelerator at the highest voltage possible. The current limit of the first linac tank is substantially increased and the very lowest frequencies and their associated frequency jumps are avoided. The high brightness of the source can be best maintained with minimal dilution during the difficult initial acceleration stage by using electrostatic acceleration with a Pierce geometry as far as practical.

We have chosen an operating voltage of 1.5 MV for our Phase 0 preaccelerator. We have high confidence that such a machine will be reliable for 50 mA operation. At this energy, a linac current limit of 25 mA can probably be achieved using conventional magnets. The preaccelerator and source have been described in detail elsewhere [1,2]; therefore, I will primarily discuss our recent experience and present status.

The current layout of our injector is shown in Fig. 2. The equipment shown is installed and operational with the exception of the independently-phased linac cavities C2 and C3. Their construction will be completed in a few months. The magnet BM1 is used for energy and charge analysis of the beam. A Faraday cup has been placed immediately behind the independently-phased cavity C1 in our initial operation. The PAPS 1 and PAPS 2 monitors provide non-destructive horizontal and vertical profiles of the beam, and the toroids T1 and T2 non-destructively measure the current. The accelerating column was high voltage conditioned to 1.4 MV and 50 mA Xe^{-1} beams were reliably extracted at 1.3 MV. A pulse length of 100 μsec and a repetition rate of 1/sec were typical during these tests. The protective grading rings on the inner surface of the accelerating column shell would not hold off the voltages involved above 1.4 MV. We also found that the ceramic at the high voltage end of the column was experiencing damage due to the overvoltages during conditioning sparkdowns. For the former problem, half of the rings were modified to increase the spacing. For the latter, a third intermediate electrode was added. This reduced the voltage across the last gap from 900 kV to 450 kV and spread this reduced transient from a sparkdown over twice as

many insulators; thereby reducing overvoltages by a factor of four. We have since conditioned to 1.1 MV with much less sparking and have experienced no additional damage. The present tests are being carried out at 1 MeV until a new outer shell has been fabricated. At that time, it will be conditioned as high as possible.

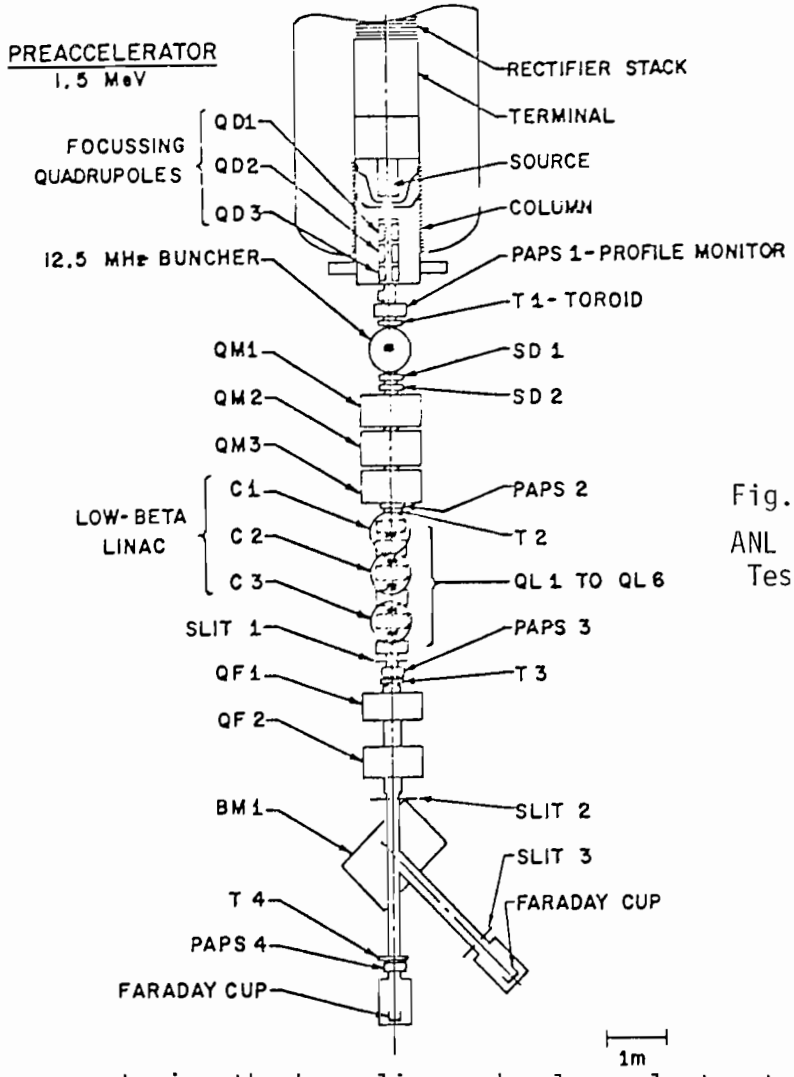

Fig. 2
ANL Injector Test Facility

At this time we are tuning the beam line and column electrostatics to minimize beam losses through the rf buncher and first accelerating cavity. Bunching factors greater than 4 have been measured at C1 at 1 MeV. In fact, this provides a fairly clean resolution of the various xenon isotopes (approximately 15 nsec/amu) when using gas which has the natural abundances. Once the beam is transported cleanly through this section, the transverse emittances will be measured. Beam scraping on the vacuum pipe has been seen to cause time-varying beam parameters (apparently due to partial neutralization developing) and forward directed electrons which are more intense than the lost ion beam. The expected normalized transverse emittances out of the preaccelerator at 1.5 MeV are 0.03 cm-mrad.

Low Beta Linac

The low beta linac consists of three independently-phased short resonators followed by 12.5 MHz Wideroe linacs. The independently-phased cavities are in essentially a $\pi/5\pi$ configuration. These are expected to transport 25 mA of Xe^{+1} to 2.3 MeV. The three Wideroe tanks which are $\pi/3\pi$, $\pi/3\pi$, and π/π will accelerate the beam to 22 MeV. A detailed description of this system is available elsewhere[4]. The three independently-phased cavities and first Wideröe tank are sketched in Fig. 3. The first independently-phased cavity (C1) is installed and operational. The next two will be completed in a few months. Construction of the first Wideröe tank has just begun; however, its completion will require more funding than is available in our FY 1980 budget.

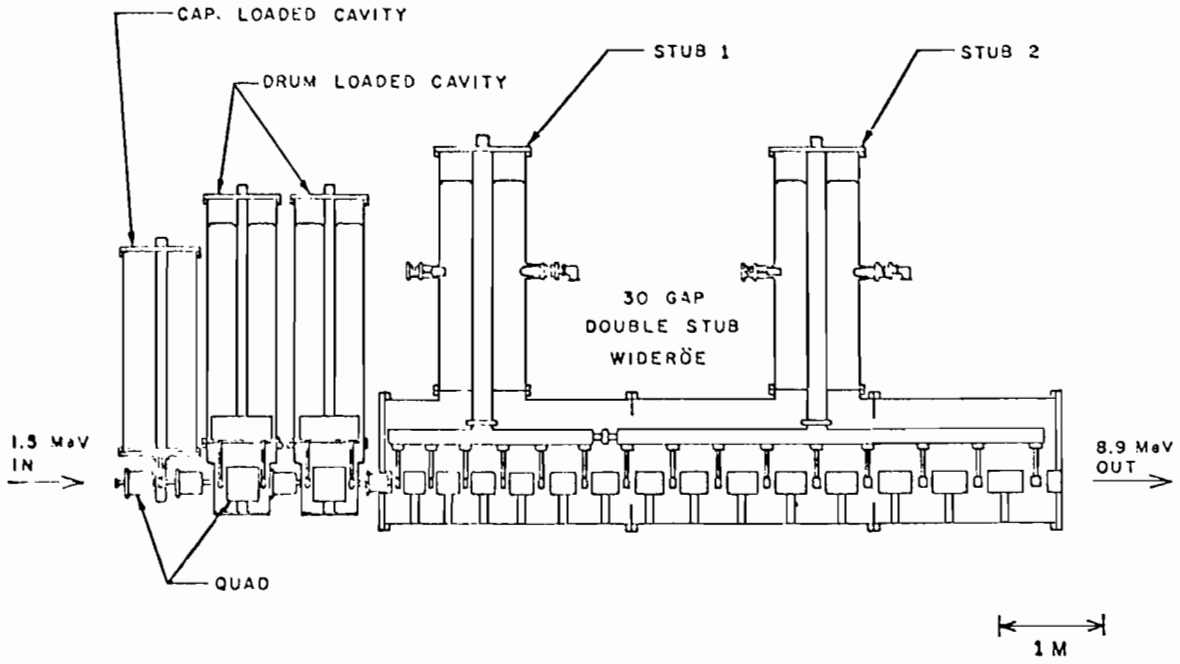

Fig. 3 30 Gap $\pi/3\pi$ Double Stub Wideröe (Tank No. 1) and Independently-Phased Cavity Linac: 1.5 MeV to 8.84 MeV

The use of independently-phased cavities provides a great deal of flexibility in attaining the injection requirements for the Wideröe linac. They can make up varying deficiencies in the preaccelerator performance and allow optimization of the accelerating gradient for minimal emittance growth. With the $\pi/5\pi$ configuration adequate focussing is available to transport the 25 mA beam.

A Wideröe linac is the only low-velocity structure with operational experience with heavy ions (albeit at low currents). After considering Wideröe's with electreostatic focussing and RFQ's, it is evident that the structure with the highest confidence of performing reliably at present is a Wideröe with magnetic focussing. Our experience has been that the reliability of electrostatic quadrupoles has been too variable. RFQ's are not yet operational; they represent a more uncertain alternative.

In Phase 0 the beam properties will be measured through the various sections of the linac. By comparison with realistic computer simulations, the optimal operating conditions for maximum current and minimum emittance growth (within reasonable economic constraints) can hopefully be defined. Preliminary results of simulations through the first Wideröe tank indicate a transverse emittance growth by a factor of three[5]. Further studies are now in progress to determine if this can be reduced by lower accelerating gradients or higher injection energies by using more independently-phased cavities[6] Also, to achieve 25 mA of Xe^{+1} through the first tank may require "overstuffing" with some beam loss. The above mentioned studies will also attempt to minimize these losses.

Conclusions

The rf linac ADF is getting underway with a high brightness beam of 50 mA of Xe^{+1} at 1.3 MeV already available. The short independently-phased linac cavities are nearing completion and construction of the first Wideröe tank has begun. Because of the stringent current and emittance requirements, realistic computer simulations are needed for initial designs of the ADF as well as for understanding the performance of each section. The experimental measurements will require a new generation of diagnostics which will accurately characterize the beam without altering it or being destroyed by it. The low beta section of the ADF is a challenge, but now appears solvable with the proper mix of simulation and experimental measurements.

References

1. J. M. Watson, et al., IEEE Trans. Nucl. Sci., Vol. NS-26, No 3, Part 1, p. 3098 (June 1979).

2. R. P. Vahrenkamp and R. L. Seliger, IEEE Trans. Nucl. Sci., Vol. NS-26, Part 1, p. 3101 (June 1979).

3. John M. Bogaty, IEEE Trans. Nucl. Sci., Vol. NS-26, No. 3, Part 1, p. 3349 (June 1979).

4. A. Moretti, et al., Proc. 1979 Linear Accelerator Conf., Montauk, N.Y. (in press).

5. S. Jorna, this workshop.

6. R. J. Burke and R. A. Sacks, this workshop.

APPLICATION OF THE RF QUADRUPOLE IN LINEAR ACCELERATORS FOR HEAVY ION FUSION*

T. P. Wangler and R. H. Stokes
Accelerator Technology Division
Los Alamos Scientific Laboratory
Los Alamos, NM 87545

ABSTRACT

The rf quadrupole (RFQ) linac structure is proposed as an alternative to a system composed of a buncher and independently phased cavities in the low-velocity acceleration section. Beam dynamics simulation studies have demonstrated that with the RFQ (1) high transmission and low beam loss are possible, (2) it is possible to use a low voltage 0.25 MV dc injector and still obtain high output beam currents, (3) the current required from the injector is reduced because of the high transmission of the RFQ, and (4) the output emittance appears to be at least comparable to that expected from a buncher and independently phased cavities.

INTRODUCTION

The low-velocity accelerator is an important element in heavy ion drivers for inertial confinement fusion. It is widely recognized that beam intensity limitations and radial emittance growth tend to occur predominantly at low velocities in linear accelerator systems. The characteristics of the RFQ make it an attractive alternative approach to other designs that have been proposed. One proposal[1,2,3] is to use a high voltage dc injector to accelerate a heavy-ion beam, for example Xe^{+1}, from the ion source to about 1.5 MeV. This is followed by an rf buncher and several independently phased cavities with magnetic quadrupoles between the cavities. At about 2.3 MeV, the Xenon beam is injected into a sequence of three Wideröe linacs and accelerated to an energy of about 20 MeV. This arrangement provides for acceleration of about 20 to 25 mA of Xe under current-saturated conditions. It is argued[3] that the high voltage of the dc injector is desired in order to obtain a high current limit and a higher starting frequency (12.5 MHz) as compared with other possible schemes which use a lower voltage injector. In this paper we suggest an alternative approach,

*Work performed under the auspices of the U. S. Department of Energy.

which would use the RFQ to accept the injector beam, bunch it and accelerate it to a few MeV. A major advantage of the RFQ is that a much lower voltage injector ($\leqslant$250 kV) can be used without lowering the space charge limit. In addition, the RFQ has the potential for adiabatic bunching, which can result in capture efficiencies in excess of 90% and minimal brightness reduction. Furthermore, as pointed out by Swenson,[4] the RFQ lends itself to array-like configurations that can be used to increase the total beam intensity. The bunches from the different beam channels in the array can easily be combined so as to interlace longitudinally, as is desirable when funneling prior to a frequency transition.

The RFQ can operate at lower beta than conventional drift tube linacs because the focusing is obtained from the rf electric fields so there is no requirement to include magnetic quadrupoles within the small cells. This opportunity to use a linear accelerator at low beta values permits adiabatic bunching of the dc beam, resulting in high capture and transmission efficiencies (>90%). Adiabatic bunching is not restricted to low energies in principle, but its application at higher energies can become very costly in length. Good transmission efficiency implies small beam loss. Reducing the amount of lost beam, and keeping the energy of lost particles low, may be important in order to minimize potential problems associated with localized heating of components by an intense beam.

RFQ Design

The LASL RFQ design approach has been reported previously.[5,6] In the most general case, it consists of combining four sections called the radial matching section, the shaper, the gentle buncher and the accelerator section. The adiabatic bunching is done in the shaper and gentle buncher sections. The synchronous phase angle is ramped from -90° to its final value at the end of the gentle buncher, so the beam reaches its minimum phase extent at this point. For this and other reasons the space charge limit typically does not occur for the dc beam at the input, but instead occurs at the end of the gentle buncher.[7] In the case where the focusing force is restricted by the maximum obtainable electric field, for a given aperture size the current limit is found to scale approximately as

$$I \propto \frac{q}{A} E_s^2 \beta\lambda^2 \qquad (1)$$

where q and A are the charge state and mass number of the ion, E_s is the maximum surface electric field, βc is the ion velocity at the end of the gentle buncher, and λ is the rf wavelength. One can also show that the length of the gentle buncher section, for a fixed energy gain ratio within the section, scales as

$$L \propto \frac{A}{q} \frac{\beta^3 \lambda}{E_s} \tag{2}$$

The length formulas for the shaper and accelerator sections are similar to Eq. (2). These formulas show that the current limit increases in proportion to β but the length increases in proportion to β^3. Thus the advantage of high energy, which raises the current limit, is soon offset by a rapidly increased structure length.

RFQ Linacs for Heavy Ions

We now present two examples of RFQ linac designs for singly charged Xenon. The first demonstrates acceleration under a current-saturated condition, which is always accompanied by high beam losses and an output emittance characterized by the geometric acceptance of the channel. The output emittance in this case is kept small by using a small bore. The second example illustrates acceleration under more lightly-loaded conditions where a smaller fraction of the input current is lost.

Both examples contain the three sections mentioned earlier, the shaper, the gentle buncher and an accelerator section. The gentle-buncher initial and final energies were chosen to be 0.25 MeV and 2.5 MeV respectively. These choices represent a compromise between good performance for high beam currents and overall length. Then the initial energy, where the shaper section begins, was chosen to be 0.242 MeV in accordance with our standard design approach.[6] A final energy of 5 MeV is arbitrary and could be increased without adding greatly to the length. A maximum surface field was assumed to be E_s = 15 MV/m, which we regard as a conservative operating point.

The computer program that we use to study the RFQ beam dynamics is called PARMTEQ[6] (a modified version of PARMILA). For the input we used a zero energy spread dc beam, whose initial transverse phase space distribution was generated by uniformly filling the volume of a 4-dimensional hyper-ellipsoid. The normalized input emittances in both x,x' and y,y' phase space, which contain 100% of

the beam, were taken to be 0.01π cm-mr. This results in 90% of the input beam within 0.007π cm-mr, and an rms input emittance of 0.0017π cm-mr.

Table I is a summary of the parameters for the two cases. The frequency is 12.5 MHz and the synchronous phase begins at -90° and ends at -32° in both cases. The initial and final vane modulation parameters m_i and m_f are listed.[5,6] V is the intervane voltage and r_o is the average radius parameter, which is equal to the initial radial aperture. The length L for both cases includes a radial matching section at the input. An important difference between linacs 1 and 2 is the aperture difference as is indicated by r_o. Notice also that although linac 2 has a larger voltage than linac 1, it is longer because of its smaller vane modulation parameter m.

Table II shows the results for linac 1 at four input beam currents. The entries include average input current, I_i, average output current I_o, and transmission efficiency T. The normalized output transverse emittance at the 90% contour is ε_{90}, and the rms normalized output emittance is ε_{rms}. Linac 1 is operated essentially at its saturated current limit of slightly more than 20 mA for input current values larger than 30 mA. The aperture limits the final normalized emittance to a relatively small value. The transmission at I_i = 30 mA of 74.7% is still higher than most conventional single gap buncher configurations.

Table III shows some results obtained for linac 2 for four input beam currents. The aperture of linac 2 is larger than linac 1 and consequently its acceptance is greater. In contrast to linac 1 there is almost no restriction caused by the aperture at I_i = 30 mA. This results in a high transmission (96.9%) and a larger output emittance (ε_{90} = 0.031π cm-mr) than for linac 1. As the input current increases we observe the expected decrease in transmission. For input currents of 40 and 50 mA, the output current approaches its saturated limit at a value greater than 30 mA.

We see from the linac 1 results that, as might be expected, it is possible to obtain a high current beam with a small output emittance at the cost of reduced transmission. However, linac 2 probably best illustrates the advantages of the RFQ. For input currents less than 30 mA it captures and transmits nearly all of the injected beam and thereby minimizes any problems associated with beam losses. The output transverse emittance ε_{90} at 5 MeV obtained from the simulation code for $I_i \leq 30$ mA is consistent with the estimate assumed in design studies using the beam from the alternative buncher-independently phased cavity

system.[8] For linac 2 at I_i = 30 mA we calculate a two-dimensional output brightness of B = 6.1 A/cm^2-mr^2, where we have defined the brightness as $B = 2I/\pi^2\varepsilon_{90}{}^2$. In addition, we have calculated the longitudinal output emittance at the 90% contour and we obtain a value of 0.85π MeV-deg.

ACKNOWLEDGMENTS

We thank R. A. Jameson and D. A. Swenson for encouragement and assistance in carrying out this work.

TABLE I

RFQ PARAMETERS

Linac	1	2
q	1	1
Ion	^{132}Xe	^{132}Xe
f(MHz)	12.5	12.5
W_i(MeV)	0.242	0.242
W_f(MeV)	5.0	5.0
ϕ_i(deg)	-90	-90
ϕ_f(deg)	-32	-32
m_i	1.00	1.00
m_f	2.00	1.48
V(MV)	0.134	0.200
r_o(cm)	1.22	1.81
L(m)	23.3	27.1

TABLE II

LINAC 1 RESULTS

I_i(mA)	I_o(mA)	T(%)	ε_{90}(cm-mr)/π	ε_{rms}(cm-mr)/π
20	18.8	93.9	0.015	0.0032
30	22.4	74.7	0.018	0.0038
40	22.4	56.1	0.021	0.0045
50	21.1	42.2	0.021	0.0045

TABLE III

LINAC 2 RESULTS

I_i(mA)	I_o(mA)	T(%)	ε_{90}(cm-mr)/π	ε_{rms}(cm-mr)/π
20	19.9	99.7	0.027	0.0056
30	29.1	96.9	0.031	0.0068
40	33.8	84.4	0.037	0.0077
50	33.9	67.8	0.041	0.0085

REFERENCES

1. R. L. Martin, "Overview of the Argonne National Laboratory Program," Proceedings of the Heavy Ion Fusion Workshop, ANL-79-41(1978), p.1.

2. J. M. Watson, "ANL Experimental Program," Proceedings of the Heavy Ion Fusion Workshop, ANL-79-41(1978), p.17.

3. J. M. Watson, et al., "A High Intensity 1.5 Megavolt Heavy Ion Preaccelerator for Ion Beam Fusion," IEEE Trans. Nucl. Sci., Vol. NS-26, No. 3, p. 3098 (June 1979).

4. D. A. Swenson, "RF Linac Approach to Heavy Ion Fusion," this workshop.

5. R. H. Stokes, K. R. Crandall, J. E. Stovall, and D. A. Swenson, IEEE Trans. Nucl. Sci., Vol. NS-26, No.3, p. 3469 (1979).

6. K. R. Crandall, R. H. Stokes, and T. P. Wangler, "RF Quadrupole Beam Dynamics Design Studies," submitted to 1979 Linear Accelerator Conference, Montauk, NY, (Sept. 9-14, 1979).

7. T. P. Wangler, "Space Charge Limits for the RF Quadrupole," to be published.

8. A. Moretti et al., "The Design of a 12.5 MHz Wideroe Linac for Ion Beam Fusion," A. Moretti et al., submitted to 1979 Linear Accelerator Conference, Montauk, NY, (Sept. 9-14, 1979).

BEAM BRIGHTNESS IN LOW BETA LINACS: A SENSITIVITY STUDY

R. J. Burke
Argonne National Laboratory

and

R. A. Sacks
Science Applications, Inc.

Introduction

Heavy ion drivers for inertial confinement fusion reactors depend on the ability to produce a high intensity, high quality beam with a minimum of in-machine loss. Deterioration of the beam quality, which subsequently leads also to beam loss, tends to occur in the early (low energy) stages of the acceleration process, since all nonlinear effects decrease with velocity. Accordingly, considerable effort has been invested[1-3] in studying the various mechanisms of emittance growth in low energy accelerators.

The current work does not directly address the specific causes for beam deterioration on a fundamental level. Rather, we present the results of a numerical study aimed at gaining an engineering characterization of the dependence of the accelerated beam quality and intensity on various parameters in the linac design, the initial beam configuration, and the initial current. A dramatic improvement is observed when injection energy is raised, and some tentative suggestions are offered for techniques of achieving this increase.

Wideroe Linacs

Table (1) lists the structures we have investigated and describes their pertinent features. All are single tank Wideroe accelerators, operating in the π-3π mode and configured to accelerate Xe^+ ions. They were designed using the WIDEROE linac code developed at Lawrence Berkeley Laboratory[4] in collaboration with GSI.[5] The gap voltages and transit time factors are, therefore, electrically consistent with the rf frequency and the drift tube table. The only exception to this statement involves the gap asymmetry introduced by the π-3π structure. This effect decreases the transit time factor in the gap upstream from a short drift tube and enhances it in the downstream gap. In an effort both to assess the importance of this effect

and to improve comparability with other reports[6] we have deleted the asymmetry from structures 3 and 4.

Focussing was achieved with a FOFODODO scheme. Quadrupole lenses were a constant length for each linac, with the length chosen so that it would fit easily within the shortest of the long drift tubes. A physical aperture with a 5 cm diameter was included throughout.

Particle Dynamics Code

Beam behavior and emittance growth were treated using the PARMILA code[7] with slight local modifications. PARMILA is a 6-D simulation code which traces macroparticle orbits. Quadrupoles are treated as thick lenses, gaps as impulse acceleration, and defocussing thin lenses including longitudinal/transverse coupling and lowest order transverse nonlinearities. The effects of momentum spread are treated naturally. Space charge effects are calculated from a direct sum of Coulomb interactions with a linear cutoff to avoid close approach singularities. These sums are computed at the midpoint of each drift tube, the midpoint of each gap, and the beginning and end points of each quadrupole. They are applied as an impulse to the particle momenta. A cylindrical aperture is included, and particles whose radii exceed the aperture are discarded.

The emittance to be reported below are computed from the normalized rms formulae

$$\varepsilon_x = 4\,\bar{\beta}\,[\overline{(x-\bar{x})^2}\,\overline{(x'-\bar{x}')^2} - \overline{(x-\bar{x})\,(x'-\bar{x}')}^2\,]^{1/2}$$
$$\varepsilon_y = 4\,\bar{\beta}\,[\overline{(y-\bar{y})^2}\,\overline{(y'-\bar{y}')^2} - \overline{(y-\bar{y})\,(y'-\bar{y}')}^2\,]^{1/2} \qquad (1)$$

In Eq. (1), a bar refers to an average over the particles that are successfully accelerated. β_i is the velocity of the i'th particle divided by the speed of light, while x_i and y_i are its transverse coordinates. The transverse momenta are measured by $x_i' = \partial x_i/\partial z = (p_x)_i/(p_z)_i$ and y_i'. The factor of 4 is appropriate for a Kapchinskij-Vladimirskij (K.V.) particle distribution[8] in which the particle coordinates uniformly cover the surface of a four dimensional hyperellipsoid in transverse phase space. For the runs using a waterbag distribution - uniformly filling the interior of that ellipsoid - the computed results have been multiplied by 3/2 to permit direct comparison of the results with those using the K.V. distribution.

Linac Tuning

The importance of properly matching the input beam and the linac is well established.[3] Unfortunately, while this concept is well defined for transport lines, the situation in accelerators, especially at low energy, is considerably less clear. The presence of acceleration, which generates momentum spread and phase dependent defocussing forces in the gaps, and results in inevitable emittance growth, invalidates the simple ideas of envelope periodicity or constant particle phase advances, except as qualitative guides. The topic of optimal input beam parameters and quadrupole settings in the context of an accelerator requires substantial effort on a fundamental level.[9]

Rather than become enmeshed at this time in an extensive investigation, we have adopted an iterative, heuristic procedure, which we call tuning. The basic concept is that at approximately the center of the short drift tube separating a horizontally focussing region from a defocussing one, the beam profile (in the x-y plane) should be circular. Furthermore, the rate of divergence in one direction should match the rate of convergence in the other. For a periodic transport line, the matched beam with $\varepsilon_x = \varepsilon_y$ satisfies these criteria exactly.

Our tuning procedure, then, consists of adjusting the quadrupole strengths in equal polarity pairs so that

$$\begin{aligned} \overline{(x - \bar{x})^2} &= \overline{(y - \bar{y})^2} \\ \overline{(x' - \bar{x}')^2} &\approx \overline{(y' - \bar{y}')^2} \end{aligned} \tag{2}$$

at the center of the short drift tube following that pair. The initial beam parameters are chosen, within the constraint of yielding the given initial emittance, to minimize both the early emittance growth and the disparity in strength between the two lenses in the first few pairs.

This procedure, of course, is <u>not</u> exact in the presence of acceleration. The results obtained by following it, however: (1) clearly form a lower bound for the obtainable optimum, (2) are sufficiently good in terms of final beam brightness to indicate that they are close to that optimum, and (3) are sufficiently consistent to allow exploration of trends and sensitivity analysis.

Results

The purpose of our investigation was to elucidate the variation in the obtainable beam quality and intensity as a function of injection energy, rf frequency, bunch length, energy spread, and initial transverse emittance. The results are displayed in Table II.

The overall trends are quite clear. The most striking is the marked improvement afforded by injecting at 5 MeV rather than 2.3. There are, of course, significant difficulties connected with achieving this injection. Increasing the beam brightness by more than a factor of 2, however, can justify some trouble. The approach that seems most promising is to extend the output energy of the combination of high voltage pre-accelerator and independently-phased rf cavities beyond the 2.3 MeV that is the present goal of the Argonne HIF Accelerator Demonstration Program. The Dynamitron is a convenient power supply for voltages of 5 MV, and oscillators with adequate power to drive the beams under consideration pose no difficulty. The accelerating column for total voltages above 1.5 MV probably should be divided into separate sections to block the path of back-streaming secondary particles. By inserting focussing lenses between the sections, it should be possible to control the growth of emittance that otherwise occurs beyond the voltage where the Pierce condition must be abandoned. Making up the difference between the pre-accelerator output energy and the desired Wideroe input energy with independently-phased cavities also seems to make electrostatic quadrupoles more practical. This is because the smaller units are easier to design around the requirements of reliable voltage holding that is the larger Wideroe structure. Further modeling of both the electrical and the transport properties of such systems is under way.

The previously reported improvement associated with increasing the rf frequency[10] is verified. Two notes of caution, however, are pertinent to this result. First, to obtain focussing in the 25 MHz schemes requires advanced technology quadrupole lenses. All 12.5 MHz linacs are tuned with a maximum magnetic field gradient of 5.5 kG/cm (13.75 kG pole tip field), corresponding to more or less standard iron core magnet technology. For the 25 MHz results, maximum gradients between 9 and 13 kG/cm are required - necessitating super-conducting quadrupoles. The second point pertains to the credibility of run Number 19, where the high frequency coupled with the low particle energy lead to short drift tube lengths of 1.5 cm at the linac entrance. With the drift tube length less than its aperture radius, many of the physical approximations made in PARMILA break down. Examples of these suspect approximations are:

(1) Assuming the electric fields vanish in the drift tube interior,

(2) Representing the transverse electric field in the gap by the first two terms in the power series of a single Bessel function,

(3) Modeling the acceleration by an impulse at the gap center.

The importance of this breakdown to the overall emittance growth has not been investigated.

Dependence on the other parameters investigated is much less dramatic. The theoretically predicted maximum bunch length for magnetic stability[11] of ± 18° appears to be somewhat conservative and better final beam brightness can be obtained by filling a ± 25° bucket to the same average charge density. The decrease in final intensity associated with filling a still longer bucket to the same charge density (Run 6) is probably associated with a failure in the tuning procedure as the losses become large. The small extend to which decreasing the input emittance improved the final brightness in Run 7 over that in Run 2 is consistent with Chasman's results[1] that there is a lower bound to the output emittance from a given linac. The more sizable improvement of Run 16 over Run 15 indicates that at the higher frequency and energy that limit has not yet been reached. Finally, the penalty associated with increasing the initial energy spread is of about the size that might be expected.

Conclusion

The numerical simulation code PARMILA has been used to describe and quantify the parametric variation of low energy Wideroe accelerators. All studies were performed on achievable engineering linac designs. The beam tuning procedure, applied consistently throughout, is a faithful operational analogue of actual hardware tuning. The striking increase in beam brightness achieved by increasing the injection energy motivates further efforts at developing advanced pre-injector techniques. One apparently achievable approach to such a pre-injector is a combination of high voltage, multi-section dc acceleration followed by independently-phased rf cavities. Another which has received considerable attention recently, is the RFQ[12] concept. Further modeling work on both of these suggestions is necessary to explore and compare their characteristics.

Table I. Description of Linacs Studied[a]

Linac No.	Energy Range (MeV)	Frequency (MHz)	Energy Gradient (MeV/m)	Number of Gaps	TTF Description	Quad Length (cm)
1	2.3→8.8	12.5	1.0	30	Realistic	17.0
2	5.0→10.3	12.5	1.0	20	Realistic	24.0
3	5.0→11.4	12.5	1.0	24	Smooth	17.0
4	5.0→9.0	25.0	0.8	40	Smooth	13.0
5	5.0→10.3	25.0	1.0	40	Realistic	13.0
6	2.5→4.83	25.0	0.65	40	Realistic	8.5

[a]The energy gradient, the average rate of increase in particle energy has been held approximately constant. The TTF description refers to whether the transit time factor realistically accounts for cell assymetry or artificially smooths the effect.

Table II. Description of Initial and Final Beam Attributes[a]

Run No.	Linac No.	$\Delta\phi$ (deg)	ΔE (MeV/nuc)	ε_T (cm-mrad)	Distribution	I_o (mA)	Maximum Quad Gradient (kG/cm)	I_f (mA)	ε_x (cm-mrad)	ε_y (cm-mrad)	Brightness (A/cm^2-$mrad^2$)
1	1	18	$5.0*10^{-4}$	.032	W.B.	25	5.5	17.7	.126	.177	.161
2	1	18	$5.0*10^{-4}$	.032	K.V.	25	5.5	18.9	.107	.113	.317
3	1	25	$3.6*10^{-4}$	.032	K.V.	25	5.5	18.9	.128	.112	.267
4	1	32	$2.81*10^{-4}$	.032	K.V.	25	5.5	16.9	.104	.112	.293
5	1	25	$3.6*10^{-4}$	.032	K.V.	34.7	5.5	22.8	.121	.110	.349
6	1	32	$2.81*10^{-4}$	.032	K.V.	44.4	5.5	17.8	.094	.112	.346
7	1	18	$5.0*10^{-4}$	.016	K.V.	25	5.5	20.0	.092	.107	.413
8	1	18	$1.5*10^{-3}$	.032	K.V.	25	5.5	13.4	.109	.099	.254
9	2	18	$5.0*10^{-4}$	.032	K.V.	25	4.1	24.0	.087	.084	.666
10	2	18	$5.0*10^{-4}$	.024	K.V.	25	4.0	24.4	.081	.081	.752
11	2	25	$3.6*10^{-4}$	.032	K.V.	25	4.2	24.3	.086	.082	.700
12	2	32	$2.81*10^{-4}$	.032	K.V.	25	4.2	23.5	.093	.085	.604
13	3	18	$2.46*10^{-4}$	.031	W.B.	25	5.5	23.7	.131	.139	.266
14	3	18	$2.46*10^{-4}$	.031	W.B.	40	5.5	31.2	.148	.140	.390
15	4	18	$2.46*10^{-4}$	.031	W.B.	25	9.4	25.0	.053	.056	1.682
16	4	18	$2.46*10^{-4}$	.016	W.B.	25	12.0	25.0	.033	.041	3.718
17	5	18	$2.46*10^{-4}$	.032	W.B.	25	10.3	25.0	.058	.063	1.388
18	5	18	$2.46*10^{-4}$	.032	W.B.	65	13.0	64.7	.080	.102	1.604
19	6	18	$3.48*10^{-4}$	.031	W.B.	25	13.0	25.0	.065	.067	1.163

[a] $\Delta\phi$ is the bunch half length in degrees (always centered on a synchronous phase of 32^o). ΔE is the energy spread in MeV/nucleon. ε_T is the initial normalized transverse emittance in cm-mrad. Under distribution, W.B. refers to an initial water-bag particle distribution, while K.V. signifies a Kapchinskij-Vladimirskij distribution. The initial and final currents are in mA. ε_x and ε_y are the normalized final transverse emittances calculated from Eq. (1). For those runs with water-bag distribution, ε_T refers to the actual size of the phase space region occupied by the beam, while the factor of 4 in Eq. (1) has been replaced by 6. The brightness is $2I/\pi^2\varepsilon_x\varepsilon_y$, given on A/cm^2 $mrad^2$.

References

1. R. Chasman, Proc. 1968 Proton Linac Conf., BNL, p. 372; Proc. 1969 Particle Accelerator Conf. (PAC), IEEE Trans. NS, June 1969, p. 202.
2. P. Lapostolle, Proc. 1971 PAC, IEEE Trans. NS, N518, No. 3, p. 1101.
3. R. A. Jameson and R. S. Mills, Proc. 1979 Linear Accelerator Conf., Montauk, N.Y. (in press).
4. J. Staples, private communication of LBL's WIDEROE program.
5. K. Kaspar, "Studies for Dimensioning a Heavy Ion Linear Accelerator of the Wideroe Type", GSI Report 73-10 and UCRL-Trans-1522 (1973).
6. S. Jorna, Proc. 1979 Heavy Ion Fusion Workshop, LBL-10301 (in press).
7. D. A. Swenson, J. E. Stovall, and J. W. Staples, private communication.
8. I.M. Kapchinskij and V. V. Vladimirskij, Proc. International Conf. on High Energy Accelerators, CERN, P. 274 (1959).
9. T. K. Khoe, private communication.
10. W. P. Lysenko, Proc. 1979 PAC, IEEE Trans. NS, June 1979, p. 3508; J. W. Staples and R. A. Jameson, Proc. 1979 PAC, p. 3698.
11. S. Jorna, private communication.
12. M. Kapchinskij and V. A. Teplyakov, "Linear Ion Accelerator with Spatially Homogeneous Strong Focussing", Nuclear Experimental Techniques, 1970 Consultants Bureau, Plenum Publishing Corp., report UDC 621.384.64 (1970).

DESCRIPTION OF THE M1 MEQALAC AND OPERATING RESULTS*

R. Adams, J. Boruch, A. Bertsche, J. Brodowski, G. Gammel, R. Glasmann, J. Keane, A. Maschke, E. Meier, R. Mobley, K. Riker, and R. Sanders

Brookhaven National Laboratory

I. Introduction

MEQALAC stands for Multiple Electrostatic Quadrupole Array Linear Accelerator. The first model, M1, was designed, built, and tested in a three month period from July to October, 1979. Within a week of operation a Xenon output current of 85% of the calculated space-charge limit was obtained.

In the following sections we will describe the M1 components and operation. Some of the design choices were made to allow hand-fabrication with available tools (principally a table-top lathe and a table-top drill press), while others were influenced by the ion source development at hand. The major goal was to demonstrate the MEQALAC principle of accelerating multiple beams through arrays of strong focussing electrostatic quadrupoles. Xenon was used since it demonstrates the principles of a low beta linac as needed for the Heavy Ion Fusion program, without the complications of a heavy-metal ion source.

II. Evolution of the MEQALAC Idea

Our original plan for a heavy ion linac was a single bore Widerӧe design operating at 2 MHz with a 500 kV Cockroft-Walton injector. (Figure 1.) It was realized early in the BNL program that magnetic focussing would be expensive due to the high momentum of heavy ions. Thus our initial design featured electrostatic quadrupoles.

Theoretical analysis of the space-charge limits ("Space-Charge Limits for Linear Accelerators"[1]) revealed no dependence of the current limit due to bore size. Moreover it was realized that electrostatic quadrupoles are amenable to small bore construction in matrix arrays, and that virtually no power is consumed for focussing. The injection energy is low enough to dispense with a Cockcroft-Walton entirely. These and other benefits of the MEQALAC concept are discussed in "MEQALAC; A New Approach to Low Beta Acceleration".[2]

*Research carried out under the auspices of the United States Department of Energy under Contract No. EY-76-C-02-0016.

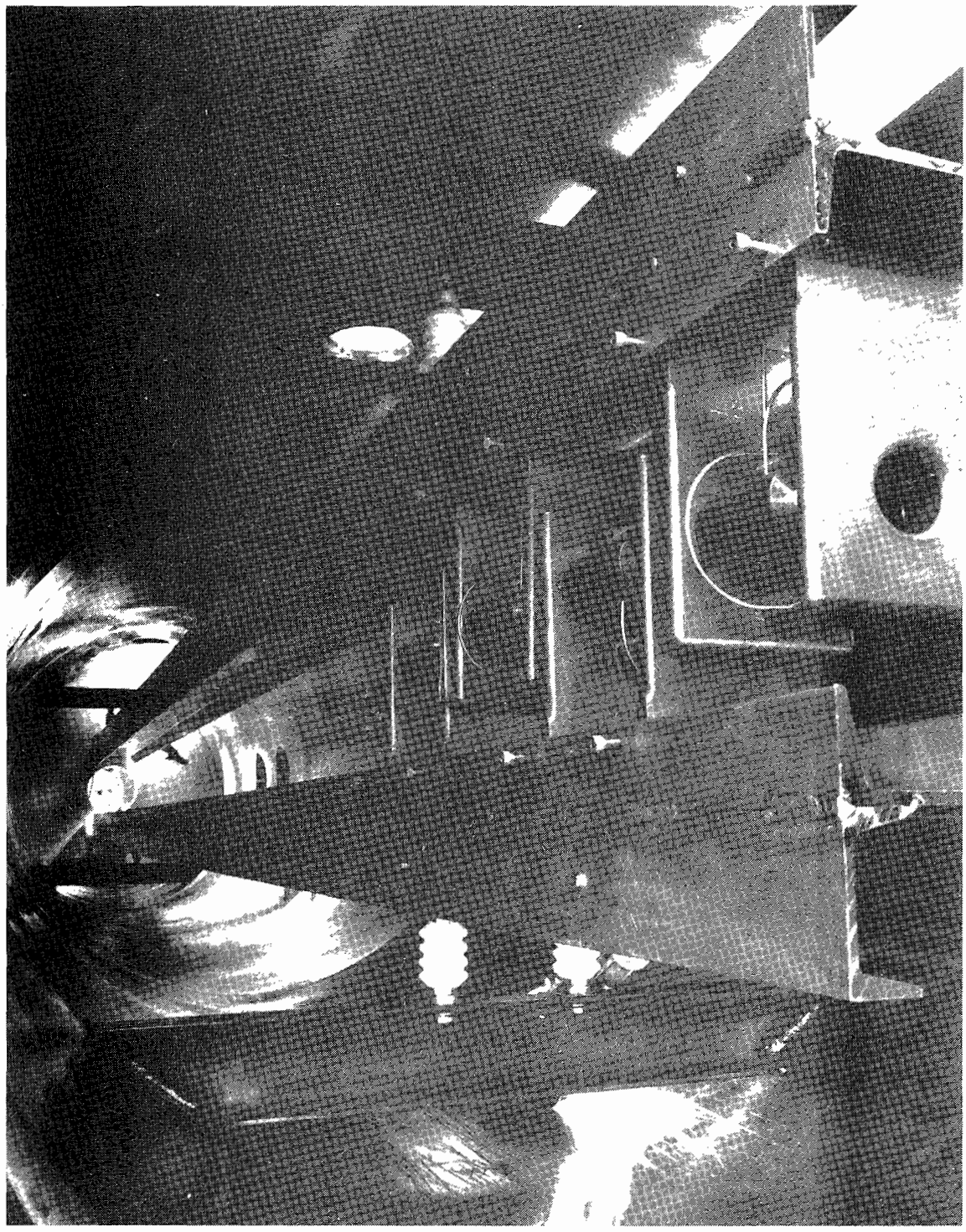

Figure 1. 2 MHz push-pull Wideroe showing four drift tubes with electrostatic quadrupoles.

III. M1 Components

a. M1 MEQALAC Assembly

Figure 2 shows the M1. Table I lists the major machine parameters. The discussion in this subsection is intended to give an overview of the machine before describing the components in detail.

TABLE I. M1 MEQALAC PARAMETERS

Ion Accelerated	Xe^{+1}
No. of Beams	9
Machine Type	Wideröe
Injection Energy	15.5-17.3 keV
Output Energy	71.5-73.3 keV
Input $\beta\lambda/2$	1.89 cm
Output $\beta\lambda/2$	3.95 cm
Rf Frequency	4 MHz
Peak Rf Voltage	5 kV
Accelerating Voltage	3.5 kV/gap
Stable Phase Angle	$\sim \sin^{-1}$ 3.5/5.0 45°
Nominal Quad Voltages	$\pm$ 2 kV
Repetition Rate	10 pps (arc supply ltd)
Pulse Length	500 usec (arc supply ltd)
Pre-Buncher	$\beta\lambda/2$, 4 MHz, 1-1.5 kV
Nominal Vacuum	10^{-5} torr
Gas Feed	Continuous
Calculated Avg. Current During Pulse - S.C.L.	3.3 mA
Measured Current	2.8 mA

The Wideröe assembly is suspended in the six inch Varian vacuum pipes shown. The ion source, operating at +15.5-17.3 kV dc, is shielded by the screen enclosure and isolated from the metal pipe by a 6 inch diameter x 6 inch long Pyrex vacuum pipe. The vacuum pump is a Welsh Turbo-Torr 1500 l/sec unit and it is mounted below the "cross" vacuum section. The upper port of the "cross"

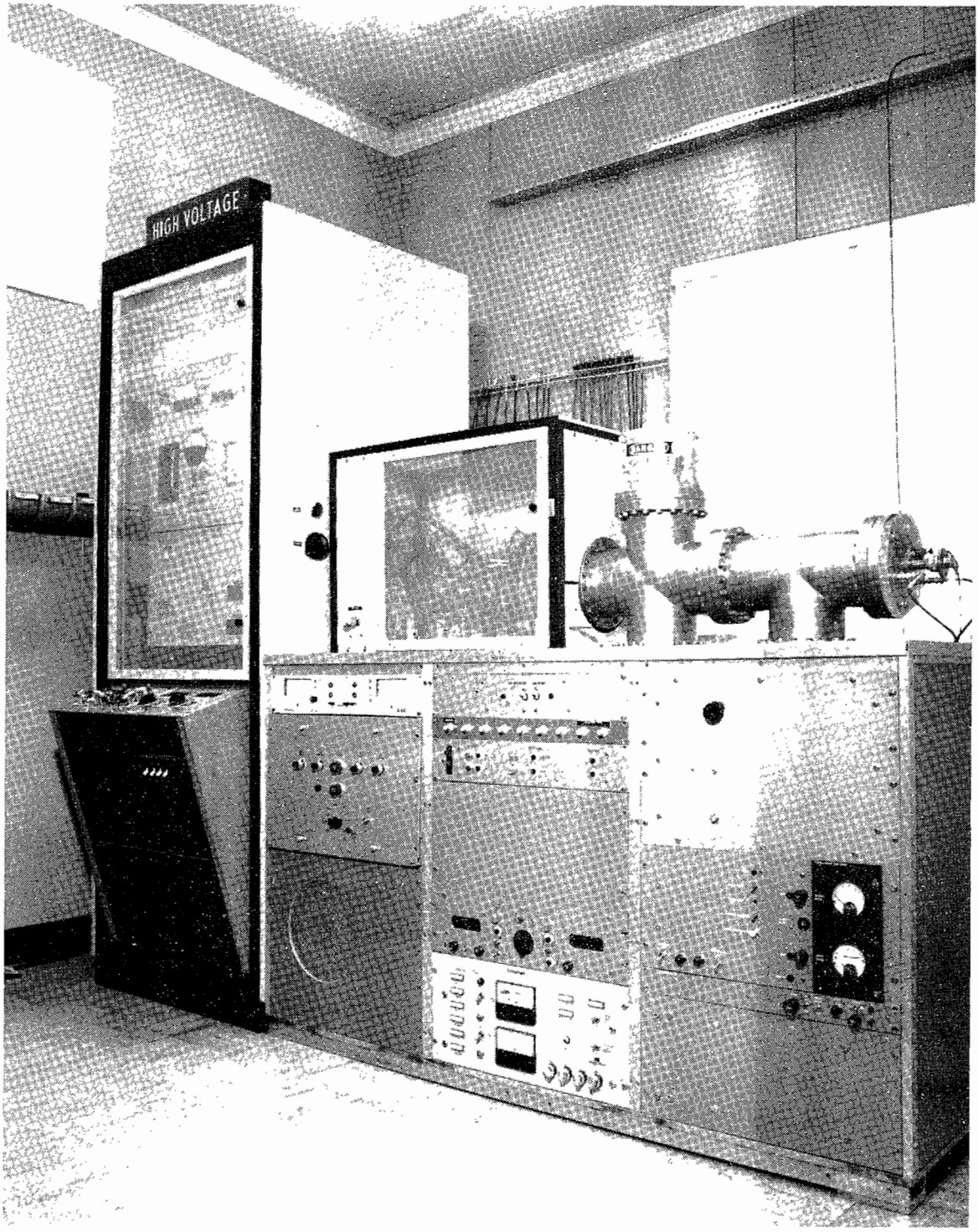

Figure 2. Assembled M1 MEQALAC.

is used for quadrupole high voltage feedthrus. The forepump sits behind the lower left panel with the circular ventilation screen.

The rf voltage is fed through the bottom of the "tee" section. The 4 MHz transmitter and tank circuit resonator are mounted in the far right rack. A Faraday cup is held on a rod inserted through a vacuum fitting on a Lucite end cover, and bias grid voltage and beam pickup connections are fed through the same cover.

The tall rack enclosure to the left is exclusive to the ion source power supplies, controls, and cooling system. The upper section contains the HV deck, which holds the arc and filament supplies for the source. The lower portion holds the HV supply, an isolation transformer for deck ac power, and a freon circulation pump and radiator. The tilted panel has the high voltage control knob and a small oscilloscope used to monitor arc current.

The accelerator has a pre-buncher "tube" or plate. The buncher tank circuit resonator is mounted beneath the ion source screen enclosure. The buncher rf is fed to the buncher tube through a Covar seal in the Pyrex pipe which isolates the ion source.

b. The Quadrupole - Drift Tube Configuration

Figure 3 shows the quadrupole array. The poles are made of 5/16 inch diameter aluminum, and arranged for nine beams with 5/16 bore diameter. It was estimated that a 1% ($\sim$.003 inch) tolerance was needed on the position of any pole tip. To accomplish this, the arrays were made on precision fixtures (see Figure 4). 1/8 inch precision-ground steel rods are pinned to the frame and pole tips in the fixtures, thus avoiding thermal expansion problems had they been soldered. The insulators at the corners were made of Rexolite.

Figure 4 shows the cover plates used to make a complete drift tube. The M1 has 8 drift tubes operating at rf potential, 7 drift tubes at ground potential, and 5 LEBT (Low Energy Beam Transport) quadrupole arrays, making 20 quad arrays in all. The LEBT and ground drift tubes are screwed to the steel alignment plate shown in the figure. This plate is hung from the top of the vacuum pipe. The rf drift tubes are suspended from 1/4" Rexolite rods which run through the side plates attached to the quad arrays as seen in Figure 3.

Rf connections are made to a copper bus bar which runs at the bottom of the vacuum pipe. Near the rf bus are two busses for the $\pm$ dc quad voltages for the rf quads. The feed lines for these are run through the resonator

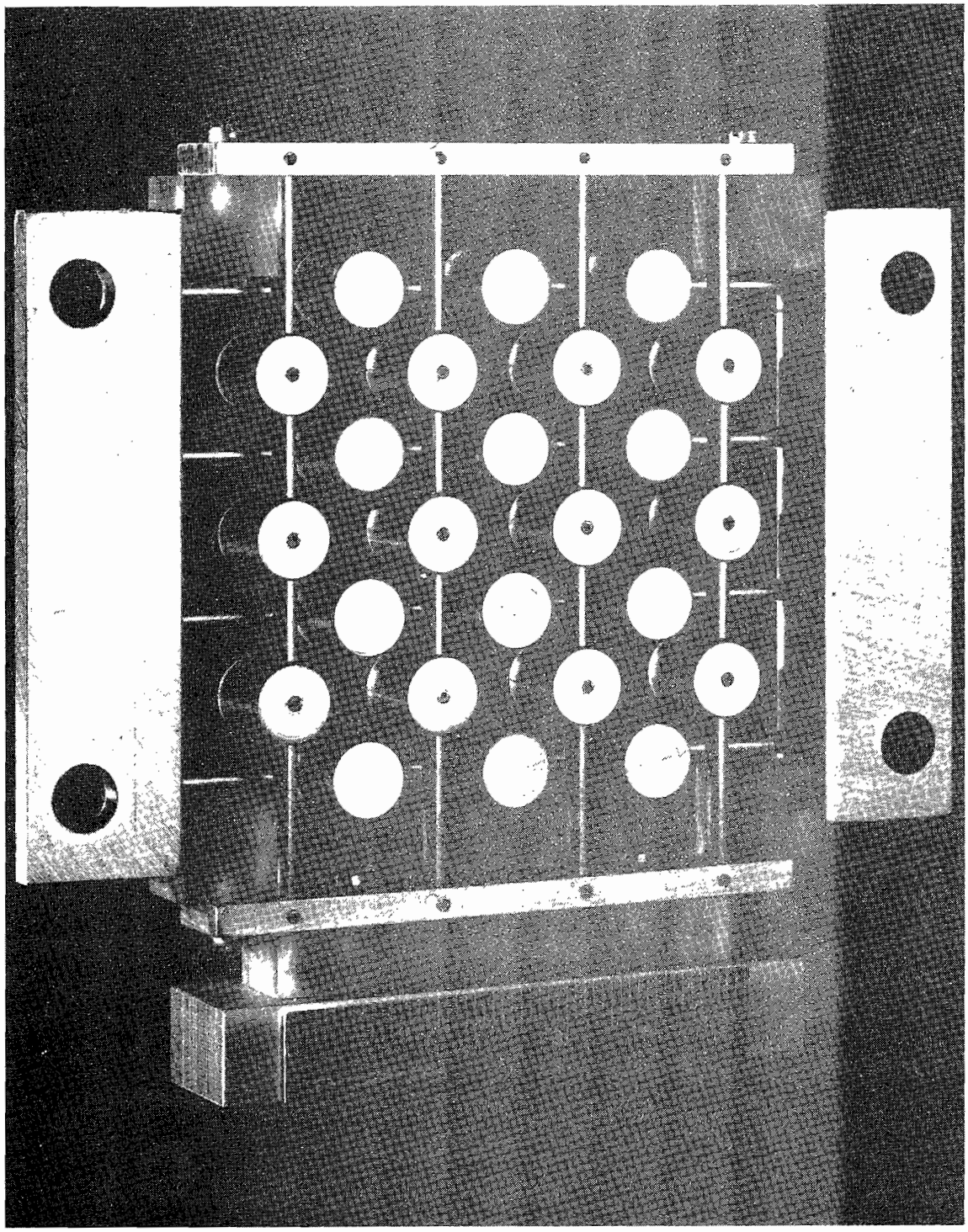

Figure 3. Nine beam quadrupole array.

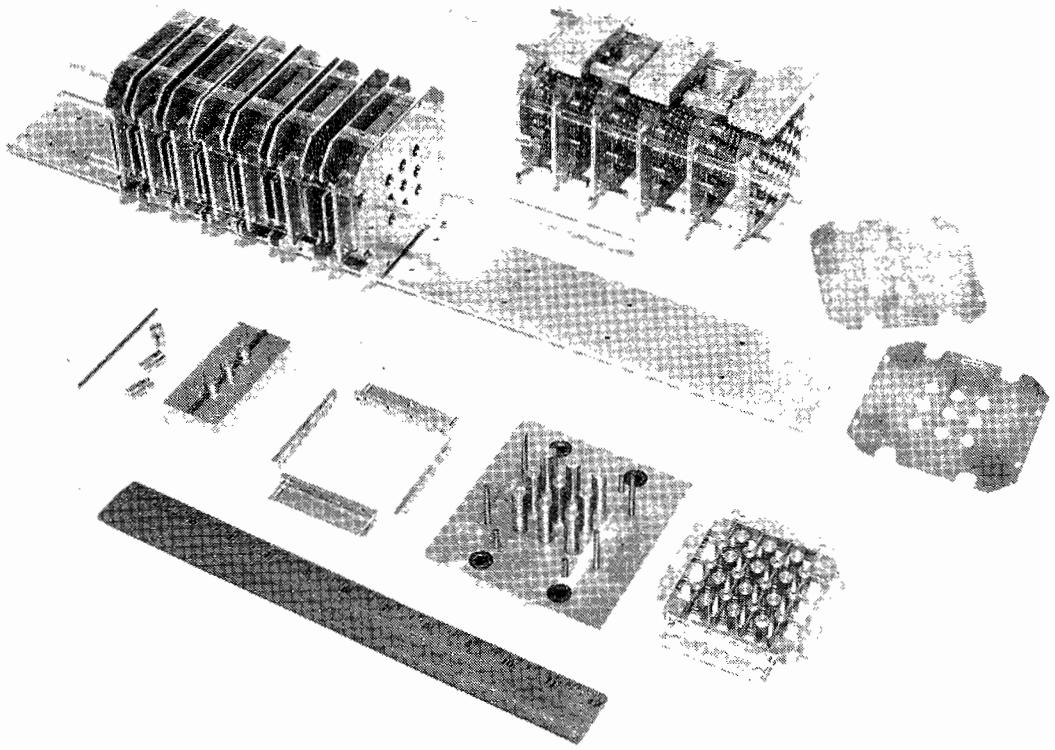

Figure 4. Quad arrays, drift tube cover plates, and precision fixtures.

coil. There are two busses above the Wideroe for the ± quad voltages for ground drift tubes. The complete assembly is shown in Figure 5.

The LEBT quads have separate busses and are run from a separate power supply. In operation, they run at a lower potential for two reasons: 1) the LEBT quads must compensate for any emittance mismatch between the ion source and the accelerating section and 2) a small rf defocussing effect in the accelerating section is expected.

The accelerating section has 16 accelerating gaps. The drift tube table (Table II) is calculated for 3.5 keV energy gain at each gap. The quadrupole lengths are proportional to the velocity of the particle. It follows that the same phase advance/cell is maintained by having the same voltage on all of the accelerator quadrupoles. Thus the M1 has a power supply which provides ± quad voltage for the accelerating section (with extra output connectors to feed the rf quads), and another which supplies ± voltage for the LEBT quadrupoles.

TABLE II. DRIFT TUBE TABLE

	DRIFT TUBE NO	ENERGY EV	TRANSIT TIME FACTOR	PARTICLE VELOCITY M/S	DRIFT TUBE LENGTH CM	DRIFT TUBE LENGTH IN	ELECTRODE LENGTH CM	ELECTRODE LENGTH IN
G	0	15500.		151262.	-	-	-	-
RF	1	19000.	0.913	166126.	1.702	0.670	0.990	0.390
G	2	22500.	0.926	181192.	1.890	0.744	1.080	0.425
RF	3	26000.	0.935	195054.	2.063	0.812	1.163	0.458
G	4	29500.	0.943	207968.	2.225	0.876	1.240	0.488
RF	5	33000.	0.949	220108.	2.376	0.936	1.312	0.517
G	6	36500.	0.953	231600.	2.520	0.992	1.381	0.544
RF	7	40000.	0.957	242539.	2.657	1.046	1.446	0.569
G	8	43500.	0.961	253000.	2.788	1.097	1.508	0.594
RF	9	47000.	0.964	263040.	2.913	1.147	1.568	0.617
G	10	50500.	0.966	272708.	3.034	1.194	1.626	0.640
RF	11	54000.	0.968	282041.	3.151	1.240	1.681	0.662
G	12	57500.	0.970	291073.	3.263	1.285	1.735	0.683
RF	13	61000.	0.972	299831.	3.373	1.328	1.787	0.704
G	14	64500.	0.973	308339.	3.479	1.370	1.838	0.724
RF	15	68000.	0.975	316617.	3.583	1.411	1.888	0.743
G		71500.		324683.				

Linac length = 41.017 + 16 x 0.375 = 47.017 cm

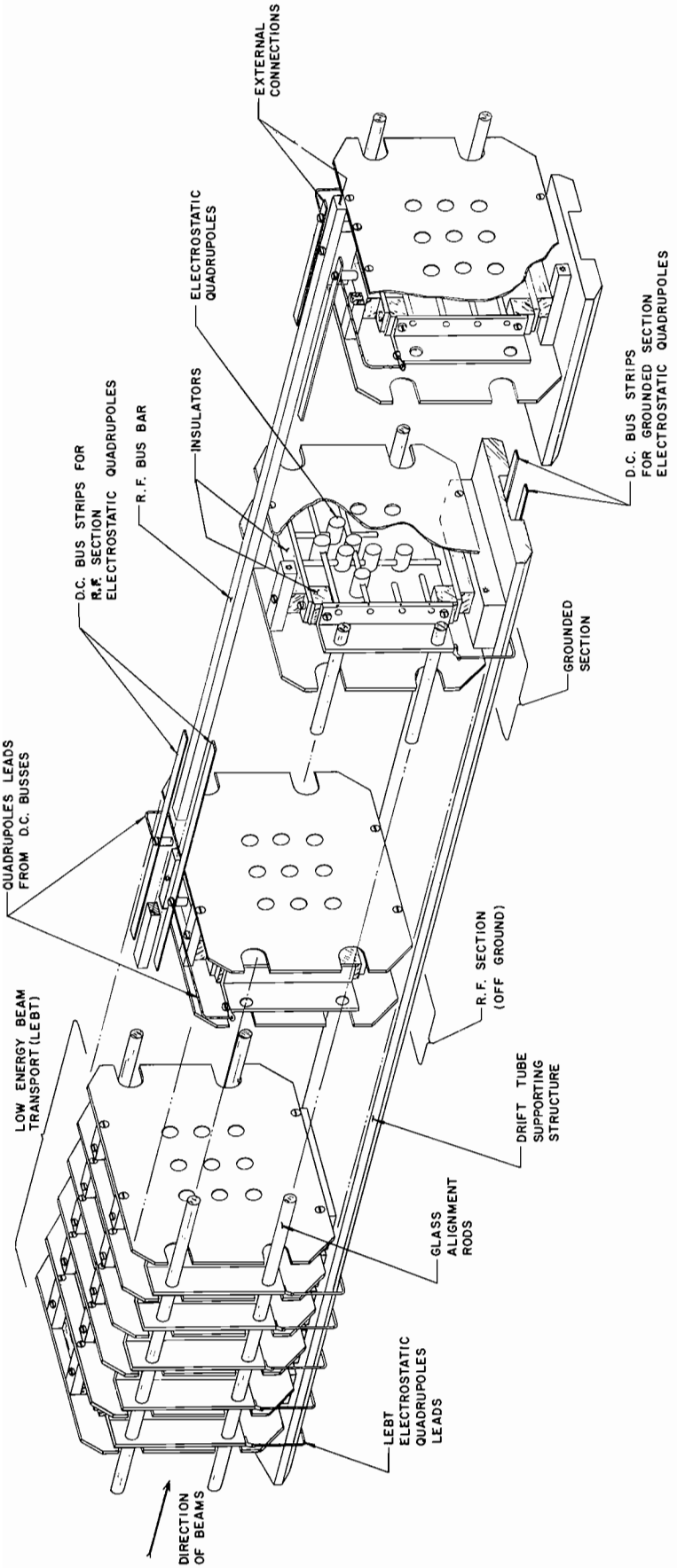

Figure 5. Schematic of M1 assembly showing bus bars. When mounted in the vacuum tank, the assembly hangs from the plate shown at the bottom.

c. Ion Source, Match to LEBT, and Pre-Buncher

The ion source is a version of the LBL-CTR ion sources (Figures 6 and 7). This type of source, with multiple distributed filaments in a chamber, produces a very quiet and uniform plasma. The electron efficiency is low, but when operated with xenon the filaments are long-lived even with cw filament operation for the modest current densities needed.

Figure 8 shows a spectrum indicating $\sim$70% Xe^{+1} purity.

Typical operating parameters are:

TABLE III. ION SOURCE PARAMETERS

Fil voltage	7.5 Vac
Fil current	150 amps ac
Arc current	25A
Arc voltage	50V
Ion current density	25 mA/cm^2

In operation, the filaments and gas run cw, and the arc voltage is pulsed. The current density is adjusted from 1-50 mA/cm^2 by varying the filament power.

Model studies were made with single channel transport systems (see Figure 9) for obtaining a good match between the source and the acceptance of the channel. The calculated acceptance area of the channel is 40 π cm-mrad (unnormalized), and the calculated space-charge limit is 3.3 mA of xenon. One must fill the acceptance of the channel uniformly in both emittance planes to approach the space-charge limit.

Previous emittance measurements with this source yielded 25 mA of Xe^{+1} into 10 π cm-mrad at 15.5 keV. Although these measurements were performed under space-charge neutral conditions after the extraction gap, it is clear that a considerable degree of emittance "spoiling" is necessary to fill the transport channel.

We have found one special solution to this highly non-linear problem experimentally. The slits shown in Figure 5 are cut in concave "dimples" of 1-1/4 inch radius in both the arc cover plate and grounded extraction plate.

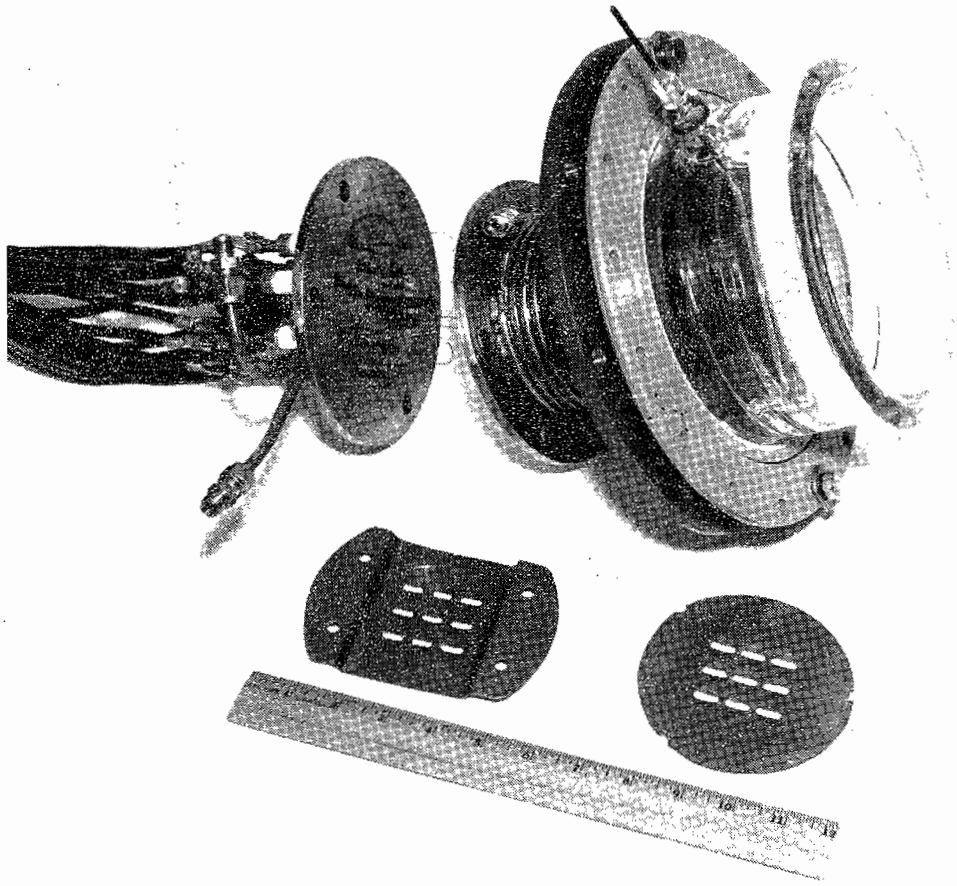

Figure 6. Ion source and Pyrex insulator.

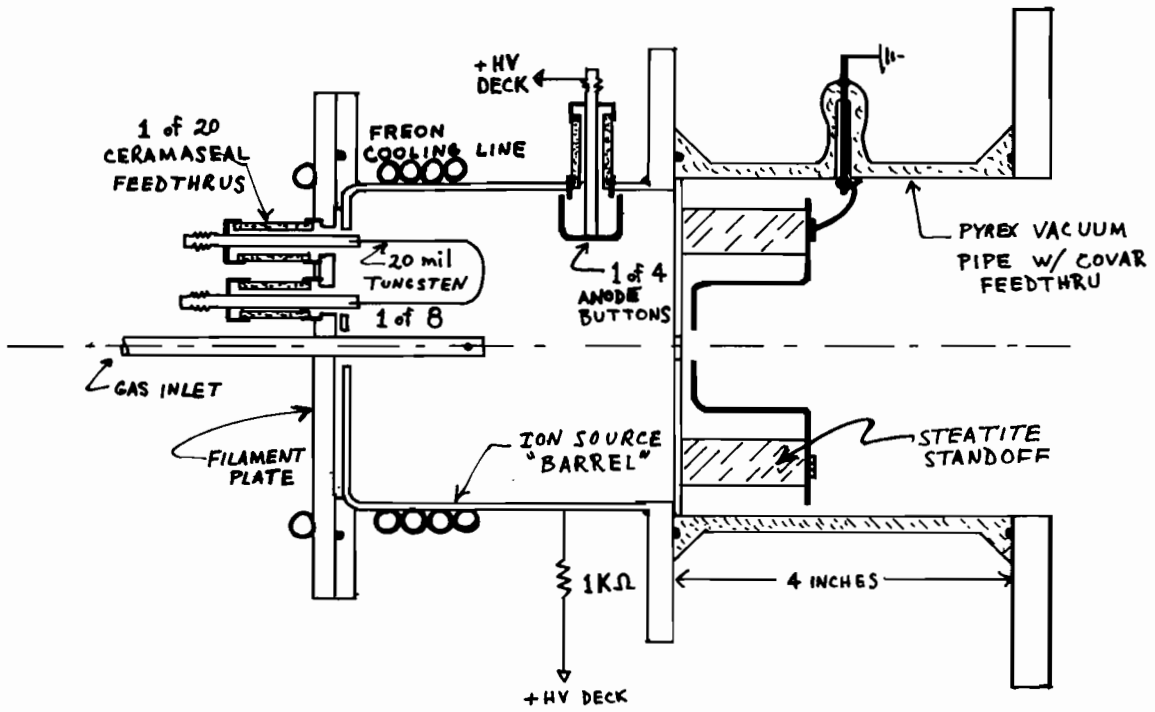

Figure 7. Schematic of ion source. The 4" dia. Pyrex pipe shown was replaced with a 6" dia. pipe.

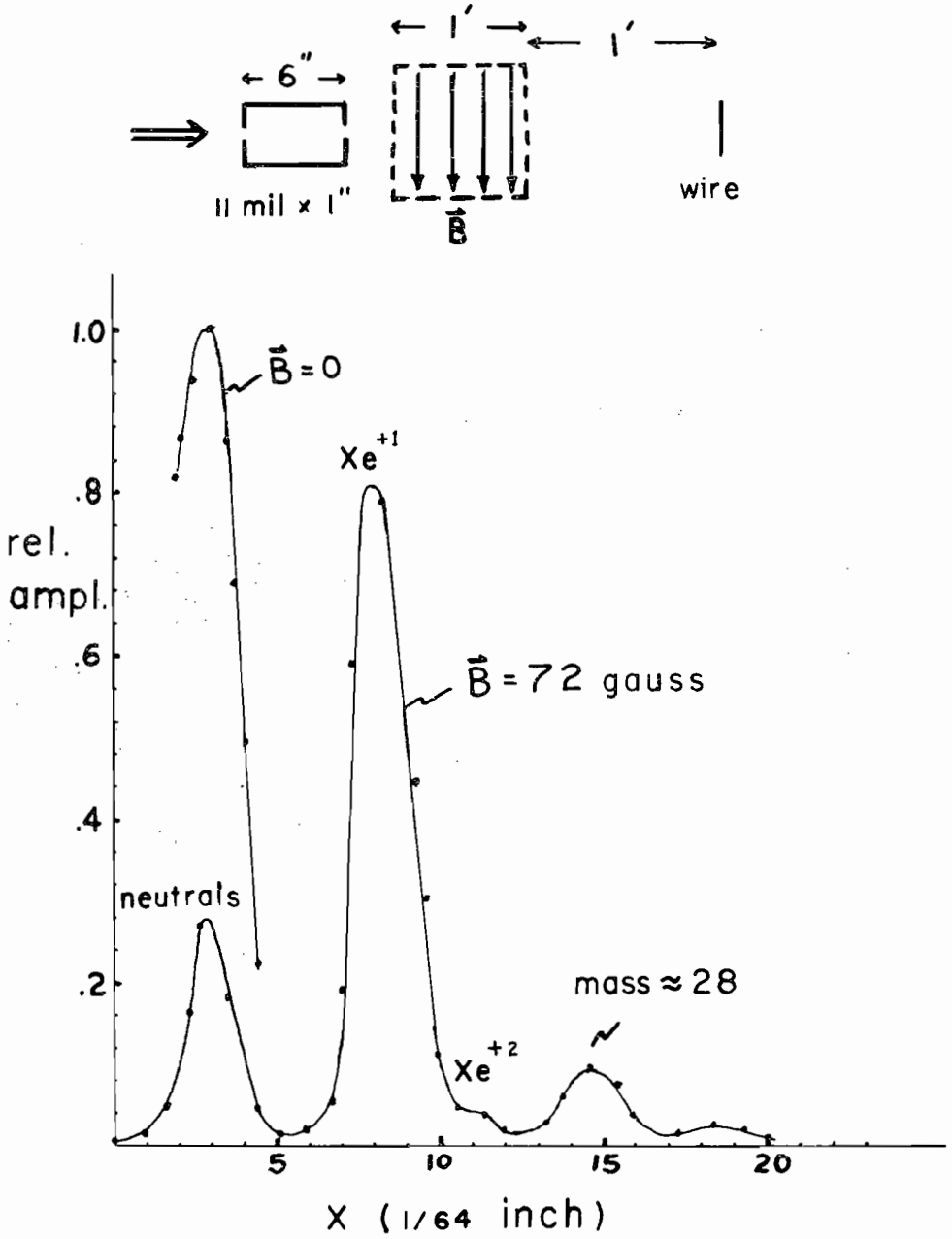

Figure 8. Spectrum of ion species from source showing $\sim 70\%$ Xe^{+}. The fact that the neutral peak is not deflected or badly distorted by the B field indicates that neutralization occurs only near the source.

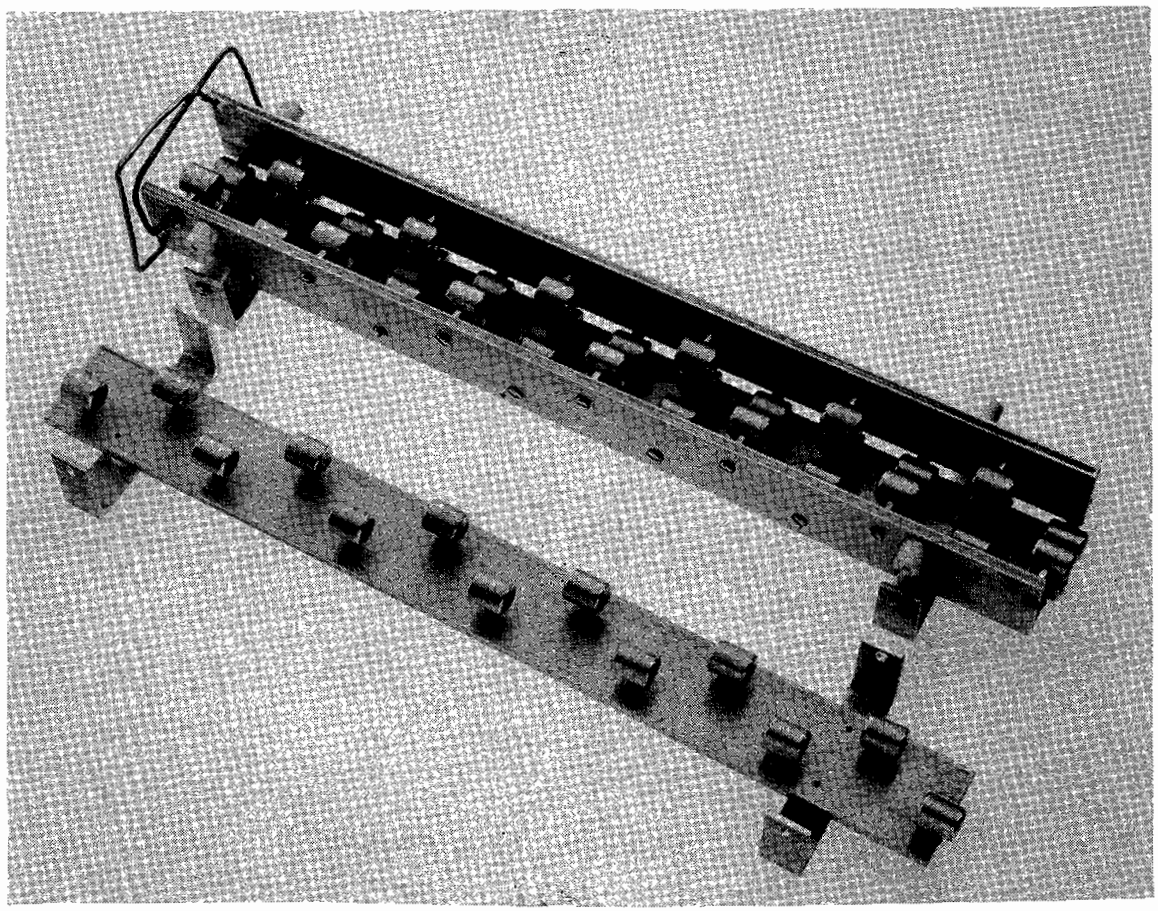

Figure 9. Transport channel for preliminary tests. This version has a 5/8" bore. Later versions were made with 5/16" bore for M1 modeling.

The area of the extraction hole is 0.35 cm^2, with an aspect ratio of 3:1. This gives us a converging beam in the dimension parallel to the slit, and a diverging beam in the direction perpendicular to the slit. We adjusted the quad channel position for maximum transported current, and obtained 2.4-2.6 mA of Xe^+ when the first quad end was 7/8 inch from the extractor plate. For the highest current levels, it was found that the arc voltage should be raised to 70-80 volts.

In this case, the total current emerging from the extractor is $\sim$8 mA, and we transport $\sim$2.5 mA. We assume that the acceptance of the channel is well filled, but this has not been measured todate.

With a 7/8" gap between the extractor plate and the first LEBT quad, we are able to insert a pre-buncher plate of 1/2 inch thick aluminum. This has nine 1/2 inch diameter holes and is suspended on the same Rexolite rods. The $\beta\lambda/2$ length between the centers of the buncher gaps is 0.75 inch.

The drift length from the buncher to the first rf gap is 4 inches (through five LEBT quad arrays). This drift length is sufficient to give a 45° phase shift with 1.5 kV buncher voltage.

The instantaneous bunch current has the same transverse space-charge limit as the dc transport limit. Therefore we have competing "bottlenecks" in the transport at each end of the LEBT. This was verified in operation of M1, by observing that the ion source could be run from 10-25 mA/cm^2 current density without changing the output current.

d. Rf System

The rf system consists of two major parts; an amplifier and a resonator.

The amplifier is a 4 MHz, 2 stage, 700 watt linear amplifier with broadband interstage coupling. The input rf amplitude range is 0 to 1 volt peak, for an output power level from 0 to maximum. The amplifier is single-ended throughout with the two output tubes driven in parallel. The input stage is operated in a class A mode with control grid modulation to compensate for beam loading. The interstage coupling is performed by a Tchebycheff filter so that tuning is unnecessary. The final stage tubes operate in a class AB_1 mode. This stage operates in a stable fashion with grid and screen parasitic suppressors but no neutralization. Figure 10 shows the rf amplifier with covers removed. In the foreground at the left is the

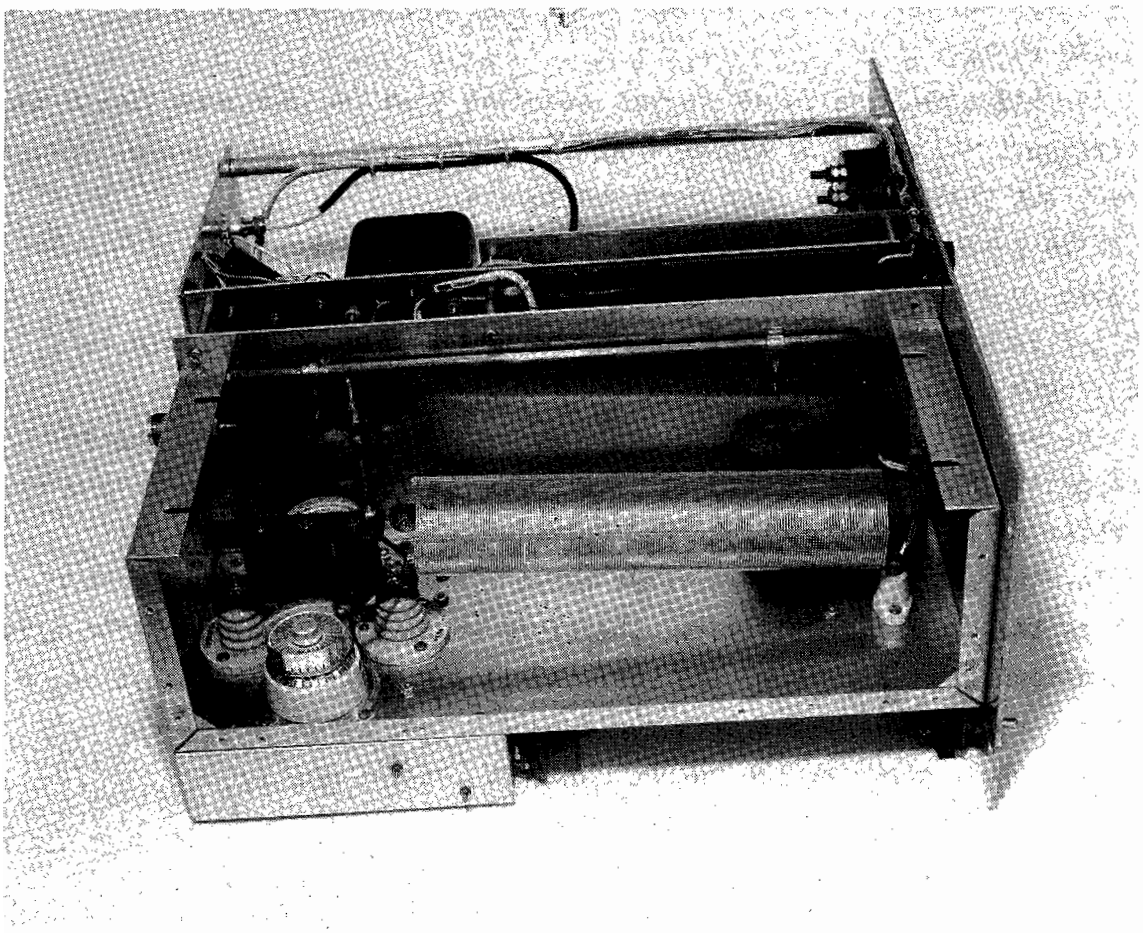

Figure 10. 4 MHz rf amplifier.

final stage showing the two 4CX350A tubes, plate choke and dc blocking capacitors. The rf plate connection is directed vertically and passes through a small duct (not shown) into the resonator compartment normally mounted above. The portions of the chassis in the background and those parts not visible in Figure 10 are the filament transformer, low voltage plate and bias power supplies, and first stage grid modulator PC board.

The resonator is a three turn coil of 3/4 inch copper tubing with a nine inch mean diameter. The amplifier plate connection is made at the first turn to give a step-up turns ratio of 1:3, thus providing 5 kV peak rf at the accelerating gaps. The unloaded Q of the resonator with the accelerating structure connected was measured at 680. The noload or tank and accelerating structure losses amount to 300 watts. The remainder of the output power is beam loading. Figure 11 shows the resonator assembly with the side panel removed. The plate tap is clearly visible, passing through the bottom panel from the first turn. The 3rd turn, or top of the coil has a flange to mate with a flanged bus from the accelerating structure just below a vacuum window. Two RG 58 coaxial cables for $\pm$ DC voltage for the rf quads can be seen entering the bottom coil mounting flange. They leave through the top mounting flange and thus have rf isolation. From the top of the resonator to ground is a 300 pF vacuum capacitor for final stage tuning. Below the tuning capacitor is a 1:1000 capacitive divider for monitoring the gap voltage.

The rf is switched at the oscillator and modulated at the first stage of the rf amplifier from timing pulses generated at a master timing panel.

The buncher is driven by a helical resonator and, in turn, driven by a commercially built wideband amplifier. The 4 MHz oscillator also provides the low level rf signal that drives the buncher amplifier. A separate rf amplitude control is provided, and a phase shifter is included so that the relative rf phase between the accelerating gaps and buncher may be tuned. Figure 12 is a block diagram of the complete rf system.

IV. M1 Operating Results

After running the M1 for several days, all systems were working together to produce the results shown in Figures 13-16, under the conditions of Table IV.

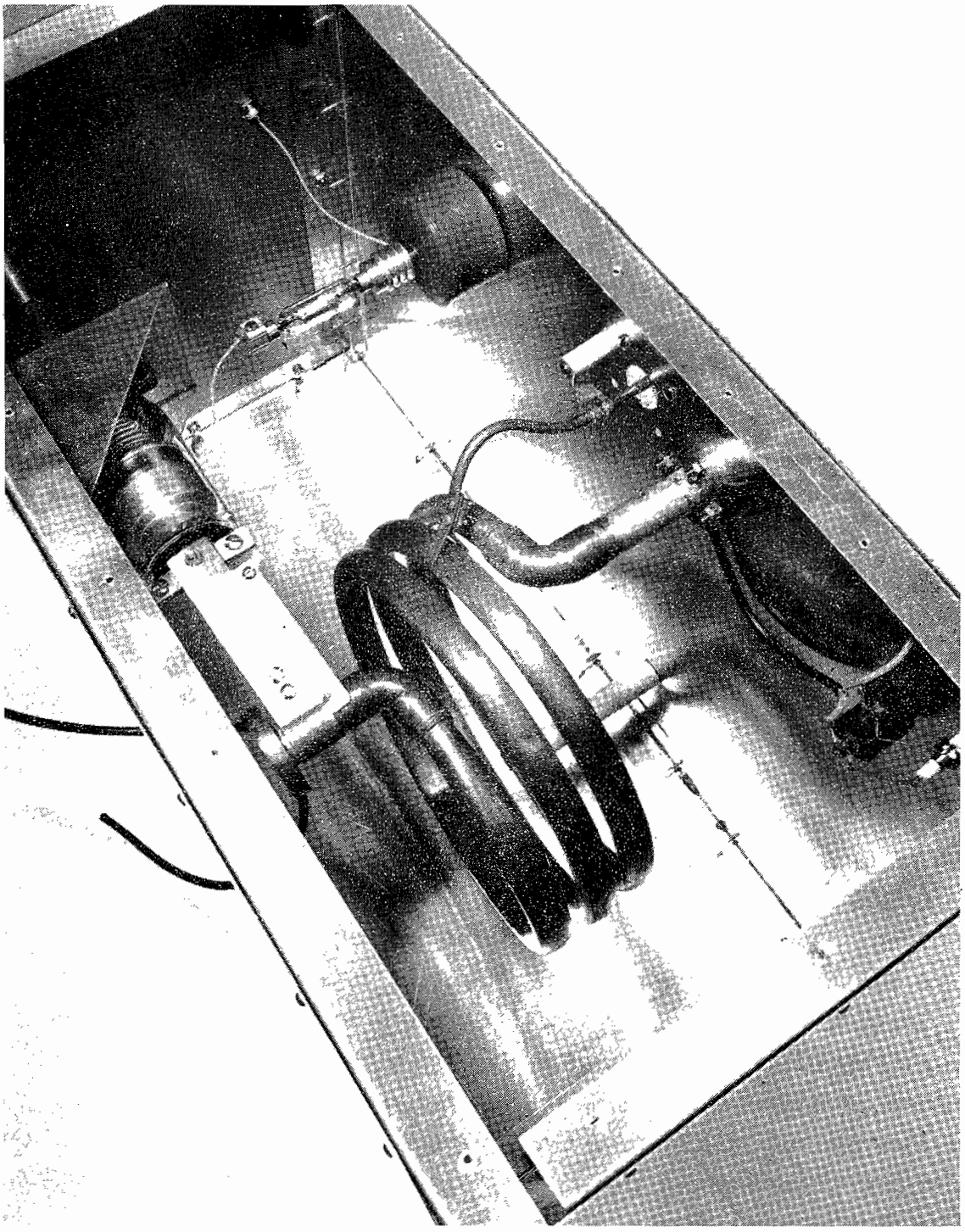

Figure 11. Rf resonator.

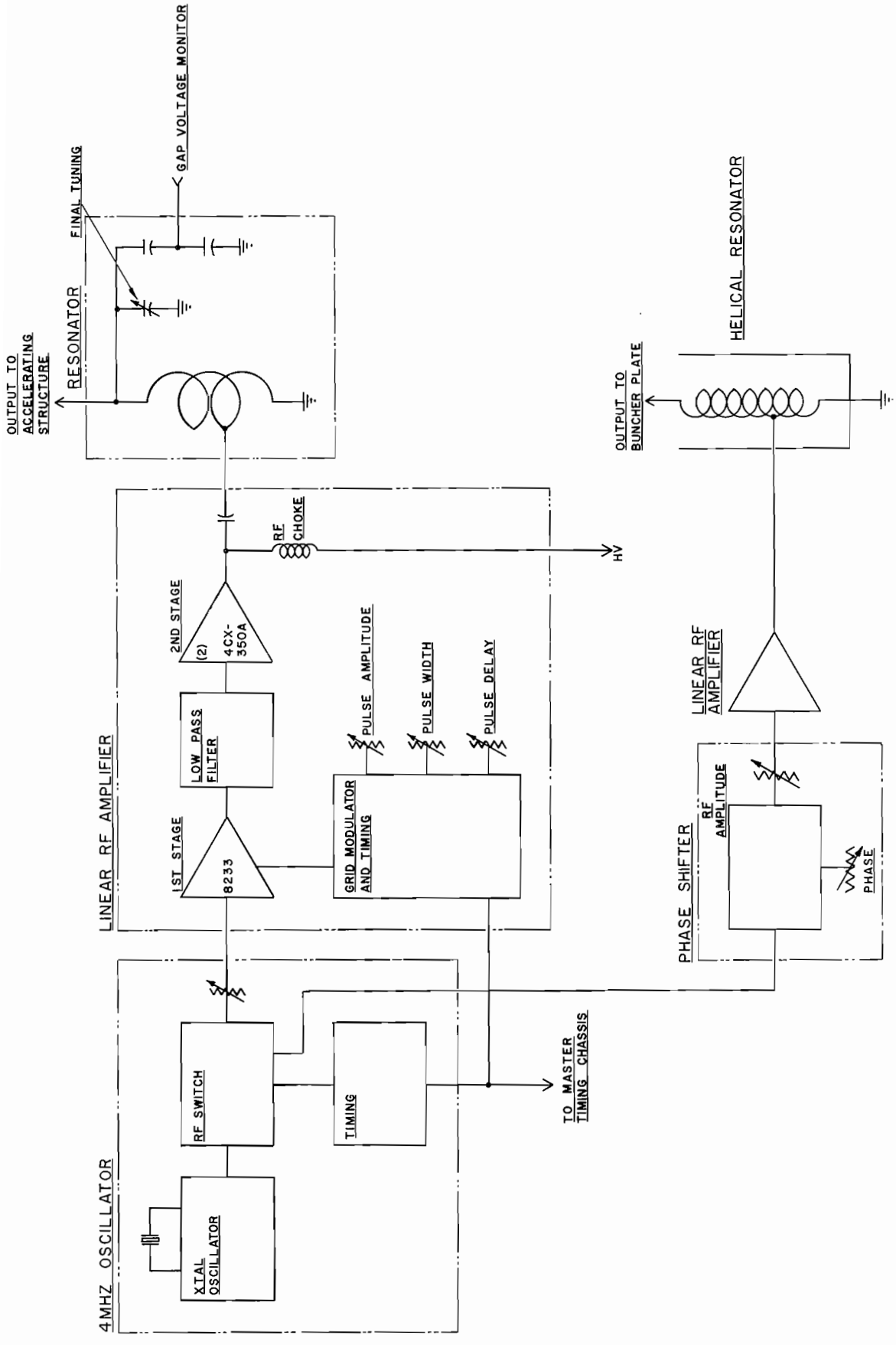

MEQALAC RF SYSTEM

Figure 12. Block diagram of rf system.

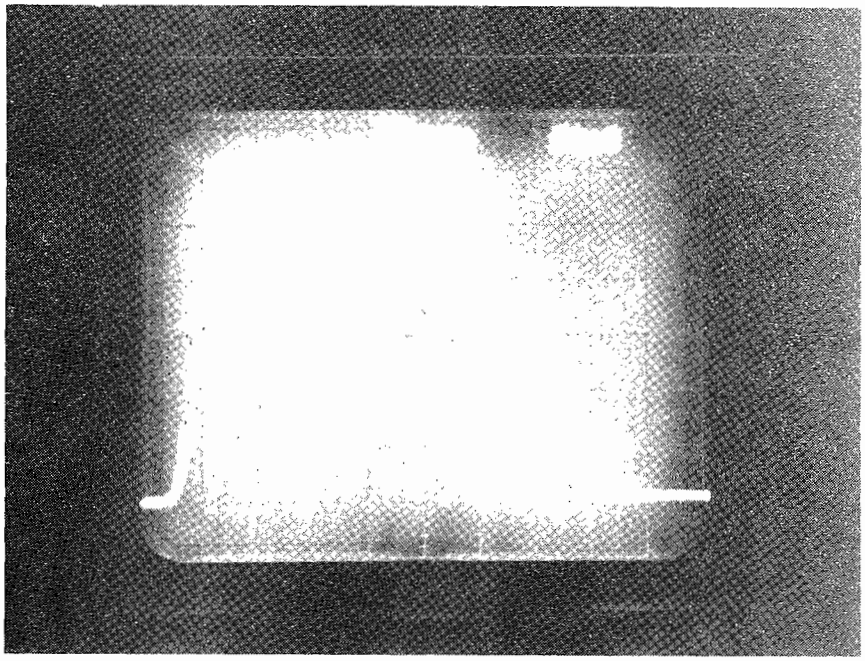

Figure 13. Full current (nine beams) at M1 output, 0.5 mA/div. vertical and 50 μsec/div. horizontal. Bunch structure is integrated.

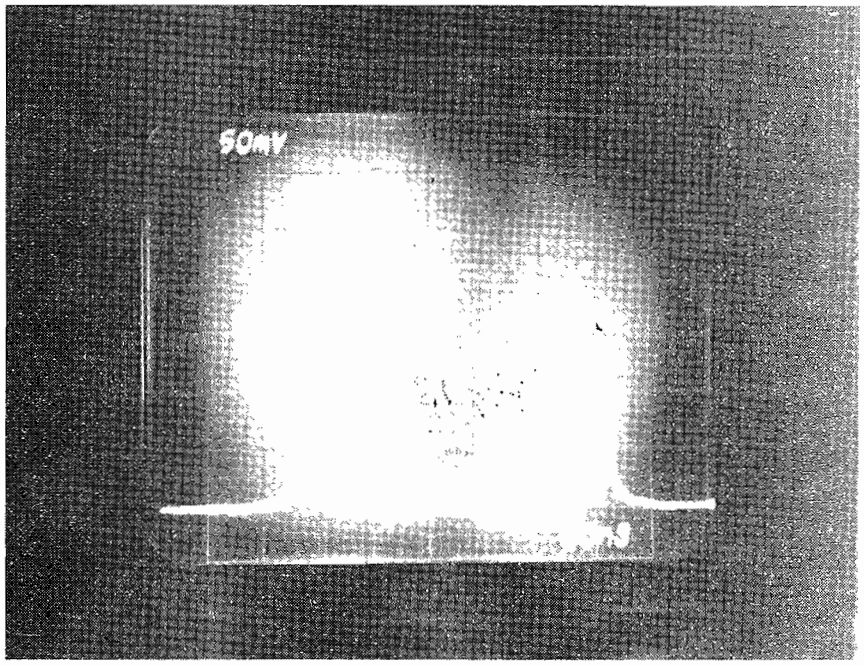

Figure 14. Single beamlet current showing 4 MHz bunches. 1 mA/div. vertical and 50 nsec/div. horizontal.

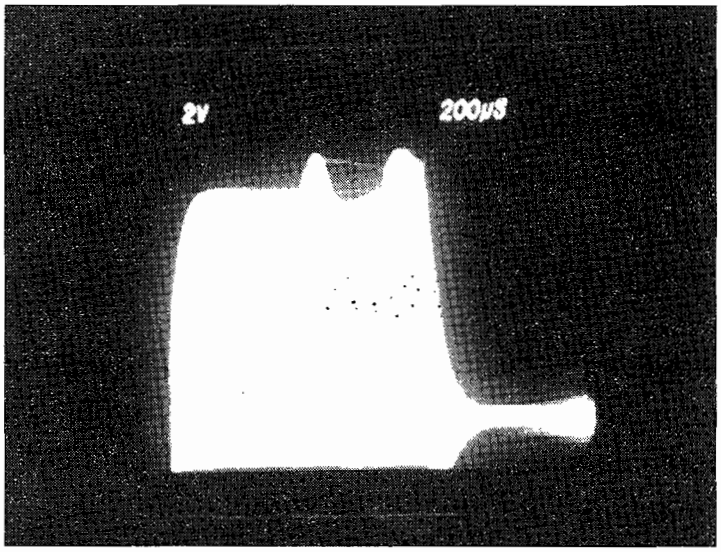

Figure 15. Rf envelope from voltage pickup on resonator. The rf amplitude is boosted ∿50 μsec before beam-on time, and the subsequent dip is due to beam loading.

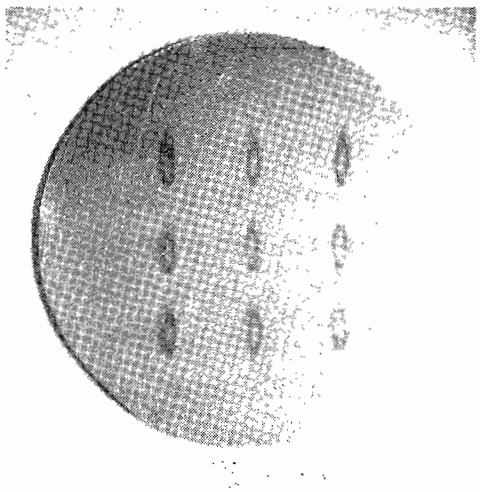

Nine Beam Witness Plate, 1"
after end of MEQALAC.

Figure 16. Aluminum plate showing beam marks.

TABLE IV. OPERATING CONDITIONS

Source		MEQALAC	
Fil Current:	133A	LEBT Quads:	±1.8 kV
Arc Current:	29A	Linac Quads:	±2.25 kV
Source Voltage:	+17.3 kV	Rf Voltage:	4.7 kV
		Buncher Voltage:	1.5 kV

Vacuum: 2×10^{-5} torr

Figure 13 shows the output current of all nine beams collected in a single Faraday cup with a -300 V biased grid. The signal was terminated in 1 kΩ with an integrating capacitor. The peak current is 2.8 mA. There is about a 10% rf signal passing the integrator.

Figure 14 shows the bunch structure in a single beamlet. This signal was terminated with 50Ω. The instantaneous peak current is 2.8 mA. We obtain an experimental rf filling factor from these two results of 11 ± 1%. This is obtained by solving the relationship

(2.8 mA/beam) x (9 beams) x (fill factor) = 2.8 mA Total Avg Current

The error quoted is an estimate of several factors including different peak currents obtained for individual beamlets, which was probably due to the coarseness of the grid bias wires compared to the small beam sizes.

The theoretical estimate of this filling factor for an optimum MEQALAC is 13.3%.[3] This estimate assumes an equality between the longitudinal and transverse space-charge limits, and so the 11% result is a measure of the validity of that assumption for the M1. We suspect that we could improve the filling factor with the addition of a 2nd harmonic buncher.

The theoretical estimate of the space charge limit is 3.3 mA total average current. We obtained 2.8 mA, or 85% of that estimate.

Figure 15 shows the rf envelope and exhibits beam loading. At beam time a square wave pulse is added to the grid modulator. The additional rf amplitude needed to compensate for beam loading is seen to be ~15%. This model is operating at greater than 30% beam loaded power.

The operation of the quadrupoles was straightforward and trouble-free. We measured 0.2 mA of current drain from the quad supplies during beam time. The optimum quad setting for a broad range of MEQALAC design is $V_Q = 0.115$ V_{input},[5] where V_{input} is the input accelerating voltage of the ion.

At V_{input} = 17.3 kV, V_Q is $\pm$ 2.0 kV. Our best results were obtained with V_Q = $\pm$ 2.25 kV. The theoretical estimate does not take into account the effect of rf defocussing.

An important consequence of the above quad voltage relationship is that the focussing channel can be arbitrarily close to the ion source extraction gap. That is to say, if the ion source operates without sparking at the extractor, then the channel shouldn't spark either. This is very favorable for future MEQALAC development since improvement calls for smaller beams and higher ion source current densities.

REFERENCES

1. A.W. Maschke, Space-Charge Limits for Linear Accelerator, BNL 51022, May 1, 1979.

2. A.W. Maschke, MEQALAC: A New Approach to Low Beta Acceleration, BNL 51029, 1 June 1979.

3. Reference 1, p. 3.

4. Reference 1, p. 6.

5. A.W. Maschke, Formulary for MEQALAC Design, BNL 51119, November 27, 1979.

SPACE CHARGE NUMERICAL SIMULATION EXPERIMENTS

P. M. Lapostolle

GANIL

Comments are presented here on the work contained in a CERN report.[a] These comments are mainly oriented toward to comparison with the work of I Haber.[b]

The CERN work was performed about 10 years ago, at the same time as both numerical computations and experimental measurements of emittance growth in a linac were being carried out, in the hope of contributing to the understanding of the phenomena or of being the start of some theory.

1. Focusing System Considered

FD Focusing:

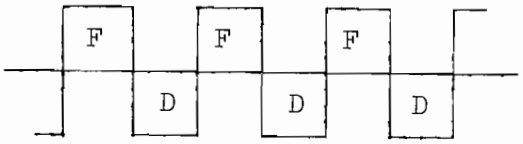

is defined by the betatron phase shift per focusing period at zero beam intensity (represented by and expressed in radians in the report; μ(radians) = σ_0 (degrees).

The intensity of space charge is expressed by the dimensionless parameter:

$$\delta \cong \frac{q}{mv^2} \frac{\lambda_o I}{\varepsilon\beta\gamma}$$

where q is the charge, m is the mass, v is the velocity of the particle, λ_0 is the betatron wavelength and I is the current (in coulombs per unit time).

---

a) Etude numerique d'effets de charge d'espace en focalisation periodique, by P. M. Lapostolle, CERN report ISR/78-13.

b) Presented at HIF Workshop, Oct. 29-Nov. 9, 1979, Claremont Hotel, Oakland, CA (See present proceedings).

There is a direct connection between δ and σ/σ_0:

for $\delta = 1.5$ $\quad \sigma/\sigma_0 \tilde{=} 0.5$,

for $\delta = 2.0$ $\quad \sigma/\sigma_0 \tilde{=} 0.4$

(The latter value is the threshold of the first Gluckstern mode for a round beam, K-V distribution.)

2. Particle Filling at the Input

In most of the runs, 2,500 macroparticles were used with a random uniform distribution inside a fixed boundary.

Such a fixed boundary only exists for continuous focusing and is then defined through a Bessel function. The boundary was approximated in actual cases by a properly sized (final adjustment empirical):

hyperellipsoid for $\delta < 2$,

uniform distribution in x,y and x'y' for $\delta > 2$.

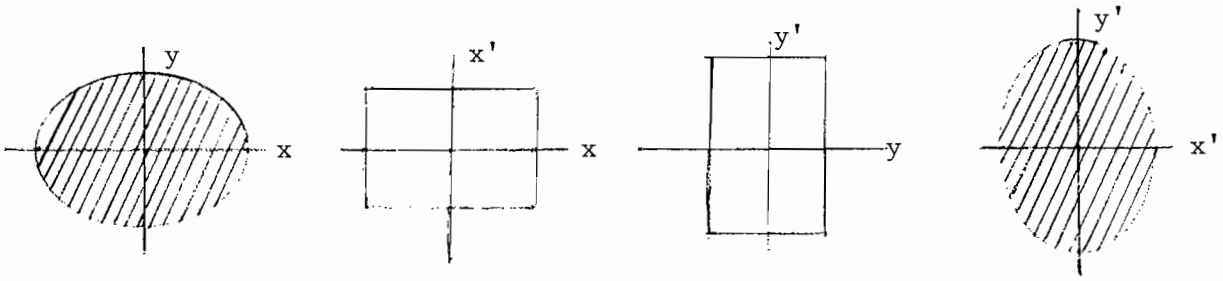

In the case, $\delta > 2$, the potential well in which particles move is no longer paraboloidal, but tends to present a flat bottom where no restoring

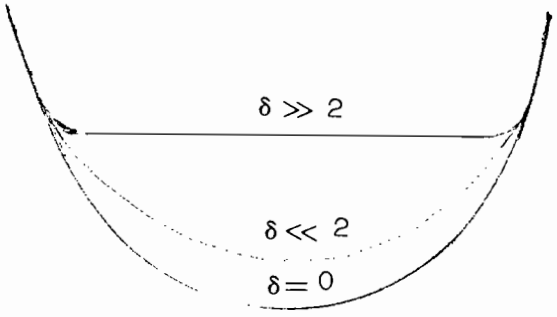

force exists, except on the edges where the force extends over a thickness equal to the Debye length.

For $\delta = 2$, the Debye length is about equal to the beam radius.

For large δ, individual particles do not perform sinusoidal oscillations and their frequency spectrum may become wide. (This was one reason not to take, during this work, σ/σ_0 as a parameter but, rather, δ, along with the fact that it was intended to keep the possibility of considering unequal sizes in x and y).

Some other distributions have been tested: a) KV, to check the stability limit (when stable, the 4-D surface immediately become slightly wrinkled due to statistical fluctuations, but with a constant thickness). b) Gaussian and uniform-gaussian have also been tested to represent the output of a source.

3. Methods of Computation

Space charge is computed in free space, but assuming a 4-fold symmetry (2-fold only in certain cases).

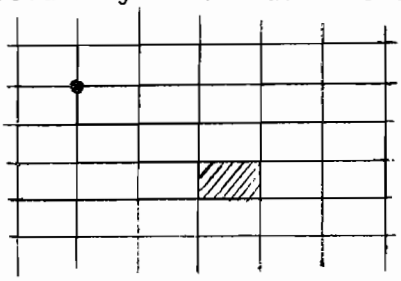

direct 10 x 10 box-to-nodes computation
or
FFT (16 x 16 or 32 x 11)
} + interpolation

The rectangular mesh is variable (sized to 1.1 outer particles) in order to keep maximum accuracy. (The potential on the boundary is computed from a series expansion of the outer potential: with a rectangular mesh of aspect ratio larger than 1.1, a 2-step computation is performed, the first is on a square mesh to compute the potential on a close boundary which would enter the circle of convergence of the expansion. For example, consider the 2-fold symmetry case illustrated here:

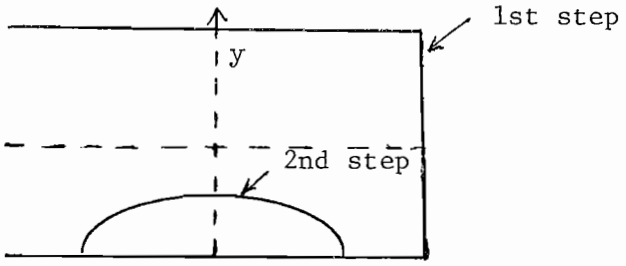

4. Results

Detailed results appear in the report quoted (a). Only a summary and some remarks are given here:

• For $\sigma_0 > 90^\circ$, even for $0.4 < \sigma/\sigma_0 < 0.6$, large emittance increases appear (as for KV). (The emittance level reached indicates an overshoot effect in this case).

• For $\sigma_0 < 90^\circ$ and large enough tune depression ($\sigma/\sigma_0 < 0.4$) slower increases are seen: the smaller the tune depression, the slower the increase, the smaller the σ_0, the slower the increase (at least in the cases computed and with 4-fold symmetry assumed in the computations; on the CERN linac, there was some experimental evidence of this effect).

• For continuous focusing, even with tune depressions as large as 95%, no deviation from the original distribution was observed (apart from the immediate statistical effect). However, no way was found to specify the absence of oscillations.

• It is mainly the outer part of the beam which is affected by higher order space charge effects; the central core almost keeps its 2-D phase space density. (The 4-D is obviously conserved.)

• It is not obvious how to determine from the simulation experiments whether or not a more stable distribution exists.

A few additional tests were performed with the simulation program:

1. Filamentation due to mismatch in a continuous focusing system, even

for cases with very large space charge,

$$x^2_{min} + x^2_{max} = ct$$

$$y^2_{min} + y^2_{max} = ct$$

The above leads, after damping has taken place, to an emittance increase. (Similar behavior was observed with a non-linear third-order field and no space charge.)

2. Some early simulation work with non-circular beams which was not followed up:

Starting with $\sigma_{ox} = \sigma_{oy}$ and unequal ε_{ox}, ε_{oy}, it was found that ε_x and ε_y become equal with their sum remaining constant (constant energy). Starting with $\sigma_{ox} \neq \sigma_{oy}$ (by a factor of $\tilde{=} 2$) nothing was seen, neither with equal initial energies in x and y, nor with equal emittances. (These runs were made when the program was not optimized, interpolations were crude and the accuracy was such that small variations were considered irrelevant.

LINAC SUMMARY

S. Penner and M. Wilson

National Bureau of Standards

Goals

To define the problem areas for both the rf and induction linac scenarios. We are not addressing engineering or cost considerations. We also did not consider the test beds.

Scenarios

Since new target parameters were presented at the beginning of the Workshop, detailed designs to match these parameters were not available. Thus, we did not do a detailed analysis of any specific design. The specific designs presented are not optimized.

RF Linacs

The problem is to take the beams available from the ion source and low-β systems (analyzed separately) with realistic current and emittance and accelerate them to the final energy, meeting the current and emittance requirements of the storage rings. An example of how this might be done is illustrated below

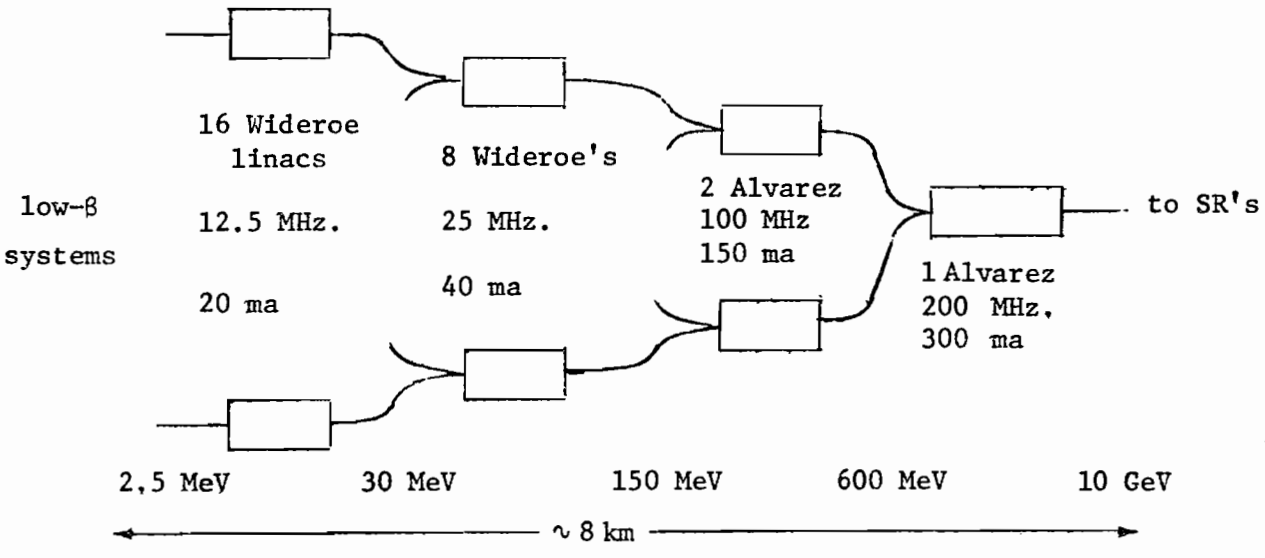

Remarks

1) Since the beams are merged by frequency multiplying, the normalized transverse emittance and the longitudinal emittance per bucket could both, in principle, be conserved. In practice, some emittance growth at injection and at each merge is anticipated.

2) The design is based on limiting the space-charge tune depression to a conservative 25% ($\mu \geq 0.75\ \mu_o$) in both transverse and longitudinal space.

3) The basic design can be varied to meet parameter changes of the low-β section, the storage rings, or target requirements.

Questions that remain to be answered

1) Calculate the emittance growth all along the system especially at the low-β end and at each merging. Numerical tools for doing this almost exist [PARMILA can correctly predict performance of existing proton linacs "for 95% of the beam" and can be applied to heavy ions as well[1]]. Other work reported in these proceedings, by Jorna and Randa treats the problem of heavy ion emittance growth and beam envelope behavior with space charge at the low energy end of the linac, but without merging.

2) Study the impedance coupling of the beam with the structure. The concensus is that transverse beam blowup is not expected at these currents, and longitudinal blowup is rather unlikely, but must be calculated.

Induction Linac

Here one takes a single high-current beam from the injector and low-β sections (12A @ 2 MV) accelerates it to final energy ($\sim$ 10 GeV) in a single accelerator (6 - 10 km long). The beam current is kept fairly close to the transverse space charge limit ($\mu > 24°$, $\mu_o \simeq 60°$) throughout the accelerator.

This implies a gradual compression (shortening) of the beam pulse which is accomplished by shaping the accelerating voltage pulses so that the back end of the pulse has slightly higher velocity than the front end. Conceptually, the difference from an rf linac is that a very large accelerating bucket is formed instead of many (2×10^5) small ones. But in the induction case, the shape of the bucket is adjusted to optimize longitudinal motion, which isn't done in the rf case.

Remarks

1) In a sense, this system is "simpler" than the rf case because there is no need to merge beams from parallel linacs, and there are no storage rings.

2) High current electron induction linacs provide some technology base, but the applications to ions is new so there are new problems. Thus, there are more questions that remain to be answered than in the rf case.

3) The number of synchrotron oscillations in the full length of the machine is of order one. The number of transverse oscillations is of order 100; very different from the rf case.

Questions that remain to be answered

1) Longtudinal dynamics - Optimization of bunch and acceleration profiles (A start on this problem is reported by S. Chattoopadhay, et al., in these proceedings. Also in these proceedings, M. Foss presents a computer design for bunching and acceleration in a high current proton induction linac, which might be applied to a heavy ion linac.).

- Study of tolerances (preliminary work is reported in these proceedings in papers by S. Chattoopadhay et al. and by A. Faltens).

- Effect of wall impedance and feedback control of beam (discussed also in the paper by A. Faltens, these proceedings).

- How do the ends of the bunch behave (erode)? (See the paper by D. Neuffer, these proceedings for more on this question.)

2) Transverse dynamics - the understanding of this in the absence of coupling to the longitudinal motion is in relatively good shape.

3) Longitudinal-transverse coupling - some of the longitudinal dynamics questions can't be adequately addressed without considering the couplings. Unlike rf linacs, the large aspect ratio of the beam bunch in an induction linac makes the full 3-dimensional particle simulation very difficult. Some proposed approaches include: two dimensional (x-z) simulation, "2-½" dimension (R-Z), full 3-D simulation of the beam ends with a simplified model for the relatively uniform central 80-90% of the beam.

Recommendations

1) Develop numerical simulation techniques which can describe the full 3-D behavior of the beams in both rf and induction linac cases. This would not be a single program for all problems.

2) Study the interaction of the structure with the beam, i.e., beam instabilities driven by the beam-structure coupling impedances. The transverse effects appear to be negligible, but the longitudinal ones need to be calculated.

3) Experimental verfications of the results of theory and numerical simulation are needed. The proposed test beds should provide the data for at least some of the effects of interest. Since the numerical work is already quite sophisticated, "crude" comparisons with experiment won't help. Very good diagnostic tools will have to be developed.

4) Alternate methods of high current transport, such as charge-neutral transport employed in the Pulselac experiments at Sandia Labs, should continue to be investigated.

Conclusions

No fatal flaws in either rf or induction linacs have been found. The concensus from preliminary simulation and analytic studies is that there probably aren't any, but more work in the areas discussed is needed.

References

1. R. Jameson, D. Swenson, LASL Private Communication.

COMPUTER DESIGN OF A HIGH CURRENT, HIGH ENERGY PROTON LINAC

M. H. Foss
ARGONNE NATIONAL LABORATORY

The accelerator produces enough beam to make the same number of neutrons on the average as 0.5 mA of 800 MeV protons. The beam is delivered to the target in 200 ns pulses at 50 Hz. The results are presented here because some of the problems are similar to HIF problems.

In the Linac discussed here, the current at each point is constant throughout the pulse. Figure 1 demonstrates this scheme: A constant current is extracted from the ion source for a time dT = 2. This beam passes an accelerating gap at D = 0. The velocity profile is adjusted so that the beam is bunched. The time required for the beam to pass a point decreases linearly from dT = 2 to dT = 0 as the distance goes from D = 0 to D = 4.

In the accelerator, all of the acceleration is done by induction cavities. The machine is divided into three sections: a buncher, a debuncher, and a main accelerator. A 7.5A, 2 ms. pulse from a 750 kV preaccelerator is compressed by a factor of 10 in the buncher and debuncher. These 200 ns pulses are then accelerated to 565 MeV.

BUNCHER

In the buncher, the speed of the leading edge of the beam is kept high enough so that the beam current never exceeds 0.2 of the space charge limit. When the beam enters a cavity, it is at 0.2 of the space charge limit. After acceleration, the beam current is the same, but the space charge limit is higher. As the beam drifts to the next cavity, the current increases again to 0.2 of the space charge limit. This process is illustrated in Fig. 2.

The trailing edge of the beam pulse is transported by the same focusing structure as the leading edge. This problem has not been studied, but it seems reasonable to allow the ions in the trailing edge to have twice the

momentum of those in the leading edge. This is illustrated in Fig. 3. The factor of two momentum spread is established in the first few accelerating gaps.

A nonrelativistic calculation gives for the length of the buncher after the space charge limit and velocity profile are established.

$$S < \frac{5}{2} T V \frac{M}{M-1}$$

where:

T = the time for the ion source beam to pass a point at the space charge limit (or fraction of the limit to be used),

V = the initial velocity of the leading edge, and

M = the ratio of the trailing edge momentum to the leading edge momentum.

The right-hand side, in the case considered here, is 120 m.

DEBUNCHER

The function of the debuncher is to reduce the momentum spread. This is illustrated in Fig. 3. Bunching continues, but at a reducing rate. The bunch length is shown in Fig. 4. The lower curve is the difference between the arrival time of the leading edge and the center of the beam pulse. The upper curve is the difference between the arrival time of the trailing edge and the center. Note that bunching is almost stopped in the debuncher.

The buncher and debuncher might require hard tube drivers to achieve the desired wave form.

Gap voltage, as a function of distance, is shown in Fig. 5. The voltage vs. time in the buncher and main accelerator is largely determined by the accelerator requirements. However, the debuncher is short and its function can be achieved with a variety of voltage vs. time curves. Keeping this voltage pattern simple is probably an important objective.

Finally, Fig. 6 shows energy vs. distance. Note that the energies in the buncher and debuncher are multiplied by 10. Also, in the first few cavities, where the velocity profile is established, the maximum mVs/m is 435.

CONCLUSION

The induction Linac presents an attractive source of protons for a pulsed neutron target. The performance could be extended by using some of the space charge safety factor in the buncher or by extending the Linac to higher energy, thus getting more neutrons per proton.

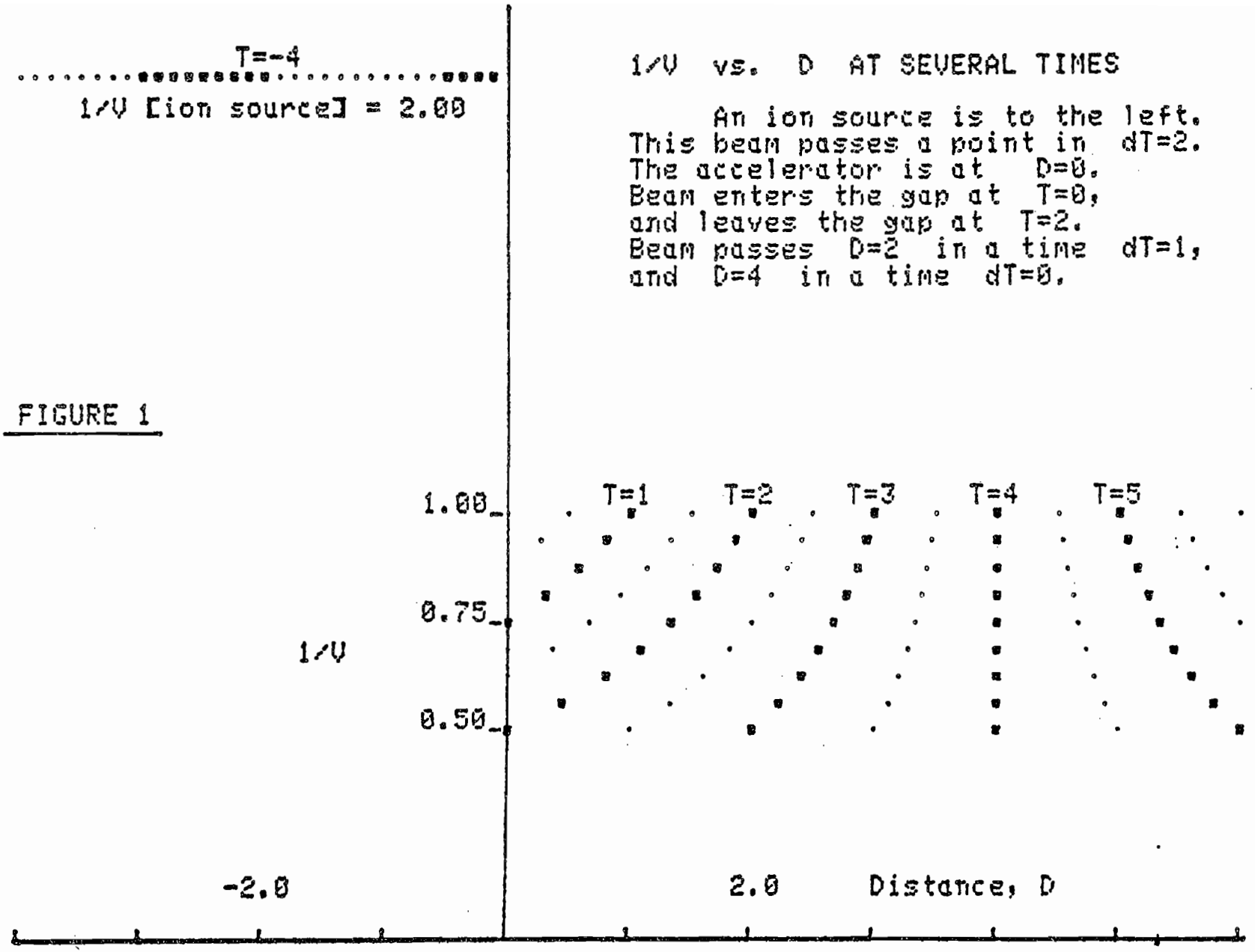
T=-4
1/V [ion source] = 2.00
1/V vs. D AT SEVERAL TIMES
An ion source is to the left.
This beam passes a point in dT=2.
The accelerator is at D=0.
Beam enters the gap at T=0,
and leaves the gap at T=2.
Beam passes D=2 in a time dT=1,
and D=4 in a time dT=0.
T=1
T=2
T=3
T=4
T=5
1.00
0.75
0.50
1/V
-2.0
2.0
Distance, D

FIGURE 1

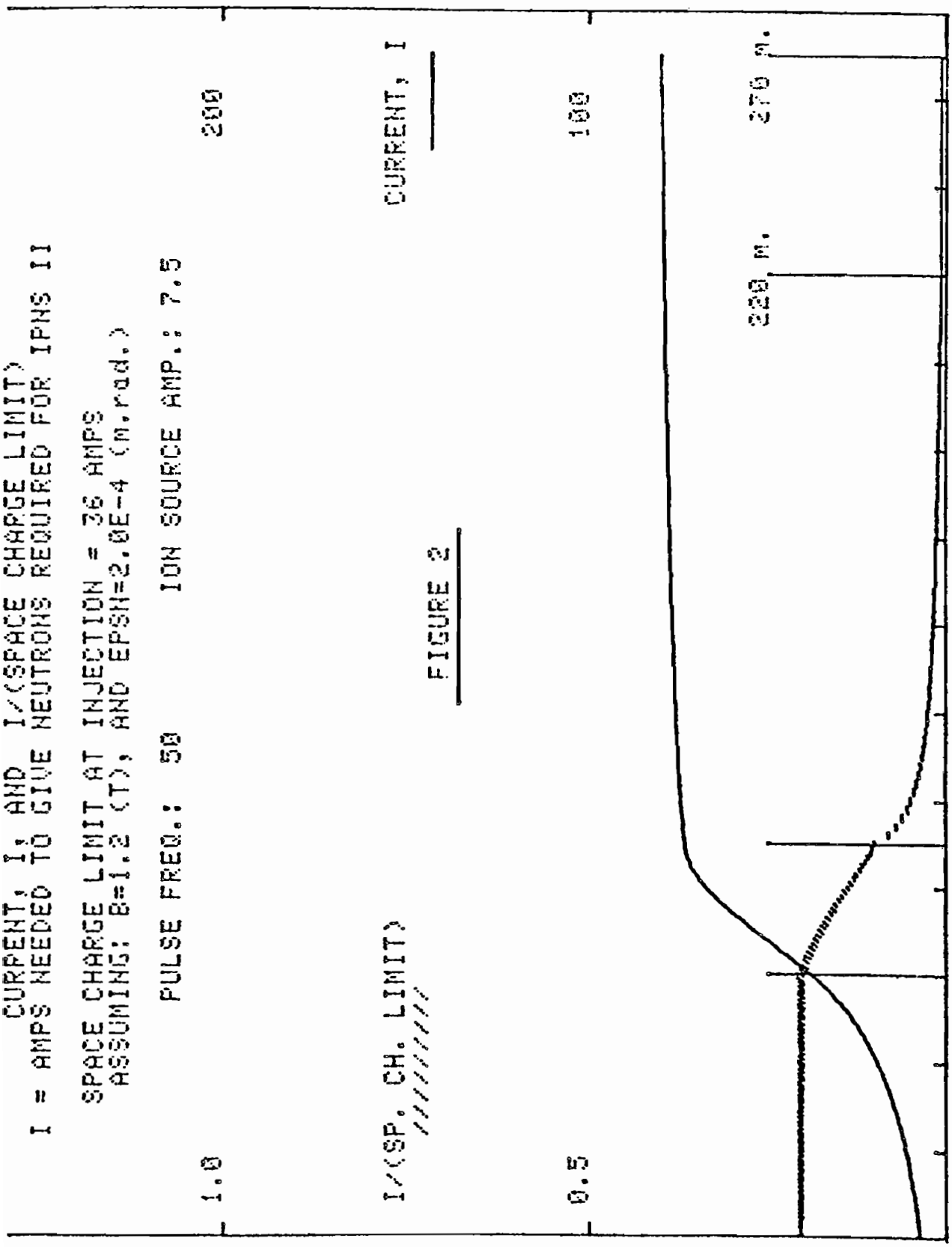
CURRENT, I, AND I/(SPACE CHARGE LIMIT)
I = AMPS NEEDED TO GIVE NEUTRONS REQUIRED FOR IPNS II
SPACE CHARGE LIMIT AT INJECTION = 36 AMPS
ASSUMING: B=1.2 (T), AND EPSN=2.0E-4 (m.rad.)
PULSE FREQ.: 50 ION SOURCE AMP.: 7.5
200
100
CURRENT, I
1.0
0.5
I/(SP. CH. LIMIT)
220 m.
270 m.

FIGURE 2

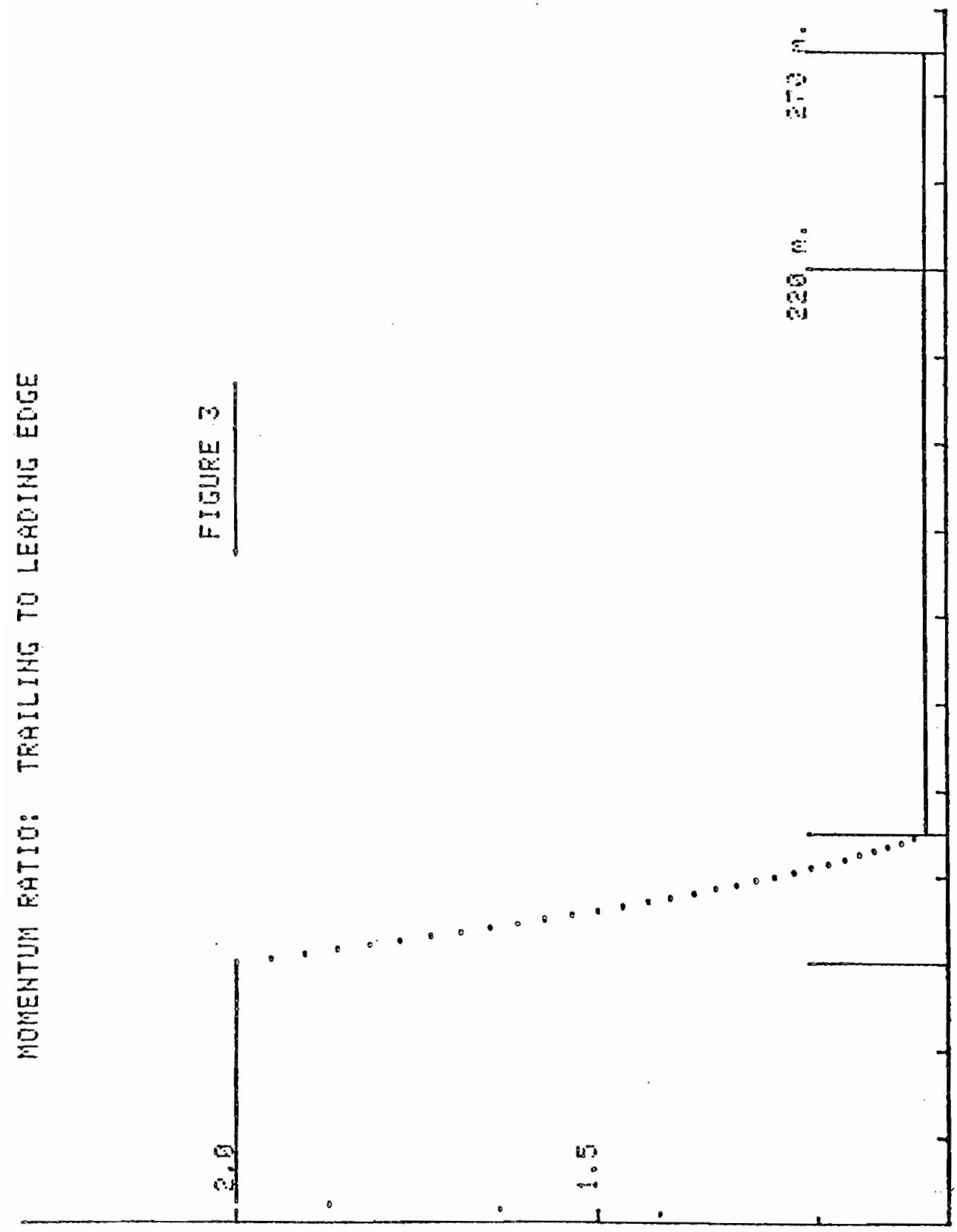

FIGURE 3

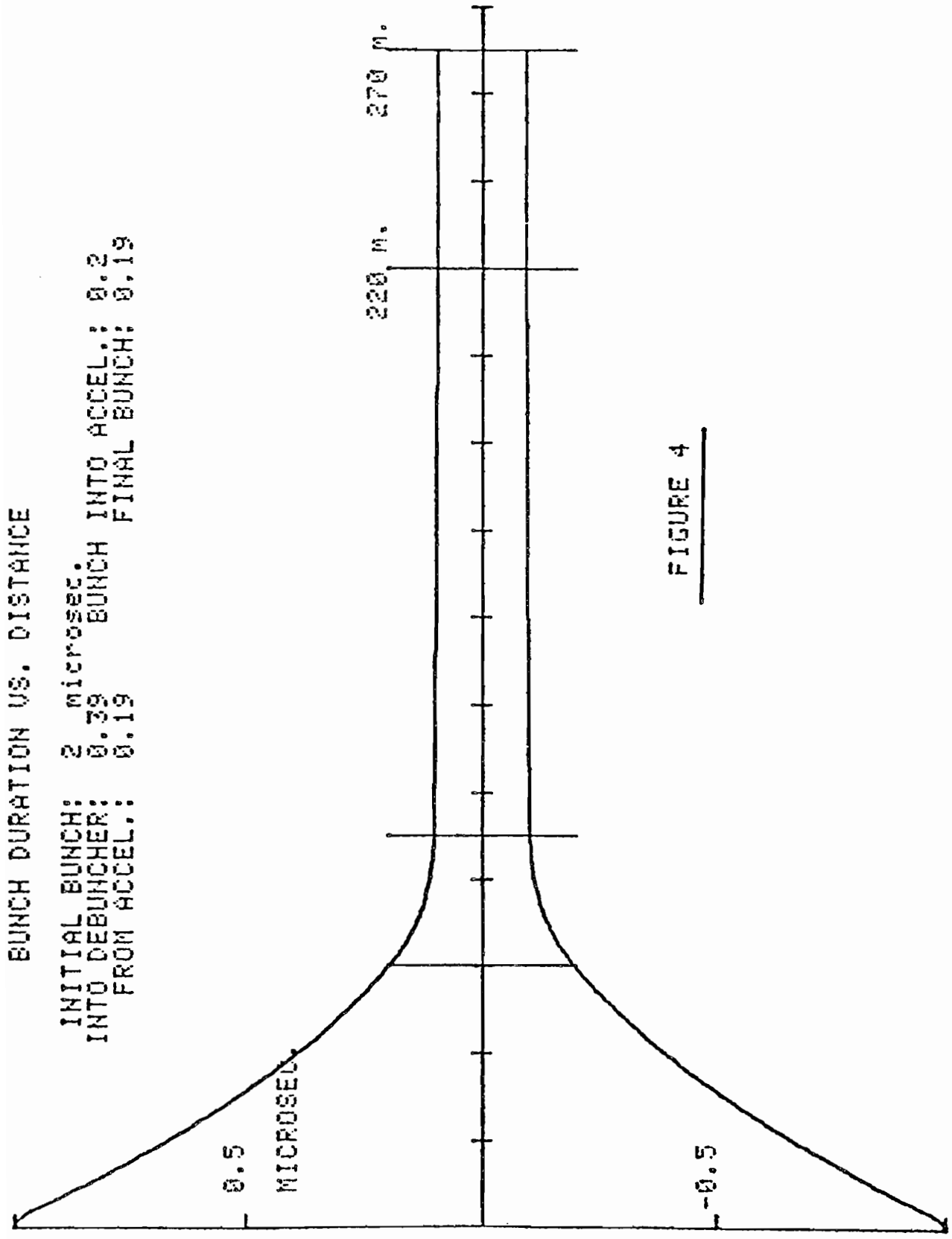
BUNCH DURATION VS. DISTANCE
INITIAL BUNCH: 2 microsec.
INTO DEBUNCHER: 0.39 BUNCH INTO ACCEL.: 0.2
FROM ACCEL.: 0.19 FINAL BUNCH: 0.19
220 m.
270 m.
0.5
MICROSEC.
-0.5

FIGURE 4

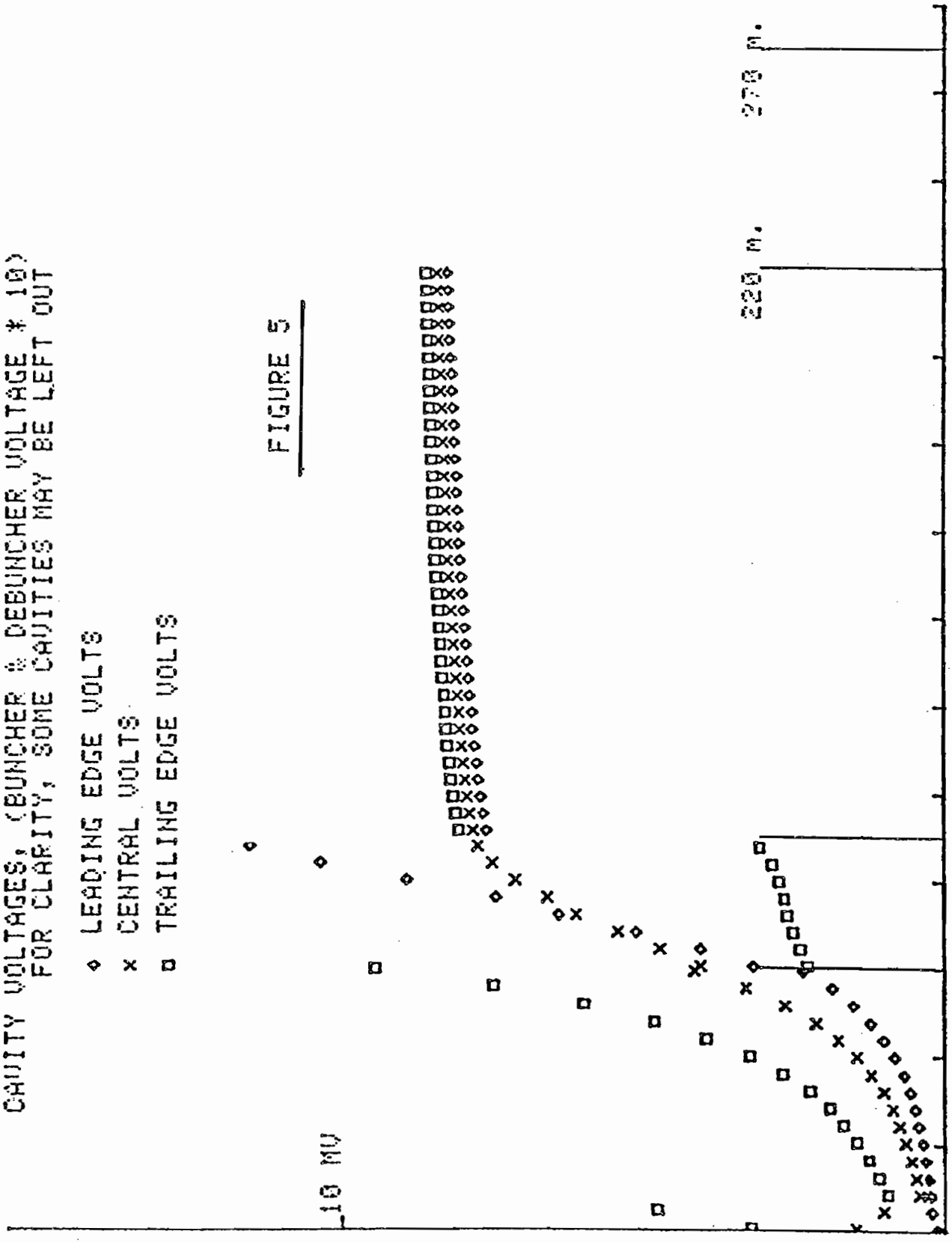
CAVITY VOLTAGES, (BUNCHER & DEBUNCHER VOLTAGE * 10)
FOR CLARITY, SOME CAVITIES MAY BE LEFT OUT
◇ LEADING EDGE VOLTS
× CENTRAL VOLTS
□ TRAILING EDGE VOLTS
10 MV
220 m.
270 m.

FIGURE 5

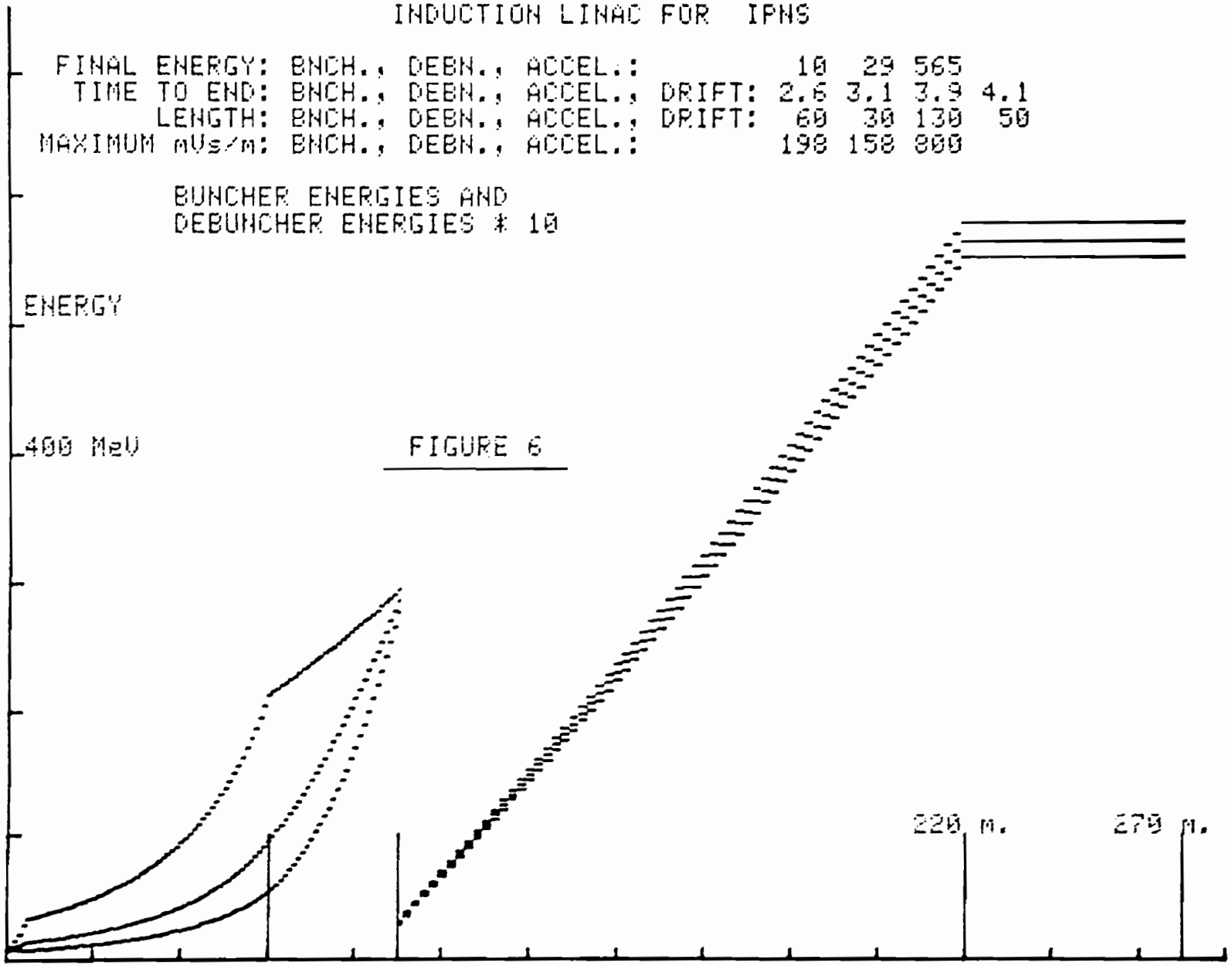
INDUCTION LINAC FOR IPNS
FINAL ENERGY: BNCH., DEBN., ACCEL.: 10 29 565
TIME TO END: BNCH., DEBN., ACCEL., DRIFT: 2.6 3.1 3.9 4.1
LENGTH: BNCH., DEBN., ACCEL., DRIFT: 60 30 130 50
MAXIMUM mVs/m: BNCH., DEBN., ACCEL.: 198 158 800
BUNCHER ENERGIES AND
DEBUNCHER ENERGIES # 10
ENERGY
400 MeV
220 M.
270 M.

FIGURE 6

ELECTRON BEAM EXPERIMENTS AT MARYLAND UNIVERSITY*

M. A. Brennan, P. Loschialpo, W. Namkung, M. Reiser
University of Maryland

J. D. Lawson†
Rutherford Laboratory

1. Introduction

Plans for an experimental study of the stability of intense electron beams in long periodic focusing systems were described at the San Francisco Accelerator Conference in February 1979.[1] At that time, extensive analytical theory on beams with a K-V distribution had been developed,[2] and good agreement with computation had been found.[3] The objective of the experiments is to extend our understanding of what happens with more realistic distribution functions and to make comparisons with numerical simulations. Even in the absence of instability, it is of interest to study the emittance growth associated with aberrations arising from the non-uniform transverse density distribution in the beam, and to compare measurements with the result of computer simulations.

In planning a program of this type, two factors should be emphasized. First, the experiment is not intended to be an exact "scale model" of any proposed ion beam system. It is to map in a flexible way the general properties of high space-charge beams as the system parameters are varied. Second, reliable, accurate diagnostics on beams are notoriously difficult to make. The first stage of the program will concentrate on simple (though not necessarily well-understood) configurations so that the familiarity with the operational aspects of the apparatus can be obtained and reliable diagnostics developed.

---

*Work supported by Department of Energy and Computer Science Center, U. of Maryland.
†Based on presentation by J. D. Lawson at Berkeley workshop.

Components of the apparatus and the proposed experimental program will now be described.

2. Beam Source.

The first experiments will be performed using a planar cylindrical Pierce gun with cathode diameter 1 cm. The perveance k can be varied by adjusting the cathode to anode spacing within the range ½ to 1 μ-amps/(volt)$^{3/2}$; this corresponds to $K = 2Nr_o/\beta^2\gamma^3$ in the range 7-15 × 10^{-3}. Later, the convergent gun described in ref. 1 will be used.

These guns will be operated in the voltage range 5-10 kV, corresponding to currents of a few hundred milliamps. Pulses with length of a few μs will be used, firstly, to avoid space-charge neutralization effects, and secondly, to limit the power dissipation to a reasonable value. This will allow the use of grids; the first gun has a gridded anode to reduce aberrations, and it is hoped that grids can be used for emittance control.

3. Characteristics of Beam from Gun.

The reference beam in all calculations to date has been the unrealizable K-V distribution. This preserves linearity in the presence of self-fields so that paraxial theory can be used. At the exit of a well-designed practical gun or ion source, the beam density is uniform in space, but the transverse velocity distribution is gaussian, with temperature corresponding to the cathode or plasma temperature kT. Such a beam cannot be matched, even in a uniform focusing system. The velocity spread produces a non-uniform density as the beam travels, and this gives rise to a non-linear defocusing force; the beam cross section varies in a non-periodic way with z, the distance along the axis. For the operating conditions quoted above, the transverse thermal velocities are small, and their effects may be masked by aberrations. The parameter range of interest includes much higher values of emittance; it is

therefore planned to increase this by the use of grids, as explained later.

4. First Experiments.

In the initial experiments, the gun is being mounted in a cylindrical vacuum vessel as shown in Fig. 1. Several ports are available for the insertion of diagnostic equipment, viewing windows, etc. In the first experiment, the space-charge spreading from the gun will be measured and compared with theory. The beam profile will be established by inserting a movable paddle into the beam until a small fraction (about 1%) is intercepted. The paddle is mounted on a shaft, which can be rotated and moved in the z-direction so that the beam radius can be found as a function of z.

The paddle also has a small hole at its center. By moving this across the beam and measuring the current intercepted by a Faraday cup, the transverse current density in the beam can be determined. By moving a straight edge across the beam emerging through the small hole, an estimate of its angular spread, and hence the beam emittance, can be made.

When the transverse temperature is negligible, the form of the "space-charge spreading" curve for a uniform beam is well known. If the spreading associated with finite temperature is appreciable, on the other hand, the way that the beam radius and density distribution vary with z must be found numerically. Calculations by I. Haber are already underway.

No lenses are required in the measurement of the beam spreading curve. The apparatus is simple, and many instrumental effects, such as secondary emission, the effects of the wall geometry, partial neutralization from residual gas, can be assessed.

5. Emittance Control.

As indicated above, it is desirable to increase the beam emittance for some experiments. This can be done with the aid of grids. Consider first

a grid of horizontal parallel wires followed by a hypothetical transparent conducting plane, as shown in Fig. 2. The grids consist essentially of an array of "aperture lenses," which deflect the electrons upwards or downwards depending on their vertical position. The emittance diagram corresponding to an initially parallel beam is shown in the figure. If now the transparent conducting plane is replaced by a grid of vertical wires, it will act as a transparent conducting plane for vertical deflections but as a deflecting grid for horizontal deflections; in this case, the grid of horizontal wires will act as the transparent screen. The properties of such a grid will be measured by placing it in the beam and measuring the additional spreading produced. It is not clear whether deviations from axial symmetry will occur; this must be checked.

6. Second Stage of Experiments.

Assuming all goes well into the first series of experiments, described above, the beam will be fed through a pair of magnetic lenses. By adjusting the two lens strengths, it is possible to produce, at a given place, a waist whose size can be varied. A preliminary design, using the K-V approximation, but including the emittance changing grids, has been established. For a real beam, however, the current distribution will be non-uniform. This will be measured and compared with numerical simulations. It will be interesting both to see how good the K-V theory is in predicting the location and rms radius of the waist, and also to assess the relative effects of the departure from a K-V distribution and of conventional lens aberrations on the form of the waist.

Once this stage of the experiment has been completed, and experience with guns, diagnostics, and the various quirks of the apparatus established, the way will be clear for the study of long beams in long solenoids, interrupted solenoids, or quadrupole arrays. In Ref. 1, the emphasis was on

interrupted solenoids. It will be interesting, however, to measure the beam behavior in a continuous solenoid, which was discussed above in section 3. This work will be essentially a continuation of earlier work, for example, by Lawson[4] and Brewer.[5]

By this time also, the convergent Pierce gun should be available. Indications are that this may have a density distribution that is higher at the outer radii than at the center, whereas the focused system will probably have higher density in the center. Comparisons between these two different distributions should prove interesting.

7. Status.

The first gun, together with paddle and Faraday cup, has now been assembled for the first tests. A good vacuum ($<10^{-7}$ torr) has been obtained, and the gun is being activated.

8. Concluding Remarks.

It is not possible to foresee in detail how this program will develop. The basic approach has been to maintain flexibility and to break down the problem into a series of easily manageable steps. The initial problems to be examined are of a general nature, and the work is in the same tradition as a great deal of experimentation in the late 1950's on microwave tube beams. We hope that the techniques can later be developed to help answer more specific questions pertaining to heavy ion fusion schemes.

9. Acknowledgement.

We look forward to the future participation of I. Haber of NRL in this program. The first calculations on the structure of a spreading beam are underway.

10. References.

1. M. Reiser, W. Namkung, and M. A. Brennan, IEEE Trans. Nucl. Sci. 26, 3026 (1979).

2. L. J. Laslett and Lloyd Smith, as above, p. 3080.

3. I. Haber, NRL Memorandum Report 3705 (Jan. 1978) and I. Haber and A. W. Maschke, NRL Memorandum Report 3787 (May 1978).

4. J. D. Lawson, J. of Electronics and Control 1, 43 (1955).

5. G. R. Brewer, J. Appl. Phys. 30, 1022 (1959).

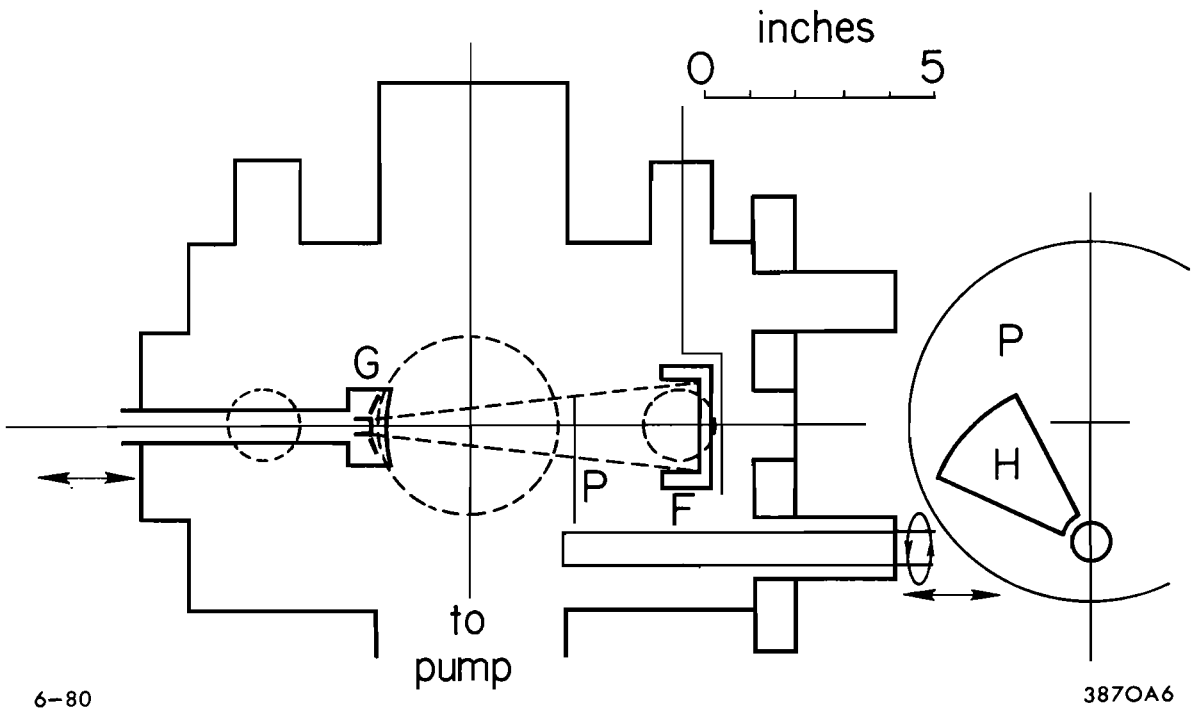

Fig. 1 Schematic plan diagram of first stage of apparatus, showing horizontal and vertical access ports (dotted circles). G = gun, P = paddle, H = pinhole, F = Faraday cup. The theoretical beam spreading curve for a 7.5 kV, 0.4 amp beam is shown ($K = 9.3 \times 10^{-3}$, $\varepsilon = 0$).

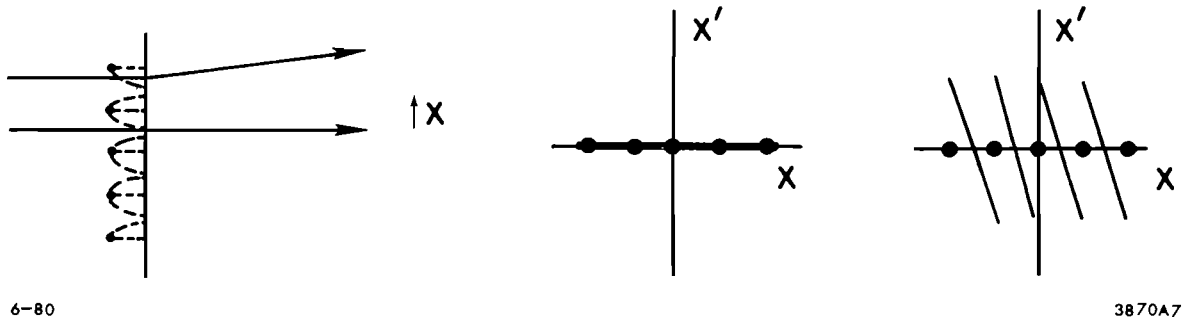

Fig. 2 Deflecting grid, showing xx' plane emittance before and after grid.

EMITTANCE GROWTH IN RF LINACS*

R. A. Jameson
Accelerator Technology Division
Los Alamos Scientific Laboratory
Los Alamos, NM 87545

ABSTRACT

As the space-charge limit is approached, the current that can be accelerated in an rf linac and the output emittance that can be expected are discussed. The role of the envelope equations to estimate limits is outlined. The results of numerical experiments to explore general properties of emittance growth are given.

In the study of beam motions through accelerator structures, the useful analytical expressions obtained from the transverse and longitudinal envelope equations give information on the effects of parameter changes over wide ranges. The effect of current is included using a linearized treatment of the space-charge forces from an ellipsoidal uniformly charged beam bunch. Steady-state emittance is included, allowing matched parameters to be calculated which provide quite good results in numerical simulations. The current limits found from the envelope equations have been found to agree well with the saturated output current obtained in computer runs, which also show that a great deal of the input current is lost before saturation is reached. As the current saturates, the output emittance also grows to a level defined by the machine acceptance. This emittance limit, found from the computer code at the onset of saturation, is found to agree well with the emittance calculated using the envelope equation at a tune shift of $\sigma/\sigma_0 = 0.4$.

The envelope equations will not, however, account for the emittance growth due to nonlinear forces seen in all real machines, and there is no theory at present for these effects. Emittance growth occurs from nonlinearities in the rf gaps, space-charge forces, and coupling effects, and would have to be analyzed as a transient problem. A detailed theory is probably impossible, and one in convenient form even less probable, but it would be very useful to have

*Work performed under the auspices of the U. S. Department of Energy.

a crude theory which would allow prediction of the size and rate of emittance growth under different parameter conditions.

Lacking any theoretical base for calculating emittance growth, except at the saturated limit, our understanding at this point comes from numerical experiments, and to a much smaller extent, from actual machines. Emittance growth is observed in all operating linacs, but production demands generally preclude machine development. It is clear that future high-performance accelerator development, such as for HIF, will require an understanding of these effects and therefore will also require accelerator experiments to be conducted--an exciting prospect.

Computer codes for linear accelerator beam dynamics have been extensively developed for over twenty years. The PARMILA code, used at LASL, LBL, and numerous other places, is the most complete and versatile code in the U. S. It can treat any type of particle in several kinds of accelerator structure, including the Alvarez, Wideröe, and RFQ. Input and output beam transport lines, including bunchers, can be handled. The code is fully six-dimensional, including nonlinear effects. Space charge can also be handled in 3-D, but present techniques are expensive, and most computations are done using a ring model on an r-z area-weighted mesh. Over the years, comparison of the code models to actual machine performance has been made whenever possible, including detailed analyses of measurement techniques. Several examples of exacting modeling studies have resulted in agreement with experimental results to a few percent. This work lends confidence to the use of the codes for detailed design work and for exploration of the causes and effects of beam characteristics such as emittance growth. The disadvantage of the numerical approach to basic studies is that the parameter space is large, making it difficult to infer general results.

Simulations (or numerical experiments) exploring the nature of emittance growth in rf linacs have been in progress at LASL for a number of years; results of some of the latest efforts were reported at the 1979 Linac Conference[1] and will be outlined below. The list of references from that paper is appended.[2-21]

The envelope equations can be expressed very compactly in terms of the phase advance per focusing period of the structure:

$$a^2 = \frac{(2n\beta\lambda)\varepsilon_t}{\sigma^t} \quad , \text{ and } \quad b^2 = \frac{(2n\beta\lambda)\varepsilon_\ell}{\sigma^\ell}$$

where a is the average beam radius over the focusing period, b is the beam bunch half-length, $(2n\beta\lambda)$ is the transverse focusing period length, ε_t and ε_ℓ are unnormalized transverse and longitudinal emittances, and σ^t, σ^ℓ are the transverse and longitudinal phase advances per transverse focusing period. We therefore decided to study emittance growth as a function of phase advance. We wanted to be able to measure the average phase advance of the particles in arbitrarily shaped bunches, as well as individual particle phase advances in the frame of the average. We also wanted to generate linacs having prescribed phase advances in both transverse and longitudinal, for arbitrary bunches. This is done using iterative, nonlinear least-squares techniques.

We have made two major sets of runs so far--both with n = 1 and $\varepsilon_t \sim \varepsilon_\ell/5$, and differing in that one set kept the accelerating gradient and synchronous phase constant at the value required to give the desired σ_0^ℓ at the first cell of each case, while the other set required the accelerating gradient to rise along the machine so that σ^ℓ was constant. The results were very similar in all qualitative aspects, the only real difference being more longitudinal emittance growth for the constant σ^ℓ case. We generated 7 linacs with zero-current phase advances of $\sigma_0^\ell \cong 42°$, and σ_0^t = 50,70,90,100,110,120, and 130°. The tune of each linac was depressed by adding current, maintaining matched conditions, and the emittance growth* observed, with the results shown in Fig. 1. For each initial condition (points on the abscissa in Figs. 1a and 1b), current was added until the longitudinal stability limit was approached. The resulting traces in Fig. 1 show the emittance growth as the tune was depressed For the $\sigma_0^t = 50°$ case, we then raised the electric field to keep some longitudinal focusing, and raised the current further (open circles, Fig. 1). The longitudinal emittance growth is shown in Figs. 1c and 1d for all the transverse cases. These studies were done with short 20-cell FDFD Alvarez linacs. No particles were lost on any of the runs. Future work will address asymptotic behavior and other aspects.

We found a violent effect on the transverse (but not longitudinal) emittance in the linacs with $\sigma_0^t > 90°$, which appears to be analogous to the envelope instabilities studied in detail by Smith, Laslett and others for K-V beams in transport systems.[4-7] This is discussed further in the Conference paper--zero-current tunes above 90° should clearly be avoided.

*Total effective emittance is found by fitting ellipses with the rms emittance parameters through each particle and taking the largest.

Below $\sigma_0^t = 90°$, the transverse emittance growth behavior indicates a preference for smaller beam radius, as would be expected to minimize the longitudinal-transverse coupling effect in the rf gaps. The other main feature is that the growth begins to increase rapidly, in both transverse and longitudinal dimensions, as the tune is depressed to about $\sigma/\sigma_0 = 0.4$ and below. This is also evidenced in the numerical runs by increasing difficulty in finding the best

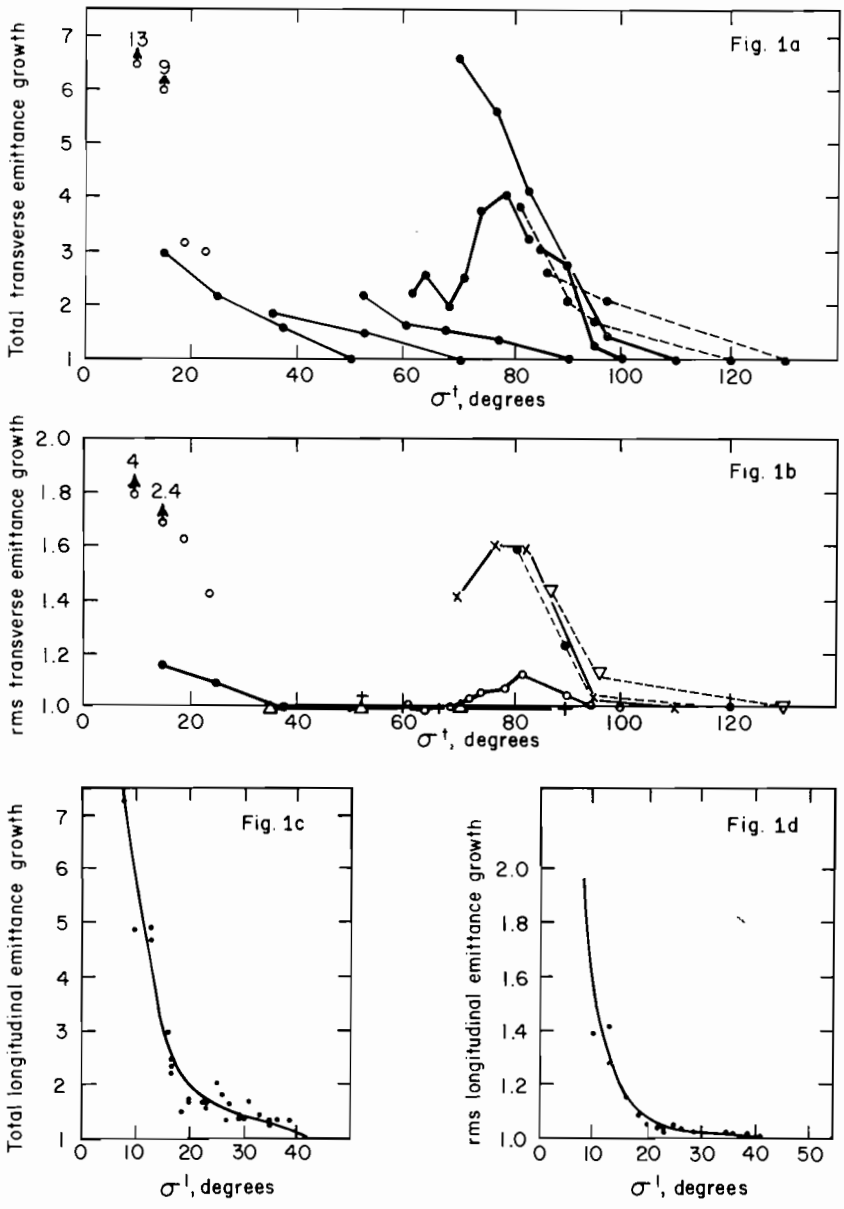

Fig. 1.
Emittance growth after 20 cells, as a function of tune shift from various initial zero-intensity phase advance per transverse focusing period.

input matching conditions to keep the beam matched in the machine. The effect of mismatching is discussed further below.

As the space-charge limit is approached, ($\sigma^t \to 0°$), we would start losing beam, as well as have the output emittance grow to the geometrically defined output limit. The growing sensitivity to matching will compound the problem. This evidence causes us to be suspicious of designs which claim operation "near the space-charge limit." This may be a matter of clarifying the definitions being used in each case - some are apparently unconcerned with beam loss and may be able to tolerate the resulting saturated output emittance. Others may use $\sigma/\sigma_0 = 0.4$ as their "space-charge limit." It does appear that by backing off on the current per channel, and/or by control of the frequency transition points in a funneled design for HIF, emittance can be kept in bounds. We need, however, to explore asymptotic behavior and the effects of frequency transitions in detail.

Since practical parameter choices for applications commonly result in $\sigma^\ell < \sigma^t$, we made a preliminary search for resonances of the $2\sigma^t = n\sigma^\ell$ type. Keeping $\sigma^t = 50°$, E_0/β was adjusted for constant σ^ℓ with n from 2 to 8. No differences in emittance growth were seen out to 60 cells, which is beyond the point to which the E_0 ramp could practically be sustained.

In considering other preliminary slices of the parameter space, we looked at some $\sigma^t/\sigma_0{}^t = 0.75$ cases in which the transverse emittance was reduced by another factor of 6 ($\varepsilon_t \sim \varepsilon_\ell/30$). Somewhat more transverse and less longitudinal growth was observed. Such transfers are commonly observed. In this case, far from the space-charge limit, the added growth was not large. The ratio of emittances is undoubtedly an important parameter, and may suggest multidimensional matching with equal emittances, especially if the parameters change along the machine.

We changed the frequency by a factor of five in each direction, keeping $a/\beta\lambda$, $b/\beta\lambda$, ϕ_s and injection energy constant, changing the accelerating gradient to keep $\sigma_o{}^\ell$ at 42° and changing σ_t to keep $a/\beta\lambda$ constant. This scaling reproduced Fig. 1 very closely.

We reran the $\sigma_o{}^t = 100°$ cases (which exhibited the instability in Fig. 1a) for input distributions uniform in 6-D, and Gaussian in 6-D (truncated at 3σ), keeping the rms emittances constant. The quadrupole strengths were those used to achieve a constant phase advance for the original distribution, approximately uniform in real space. The 6-D distributions grew more rapidly in the first two

to three cells. From Cells 3-20 the growth in total emittance was very similar, but the rms growth for the 6-D cases was about double that of the 3-D case. The 6-D cases became somewhat mismatched as the beam progressed through the cells. We could reset the quads for each particular distribution; we expect that this would smooth but not necessarily reduce the growth--it may in fact increase (see below). The unstable mode evidenced in Fig. 1 is thus not the result of a particular particle distribution. Similar general influences of the distribution have also been observed for other choices of parameters. Figure 2 shows a typical redistribution of emittance. We conclude that the shape of the distribution does influence emittance growth, with greater effect as the beam brightness is increased, and with greater growth as the central density is increased.

Mismatched beams will be smeared by the action of nonlinear space-charge forces and eventually will assume an emittance congruent with the machine acceptance. Figure 3 demonstrates how emittance growth is affected by mismatching the input beam size up to a factor of $\sqrt{2}$ at injection, for the range of linac parameters we have been discussing. (Note that these cases have constant accelerating voltage gradient, E_0, rather than constant σ_0^{ℓ} as in Figs. 1 and 5.) At a given σ_0^{t}, the sensitivity to matching becomes more pronounced as the tune is depressed. As σ_0^{t} increases, the sensitivity for a given tune depression increases, an effect of the alternating gradient. The smaller absolute size of the beam (in one dimension) also becomes more important in terms of the required measurement resolution. For K-V beams, a "mismatching" instability mode has been identified[5] for $\sigma_0^{t} > 90°$; its analog for these distributions may be a factor here.

In the vicinity of the unstable mode, the behavior becomes somewhat unpredictable. For the parameters in Fig. 3, the betatron oscillations generally subjected the beam to a lower average μ_t (higher σ^t) over the 20 cells, sometimes resulting in less growth. The $\sigma^t/\sigma_0^{\ t} = 70°/110°$ case is particularly dramatic in this respect. The changes in transverse emittance growth from mismatching are generally rather uniform with respect to the shape of the distribution function, as shown in Fig. 4, or sometimes show more growth for higher percentages.

We then considered off-axis beams. For a single gap without space charge, Crandall[11] showed that the increase in total emittance is proportional to $(a^2 + d^2)$ if $|d| \leqslant a$, and $2da$ if $|d| \geqslant a$, where a is the half-width of the beam and d is the displacement of the beam center from the axis. The increase in rms emittance is proportional to $(1 + d^2/\overline{a^2})$, where $\overline{a^2}$ denotes the mean square

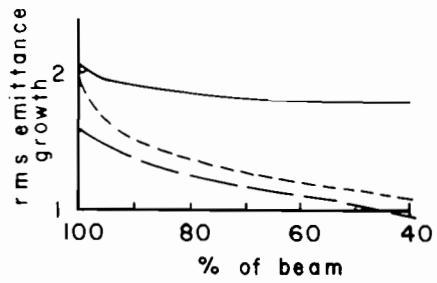

Fig. 2.
Typical variation in rms transverse emittance growth with input distribution.
—— —— Uniform in 3-D real space
------- Uniform in 4-D transverse space, separate 2-D longitudinal
——— Gaussian in real space, truncated at 3σ

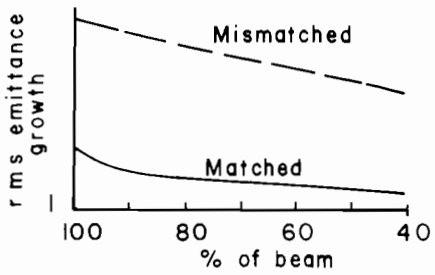

Fig. 4.
Typical redistribution of transverse emittance growth for mismatched beams.

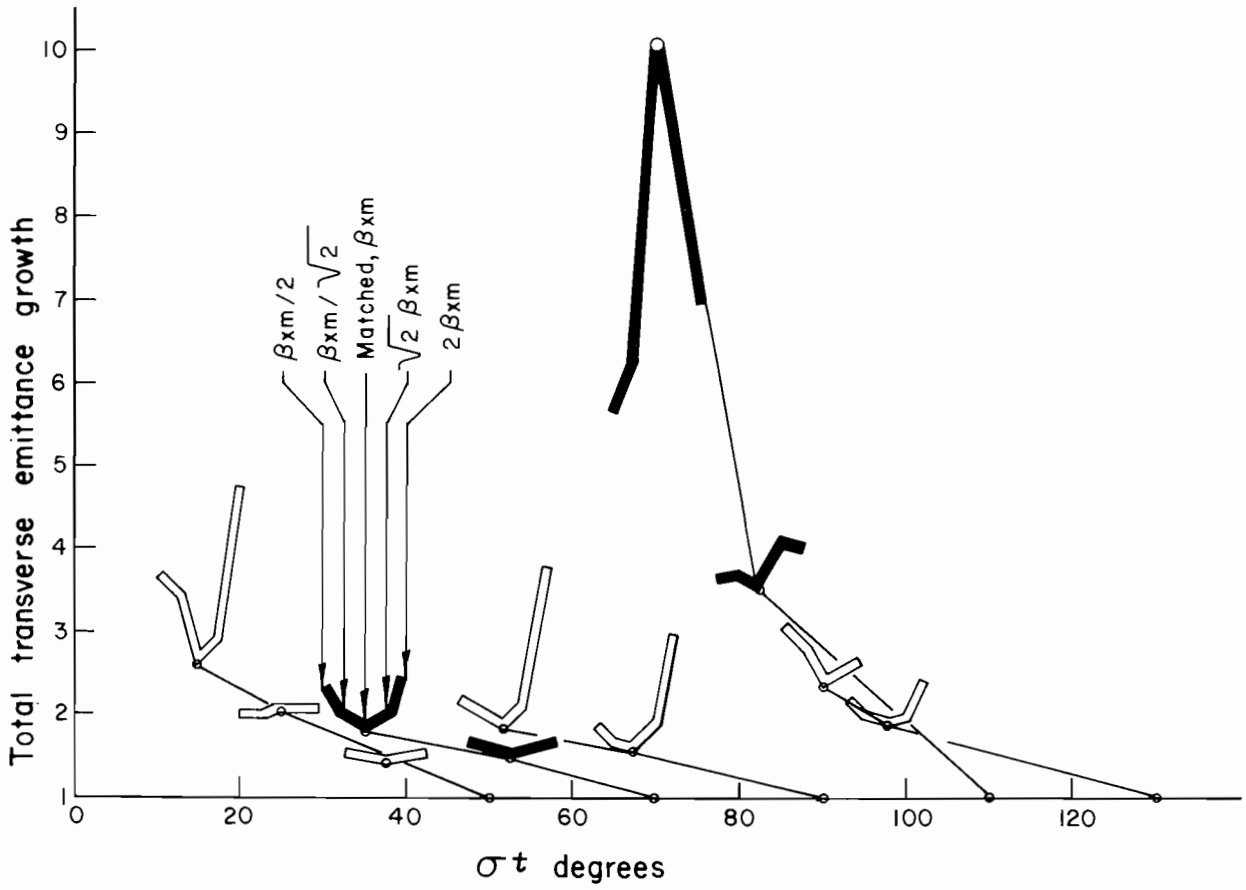

Fig. 3.
Sensitivity of transverse emittance growth to input matching. Linac has constant accelerating gradient E_0. At each tune, the smaller dimension of the input beam is varied by changing the input matching-ellipse parameter β by $\pm\sqrt{2}$ and ±2. The y and z inputs are matched. Growth is shown after 20 cells.

half-width of the beam. It is seen that the rms emittance grows relatively faster than the total emittance. The growth over n gaps will depend on what happens to the relative sizes of a and d. Figure 5 shows the emittance growths for (x-off-set/average input-beam radius) = 1.0 for five of the cases of Fig. 1. Again the sensitivity increases for larger tune depressions and for higher σ_0^t.

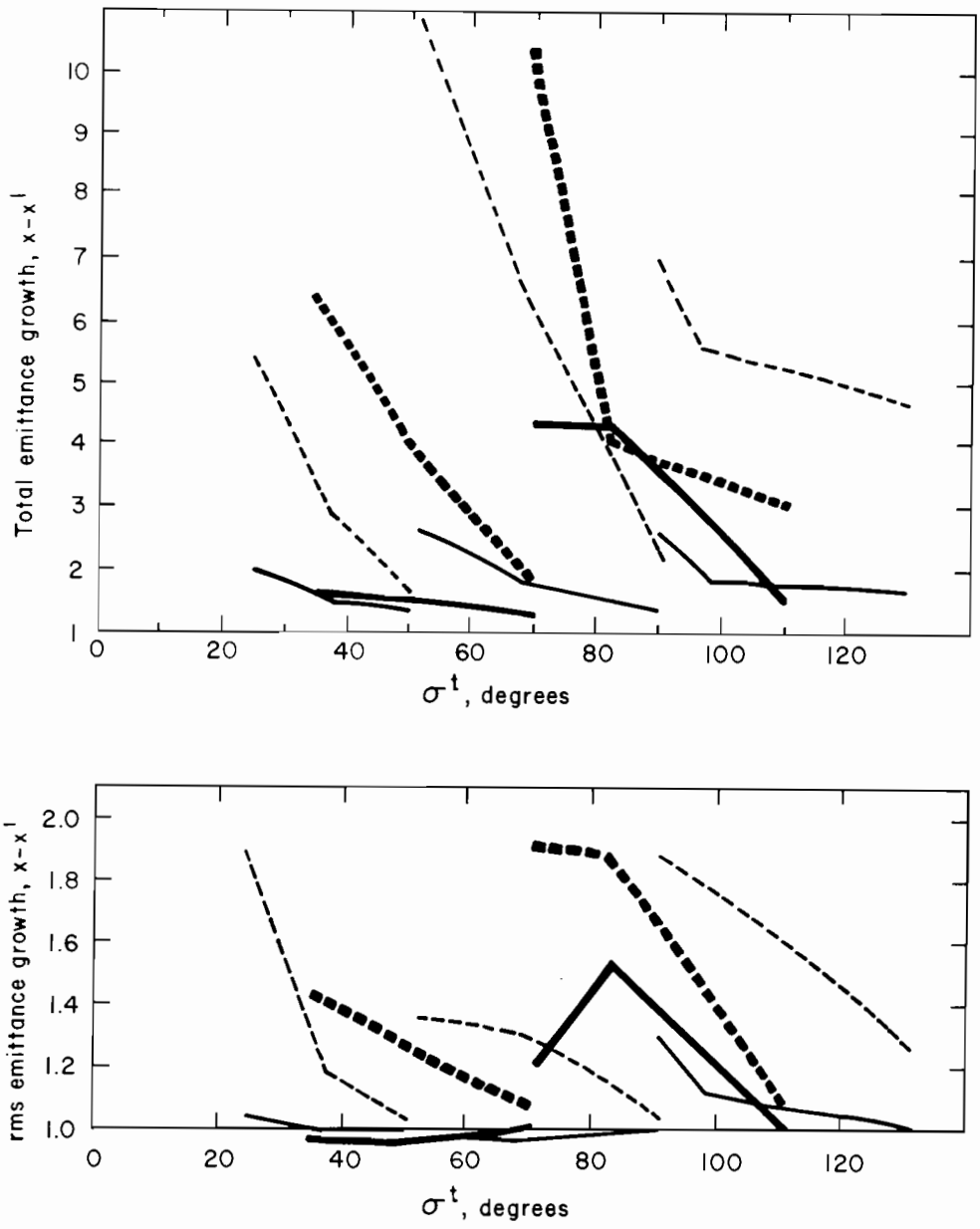

Fig. 5.
Sensitivity of transverse emittance growth, after 20 cells for 100% of beam, to horizontal offsets equal to the average input beam radius. Solid - no offset; Dashed - offset.

The interaction of off-axis beams with the envelope mode is complicated. The longitudinal emittance growth also is increased by the transverse oscillation. Figure 6 shows the typical redistribution that occurs in the transverse-phase space. This feature, and the contrasting signature of the mismatched beam, Fig. 4, can be valuable aids in machine tuning for detecting the presence of a centroid oscillation or mismatch.

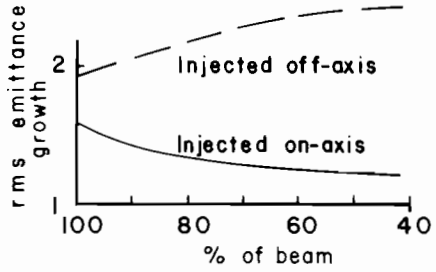

Fig. 6.
Typical redistribution of transverse emittance growth for missteered beams.

There are clearly many more things to be done. This initial work is encouraging in the sense that at least some scalings over wide ranges appear to produce the same emittance growth behavior. The effect of constraints on parameters as scaling is done must be investigated.

REFERENCES

1. R. A. Jameson and R. S. Mills, "On Emittance Growth in Linear Accelerators," 1979 Linac Conference, Montauk Point, Long Island.

2. R. Gluckstern, R. Chasman, K. Crandall, Proc. 1970 Linac Conference, Batavia, pp. 823-849.

3. R. Chasman, Proc. 1968 Proton Linac Conf., BNL, p. 372; Proc. 1969 Particle Accelerator Conf. (PAC), IEEE Trans. NS, June 1969, p. 202.

4. P. Lapostolle, Proc. 1971 PAC, IEEE Trans. NS N518 No. 3, p. 1101; various CERN reports, summarized in CERN-ISR/78-13.

5. L. J. Laslett, L. Smith, Proc. 1979 PAC, IEEE Trans NS, June 1979, p. 3080.

6. I. Hofmann, Proc. 1979 PAC, op. cit. p. 3083.

7. S. Penner, A. Galejs, Proc. 1979 PAC, op. cit. p. 3086.

8. I. Haber, Proc. 1979 PAC op. cit. p. 3090.

9. M. Reiser, Particle Accelerators, 1978, Vol. 8, pp. 167-182.

10. W. P. Lysenko, LASL Report LA-7010-MS, Oct 1977; and Proc. 1979 PAC op. cit. p. 3508.

11. K. R. Crandall, "Transverse Emittance Increase in an RF Gap," LASL Priv. Comm. MP-9, Jan. 12, 1978, and "Transverse Emittance Growth Due to a Sequence of RF Gaps," with R. S. Mills, LASL Priv. Comm. MP-9, Feb. 28, 1978.

12. R. A. Jameson, R. S. Mills, "Factors Affecting High-Current, Bright Linac Beams," April 8, 1977, LASL Priv. Comm.

13. J. W. Staples, R. A. Jameson, Proc. 1979 PAC, op. cit. p. 3698.

14. K. R. Crandall, R. H. Stokes and T. P. Wangler, "RF Quadrupole Beam Dynamics Design Studies," to be presented at 1979 Linear Accelerator Conference.

15. O. R. Sander, R. A. Jameson, R. D. Patton, Proc. 1979 PAC, op. cit. p. 3417.

16. K. R. Crandall, "Summary of 805-MHz Linac Length Corrections," LASL Priv. Comm., March 26, 1975.

17. R. A. Jameson, W. E. Jule, "Longitudinal Tuning of the LAMPF 201.25 MHz Linac without Space Charge," LA-6863, March 1978, LASL.

18. R. A. Jameson, "Emittance Growth in the New CERN Linac - Transverse Plane; Comparison Between Experimental Results and Computer Simulation," LASL Priv. Comm. AT-DO-377(U), Jan. 15, 1979.

19. O. R. Sander, G. N. Minerbo, R. A. Jameson, D. D. Chamberlin, "Beam Tomography in Two and Four Dimensions," Proc. this conference.

20. P. Channell, LASL, Priv. Comm.

21. A. Chabert, et al., Proc. 1979 PAC op. cit. p. 3612.

EMITTANCE STUDIES FOR HEAVY ION LINAC

BY

S. JORNA
R. JANDA

THIS EFFORT SUPPORTED BY
ARGONNE NATIONAL LABORATORY
UNDER CONTRACT 31-109-38-5049

PHYSICAL DYNAMICS, INC.
LA JOLLA, CA. 92038

1. Summary

Our three-dimensional linear accelerator code has been applied to calculate transverse and longitudinal phase space dilution for beams of Xe^+ ions carrying average currents in the 15 to 25 mA range. The calculations have been confined to a FOFODODO Wideroe structure operating in the π-3π mode generally with a gap voltage gradient of 5 MV/m; but we have also considered the effect on emittance growth of lowering the gap fields. The r.f. wavelength is 2400 cm, the synchronous phase is -32^o, and the quadrupole fill factor ranges from 50-60 percent. The quadrupole lengths are $\beta_s\lambda$ and the magnetic field gradient is varied with the synchronous particle momentum to keep $\int B'dz$ essentially constant. The magnitude of the field gradient is fixed by stability requirements. These then also set the maximum phase spread. Typical beam parameters are: normalized transverse emittance $\gamma\beta_s\varepsilon_t$ = 0.3mm mrad, longitudinal emittance 10^{-4} cm, $\beta_{initial}$ = 0.0061.

The code has usually been run for 160 particles distributed in the transverse phase-space as a K-V distribution. Provided the mesh for the space charge calculations is chosen carefully, this number appears to be entirely adequate for parametric studies. Once matched beam parameters have been found, a 1000-particle case is run, and one typically finds that the emittances are 20-25 percent below those for the 160-particle case. Our experience has been that very little further change results when more than 1000 particles are used. Collective modes which might render the beam unstable cannot be studied with such small particle numbers but they are probably not important here due to the phase mixing in the gaps.

With the focusing gradient and phase spread of the beam set by the stability conditions, the equilibrium beam radius, R, say, is then also determined (by the matching requirement). The calculations show that as a general rule the emittance increases rapidly in the first cell. The perveance

$K = 4.9 \times 10^{-10}\ I(A)/\beta^3$ for Xe^+ ions; I(A) is the current in amperes. Thus the beam is space charge dominated for the emittance considered here at I = 25 mA, $\beta = 0.0061$. The matched radius for a quadrupole gradient $g = 0.031/\beta$ KG/cm turns out to be about 2.4 cm and the transverse emittance grows rapidly by a factor of 3.7. Thereafter, the emittance continues to increase slowly due to a combination of the space charge forces, nonlinear transverse-longitudinal coupling in the gaps, and mismatch due to the finite bunch length. Scatterplots of the particle distribution in the phase spaces indicate that dilution takes place due to the latter effect, but it does not appear to be the dominant contribution.[2] This has been substantiated by code calculations in which the beam was given zero spread. For the 25 mA beam the normalized emittance for a final particle energy of 8.4 MeV increases by a factor of 8 for 100 percent of the particles and by about 6 for 80 percent of the particles. For 15 mA the initial matching radius is about 1.8 cm, and the emittance for a final energy of 8.4 MeV increases for 100 percent of the particles by a factor 5; for 90 percent of the particles the envelope radius is held to a little over 2 cm and the emittance increases by about 4.5. The gain in longitudinal emittance ranges from 3 for 15 mA to 4 for 25 mA.

We have also studied the extent to which emittance increase can be curtailed by lowering the gap fields. For a 25 mA beam, lowering the gap field from 5 to 4 MV/m results in a 20 percent reduction in transverse emittance growth for 80 percent of the particle number when the results are compared at a final particle energy of 7 MeV; from 5 to 2.5 MV/m the reduction is almost 50 percent. For 15 mA the corresponding reduction is about 15 percent in going from 5 to 4 MV/m. Also, 90 percent of the particles are contained with a 2 cm radius, and about 10 percent of the particles are lost from the

"bucket" because of the increased influence of the space charge. The 2 cm limit on the radial excursion does not mean that these results are recovered when particles reaching beyond 2 cm along the accelerator are discarded. This is because particles which are beyond 2 cm at one point will be within this radius further along. The case with a physical stop of a given radius will be considered separately.

The gap defocusing forces will also be reduced by operating with a smaller phase angle, although the space charge forces will then be increased for a given current due to the reduced phase spread, and the accelerator efficiency will suffer if the separatrix length is less than the spread allowed by the stability limits.

In the remainder of this report we discuss these matters in greater detail. Section 2 contains a description of the phenomena which limit the allowable parameter range for beam and accelerator. In Section 3 we present the emittance calculations for some typical beam parameters and the Wideroe structure mentioned above.

2. Constraints

There are two constraints on the length of the bunch. One is set by the separatrix length and is given approximately by the inequalities

$$(1 - S)\phi_s < (\phi - \phi_s) < -2(1 - S)\phi_s \quad ,$$

where S is the ratio of the defocusing space charge to the accelerating force:

$$S = M2\rho\beta_s\lambda/E \sin \phi_s \quad ,$$

where ρ is the space charge density in the bunch, E the r.f. amplitude of the accelerating field, λ its wavelength. The proportionality constant M, whose magnitude ranges from 0 to 1, is determined by the shape of the bunch.

The other is governed by the magnetic focusing stability limits determined by the condition that "μ" be real. For E_{gap} = 5 MV/m and a magnetic fill factor of 50 percent, these limits are for the Wideroe under discussion given by Figure 1 (in the absence of space charge). Here,

$$-\Delta = -0.001294\ E_{gap}(MV/m) \sin \phi \ ,$$

is the strength of the thin lens representing the gap field and g^2 is the square of the quadrupole gradient in kG/cm. The magnetic field gradient is chosen such that for $\phi = \phi_s$ the operating point lies at $\mu = \pi/2$. The maximum phase spread then follows from the range in ϕ which keeps $-\Delta$ between the cos $\mu = \pm 1$ lines. Because instability is due to overfocusing and space charge corresponds to reduced focusing, this should also be the stable regime for non-zero currents. For E_g = 5 MV/m, we find that a focusing gradient of 5.1 kG/cm is required, while for E_g = 4 MV/m this is reduced to 4.9 kG/cm. For the former case, the maximum range in ϕ is $\phi \simeq \phi_s \pm 18^o$ as ϕ ranges from -50^o to -13^o. The maximum phase spread $(\phi - \phi_s)m = (3/2)(1 - S)|\phi_s|$ imposes

the following relation between S and the current (λ = 2400 cm)

$$\frac{1}{4} \geq S(1 - S) \geq 0.049 \frac{I(mA)M}{a_x a_y E(MV/m)} ,$$

where the geometric factor is a function of S and set by the ratio of the mean transverse bunch dimension to its half-length. For $(a_x a_y)^{1/2}/(z - z_s)_m$ = 1.8, the maximum value of $S(1 - S)/M \simeq 0.4$ for $S \simeq 0.4$. Thus, the maximum transportable current $I_{max}(mA) \simeq 8.1 a_x a_y E(MV/m)$ or with $(z - z_s)_m$ = 0.7 cm $I_{max} \simeq 13$ mA for E = 1 MV/m. The maximum bunch length is set by ϕ_s and S.

If the transverse beam dimensions are greater than the bunch length, the optimum value of S is relatively constant at 0.4. Thus, the maximum theoretical bunch length set by these considerations is about 2.3 cm corresponding to ϕ ranging from -51.2^o to 6.4^o. The phase range permitted by the magnetic stability limits is within these limits, corresponding to a bunch length of about 1.5 cm. Thus, adopting $(z - z_s)$ = 0.7 cm would appear to be conservative.

To determine how stringent the current limit of 13 mA is requires a more precise determination of the space charge forces and the effect of applying acceleration only in the gaps. The actual transverse beam dimension will, of course, be determined by the matching conditions.

Rather than adopting the envelope equations to obtain the matched beam parameters, we have found it expeditious to start from the matched parameters for zero current (obtained from a separate matrix code) and then to increase the current while keeping the beam matched. One only needs to use a few particles and run the code out to a few periods, paying particular attention to the symmetry points. This has the advantage over the envelope equation approach that a K-V distribution need not be assumed and the emittance is not assumed constant. Convergence to the desired optimum parameters is fast so

that automating this search is a practical possibility. In the occasional event that this process becomes tedious, a matrix code is used with space charge and gap defocusing forces represented by delta functions in the gaps. The changing values for β are predetermined in this case.

3. Results

To reiterate, most of our calculations have been run for the following parameters: particle number: 160; initial β: 0.0061; input normalized emittance: 0.32 mm mrad; bunch length: 1.4 cm; initial velocity dispersion: 1 percent; magnetic fill factor: 50 percent; synchronous phase: -32^{o}; magnet arrangement: ++--; accelerating mode: π-3π; gap length: 0.2 $\beta\lambda$.

The injection point has for simplicity been chosen halfway between the x-focusing magnets: the phase-space ellipses are upright here and x and y have extremal values.

To ensure that no spurious emittance growth is generated, a matched beam was passed through the accelerator at zero current. The matching parameters were obtained from a separate matrix code in which the gap acceleration was simulated by thin lenses in the middle of the gaps. The results show that the equations and the difference scheme clearly preserve the normalized emittance.

Unless otherwise stated, the emittances referred to in this paper are normalized r.m.s. values calculated from the relations

$$\varepsilon_x = \beta \left\{ \overline{x^2}\ \overline{x'^2} - \overline{xx'}^2 \right\}^{1/2}, \quad \varepsilon_y = \beta \left\{ \overline{y^2}\ \overline{y'^2} - \overline{-yy'}^2 \right\}^{1/2},$$

$$\varepsilon_z = \left\{ \overline{(z - z_s)^2}\ \overline{(\beta - \beta_s)^2} - \overline{(z - z_s)\ (\beta - \beta_s)}^2 \right\}^{1/2}.$$

These quantities are exactly preserved in linear systems. They have the further advantage of allowing in an r.m.s. sense for non-uniform distribution. The normalizing factor of 1/4 for the K-V distribution assumed here should be kept in mind when comparing absolute values for the emittance with those obtained from uncorrelated distributions. Also, although for 100 percent

transmission our calculated emittances are just those usually referred to as r.m.s. emittance, the emittances for smaller fractions of the beam are determined with reference to a circular hole transmitting a particular percentage of the total number of particles in the beam. To avoid confusion in comparing our results with other calculations these quantities might be more appropriately referred to as transmitted emittances.

Results for I = 15 mA and 25 mA are given in Figures 2 and 3. The curves represent 60, 70, 80 and 100% of total particle numbers, a fifth curve represents 90%. In the legend on each figure, I represents the current (in Amp); x, xp, y and yp represent the input values for the transverse beam dimensions and the envelope gradients (in cgs units). The quantity AL1 is a measure of the magnet fill factor, g is the initial guadrupole gradient in kG/cm, and

$$CCS = 2eE_{gap} \cos \phi_s / Am_1 c^2$$

$$= 1.38 \times 10^{-7} E_{gap}(MV/m) \text{ for } Xe^+ \quad .$$

Since ε_x and ε_y remain about equal, we give only plots of their geometric mean. The scales are compatible with the accuracy of these calculations.

It will be noted that if the beam envelope radius is to be kept below 2 cm, 20 percent of the particles will be lost for I = 25 mA, while almost 90 percent will pass for 15 mA. A physical stop will be imposed later; we examine first the idealized case. The emittance increase is also substantially less for the lower current (cf., Figure 5). As we have already noted, much of the emittance adjustment occurs in the first period ($\sim$120 cm) with a continually decreasing rate of increase thereafter. There should therefore be little emittance increase in the second and third tanks if the matching can be preserved.

Emittance is only a crude indication of beam quality and a better representation can be obtained from a scatter plot giving the distributions of the macro-particles in phase space and real space. An example is Figure 4 for I = 25 mA and 320 particles. This case corresponds closely to that of Figure 3, except that a slightly smaller value of Y was used. The quantity z on these graphs is the distance along the accelerator. It is particularly interesting to note the progressive deterioration of the beam in the x - x' and y - y' phase-spaces, and the emittance dilution at z = 695.3 cm represented by the appearance of four wings is apparent. It is also clear that beam match cannot be maintained.[2]

Since the defocusing effect of the gaps is reduced by lowering the gap fields, and since the beam is then also handled more gently, one might expect reduced beam quality deterioration as a result. Another benefit is the reduced quadrupole gradients, which we have again determined from Figure 1. In Figure 5 we have plotted the variation of the ratio of final emittance to input emittance at a particlar final particle energy (7 MeV) with beam current. The curves for 80 percent of the particles are most representative as they discount the disproportionate contribution from a few particles. Results are given for gap fields of 5, 4 MV/m, and 2.5 MV/m. In the current range 15-25 mA, the relative emittance varies linearly with current. The proportionality constant ranges from 0.17 for a gap field of 5 MV/m to 0.023 for a gap field of 2.5 MV/m. In the latter case, therefore, the emittance gain is relatively independent of current.

In practice, the transverse excursions of the particles are limited by the bore size and the beam must be matched to the LINAC acceptance. To simulate this constraint, we have imposed an upper limit on the radius of

the beam, dropping particles if they exceed this value. An example is Figure 6 for which the initial current is 25 mA and the gap fields ≃ 2.5 MV/m. The radial cutoff is 2.5 cm and the curves indicate the axial positions at which particles are dropped. About 15 percent of the particles are lost. These include the losses from the "bucket." The increase in bunch length due to straggling particles is evident in Figure 6b. Thus, the transmitted current is about 20 mA for this case of gentle acceleration.

As the current is increased beyond 25 mA, there will come a point where a larger percentage is lost because the increase in the "bucket" size along the accelerator does not keep up with the spread due to longitudinal forces. The advantage of a larger separatrix fill factor would then be lost. Where this occurs depends on the initial distribution and to some extent on the details of the accelerating structure. These results indicate that it may be worthwhile to run at currents higher than the theoretical maximum and to use gradually increasing voltages in the first few gaps.

REFERENCES

1. T. Khoe, private communication.

2. J. W. Staples and R. A. Jameson, 1979 Particle Accelerator Conference NS26 No. 3 (San Francisco, March 1979).

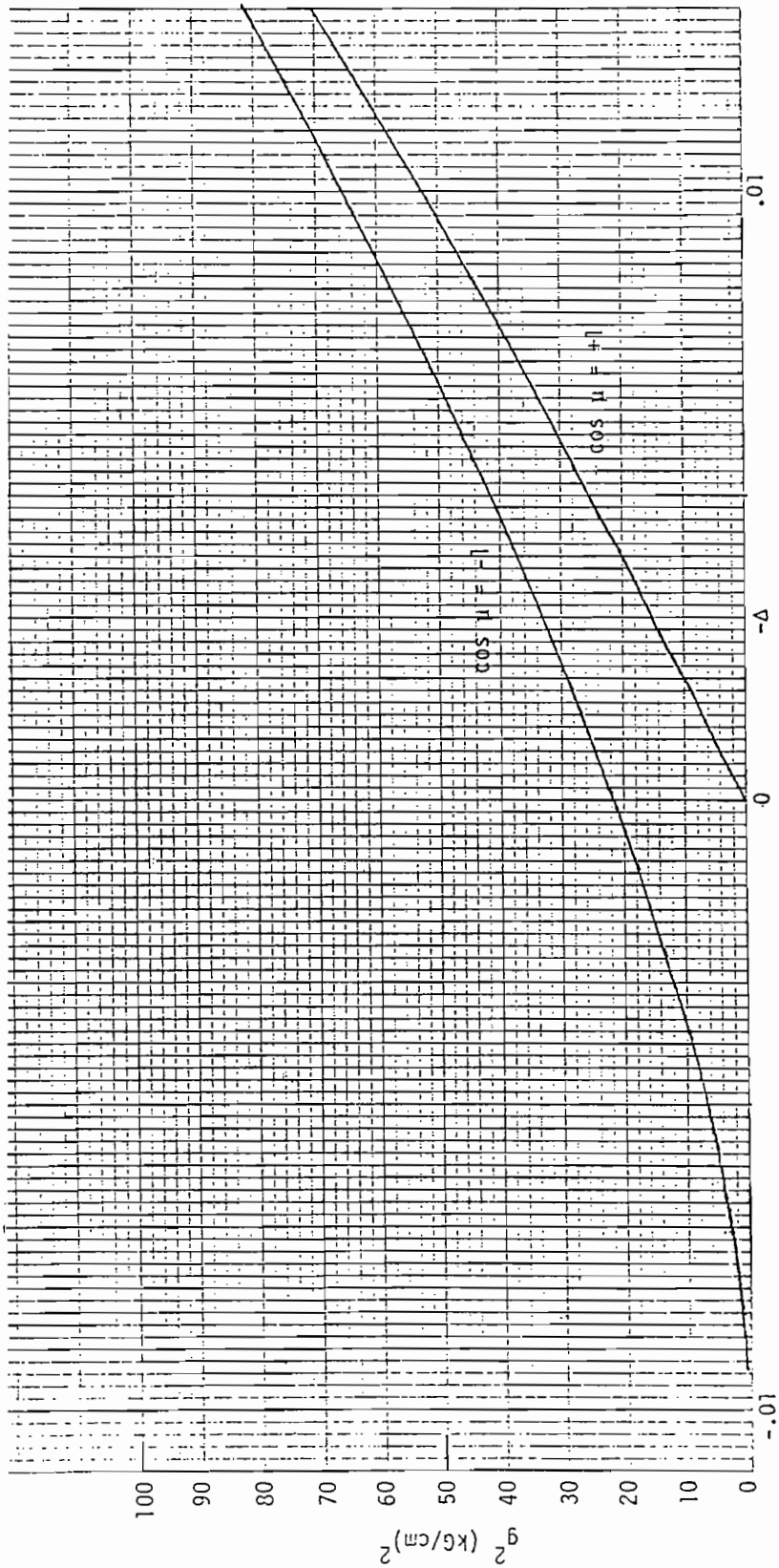

Figure 1. Magnetic Stability Limits for ++-- Geometry.

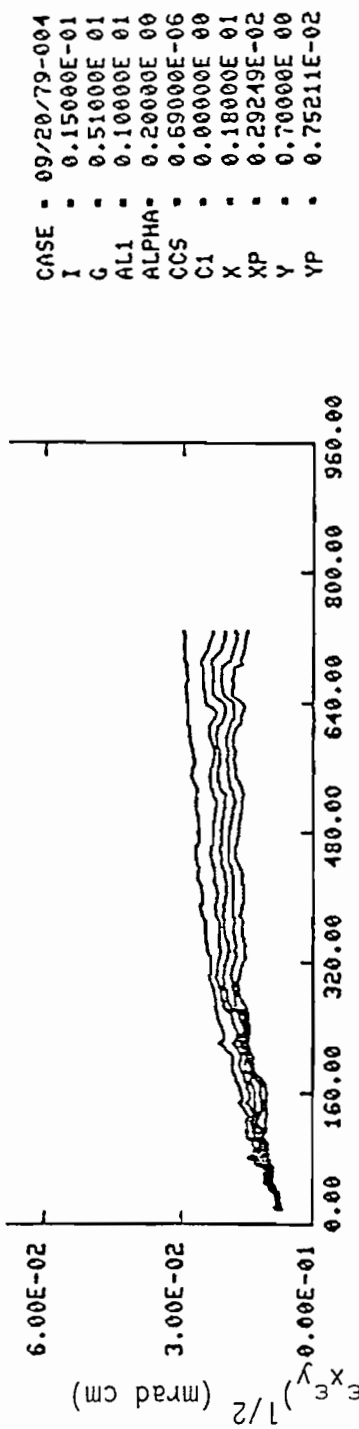

Figure 2a. Mean Transverse Emittance

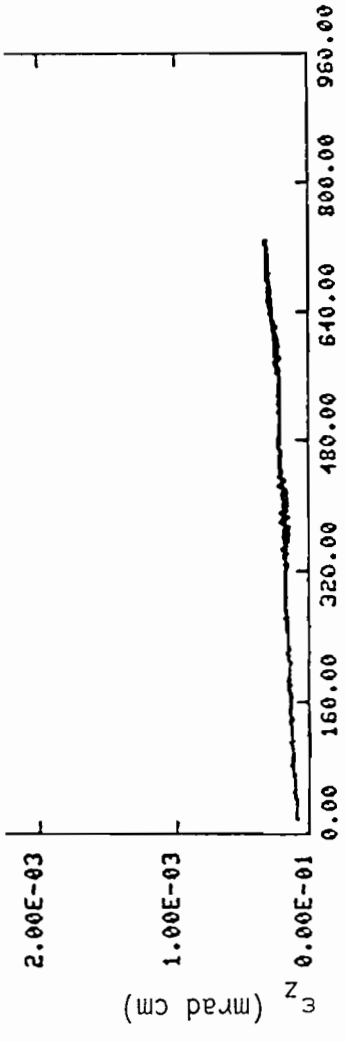

Figure 2b. Longitudinal Emittance

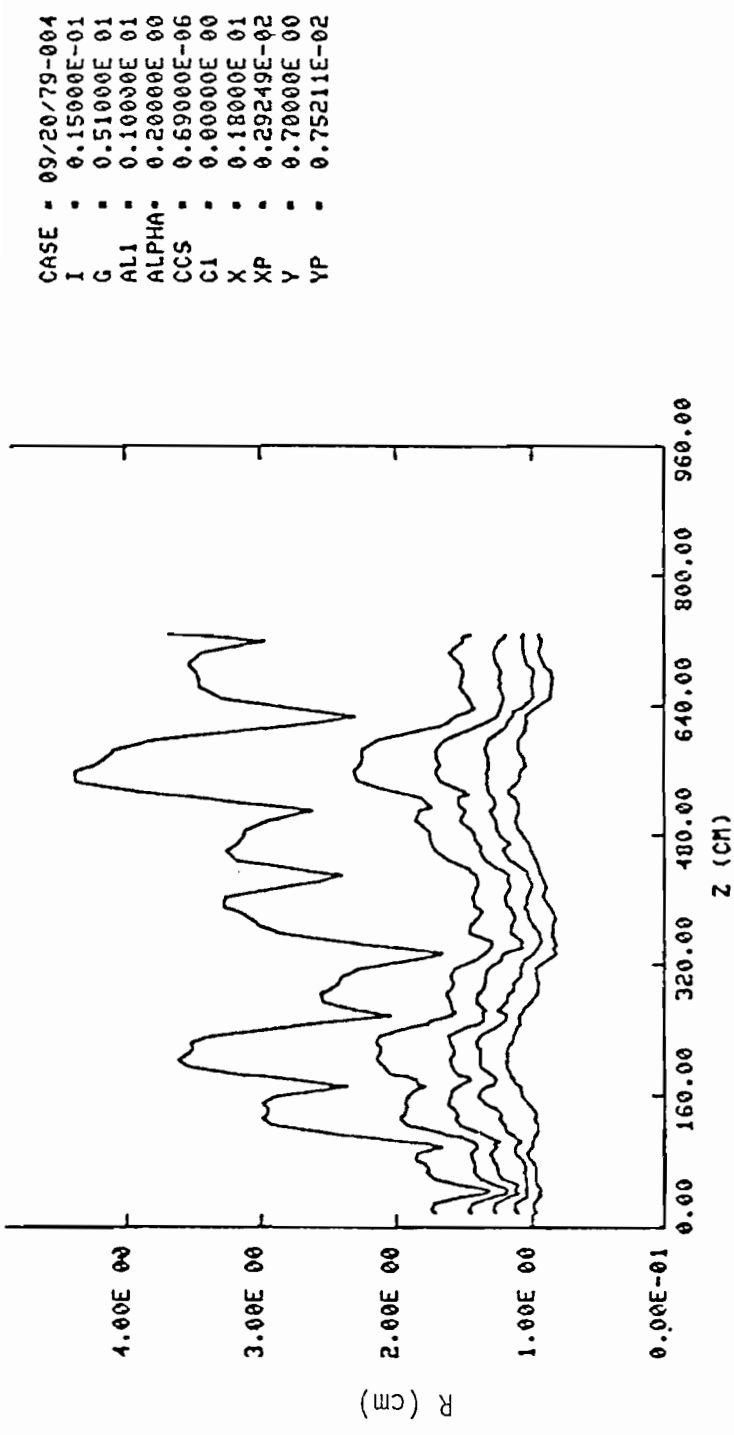

Figure 2c. Beam Radius

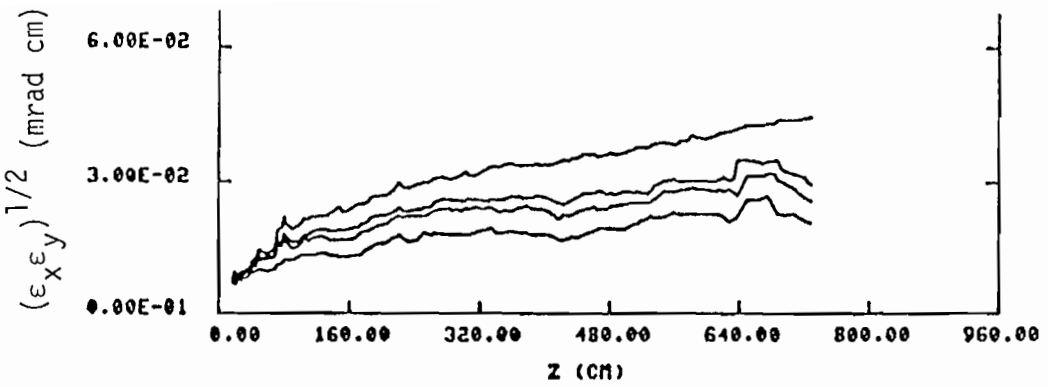

CASE = 09/12/79-004
I = 0.25000E-01
G = 0.51000E 01
AL1 = 0.10000E 01
ALPHA = 0.20000E 00
CCS = 0.69000E-06
C1 = 0.00000E 00
X = 0.21950E 01
XP = 0.23985E-02
Y = 0.93705E 00
YP = 0.56187E-02

Figure 3a. Mean Transverse Emittance

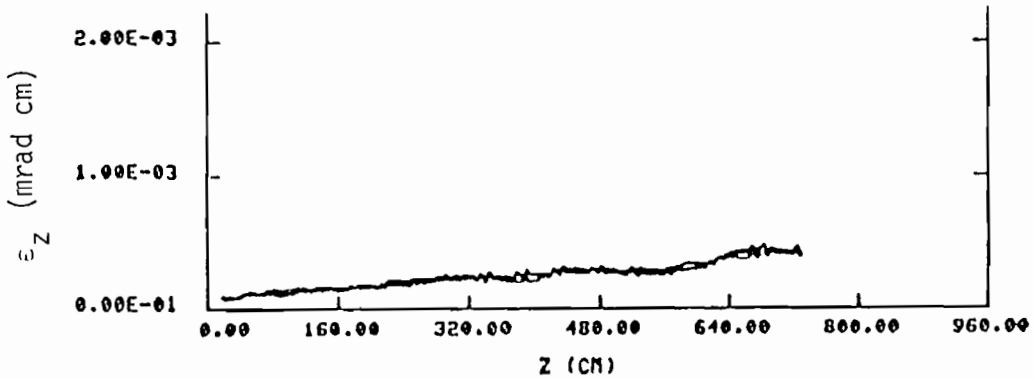

Figure 3b. Longitudinal Emittance

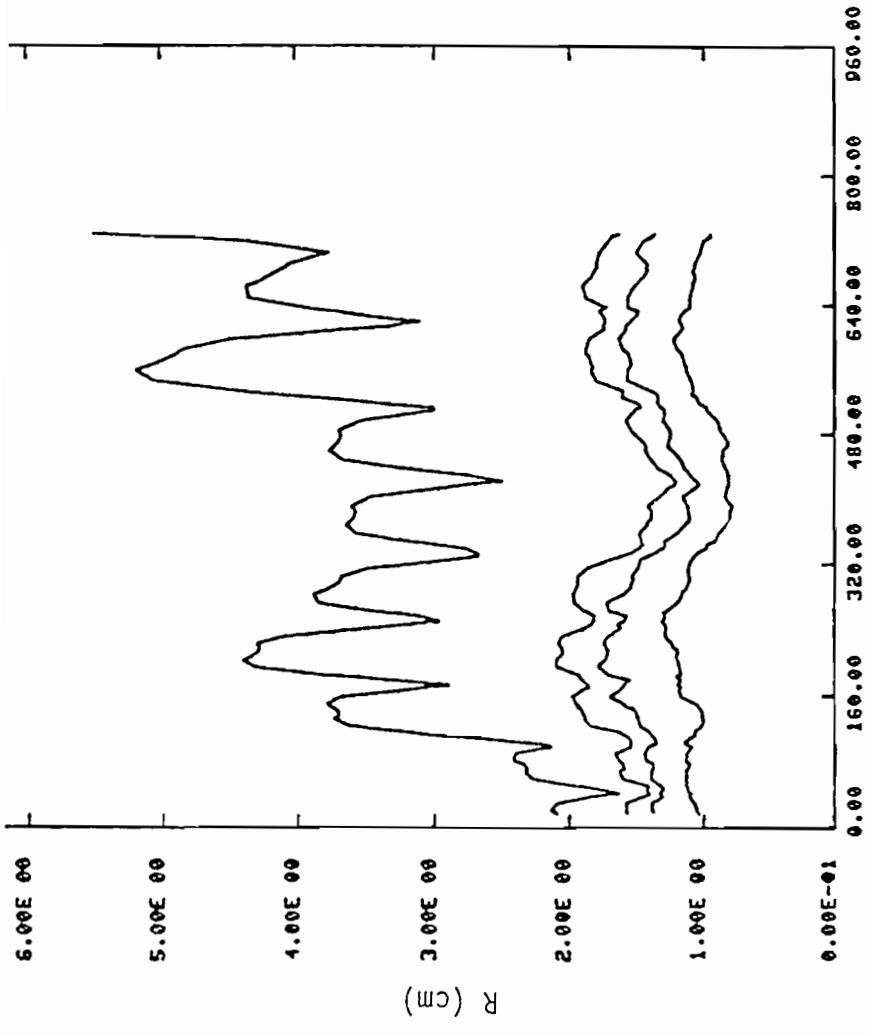

Figure 3c. Beam Radius

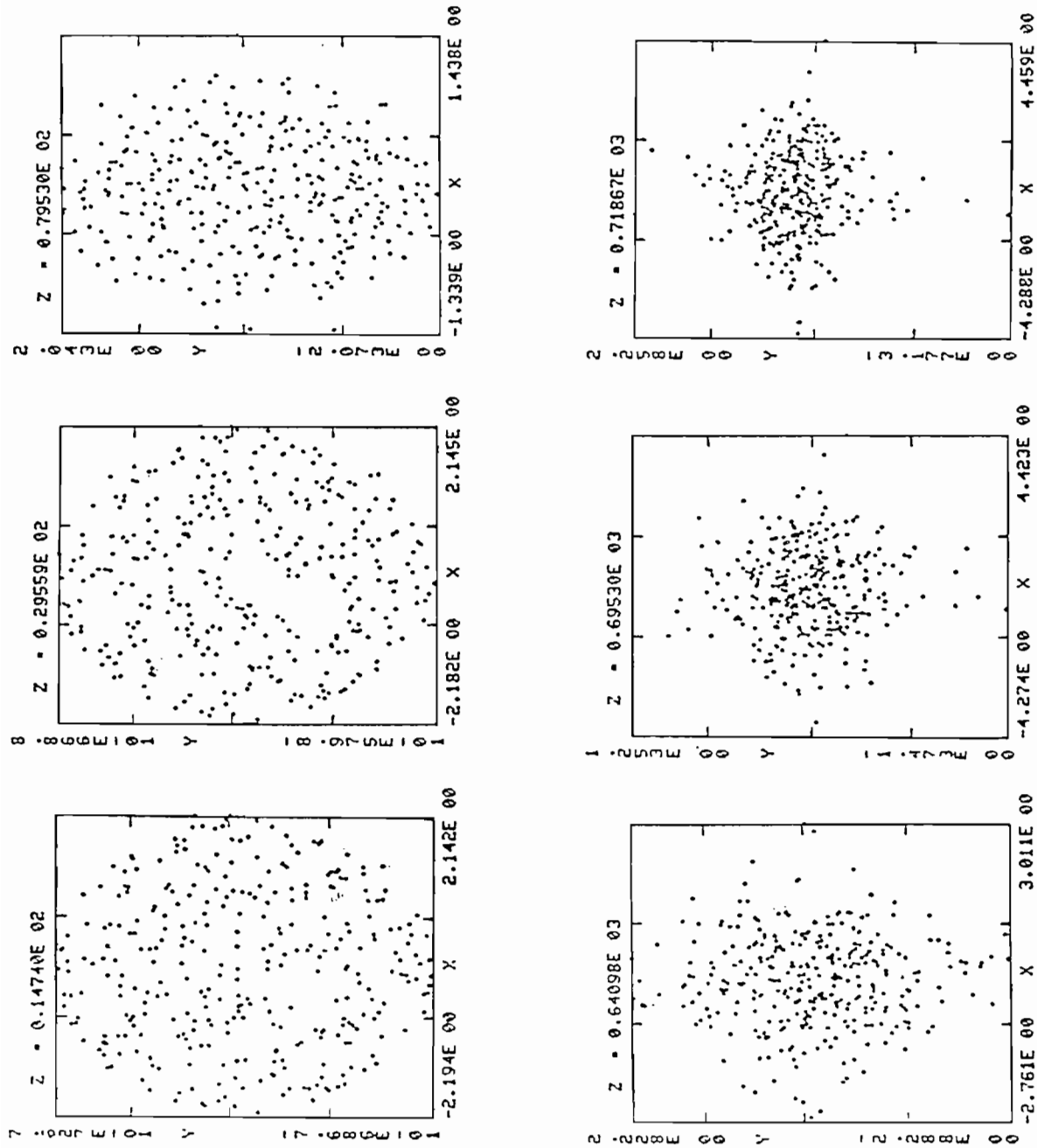

Figure 4.1. Space (x-y) Particle Distribution

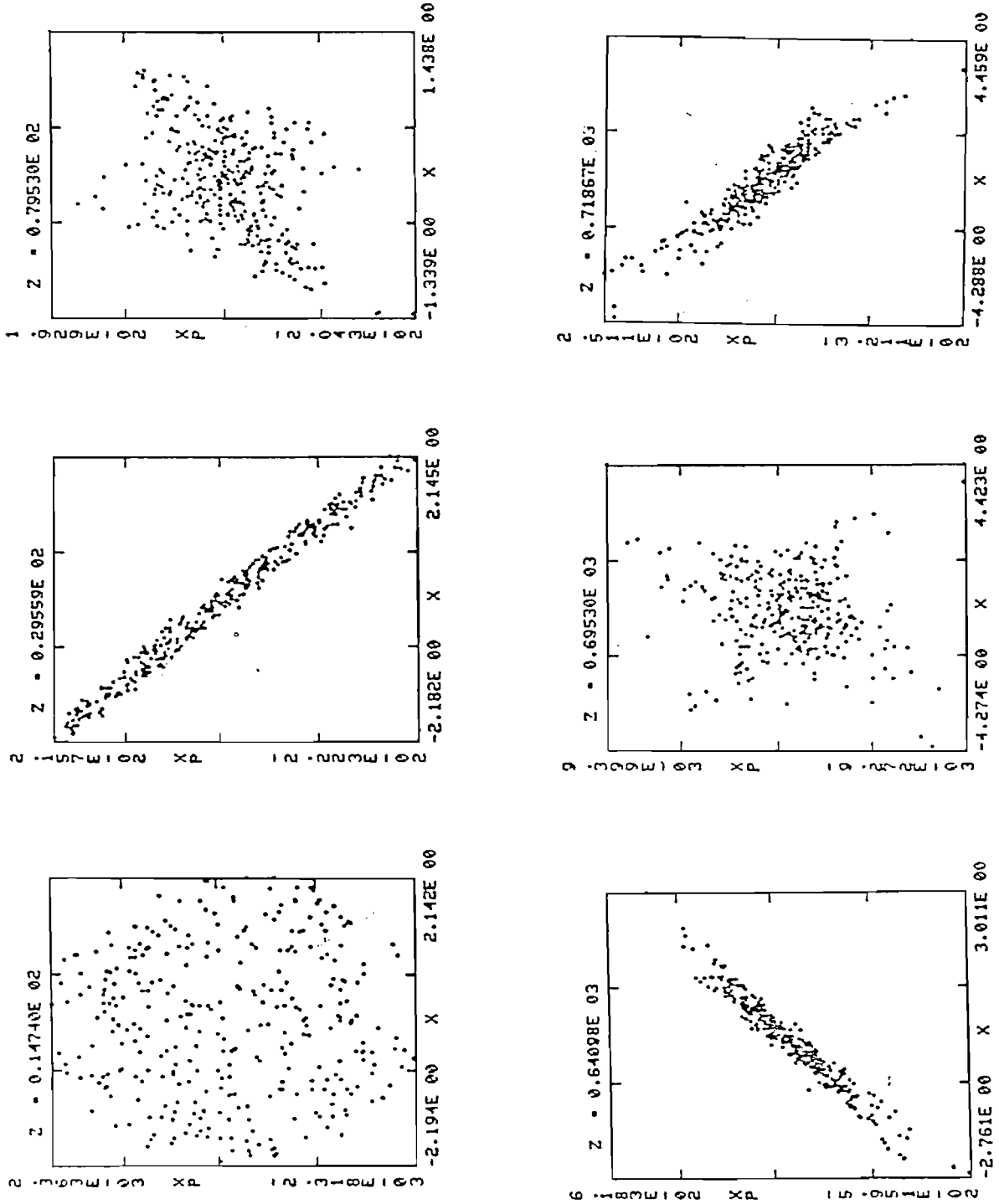

Figure 4.2. Phase-Space (x-xp) Particle Distribution

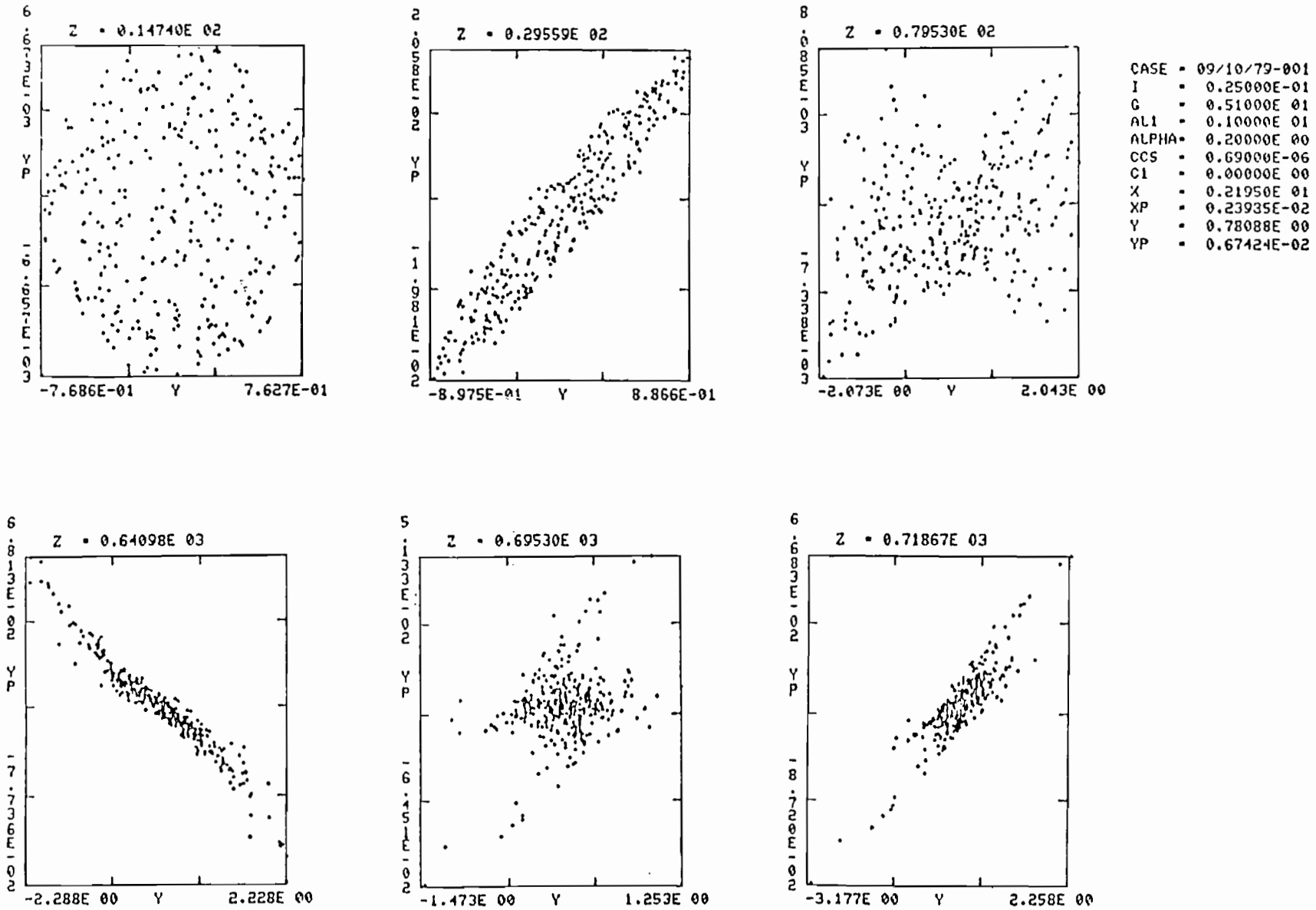

Figure 4.3. Phase-Space (y-yp) Particle Distribution

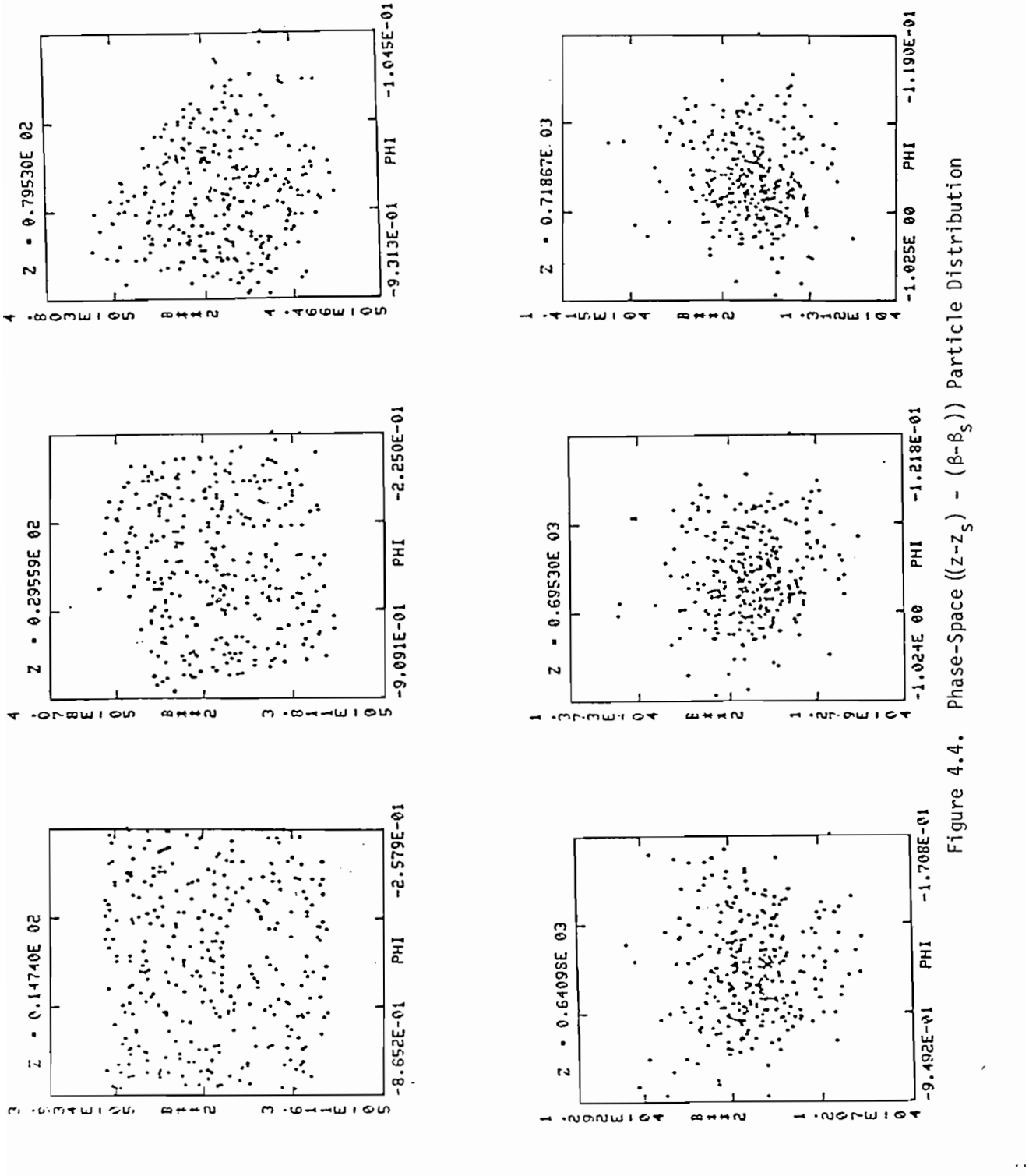

Figure 4.4. Phase-Space $((z-z_s) - (\beta-\beta_s))$ Particle Distribution

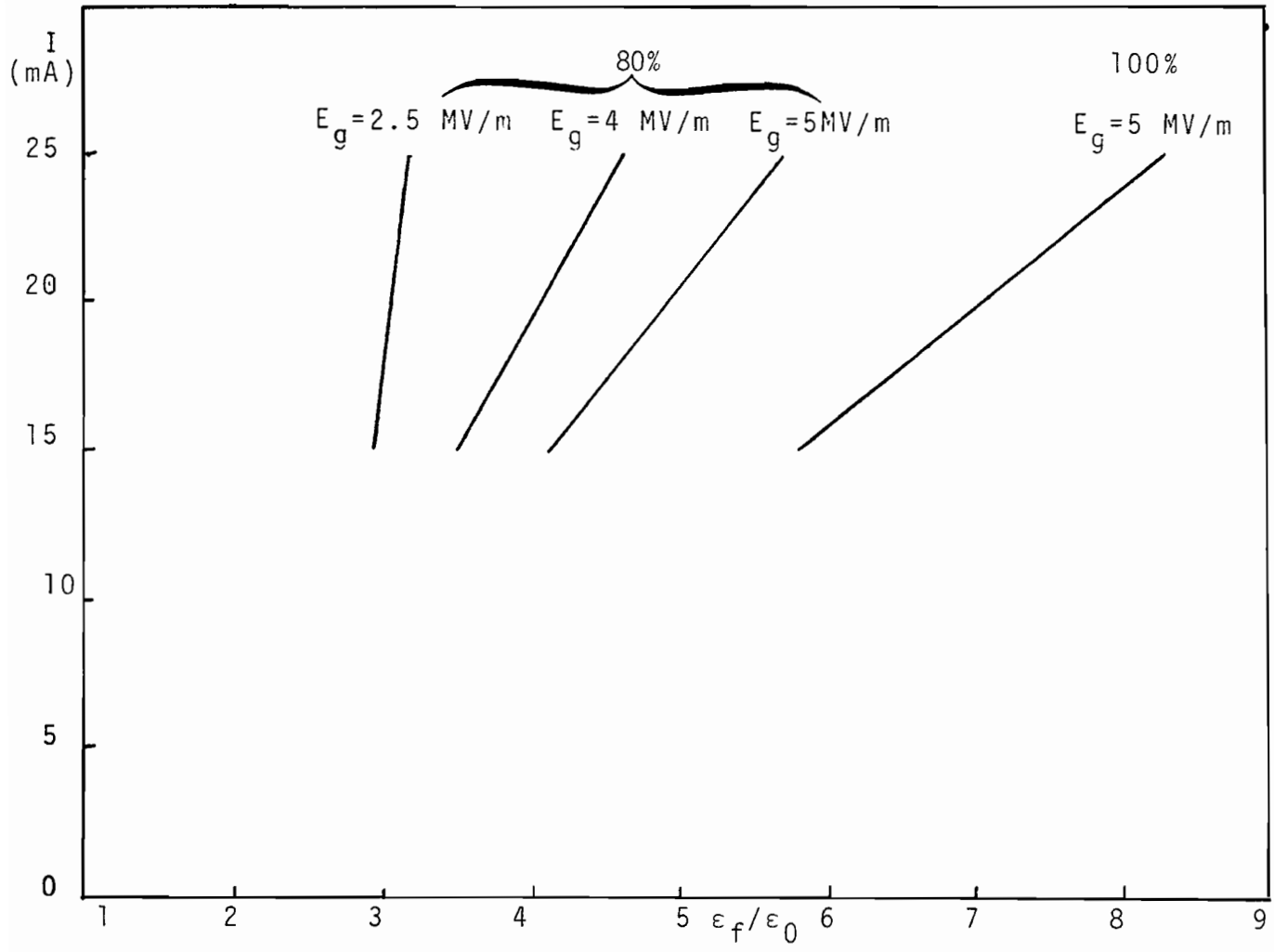

Figure 5. Emittance Variation with Current and Gap Field for Final Energy of 7 MeV.

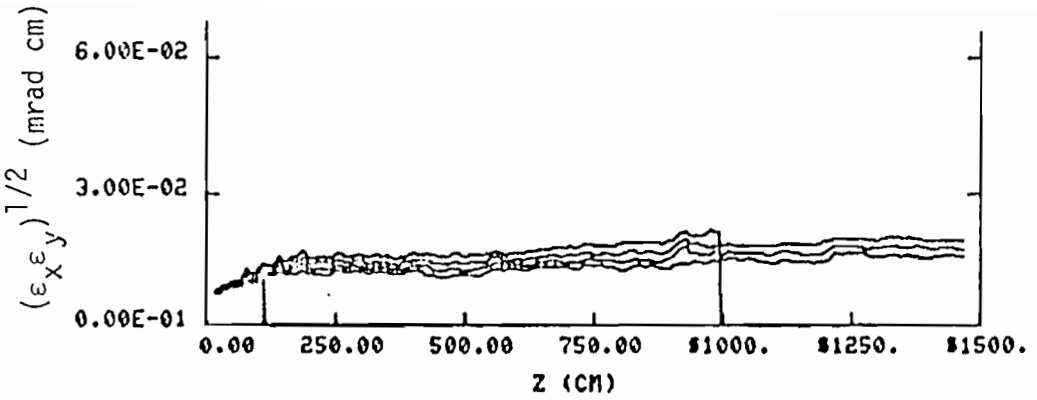

CASE = 10/02/79-001
I = 0.25000E-01
G = 0.43600E 01
AL1 = 0.10000E 01
ALPHA= 0.20000E 00
CCS = 0.34770E-06
C1 = 0.00000E 00
X = 0.18000E 01
XP = 0.29240E-02
Y = 0.85700E 00
YP = 0.61930E-02

Figure 6a. Mean Transverse Emittance

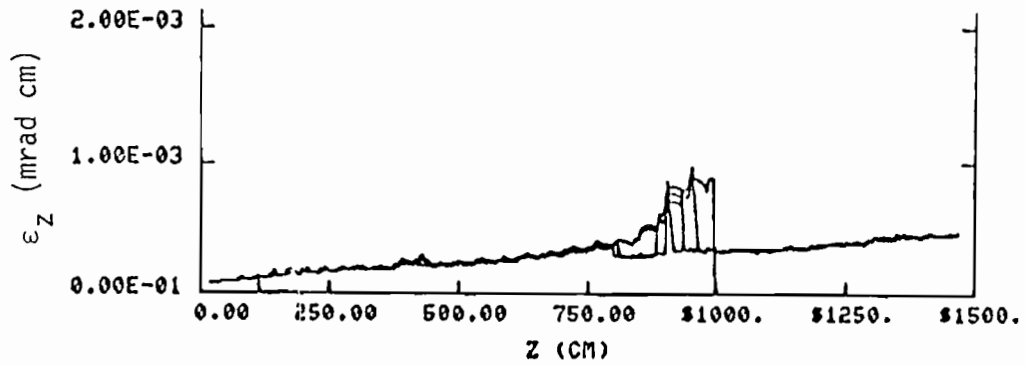

Figure 6b. Longitudinal Emittance

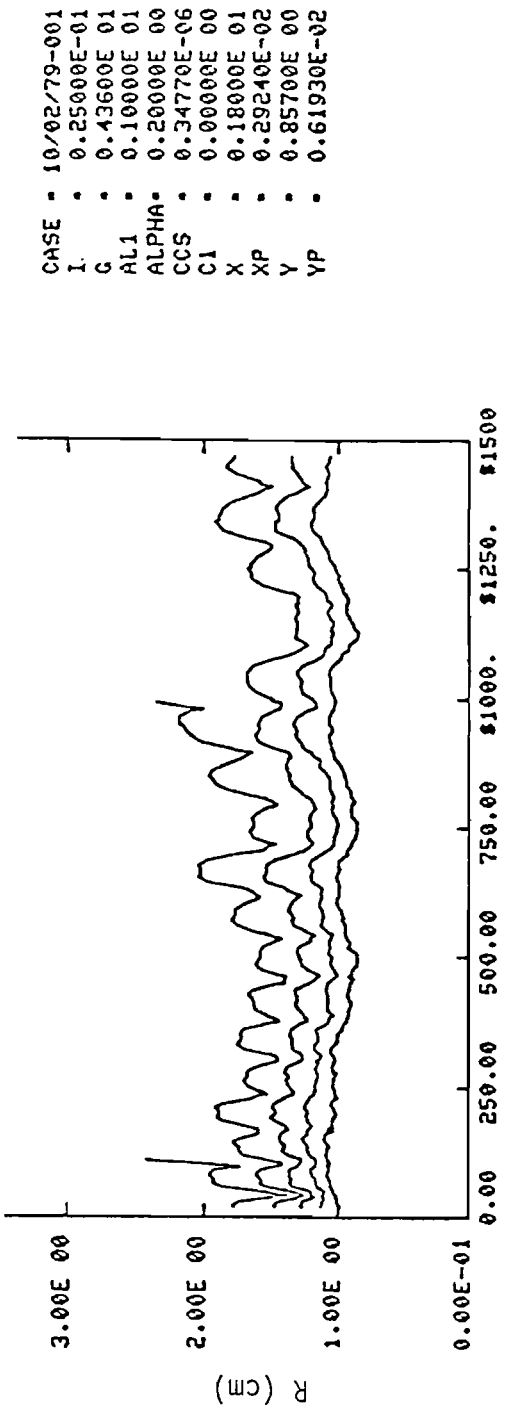

Figure 6c. Beam Radius

EXCITATION OF HIGHER ORDER MODES IN ALVEREZ LINAC STRUCTURES*

John T. Keane

Brookhaven National Laboratory

I. INTRODUCTION

For overall system efficiency it is desirable to run the high beta linac as heavily beam loaded as practical. One limitation is the effect of higher order rf mode excitation on beam stability.

The excitation of these modes is reviewed. A possible excitation mechanism with synchronous particles is introduced.

II. RESONANCE POSSIBLE IN HOLLOW CYLINDRICAL GUIDES

Table 1 lists the modes that can propogate in a hollow cylindrical guide. The cutoff frequency, f_c, below which no field can propogate, is dictated by the transverse dimension namely radius, a. When the guide is closed a resonance cavity is formed whose frequency is determined by the longitudinal dimension, z.

TABLE 1

Mode	λ_c	Freq (MHz)	Field Components
TM_{01}	2.61a	200	Ez, Hϕ
TM_{02}	1.14a	457	Ez, Hϕ
TM_{11}	1.64a	318	Ez, Hr, Hϕ
TE_{01}	1.64a	318	Hz, Hr, Er
TE_{11}	3.41a	153	

An Alverez cavity is a cylindrical guide operated in the TM_{010} mode (at cutoff). The drift tube causes a frequency perturbation. A guide operating in the TM_{01} mode can support numerous longitudinal resonances corresponding to guide wavelengths in the longitudinal direction ($\lambda/2$, λ, $3\lambda/2$, etc.). If the length is much greater than the diameter, then their frequency will be close to the TM_{010} mode. Similarly the other cylindrical guides have resonances corresponding to "n" longitudinal wavelengths. (See Figure 1).

*Research carried out under the auspices of the United States Department of Energy under Contract No. EY-76-C-02-0016.

Due to the large frequency separation between the operating mode and the other cylindrical guide modes, only TM_{01n} modes appear to be worrisome. This assumes that the higher mass of heavy ions will exclude the deflection mode (TM_{11}) blowup observed in electron linacs. This should be verified however.[1,2,3]

The field distribution of the TM_{01n} modes are shown in Figure 2.

III. TRANSIENT MODAL EXCITATION BY RF POWER AMPLIFIER

Due to the Fourier components existing during the rf turn on, the TM_{011} and TM_{012} modes have been observed in Alverez accelerators during the rf buildup period.[4] These fields exponentially decay before the beam is turned on.

From Figure 2 it can be seen that by placing the rf drive points at the 1/4 and 3/4 L points these modes cannot be driven. The moding effect has been further reduced by the use of dummy stems which push the frequency of the higher order TM_{01n} modes further away from the TM_{010} operating frequency.[5] The motivation for suppressing these higher order modes is the desire to minimize the transient effect when the rf is increased for beam compensation. The excitation of these modes has been from the generator and not the synchronous beam.

IV. BEAM EXCITATION OF TM_{011} and TM_{012} MODES

The beam which is in synchronism to the TM_{010} operating frequency has not been observed to cause higher order mode excitation. This is to be expected because of the distribution of the H field. Excitation from the synchronous beam in one section of the tank tend to be canceled out by the field induced (180° out of phase) in other sections of the structure (see Figure 2). One means of coupling can be envisioned, however.

Since the frequency of a TM011 mode is slightly higher than that of the TM_{010} mode, a synchronous particle traveling the length of the tank will see a phase advance of any TM_{011} electric field that exists. Figure 3A assumes that the synchronous beam enters the first drift tube gap during the maximum accelerating phase of the longitudinal electric field. If there is a total of 180° phase advance this particle will receive kinetic energy. In Figure 3B the synchronous beam particle enters the first gap during the de-accelerating part of the TM_{011} mode. With a 180° phase advance this particle gives up kinetic energy. Under the condition cited the beam would act as a modulating system, alternately acting as an rf generator and rf load. The modulating rate would be equal to the difference frequency between the TM_{010} and TM_{011} natural excitation frequencies.

IV.A DETERMINING DIFFERENCE FREQUENCY

The required beta and accelerator length to produce 180^{0} phase shift can be found.

$$\Delta f = f_{011} - f_{010}$$

where

f_{011} = frequency of TM_{011} mode

f_{010} = frequency of TM_{010} mode

$\left(\frac{\Delta f}{f_o}\right)(360°)$ = degree advance/drift tube

Assuming that the relative beam velocity, β, is constant through the accelerating structure.

$$\frac{\Delta f/f(360^{0})}{\beta\lambda} = \text{degree advance/cell length}$$

The difference frequency required to produce 180° phase shift in an accelerator tank of length, Z, is found to be

$$\Delta f = \frac{\beta c}{2Z} \qquad c = \text{velocity light} \qquad (1)$$

The cavity dimension required to set up a particular Δf can be approximated by assuming an unperturbed cylindrical guide.

$$f_{01n} = \left(\frac{2.405}{a}\right)\left(\frac{c}{2\pi}\right)\left[1 + \left(\frac{n\pi a}{2.405Z}\right)^{2}\right]^{\frac{1}{2}}$$

where

a = radius

Z = length

Since $a << Z$

$$f_{011} \cong (f_{010})\left[1 + \frac{1}{2}\left(\frac{\pi}{2.405}\frac{a}{Z}\right)^{2}\right]$$

$$\Delta f = \left(\frac{1}{8\ f_{010}}\right)\left(\frac{c}{Z}\right)^{2} \qquad (2)$$

By equating 1 and 2 the appropriate β and λ to set up a 180^{o} phase shift are found.

$$\Delta f = \frac{\beta c}{2Z} = \frac{c^2}{L^2 (8 f_{010})}$$

$$\beta = \frac{\lambda}{4c} \qquad (3)$$

where λ = free space wavelength of TM_{010} mode

$$\beta\lambda = \frac{\lambda^2}{4Z}$$

Practical values of $\beta\lambda$ are between .1 and 1 meter and Z between 10 and 20 meters which would suggest a frequency range of between 30 to 150 MHz. This corresponds to a range of betas from .025 to .1. The most likely range is the lower beta, higher frequency range. Picking values of Z = 15 meter, f_{010} = 100 MHz, from equation 3 we obtain:

$$\beta = \frac{3}{60} = .05$$

For this case the frequency difference would be as follows:

$$\Delta f = \frac{\beta c}{2Z} = \frac{(.05)\ (3 \times 10^8)}{30} = 500 \text{ kilohertz}$$

The bandwidth of an Alverez structure is approximately 5 kilohertz however. Since energy is alternately being supplied to and delivered by the beam at a 500 kilohertz rate it is most unlikely that the higher mode would build up. If for some reason the loading effect on the beam is not equal to the generating effect of the beam the mode could build up.

V. CASE OF CHANGING BETA

The above analysis was not rigorous since it assumed constant beta through the accelerating tank and did not consider the effect of dummy stems in the structure. It did indicate areas where problems could occur.

To see the effect of changing beta in an acccelerating section let the following specifications apply:

Input Energy = 2 MeV
Output Energy = 20 MeV
f_{010} = 80 MHz
Z = 18 meters
β_{in} = .046
β_{out} = .146
# of Cells = 55
Beam Current = 100 milliamps
Rf Power = 3.5 megawatts

The approximate separation of the TM_{011} mode from the operating mode is found by using Eq. (2).

$$\Delta f = \frac{c^2}{2^2(8\ f_{010})} = 434 \text{ kilohertz}$$

The phase advance per cell is given as follows:

$$\frac{\Delta f}{f_{010}}\ 360^{o} = 1.95^{o}/\text{cell}$$

55 cells x 1.950/cell = 107° total advance

If the actual Δf is higher because of dummy stems the phase advance per cell will be larger. Since the beam kinetic energy is low any moding will effect the particle velocity.

Figure 4 suggests a mechanism for initiating the TM_{011} buildup. It is noted that there can be unsymmetrical excitation from the beam at 90° phase advance. Figure 5 indicates the excitation versus entrance angle at the first gap. The phase advance is reduced by the particles gaining kinetic energy thus tending to approach synchronism with the TM_{011} wave. If synchronism is reached, these particles no longer act as an absorber since energy gain will equal energy lost. Particles losing energy in the first gap, however, will tend to increase their phase advance toward the 180° required for strong coupling. For this case symmetry between the driving function (decreasing beam K.E.) and the absorption function does not exist. Particles entering the 1st gap at 270° could loose as much as 2 MeV kinetic energy (200 kilowatt instantaneous) while particles entering at 360° could loose 10 MeV kinetic energy (1 megawatt instantaneous).

VI. CONCLUSIONS

The excitation of higher order TM_{01} modes produced during the rf build-up period has been observed and compensated for over the years.

Synchronous beam excitation of these modes has not been observed. A possible, though unlikely, mechanism for beam excitation has been presented. This would occur only in a very specific section of the machine (low beta).

There is no strong reason to expect poor beam quality for currents near 160 milliamperes but further studies into the effect of heavy beam loading should be persued.

REFERENCES

1. O. Altenmueller, et. al., "Beam Break-Up Experiments at SLAC", Proceedings of the 1966 Linear Accelerator Conference, October 1966, p. 267.

2. W. Visscher, "Simple Modes for Beam-Blow Up", Proceedings of the 1966 Linear Accelerator Conference, October 1966, p. 284.

3. R. Gluckstern, "Transverse Beam Growth Due to Longitudinal Coupling in Linear Accelerators", Proceedings of the 1966 Linear Accelerator Conference, October 1966, p. 207.

4. T. Nishikawa, "Beam Loading Effects in Standing Wave Linacs, Proceedings of the 1966 Linear Accelerator Conference, October 1966, p. 294.

5. S. Giordano and J. Hannwacker, "Measurements on a Multisystem Drift Tube Structure", Proceedings of the 1966 Linear Accelerator Conference, October 1966, p. 88.

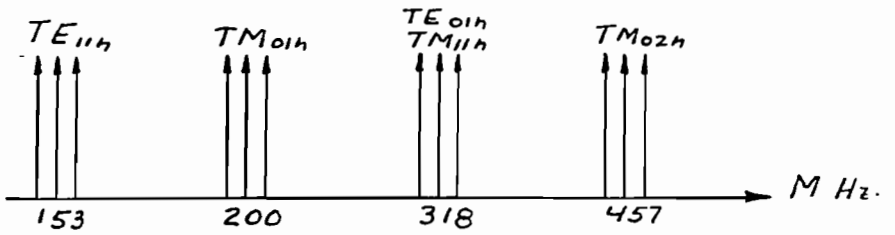

Figure 1. Modal Separation of Cylindrical Guide (2 = .57 Meters).

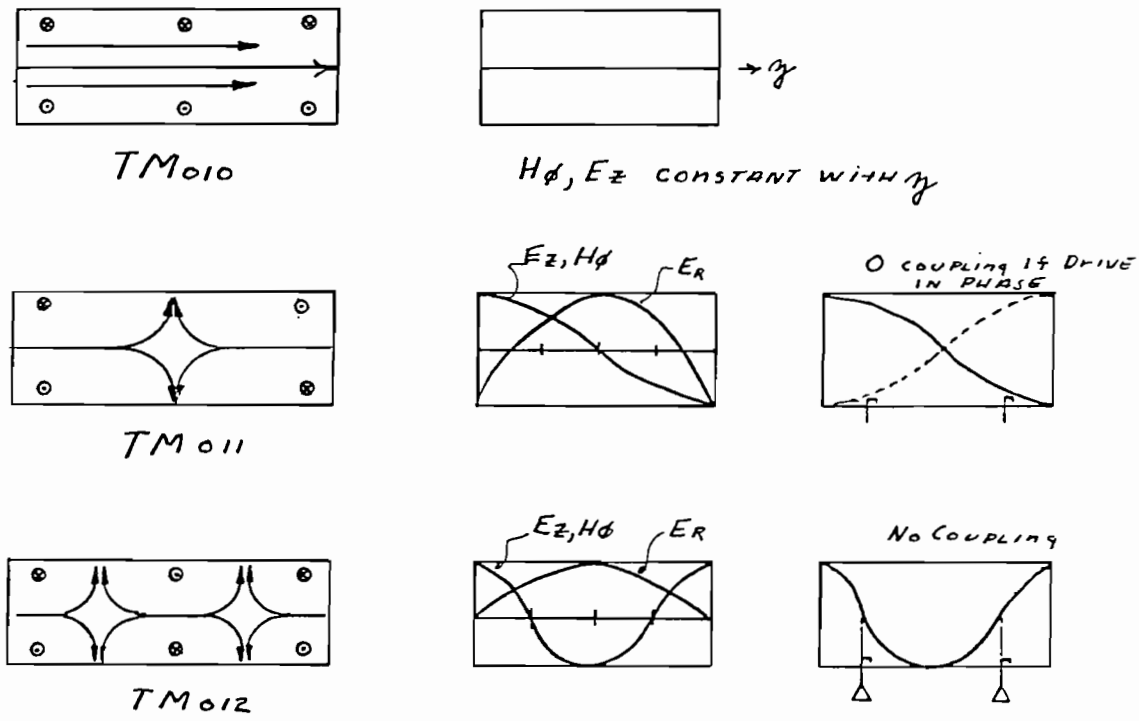

Figure 2. Field Distribution of TM_{01n} Modes.

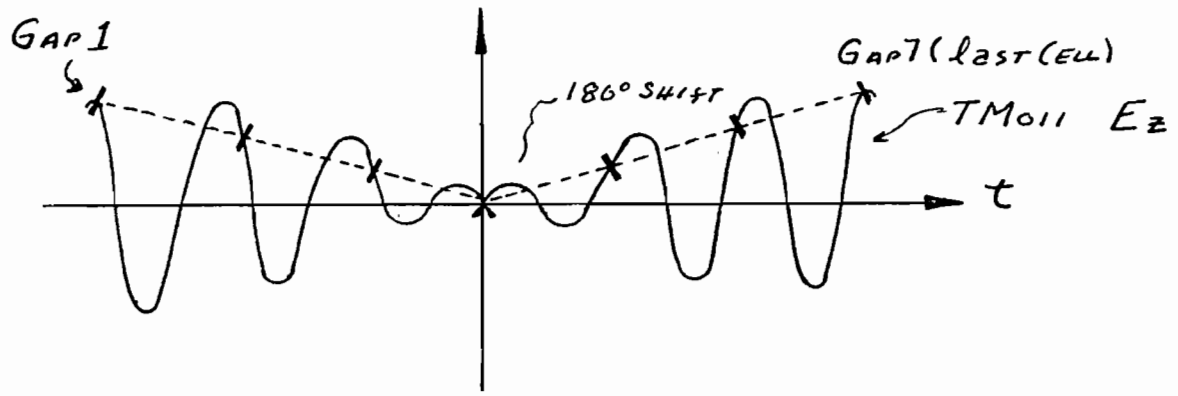

A. Particle Gaining Kinetic Energy - 90^{o} Entrance Angle

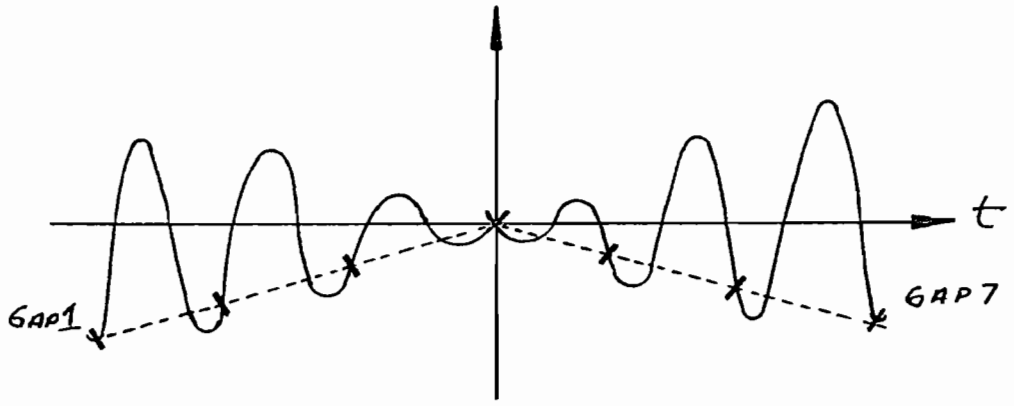

B. Particle Loosing Kinetic Energy - 270^{o} Entrance Angle.

Figure 3. 180^{o} Phase Advance of TM_{011} Longitudinal Electric Field As Synchronous Particle Passes Through Structure.

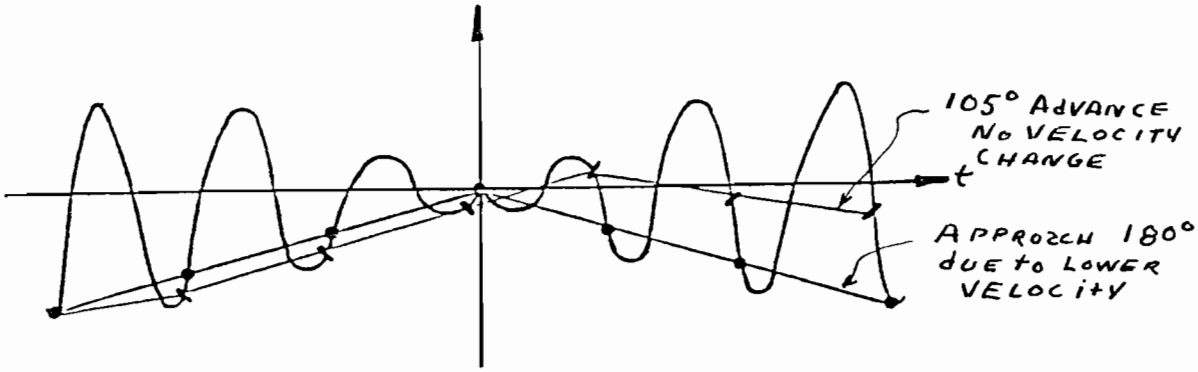

A. Effect of Reduced Velocity on Driving Particle

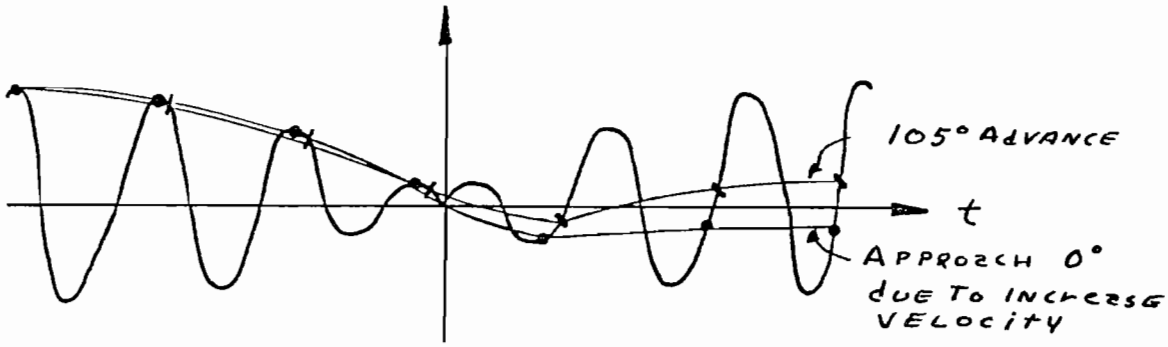

B. Effect of Increased Velocity on Absorbing Particle

Figure 4. Velocity Change Resulting in Anti-symmetric Driving and Absorbing Function (105° Phase Advance).

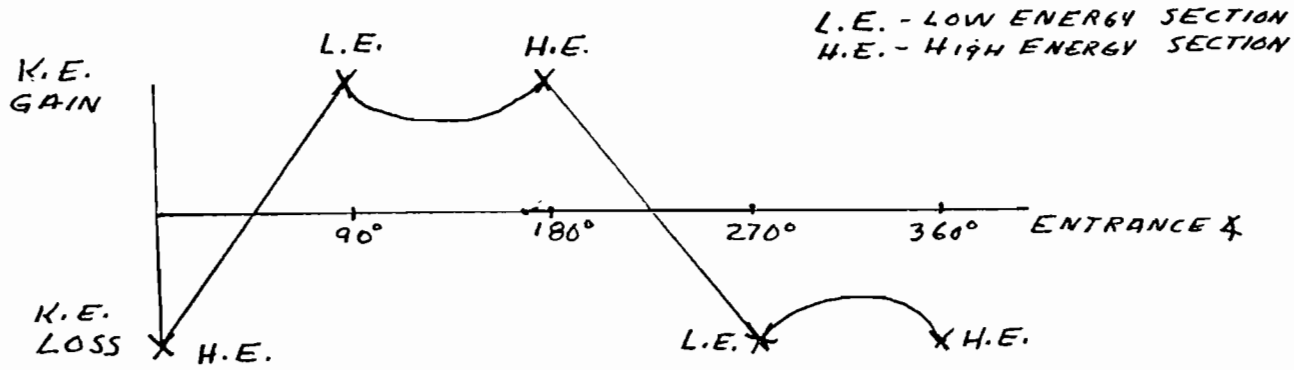

Figure 5. Location of Energy Interchange Versus Entrance Angle at First Gap (90° Phase Advance)

IMPEDANCES FOR ELECTRON LINACS AND STORAGE RINGS

Perry B. Wilson

Stanford Linear Accelerator Center

In this note some basic concepts and results are presented concerning the impedances of electron linacs and storage rings. The impedance of an accelerator or ring completely characterizes the interaction of the beam with its environment. Not only does the impedance (or its Fourier transform, the wake potential) determine the energy loss by a bunched beam to its environment, but it is also the chief ingredient required for any calculation of beam stability.

As the title implies, we will be concerned mainly with particles moving close to the velocity of light. The assumption $v \approx c$ makes possible certain important simplifications in the impedance-wake potential formalism but, unfortunately, it is clearly violated in the case of heavy ion accelerators. In several instances we will point out where it might be possible to extend the results to the more general case.

Another limitation in the present note is that it is concerned almost entirely with the longitudinal impedance. A parallel development is often possible for the case of the transverse impedance, but the analysis, measurement methods and computer programs tend to be more complicated. At SLAC, the effort being directed to the measurement and computation of transverse impedances is just now reaching the level that was earlier devoted to the longitudinal impedance problem. For example, a computer program is just being completed for calculating the transverse deflection modes in the SLAC linac structure.

Some Definitions

A loss parameter $k(\sigma)$, defined by

$$k(\sigma) = \frac{\Delta U}{q^2}$$

gives the total energy loss ΔU given up to a component by a bunch with charge q and bunch length σ. For a periodic train of bunches spaced in time by T_b, the loss parameter determines the average power loss to a component by

$$P = I_o^2 k T_b = I_o^2 Z_\ell \tag{1}$$

where $Z_\ell = kT_b$ is the loss impedance and I_o the average current. The impedance function for a component is defined by (see Fig. 1),

$$Z(\omega) = \frac{V(\omega)}{I(\omega)} .$$

The wake function, or wake potential $w(\tau)$, is the potential seen by a non-perturbing test charge following at time τ behind a unit charge passing through a component. The net potential at time t in a charge distribution I(t) is then obtained as

$$V(t) = \int_{-\infty}^{t} w(t-\tau) I(\tau) d\tau, \tag{2}$$

The following transform relations between the frequency and time domain can be shown to hold (a tilda indicates the Fourier transform):

$$I(\omega) = \tilde{I}(t)$$

$$V(\omega) = \tilde{V}(t)$$

$$Z(\omega) = \pi \tilde{w}(t).$$

Some Consequences

The impedance function $Z(\omega)$ is in general a complex function,

$$Z(\omega) = Z_R(\omega) + jZ_I(\omega).$$

If we take $w(\tau)$ to be a real function of time, then it follows that

$$Z_R(\omega) = Z_R(-\omega) \qquad \text{(an even function of } \omega)$$
$$Z_I(\omega) = -Z_I(-\omega) \qquad \text{(an odd function of } \omega).$$

If the velocity of a particle passing through a component is close to the velocity of light, then the wake potential is causal, or nearly so. That is, $w(\tau) \equiv 0$ for $\tau < 0$. Then we can show that $Z_R(\omega)$ and $Z_I(\omega)$ are related by the Hilbert transform,

$$Z_I(\omega) = \frac{1}{\pi} \int_{-\infty}^{\infty} \frac{Z_R(\omega')}{\omega' - \omega} \, d\omega'. \tag{3}$$

Thus a knowledge of $Z_R(\omega)$ is sufficient to determine $Z_I(\omega)$. However, the wake induced in a component by a charge will not vanish ahead of the charge. The assumption of a causal wake potential also implies that

$$w(\tau) = \frac{2}{\pi} \int_0^{\infty} Z_R(\omega) \cos\omega\tau \, d\omega. \tag{4}$$

Under the assumption that $I(t)$ is a real function of time, the loss parameter $k(\sigma)$ can also be related to the real part of the impedance function by

$$k(\tau) = \frac{\pi}{q^2} \int_0^{\infty} I^2(\omega) \, Z_R(\omega) \, d\omega \, .$$

For a Gaussian bunch this reduces to

$$k(\tau) = \frac{1}{\pi} \int_0^\infty Z_R(\omega) e^{-\omega^2 \sigma_t^2} \, d\omega. \tag{5}$$

Application to Resonant Modes

For a high-Q parallel resonant circuit, we have

$$Z(\omega) = \frac{R}{1+j2Q\delta}$$

$$Z_R(\omega) = \frac{R}{1+(2Q\delta)^2}$$

where $\delta = (\omega - \omega_0)/\omega_0$. From this relation and Eq. (4) in the preceding section we derive for the n^{th} mode,

$$w(\tau) = 2k_n \cos \omega_n \tau$$

$$k_n = \frac{\omega_n}{4} \left(\frac{R}{Q}\right)_n = \frac{V_n^2}{4W_n}$$

where V_n is voltage gain for a non-perturbing test charge when W_n is the stored energy. The total wake potential for a resonator is the sum over all modes,

$$\omega(\tau) = 2 \sum_n k_n \cos\omega_n \tau \quad . \tag{6}$$

The total loss parameter for a bunch with bunch length σ_t is

$$k(\sigma_t) = \sum_n k_n e^{-\omega_n^2 \sigma_t^2} \quad . \tag{7}$$

Two computer programs exist for computing ω_n and k_n for the fundamental and higher-order longitudinal modes in cavities and structures. The program KN7C[1] computes modes for a periodic structure characterized

by the four parameters a, b, g and d shown in Fig. 2. A single resonant cell can be modeled by setting d - g >> a. Similarly, the program SUPERFISH[2] computes modes for a single axi-symmetric cavity having any boundary in the r-z plane. That is, the function r(z) representing the surface can be arbitrary, even multiply connected. However, any cross-section in the r-ϕ plane must be a circle. In addition to values for ω_n, k_n and Q_n, the E and H fields at any point in the cavity can also be obtained from the output. By putting a taper in the beam tube as shown at the right in Fig. 1, the loss to small discontinuities such as a gap or iris can be obtained from SUPERFISH, even though there are no standing-wave modes in the gap or iris region.

An example of the power of SUPERFISH is its application to the computation[3] of modes in the RF cavities for PEP and the proposed LEP storage ring (which uses PETRA-type cavities scaled to 353 MHz). Fig. 3 shows the cavity dimensions, and Fig. 4 gives sketches of the electric field patterns for the first 9 higher-order modes in the PETRA-type cavity. Table I gives numerical values for the properties of the 19 standing-wave modes below cutoff of the beam tube. These results define, in fact, the impedance function for this RF cavity. For large rings such as PEP or PETRA the impedance of the RF system is the major part of the total ring impedance. Thus for these rings there is little uncertainty as to the ring impedance, since the largest contribution can be computed with good accuracy. Finally, Fig. 5 shows how the loss parameter for loss to higher order modes (k_{hom}) and the total loss parameter (k_{tot}) for these cavities depend strongly on bunch length.

Table I

PETRA CAVITY MODES

Mode Number and Type				Frequency (MHz)	R/Q (ohms)	Q_o (x 10^{-3})		k (V/pc)
1	Even	11,00		359.2	250.4	47.2		0.1413
2	Odd	11,11		525.0	55.6	40.5		0.0458
3	Even	21,20		886.5	9.4	71.5		0.0130
4	Odd	22,11		974.0	44.2	26.1		0.0677
5	Even	22,22		1221.1	17.0	39.8		0.0327
6	Odd	21,31		1237.4	4.1	26.5		0.0080
7	Even	33,00		1396.0	7.7	99.5		0.0168
8	Odd	32,31		1466.1	2.3	24.6		0.0054
9	Odd	22,33		1564.8	5.5	20.9		0.0134
10	Even	21,42	(31,22)	1588.0	6.6	38.2	(68.5)	0.0165
11	Even	32,42		1700.6	4.6	71.4	(66.7)	0.0123
12	Even	33,40	(43,20)	1854.7	1.9	--	(59.9)	0.0054
13	Odd	43,31		1888.3	4.3	71.4	?	0.0129
14	Even	24,40		1931.5	0.2	108.5		0.0007
15	Odd	44,11		1990.3	6.6	23.4		0.0206
16	Odd	12,53		2035.5	1.4	18.1	(70.4)	0.0045
17	Even	43,42		2107.3	0.3	72.8		0.0011
18	Odd	32,31		2220.0	0.4	70.2		0.0016
19	Even	34,42	(44,22)	2261.2	6.2	78.2		0.0219
	Cutoff Frequency			(2295)				
20	Odd	43,53		2355.4				0.0030
21	Even			2372.3				0.0002
22	Even			2416.9				0.0005
23	Odd			2429.2				0.0012
24	Even			2492.2				0.0036
25	Even			2558.8				0.0001
26	Odd			2587.6				0.0002

A transverse version of KN7C has just been completed[4]. This code will calculate the deflection modes for the periodic structure shown in Fig. 2. The first use of the program will be to compute the transverse deflection mode for the SLAC two-mile linac in order to predict the emittance growth for single bunches. This computation is important for predicting the luminosity that can be achieved by the proposed linac collider project.

Measurement Techniques

Figure 6 shows the measurement method, originally proposed by Sands and Rees[5], that has been used to measure the loss parameter $k(\sigma)$ for the PEP ring components. Elaborations of this method were also used at PETRA and CESR[6]. In this method, an approximately Gaussian pulse is sent along a wire on the axis of the component to be tested. The pulse will interact with any mode having (in the absence of the wire) an E_z field on the axis. The excited fields or modes will induce a secondary pulse, $I_s(t)$, on the wire. As shown in Fig. 7, the net pulse $I_1(t)$ observed at the output of the component is a superposition of $I_s(t)$ and the incident pulse $I_0(t)$: $I_1(t) = I_0(t) + I_s(t)$. The incident pulse is obtained by substituting a smooth reference pipe for the component. If the incident pulse could be made arbitrarily short (a delta-function), then for $t > 0$, $I_s(t) = I_1(t)$ would be proportional to the wake potential $w(t)$.

The total loss parameter is given[5] by

$$k = \frac{2Z_0}{q^2} \int I_0(t)\ I_s(t)\ dt$$

$$q = \int I_0(t)\ dt$$

where Z_0 is the characteristic impedance of the reference pipe with the wire in place. By using incident pulses of different length, the

Again, only the R/Q's of resonant modes can be measured in the frequency domain, losses, corresponding to the short-range wake in the time domain.

Wake Potential for the SLAC Linac

The structure shown in Fig. 2a is a reasonable approximation to the disk-loaded structure of the two-mile SLAC linac. Using output from KN7C in Eq. (6) for 416 modes, the wake function for SLAC was computed[9]. The result is shown in Fig. 10. In addition to the wake computed from the modes, the result also includes the contribution of an "analytic extension", which takes into account the effect of modes beyond the highest frequency reached by the computer calculation. The analytic extension uses the Sessler-Vainshtein optical resonator model described in Ref. 1. It covers the frequency range from $\omega = 6.1 \times 10^{11}$ (for the 416th mode) to $\omega = 8 \times 10^{13}$. (The fundamental mode is at $\omega = 1.8 \times 10^{10}$.) The contribution of the analytic extension is important only for the first picosecond or so.

Using Eq. (7) the average energy loss per particle can be computed. The computed loss is 40 MeV per electron, while the measurements give 50 MeV. Considering the possible experimental errors in the measurement, this is reasonable agreement. The average energy loss is related to the intercept of the wake potential at t = 0. From Eqs. (6) and (7), $w(0) = 2k$ for a point bunch. The time dependence of the wake affects the detailed shape of the energy spectra. In Ref. 9 it is shown that detailed agreement between measured energy spectra and spectra computed from the wake in Fig. 10 is very good, if the amplitude of the computed wake is multiplied by a factor of 1.3.

The SPEAR Impedance Function

The impedance function for SPEAR is shown in Fig. 11. The form of this function was obtained as follows. From data[10] on bunch lengthening in SPEAR, it can be shown[11] that at high frequencies the real part of the impedance must vary as $Z_R(\omega) \sim \omega^{-0.68}$. However, at low frequencies the impedance must fall to zero. Quite arbitrarily the low frequency portion is represented by a linear dependence on frequency. Thus, $Z_R(\omega)$ has a maximum value Z_0 at some frequency $\omega_0 = 2\pi f_0$ where the two curves intersect. Using Eq. (5), Z_0 and f_0 can be adjusted to fit measured energy loss data for SPEAR. This loss is represented quite accurately for SPEAR by

$$k(\sigma) = \left[50\ \sigma_Z(\text{cm})\right]^{-1.21}\ \text{V/pC}. \qquad (8)$$

The result of the fitting procedure (described in Ref. 12) is Z_0 = 8000 ohms and f_0 = 1.2 GHz.

The imaginary part of the impedance can be computed, if the real part is given, using the Hilbert transform in Eq. (3). The result[13] is shown in normalized form in Fig. 11. The ratio Z/n is also of interest in predicting the threshold for various beam instabilities, where n is the harmonic number of the revolution frequency (1.28 MHz for SPEAR). From Fig. 11 we readily compute Z_R/n = 8.5 ohms. The total impedance $|Z|/n$ is on the order of 20 ohms.

Comparison of SPEAR and PEP Impedances

Some impedances for SPEAR and PEP are compared in Table II below. Using Eq. (7) and the definition of the loss impedance, $Z_\ell = T_b k(\sigma)$,

the total SPEAR impedance at a bunch length of 2.0 cm is computed to be Z_ℓ = 17 MΩ. Computer calculations using SUPERFISH and KN7C give a loss impedance of 3 MΩ for higher-order modes in the RF cavities. This leaves 14 MΩ for the vacuum chamber loss. Thus, losses in the vacuum chamber external to the RF cavities are dominant for SPEAR. PEP has six times more RF cavities than SPEAR, but the beam hole size is somewhat smaller on the average and the loss per cavity is about 24% greater. Remember also that the loss impedance for a given component scales in proportion to the time between bunches: $T_b(\text{PEP})/T_b(\text{SPEAR}) = 3.13$. Applying these factors gives a loss impedance for the PEP cavities of 69 MΩ. The loss for the PEP vacuum chamber, on the other hand, has been measured to be about 8% of the loss per unit length for SPEAR. The total circumference of PEP is greater by a factor of 9.4. Multiplying the SPEAR vacuum chamber impedance by 3.13 x 9.4 x .08 gives 33 MΩ for PEP. We see that for PEP the cavity impedance is about twice the vacuum chamber impedance. Estimated values for Z_R/n and $|Z|/n$ are also given in Table II for SPEAR and PEP.

TABLE II

Impedances for SPEAR and PEP

at σ_z = 2.0 cm

		SPEAR	PEP
Z_ℓ(rf)	MΩ	3 (18%)	69 (68%)
Z_ℓ(vac)	MΩ	14 (82%)	33 (32%)
Z_ℓ(tot)	MΩ	17	102
Z_R/n	ohms	8.5	1.8
$\|Z\|/n$	ohms	≈ 20	≈ 4

Impedances, Wakes and Stability

Analytic stability criteria have been developed so far mainly in the frequency domain. A solution in the form of an expansion in modes is first obtained, with mode frequencies that may be complex. As some parameter (such as charge per bunch) is increased, the imaginary part of the frequency for a particular mode may change sign, indicating a transition from damping to exponential growth. However, in order to carry the procedure past the stage of a very general expression, simplifying assumptions are usually introduced which limit the predictive power of the model.

In the time domain, non-linear problems are usually attacked by computer simulations using a limited number of superparticles. The coupling between particles is characterized by the wake potential, rather than the impedance. It is difficult, however, to develop analytic criteria for stability. A recipe for obtaining stability criteria similar to that outlined above for the frequency domain, does not appear to exist. The situation may be changing with the recent interdisciplinary surge of interest in non-linear dynamics[14]. For the case of turbulent bunch lengthening an unusual time-domain stability criteria has been developed[15], which may have an application to other aspects of the problem of the interaction of a charged beam with its environment.

References

1. E. Keil, Nucl. Instr. Methods 100, 419 (1972).

2. K. Halbach and R.F. Holsinger, Part. Accel. 7, 213 (1976).

3. P.B. Wilson, LEP-70/69, CERN (May 1978).

4. B. Zotter and K. Bane, PEP Note-308, SLAC (1979).

5. M. Sands and J. Rees, PEP-95, SLAC (1974).

6. M.G. Billing, J.L. Kirchgessner and R.M. Sundelin, IEEE Trans. Nucl. Sci. NS-26, 3583 (1979).

7. J.N. Weaver, P.B. Wilson and J.B. Styles, IEEE Trans. Nucl. Sci. NS-26, 3971 (1979).

8. P.B. Wilson, J.B. Styles and K.L.F. Bane, IEEE Trans. Nucl. Sci. NS-24, 1496 (1977).

9. R.F. Koontz, G.A. Loew, R.H. Miller and P.B. Wilson, IEEE Trans. Nucl. Sci. NS-24, 1943 (1977).

10. P.B. Wilson et al, IEEE Trans. Nucl. Sci. NS-24, 1211 (1977).

11. A.W. Chao and J. Gareyte, SPEAR-197/PEP-224, SLAC (1976).

12. P.B. Wilson, PEP-233, SLAC (1977).

13. K. Bane and P. Wilson, PEP-261, SLAC (1977).

14. Siebe Jorna, ed. Topics in Nonlinear Dynamics, AIP Conf. Proc. No. 46 (American Inst. of Physics, NY, 1978).

15. P.B. Wilson, PEP-232, SLAC (1977).

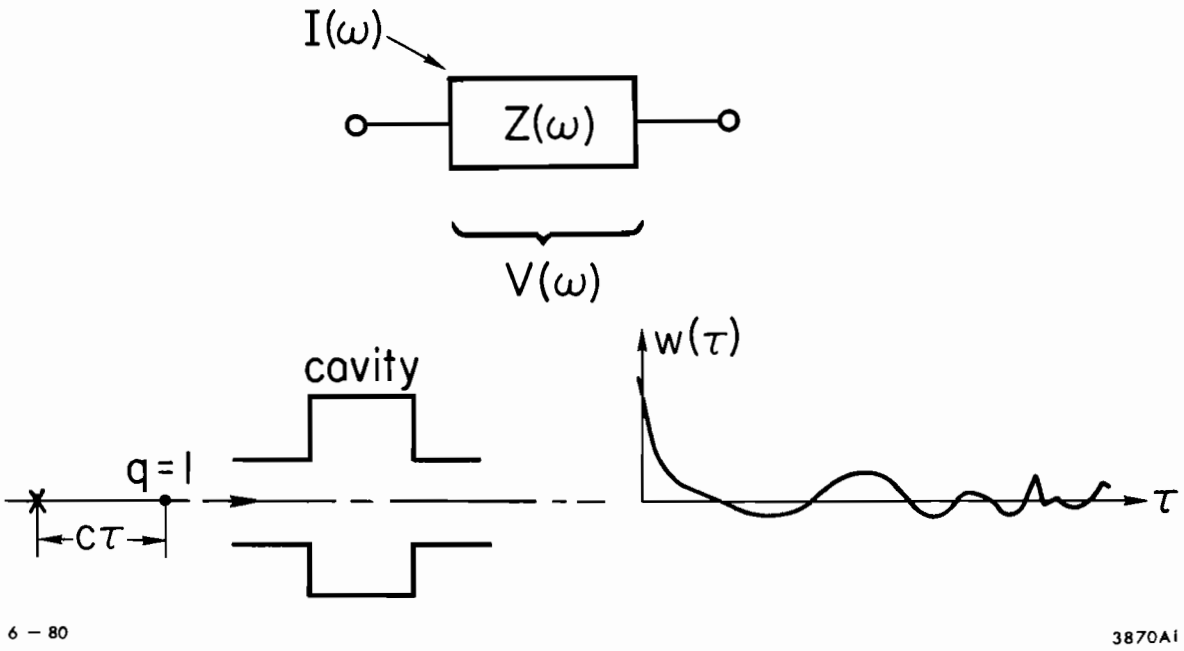

Fig. 1 -- Physical meaning of the impedance functions $Z(\omega)$ and wake potential $w(\tau)$.

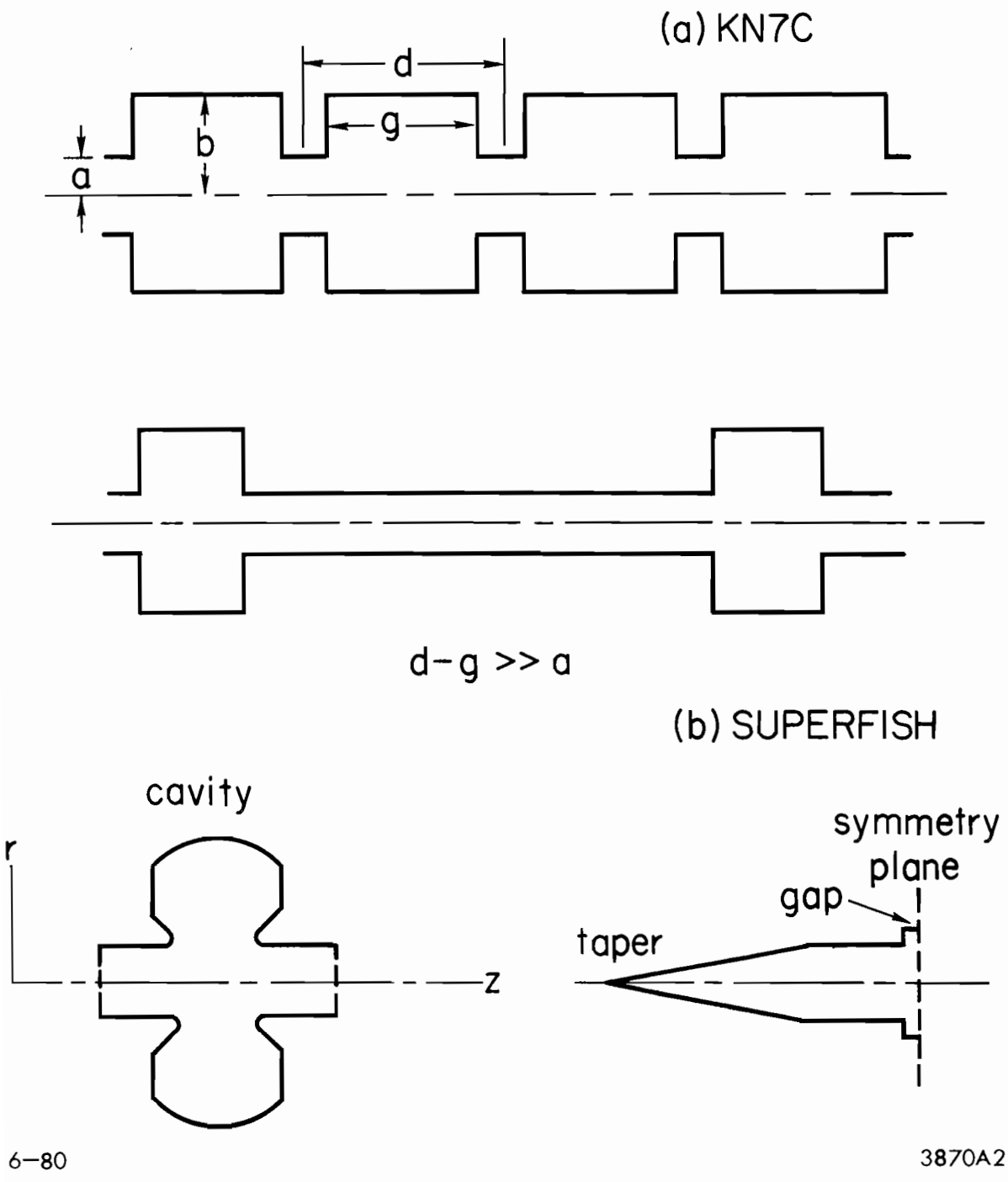

Fig. 2 -- Structures that can be computed by KN7C and SUPERFISH.

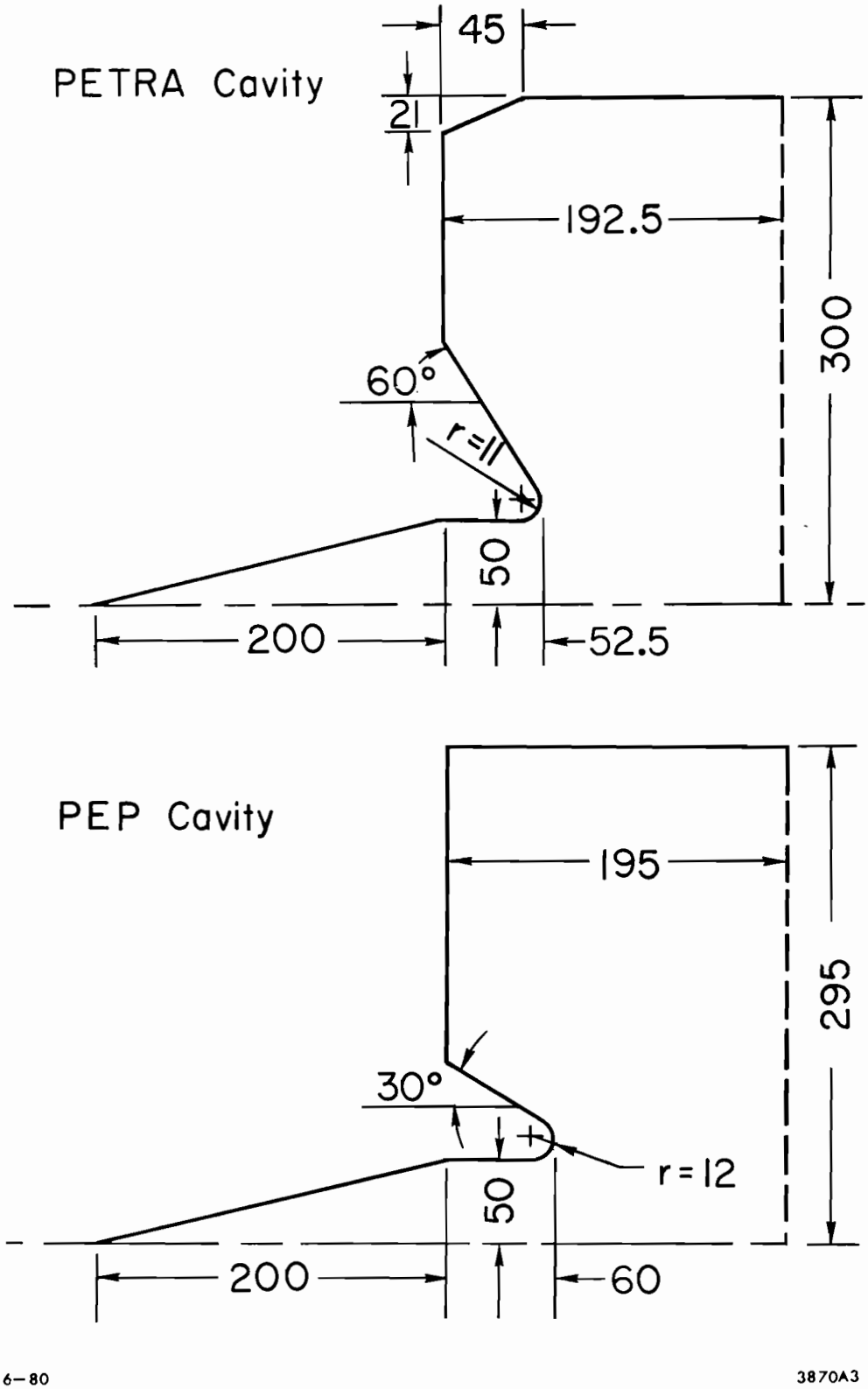

Fig. 3 -- Dimension of the PEP and PETRA cavities.

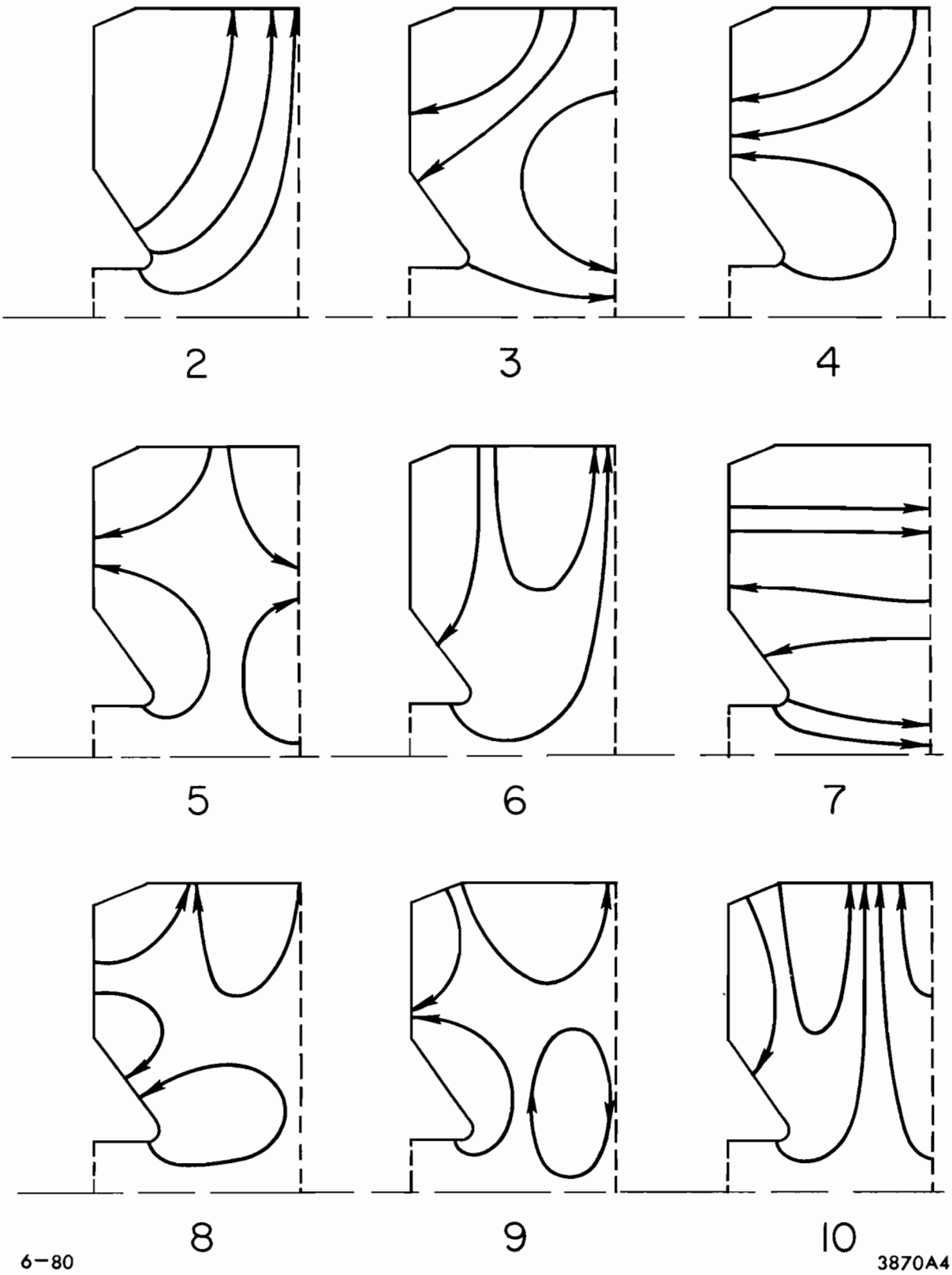

Fig. 4 -- Electric field for the first 9 higher-order modes in the PETRA-type cavity.

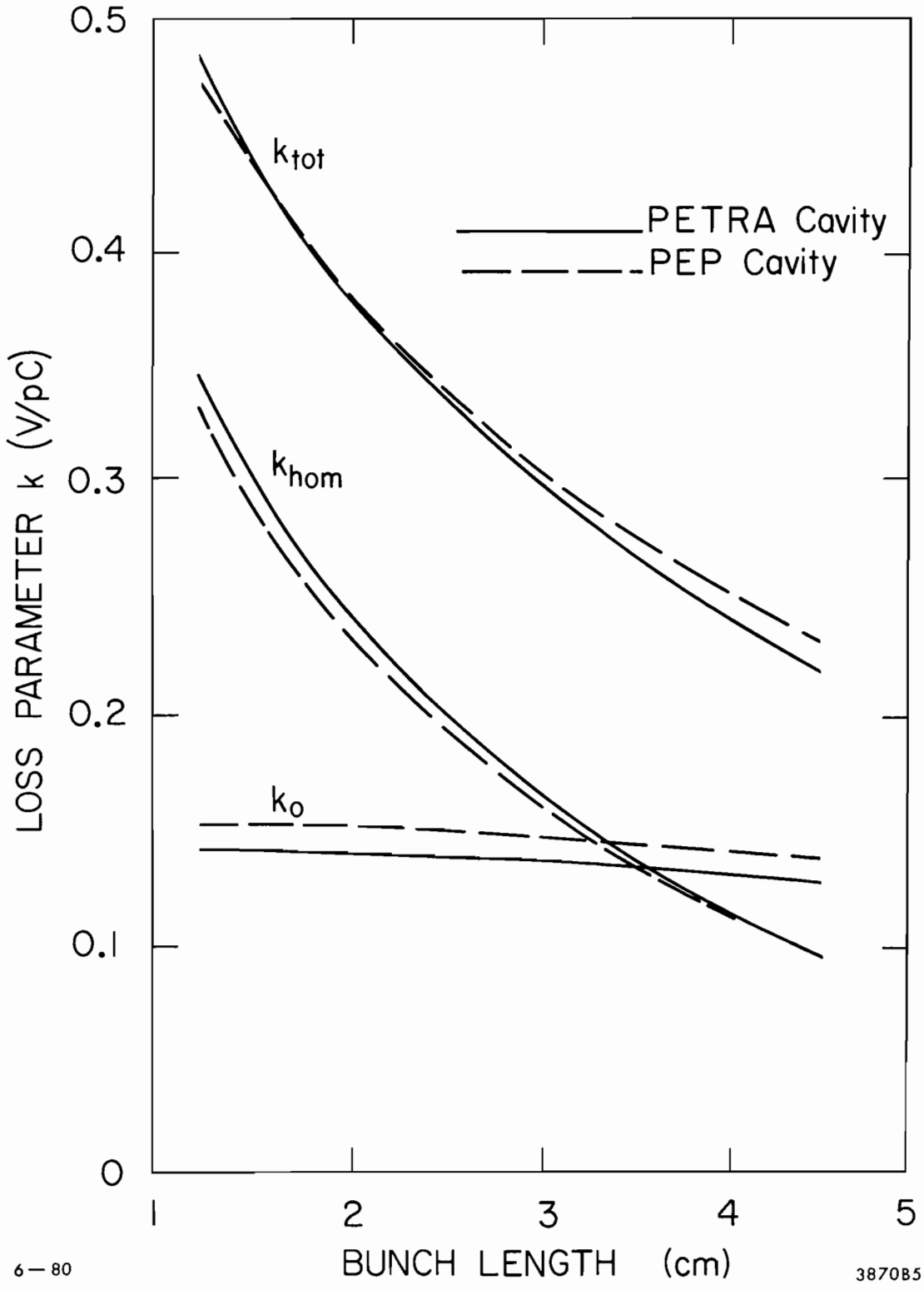

Fig. 5 -- Loss parameter as a function of bunch length for the PEP and PETRA cavities.

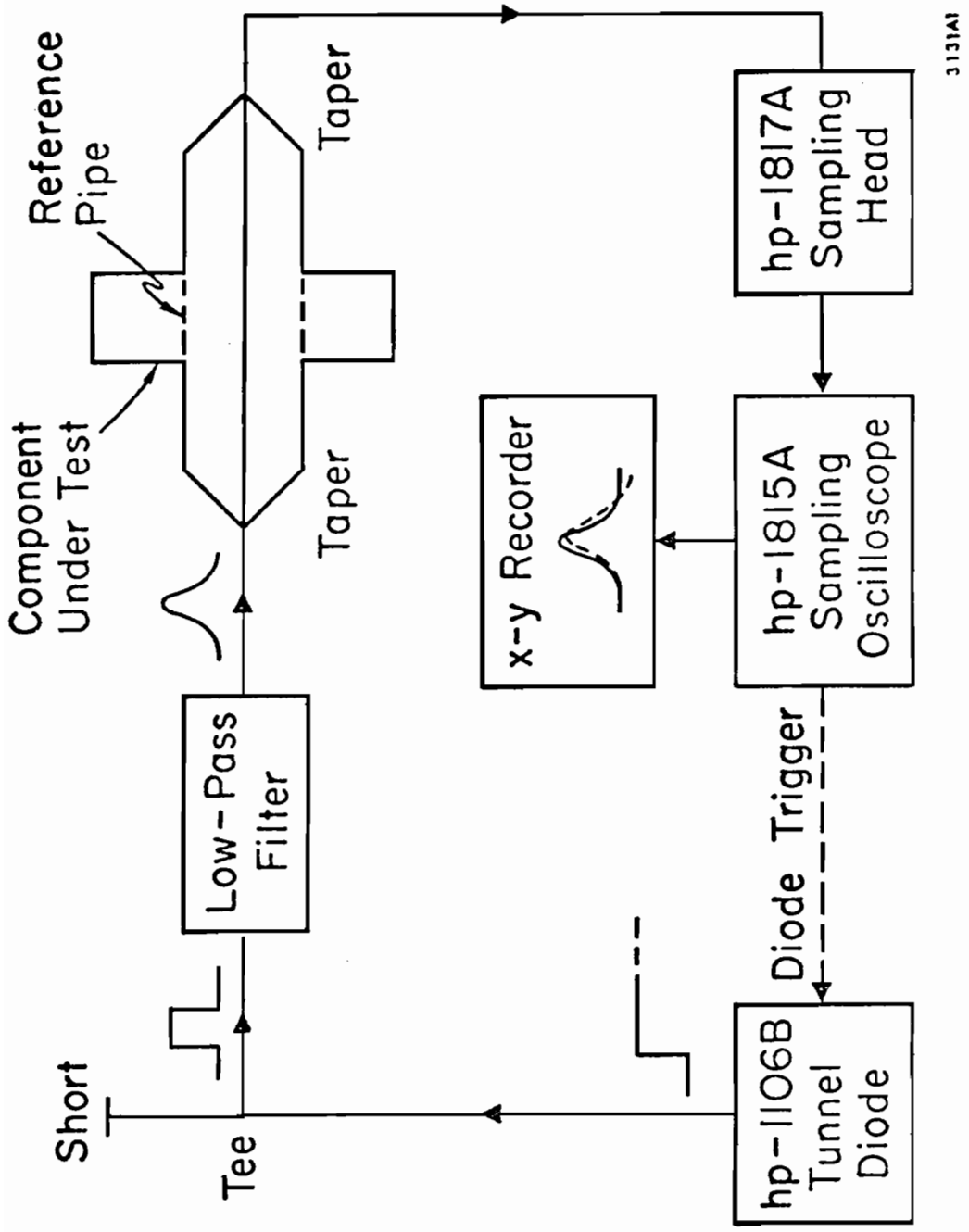

Fig. 6 -- Instrumentation for measuring the loss parameter.

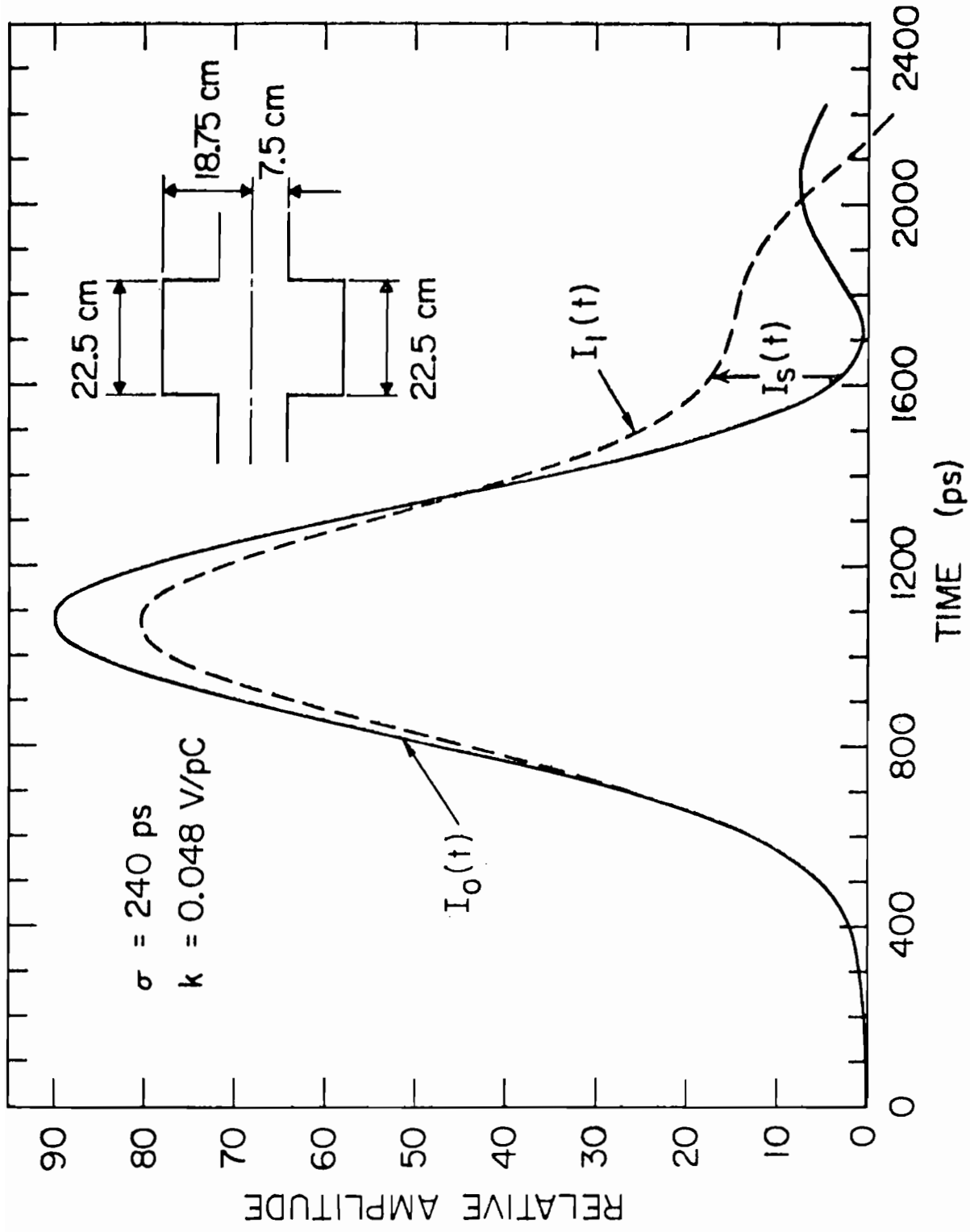

Fig. 7 -- Recorded output pulses $I_0(t)$ for the reference pipe and $I_1(t)$ for a cylindrical cavity having the dimensions shown.

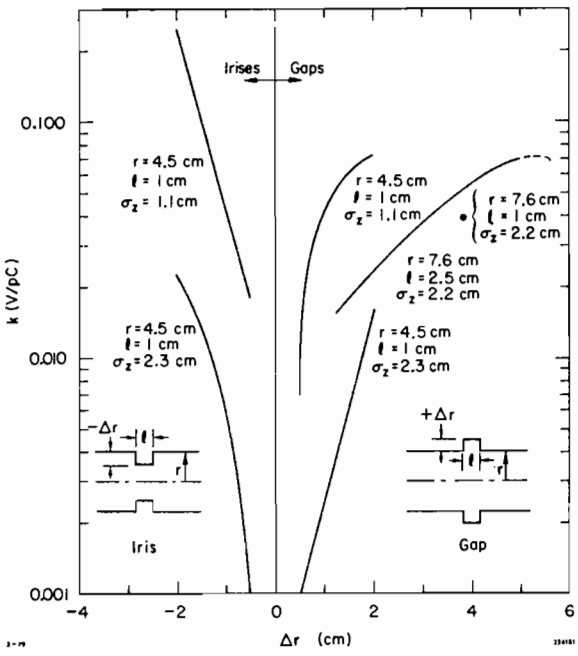

Radial gaps and irises.

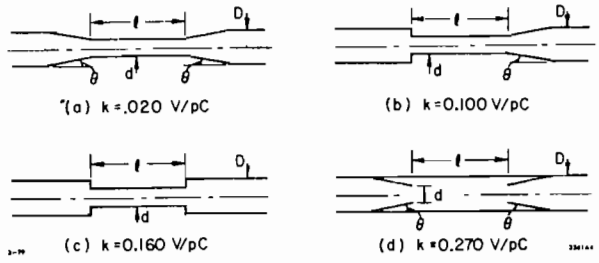

Collimator chambers. D = 20 cm diam, d = 10 cm diam, $\theta = 10^{\circ}$, ℓ = 56 cm and σ_z = 2.5 cm.

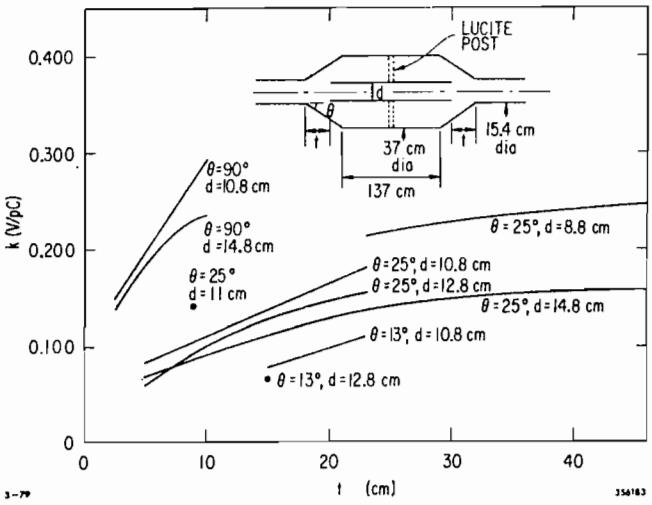

Separating plates model (σ_z = 2.3 cm).

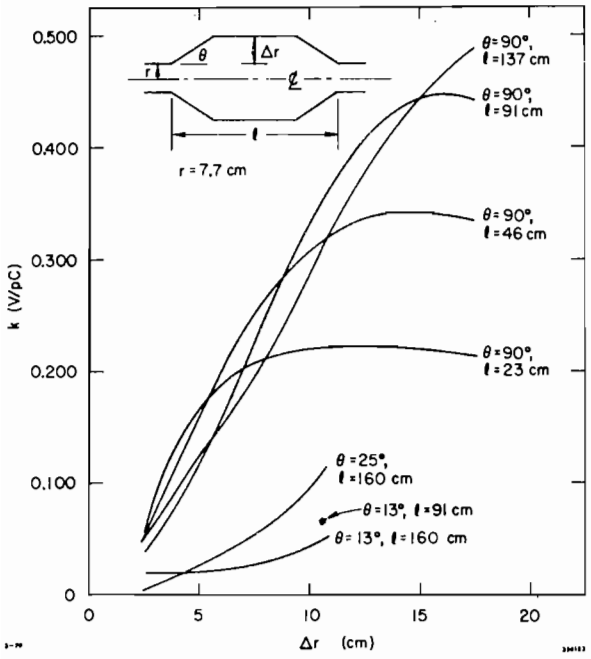

Tapers with various angles and spacings between tapers (σ_z = 2.3 cm).

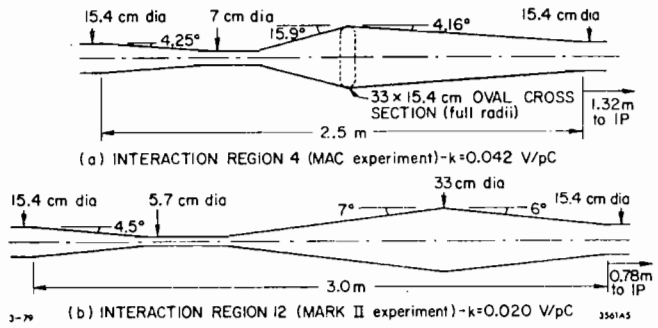

Interaction region chambers (σ_z = 2.3 cm). There is symmetry about the interaction point (IP), so the total loss is twice that given above.

Fig. 8 -- Loss parameters for some representative PEP components.

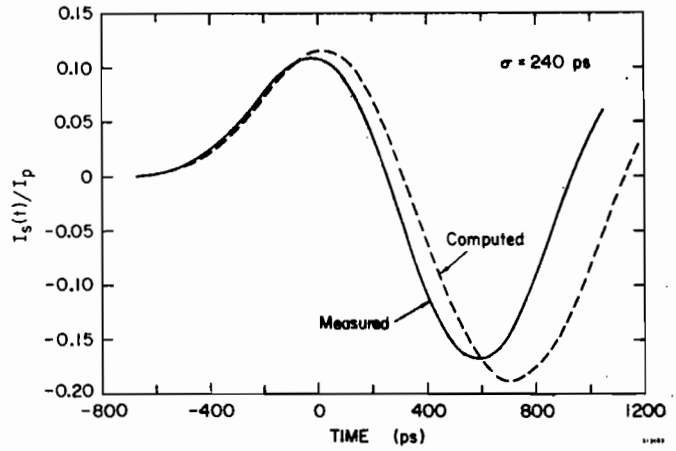

Fig. 9a Computed and measured functions $I_s(t)/I_p$ for the cavity shown in Fig. 7 for a bunch length $\sigma = 240$ ps.

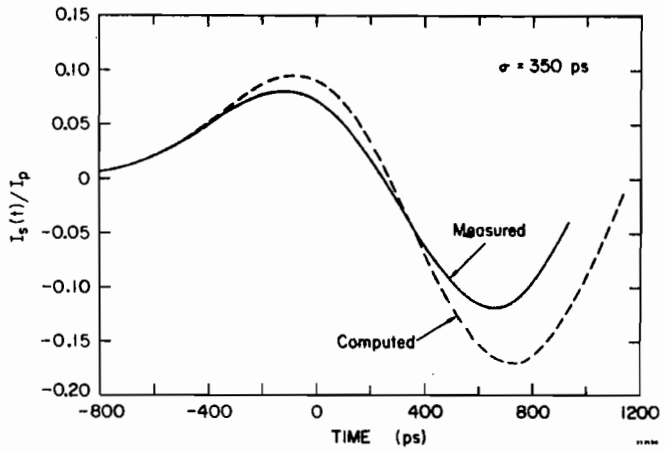

Fig. 9b Computed and measured functions $I_s(t)/I_p$ for the cavity shown in Fig. 7 for a bunch length $\sigma = 350$ ps.

Fig. 9 -- Computed and measured functions $I_s(t)/Ip$ for the cavity shown in Fig. 7.

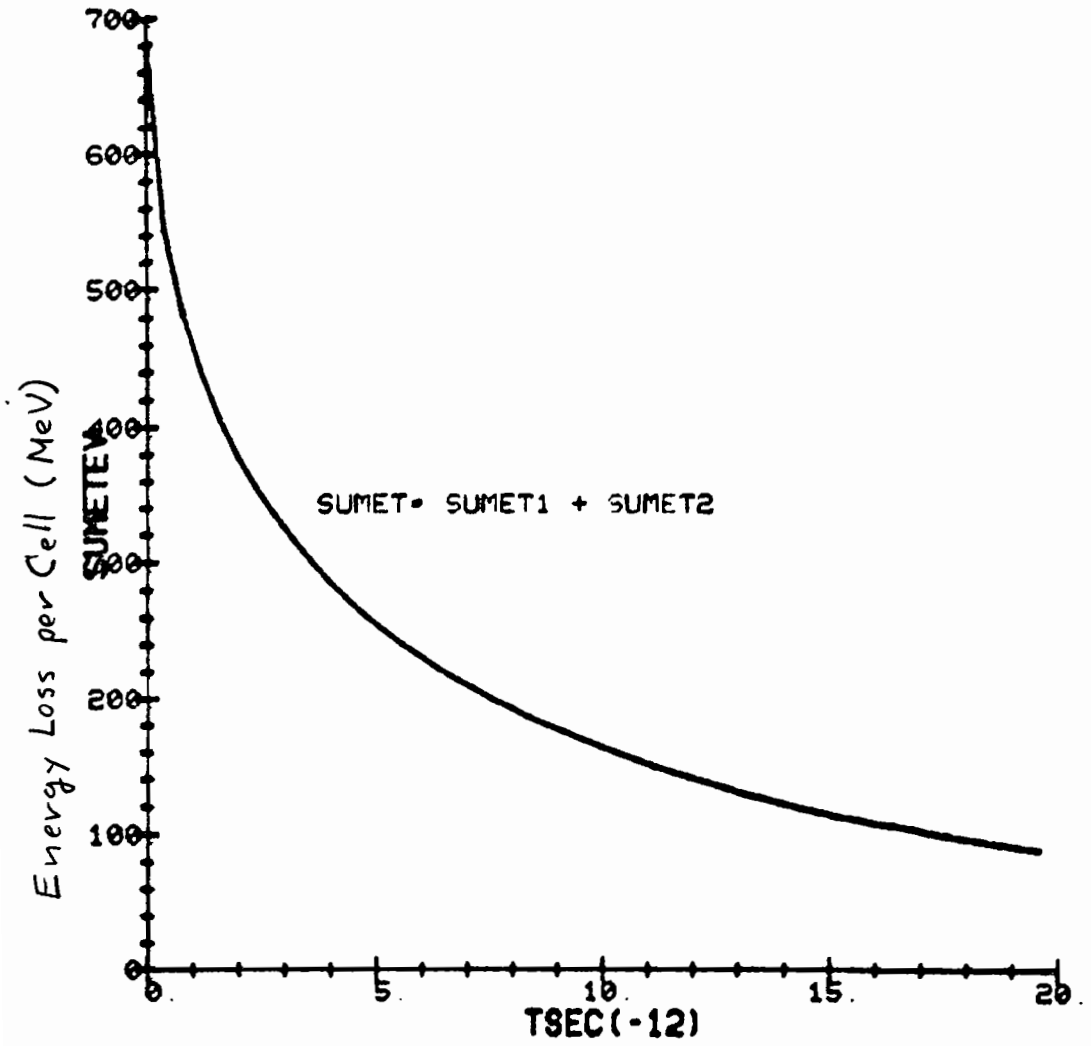

Fig. 10 -- Wake potential for the SLAC linac structure for a point bunch of 5 x 10^8 electrons.

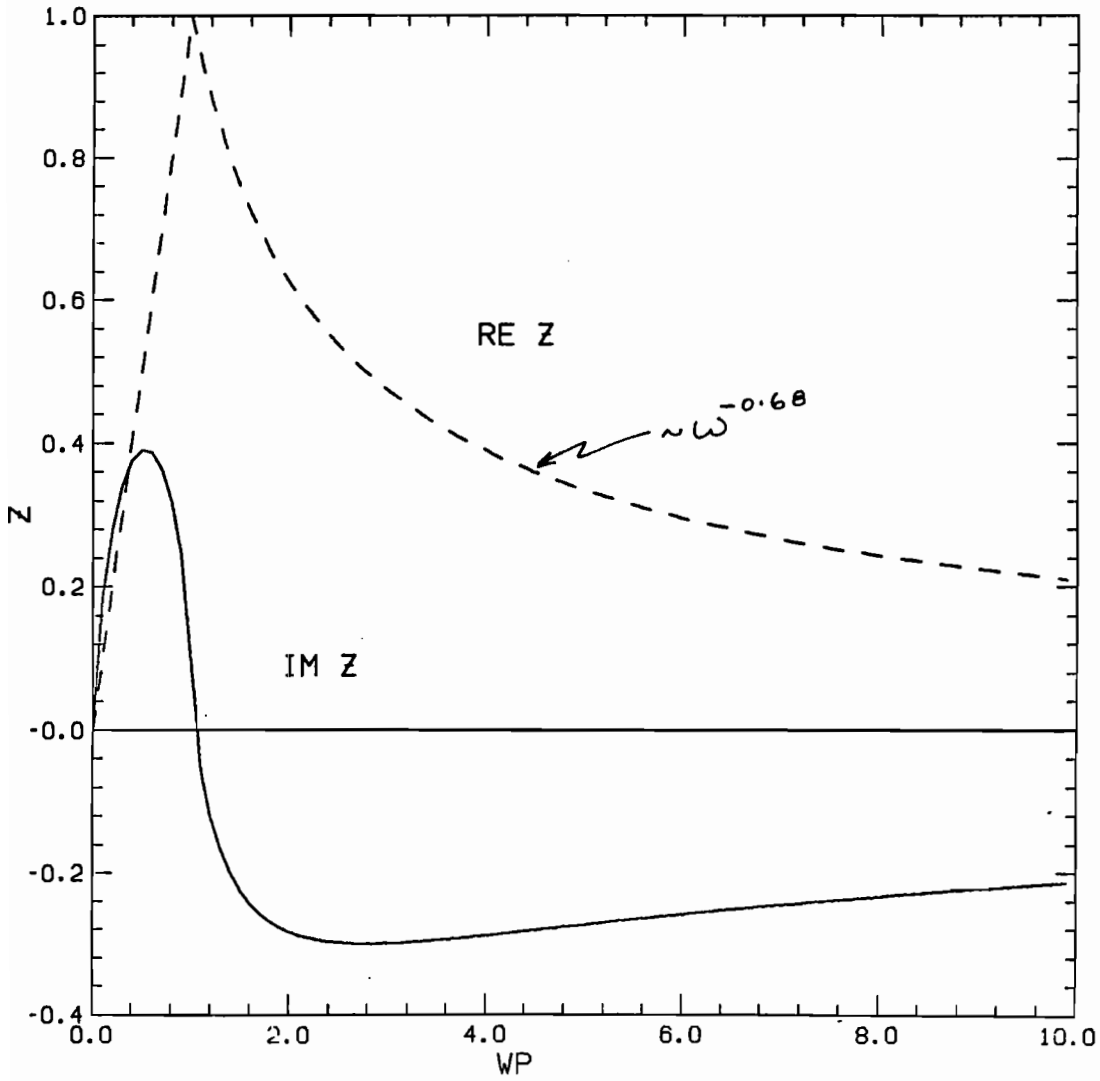

Fig. 11 -- SPEAR impedances normalized to a frequency of 2π x 1.2 GHz and a peak value of 8000 ohms for Re Z.

INVESTIGATION OF TOLERANCES FOR THE PARAMETERS OF THE PROPOSED LBL TEST-BED LINEAR INDUCTION ACCELERATOR

S. Chattopadhyay, A. Faltens, L. J. Laslett, and L. Smith
University of California Lawrence Berkeley Laboratory

I. INTRODUCTION

The Lawrence Berkeley Laboratory has proposed the construction of a Test-Bed linear induction accelerator[1] to test the technique of accelerating heavy ions by use of induction modules and to investigate the transverse focusing of the ion beam by a FODO sequence of magnetic quadrupole lenses. The induction accelerator is intended to accept a 6-μsec bunch of Cs^{+1} ions with 3-MeV kinetic energy ($\beta_0 \cong 0.007$) from a sequence of a few pulsed drift tubes and to accelerate these ions to a kinetic energy of approximately 25 MeV ($\beta \cong 0.020$) in a distance $\cong 10^2$ meter. The approximately 3-fold increase of velocity, combined with bunching of the beam by a factor of two, would result in a six-fold increase of current. A favorable value of transverse emittance -- e.g., $\pi\varepsilon_N = (2.5\times10^{-5})\pi$ meter radian, normalized -- then could be expected to permit a beam current that increases from $I_0 = 2.5$ A ($\cong 15$ μC) to $I \cong 15$ A to be accommodated within an acceptable aperture.[2]

To facilitate the investigation of tolerance limits that would be desirable to impose on the acceleration wave-forms -- and, more generally, to permit study of the expected dynamical behavior of beams of different quality and intensity -- we have constructed an illustrative schedule for the acceleration wave-forms and have prepared programs for the numerical examination of the consequences that could result from errors in wave-form magnitude, timing, or etc. and from variations in the initial characteristics of the beam. The design of appropriate wave-forms was initially undertaken by treating the longitudinal field $E(z,t)$ as a continuous function of z, but, with such work as a guide, impulsive wave-forms were then adopted for application at intervals (e.g., at 1-meter intervals) along the accelerator. A check of the uniformity of the linear charge density at various fixed times indicated that this transition to impulsive fields could be made successfully if the acceleration and bunching begin gradually. Considerations that entered irto the wave-form design are summarized in Sect. II and some tolerance questions that warrant attention are discussed in Sect. III. The investigation of tolerance limits was begun only very shortly prior to the start of the Workshop (and continued to a limited degree during the Workshop); accordingly, although initial results appeared favorable, it clearly would be premature to report tolerance results at this time.

Following the acquisition of sufficient information concerning the tolerance restrictions for longitudinal acceleration, for a satisfactory representative set of wave-forms, we are prepared to extend the computational work to a similar investigation of beam-envelope behavior in the FODO transport system of the accelerator. It is planned, for convenience, initially to consider this transport system to be strictly periodic spatially (occupancy factor, $\eta = 1/2$; half-period, $L = 1$ meter), although a final design of quadrupole lenses meriting subsequent examination well might divide the Test-Bed into two or three sections characterized by successively increasing values of L and certainly will require space for occasional pumping ports, etc. The work in progress does not take collective effects into account explicitly, but parameters controlling potential collective instabilities have been the subject of other theoretical and computational investigations.

II. THE LONGITUDINAL ACCELERATING FIELD

1. Specifications

Cs^{+1} to be accelerated from

$\beta_0 = 0.007$ to $\beta \cong 0.020$;

Little initial spread of β;

Inject for an interval $\cong 6$ μsec;

Accelerate with spatial bunching by a factor $\cong 2$;

Maintain the linear ion density substantially constant, vs. z, at every fixed t;

Assume that one will subsequently design and provide "ears" to the applied wave-forms, to compensate for longitudinal space-charge forces at the ends of the bunch;

Conform to technological restrictions concerning the magnitude, shape, and volt-sec of the applied wave-forms (e.g., E less than circa 0.30 or 0.35 MV/m and $\Phi \lesssim 0.8$ volt-sec).

The specification that the linear charge density along the bunch shall be constant at any fixed time is favorable with respect to avoidance of excessive transverse space-charge defocusing forces, and the avoidance of a significant $d\lambda/dz$ in the interior implies that the wave-forms require only the addition of modest corrective fields ("ears") at the ends in order to compensate for longitudinal space-charge forces.

2. Continuous Longitudinal Fields

In the work that follows we make frequent use of "scaled" variables τ and F, where $\tau = ct$ and $E = \frac{A_i c^2}{qe} F$. If the requirement that the longitudinal density remain constant along the beam (at fixed t) is to be maintained, it is clear that no particle should experience a longitudinal electric field until the entire beam is within the accelerator. Accordingly, if injection occurs within the interval $0 < \tau < 1800$, one may arrange that $E \neq 0$ only for $\tau > \tau_G$ where, for example, $\tau_G = 1850$. Subject to this restriction, one can prescribe the functional form of the field $F(z(\tau))$ acting on a reference particle (e.g., on a particle injected at the mid-point of the bunch) and also a function $w(\tau - \tau_G)$ that describes the factor by which the bunch length is shortened. The requisite wave-forms, $F(z,\tau)$, then may be derived (in practice, numerically) so that the desired constancy of $\lambda(z)$ is achieved -- Note 1.

An example of a selected bunching function, $w(\tau - \tau_G)$, is shown in Fig. 1. Figure 2 shows, also as an example, the form of the function $E(z(\tau))$ chosen in this initial work to represent the field acting on the reference particle, together with the corresponding fields acting on particles at the head and tail of the beam. In anticipation of the use of localized fields it has appeared desirable that the acceleration and bunching begin gradually -- most particularly if the constancy of linear density vs. z is to be maintained throughout the acceleration -- and the functions illustrated in Figs. 1 and 2 were designed with this intent. Subsequent to this gradual onset, the fields are permitted to grow comparatively rapidly to attain values limited chiefly by technological considerations. There has been no attempt, in the work described here, however, to construct a fully optimized design, since the object of this work is an investigation of tolerances.[3]

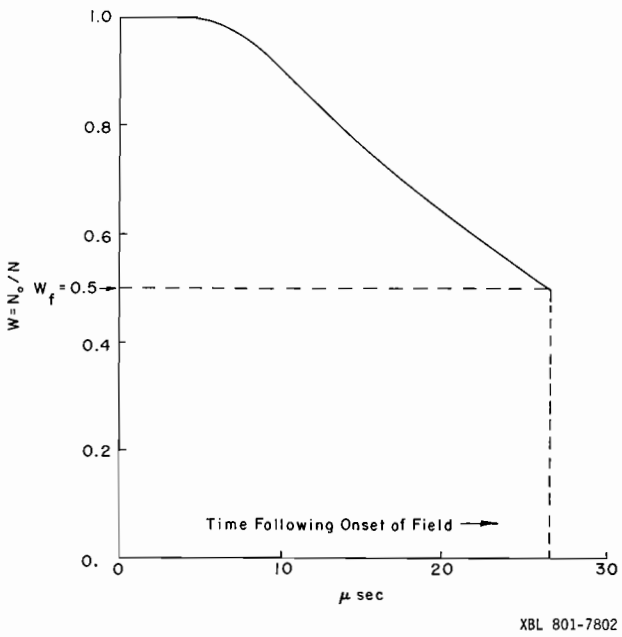

Fig. 1. An example of the bunching function, $w(\tau - \tau_G)$.

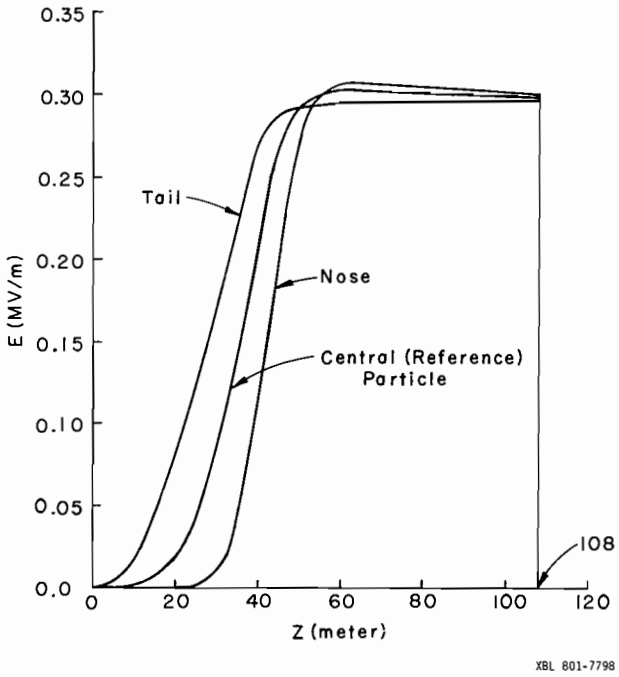

Fig. 2. An example of the field on a reference particle, and of the associated fields on the nose and tail particles when the bunching function is that shown in Fig. 1.

3. Discrete Impulsive Fields

Prior to the investigation of tolerances, the continuous longitudinal field (Sub-section 2) was discretized into a sequence of impulsive fields (nominally at 1-meter intervals). Values of F at each of the discrete z values were obtained at seven values of τ (within the interval during which the beam would be present) and the corresponding wave-forms were obtained as a least-squares fit to a polynominal of the form

$$F(\tau) = E_c + A_1 D + A_2 D^2 + A_3 D^3 + A_4 D^4,$$

where

$$D = \tau - A_o,$$

$$A_o = \tau - A_{Ref.},$$

and

$$E_c = F(\tau_{Ref.}).$$

The parameters E_c and A_i (i=0,...4) are dimensioned variables, with each index value corresponding to a discrete z value, and are stored for subsequent use in other programs.

A few representative wave-forms, as given by such polynominals, are shown on Fig. 3 for the field sketched (prior to discretization) in

Fig. 2. The corresponding flux-changes per meter, $\int E dt$, are shown as a function of z on Fig. 4.

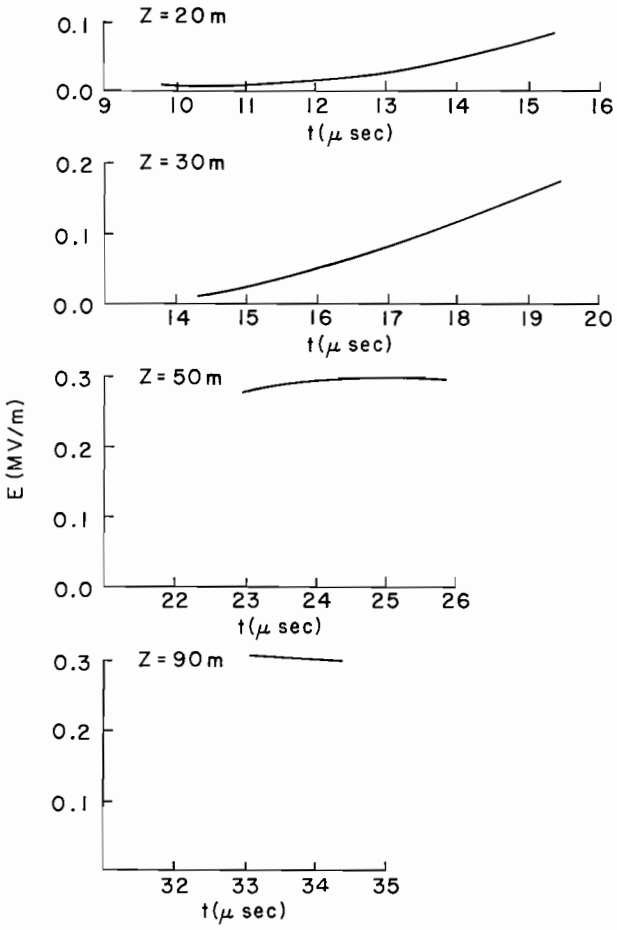

Fig. 3. Representative wave-forms for the acceleration schedule of Figs. 1 and 2.

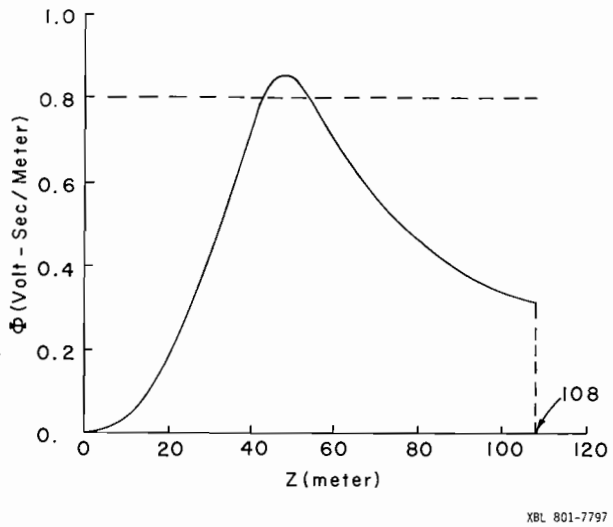

Fig. 4. The flux swing per meter for the acceleration fields of Figs. 1 and 2.

The longitudinal dynamics of particles moving under the action of a sequence of impulsive fields can be supplemented by evaluations of the local bunching (specifically of N_0/N), as indicated in Note 2, and the bunching appears to remain substantially constant with respect to z at fixed time. For the specific longitudinal field mentioned here, the resulting increase of β is as shown on Fig. 5 and the bunching is such that $N_0/N = 0.5$, implying an increase of current by a factor[4] approximately 3/0.5 = 6.

Although the incident beam is presumed to be composed of particles with substantially identical values of β_0, phase plots (e.g., of β vs. z, at fixed time) can be constructed by performing computations for particles with somewhat different values of β_0. The evolution of such phase plots, for an overall spread of β_0 much greater than would be expected in practice, is illustrated in Fig. 6. Corresponding plots of kinetic energy vs. t (at fixed z) are shown on Fig. 7.

III. THE STUDY OF TOLERANCES

We have begun to investigate the sensitivity of the acceleration process to the complete or partial failure of one or more acceleration cavities -- with initial results that appear to be favorable. One effect that can result from failures of this type is illustrated in Fig. 8, from which one sees that the failure of a cavity may result in a particle quite near the tail of the beam drifting (as indicated by the broken dashed line) outside the region covered by the

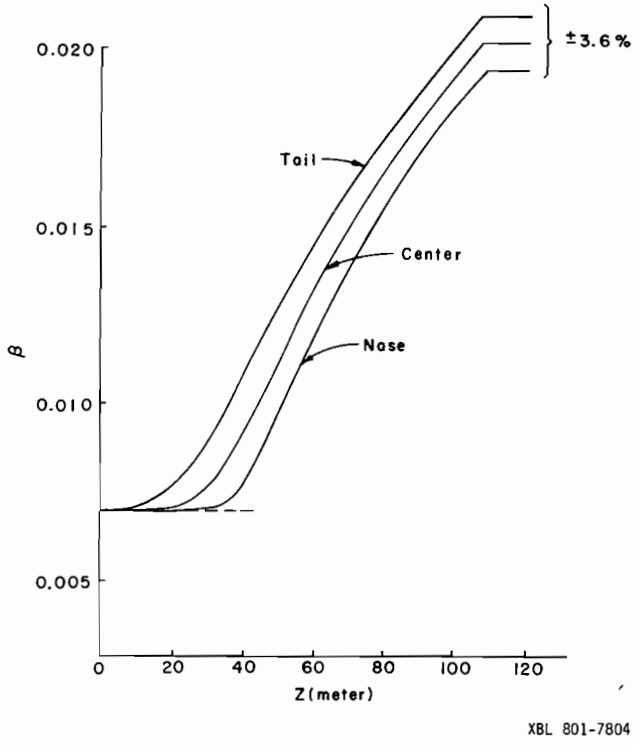

Fig. 5. The growth of β, from an intial value $\beta_0 = 0.007$, for the fields of Figs. 1 and 2.

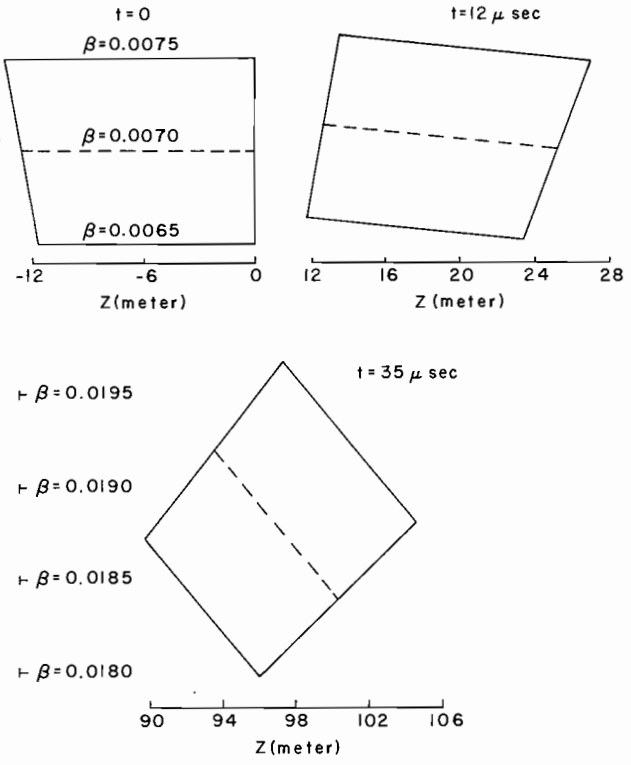

Fig. 6. Evolution of phase diagrams, β vs. z at constant t, with the initial spread of β markedly greater than would be expected in practice.

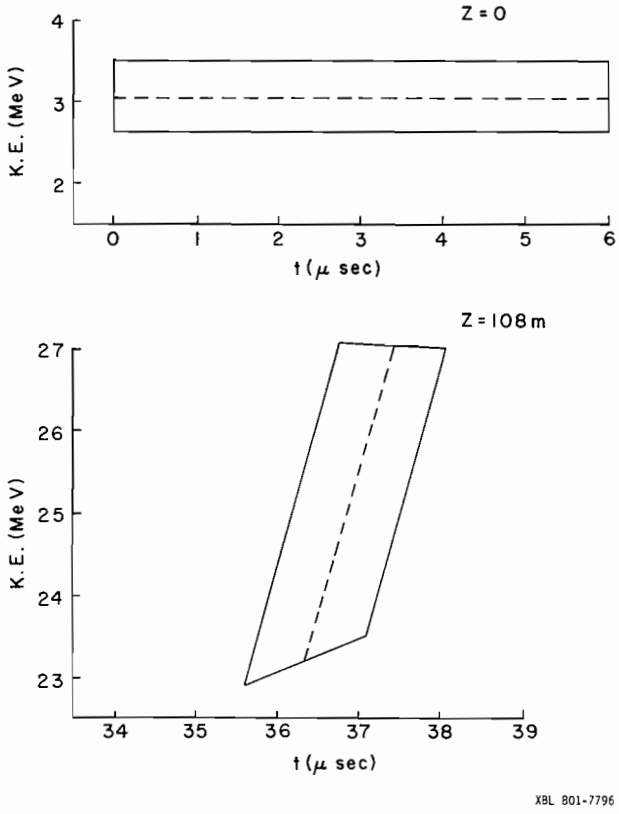

Fig. 7. Plots of kinetic energy vs. t, at constant z, for the case illustrated in Fig. 6.

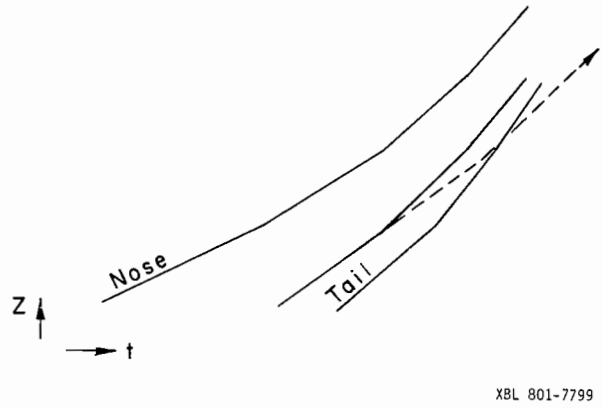

Fig. 8. An illustration of a possible effect, on a particle near the tail of the beam, of a cavity failure.

applied wave-forms (region bounded by the solid lines). A more detailed investigation of this and related effects (such as the response to timing errors, variations of β_0, etc.) ultimately may require the extension of the wave-forms into regions where a field is not required under ideal conditions, in addition to the provision of some supplemental fields near the ends in order to compensate for longitudinal space-charge forces.

NOTES

Note 1. The Bunching Factor in the Case of Continuous Fields

Denoting the z and τ values for a reference ion by $\bar{z}$ and $\bar{\tau}$, we specify $F(\bar{z})$ for the reference particle and have

$$d(z-\bar{z})/d\tau = \beta-\bar{\beta} \text{ and } d(\beta-\bar{\beta})/d\tau = F(z,\tau)-F(\bar{z}(\tau)).$$

With $w(\tau-\tau_G)$ [$= N_0/N$] also specified, we wish (for notation, see Fig. 9)

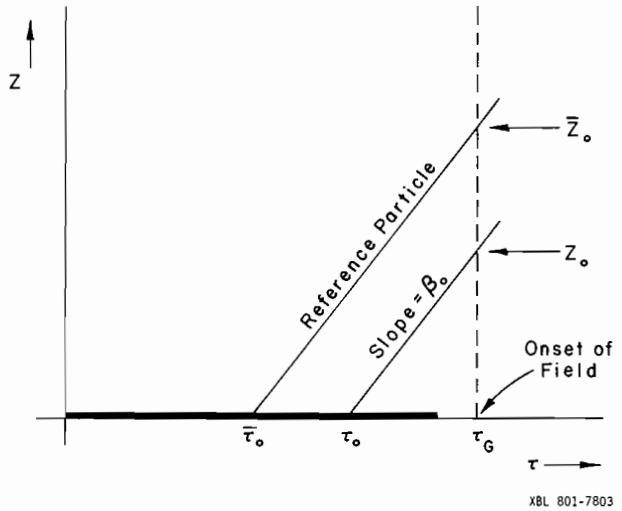

Fig. 9. Illustration of notation employed in Note 1, leading to the relation $z - \bar{z} = (z - \bar{z})_0 \cdot w = \beta_0(\bar{\tau}_0-\tau_0)\cdot w$.

$$z - \bar{z} = (z - \bar{z})_0 \cdot w$$

$$= \beta_0(\bar{\tau}_0 - \tau_0)\cdot w,$$

so that

$$\beta - \bar{\beta} = \beta_0(\bar{\tau}_0 - \tau_0)\frac{dw}{d\tau}$$

or $$\beta = \bar{\beta} + \beta_0(\bar{\tau}_0 - \tau_0)\frac{dw}{d\tau} \qquad (N1)$$

and

$$F(z,\tau) - F(\bar{z}(\tau)) = \beta_0(\bar{\tau}_0 - \tau_0)\frac{d^2w}{d\tau^2} \quad \text{or}$$

$$F(z,\tau) = F(\bar{z}(\tau)) + \beta_0(\bar{\tau}_0 - \tau_0)\frac{d^2w}{d\tau^2}. \qquad (N2)$$

Equation (N2) thus provides the desired values of F for particles crossing the location z at time $\tau = ct$. The corresponding β is given by Eqn. (N1), or may be obtained by integration of $d\beta/d\tau = F$, while z is obtained from $dz/d\tau = \beta$. If, in practice, one integrates with respect to z (in order to obtain results at regularly spaced z values), one must interlace integrations with respect to τ in order to obtain the reference field $[F(\bar{z}(\tau))$, required by Eqn. (N2)] at values of τ common to the reference and trial particles.

If the function $F(z,\tau)$ is not specified through use of the bunching function $w(\tau - \tau_0)$, the local value of N_0/N may be evaluated for any explicit specification of F through introduction of auxiliary variables $u = [\partial\tau/\partial\tau_0]_{z=\text{const.}}$ and $v = \beta[\partial\beta/\partial\tau_0]_{z=\text{const.}}$ (with $u_0 = 1$, $v_0 = 0$). One then employs the coupled total differential equations

$$\left.\begin{aligned} \frac{d\tau}{dz} &= \frac{1}{\beta} \\ \frac{d\beta}{dz} &= \frac{F}{\beta} \\ \frac{du}{dz} &= -\frac{v}{\beta^3} \\ \frac{dv}{dz} &= u\frac{\partial F}{\partial\tau} \end{aligned}\right\} \quad \text{or} \quad \left\{\begin{aligned} \frac{dz}{d\tau} &= \beta \\ \frac{d\beta}{d\tau} &= F \\ \frac{du}{d\tau} &= -\frac{v}{\beta^2} \\ \frac{dv}{d\tau} &= \beta u\frac{\partial F}{\partial\tau} \end{aligned}\right.$$

and computes the local density ratio as

$N_0/N = \frac{\beta u}{\beta_0}$. In the particular case that $F(z,\tau)$ is given by Eqn. (N2), the ratio $\ddot{w}/w$ (with dots denoting $d/d\tau$) is independent of z and may be identified with $\partial F/\partial z$. With β and $\dot{w}$ initially zero, the auxiliary variables u and v then will be

$$u = (\beta_0/\beta)w \text{ and } v = \beta_0\dot{\beta}w - \beta_0\beta\dot{w},$$

with $\frac{1}{\beta u}\frac{dv}{d\tau} = \ddot{\beta} - \beta\ddot{w}/w = dF/d\tau$

$= dF/d\tau - \beta\partial F/\partial z = \partial F/\partial\tau$, as required.

Note 2. The Bunching Factor in the Case of Impulsive Fields.

A(i). Between cavities:

$$\Delta\tau = \frac{1}{\beta}\Delta z, \quad \text{i.e., } \tau_{n+1} = \tau_n + \frac{1}{\beta_n}(z_{n+1} - z_n),$$

while β remains unchanged.

(ii). Traversing a cavity:

τ is unchanged,

and

$$\beta_{n+1} = \sqrt{\beta_n^2 + 2F_{n+1}}\,.$$

B. For infinitesimally neighboring trajectories ($D\tau$ and $D\beta$):

(i). In passing from one cavity to the next:

From Fig. 10,

$$\frac{\delta z_n}{\delta z_{n+1}} = \frac{[(\beta_n + \beta_{n-1}) - (D\beta_n - D\beta_{n-1})]D\tau_n}{[(\beta_{n+1} + \beta_n) - (D\beta_{n+1} - D\beta_n)]D\tau_{n+1}}$$

is a factor that may be applied to convert the old density ratio (initially unity, at z = 0) to the new density ratio, where

$$D\tau_{n+1} = D\tau_n - \frac{D\beta_n}{\beta_n^2}\Delta z$$

and

$$D\beta_{n+1} \cong \frac{\beta_n D\beta_n + (\partial F_{n+1}/\partial\tau)D\tau_{n+1}}{\beta_{n+1}}\,.$$

(ii). In moving between two cavities:

To update linear ion density (N) between cavities ($\delta z < \Delta z$), one recalls that, from B(i) above (with n+1 replaced by n), one employs a denominator $\delta z_n = [(\beta_n + \beta_{n-1}) - (D\beta_n - D\beta_{n-1})]D\tau_n$ in evaluating $\delta z_{n-1}/\delta z_n$. From Fig. 11 it is evident that to obtain the density ratio at a point between z_n and z_{n+1} one should replace δz_n by $s_U + s_L$ -- i.e., the density factor at $z = z_n$ should be corrected by the factor

$$\frac{\delta z_n}{s_U + s_L} = \frac{\text{denominator}}{2[\beta_n D\tau_n - (\delta z/\beta_n)D\beta_n]}$$

to obtain the ratio at $z = z_n + \delta z$.

In practice the infinitesimal quantities $D\tau$ and $D\beta$ may be initialized to 1 and 0, respectively, since only their relative values are of significance.

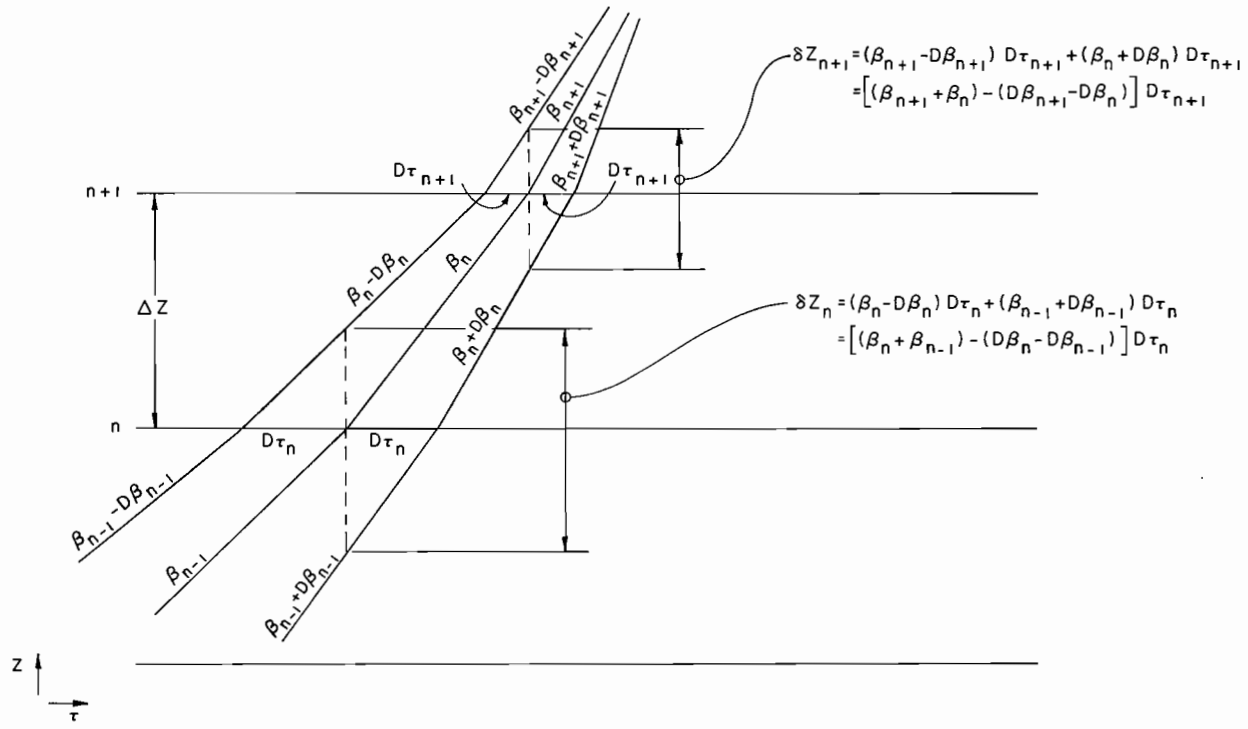

XBL 801-7806

Fig. 10. Kinematics relevant to the change of particle density in passing from one cavity to the next.

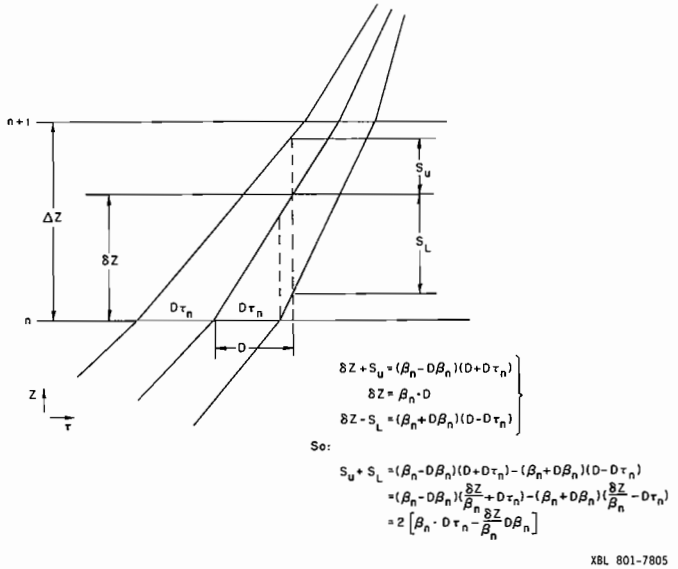

XBL 801-7805

Fig. 11. Kinematics relevant to the change of particle density in passing between induction cavities.

REFERENCES AND NOTES

1. See presentation by A. Faltens -- this Workshop. See also LBL Report PUB-5031 (September 1979) and earlier LBL Report HIFAN-67 (16 January 1979).

2. Experiments now in progress at the Lawrence Berkeley Laboratory are directed to a study of the optical characteristics of a contact-ionization Cs^{+1} source.

3. In a separate investigation, to which we have returned following the Workshop, further consideration is being given to the specification of wave-forms and lattice structures that may prove to be significantly more economical than those mentioned in the present report.

4. The acceleration and bunching produced by the fields described by Figs. 1-3, and by similar field systems[3] to which we have given consideration, results in a current that increases slightly less rapidly than in direct proportion to the kinetic energy. Such current increases permit the transport of a non-relativistic Kapchinskij-Vladimirskij beam through a periodic focusing system of constant K and η without the space-charge tune depression during the course of acceleration becoming more pronounced than initially (for the reference particle).

ION INDUCTION LINACS: REFERENCE DESIGN AND PROPOSED TEST-BED

Andy Faltens and Denis Keefe

Lawrence Berkeley Laboratory

I. INTRODUCTION

The LBL HIF program has concentrated on the induction linac approach because this type of machine is able to accelerate the entire charge required for fusion in a single, high current bunch, and because of our experience ten years ago using the Astron induction linac at LLL and subsequently building and operating our own machine at LBL. The operation of an r.f. linac with storage rings, Fig. 1, is based on an operating line where, excluding the tree of linacs at the lowest energies, acceleration is along a constant current trajectory to peak energy, and then along a constant energy trajectory as the current is compressed and multiplied to reach the required of beam power (> 100 TW). The operation of the linear induction accelerator, Fig. 2, is along a trajectory where the energy and current are increased simultaneously; at the end of acceleration the beam is split transversely into two groups of beams to provide for higher peak power and a left-right symmetrical pellet bombardment.

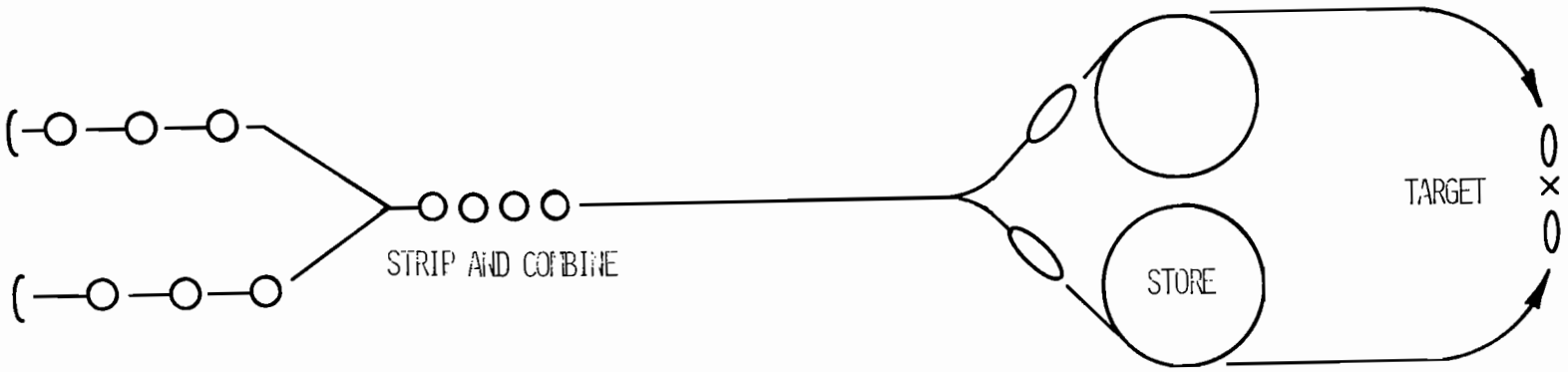

R&D NEEDED: ION SOURCE AND LOW-BETA ACCELERATOR
PHASE SPACE DILUTION AT EACH MANIPULATION
VACUUM AND CHARGE EXCHANGE CROSS SECTIONS
COST OPTIMIZATION

XBL 806-10083

Fig. 1 - RF Linac with Storage Ring Current Multipliers

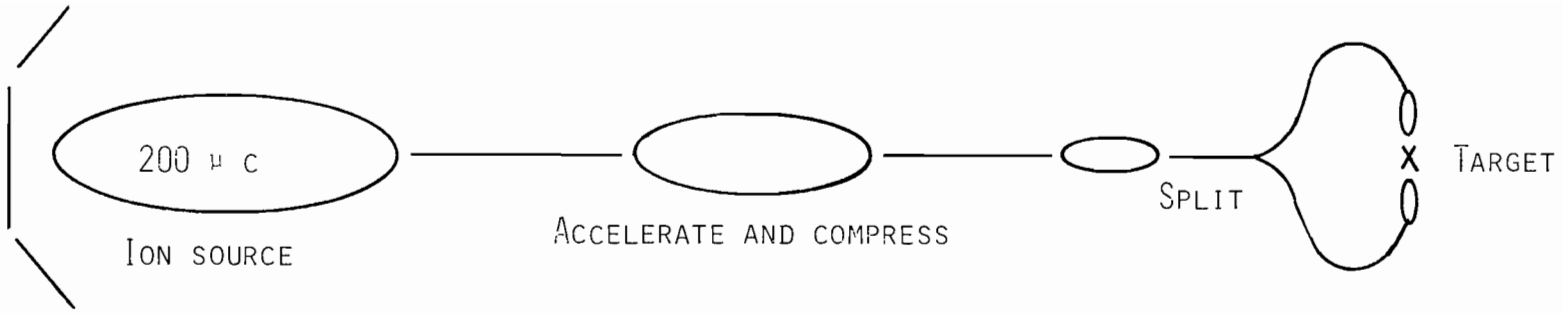

R&D NEEDED: ION SOURCE AND LOW-BETA ACCELERATOR
MATCHING AND PHASE SPACE DILUTION
HIGH-CURRENT BEAM TRANSPORT
COST OPTIMIZATION

XBL 806-10084

Fig. 2 - Linear Induction Accelerator "Single-Pass" System

2. REFERENCE DESIGN FOR 1 MEGAJOULE DRIVER

The parameters of our 1 MJ reference design are as follows:

Beam charge = 210 μC (electrical) of U^{+4}

Q = 1 MJ	P = 160 TW
T = 19 GeV	R = 0.5 gm/cm^2
$\varepsilon_N = 3 \times 10^{-5}$ radian-meters	Pellet radius = 1.25 mm

The major cost, about 80% , of the LIA conceptual design is in the induction accelerator itself, with the injector and source requiring about 10% and the final transport and focusing another 10%. The earliest concept (three years ago) for an induction linac driver was based on a large-aperture (radius ~ 50 cm) ion-emitter which could provide 5 amperes of beam current for injection into a drift tube accelerating structure, followed by iron core induction units at long pulse durations and ferrite core units at short durations. The 1979 version of the system looks very similar, although most components of the system have been examined and cost optimized. The major differences are: that the source current may be increased as required by using multiple beamlets with electrostatic focusing, as proposed by Herrmannsfeldt,[1)] thereby eliminating the need for unwieldy magnetic quadrupoles at low energies; that the induction acceleration may begin economically near the 10 MeV point instead of near 100 MeV; that the magnet occupancy factor (fraction of length occupied by magnets) may be decreased from 50% to about 10% as the energy is increased; that acceleration of bunches less than 100 ns in duration is not necessary; and that final focusing may be greatly improved by splitting the beam into many beamlets near the target chamber. A computer program, LIACEP, has been used for cost optimization of the accelerator portion of the system and has generated the desired operating

parameters shown in Fig. 3. As the pulse duration is decreased with increasing beam voltage, the appearance of the accelerating modules changes gradually, from being similar to the modules designed and built at NBS for a 2 μsec., 400 kV pulse, Fig. 4, to being similar to the LLL Astron Injector 300 ns, 300 kV modules shown in Fig. 5, to finally being similar to the LBL ERA 250 kV 45 ns modules, Fig. 6. The applied voltage waveforms used in the electron induction machines shown were flat; for ion acceleration they need shaping as shown in Fig. 7, the details of which are being refined at this time as reported at this workshop by L. Jackson Laslett. Interspersed between the accelerating modules are superconducting quadrupoles whose pole tip field has been assumed to be 4 Teslas for design purposes.

There is still room for invention and improvement at both ends of the machine. At the front, the source parameters as used in the Reference Design were as follows:

Area ≈ 0.5 m^2	Current = 7.5 amps of U^{+1}
Voltage = 1 MV	Beam Charge = 150 μC of U^{+1}
Pulse Duration = 20 μsec	Current Density = 2 mA/cm^2

There is a wide variety of other choices that could be explored for future applications. At present, we are routinely using a large-aperture contact-ionization source for Cs^{+1} ions - this type of source can be used to produce U^{+1} ions. We have successfully tested a smaller alumina-silicate source for producing Cs^{+1} ions - such sources offer significant advantages

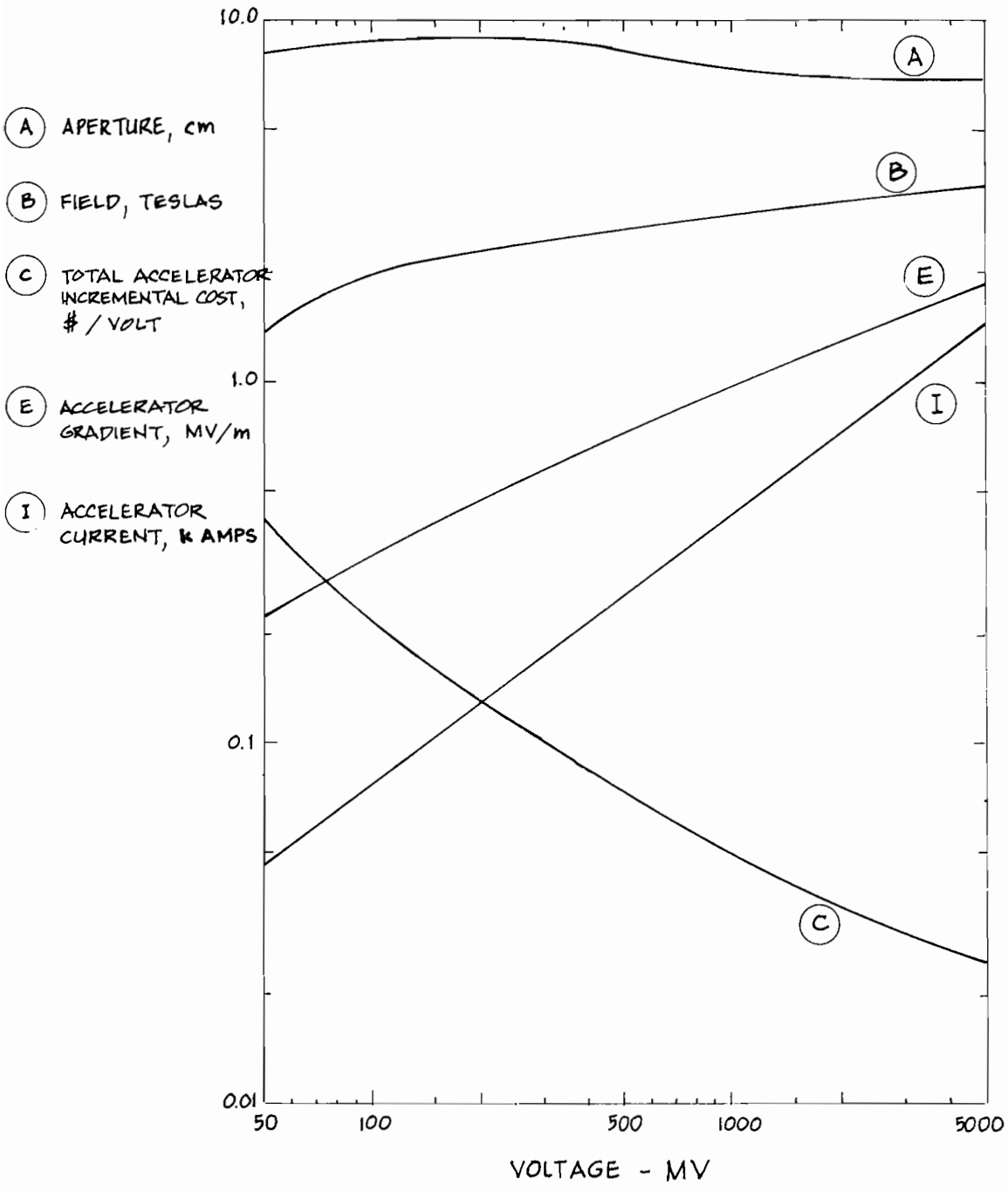

XBL 806-10085

Fig. 3 - 19 GeV U^{+4} 1 MJ Induction Linac Parameter

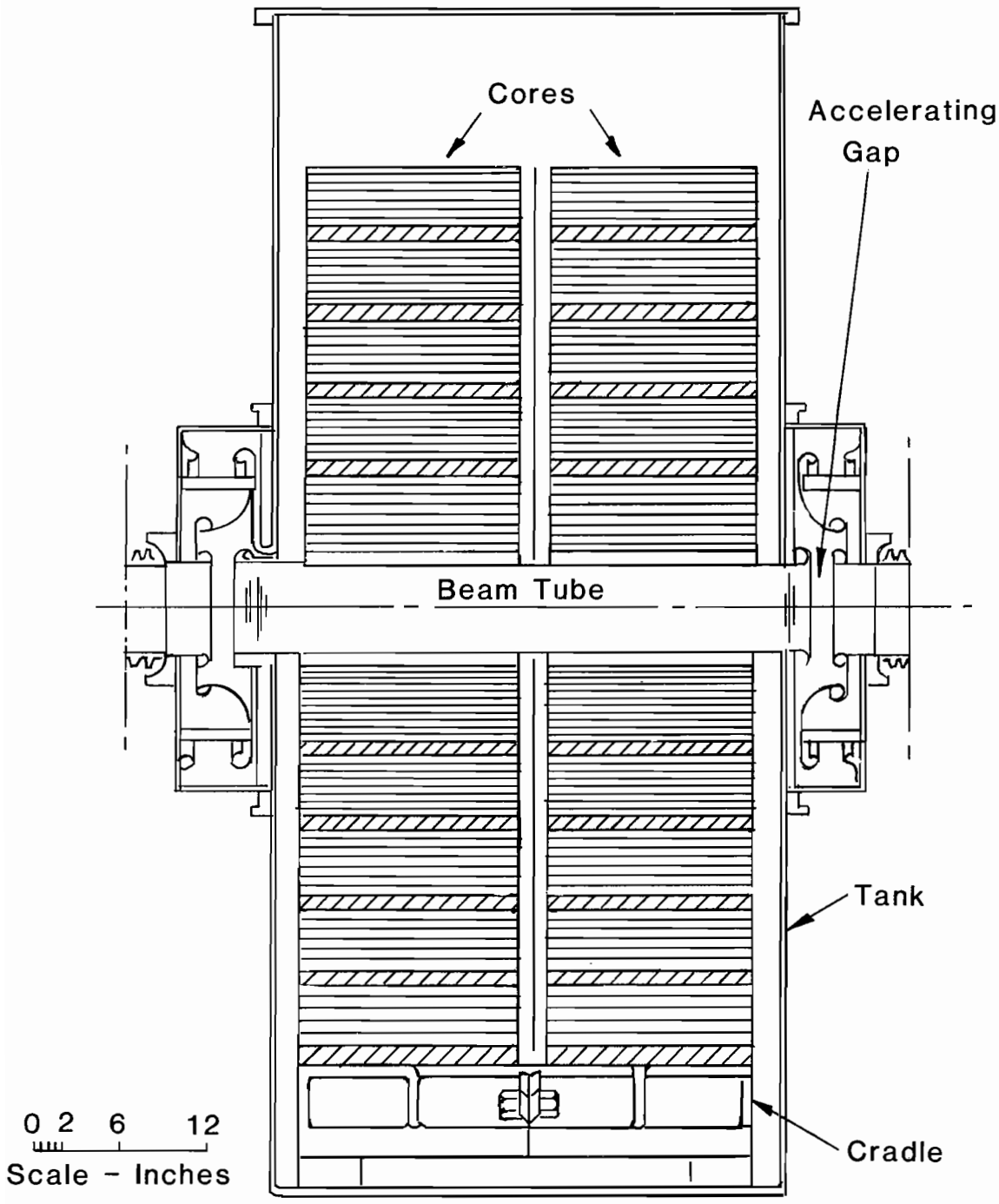

400 kV, 2μs LIA INDUCTION MODULE DEVELOPED AT N. B. S.

Fig. 4 - Schematic cross-section of NBS accelerator module for 400 kV, 2 μs pulses.

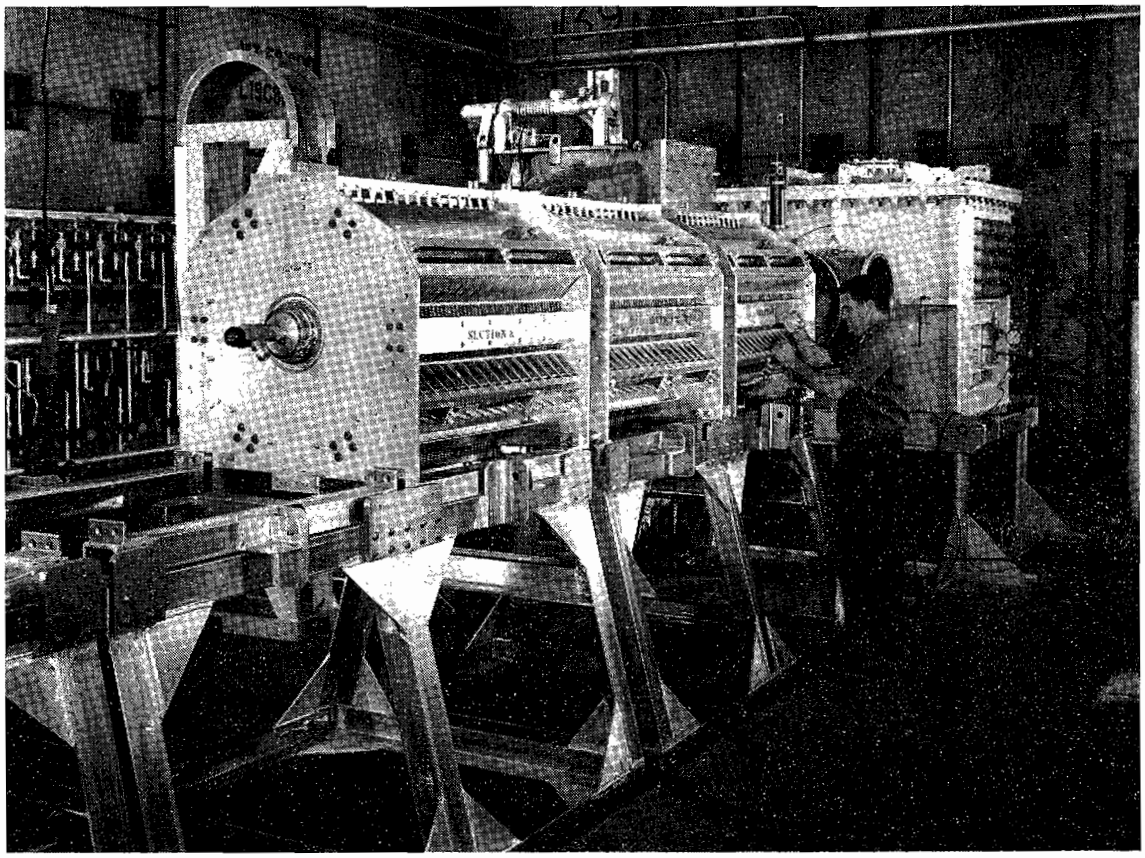

Fig. 5 - LLL Astron Injector accelerator modules for 300 kV, 300 ns pulses.

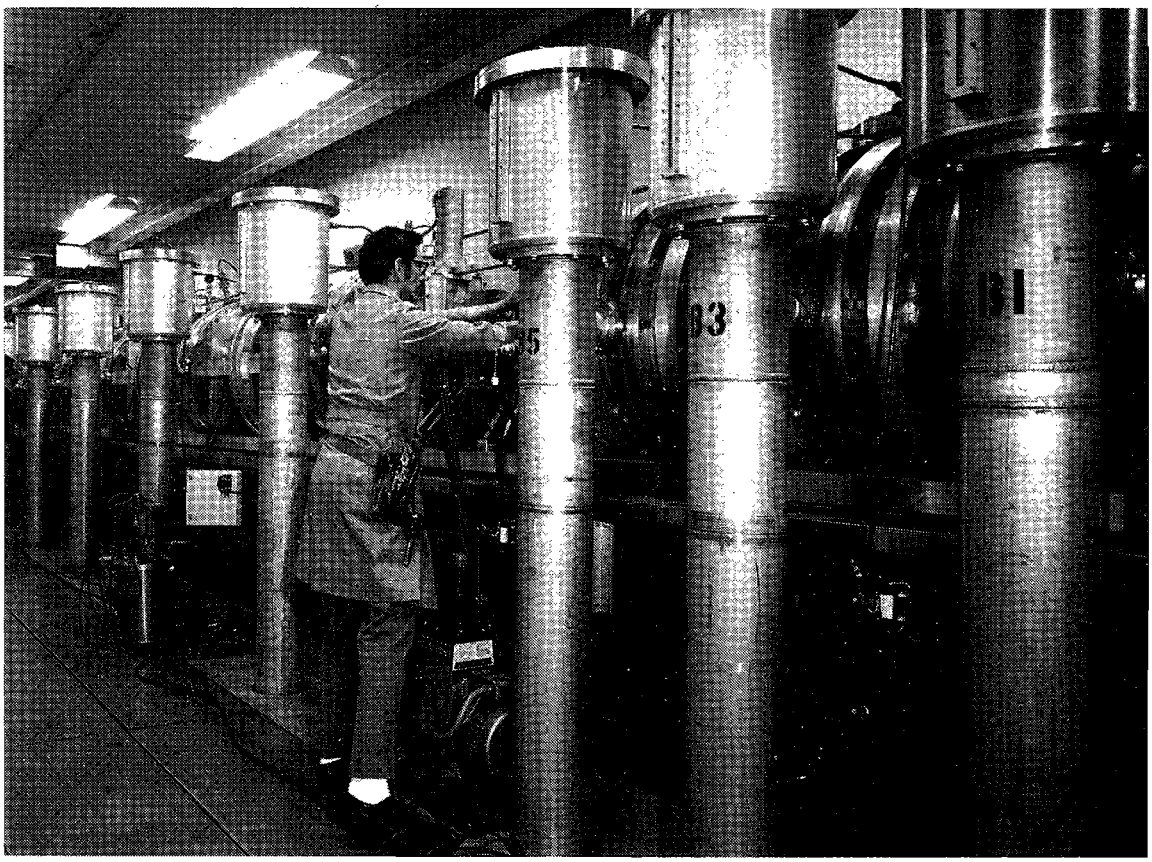

Fig. 6 - LBL ERA Injector Accelerator modules for 250 kV, 45 ns pulses.

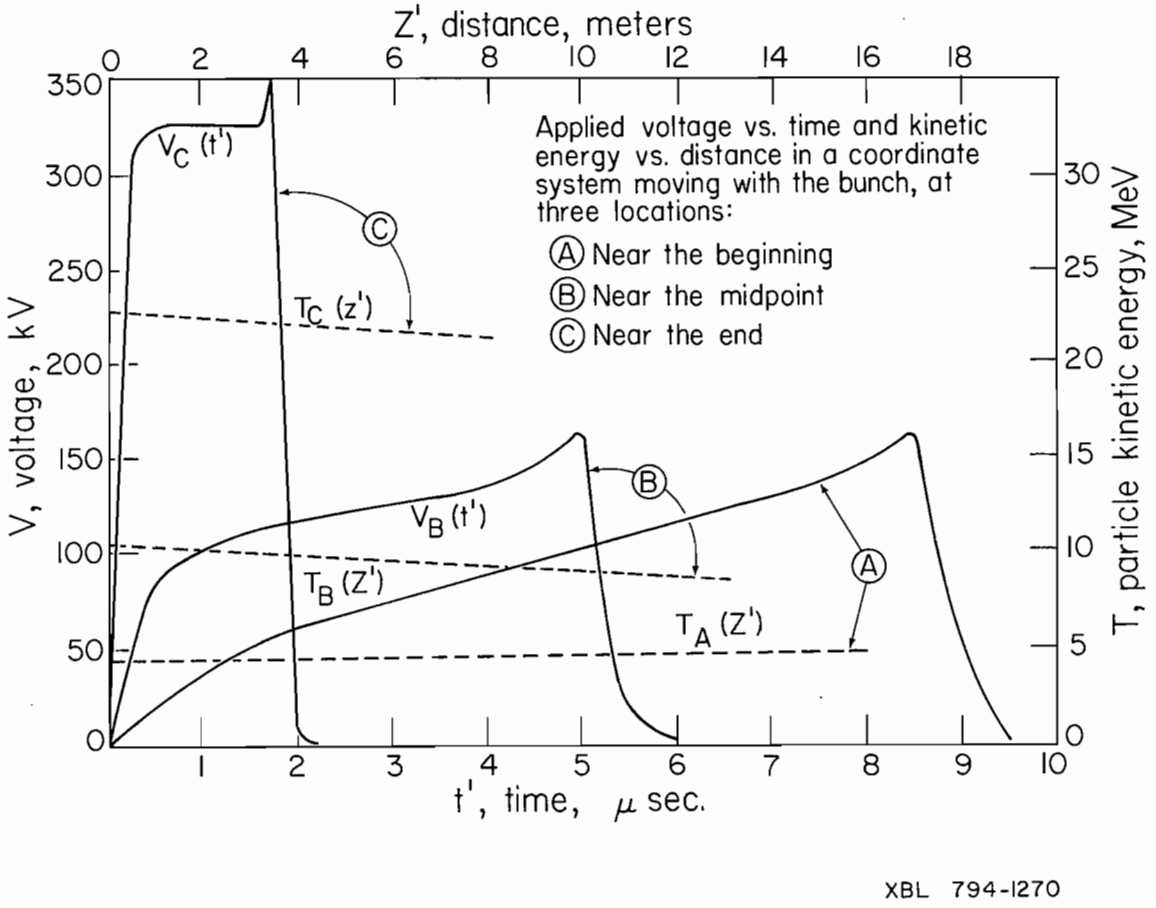

Fig. 7 - Ion Induction Accelerator Waveforms

for the production of thallium ions (mass number: 204). Finally, large-aperture sources, approaching the sizes needed, have been developed at LBL for plasma heating in Tokamaks and would allow production of a wide choice of ion species. One such Ehlers-type source has already produced amperes of xenon ions.

The total source current for some ions such as Cs^{+1} is limited by the downstream transport system rather than by the source itself; likewise, the large diameter sources and beams are dictated by the desire to decrease the transverse space charge fields, rather than by the current density emission limit. No major effort at LBL has been devoted to obtaining ions with masses higher than Xe and Cs, both of which have been generated in sufficient amounts, even though there has been a small advantage shown for heavier ions in some of the conceptual designs. The LBL contact ionization Cs source is shown in Fig. 8. Its emission density is adequate for a 1 MJ driver and would require scaling only in dimensions and voltage.

The injector for the reference design has three pulsed drift tubes. The first two are used to accelerate 150 μC of U^{+1} to an energy of 5 MeV, at which point a helium gas-jet stripper is introduced and an emergent beam with 210 μC (electrical) of U^{+4} ions is created and separated[2]. This beam is accelerated by a further 8 MeV by passage through the third drift tube, and then enters the induction linac.

Other injector options need careful evaluation in the future. Solenoid focussing has been examined in some detail and while workable, is too cumbersome an approach. The limits of applicability of grid focussing needs

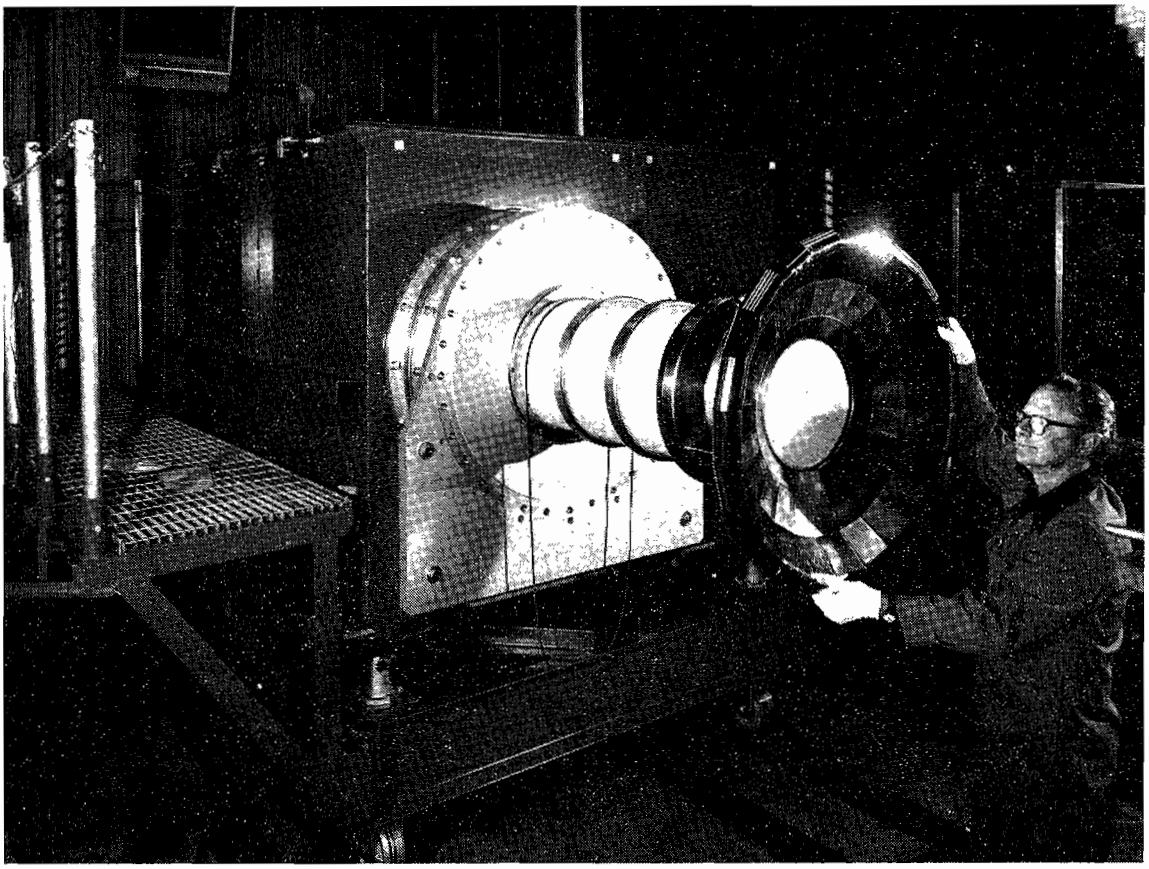

Fig. 8 - 1 Amp Cs^{+1} Contact Ionization Source.

more study and also the use of electrostatic quadrupoles within the drift-tubes (either large-aperture or stacked small-aperture arrays as suggested by Maschke at this meeting) remain to be evaluated. The multiple beam electrostatic focusing system designed by Herrmannsfeldt has been simulated computationally, including space charge, and Figures 2-7 of Reference 1, show the rectangular and annular ribbon configurations as well as particle trajectories through enough of the system to show that it is extendable indefinitely.

Another injector possiblity, the recirculator shown in Fig. 9, allows the acceleration structure to be used several times in one pulse. The magnetic focussing lenses are held at fixed field. The recirculator is limited to long intervals between bunch passage times by the recovery time limitations of existing switches. With any of the alternative concepts shown, and future ones yet to be discovered, the decision on their suitability for use is on the basis of economic comparison. In general the magnetic quadrupoles have proven to be preferable as the energy is increased and the optimum energy for changing from electrostatic to magnetic lenses remains to be determined. At the present stage of conceptual designs, it is significant that at least one source and one injector concept exist, and that their costs are not dominant for the entire system.

A similar mix of technical and economic considerations applies to the final focusing problem. It is clear that the peak power delivered to the pellet may be greatly increased by proliferating the number of incident beams and final focusing elements. An apparently more stringent requirement for the subdivision into several beams is set by the need to keep the emittance of

RECIRCULATOR CONCEPT

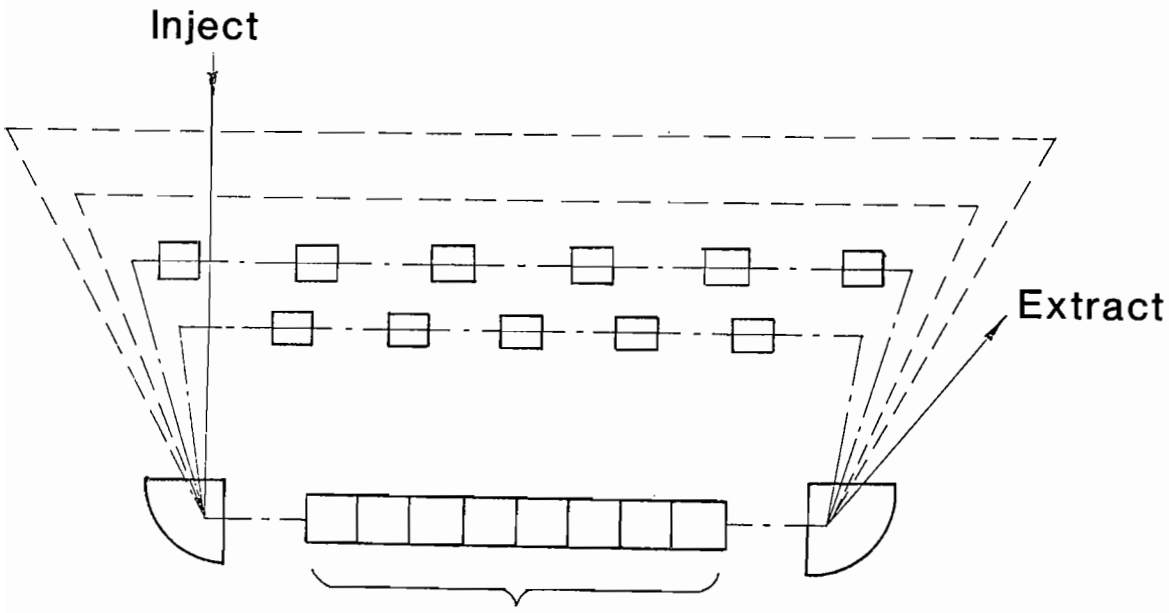

Induction Accelerator (5 MV)

Burst Mode: 5-10 pulses with
20 μsec cycle

Current = Constant

Pulse Duration = Constant

Fig. 9.

each beamlet small enough to avoid third-order aberrations in the final focussing lenses[3,4]. To accomplish such splitting the beam has to be enlarged greatly in transverse dimensions before passage through vertical and horizontal splitting magnets (see Fig. 5 of Reference 4); a necessary condition is that the energy density deposited in the septum edge be less than about 1 kJ/gm to avoid spalling. The gases liberated from the surfaces move too slowly to affect the beam during the passage time of the bunch. Just before the septum splitters that create the major subdivision into two pairs of beams an energy tilt is introduced into the bunch by strongly ramping the voltages in the final 280 meters of induction cores. This will cause the bunch length to collapse from 175 nsec, at the end of acceleration, to 10 nsec at the target, after it has traversed the full length of the transport line. A drawing of part of the final transport system is shown in Fig. 10. All of the estimates for the conceptual design are based on final focusing in a vacuum environment, with perhaps charge neutralization near the pellet. A completely different alternative is for a charge and current neutralized final transport in a low pressure gas, or a co-streaming electron beam. If such a scheme were viable, it would greatly reduce the complexity of the final focusing array of magnets and reduce some of the stringent requirements during the acceleration process.

3. CURRENT AND PROPOSED LBL PROGRAM

The ongoing experimental program at LBL and the proposed one for the accelerator development facility (ADF) are aimed at verifying the design criteria experimentally and developing machine specifications. Basic to all HIF drivers is the question of the transverse stability limit in a focusing

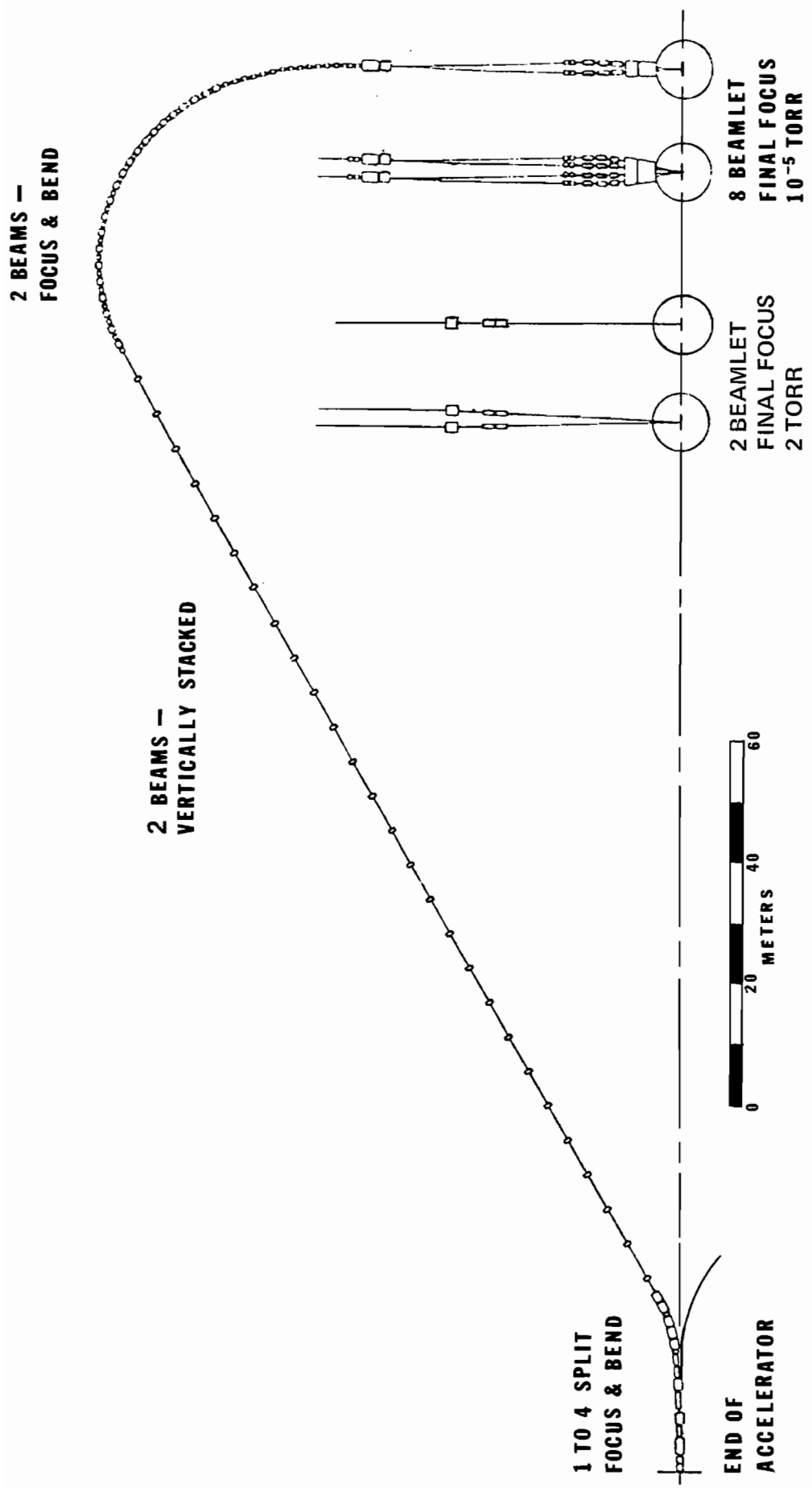

FINAL BEAM TRANSPORT AND FOCUS

channel, which has been investigated analytically and computationally, but not yet experimentally. The 1 Amp 2 MeV Cs^{+1} beam propagation experiment, Fig. 11, is a first step towards an experimental verification of the transport theory. It would investigate matching into a quadrupole lattice with intense space charge and a finite bunch, and could roughly check regions of stability and instability. A substantially longer transport system is required for investigating the region near the threshold of instability.

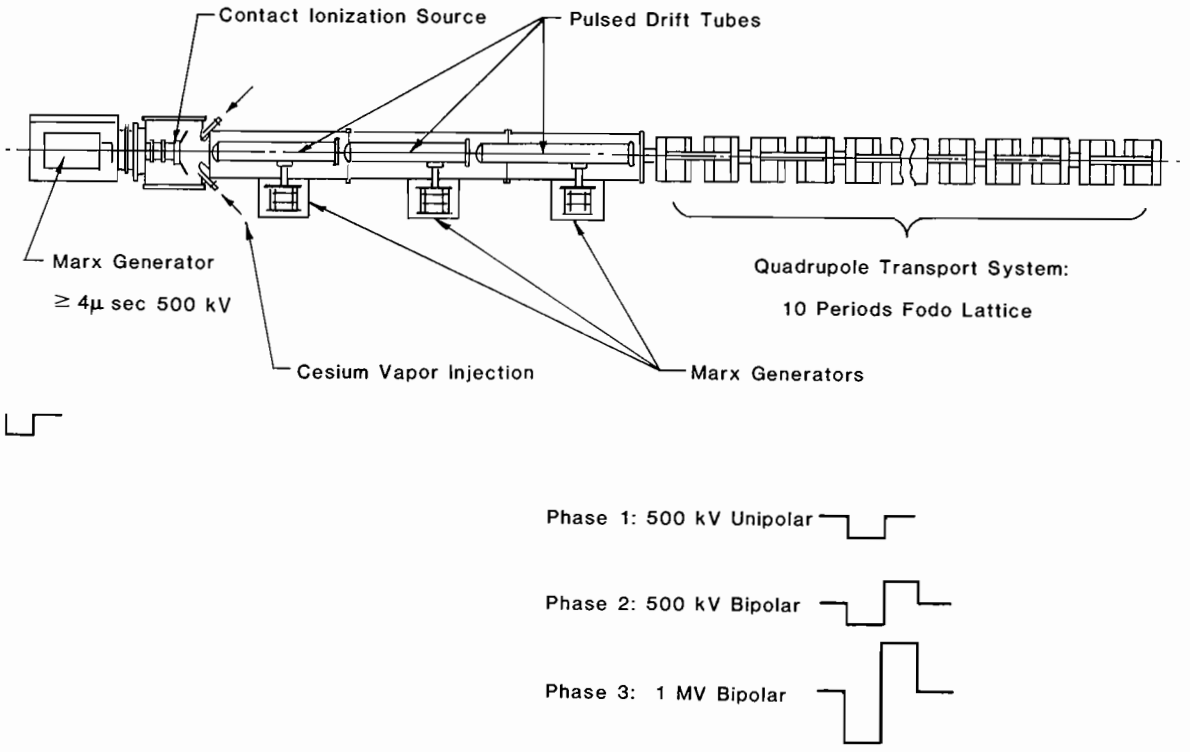

1 AMP, 2 MeV, Cs^{+1} BEAM PROPAGATION EXPERIMENT

Fig. 11.

Figure 12 shows where the present and proposed experiments are in relation to the end goals, and where the research machines for heavy ion collisions are on the same scale; Table I tabulates some of the desirable values. These figures do not include the latest desire of the target designers to move toward lower particle energies.

TABLE I

BEAM VOLTAGE AND CHARGE FOR SINGLY-CHARGED CESIUM*

Example	Charge (μC)	Kinetic Energy (MeV)
1. 4 J (Current experiment)	2	2
2. 500 J	20	25
3. 100 kJ	$\geq$ 45	$\leq$ 2,200
4. 1 MJ	$\geq$ 80	$\leq$ 12,000

* For Uranium the beam charge needed is, typically, one-half that for Cesium.

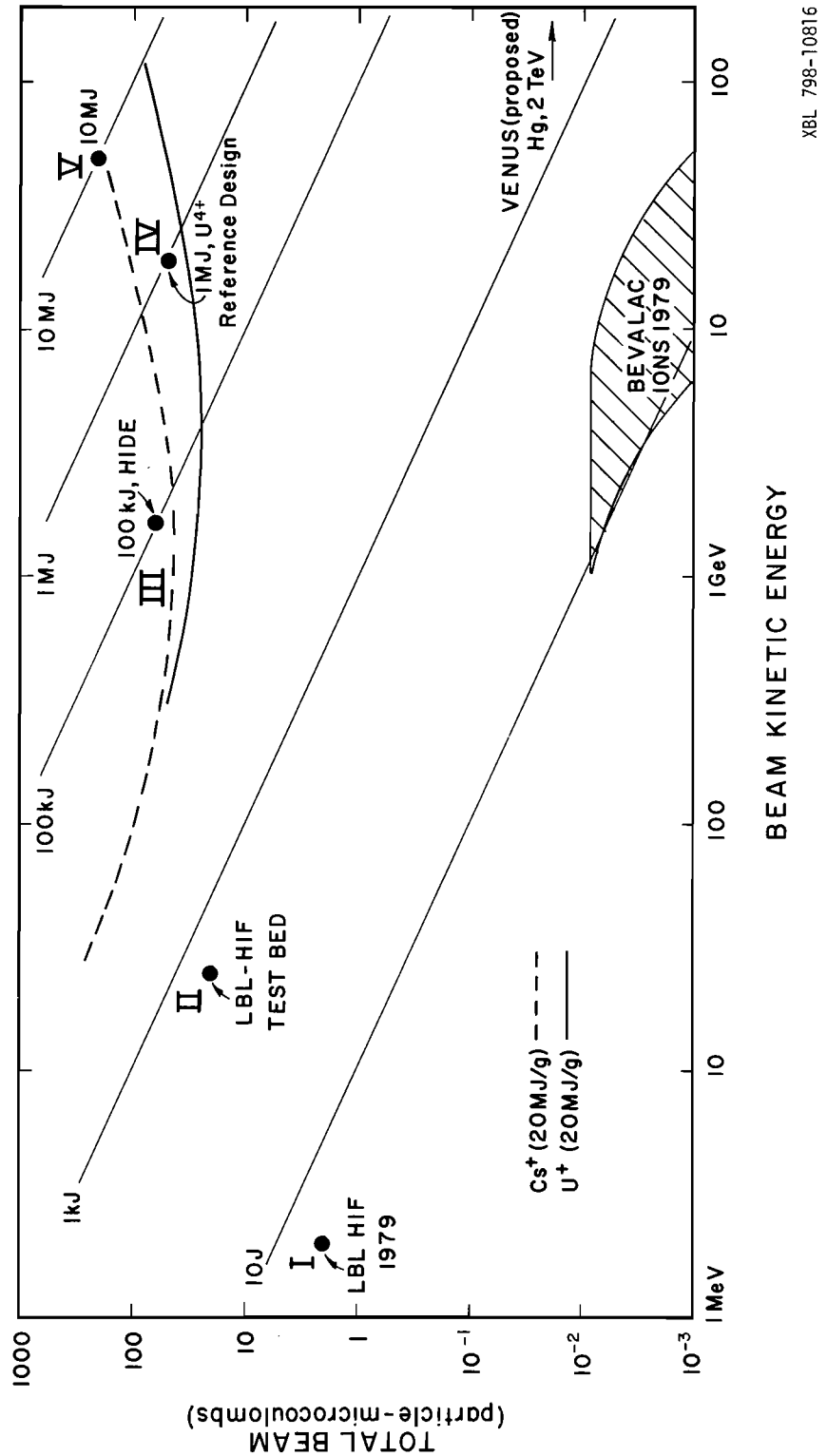

Fig. 12 - Present and proposed Heavy Ion Accelerators

The logical next step in increasing knowledge and experience in the acceleration of a large charge of heavy ions is the building of an ADF to answer some of the following physics questions:

-Beam Quality:

- Prepare and launch beam of significant current and charge into an induction linac structure.
- Show bunching by pulse compression (x1/5) in this structure.
- External bunching by further factor (x1/3).
- Demonstrate satisfactory 6-D phase volume.
- Explore instability limits.
- Realistically evaluate effects of imperfect operation of multi-element system.

-Beam Experiments:

- Focus (<1 cm)
- Bunch.
- Gains from neutralization
- "Damage" in slab geometry
- Beam Splitting

-Accelerate other ions (e.g. Potassium 39)

In parallel it is vital to develop engineering experience that will be needed for the design of HIDE and subsequent machines. Among the engineering goals are:

-Component Development:

- Induction Modules
- Superconducting Quadrupoles
- Periodic Internal Focusing Structure
- Beam Splitter
- Gas Stripper and Analyzer

-A Working Induction Linac to provide a Viable Framework for Higher Energy Designs

-Operating Experience with Emphasis on:

Component Performance

Sensitivity of Timing, Synchronization, Wave Form Errors

Some of the desiderata for ADF are listed in Table III

TABLE II.

One Would Like:	LBL Proposal:
Energy ~ 1 kJ	500 J
$L_{Accelerator} >> L_{Bunch}$ (20 m)	100 m
No. of Betatron Periods > 1	2
$\sqrt{\text{No. of Modules}} >> 1$	$\sqrt{81 \text{ modules}}$
$\sqrt{\text{No. of Switches}} >> 1$	$\sqrt{1000 \text{ switches}}$
Particle Interchange Between Front and Back of Bunch	some

While there are no firm values for the minimum number of elements required and for the other parameters, the values shown are about an order of magnitude above existing capabilities for most parameters, and furthermore, they occur

in the most sensitive and interesting part of an ion induction linac. At the low energy end the beam is subjected to the most violent manipulations transversely and longitudinally, excluding its encounter with a pellet, in the entire system. Subsequent acceleration approaches a steady state condition, with a small fractional energy change per accelerating gap and only a modest bunching field required.

The appearance of the ADF is sketched in Fig. 13, and its operating parameters are shown in Fig. 14. The focusing quadrupoles are placed within the accelerating modules because of the low energy transport limits. Within the short length of the ADF, the bunch experiences many of the same maneuvers required in HIDE - specifically, a several-fold increase in the beam current, a physical shortening of the bunch length, and acceleration by a large number of independent pulsed devices which will have practical imperfections. Specifications for desirable waveforms are being developed, as described in the talk at the workshop by Jackson Laslett, and have the trend shown in Fig. 7. Further details are given in Reference 5.

REFERENCES

1. W. B. Herrmannsfeldt, Proc. H.I.F. Workshop, ANL, Sept. (1978), p. 273, ANL Report Number, 79-41.

2. W. B. Herrmannsfeldt, ibid., p. 267.

3. D. Neuffer, ibid., p. 333.

4. A. Faltens, E. Hoyer, D. Keefe, L. J. Laslett, ibid., p. 31.

5. Ion Induction Linac Test Bed, LBL Report PUB-5031 (Sept. 1979).

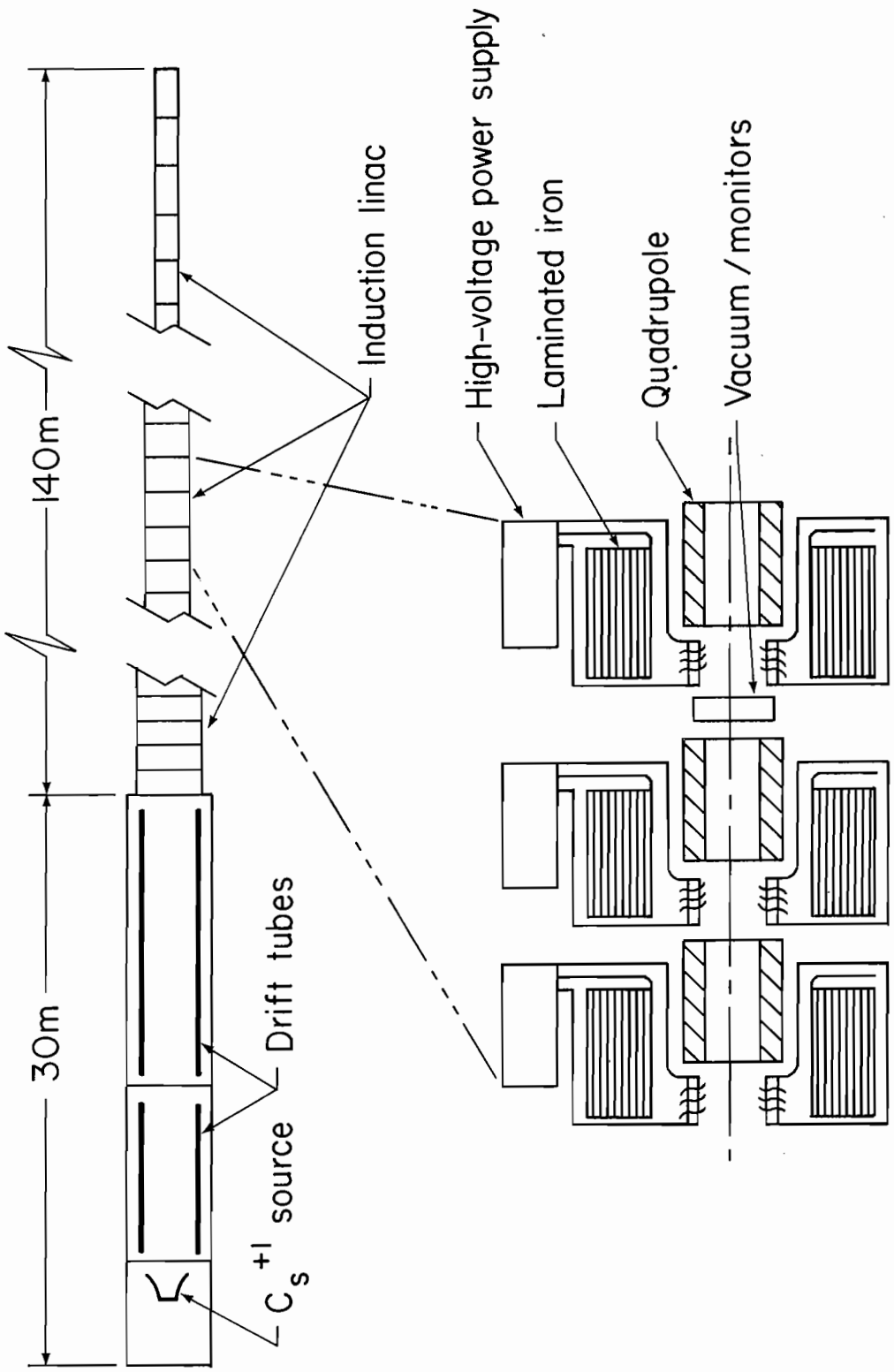

Fig. 13 - 25 MeV Cs^{+1} 500 Joule Induction Linac Test Bed

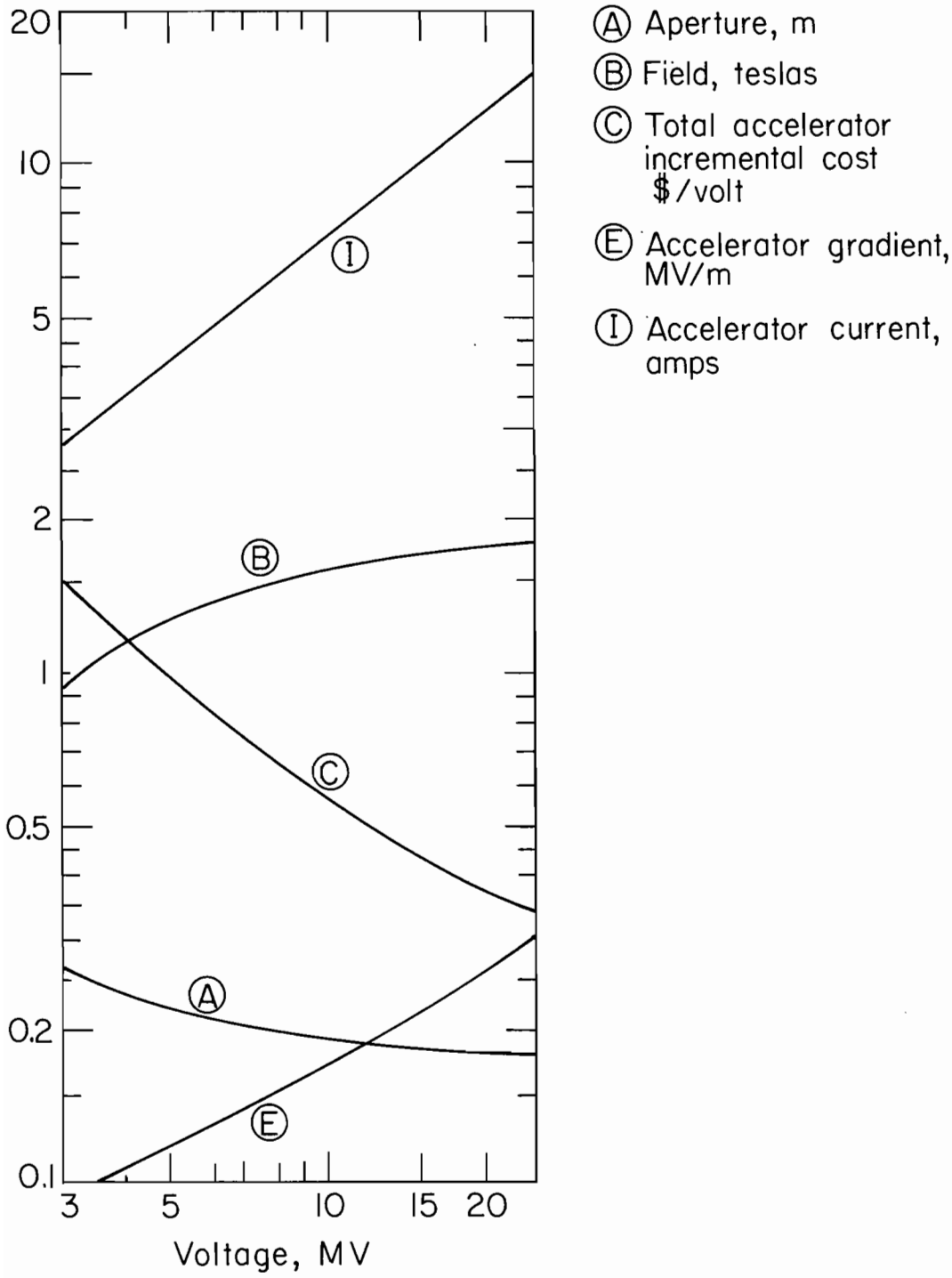

Fig. 14 - 25 MeV Cs^{+1} 500 Joule Induction Linac Parameters

LIA LONGITUDINAL COUPLING IMPEDANCE

Andris Faltens
Lawrence Berkeley Laboratory

The beam generated fields enter into the problems of waveform generation and longitudinal stability. In the former, provision must be made for the longitudinally defocusing forces due to the space charge and the beam loading effects on the accelerating voltage due to the current of a presumably known bunch. In the latter, the concern is for the growth of unintentional perturbations to unacceptably large values through the interaction of the charge and current fluctuations with the rest of the beam and the surrounding structures. These beam generated electric fields may be related to the beam current through a coupling impedance, $Z' = \frac{E_z}{I}$.

The problem of longitudinal stability and its dependence on the coupling impedance is well known in the design of proton storage rings and other circular machines, where it often limits attainable intensities; some of the theory and formalism may be applied to linear machines, with suitable modifications. For circular machines the usual definition has been

$$Z_n = \frac{V_n}{I_n} = \frac{2\pi R E_n}{I_n} \quad ,$$

where E_n is the peak azimuthal electric field generated by a sinusoidally modulated current, I_n, of the spatial harmonic number n in a machine of radius R. The theory of space charge waves as developed for microwave tubes is analogous, though less known in the accelerator community, and uses an interaction or Pierce impedance which relates the longitudinal electric field in the region of the beam to the average power flow through an external circuit,

$$Z_p = \frac{E_z^2 \lambda^2}{8\pi^2 P_{av}} \quad ,$$

for a beam wavelength, λ, and a wall impedance

$$Z_w = \left.\frac{E_z}{H_\theta}\right|_{wall} \quad ,$$

which is useful for matching fields at a wall boundary. Both of the microwave tube impedances emphasize the surrounding structure, while the accelerator coupling impedance combines the effects of space charge and external structure.

For the purposes of a high current linear accelerator it appears useful to maintain some distinction between the space charge fields and the fields due to the interaction of the beam current with structure, and to define

$$Z'(\omega) = Z'_q(\omega) + Z'_{ext}(\omega) = \frac{E(\omega)}{I(\omega)} \quad ,$$

where the subscript q refers to the space charge contribution, and the subscript ext refers to the external structure. $Z'(\omega)$ is the ratio of the electric field to the beam current amplitudes for a sinusoidally modulated current at angular frequency ω, has the dimensions of ohms per meter, and in general is complex because the electric field is usually phase shifted with respect to the current. No special emphasis is given to any particular set of harmonics in the LIA because a single bunch is accelerated in a non-steady-state manner.

Z_q

The self-fields are within a factor of $1-\beta^2$ the electrostatic fields of the modulated charge, and may be calculated by transforming the electrostatic fields of a stationary charge distribution to a moving coordinate frame. For the HIF applications $\beta^2 << 1$ because of the low particle speed, βc. For modulation wavelengths long compared to the chamber radius, b, a beam of radius a has

$$Z'_q(\omega) = j\omega"(-L)" \simeq \frac{j\omega\mu_o}{2\pi\beta^2}\left(\ell n\,\frac{b}{a} + \frac{1}{2}\right),$$

where the factor, $\ell n\,\frac{b}{a} + \frac{1}{2}$, often called g for a geometry factor, applies to the particles at the center of the vacuum chamber and a factor $\ell n\,\frac{b}{a} + \frac{1}{4}$ is more appropriate if the average electric field over all particles is required. Insofar as this g factor is of order unity and changes slowly with the beam-chamber geometry, $Z'_q(\omega)$, the self-field contribution, is of the same order of magnitude at low frequencies for the induction linac, the rf linac, or the storage ring, depending mainly on the velocity of the particles. The sign of Z'_q is capacitive, that is, in the sense that the bunch would be caused to expand longitudinally, but the frequency dependence is like that of an inductor, therefore, it acts as a negative inductance, "-L". In principle, the self-impedance could be partly compensated by a positive inductive wall impedance, with inductances comparable to those in the induction acceleration cores. The compensation could only be partial because of the field variation across the beam and because of frequency dependent transit time effects.

The frequency range where the long wavelength approximation fails depends on the chamber dimensions. Physically, for short wavelengths the electric field preferentially goes from regions of greater charge density to regions of lower density within the beam, rather than to the wall as in the low frequency limit. The boundary between the long and short wavelength approximations is in the region where

$$ka \simeq kb = \frac{\omega b}{v} = \frac{2\pi b}{\lambda} \simeq 1, \text{ or } \omega \simeq \frac{\beta c}{b} \quad .$$

In the short wavelength limit,

$$Z_q'(\omega) = \frac{1}{j\omega "C"} \simeq \frac{1}{j\omega\varepsilon_o \pi a^2} ,$$

and it behaves as a capacitor, "C".

The maximum value of Z_q' therefore is in the region $\omega \simeq \frac{\beta c}{b}$ and has the values

$$Z_q' \text{ max} \simeq - \frac{j60}{\beta b} \frac{(\ell n \frac{b}{a} + \frac{1}{2})}{} \text{ or } \frac{-j120}{\beta a}$$

in the two limits. The lower of these, for $(\ell n \frac{b}{a} + \frac{1}{2}) \simeq 1$, gives

$$Z_q' \text{ max} \simeq - \frac{j600}{\beta} \Omega/m \text{ for } b \simeq 10 \text{ cm} ,$$

as would be typical in the induction linac or storage ring, and Z_q' max $\simeq - \frac{j6000}{\beta} \Omega/m$ for $b \simeq 1$ cm as in a typical rf linac, with $\omega_{max} \simeq 3\times10^9\beta$ and $3\times10^{10}\beta$ respectively. Since β has a maximum value of about 1/3 for HIF, the space charge impedance peaks in the neighborhood of 100 MHz and 1000 MHz for the large and small chamber machines, respectively.

A sketch of the self-field impedance is shown in Figure 1 for a range of β's and chamber radii that span the HIF range.

Z_{ext}

The external or wall impedance, Z_{ext}', includes the effects of the accelerating gaps and other discontinuities in the beam line as well as a relatively unimportant contribution from the skin or surface impedance of the chamber wall itself. Z_{ext}' is easier to estimate and manipulate in an induction linac than in other accelerator structures because the LIA "cavity" is filled with rf absorbing material and is tightly coupled to a low impedance generator. By contrast, an rf cavity is a high-Q structure designed to attain an impedance of several Meg Ω/m on resonance, and usually is loosely coupled to a generator.

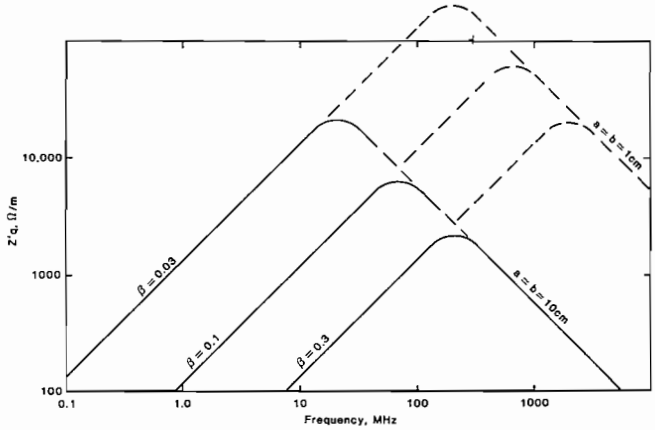

The Self-field Contribution, Zq, to the Coupling Impedance for β 0.03, 0.1, and 0.3 and Radius 10 cm (LIA) and 1 cm (rf Linac)

Figure 1

While phase and amplitude feedback may regulate the fundamental mode voltage and thereby lower the impedance seen by the beam, little seems to be known about the higher modes other than that they shouldn't be harmonically related to the fundamental of the rf. Because of these differences in the structures and coupling, Z_{ext} in an LIA cavity is to a large extent determined by the generator which drives it, while in an rf cavity it is mainly a property of the structure itself.

The LIA Z_{ext}' is well represented over the most important frequency range by the circuit shown in Fig. 2., which may be directly related to the induction module and drive circuit shown in Fig. 3. The generator impedance, Z_o, is the characteristic impedance of the pulse forming network or line used to drive the module, and is the dominant element for frequencies of the order of the reciprocal of the pulse duration. At higher frequencies, the generator impedance is shunted by the gap capacity, C_g, which is about two orders of magnitude higher than the usual gap capacity of an rf cavity. The induction core has a relatively minor role compared to the first two elements. Because of the non-ideal behavior of the induction core, whether it is ferrite or iron, eddy current and magnetization currents have the appearance shown in Fig. 4, for a constant applied voltage, rather than the linearly increasing and smaller current which is shown dashed in Fig. 4. The actual current response suggests an equivalent circuit for the core which consists of a parallel R_c-L_c combination, with the resistive part, R_c, dominant. At very low frequencies the core does have inductive behavior. An optional compensation network, shown as the L_{comp}-R_{comp}-C_{comp} series string may be used for pulse shaping purposes, such as speeding up the rise time and modifying the slope of the voltage, or the same function may

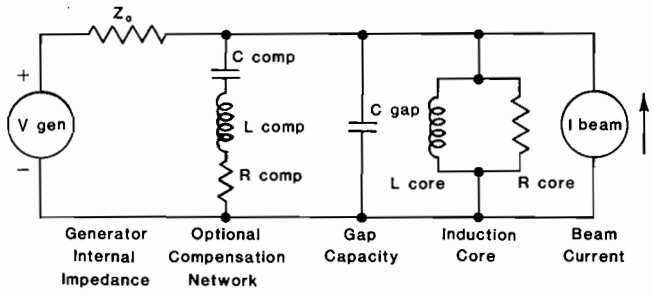

Representative values:
L core $\simeq 10^{-4}$ - 10^{-3} Hy
R core $\simeq$ 1-2 kΩ
C gap $\simeq$ 100-200pF
Z_o $\simeq$ 100-1000Ω

Accelerator Equivalent Circuit

Figure 2

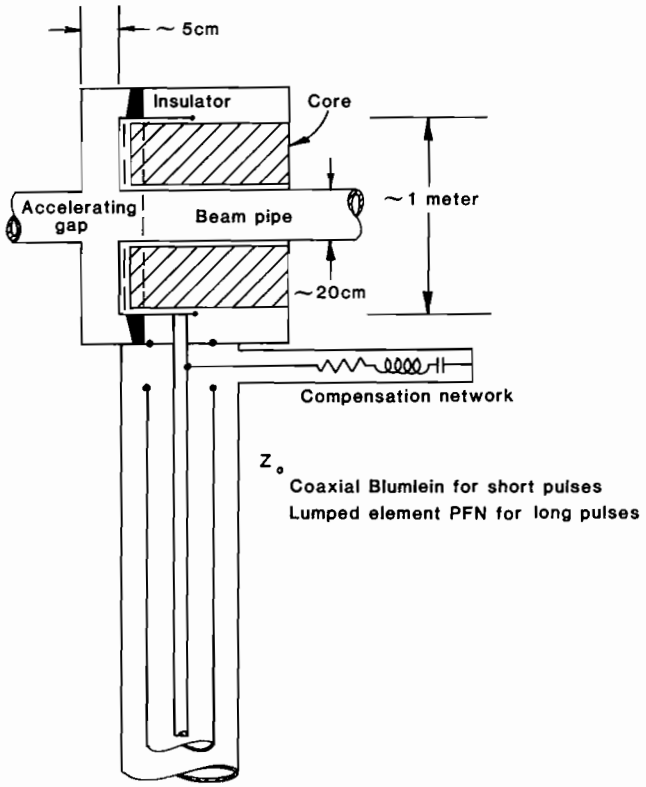

Induction Acceleration Cavity and Voltage Generator

Figure 3

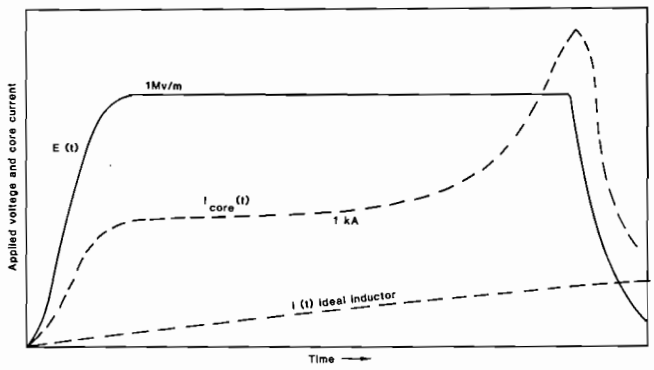

Approximate Form of Core Excitation Current

Figure 4

be obtained by tailoring the generator impedance. A desirable core has

$$R_{core},\ R_{comp} >> Z_o \ ,$$

and

$$Z_o \simeq \frac{V_{gap}}{I_{beam}} \ ,$$

Most of the effort has been expended on decreasing the core losses, which allows Z_o to be raised.

The choice of the generator impedance, Z_o, is influenced by efficiency considerations. The voltage appearing across the accelerating gap is the sum of the applied voltage and the beam generated voltage, with the approximations that the source is a generator matched to a transmission line with a characteristic impedance, Z_o, that the gap capacity is negligible, that the core impedance is infinite, and that all components are linear.

$$V_{gap} = V_{incident} + V_{reflected} - I_{beam}\, R_{beam} \ ,$$

where R_{beam} is the parallel combination of Z_o and R_{core}

$$R_{beam} \equiv R_b \simeq Z_o \,||\, R_{core} \ ,$$

and is equal to the external coupling impedance, Z'_{ext} in this approximation.

For this model, the acceleration efficiency, η, is

$$\eta = \left(\frac{R_{core}}{Z_o + R_{core}}\right)\left(\frac{I_{beam}\, Z_o}{V_{incident}}\right)\left(2 - \frac{I_{beam}\, Z_o}{V_{incident}}\right) ,$$

with a maximum value

$$\eta_{max} = \frac{R_{core}}{Z_o + R_{core}} \ ,$$

which may approach 1. The efficiency in terms of the external coupling impedance is

$$\eta = \frac{4 I_b\, Z_{ext}^2\, V_{gap}}{Z_0 (V_{gap} + I_b\, Z_{ext})^2} \ .$$

η is plotted versus Z_{ext} in Fig. 5. Near the maximum efficiency point the function is flat; therefore, Z_{ext} may be reduced by a factor of two or three without a comparable loss of efficiency. Lowering the generator impedance is

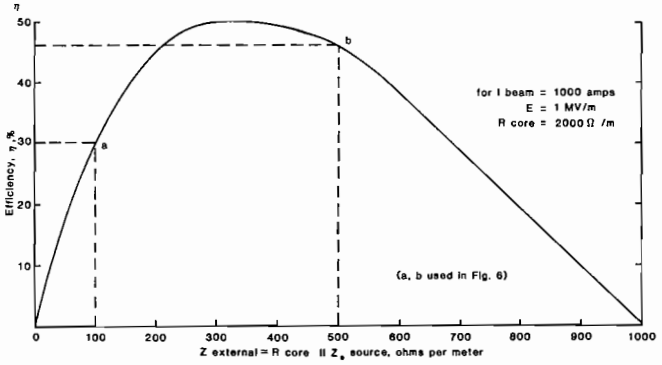

Dependence of Efficiency on the External Coupling Impedance at the Peak of the Z(ω) Curve

Figure 5

advantageous in the short pulse region, where transmission lines are acceptable voltage sources, because it is difficult to build high voltage, high impedance lines, and because a lower impedance line allows the gap capacity to be charged faster.

At frequencies comparable to the reciprocal of the acceleration pulse rise time, the wall impedance is dominated by the gap capacity. For the gap capacity to be treated like a lumped element, the two way travel time for electromagnetic waves from the inner radius to its outer radius should be less than a quarter cycle,

$$\frac{2\Delta r}{c} < \frac{T}{4} \text{ , or equivalently } \Delta r < \frac{\lambda_{\text{free space}}}{8} .$$

where Δr is the difference between the outer radius, A, and the bore radius, b. A typical Δr is 50 cm, therefore, the lumped element approximation is satisfactory for f < 75 MHz. The actual value of the gap capacity

$$C \simeq \frac{\varepsilon_o \pi A^2}{d} ,$$

for a gap of width d, depends to a large extent on d. Within bounds, d is a free parameter, with the minimum set by voltage breakdown, and a value near 5 cm satisfactory, for which C ≃ 140 pF. The inclusion of the gap capacity leads to a lower value of the wall impedance;

$$Z_{ext} \rightarrow \frac{R}{1 + j\omega RC} = \frac{R}{1 + (\omega RC)^2} - \frac{j\omega R^2 C}{1 + (\omega RC)^2} ,$$

with the dependences

$$\left| Z_{ext} \right| \propto \frac{1}{\omega} \text{ and } \mathrm{Re}(Z_{ext}) \propto \frac{1}{\omega^2} ,$$

as the frequency is increased.

Transit time function, T_r

In the frequency region where the gap capacity becomes important and above, the effects due to the change in the electric field during the transit of the particles through it becomes significant also, and tend to lower the external impedance by the factor T_r^2, where

$$T_r = \frac{< \int_{-\infty}^{\infty} E(r,z)\cos\omega t dz >}{< \int_{-\infty}^{\infty} E(r,z) ds >}$$

along the particle trajectories. In a gridded gap with uniform fields, $T_r = \frac{\sin\pi d/\lambda}{\pi d/\lambda}$, and has a null at about 600 MHz for our example, with β ≃ 1/10. In an open geometry such as the real accelerating gap, T_r will start decreasing at lower frequencies because of the extension of the field into the bore tube, say, at 300 MHz for the previous example. At any β, T_r will also decrease when the frequency approaches the waveguide cutoff frequency of the vacuum chamber, which is ~ 1.1 GHz for this example. The detailed geometry of the gap region may be adjusted rather freely to change T_r without affecting the functioning of the cavity.

High Frequency Limit

At the highest frequencies, the accelerating gap geometry may be approximated as a radial transmission line. If the line were tapered to achieve a constant impedance, its value would be

$$Z_{radial} \simeq \frac{60d}{a} \simeq 30\ \Omega \text{ (resistive)} ,$$

while in the parallel disc geometry it would be less. At the cavity outer radius, the radially outgoing radiation is well absorbed by the magnetic core material, which may be facilitated by making a gradual rather than abrupt transition into the material (e.g., ferrite). This is quite the opposite from the usual situation in an rf cavity, where the reflection of waves is essentially lossless, and results in a series of resonant peaks in the impedance at the frequencies where the reflections all add up in phase. In an induction cavity, because of the loading with rf absorbing magnetic material, only the vestiges of the usual resonant behavior remain, and these are bounded in magnitude to some tens of ohms. The impedance function is modulated by the transit time factor squared, and therefore the resonant peaks have a $\frac{1}{\omega^2}$ dependence at high frequencies, roughly in the range between 100 and 1000 mHz.

The various ingredients of Z_{ext} and the frequency ranges where they apply are shown in Fig. 6. It should be noted that the peak of the impedance function is well below the microwave region, and that this peak is determined by the external circuitry rather than being an intrinsic property of the structure. The 500Ω line shown is near the maximum attainable impedance for a generator matched to the beam in a cavity using available core materials; the 100 Ω line is for a mismatched source. If

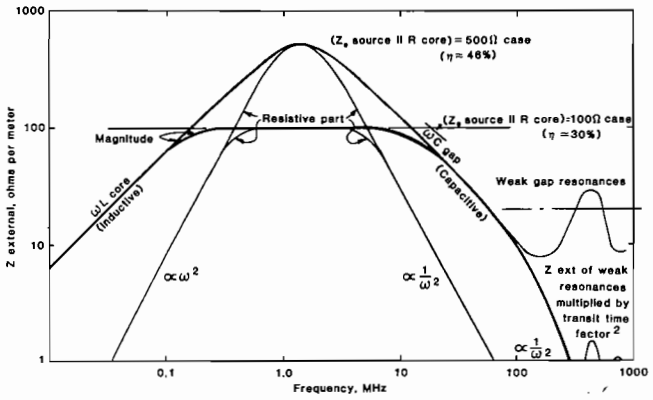

The External or Wall Impedance Part of the Coupling Impedance for (Z source Source II R core)=100Ω/m and 500Ω/m

Figure 6

necessary, the impedance could be lowered below the values shown by modifying the external circuitry.

Applications

The coupling impedance enters into the calculation of the applied voltages and into the longitudinal stability problem. The voltage seen by the bunch is the sum of the applied voltage and the beam generated voltage: this latter is composed of two parts, which may be approximated as

$$E_{beam} = - I_{beam} R' + "L" \frac{dI_{beam}}{dt} ,$$

where R' is the resistive impedance seen by the beam and "L" is a measure of the space charge forces generated by charge density gradients with the bunch. In a long bunch the charge density gradient is expected to be localized near the ends of the bunch. When the applied and beam generated forces are added together, the field seen by any particle is constant anywhere within the bunch. A small additional field is required at the tail of the bunch to reflect off-momentum particles and create the equivalent of a synchrotron bucket, with the major difference that the applied voltages are not constrained to be sinusoidal. These major components are shown in Fig. 7. One of the areas of active investigation at LBL is the sensitivity of the bunch to errors in the applied waveforms, and the growth of the longitudinal emittance by "noise" in the

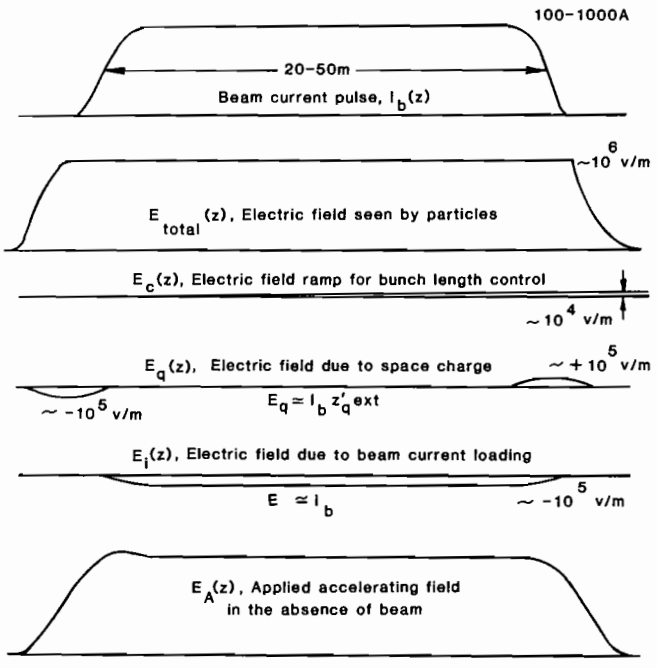

Applied, Beam Generated, and Total Electric Field and Bunch Current Waveforms

Figure 7

acceleration process. On a single particle basis, as would apply to a particle in the middle of the bunch, most of the voltage errors, if random, are expected to average out, and the energy spread should grow as $\frac{\Delta E}{E} \simeq \frac{1}{\sqrt{n}} (\frac{\Delta V}{V})$ where n is the number of acceleration gaps, about 10^4, and $\Delta V/V$ is the fractional voltage error per gap.

The longitudinal stability of the beam against small perturbations depends on the detailed nature of the coupling impedance, the form of the particle distribution function, and the square of the velocity spread. In recent years the complex stability criterion has been approximated as depending on the magnitude of Z divided by the frequency, and the coasting beam stability criterion has been applied to bunched beams. To improve on this less than satisfactory state of affairs computational work has been in progress for about a year to study a bunched beam, as reported by David Neuffer at this conference, and will continue, with the coupling impedance as a necessary input.

In all of the preceding no emphasis has been placed on the within bunch harmonics, either spatially or temporally. Such a harmonic analysis would be helpful if either the particles or the space charge waves executed many oscillations during the passage of the bunch through the accelerator. In the LIA case, a single particle on the average makes less than one synchrotron oscillation, while the space charge waves make at most two or three oscillations. The physical situation is better approximated by a middle portion, which is very much like a "coasting beam", and two bunch ends.

Feedback

The low speed of the ions and the long acceleration pulse duration make it possible to consider active feedback for longitudinal stabilization and waveform correction purposes. If the difference between an actual voltage and a desired voltage is detected and fed back to the beam, then the external impedance becomes zero. For such a scheme to be at all practical, as many known effects must be included in the voltage waveform as possible, so that only a small error signal has to be dealt with. Because of the low speed of the ions and the much lower intra-bunch velocities, the error signal could be accumulated over, for example, a 100 meter interval, and the correction applied further downstream. The most serious types of error are probably excessive tilts in energy, which could lead to premature bunching of the beam, and gross deficiencies in accelerating voltage such as might be caused by several misfires, which would tend to make the bunch slip out of its accelerating bucket. The correction for these types of errors would be a few cavities held in reserve, and triggered as required, to either change the average energy of the bunch or its variation along the bunch. The use of linear amplifiers would certainly work, but would be more expensive than the above method.

LONGITUDINAL DYNAMICS OF BUNCHED BEAM IN A MODEL LINAC

Kwang Je Kim
Lawrence Berkeley Laboratory

In this note, I will report on some analytical efforts to understand the longitudinal bunched beam dynamics in an induction linac as currently stipulated for the HIF program. The analysis is carried out within the framework of a simple model. It is found that a bunched beam tends to be stable. Further work is necessary to extend the results to a more realistic case.

I. THE MODEL

Since the subject is analytically quite involved, some mathematical idealization is inevitable. The model linac to be considered here has the following features:

a) The external force is described by a rectangular-well potential shown in Fig. (1).

b) The self-force F_s is given by

$$\boxed{F_s = - e^2 \frac{Z_R}{L} p_o \lambda(x) - e^2 Z_C \frac{\partial}{\partial x} p_o \lambda(x)} \qquad (1)$$

Here, e = the proton charge, p_o = the velocity of the bunch center, L = the bunch length, $\lambda(x)$ = the line density, and Z_R and Z_C are the resistive and the capacitive parts of the impedance, respectively. They are taken to be real and positive.

The main motivation for introducing the model is the calculational simplicity. However, it should be noted that the external potential in induction linacs resembles more or less the rectangular well. Also, Eq. (1) represents the simplest possible form of the force incorporating both the space charge repulsion and the deceleration due to the cavity impedance.

The relevant magnitudes for Z_R and Z_C are

$$Z_R \sim Z_C \sim 10^3 \text{ ohms.} \tag{2}$$

The motion in phase space under the influence of the rectangular-well potential is shown in Fig. (1.b). Here and in the following, p is the velocity of the particle relative to the bunch center. A particle is reflected instantaneously when it reaches the edge of the potential well. Therefore, one should identify the points B and C, and also the points A and D. In terms of the distribution function $\psi_T(t,x,p)$ (T for the total, unperturbed plus perturbed), one obtains

$$\psi_T(t,o,p) = \psi_T(t,o,-p), \psi_T(t,L,p) = \psi_T(t,L,-p). \tag{3}$$

Eq. (3) supplies the relevant boundary conditions for the longitudinal motion of the bunched beam for our idealized linac.

The linearized Vlasov's equation for the present problem is

$$\frac{\partial \psi}{\partial t} + p \frac{\partial \psi}{\partial x} - f(p) \left[\alpha \frac{\partial}{\partial x} + \beta\right] \lambda(x) = 0, \tag{4}$$

where

$$f(p) = \frac{\partial \psi_o(p)}{\partial p}, \quad \lambda(t,x) = \int dp\, \psi(t,x,p), \tag{5}$$

$$\alpha = \frac{e^2 p_o Z_C}{m\gamma^3}, \quad \beta = \frac{e^2 p_o Z_R}{m\gamma^3 L}. \tag{6}$$

In the above, ψ_o and ψ are the unperturbed and perturbed parts of ψ_T, m is the rest mass of particle and γ is the ratio relativistic mass/rest mass. The boundary conditions (3) become the following statement:

$\psi_o(p)$, $\psi(t,o,p)$ and $\psi(t,L,p)$ are even functions of p. (7).

II. METHOD OF ANALYSIS

The boundary value problem specified in the above can be solved in the following steps: First, one seeks a solution in the following form:

$$\psi(t,x,p) = e^{i\omega t} \sum_{k} e^{-ik.x} A(k,p) \ . \tag{8}$$

From Eq. (4), one obtains

$$A(k,p) + \frac{k\alpha + i\beta}{\omega - kp} f(p) \int A(k,p)\, dp = 0, \tag{9}$$

$$1 + (k\alpha + i\beta) \int dp\, f(p) \frac{1}{\omega - kp} = 0. \tag{10}$$

Next, one solves the dispersion relation (10) to obtain k as a function of ω. In general, there will be many branches $k_\ell(\omega)$, $\ell = 1, 2, \ldots$. In view of Eqs. (8) and (9), the solution has the following structure:

$$\psi(t,x,p) = e^{i\omega t} \sum_{\ell} e^{-ik_\ell(\omega) \cdot x} \frac{k_\ell(\omega) \cdot \alpha + i\beta}{\omega - k_\ell(\omega)p} f(p)\, A_\ell, \tag{11}$$

where $\left\{ A_\ell \right\}$ is a set of constants. The requirement that the function ψ must satisfy the boundary condition (7) results in a discrete set of eigenvalues ω_n. Going back to Eq. (11), one determines the eigenfunction corresponding to ω_n in the following form:

$$\psi_n(t,x,p) = e^{i\omega_n t} \ U_n(t,p). \tag{12}$$

This completes the sketch of the general procedure to obtain the eigenvalues and the eigenfunctions.

It is instructive to compare the situation to the case of a coasting beam circulating in a ring. In this case, Eq. (4) remains the same while the boundary condition (7) is replaced by

$$\psi(t,x,p) = \psi(t,x + C,p), \tag{13}$$

where C is the circumference of the ring. Eq. (13) determines immediately that $k = k_n = 2\pi n/C$, $n = 1, 2, .$ The eigenvalue ω_n is then obtained from Eq. (11).

To compare the theory with numerical simulation, one has to consider the initial value problem. This is easily solved if one could determine the coefficients C_n in the expansion of the initial distribution $\psi(o,x,p)$;

$$\psi(o,x,p) = \Sigma\ C_n\ \psi_n(x,p). \tag{14}$$

For this purpose, it is necessary to consider the following adjoint equation á la Van Kampen[1]:

$$\frac{\partial\phi}{\partial t} + p\ \frac{\partial\phi}{\partial x} - (\alpha\ \frac{\partial}{\partial x} - \beta)\ \int dp\ f(p)\ \phi(t,x,p) = 0. \tag{15}$$

The function $\phi(t,x,p)$ is subject to the same boundary condition as $\psi(t,x,p)$. Following similar steps as in the above, one obtains the eigenvalues $\bar{\omega}_n$ and and the eigenfunctions $V_n(x,p)$ for the adjoint system. The following orthogonality theorem is easily derived:

$$(V_m,U_n) \equiv \int_0^L dx \int dp\ V_m^*(x,p)\ U_n(x,p) = 0 \text{ if } \omega_n \neq \bar{\omega}_n^*. \tag{16}$$

The coefficients C_n can now be determined by making use of (16).

III. A SIMPLE EXAMPLE

In this section, the general procedure described in the previous section will be illustrated for a special case in which the unperturbed distribution $\psi_o(p)$ is a simple step function as shown in Fig. (2). One has

$$f(p) = \frac{\partial \psi_o(p)}{\partial p} = \frac{N}{2L\Delta}\,[-\delta\,(p-\Delta) + \delta\,(p+\Delta)], \tag{17}$$

where N is the total number of the particles in the bunch. From the structure of Eq. (4), it is convenient to write

$$\psi(t,x,p) = \psi_I(t,x,p) + \delta(p-\Delta)\,A(t,x) + \delta(p+\Delta)\,B(t,x). \tag{18}$$

The functions ψ_I, A and B satisfy the following equations:

$$\frac{\partial \psi_I(t,x,p)}{\partial t} + p\,\frac{\partial \psi_I(t,x,p)}{\partial x} = 0 \tag{19}$$

$$\left[\frac{\partial}{\partial t} + \Delta \begin{pmatrix} 1 & 0 \\ 0 & -1 \end{pmatrix} \frac{\partial}{\partial x} + \frac{N}{2L\Delta} \begin{pmatrix} 1 & 1 \\ -1 & -1 \end{pmatrix} \left(\alpha \frac{\partial}{\partial x} + \beta\right)\right] \begin{pmatrix} A \\ B \end{pmatrix} + \frac{N}{2L\Delta} \left(\alpha \frac{\partial}{\partial x} + \beta\right) \begin{pmatrix} \lambda_I \\ -\lambda_I \end{pmatrix} = 0. \tag{20}$$

In the above, $\lambda_I(t,x)$ is the charge density associated with ψ_I;

$$\lambda_I(t,x) = \int dp\ \psi_I(t,x,p) \tag{21}$$

The function ψ_I satisfies the same boundary condition as ψ, Eq. (7), while the boundary condition for A and B becomes

$$A(t,o) = B(t,o),\ A(t,L) = B(t,L). \tag{22}$$

The boundary value problem for ψ_I is easily solved. One gets

$$\psi_I(t,x) = g_n(p) \cos K_n(pt \pm x), \text{ or } h_n(p) \sin K_n(pt - x). \tag{23}$$

In the above, $g_n(p)$ ($h_n(p)$) is an arbitrary even (odd) function of p, and

$$K_n = \pi n/L \tag{24}$$

Eq. (23) describes waves that move with phase velocity p.

Now consider the "edge wave" described by Eqs. (20) and (22). If ψ_I does not vanish, it drives the edge wave through the last term in Eq. (20). Let us first consider the case $\psi_I = 0$. The resulting system can be solved following the general outline described in the previous section. The details can be found in Reference (2), and the result is

$$\begin{pmatrix} A \\ B \end{pmatrix} = e^{i\omega_n t} e^{-Qx} \left[e^{-iK_n x} \begin{pmatrix} \omega_n + k_n^{+}\Delta \\ -\omega_n + K_n{}^{+}\Delta \end{pmatrix} + e^{iK_n x} \begin{pmatrix} -\omega_n - k_n^{-}\Delta \\ \omega_n - k_n^{-}\Delta \end{pmatrix} \right] \tag{25}$$

Here

$$Q = \frac{\beta'}{2L(1+\alpha')}, \quad \alpha' = \frac{N\alpha}{\Delta^2 L}, \quad \beta' = \frac{N\beta}{\Delta^2}, \tag{26}$$

$$\omega_n^2 = (1+\alpha')\,\Delta^2 (K_n^2 + Q^2), \; k_n^{\pm} = iQ \pm K_n \; . \tag{27}$$

The factor e^{-Qx} in Eq. (25) means that the particles tend to pile up in the rear part of the bunch (The bunch moves to the positive x-direction). This is due to the fact that the resistive part Z_R of the impedance causes a decelerating force through the first term in Eq. (1). For a machine with a peak current $I = ep_o N/L \sim 10^4$ Amp, velocity spread $\Delta/p_o \sim .1\%$, energy $mp_o^2 \sim 10$ GeV and $\gamma \sim 1$, the dimensionless constants α' and β' are numerically equal to the impedances Z_C and Z_R expressed in ohms. From Eqs. (2) and (26),

the attenuation factor for such a machine is

$$e^{-QL} \sim e^{-.5} \sim .6 \ . \tag{28}$$

It is perhaps surprising that the eigenfrequency given in Eq. (27) is real so that no instabilities develop for the bunched beam case. This is in sharp contrast to the coasting beam case where the beam is unstable as long as $Z_R \neq 0$. The usual interpretation is that, while the wave grows along the line C → D in Fig. (1.b), it damps on travelling along the line A → B, the net result being stable. Notice that the growth along C → D (or damping along A → B) is consistent with the explanation given in the previous paragraph.

To complete the solution, one has to consider the effect of the last term in Eq. (20), which is analogous to the driving term in an oscillator problem. It is then necessary to expand the last term in terms of the eigenfunctions (25). This is done easily with the help of the adjoint eigenfunctions obtained below. The behavior of the complete solution can only be analyzed numerically, and will not be discussed further in this paper.

The adjoint equation defined by Eq. (15) is, if written in the matrix notation as in Eq. (20), as follows:

$$\left[\frac{\partial}{\partial t} + \Delta \begin{pmatrix} 1 & 0 \\ 0 & -1 \end{pmatrix} + \frac{N}{2L\Delta} \begin{pmatrix} 1 & -1 \\ 1 & -1 \end{pmatrix} \left(\alpha \frac{\partial}{\partial x} - \beta\right)\right] \begin{pmatrix} C \\ D \end{pmatrix} = 0 \ . \tag{29}$$

The functions C and D satisfy the same boundary condition as in Eq. (22). The solution of the adjoint system is quite analogous to the original system. One finds that is has the same set of eigenvalues ω_n, and the corresponding eigenfunctions are as follows:

$$\begin{pmatrix} C \\ D \end{pmatrix} = e^{i\omega_n t} \, e^{Qx} \left[e^{-iK_n \cdot x} \begin{pmatrix} \omega_n/k_n^{+} + \Delta \\ \omega_n/k_n^{+} - \Delta \end{pmatrix}^{*} \; -e^{iK_n \cdot x} \begin{pmatrix} \omega_n/k_n^{-} + \Delta \\ \omega_n/k_n^{-} - \Delta \end{pmatrix}^{*} \right]. \tag{30}$$

In the above, * denotes the complex conjugate. After a lengthy algebraic computation, one confirms that the functions in Eq. (25) are orthogonal to those in Eq. (30) for $n \neq m$.

IV. EXTENSION

For an arbitrary shaped unperturbed distribution $\psi_o(p)$, it is convenient to introduce a new set of canonical variables (ρ,θ) as follows:

$$\begin{cases} \rho = |p| \\ \theta = x\, E(p) \end{cases} \quad \text{or equivalently} \quad \begin{cases} p = \rho\, E(\theta) \\ x = |\theta| \end{cases} \tag{31}$$

Here $E(z)$ is a step function defined to be +1 (-1) when $z > 0$ ($z < 0$). The variables (ρ,θ) are analogous to the polar variables in phase plane.

The Vlasov's equation becomes

$$\frac{\partial}{\partial t}\psi(t,\theta,\rho) + \rho\,\frac{\partial\psi(t,\theta,\rho)}{\partial\theta} + f(\rho)\left(\alpha\,\frac{\partial}{\partial\theta} + \beta\, E(\theta)\right)\lambda(t,\theta) = 0,$$

$$\lambda(t,\theta) = \int_0^\infty dp[\psi(t,\theta,\rho) + \psi(t,-\theta,\rho)]. \tag{32}$$

The boundary condition (7) can be translated as follows:

$$\boxed{\psi(t,\theta,\rho) \text{ is continuous at } \theta = 0 \text{ and } \psi(t,L,\rho) = \psi(t,-L,\rho).} \tag{33}$$

It follows that $\psi(t,\theta,\rho)$ can be regarded as a continuous periodic function of period 2L in θ. Therefore, an eigenfunction with frequency ω must have the following expansion:

$$\psi = e^{i\omega t}\sum_n e^{ik_n\cdot\theta} A_n(\rho). \tag{34}$$

Inserting Eq. (34) into Eq. (32), one obtains a recursion relation (of infinite order) to determine $A_n(\rho)$. The eigenvalue condition involves an infinite determinant as follows[3]:

$$\begin{vmatrix} \lambda_1(\omega), & \frac{1}{3}, & 0, & \frac{1}{15}, & 0, \ldots \\ -\frac{1}{3}, & \lambda_2(\omega), & \frac{1}{5}, & 0, & \frac{1}{21}, \ldots \\ 0, & -\frac{1}{5}, & \lambda_3(\omega), & \frac{1}{7}, & 0, \ldots \\ -\frac{1}{15}, & 0, & -\frac{1}{7}, & \lambda_4(\omega), & \frac{1}{9}, \ldots \\ \ldots\ldots & \ldots\ldots & \ldots\ldots & \ldots\ldots & \ldots\ldots \end{vmatrix} = 0 \qquad (35)$$

Here

$$\lambda_n(\omega) = \pi \cdot \frac{1 + \alpha K_n D_n(\omega)}{4\beta n D_n(\omega)}, \quad D_n(\omega) = \int_{-\infty}^{\infty} dp\, f(p) \frac{1}{K_n p - \omega}. \qquad (36)$$

Eq. (35) could probably be analyzed numerically.[4]

For the case where the unperturbed distribution consists of two steps as shown in Fig. (3), the procedure described in Section II is still tractable. The dispersion relation (10) becomes a quartic equation in k, which could in principle be solved to obtain $k_\ell(\omega)$, $\ell = 1, 2, 3, 4$. The eigenvalue equation is a complicated transcendental equation involving $k_\ell(\omega)$, which is presently being studied numerically. In some limiting cases, the equation can even be studied analytically. For example, suppose that the shaded area in Fig. (3) is very small compared to the unshaded one. One can then set up a perturbation series $\omega_n = \omega_n^{\circ} + \omega_n^{1} + \omega_n^{2} + \ldots$. Here ω_n° is the frequency for the simple step function discussed in Section III. The lowest order frequency shift ω_n^{1} was computed. Although the formula is too lengthy to be recorded here, ω_n^{1} was found to be real for all values of Z_R and Z_C. Therefore, the motion is again stable.

With the examples treated so far, one may get the impression that a bunched beam in our model linac is always stable. However, that is not generally so. A simple example is the case in which $\beta = 0$ and $\psi_o(p)$ has a dip as in Fig. (4). It is not hard to show that when $\beta = 0$, the wave vector k_n is real and given by

$$k_n = K_n \tag{37}$$

Since k_n is known, ω_n is determined from the dispersion relation (10). The situation here is quite similar to the coasting beam case. Now, it is well-known that a coasting beam can develop instability if $\psi_o(p)$ has a dip as shown in Fig. (4) even when the resistive part β vanishes. Thus, one concludes that the longitudinal motion of our model linac can be unstable. However, the instabilities seem to be driven mainly by the geometrical parameters of $\psi_o(p)$, and not by the resistive part of the impedance.

V. DISCUSSIONS AND CONCLUSIONS

In this paper, a linac specified by a) and b) in Sec. (I) is discussed in detail, limiting ourselves to analytical methods. The results obtained here are encouraging in the sense that a sensible theoretical approach to the longitudinal dynamics of bunched beam could be formulated and solved. However, a lot of further work is necessary both within the framework of the present model and beyond. The paper will be concluded by listing some of the immediate problems.

First, within the framework of the model, they are a) the problem of obtaining eigenfunctions and eigenvalues for a general distribution $\psi_o(p)$;

this problem was briefly touched on in Section IV. One might try, for example, to solve the determinant equation (35) by numerical method. b) The initial value problem; given an intitial disturbance at t = 0, how does it develop in time? By analyzing this problem, one would like to understand how the wave disperses and how it reflects at the walls of the potential. The results of Section III should be useful for this analysis.

The model studied in this paper was shown to be stable in most cases (except when $\psi_0(p)$ has a dip), and it does not explain the microwave instabilities observed at CERN and FNAL. Therefore, it is important to consider a more realistic model. In doing so, there are the following problems: c) Replacing the rectangular well potential by a more realistic potential. A realistic potential cannot be rectangular. Also, one would like to understand the differences between the longitudinal dynamics in induction linacs and in storage rings. d) Replacing the self force (Eq. (1)) by a more realistic one. For this purpose, one has to start from a first principle, Maxwell's equations, etc. A possible improvement of Eq. (1) is proposed by L. Smith, who suggested that the factor $p_0\lambda(x)$ in Eq. (1) be replaced by

$$p_0\lambda(x) \to \int (p_0 + p)\, \psi(t,x,p)\, ds \ . \tag{38}$$

The above replacement is made plausible by arguing that the force should be proportional to the current rather than charge density. With this modification, the Vlasov's equation can again be solved exactly when $\psi_0(p)$ is given by Fig. (2). Following similar steps as in Section III, one finds that the eigenvalues for the edge waves are given by

$$\omega_n = \frac{i\gamma \ \pm \sqrt{-\gamma^2 + (1+\delta)(1+\alpha')\ \Delta^2(k_n^2 + Q^2)}}{1+\delta} \ , \tag{39}$$

where

$$\gamma = \frac{\varepsilon\beta'(1+\alpha')}{4(1+\alpha')}\left(\frac{\Delta}{L}\right) , \quad \delta = \frac{\alpha'\varepsilon}{4(1+\alpha')} , \quad \varepsilon = \frac{\Delta}{p_o} . \tag{40}$$

Notice that ω_n now has a positive imaginary part. Therefore, the perturbation is damped, and again there is no instability. This is easy to understand because the growth rate along C → D in the phase plane is less than the damping along A → B due to the replacement Eq. (38).

Acknowledgement: I thank Dr. A. M. Sessler and Dr. L. Smith for many helpful suggestions and discussions.

REFERENCES AND FOOTNOTES

1. N. G. Van Kampen, Physica 21, 949 (1955); See also F. Sacherer, CERN/SI-BR/72-5.

2. K. J. Kim, LBL-9741, presented at 1979 ISABELLE Workshop (to be published).

3. The eigenvalue problem for the Neuffer's model (D. Neuffer, IEEE Trans. NS-26, 3031 (1979)), properly extended to incorporate the resistive part of the impedance, can also be formulated in terms of an infinite determinant, as shown by L. Smith (private communication).

4. Eq. (35) was tested for $\psi_0(p)$ given by Fig. (2). The infinite determinant is approximate by retaining only the first two rows and columns. The approximate eigenvalues so obtained was in good agreement with the results of Section III.

Fig. (1)

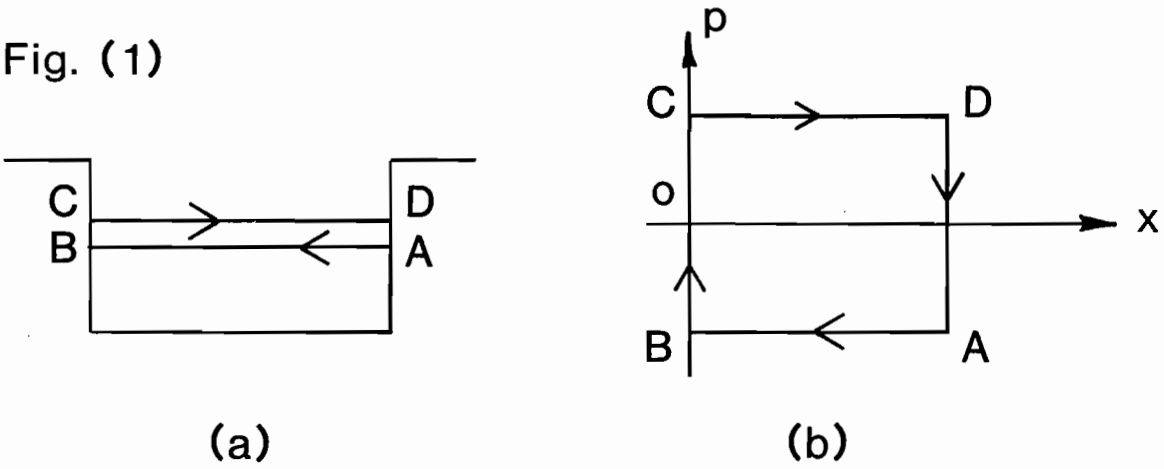

Fig. (2)

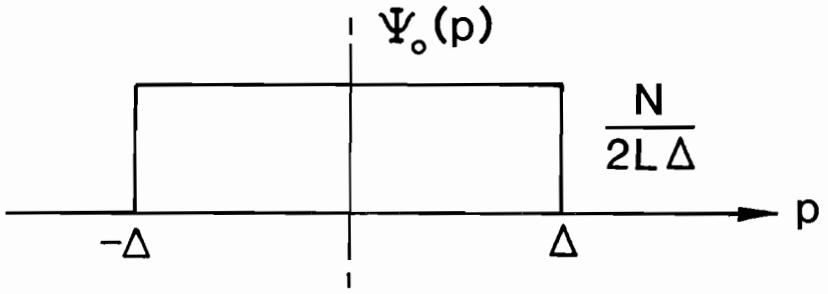

Fig.(3)

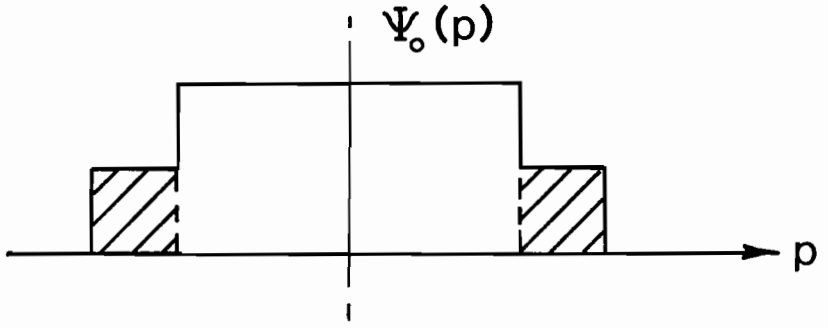

Fig. (4)

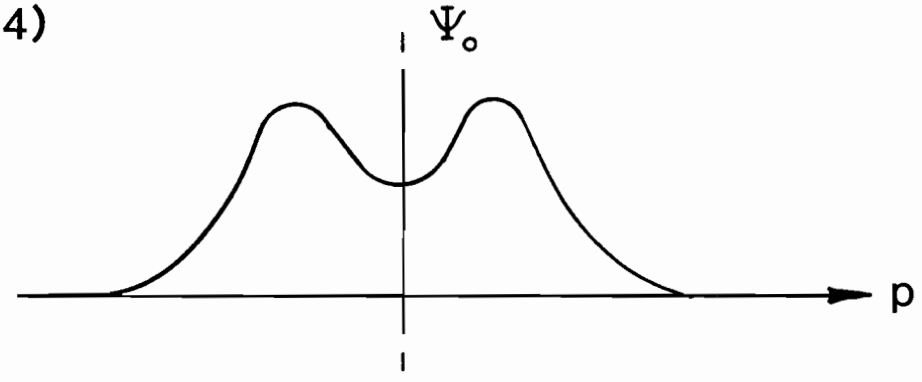

LONGITUDINAL DYNAMICS IN HEAVY-ION INDUCTION LINACS FOR INERTIAL-FUSION POWER PLANTS

David L. Judd

Lawrence Berkeley Laboratory

I. INTRODUCTION

All induction linacs thus far constructed have accelerated relativistic electrons. Because these move with almost the speed of light, there were few longitudinal dynamics problems to solve. In contrast, heavy-ion induction linacs for inertial-fusion power plants will handle ions in the range $0.1 \lesssim \beta \lesssim 0.5$ ($\beta = v/c$); the controlled variation of bunch length during acceleration is not only a very useful new property but also introduces a new set of problems.

In this paper we first point out that the requirements for pellet ignition in commercial-scale power plants, and the limitations of final focusing lens systems, place stringent bounds on the allowable random spread of longitudinal velocities, or equivalently on the longitudinal "temperature". We evaluate these bounds; the result is that the shapes of the applied voltage pulses must, on the average, fit those required to compress the bunches and cancel their space-charge repulsion like a glove fits a hand, within very tight tolerances.

Next we show that at any point within a bunch there is a characteristic longitudinal velocity with which small "signals" (departures from the desired number λ of ions per unit length) are propagated. This velocity turns out to be of the same order of magnitude as that of ions at bunch ends (relative to a bunch center) due to bunch compression in accelerator designs currently being studied. Both of these velocities are about an order of magnitude greater than the maximum random velocity spread allowed by pellet and final lens requirements. Therefore the longitudinal propagation of small error signals (density waves) may with good approximation be

studied as if the ions had a negligible longitudinal temperature, in analogy with the propagation of waves in a cold plasma.

Next it is shown that the linearized wave equation for these small disturbances may be dealt with by the method of separation of variables for a wide class of bunches whose variation of λ along the bunch and variation of length during acceleration are characterized by two independent arbitrary functions. The requirement for separation is that the bunch behavior is scaling; that is, the bunch shape in terms of λ depends only on the ratio $z/z_o(t)$ with z the distance from the bunch center and $z_o(t)$ the varying bunch half-length. [Normalization to a fixed total number of ions in the bunch requires that λ be also inversely proportional to $z_o(t)$.] Although the bunch behavior desired in current designs is not exactly of this scaling form, solutions obtainable from the separated equations are sufficiently general to give a good understanding of the dynamic response of a variety of bunch shapes to small errors in initial conditions and in applied voltage, and to provide a basis for comparison with computer simulation results.

Such computer simulations of longitudinal bunch dynamics will follow in time the variations of two-dimensional longitudinal phase space density. Neuffer[1,2] has derived a particular form of non-stationary distribution function, in which λ is a parabolic function of z. In the concluding section of the present paper we show how to generalize this type of distribution so as to provide not only an arbitrarily varying rate of bunch compression but also (in principle) an arbitrary scaling bunch shape. Examples illustrating this wider class of non-stationary distributions are presented.

II. IMPLICATIONS OF LONGITUDINAL PHASE SPACE CONSTRAINTS

1. Velocity Spread and Longitudinal Temperature

Present conceptual designs of induction linac systems for commercial-scale power production by inertial-confinement fusion are based on the assumption that after acceleration an individual ion bunch will be split in transverse phase space into many beamlets but will not be chopped longitudinally into segments. Therefore the longitudinal phase area of a bunch may not exceed that acceptable at a final lens system or at the traget.

This requirement may be written, for ions of mass $m = Am_p$, as

$$\frac{(\varepsilon_L)_{linac}}{(\varepsilon_L)_{final}} = \frac{\frac{1}{2}(L\Delta p_z)_{linac}}{\frac{1}{2}(L\Delta p_z)_{final}} = \frac{L_s \gamma_s^3 \, Am_p (\Delta v_z)_s}{(\beta_f c\tau_f)[\beta_f \gamma_f Am_p c(\Delta p_z/p_z)_f]} < 1,$$

with bunch length L, velocity spread $\pm\Delta v_z$, and γ varying along the linac; the subscript s denotes evaluation at a distance s along it. The final beam duration time τ_f, relative momentum spread $\pm(\Delta p_z/p_z)_f$, β_f, and γ_f are evaluated at final lens or target. Our purpose here is to obtain estimates, so we neglect relativistic corrections and factors such as $4/\pi$ related to phase space shapes (e.g., elliptical vs. rectangular). We use the relations

$$L_s = \beta_s c\tau_s = \beta_s cQ/I_s, \quad Q = qeE/T_f$$

with Q the electric charge per bunch, I the mean electric current, E the delivered energy, qe the charge per ion, and T the kinetic

energy per ion. Then

$$(\Delta v_z/v_z)_s \; < \sim \; (T_f^2/T_s E)(\Delta p_z/p_z)_f (\tau_f/e)(I_s/q) .$$

It is convenient to express T_f, T_s in GeV, E in megajoules, and τ_f in nanoseconds, and to define $\mathcal{J}_s = I_s/q$ as the particle current in particle-Amperes. Then

$$(\Delta v_z/v_z)_s < \sim 10^{-6} \left[\frac{T_f^2(\text{GeV})\,\tau_f(\text{nsec})(\Delta p_z/p_z)_f}{E(\text{MJ})}\right] \left[\frac{\mathcal{J}_s(\text{Part.-Amp})}{T_s(\text{GeV})}\right]$$

in which the first bracket's value is fixed by the system design, and that of the second varies along the linac. We employ Neuffer's estimate,[3] modified by a hoped-for sextupole improvement factor $F \geqslant 1$, for allowable momentum spread at the final lens;

$$(\Delta p_z/p_z)_f \; < \sim \tfrac{1}{2}(r_s/X)F$$

with spot radius r_s and quadrupole lens bore radius X. In the numerical estimates below we use the value 2×10^{-3} F (r_s = 1 mm, X = 25 cm).

Another measure of this constraint is the maximum allowed disordered ion longitudinal kinetic energy as seen in the moving frame, which may be expressed as a longitudinal "temperature" Θ_z in electron-Volts:

$$\Theta_z \; \tilde{=} \; \tfrac{1}{2}Am_p(\Delta v_z)^2 .$$

This quantity must be limited, using the units above, by

$$(\Theta_z)_s <\sim 10^{-3}\left[\frac{T_f^2(\text{GeV})\,\tau_f(\text{nsec})\,(\Delta p_z/p_z)_f}{E(\text{MJ})}\right]^2\left[\frac{\mathcal{J}_s^2(\text{part.-Amp})}{T_s(\text{GeV})}\right]\ \text{eV}.$$

As an illustration we take $T_f = 20$ GeV, $E = 1$ MJ, $\tau_f = 6$ nsec, $A = 200$. Then $Q = 50q$ μCoul so that $\mathcal{J} = 50/\tau(\mu\text{sec})$; the constraints become

$$(\Delta v_z/v_z)_s <\sim 2.4 \times 10^{-4} F/[\,\tau_s(\mu\text{sec})\,T_s(\text{GeV})\,],$$

$$\Theta_s <\sim 58F^2/[\,\tau_s^2(\mu\text{sec})\,T_s(\text{GeV})\,]\ \text{eV}.$$

To proceed with the illustration we take a specific design[4] developed at the Lawrence Berkeley Laboratory, for which $q = 4$. The pulse duration and current shown there are moderately well reproduced by

$$\tau(\text{nsec}) \sim 1380\,[T(\text{GeV})]^{-0.8},\quad I(\text{Amp}) \sim 145[\,T(\text{GeV})\,]^{0.8},$$

which lead to the following values:

T(GeV)	β	τ (μsec)	L(m)	I(Amp)	$\mathcal{J}$(p.A)	$\Delta v_z/v_z$	Δv_z(m/sec)	Θ(eV)
0.2	0.045	5	68	40	10	$2.4F \times 10^{-4}$	$3.2F \times 10^{3}$	$11F^2$
1	0.1	1.4	41	144	36	$1.7F \times 10^{-4}$	$5.1F \times 10^{3}$	$30F^2$
4	0.2	0.46	27	440	110	$1.3F \times 10^{-4}$	$7.9F \times 10^{3}$	$70F^2$
10	0.32	0.22	21	920	230	$1.1F \times 10^{-4}$	$10F \times 10^{3}$	$120F^2$
20	0.45	0.125	17	1600	400	$1.0F \times 10^{-4}$	$13F \times 10^{3}$	$184F^2$

These velocities and temperatures are very small indeed.

2. Relative Distance of Travel

The distance of travel, relative to the bunch center, by an ion having maximum velocity defect depends on the designed variations of both mean bunch velocity and bunch length along the linac;

$$\Delta z(s) = \int_0^s (\Delta v_z/v_z)_s ds.$$

The integrand is proportional to $(v_z L)^{-1}$; thus

$$\Delta z_f = (\Delta v_z/v_z)_i \, s_f \int_0^1 \left[L_i/L(\sigma)\right]\left[v_i/v(\sigma)\right] d\sigma = (\Delta v_z)_f t_f \int_0^1 \left[L_i/L(\mu)\right] d\mu$$

with i and f initial and final values and $\sigma = s/s_f$, $\mu = t/t_f$. The product $v_z L$ varies by only a small factor; it is proportional to $T\tau(T)$, which is proportional to $T^{0.2}$ in the example design approximated above. If the mean accelerating field is assumed uniform along the linac, $T - T_i$ is proportional to s so that the first dimensionless integral above is an elementary one, closely approximated by $[(T_i/T_f)^{0.2}]/0.8$, which equals 0.5 for this design. Numerical experiments have shown that if $\mathscr{E}$ is linear in s with space-average $\bar{\mathscr{E}}$ this integral is only larger by $\leqslant \sim 6\%$ if $\mathscr{E}$ varies by a factor $\leqslant 3$. For $\mathscr{E}$ linear in s, $s_f = (T_f - T_i)/qe\bar{\mathscr{E}}$. For the example design

$$\Delta z_f \sim (\Delta v_z/v_z)_i (T_f - T_i)/2qe\bar{\mathscr{E}} = 0.57F/\bar{\mathscr{E}} \text{ (MV/m) meter.}$$

For the reasonable assumptions $F \leqslant 3$, $\bar{\mathscr{E}} \geqslant 1$ MV/m this travel is less than 10% of the final bunch length of 17 m in this design.

Estimates based on simple assumptions about the low-beta section (from ~ 1 MeV to 0.2 GeV) and the final compression system after acceleration in this example indicate that comparable or lesser fractions of a bunch length may be traversed in these sections by an ion having maximum velocity defect. Thus it appears that for systems with parameters in this range it is not merely desirable, but required, that individual ions shall not move along a bunch by more than a fraction of its length during acceleration and compression. This might tend to reduce concern about nonlinear couplings between longitudinal and transverse motions of ions during multiple reflections from steep longitudinal potential "walls" near the bunch ends during most of the acceleration; however, the tolerances required to create and maintain such low longitudinal temperatures are extremely stringent.

III. BEHAVIOR OF SMALL DISTURBANCES ON A BUNCH VARYING IN SPACE AND TIME

We employ the commonly used assumption[5] that the longitudinal space-charge field of a beam of charged particles moving inside a conducting pipe is given (non-relativistically) by*

$$\mathscr{E}_{z_{sc}} \simeq - gqe\ \partial\lambda/\partial z$$

with λ the number of ions per unit length, g a geometrical factor of order unity, and z distance along the bunch measured from its center, for ions of charge qe and mass m. Just as a plasma frequency is defined by ion charge, mass, and number per unit

* Introduction of a more general assumption would allow consideration of resistive-wall and related effects which are not considered here.

volume, so is a charateristic velocity V defined here by charge, mass, and number per unit length. It is given by

$$V^2 = g(qe)^2/m \text{ (cgs)}.$$

To show this consider a uniform bunch (constant λ_o) at rest. For a small density perturbation $\delta\lambda(z,t) = \lambda(z,t) - \lambda_o$ and correlated small velocity perturbation $\delta u(z,t)$, the equation of continuity is

$$\frac{\partial\lambda}{\partial t} + \frac{\partial}{\partial z}(\lambda u) \simeq \frac{\partial\lambda}{\partial t} + \lambda_o \frac{\partial u}{\partial z} \doteq 0$$

and the equation of motion is

$$a \simeq \frac{\partial u}{\partial t} = -\frac{g(qe)^2}{m}\frac{\partial\lambda}{\partial z} .$$

Evaluating $\partial^2\lambda/\partial z\partial t$ from each equation and equating, we have

$$\frac{\partial^2 u}{\partial z^2} - \frac{1}{V^2}\frac{\partial^2 u}{\partial t^2} = 0 ,$$

the wave equation, with V^2 as given above.

For $g \sim 2$, ions of mass Am_p, and a uniform bunch of length L meters containing a total charge Q microcoulomb, one finds

$$V \sim 1.3\,(qQ/AL)^{\frac{1}{2}} \times 10^6 \text{ m/sec} .$$

For example, if $q = 4$, $Q = 200$ μcoul, $A = 200$

$$V \sim 2.7\,L^{-\frac{1}{2}} \times 10^6 \text{ m/sec} .$$

This velocity is to be compared with that of a bunch end toward its center during bunch compression in an induction linac, which we denote by u_{max}. If a bunch is compressed from $L \sim 75$ m to $L \sim 15$ m during an acceleration time $\sim$ 60 μsec, the average value of u_{max} is $\sim 0.5 \times 10^6$ m/sec, so that V and u_{max} are comparable, being equal in this example at $L \sim 30$ m.

As shown earlier, target requirements and final lens parameters constrain the maximum allowable longitudinal thermal (random) velocity. It is a general property of system designs presently under consideration that this velocity is smaller by more than an order of magnitude than the characteristic signal velocity V and the bunch end velocity u_{max}. Therefore it is reasonable to neglect thermal spread and to regard the medium as being at zero temperature when discussing the propagation of small disturbances along a bunch in which density λ and unperturbed ion velocity u (relative to the bunch center) vary in both space and time. We now derive the linearized wave equations for disturbances on such bunches.

We assume that in the absence of perturbations the density and velocity $\lambda_o = \lambda_o(z,t)$ and $u_o = u_o(z,t)$ satisfy the equation of continuity

$$\partial\lambda/\partial t + \partial(\lambda u)/\partial z = 0$$

and are consistent* with the unperturbed externally applied and

---

* See Section IV below.

space-charge fields. With perturbations present,

$$\lambda = \lambda_o + \phi(z,t), \quad u = u_o + \psi(z,t)$$

with ϕ, ψ small of first order. Neglecting the second-order term, the equation of continuity is

$$\partial\phi/\partial t + \partial(u_o\phi + \lambda_o\psi)/\partial z = 0. \tag{1}$$

The equation of motion is

$$du/dt = \left[\frac{\partial}{\partial t} + u\frac{\partial}{\partial z}\right] u = \partial(u_o + \psi)/\partial t + (u_o + \psi)\,\partial(u_o + \psi)/\partial z$$

$$= qe\mathscr{E}/m;$$

again neglecting the second-order term and cancelling those present in the absence of perturbations,

$$\partial\psi/\partial t + \partial(u_o\psi)/\partial z = -[g(qe)^2/m]\partial\phi/\partial z + \delta a_{ext}(z,t) \tag{2}$$

in which δa_{ext} is the acceleration due to departures of the external field from the form required for consistency in the absence of perturbations.

The two coupled first-order partial differential equations (1) and (2) for ϕ and ψ contain the unspecified functions u_o and λ_o which are constrained as indicated above. In order to proceed analytically it has been found desirable to further

constrain these functions so that they represent scaling bunch shapes as described in the introduction. Such bunches have linear densities of the form

$$\lambda_o(x,t) = \text{const. } S(x)/z_o(t)$$

in which $x = z/z_o(t)$ is distance from the bunch center measured in units of the (arbitrarily) varying bunch half-length. The equation of continuity then requires that the form of u_o be

$$u_o(z,t) = z(dz_o/dt)/z_o = x\, dz_o/dt.$$

Thus scaling bunches are characterized by two independent arbitrary functions, the shape function $S(x)$ and the half-length $z_o(t)$, which we express in terms of its initial value z_{oo} as a dimensionless reciprocal compression factor $R(t) = z_o(t)/z_{oo}$ having initial value unity. Similarly we normalize $S(x)$ so that $S(0) = 1$, leading to

$$\lambda_o(z,t) = \lambda_{oo} S(x)/R(t)$$

with λ_{oo} the initial value of λ at the bunch center. We change variables from (z,t) to (x,t) using the relations

$$\partial/\partial z\big|_t = z_o(t)^{-1} \partial/\partial x\big|_t ,$$

$$\begin{aligned} \partial/\partial t\big|_z &= \partial/\partial t\big|_x + \partial x/\partial t\big|_z \, \partial/\partial x\big|_t \\ &= \partial/\partial t\big|_x - (z/z_o^2)\ (dz_o/dt)\partial/\partial x\big|_t . \end{aligned}$$

After some manipulation eqs. (1) and (2) become

$$[R(t)\ \partial/\partial t]\ (R\emptyset) + (\lambda_{oo}/z_{oo})\partial(S\psi)/\partial x = 0,$$

$$\partial(R\emptyset)/\partial x + (\lambda_{oo} z_{oo}/V_{oo}^2)\{[R\partial/\partial t](R\psi) - R^2\delta a\} = 0 ,$$

in which $V_{oo} = qe(g\lambda_{oo}/m)^{\frac{1}{2}}$ is the initial mid-bunch value of the characteristic velocity. From this form it is evident that the appropriate time variable is

$$\tau(t) = \int_0^t R(t')^{-1} dt' .$$

In terms of τ the equations are

$$\partial(R\emptyset)/\partial\tau + (\lambda_{oo}/z_{oo})\partial(S\psi)/\partial x = 0,$$

$$\partial(R\psi)/\partial\tau + (V_{oo}^2/\lambda_{oo} z_{oo})\partial(R\emptyset)/\partial x = R^2\delta a .$$

The dependent variable $R\emptyset$ may now be eliminated, yielding the desired wave equation for ψ ;

$$\partial^2(R\psi)/\partial\tau^2 = (V_{oo}/z_{oo})^2\partial^2(S\psi)/\partial x^2 + \partial(R^2\delta a)/\partial\tau .$$

We now confine our attention to the normal-mode (standing-wave) solutions of the homogeneous equation in the absence of external perturbations δa. Separating the variables by setting $\psi(x,\tau) = X(x)T(\tau)$, we have

$$T^{-1}d^2(RT)/d\tau^2 = (V_{oo}/z_{oo})^2 X^{-1}d^2(SX)/dx^2$$

$$= \text{constant} = -\omega_o^2 ,$$

yielding th two ordinary differential equations

$$d^2(RT)/d\tau^2 + (\omega_o^2/R)(RT) = 0 ,$$

$$d^2(SX)/dx^2 + (\kappa_o^2/S)(SX) = 0 ,$$

with $\kappa_o = \omega_o z_{oo}/V_{oo}$ the radian wave-number at the bunch center (dimensionless, in units of x^{-1}) corresponding to angular frequency ω_o of a mode at $t = 0$.

From the form of these equations we may gain a picture of the scaling in space and time of small perturbations in the idealized system to which these equations apply. Consider, for example, the temporal behavior of modes with frequencies high enough that the variation of R may be regarded as adiabatic. [This requires that $|\Delta R/R| << 1$ in one period $\Delta t = R\Delta\tau \sim R^{3/2}/\omega_o$.] Then from the WKB approximation RT is proportional to the real part of

$$R^{\frac{1}{4}} \exp[i\omega_o \int^{\tau} R^{-\frac{1}{2}}(\tau')d\tau']$$

so that the real-time variation of the velocity perturbation in such a mode is

$$T(t) \propto R(t)^{-3/4} \, R\ell \, \exp\left[i\omega_o \int^{\tau} R^{-3/2}(t')dt' \right] .$$

Similarly, some wavelengths are short enough that the variation of S may be regarded as adiabatic in space. [This requires that $|\Delta S/S| \ll 1$ over the spatial region $\Delta z = z_o \Delta x = z_o S^{\frac{1}{2}}/\kappa_o$.] In the same way the spatial variation of the velocity perturbation is

$$X(x) \propto S(x)^{-3/4} \, R\ell \, \exp\left[i\kappa_o \int^{z} S^{-\frac{1}{2}}(x')dx' \right].$$

Thus the amplitude of such a mode's velocity perturbation is $\psi_{oo}[R(t)S(x)]^{-3/4}$, with local frequency $\omega_o/[R(t)^{3/2}]$ and radian wave-number $\kappa_o/[S^{\frac{1}{2}}(x)z_o(t)] = \kappa_o/[z_{oo}S^{\frac{1}{2}}(x)R(t)]$ in physical units (length^{-1}).

The density perturbation $\emptyset$ is found from

$$\emptyset(x,\tau) = - R^{-1}(\tau)(\lambda_{oo}/z_{oo}) \int^{\tau} \frac{\partial(S\psi)}{\partial x} \, d\tau$$

$$= - R^{-1}(\tau)(\lambda_{oo}/z_{oo}) \, \frac{d}{dx} \, (SX) \int^{\tau} T(\tau')d\tau'.$$

In the spirit of the WKB approximation, the operations are applied only to the rapidly varying phases in SX and T;

$$d(SX)/dx \tilde{\propto} S^{\frac{1}{4}} R\ell \left[(i\kappa_o S^{-\frac{1}{2}}) \exp(i\kappa_o \int^{x} S^{-\frac{1}{2}} dx') \right] ,$$

$$\int^{\tau} T(\tau')d\tau' \tilde{\propto} R^{-3/4} R\ell \left[(i\omega_o R^{-\frac{1}{2}})^{-1} \exp(i\omega_o \int^{\tau} R^{-\frac{1}{2}} d\tau' \right].$$

Thus the amplitude of the density perturbation is

$$(\psi_{oo}/R)(\lambda_{oo}/z_{oo})(\kappa_o/\omega_o)(S^{\frac{1}{2}}/R^{3/4})(R/S)^{\frac{1}{2}}$$

$$= \phi_{oo} R(t)^{-5/4} S(x)^{-1/4}$$

with ϕ_{oo}, ψ_{oo} the amplitudes at $z = 0$, $t = 0$, satisfying the relation

$$|\phi_{oo}/\psi_{oo}| = \lambda_{oo}/V_{oo} \quad .$$

For lower frequencies, longer waves, and in regions of the bunch where $S(x)$ is changing rapidly the WKB approximations are not valid. To illustrate what can be done with the equations we give here exact solutions of the equation for T for a one-parameter family of functions $R(t)$ which has some generality, and an exact solution of the equation for X for the parabolic shape $S(x) = 1 - x^2$. We set $R(t) = (1 + \alpha\nu t)^{-1/\alpha}$, in which α is a parameter determining the functional form of the bunch compression; since $dR/dt = -\nu$ for all α, ν is the initial fractional compression rate. The form of $R(\tau)$ is found from

$$\tau(t) = \int_0^t R^{-1}(t')dt' = \left[(1 + \alpha\nu t)^{(\alpha+1)/\alpha} - 1\right]/\nu(\alpha + 1)$$

so that

$$R(\tau) = (1 + \beta\nu\tau)^{-1/\beta} \text{ with } \beta = 1 + \alpha.$$

As examples we list

1. Steady compression $(\alpha = -1, \beta = 0)$, $R(t) = 1 - \nu t$, $R(\tau) = e^{-\nu\tau}$
2. Exponentially increasing compression $(\alpha = 0, \beta = 1)$, $R(t) = e^{-\nu t}$, $R(\tau) = (1 + \nu\tau)^{-1}$
3. An intermediate case $(\alpha = -\frac{1}{2}, \beta = \frac{1}{2})$, $R(t) = (1 - \frac{1}{2}\nu t)^2$, $R(\tau) = (1 + \frac{1}{2}\nu\tau)^{-2}$

[In the first two examples one must use the limiting form

$$\lim_{n \to 0} (1 + nx)^{1/n} = e^x .]$$

For this family $R(\tau)$ the equation may be written as

$$d^2(RT)/d\xi^2 + (\omega_o/\beta\nu)^2 \xi^{1/\beta}(RT) = 0 ,$$

with $\xi = 1 + \beta\nu\tau$. Its solution is

$$RT = \xi^{\frac{1}{2}}[AJ_p(\zeta) + BY_p(\zeta)]$$

where the order p of the Bessel functions is $\beta/(2\beta + 1) = (\alpha + 1)/(2\alpha + 3)$ and their argument ξ is $(\omega_o/\nu)(\beta + \frac{1}{2})^{-1} \xi^{-(\beta + \frac{1}{2})/\beta}$; A and B are arbitrary constants. It is more useful to express T in terms of R and α since the latter gives the dependence of R on real time t directly;

$$T = R^{-(\alpha+3)/2}[AJ_p(\zeta) + BY_p(\zeta)]$$

with $\zeta = (\omega_o/\nu)(\alpha + 3/2)^{-1} R^{-(\alpha+3/2)}$.

This form of solution fails for the first example above (steady compression) because R is not a power of ξ for $\beta = 0$. For this case it is simpler to express the equation in terms of t though $\xi = 1 - \nu t$;

$$\xi (d/d\xi)[\xi (dT/d\xi)] + (\omega_o/\nu)^2 T = 0.$$

The solution is $T = A \cos[(\omega_o/\nu) \ell n(1 - \nu t) + \delta]$ with A, δ constants.

The Bessel form of solution is also invalid for the special case $\alpha = -3/2$, $\beta = -\frac{1}{2}$, for which the order p becomes infinite. In this case the equation is

$$d^2(RT)/d\xi^2 + (2\omega_o/\nu)^2 \xi^{-2} (RT) = 0.$$

The form of solution depends on the value of the parameter $\mu = (2\omega_o/\nu)^2$. For $\mu < \frac{1}{4}$ it is $T(\xi) = \xi^{-3/2} [A\xi^{(\frac{1}{4}-\mu)^{\frac{1}{2}}} + B\xi^{-(\frac{1}{4}-\mu)^{\frac{1}{2}}}]$;

for $\mu > \frac{1}{4}$, $T(\xi) = A\xi^{-3/2} \cos[(\mu - \frac{1}{4})^{\frac{1}{2}} \ell n \xi + \delta]$, and for $\mu = \frac{1}{4}$, $T(\xi) = \xi^{-3/2} [A + B \ell n \xi]$.

In considering normal modes of small oscillations on a finite bunch the equation for $X(x)$ is to be solved subject to appropriate boundary conditions at its ends, thereby defining spatial eigenfunctions X_n and associated eigenvalues κ_{o_n} leading to eigenfrequencies ω_{o_n} through the relation $\omega_o/\kappa_o = V_{oo}/z_{oo}$. The simplest non-trivial example of a shape function appears to be the parabolic one, $S(x) = 1 - x^2$, for which the equation is

$$d^2[(1 - x^2)X]/dx^2 + \kappa^2 X = 0;$$

it may be written in the form

$$(x^2 - 1)X'' + 4x\,X' + (2 - \kappa^2)\,X = 0,$$

which is Gegenbauer's equation[6] with its parameters α and β (not the α and β used above) given by $(\alpha + 1)(\alpha + 2) = \kappa^2$, $\beta = 1$. For this value of β, the general solution is[7]

$$X(x) = (d/dx)[\,AP_{1+\alpha}(x) + BQ_{1+\alpha}(x)]$$

in which P and Q are Legendre functions.

To proceed further one must establish boundary conditions. Unfortunately, both the physical assumption $\mathscr{E}_{sc} \propto \partial\lambda/\partial z$ and (therefore) the mathematics become inadequate near the bunch ends where $\lambda \to 0$; the bunch ends are singular points of the differential equation, at which only a single specific linear combination of the P and Q terms is non-singular for any given value of α. For such solutions the ratio of slope to value at these points is $(X'/X)\big|_{x=\pm 1} = \pm\frac{1}{4}\alpha(\alpha+3)$, leaving no freedom to impose a physical condition on the ratio. The problem will not be pursued further here because with our assumptions there is no clear justication for any particular boundary condition. More work might be appropriate should analytic solutions be desired for comparison with a computer simulation, provided the latter embodies a well defined bunch-end condition.

After establishing by some means a set of normal modes, examination of the inhomogeneous equations ($\delta a \neq 0$) could lead to an evaluation of tolerances on allowable departures of the applied electric field from that required for the equilibrium distribution.

Among additional topics remaining for future study are inclusion of the space periodicity of the surrounding structure and its applied electric field, and of its finite resistivity.

IV. GENERALIZATIONS OF NEUFFER'S SELF-CONSISTENT PHASE SPACE DISTRIBUTIONS

Neuffer has derived a "self-consistent" stationary distribution for longitudinal transport of a beam bunch, and a similar nonstationary distribution together with its envelope equation[1]. In subsequent work[2] he has analyzed the stability of these "standard longitudinal distributions" in continuous and periodic transport systems. His distributions are characterized by longitudinal self-fields and external fields proportional to the distance z from the bunch center [based on the usual approximation[5] $\varepsilon_z(\text{sp.chg.}) \simeq -gqe\, d\lambda/dz$] and therefore by parabolic dependence of the number of ions per unit length λ on z. Although these dependences provide analogies with the K-V distribution[8] (which has appeared to be uniquely tractable for analytic stability studies), they are very different from those for the nearly uniform λ expected over most of the bunch length (beginning at injection and continuing over a large part of the acceleration) in an induction linac driver for a heavy-ion inertial-fusion power plant. The generalizations described below were

developed in an effort to arrive at forms more relevant to the physical situation in such a linac. Here, as in Neuffer's work, relativistic corrections are ignored.

It is perhaps worth noting that the property of self-consistency is in one sense a matter of definition. If a distribution function is specified there will exist some external force field which, together with the self-field, is required to produce it; the total field can be calculated from conservation of phase space density (Vlasov equation). However, in our application and many others a velocity dependence of the force due to this field is unacceptable; the general problem of finding distributions without velocity dependence of the force is a difficult one. In Neuffer's work the desired forms of λ and the corresponding consistent total field (parabolic and linear, respectively, in z) were established in advance.

Here we explore in turn alternatives to the following assumptions made by Neuffer:

1. $\lambda(z)$ is required to be parabolic.
2. The stationary distribution function $f(z, z') = f(H)$ is a <u>specific</u> function of the single-ion Hamiltonian $H(z, z')$; $f = \text{const.}(H_{max} - H)^{\frac{1}{2}}$.
3. The nonstationary distribution function $\lambda(z, s)$ is required to be parabolic in z.
4. The bunch is coasting; its center has zero acceleration.

In what follows the shape function is denoted by $F(x)$ rather than $S(x)$, and the meanings of the symbols p, q, r, S, R, T, μ, ν, ξ, ζ, ϕ, and ψ are not related to those above.

1. Stationary Distributions

First we explore alternatives to the first assumption, retaining the others. Consider the class of stationary distribution functions for which

$$f(z, z') = (3N/2\pi\varepsilon)(\nu/\mu)\,[F(x) - (\nu z_o/\varepsilon)^2 z'^2]^{1/2}$$

within the area in $z - z'$ space where the square root is real and $f = 0$ outside it. Here $F(x)$ is a dimensionless shape function; $x = z/z_o$, with z_o the bunch half-length, and $F(\pm 1) = 0$; N is the total number of particles; ε is the un-normalized emittance = (occupied area in $z - z'$)/π; primes are d/ds with s, the independent variable, equal to vt for a coasting beam; μ and ν are constants defined by

$$\mu = (3/4)\int F(x)\,dx, \quad \nu = (2/\pi)\int F^{1/2}(x)\,dx,$$

and unstated limits of integration here and below are those at which the integrand vanishes. The quantity within the square root is proportional to $H_{max} - H(z, z')$ with the Hamiltonian H the sum of kinetic and potential energies; the potential energy per particle is

$$V(z) = V_{ext} + V_{sc}$$

and the space charge potential energy is

$$V_{sc} = g(qe)^2\lambda(z)$$

with λ the number of particles per unit length;

$$\lambda(z) = \int f\, dz' = (3N/4z_o)\mu^{-1}F(x) .$$

For a coasting beam the total force on an ion is mv^2z'', and from the Vlasov equation $z'' = -z'(\partial f/\partial z)/(\partial f/\partial z') = \frac{1}{2}(\epsilon/\nu z_o)^2 dF/dz$; the total force is also given by $-d(V_{ext} + V_{sc})/dz$. Combining the expressions above, the self-consistent potential energy per ion of the external force is found to be

$$V_{ext}(z) = -\left[1 + 2(S/R)(\mu/\nu)^2\right] V_{sc}(z)$$

in which

$$2S/R = (2mv^2\epsilon^2)/(3gq^2e^1Nz_o) ;$$

S and R are dimensionless parameters I introduced in an earlier work[9] on longitudinal dynamics [in which $F(x) = 1 - x^2$ as in Neuffer's distribution and $\mu = \nu = 1$] as measures of the emittance and space charge terms. The external force must not only cancel that due to space charge but in addition must contain the thermal pressure of the bunch which is proportional to ϵ^2.

Thus we have constructed a family of stationary distribution functions generalized from that of Neuffer which allow an arbitrary linear density $\lambda(z)$ and have determined the corresponding self-consistent external field; for this family it has the same form of space dependence as $d\lambda/dz$.

Next we explore alternatives to the second assumption, retaining the first and last ones. Consider the class of stationary distribution functions

$$f(z,z') = (3N/2\pi\varepsilon)(\nu/\xi)\ f\left[F(x) - (\nu z_o/\varepsilon)^2 z'^2\right]$$

with the same definitions and conditions as before; the function $f(H_{max} - H)$ is assumed to be such that the integral $\int f\, dz'$ can be performed analytically so as to obtain an analytic expression for $\lambda(z)$. We define a function $G(F(x))$;

$$G(F(x)) = F^{\frac{1}{2}} \int_{-1}^{1} f\left[F(1 - \zeta^2)\right] d\zeta$$

The constants ν and ζ are defined by

$$\nu = (2/\pi)\int F^{\frac{1}{2}}(x)\, dx, \quad \xi = (3/2\pi)\int G\, dx.$$

Then

$$\lambda(z) = (3N/4z_o)\xi^{-1}G$$

Following the same procedure as before, we find

$$V_{ext}(z) = -\left[V_{sc}(z) + 2m(v\varepsilon/\nu z_o)^2\ F(x)\right]$$

Thus we have constructed a more general family of stationary distribution functions which allow an arbitrary density $\lambda(z)$, and have determined the corresponding self-consistent external field; for this wider class the part of the external field which contains the thermal pressure has in general a form of dependence on z which differs from that of $d\lambda/dz$.

As examples of this class we display the results for $f(h) = h^{\eta}$ with η an arbitrary number, restricted to avoid non-integrable singularities. Then

$$\lambda(z) = (N/z_o)\, F^{\eta+\frac{1}{2}} / \int F^{\eta+\frac{1}{2}}(x)\, dx .$$

For $\eta = \frac{1}{2}$ we reproduce the results for the less general family above. For $\eta < \frac{1}{2}$ the space charge field becomes singular at the bunch ends where $F(x) \to 0$, unless $dF/dx \to 0$ there. For $\eta = 0$ the distribution function is constant within the boundary in $z - z'$ space for any $F(x)$; to avoid a singularity in the space charge field at the bunch ends one must require $F^{-\frac{1}{2}} dF/dx \to 0$ there. As $\eta \to -\frac{1}{2}$, $\lambda(z) \to N/(2z_o)$ = constant within the bunch for any $F(x)$, and the distribution function becomes increasingly singular toward the boundary in $z - z'$ space, approaching a square root singularity. For Neuffer's choice $F(x) = 1 - x^2$, the external field required will always be proportional to z while λ varies as $[1 - (z/z_o)^2]^{\eta}$ for any value of η .

These examples serve to indicate a special feature of Neuffer's distribution $\left[F(x) = 1 - x^2,\ \eta = \frac{1}{2}\right]$; all forces (space charge,

external, and thermal) are linear in z. This feature no doubt contributes to the tractability of analytic stability analyses. More importantly, the examples show that the z dependence of the external field required to maintain a bunch in equilibrium will depend on the form of its distribution function's dependence on z', even for a fixed $\lambda(z)$. Should actual distributions have thermal pressures requiring applied containing-field components of magnitude greater that the smallest allowable error fields it will be necessary to determine their z dependences.

2. Nonstationary Distribution Functions

Here we explore alternatives to the third assumption, considering not only the specific functional dependence of the second assumption but also more general ones. The requirement that the forces be velocity-independent $(\partial z''/\partial z' = 0)$ is

$$(\partial/\partial z')[\,(\partial f/\partial s + z'\, f/\partial z)/(\partial f/\partial z')\,] = 0$$

which imposes a constraint on the form of the distribution function $f(z, z', s)$ and leads to the expected conservation equation

$$\partial\lambda/\partial s + \partial(\lambda u)/\partial z = 0,$$

in which $\lambda(z, s) = \int f\, dz'$ and $u(z, s) = \langle z' \rangle = \int z'\, f\, dz'/\lambda$, obtained by integrating the Vlasov equation over z' and noting that $f = 0$ at the limits of integration.

The severity of this constraint on the form of f may be seen by considering f to be <u>any</u> appropriate function of $H_{max} - H(z,z',s)$

and assuming the somewhat general form

$$H_{max} - H = \phi(z,s) - \psi(s)[z' - u(z,s)]^2 .$$

Then

$$\lambda(z,s) = (\phi/\psi)^{\frac{1}{2}} \int_{-1}^{1} f[\phi(1-\zeta^2)]\,d\zeta = \psi^{-\frac{1}{2}} G(\phi(z,s)).$$

After some calculation one finds that the constraint requires

$$2\psi z'(z' - 2u)\left[(\partial u/\partial z) - \frac{1}{2}\psi'/\psi\right] - [\phi' + u(\partial\phi/\partial z)] = 0$$

for all z', which can be satisfied only if

$$u(z,s) = \frac{1}{2}(\psi'/\psi)z$$

and

$$\phi' + u\partial\phi/\partial z = 0.$$

Using this form for u, the continuity equation becomes

$$\psi^{-\frac{1}{2}}(dG/d\phi)(\phi' + u\partial\phi/\partial z) = 0 ,$$

showing consistency; $\phi(z,s)$ must be of the form $\phi\left[z/\psi^{\frac{1}{2}}\right]$. All such distribution functions are <u>scaling</u>; the rate of dilation (change of length per unit length per unit change of the independent variable s) is independent of z, so that the <u>shape</u> of $\lambda(z,s)$ is preserved.

Should one try a more general form by allowing ψ to depend on z as well as on s, the requirement $\partial z''/\partial z' = 0$ forces the condition $\partial\psi/\partial z = 0$. The problem of developing non-scaling non-stationary distributions appears to be a difficult one, and will not be attempted here.

All of the generalized stationary distributions derived above may be converted into scaling nonstationary ones, with arbitrary shape function and arbitrary dilation dependence on s, in the following way:

$$f(z,z',s) = (3N/2\pi\varepsilon)(\nu/\S)f\left[F(x) - \{\nu z_o(s)/\varepsilon\}^2\{z' - (z_o'z/z_o)\}^2\right]$$

in which f is any suitable function of the argument in the square brackets; $z_o(s)$ is any function; $x = z/z_o(s)$;

$$\nu = (2/\pi)\int F^{\frac{1}{2}}(x)dx, \quad G(F(x)) = F^{\frac{1}{2}} \int_{-1}^{1} f\left[F(1-\zeta^2)\right] d\zeta$$

with f the function selected and $F(1-\zeta^2)$ its argument, and

$$\xi = (3/2\pi)\int G(F(x))dx.$$

The density is

$$\lambda(z,s) = [3N/4z_o(s)]\ \xi^{-1}G(F(z/z_o)).$$

The potential energy per ion of the external force required by self-consistency is

$$V_{ext}(z,s) = - V_{sc}(z,s) - \frac{1}{2}mv^2 \left[(\varepsilon/\nu z_o)^2 F + (z_o"/z_o)z^2\right]$$

for a coasting beam with constant v. The force due to the second term in the bracket is that required to produce the specified dilation.

3. Effect of Acceleration

Here we consider the correction needed if the fourth assumption is not valid. For an accelerating bunch

$$d^2z/dt^2 = z"v^2 + z' a$$

with $a = dv/dt$. We will estimate the importance of the second term by evaluating the ratio

$$R = z'a/z"v^2$$

on the assumption that the acceleration is constant and that the bunch length varies as a power of the ion kinetic energy T. (In the example design[4] used above the pulse duration τ is approximately proportional to $T^{-0.8}$, so that bunch length $L \propto T^{-0.3}$.) With $L \propto T^{-p}$, and dT/ds constant,

$$R = L'(T'/m)L"(2T/m) = (dL/dt)/\left[2T(d^2L/dt^2)\right] = - \left[2(1+p)\right]^{-1}$$

and if $p = 0.3$ the correction ratio $|R| \sim 40\%$.

The correction ratio R is even larger if the acceleration increases with distance along the accelerator. Retaining the

power law assumption for $L(T)$ but assuming the acceleration to increase linearly with distance s from an initial value a_i to a final value a_f, the value of R is

$$R = -\frac{1}{2}\{(1 + p) - d[\ln(dT/ds)]/d(\ln T)\}^{-1}$$

and the logarithmic derivative is

$$\frac{1}{2}(1 - q)r/[q + (1 - q)r]$$

with $q = (a_i/a_f)^2$ and $r = (T - T_i)/(T_f - T_i)$. This term (and therefore also $|R|$) attains its maximum value $\frac{1}{2}(1 - q)$ at the final energy, where

$$|R|_{max} = (1 + 2p + q)^{-1} ;$$

if the accelerating field increases by a factor ~ 3, as suggested in some designs, $q \sim 0.1$ and $R \sim -0.6$; the ratio $z''v^2/(d^2z/dt^2)$ becomes as large as ~ 2.4, compared with unity for a coasting beam.

ACKNOWLEDGEMENT

I am grateful to Dr. Lloyd Smith for pointing out an ambiguity of interpretation in the first draft of Section IV. Supported in part by the High Energy Physics Division of the U. S. Department of Energy under contract No. W-7405-ENG-48.

REFERENCES

1. Lawrence Berkeley Laboratory Report LBL-8387

2. Lawrence Berkeley Laboratory Internal Reports HI-FAN 72, HI-FAN 83, HI-FAN 85

3. See, for example, Argonne National Laboratory Report ANL-79-41, p. 239.

4. Lawrence Berkeley Laboratory Report LBL-9019 UC-21, Appendix B, p. 3, Fig. 5.

5. E.g., Ref. 1, eq. 1.

6. Morse and Feshbach, Methods of Theoretical Physics, McGraw-Hill, 1953, Vol I, p. 547.

7. Ref. 6, pp. 601-603.

8. Proc. Int. Conf. on High Energy Accelerators, CERN (1959), p. 274.

9. Brookhaven National Laboratory Report BNL 50769, p. 34.

PULSELAC PROGRAM

S. Humphries, Jr., J. R. Freeman, G. W. Kuswa, C. W. Mendel,
J. W. Poukey, and J. P. Quintenz
Sandia Laboratories, Albuquerque, NM 87185

I. Introduction

The Pulselac Program at Sandia Laboratories is a recent addition to the Heavy Ion Fusion Program. The purpose of this paper is to give a brief introduction to the work performed to date and future plans for the development of high current accelerators. The basis of the program is the investigation of practical methods of neutralizing the space charge of intense ion beams both in accelerating and transport regions. Alleviation of space charge constraints on ion beam transport would open up a broad range of new options for accelerator fusion drivers.[1,2,3] The method to be employed is the introduction of electrons from external sources into the volume of the ion beam, allowing the relaxation towards a state of lower potential energy. Both the spatial location and velocity distribution of the electrons must be controlled. Our approach is to utilize weak magnetic fields, which have negligible effect on the ion orbits, to accomplish this. The physics of the electron control and magnetic field geometry requires an ion beam with annular geometry.

The program has two major goals. The first is to gain an understanding of the general phenomenon of beam neutralization. The second is to demonstrate the technological feasibility of the utilization of these principles to produce multi-kiloampere ion beams in a controlled and reproducible manner. It should be emphasized that we are investigating new methods of beam transport; actual beam acceleration is conventional. In particular, the inductive linear accelerator technology under development at LBL would be ideally matched to the high current beam transport systems.

The physical basis of neutralized beam transport has been discussed in the proceedings of the Argonne National Laboratory Workshop, 1978 (3) as well as in a number of other references.[4,5,6] In this paper, progress since the Argonne Workshop will be reviewed, and plans for a fusion demonstration accelerator, Pulselac C, to be built over the next 2.5 years, will be discussed.

II. Theoretical Work

Neutralized beam propagation presents a number of novel research areas, both for the plasma physicist and accelerator theorist. The microscopic problems of gap behavior and local neutralization must be combined with systems considerations. A wide diversity of new phenomena can occur because of the two-particle nature of the problem. The electron dynamics is of equal importance to that of the ions in determining the behavior of the system. Familiar techniques in accelerator theory, such as the treatment of space charge as a perturbation and

the approximation of focusing forces as linear away from the axis of symmetry, must be completely discarded. We have made initial efforts to construct a theory of neutralized beams; results are summarized in this section.

A. Ion Beam Neutralization

One-dimensional computer simulations have confirmed that space charge in ion beams can be almost completely cancelled by electrons introduced from sources external to the beam.[7] Basic scaling laws for the time-dependence of the neutralization process have been verified.

B. Two-Dimensional Particle Simulations

A two-dimensional particle simulation model has successfully demonstrated a number of the physical aspects of the Pulselac gap. The code follows individual, self-consistent particle orbits to look for quasi-steady-state solutions. Virtual cathode formation and drift tube neutralization are clearly demonstrated. The computer results also indicate two important constraints on the time response of neutralization; the access of the electrons to the beam volume (which may be affected by magnetic field line contours), and the rate of relaxation of the electron velocity distribution.

C. Neutralized Beam Propagation

The problem of the propagation of neutralized ion beams in free space (plasmoids) is not trivial when the beam changes dimension, as in a transverse or longitudinal focus. Possible problems arising from the transfer of energy from the ions to electrons by adiabatic compression were mentioned in an earlier reference.[8] Recent two-dimensional computer simulations of focused neutralized beams in vacuum have verified that the beam focus can be limited by thermoelectric effects in the electron cloud. This disturbance can grow unstably if the beam pulselength is too long. These considerations set requirements on the quality of the neutralizing electron distribution and the beam pulselength.

D. Transport of Beams in Non-linear Focusing Systems

Analytic studies have been published[6] which describe methods for treating the transverse confinement of beams in focusing systems that vary non-linearly with distance from the symmetry axis. The most important results of these studies are that beams can be transported in highly non-linear systems without emittance growth once the beam has reached an equilibrium distribution appropriate to the system, and that non-linear systems may have advantages from the point of view of beam stability because of the large spread in transverse oscillation frequencies.

E. Longitudinal Instabilities

Velocity bunching in accelerators of neutralized ion beams can be a serious problem. The ions are generally non-relativistic, the individual gaps are strongly loaded by the beam and longitudinal space charge effects (which impede bunching) have been greatly reduced. A particle simulation model has been used to investigate such instabilities in the case where space charge effects are absent. A longitudinal velocity spread (which can be simply related to the impedance of the gap driving circuits) can provide stability. The required spread does not preclude a macroscopic beam bunching for power compression to

the target. The non-linear development of the instability can be followed. Since the instability increases the longitudinal velocity spread, it is self-stabilizing.

III. Experimental Work

Experimental work on neutralized beam propagation has been carried out for the past two years at Sandia Laboratories. The purpose of these experiments was to investigate a wide diversity of problems associated with neutralized beams in order to form a basis for the design of practical systems. Considerable work has been carried out on injector gaps and on a two-gap system with independently applied voltage. These results are reported in Ref. 8.

Recently, a five gap accelerator has been operated with encouraging results. Peripheral work has been performed on the development of large area electron sources and pulsed guns for intermediate ion mass plasmas.

A. Injector Development

A novel injector has been developed which holds great promise for technological development. It is the first intense ion gun to use plasma injection into the anode plane from independent plasma sources. Initial operation was with carbon plasmas. Extracted carbon ion beams in the range 100-200 keV and 3-4 kA have been obtained. The injectors can be fired repetitively, limited mainly by the performance of the plasma guns. They operate at 20-30 A/sq. cm, roughly 10 times the Child-Langmuir limit. This current density enhancement is due to electrons trapped in the magnetic fields of the acceleration gap. The beams can be aimed by shaping the electron distributions through magnetic field curvature. Parallelism better than three degrees has recently been obtained.

B. Post-Acceleration

Experiments have been performed to post-accelerate beams in a number of gaps. These are the first such experiments with intense ion beams. Most recently, a five gap system has been operated. The final energy of the beam agrees closely with the sum of voltages on the acceleration gaps. Carbon beams at over 600 keV, 3 kA have been measured at the output. Pulselength is about 0.5 microseconds. Of greatest importance, the divergence angle of beams emerging from the five gap injector have been measured to be about 0.7 degrees, better than any results with single gap, intense ion beam injectors.

C. Beam Neutralization

It has been difficult to perform controlled measurements on beam neutralization phenomena in the close confines of the accelerator. Nonetheless, measurements of current density as a function of longitudinal position are useful since the ion orbits are sensitive to any imbalance in the space charge. These measurements imply an average upper limit of 0.2% in the imbalance of space charge during the propagation of the ion beams in the downstream drift regions. Roughly 2/3 of the beam current is measured 30 cm downstream from the injector. Without neutralization, the beam would be expected to blow up within 2 mm of the extractor.

D. Electrostatic Focusing

By purposely introducing curvature into the magnetic fields of post-acceleration gaps, the acceleration fields can be used to apply transverse electrostatic focusing forces to the ions because of the curved virtual electrode surfaces. Such experiments were performed using scintillation image detectors and probe arrays to measure the convergence of the ion beam. Tight azimuthal line foci were obtained (when the post-acceleration gap voltage was applied), in good agreement with calculations of the field line curvature. These tests provided a dramatic demonstration of virtual electrode effects.

E. Electron Sources

A critical requirement for the success of beam neutralization methods is the development of large area sources of electrons that can supply multi-kiloampere pulsed current. Steady state sources (such as thermionic sources) are clearly impractical in an application with a duty cycle 1/1,000,000. Secondary emission electrons from the walls produced by a blow-up of the head of the beam have provided neutralization in first generation experiments. This is not extrapolatable to multi-gap systems. We have been investigating the use of surface sparks to produce dense plasmas localized at the drift tube walls to act as a zero work function source of electrons. These require only a small energy investment (a few joules per sq. m). We have recently had success towards development of a practical source. It uses a unique method of capacitive ballasting to produce many sparks (possibly thousands) with one voltage input. The plasma is in good contact with a grounded metal screen. The unit can be shaped and is only 2 mm thick, so it can be easily mounted inside the accelerator drift tubes.

IV. Pulselac C

It has recently been decided that we should proceed with the construction of a demonstration fusion accelerator based on neutralization principles. This device, Pulselac C, will be a 4 MeV linear induction accelerator designed to accelerate 5 kA of ions in a 50 ns pulselength. Total beam output energy will be 1 kJ. Design parameters of the accelerator are listed in Table 1. The goal is to build an accelerator with technology within the range of existing devices. It will have enough gaps to study system problems of intense ion beam transport. The curvature of the gap magnetic field lines will be externally adjustable to allow investigation of transverse focusing. The pulselines will store four times the energy required by the gaps. This will allow investigation of the stabilization of longitudinal velocity space instabilities and permit the application of time-ramped voltages using passive shunt circuits for beam bunching experiments. The Pulselac C accelerator will be a test bed for neutralized transport; it will be built on a scale that will allow it to either succeed or fail unambiguously. A scale drawing of an acceleration gap and core module is shown in Fig. 1 to demonstrate the compatibility of the neutralized transport system and inductive LINAC technology.

References

1. S. Humphries, Jr. G. W. Kuswa, C. W. Mendel, and J. W. Poukey, IEEE Trans. Nucl. Sci. NS-26, 4220 (1979).
2. S. Humphries, Jr., G. Yonas, and J. W. Poukey, in COLLECTIVE METHODS OF ACCELERATION, edited by N. Rostoker and M. Reiser (Harwood Academic Publishers, New York, 1979), 595.
3. S. Humphries, Jr., in Proc. of the Heavy Ion Fusion Workshop, Argonne National Laboratory, edited by R. C. Arnold (ANL-79-41, 1978), 93.
4. S. Humphries, Jr., J. Appl. Phys. 49, 501 (1978).
5. S. Humphries, Jr., in Proc. of the 2nd Int'l Topical Conf. on High Power Electron and Ion Beam Research and Technology, edited by J. A. Nation and R. N. Sudan (Laboratory of Plasma Studies, Cornell University, 1977), 83.
6. S. Humphries, Jr. and J. W. Poukey, Particle Accelerators 10, 71 (1979).
7. J. W. Poukey and S. Humphries, Jr., Appl. Phys. Lett 33, 122 (1978).
8. S. Humphries, Jr. J. R. Freeman, J. Greenly, G. W. Kuswa, C. W. Mendel, J. W. Poukey and D. W. Woodall (Sandia Laboratories Internal Report SAND79-1673), condensed version to be published, J. Appl. Phys.

TABLE I. Pulselac C Parameters

Accelerator length	6 m
Number of gaps	16
Voltage per gap	250 kV
Beam current	5 kA
Pulseline impedance	12.5 ohm
Pulselength	50 ns
Gap efficiency	25%
Drift tube cross sectional area	200 cm sq.
Average gap magnetic field	4 kG
Longitudinal potential gradient	0.67 MV/m
Injector voltage	100 kV
Injector pulselength	1 microsecond
Ion species	C+
Beam bunched pulselength	20 ns
Beam output power (bunched)	50 GW
Beam output divergence	Less than 0.5 degree
Focused beam area	1 cm sq.
Total beam energy	1 kJ
Repetition rate	1 ppm

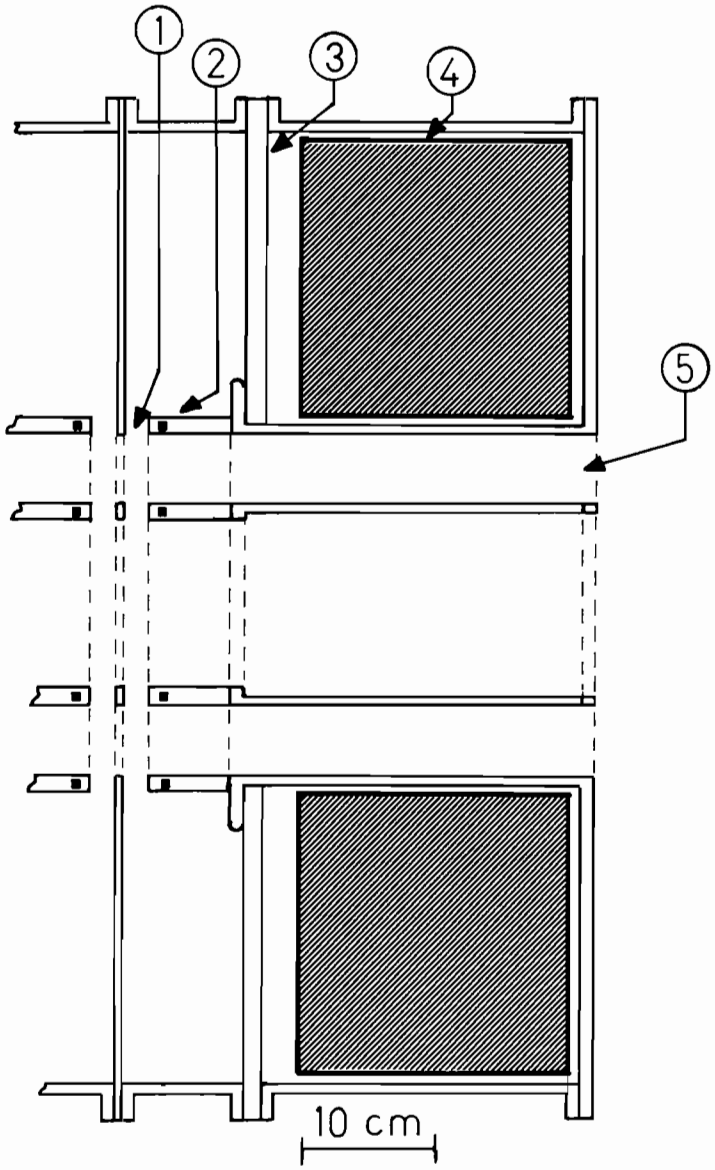

Figure 1. Pulselac C Acceleration Module. 1) Magnetically insulated acceleration gap. 2) Coaxial drift tube structure with magnetic coils. 3) Vacuum insulator. 4) Ferrite core (250 kV, 50 nsec). 5) Annular drift region.

RF LINAC APPROACH TO HEAVY ION FUSION*

D. A. Swenson

Accelerator Technology Division
Los Alamos Scientific Laboratory
Los Alamos, NM 87545

ABSTRACT

The necessary properties of "funneling" particle beams from multiple accelerators into combined beams having higher current are outlined, and methods are proposed which maximize the efficiency of this process. A heavy ion fusion driver system example is presented which shows the large advantages in system efficiency to be gained by proper funneling.

The rf linac, when operated at sufficiently high currents of singly-charged heavy ions in the range of 1 to 10 GeV at frequencies in the range of 100 to 400 MHz, is an efficient accelerator, where most of the power is transferred to the beam. Under these conditions, the total rf power required to accelerate a given particle to a given particle energy is essentially independent of the charge state; thus if the singly-charged heavy ion, with its low charge-to-mass ratio, is the preferred particle for reasons associated with other parts of the facility, it is quite acceptable from the rf linac point of view. Furthermore, the relatively high current reduces the required linac pulse length, causing the optimum acceleration gradient to be higher** and the optimum accelerator length to be shorter than would be the case for lower currents of similar ions.

Filling such machines, on the other hand, is a major problem, requiring a multiplicity of low-frequency linacs at the lowest energy with relatively low

---

*Work performed under the auspices of the U. S. Department of Energy.

**In low-duty applications, where the rf power sources are peak-power limited, the power-related costs are proportional to the peak power and the optimum acceleration gradient is independent of the beam current. In fixed high-duty applications, where the rf power sources are average-power limited, the power related costs are proportional to the average power, which is also proportional to the peak power, and the optimum accelerator gradient is independent of the beam current. In fixed average-current applications, the duty factor is inversely proportional to the peak beam current, and in those cases which are average-power limited, the optimum acceleration gradient is proportional to the square root of the peak beam current.

currents, followed by smaller numbers of linacs at higher energies with higher frequencies and currents, culminating in a single linac at the highest frequency and current for the major portion of the facility.

Let us define "funneling" as the interlaced filling of one linac of frequency Nf from N linacs of frequency f. For a number of reasons, the most interesting value of N is 2. For N = 2, funneling implies a doubling of the frequency whenever the space charge limits of the structure permit and a combination of the beams from two linacs at the old frequency into each linac at the new frequency. In principle, it is possible to accomplish the funneling with no increase in the transverse phase space and a simple addition of the longitudinal phases from the two linacs using an rf deflector.

Funneling is an important concept. It implies the filling of every bucket at each new frequency, thereby realizing the full space charge capabilities of each portion of the linac. It maximizes the frequency and consequently minimizes the size and power consumption of each portion of the structure. Empty buckets represent a valuable resource that must not be wasted. They represent prime space in which additional beam can be accelerated with no additional hardware, real estate, or pulse length, and with only the additional power required for the additional beam. The additional beam current serves to reduce the linac pulse length and to reduce the severe requirements on the final bunching system involving multiple accumulator rings and linear induction bunchers.

The concept of funneling was invented at the 1977 Heavy Ion Fusion Workshop. Since then, neither the ANL nor BNL designs have fully exploited this concept, having only one-eighth to one-twelfth of the buckets filled, and particle currents that are factors of 10 to 100 below what they could be. This causes the pulse lengths to be longer, the optimum gradients to be lower, and the linac lengths to be longer in those designs than in the designs which fully exploit funneling.

Strict funneling implies a constant ratio between the beam current and the frequency of each portion of the linac. The relative difficulty of funneling depends on the ratio of the physical separation of the beams to their particle wavelength ($\beta\lambda$). The larger this ratio, the more difficult the funneling. At the lowest betas, it is attractive to consider arrays of linac channels within a common linac structure, where the beam-to-beam spacings can be quite small.

The radio frequency quadrupole (RFQ) linac structure promises to be the best low-beta linac structure, offering high capture of very low energy beams

and acceleration with a minimal emittance growth.* Furthermore, the RFQ lends itself to array-like configurations as shown in Fig. 1, which can be driven by external resonant circuits in the same manner as Wideröe linacs. By staggering the geometrical modulations that produce the accelerating voltages, the beams can be made to interlace as required by funneling, without the necessity for introducing varying lengths into the funneling transport lines.

Candidates for the second linac structure in the system are an RFQ linac, an electrostatically-focused π, 3π Wideröe linac, and a magnetically-focused π, 3π Wideröe linac. At a few MeV, the electrostatically-focused π, 3π Wideröe linac seems to be the best choice, because the RFQ efficiency is dropping, while the required magnet strengths are still impractical.

If the original array of RFQ linacs involves more than two interlaced beam channels, the second structure must also accommodate an array of more than one interlaced channel. It should be noted that multiple-holed drift tubes in a Wideröe or Alvarez configuration do not satisfy the interlaced requirements of funneling. Figure 2 suggests the basic features of a double-barreled, electrostatically-focused π, 3π Wideröe linac which does satisfy this requirement and would seem to have some attractive rf and mechanical properties. This idea could be extended to a larger number of beams at the cost of further complication.

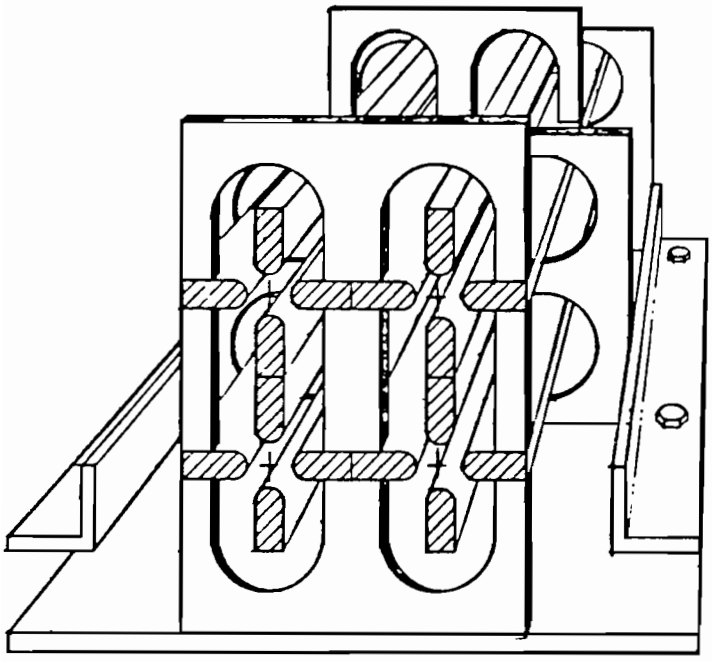

Fig. 1.
Array of Four RFQ Channels

A multiple-channel, magnetically-focused π, 3π Wideröe linac could be based on the same idea, where the magnetic quadrupoles could have an outer diameter equal to the channel separation (not an undue constraint). In this case, it would seem preferable to limit the vacuum to the rf accelerating regions and the interior of a beam

*It is the best transition that we know of between a dc injector and an rf linac.

tube passing through the magnetic quadrupoles. This would leave the magnetic quadrupoles completely exposed on top of the structure to facilitate alignment and services.

We realize that requirements on brightness have a strong influence on how close we can operate to the space charge limit. However, the important properties of funneling and the impact outlined above on structure selection are equally valid for lower currents. We are proceeding with more detailed design of a facility configuration using these ideas; in the following paragraphs, we outline a preliminary, idealized configuration which illustrates the potential advantages of full funneling.

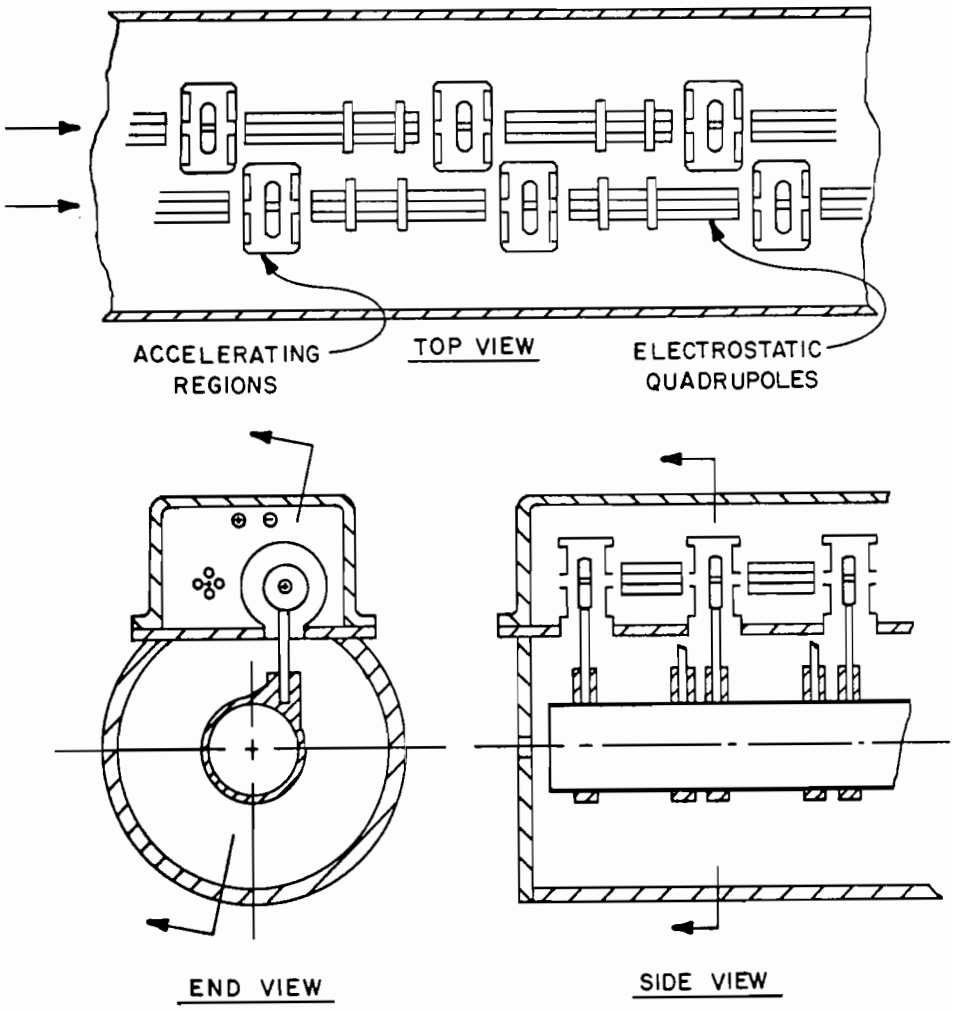

Fig. 2.
Double-barreled, electrostatically focused, π, 3π Wideröe linac.

We believe that the space-charge limit for Xe^{+1} in a magnetically-focused rf linac is approximately one ampere at 1 GeV and 100 MHz, based on a uniformly-filled, three-dimensional ellipsoidal model and a smooth approximation of the transverse focusing forces.[1] This limit increases with energy and decreases with frequency, such that at 3 GeV and 400 MHz the limit is also approximately one ampere. Thus for the major portion of a 10 GeV heavy ion fusion facility based on the rf linac approach, one can accommodate currents in the order of an ampere at frequencies as high as 400 MHz. If one shoots for 800 mA at 400 MHz in the major portion of the facility, one is obliged to start out with 32 linac channels, each carrying 25 mA at 12.5 MHz followed by five stages of funneling.

A schedule of linac structures which, if combined through funneling, would produce an 800 mA beam of Xe^{+1} at 10 GeV is given in Table I. Each structure, after the initial RFQ section, is close to its space charge limit at the low energy end and significantly below its space charge limit at the high energy

TABLE I

SCHEDULE OF LINAC STRUCTURES

Structure	1	2	3	4	5	6
Type	RFQ	EFW	MFW	MFA	MFA	MFA
Number	32	16	8	4	2	1
Current (mA)	25	50	100	200	400	800
Frequency (MHz)	12.5	25	50	100	200	400
Energy in (MeV)	0.2	6	28	190	750	3000
Beta in	0.002	0.010	0.021	0.056	0.110	0.217
Beta*Lambda (m)	0.043	0.118	0.128	0.166	0.165	0.163
Energy out (MeV)	6	28	190	750	3000	10000
Length (m)	21	26	125	373	1125	1750
Total length (m)						3420

RFQ = Radio frequency quadrupole linac.
EFW = Electrostatically-focused Wideröe linac.
MFW = Magnetically-focused Wideröe linac.
MFA = Magnetically-focused Alvarez linac.

end. Detailed studies of the beam dynamics in these structures have not been made, nor have studies been made of the problems associated with funneling.

The transition energies in Table I are based on a ratio of the space charge force to the focusing force of 0.5, which corresponds to an allowed tune depression of about 30%.[1] Within the RFQ, this limit is evaluated at the end of a bunching subsection. For all other cases, these limits apply at the input or transition energy to each new structure. If we decide, because of emittance growth or current loss, to operate further from the space charge limit, we can delay the transitions to somewhat higher energies where the limiting currents are higher.

The total length of the linac is only 3.4 km, which is quite short compared to previous designs. This is the result of the relatively high acceleration gradients in the latter portions of the facility, namely, 1.5 MeV/m at 100 MHz, 2.0 MeV/m at 200 MHz, and 4.0 MeV/m at 400 MHz. These gradients at these frequencies are known to be technically feasible, and they can be shown to be economically attractive because of the high frequencies and high peak beam currents that result from funneling.

In our present stage of thinking, we would propose to configure the 32 channels of the first structure as eight independent arrays of four channels as shown in Fig. 1, the 16 channels of the second structure as eight independent double-barreled structures as shown in Fig. 2, and the 8 channels of the third structure as 8 conventional 50 MHz Wideröe structures. As such, the early stages of the facility, those with the highest multiplicities, would take the form of eight identical assemblies, each accommodating a total current of 100 mA. This configuration lends itself to the possibility of developing, prototyping and testing one-eighth of the total configuration in a staged development of the total facility.

ACKNOWLEDGMENTS

The author wishes to acknowledge many useful discussions on these topics with his colleagues, R. H. Stokes, T. P. Wangler, K. R. Crandall, and R. A. Jameson.

REFERENCE

1. "Space Charge Limits in Linacs," T. P. Wangler, to be published.

STABILITY OF LONGITUDINAL MOTION IN INTENSE ION BEAMS

David Neuffer
Fermi National Accelerator Laboratory

Inertial confinement fusion using high energy heavy ion beams requires focussing of the igniting ion beams in longitudinal, as well as transverse, space at the pellet target. The focussing requirements set limits on the size of the beam emittances at the target, and obtaining sufficiently small emittances at the target requires sufficient stability in beam transport and acceleration from source to target, and an analysis of that stability is necessary for heavy ion fusion (HIF) accelerator design. Theoretical analysis is necessary since practical accelerator experience with high intensity non-relativistic ion beams has been limited. This analysis is particularly important for the case of a heavy ion induction linac, since previous induction linacs have been electron accelerators, and the highly relativistic electrons have negligible longitudinal motion. In this paper we present some results of our analysis of the of the stability of longitudinal motion.

I. Equations of Motion

The equations of longitudinal motion which we use are obtained by solution of Maxwell's equations with simplifying assumptions. We assume that the transverse (x-y) and longitudinal (z) motions of particles in the beam are completely decoupled with the beam length much greater than the beam radius. We choose the longitudinal distance from the center of the bunch z and the position of the center of the bunch s as the dependent and independent variables. We will assume the motion is non-relativistic and that the center of the beam bunch is not accelerating but moves with constant speed βc. If the beam pipe is perfectly conducting, we find the following equation of motion (in MKS units):

$$\frac{d^2z}{ds^2} \cong z'' = -\frac{q^2e^2}{M\beta^2c^2}\,\frac{g}{4\pi\varepsilon_0}\,\frac{d\lambda}{da} + \frac{qe}{M\beta^2c^2}\,E_z \qquad (1)$$

where e is the proton charge, q is the ion charge state, M is the ion mass, λ is the number of ions per unit length, and g is a geometric factor of order unity. For the particular case of an ion at the center of a constant transverse density round beam of radius a inside a round pipe of radius b, $g = 1 + 2\,\ell n\,(b/a)$. We assume that transverse variations simply produce some average g, which we treat as constant. In equation 1, we have added an external bunching field E_z to the space charge self-field.

Analysis of design studies of HIF accelerators indicates that the assumption of perfectly conducting walls may not be adequate. If we assume a resistive coupling per meter R', a term

$$\left(\frac{d^2z}{ds^2}\right)_{resistive} = -\frac{q^2e^2}{MBc}\,\lambda\,R' \qquad (2)$$

must be added to equation 1. In sections II and III we will assume that the walls are perfectly conducting (R' = 0) and in later sections we will consider the effects of non-zero R'.

II. Envelope Equation for Longitudinal Motion

Unperturbed longitudinal motion of a beam bunch through a transport system can be calculated using the envelope equation derived before.[1] This envelope equation applies to a bunch transported through a system with linear bunching fields; that is

$$E_z(s,z) = \frac{dE}{dz}(s)\cdot z \qquad (3)$$

The equation of motion (1) is rewritten as:

$$z'' = \frac{qe}{M\beta^2c^2}\,\frac{dE(s)}{dz}\,z - \frac{q^2e^2}{M\beta^2c^2}\,\frac{g}{(4\pi\varepsilon_0)}\,\frac{\partial\lambda}{\partial z} \qquad (4)'$$

$$\equiv -K(s)\,z - A\,\frac{\partial\lambda}{\partial z}$$

The particle distribution which is a solution to the Vlasov equation with this equation of motion is:

$$f(z,\ z',\ s) = \frac{3N}{2\pi\epsilon_L}\sqrt{1 - \frac{z^2}{z_o^2} - \frac{z_o'^2}{\epsilon_L^2}\left(z' - \frac{z_o'}{z_o}z\right)^2} \qquad (5)$$

defined wherever the square root is real (f = 0 otherwise), and where N is the total number of ions in the bunch, ϵ_L is the longitudinal emittance, and z_o is the envelope amplitude. This distribution has a parabolic particle density:

$$\lambda(z,\ s) = \int f(z,\ z's)dz' = \frac{3N}{4z_o}\left(1 - \frac{z^2}{z_o^2}\right) \qquad (6)$$

and z_o is a solution of the envelope equation:

$$z_o'' = \frac{d^2z_o}{ds^2} = \frac{\epsilon_L^2}{z_o^3} + \frac{3}{2}\frac{AN}{z_o^2} - K(s)\ z_o \qquad (7)$$

where the initial conditions (z_o (s=0, z_o(s=0)) may be chosen arbitrarily.

This solution can be, and has been, used to check computer programs which integrate the Vlasov equation numerically, such as the code of Neil, Buchanan, and Cooper.[2]

An analysis of perturbations of this distribution can also be used to evaluate longitudinal transport stability analytically.

III. Stability of Space Charge Perturbations

Following techniques previously developed by L. Smith and others for analyzing transverse stability,[3, 4, 5] and analysis of the stability of space charge perturbations of the distribution of section II has been presented and in this section we summarize the results of the analysis.[6]

We first consider the case of the stationary distribution, the particular solution of equations 4-7 in which K(s) is constant, and z_o is chosen such that $z_o''(0) = z_o'(0) = 0$. Our unperturbed distribution is (v ≡ z'):

$$f_o(z,v) = \frac{3N}{2\pi v_o z_o}\sqrt{1 - \frac{z^2}{z_o^2} - \left(\frac{v}{v_o}\right)^2} \qquad (8)$$

Stability is determined by adding a small perturbation f_p (z, v, s) to f_o (z, v) and solving the linearized Vlasov equation for f_p (z, v, s) and λ_p (z, s) with our solutions of the form

$$f_p(z,\ v,\ s) = f_n(z,\ v)\ e^{-i\omega_n s}$$

$$\text{and}\quad \lambda_p(z,\ s) = \lambda_n(z)e^{-i\omega_n s} = \int f_n(z,v)\ dv\ e^{-i\omega_n s} \qquad (9)$$

Instability exists where Im(ω) ≠ 0. As reported in reference 6, the solutions have the following properties:

$$\lambda_n(z) \propto P_n\left(\frac{z}{z_o}\right) \quad \text{(Legendre polynomials)}$$

and ω_n is a solution of

$$\frac{\nu^2 + \omega p^2}{\omega_n^2} = \omega_p^2 \sum_{m=-n}^{n} \frac{1}{4^n}\binom{2m}{m}\binom{2n-m}{n-m} \times \frac{1}{\omega^2 n - ((n-2m)\nu)^2} \qquad (10)$$

with $\omega_p^2 \equiv \frac{3}{2}\frac{AN}{z_o^3}$, $\nu^2 \equiv K$.

It can be shown that all ω_n which are solutions of (10) are real, which indicates that small space charge perturbations are stable, unlike the transverse case.[4]

The analysis has been extended to the case where K(s) is periodic, and it is found that instabilities can exists where the eigenfrequency of the normal mode ω_n and the period of K(s) are near resonance.

The largest such resonances are:

1. A second order resonance (n = 2) which can occur if the phase shift of individual particle longitudinal motion over a period of K(s) is between 90° and 104° at zero current. This has a growth rate of ~ 1.1 per period.

2. A fourth order resonance (n = 4) which can occur for longitudinal phase shifts between 45° and 57° per period. The growth rate is ~ 1.03.

For most accelerators considered to date, such as the HIF induction linac, the longitudinal phase shift per period of structure is quite small, so periodic space charge instabilities can occur only in very high order n and the analysis indicates that these instabilities become vanishingly small. The only possible exception proposed to date would be a bunching ring with a very large ($\tilde{>}$ 30°) longitudinal phase shift per turn at peak field. Such bunching rings should be designed to avoid the largest low order resonances.

IV. Resistive Wall Instability

Faltens[7] has suggested that particle motion, particularly in an induction linac, may show significant resistive coupling. In that case the equations of motion are modified as described in section 1. The self forces are given by

$$z'' = -\frac{q^2e^2}{M\beta^2c^2}\frac{g}{4\pi\epsilon_o}\frac{\partial\lambda}{\partial z} - \frac{q^2e^2R'}{M\beta c}\lambda \equiv -A\frac{\partial\lambda}{\partial z} - B\lambda$$

The value of R' depends upon the current, acceleration and efficiency requirements of the induction linac; Faltens[8] suggests that for HIF it will be of the order of 100 Ω/m.

To show the effects of resistive coupling we use an approximate analysis previously presented by L. Smith.[9] We start with an unperturbed distribution with constant density in z and with a step function in z':

$$f_o(z, z') = \frac{N'}{2\Delta}\Big(S(z' + \Delta) - S(z' - \Delta)\Big)$$

and consider perturbing waves of the form

$$f_1(z, z's) = f_1(z')\, e^{i(kz-\omega s)} \qquad (11)$$

We then solve the linearized Vlasov equation to find ω(k).

$$-i(\omega - kz')\, f_1(z') + \frac{\partial f_o}{\partial z}(-iAk - B)\int f_1(z')dz' = 0 \qquad (12)$$

The result is: $\omega^2 = k^2\Delta^2 + k^2AN' - ikBN'$

or

$$\omega^2 = k^2\Delta^2 + k^2\frac{N'q^2e^2}{M(\beta c)^2}\frac{g}{4\pi\epsilon_o} - ik\frac{q^2e^2}{M\beta c}N'R' \qquad (13)$$

Instability can occur since $\mathrm{Im}(\omega) \neq 0$.

With parameters suitable for fusion induction linacs, the waves of equations 11-13 show some interesting characteristics:

1. The requirement of small energy spread for final focussing sets Δ quite small, so that in equation 13 the velocity dependent term $k^2\Delta^2$ is negligible to a first approximation. As a corollary to this, the wave velocity ($\mathrm{Re}(\omega/k)$) of disturbances in the bunch is much greater than individual particle velocities.

2. The space charge term of equation (13) k^2AN' is usually larger than the resistive term $ikBN'$ in absolute value, if $R' < 200\ \Omega/m$. With this approximation, we have $\mathrm{Re}(\omega) \cong \pm\sqrt{k^2AN'}$ and we find that the wave velocity ($\mathrm{Re}(\omega/k)$) is independent of k, so that propagating wave packets do not disperse but travel together coherently.

3. Also with space charge dominant we have the relation

$$\mathrm{Im}(\omega) \cong \frac{1}{2}\frac{kBN'}{|k|\sqrt{AN'}} \cong -\frac{k}{|k|}\frac{1}{2}qeR'\sqrt{\frac{4\pi\epsilon_o N'}{gM}}$$

so that the magnitude of the growth parameter is independent of k. Waves change in amplitude as $e^{\mathrm{Im}(\omega)s}$ and the sign of

$\mathrm{Im}(\omega)$ is correlated with $\mathrm{Re}(\omega/k)$ so that for $\mathrm{Re}(\omega/k) > 0$ ("fast" wave) we have $\mathrm{Im}(\omega) > 0$ and the wave decays, while with $\mathrm{Re}(\omega/k) < 0$ ("slow" wave) we have $\mathrm{Im}(\omega) > 0$ and the wave grows.

Typical parameters for HIF can be substituted into equation (13) to find sample values of $\mathrm{Re}(\omega/k)$ and $\mathrm{Im}(\omega)$. For example, with $R' = 100\ \Omega/m$, $N' = 3 \times 10^{13}$ ions/m., $q = 4$, $g = 2$, $M = 238\ m_p$, and $\beta = .33$, we find

$$1)\quad \mathrm{Re}\left(\frac{\omega}{k}\right) = 7.4 \times 10^{-3}$$
$$2)\quad \left|\mathrm{Im}(\omega)\right| = 2 \times 10^{-3}\ m^{-1} = (500\ m)^{-1} \qquad (14)$$

The growth distance is about 500 m., which is less than the total length of the HIF induction linac (a few km.), but it is a substantial fraction of it.

This wave motion in a beam bunch can be simulated numerically. In figures 1 we show wave propagation in a perturbed beam bunch, calculated using the program of Neil, Buchanan and Cooper, which numerically integrates the longitudinal Vlasov equation. In this case an initial disturbance at the center of the bunch splits into forward-going "fast" and backward "slow" wave packets which decay and grow respectively. The behavior agrees closely with equation (13) and the discussion above.

V. Effect of the Resistive Coupling on Beam Stability

In the previous section, we demonstrated that a resistive coupling can lead to growth of perturbations in a beam bunch with HIF parameters. We need to determine the amount of growth by resistive coupling which can be permitted without endangering HIF performance. To estimate this, we must include the effects of the finite bunch size, which means that a propagating disturbance will reach the end of the bunch in a finite time.

A naive expectation is that a growing "slow" wave will reach the end of the bunch, be immediately reflected to a decaying "fast" wave by the external bunching field, and therefore produce no net instability. With this expectation, we can set a limit on the allowable growth by requiring that an individual wave packet not grow by more than some factor F in traversing the bunch length L_B. This requirement can be written as:

$$G = \left|\mathrm{Im}(\omega) \cdot \frac{L_B}{\mathrm{Re}(\omega/k)}\right| \cong \frac{4\pi\varepsilon_0}{2g}\,\beta c R'\, L_B < \ell n\,|F| \qquad (14)$$

For the sample case of section 4, with $L_B = 10$ m., we have $G \cong 2.5$ or $F > 12$. This amount of growth may be tolerable provided that initial wave packet perturbations are limited to a few per cent.

Numerical simulation seems to indicate that longitudinal motion does not fit this naive picture. To observe wave packet reflection at the bunch end, we calculate a case with $R' = 0$ so that waves neither grow nor decay. In this example (shown in figures 2) the disturbances propagate to the bunch ends from the center in about 800 m., then remain localized at the ends for 800 m. while particle motions reverse, and then propagate back toward the center. Wave packet reflection is substantially delayed.

The same type of delayed reflection exists in numerical simulation with $R' \neq 0$. However substantial wave packet distortion occurs on reflection and this distortion is not fully understood. Future analysis will attempt to understand this reflection distortion, and to determine its importance in describing the stability of longitudinal transport.

ACKNOWLEDGEMENTS

We thank A. Faltens and L. Smith for many useful conversations on this problem. We also thank E. Close for programming and graphics assistance.

REFERENCES

1. D. Neuffer, IEEE Trans. on Nuclear Science, NS-26, 3031 (1979).
2. V.K. Neil, H.L. Buchanan, and R.K. Cooper, Particle Accelerators, 9, 207 (1979).
3. L. Smith, S. Chattopadhyay, I. Hofmann, and L.J. Laslett, "Stability of K.-V. Distribution in Long Periodic Systems", LBL HI-FAN-13, -14, and -15 (1979).
4. R.L. Gluckstern, Proceedings of the NAL Linear Accelerator Conference, September 1970, 823 (1971).
5. F.J. Sacherer, Ph.D Thesis, University of California, Berkeley, UCRL-18454 (1968).
6. D. Neuffer, to be published in Particle Accelerators (1980).
7. A. Faltens, 1979 HIF Workshop, Berkeley, California.
8. A. Faltens, private communication (1979).
9. L. Smith, unpublished communication (1974).

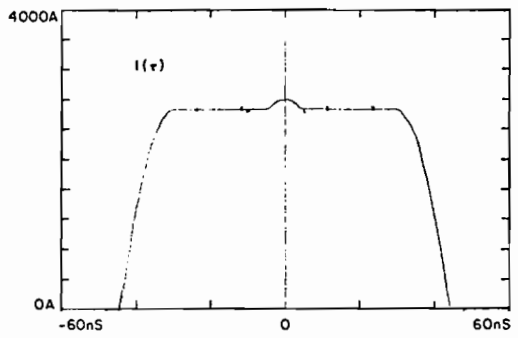

1A : S = 0m.

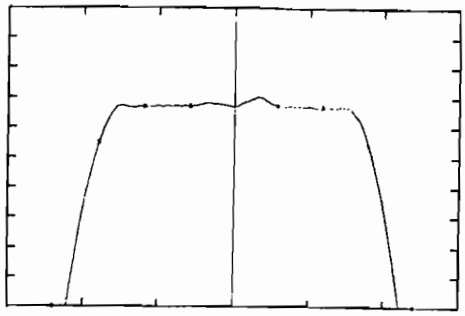

1B : S = 100m.

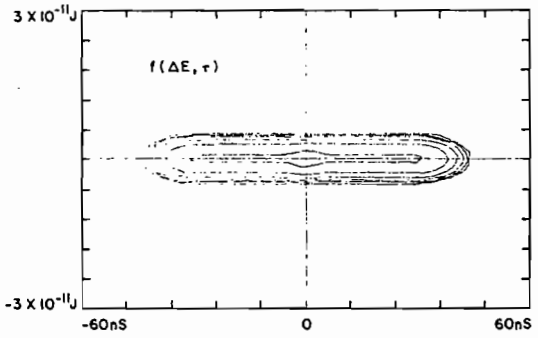

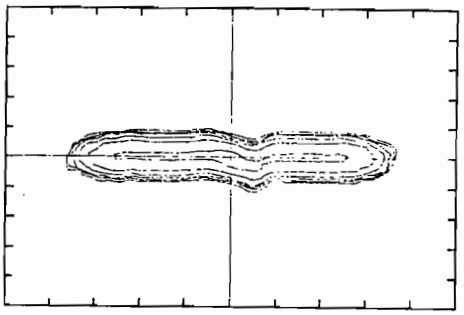

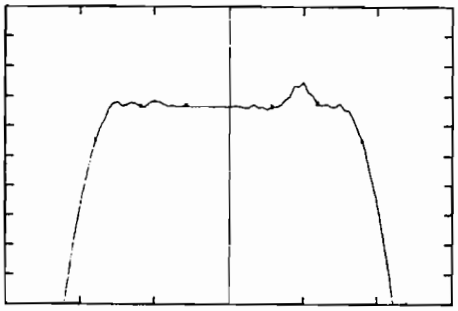

1C : S = 300m.

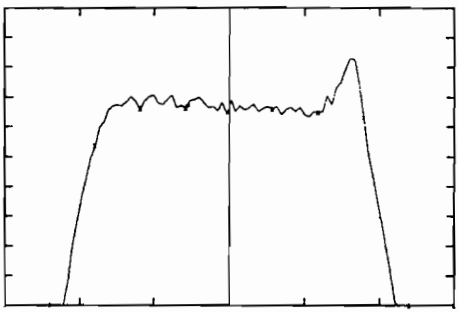

1D : S = 500m.

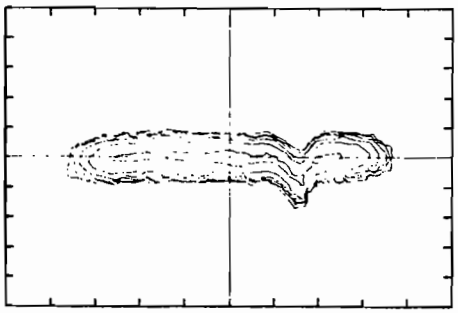

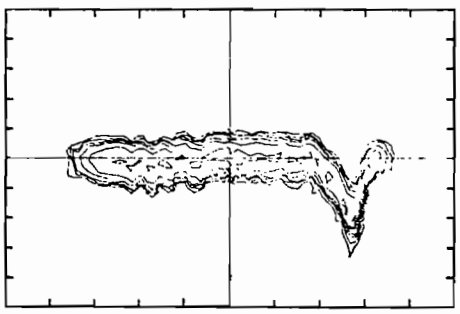

1:A-D. Wave propagation in a perturbed beam bunch. In this case we have R' = 200 Ω/m., N'_{max} = 3 x 10^{13} ions/m., q = 4, g = 2, M = 238 m_p, and β = .35. An initial disturbance shown in A (s = 0 m.) separates into "fast" and "slow" waves at B (s = 100 m.) with the "fast" wave rapidly decaying and the "slow" wave growing at C (s = 300 m.). At D (s = 500 m.) the waves have reached the ends of the bunch.

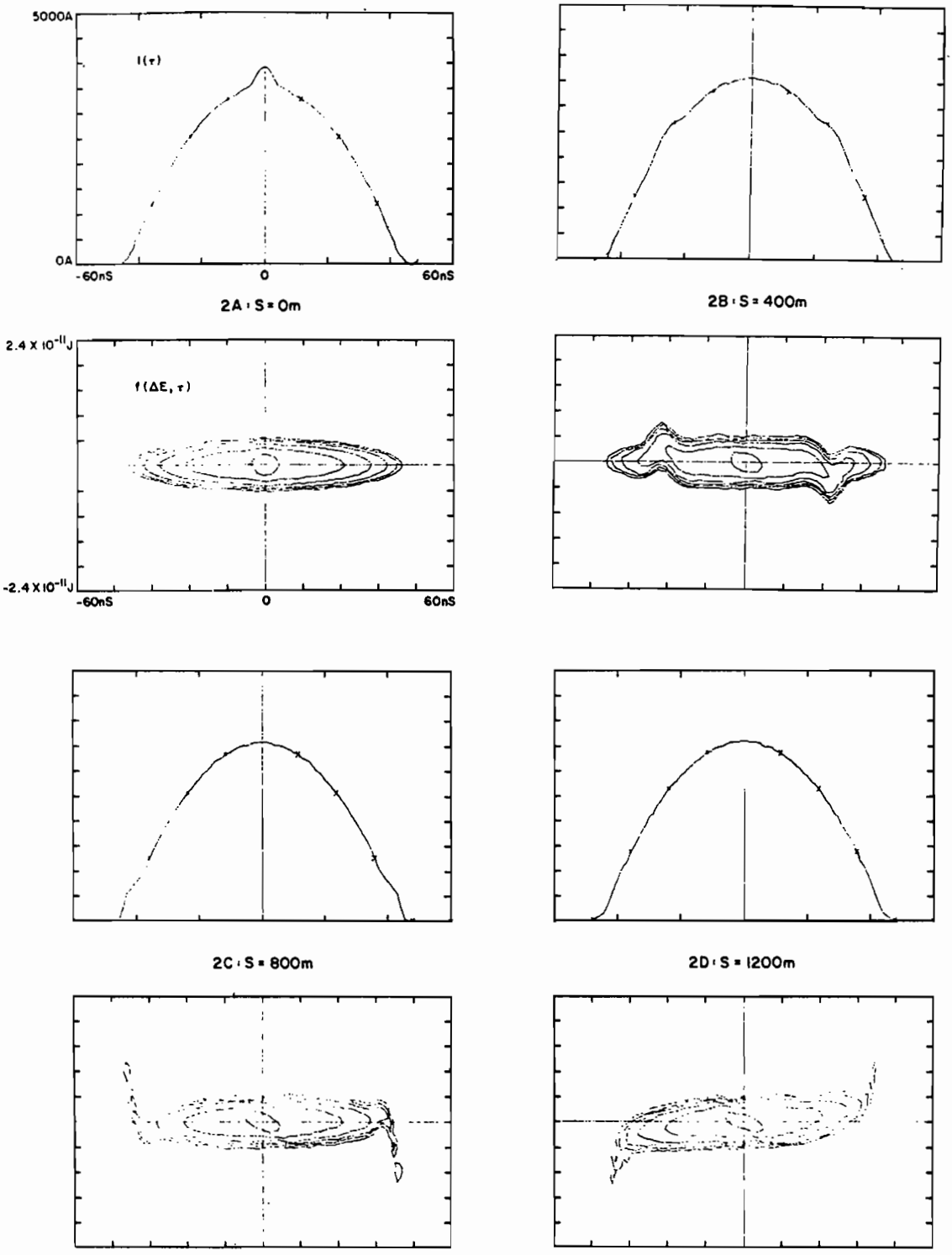

2:A-F Wave propagation and reflection with R' = 0. The other parameters (N', q, g, M, β) are the same as in Figures 1, A-D, except the beam bunch is parabolic. In this case the "fast" and "slow" waves travel to the ends of the bunch from s = 0 m., to s = 800 m. (A, B, C). From s = 800 to s = 1600 (C, D, E) the beam bunch reflects the distrubance. The reflected waves (reversed in sign and direction) appear clearly in figure F (s = 2000 m.). Reflection is not instantaneous in any usual approximation.

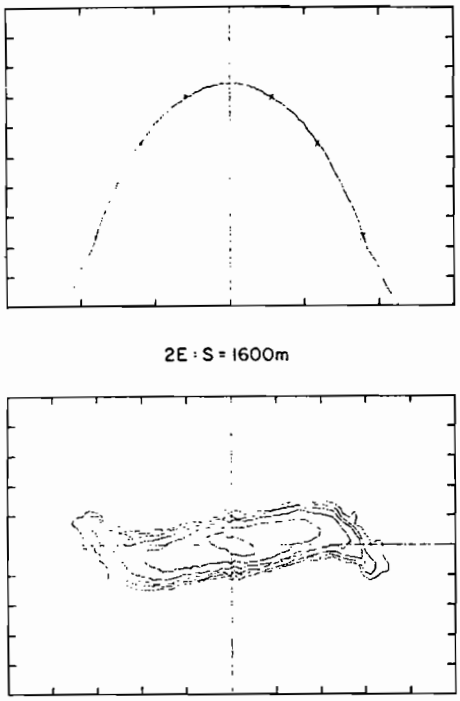

2E : S = 1600m

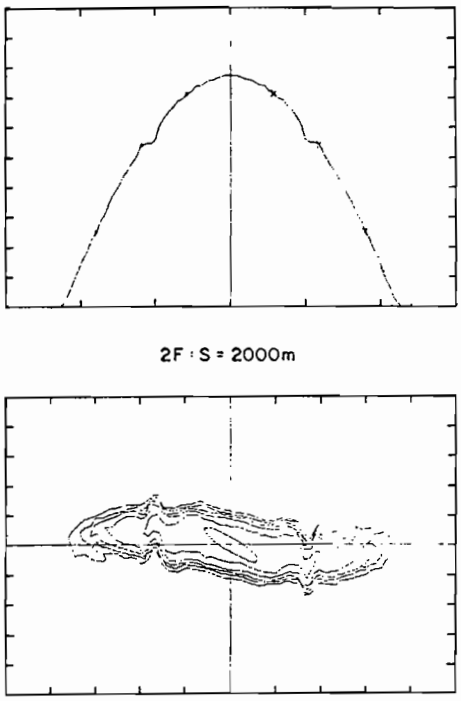

2F : S = 2000m

Each of these figures (1(A–D), 2(A–F)) contains two plots. The upper plots graph the current I as a function of position τ, where $\tau = -\beta cz$. The lower plots are contour plots of the distribution function $f(\Delta E, \tau)$ which is proportional to $f(z', z)$. In both plots the horizontal axis is position τ.

STORAGE RING GROUP SUMMARY

N. Marshall King
Rutherford Laboratory

Storage Ring Group: R. Burke, Y. Cho, M. Cornacchia, E. Courant†, M. Foss, K. Johnsen, L. Jones, T. Katayama, N.M. King*, J. Le Duff, J.R. Maidment, R. Martin, R. Mobley, D. Möhl, A. Noda, G. Plass, G.H. Rees, L.C. Teng.††

(*Chairman, †Co-Chairman, Week 2, ††Co-Chairman, Week 1).

1. INTRODUCTION

The Storage Ring Group set out to identify and pursue salient problems in accelerator physics for heavy ion fusion, divorced from any particular reference design concept. However, it became apparent that some basic parameter framework was required to correlate the different study topics.

Accordingly, three sets of skeleton system data were developed, starting from target estimates provided by R. Bangerter[1], repeated here as Table I along with some immediate implications on accelerated beam requirements.

Further definition of storage ring parameters involved feedback from the work in progress in the RF Linac Group[2] and the Final Beam Transport Group.[3]

As the Workshop progressed, ring parameters were modified and updated: Consequently, the accompanying papers on individual topics will be found to refer to slightly varied parameters, according to the stage at which the different problems were tackled.

1.1 Effects of Latest Target Data

In contrast to earlier HIF Workshops, the latest target data referred to lower kinetic energies exemplified by 5 GeV U^+ ions for 1 MJ

TABLE I
SAMPLE TARGET DATA SETS[1], U^{+1} IONS,
AND IMPLICATIONS ON ACCELERATED BEAM PARAMETERS

CASE		A	B	C
Beam Stored Energy	E(MJ)	1	3	10
Beam Kinetic Energy	T(GeV)	5	10	10
Total No. of Ions	N($\times 10^{15}$)	1.25	1.875	6.25
Pulse Time	t(ns)	20	40	70
Pulse Time at Peak Power	t_p(ns)	6	16	20
Pulse Length at Target	ℓ_b(m)	1.25	3.49	6.10
Power in Pulse Peak	P_p(TW)	100	150	300
Beam Stored Energy in Peak	E_p(MJ)	0.6	2.4	6.0
No. of Ions in Peak	N_p($\times 10^{15}$)	0.75	1.5	3.75
Peak Current	I_p(kA)	20	15	30
Average Current in Pulse	I_{av}(kA)	10	7.5	14.3
Beam Momentum	P(GeV/c)	47.349	67.334	67.334
	γ	1.0226	1.0451	1.0451
	β	0.2089	0.2906	0.2906
	$\beta\gamma$	0.2136	0.3037	0.3037
Beam Radius at Target	r(mm)	2.0	2.5	4.0
Approx. Target Gain	g	8	30	120

stored energy in the beams (Case A), and 10 GeV U^+ ions for either 3 MJ (Case B) or 10 MJ (Case C) stored energy. For the great majority of storage ring problems, Case A was identified to be extremely difficult, due to space charge effects at the low kinetic energy. Most of the later detailed work was carried out for Case B, where the problems already looked tractable.

Another striking aspect of the target data was the much more conservative estimate of target gain than heretofore: the basis for a heavy ion fusion demonstration plant now seemed to be above 1 MJ, and the 3 MJ case looked much more appropriate in that context.

On the other hand, encouraging features of the new target data concerned the larger pellet radii and longer pulse times than had been quoted previously, leading to considerable easing of the space-charge-dominated accelerator problems.

1.2 Ion Charge State

From the outset, the decision was made to consider singly-charged ions exemplified throughout the study by U^{+1}. Although higher charge states were not analyzed in detail, the space-charge problems encountered were sufficiently formidable that, as a general concensus of opinion, anything other than a very low charge state was regarded with some scepticism.

1.3 Basic Framework

The basic framework envisaged for a storage ring system involved the following features:

(i) Injection from a 'funnelled' RF linac system, starting from 16 ion sources, each providing about 20 mA. Allowing for losses in the linac system, a total linac current at injection, I_{lin} = 300 mA was taken[2].

(ii) Stacking a total of S turns into each of N_{SR} storage rings, accomplished via $\sqrt{S}$ turns into each transverse plane.[4],[5],[6] In parctice, this probably requires one or more large accummulation rings feeding into the smaller storage rings in turn.

(iii) Bunching and Bunch Compression in the storage rings to give a number of bunches 'N_{bunch}' and a compression factor 'C_{SR}' in each ring.[13],[14]

(iv) Ejection of each bunch into a separate beam line to give a total number of beams $N_b = N_{bunch} \times N_{SR}$ directed towards the target.

(v) Further Bunch Compression in the beam lines by a factor 'C_b'.

The final current reaching the target is therefore given by:

$$I = I_{lin} \cdot S \cdot C_{SR} \cdot C_b \cdot N_b . \qquad (1)$$

As storage ring bunch compression studies progressed,[13] it became clear that a factor C_{SR} greater than about 7 would be difficult to achieve, whereas the total compression factor $C_{SR} \times C_b$ needed to be about 50. Accordingly, the factor C_b = 50/7 was assumed to be accomplished in the final beam line, notionally using induction linac modules. The consequences of this latter requirement (e.g., on beam transport length and power required) were not analyzed in detail by the Storage Ring Group.

Inserting the above values for I_{lin}, C_{SR}, and C_b, the final current at the target is given by:

$$I_{kV}(kA) = 0.0147 \times S \times N_b \qquad (2)$$

A glance at Table I shows that the product $S \times N_b$ has to be in the range 500-1000 for all three cases: immediate problems were therefore to examine how space charge limits in the beam lines and storage rings would determine the product $N_b = N_{bunch} \times N_{SR}$, and how emittance dilution during stacking would limit the number of possible injected turns S.

1.4 Problems Identified and Studied

The following broad pattern of problems emerged during the course of the Study. All References given are to other papers in these Proceedings.

(i) Injection
Emittance and Momentum Spread from Linac[2]
*Multi-turn stacking in 2 Transverse Planes: Emittance Dilution[4],[5]
R.F. Stacking[6],[7]
*Beam loss on Septa[8]

(ii) Accumulation and Storage
Laslett Tune Shift
*Longitudinal and transverse microwave instabilities: thresholds and growth rates[9],[10],[6]
Beam loss and lifetime due to Ion-Ion charge exchange and ionization scattering[11],[6]
Storage Ring Parameters

(iii) Bunch Compression[13],[14]
*Compression factor attainable: RF system requirements
momentum spread
Integer and Half-Integer Resonance Crossing: Non-Linear Effects and Emittance Growth.

(iv) Extraction
Mechanism: Kickers
Possible Beam Loss

(v) Final Beam Line and Focussing onto Target
Space charge limit in beam lines
*Effective Emittance Growth due to Aberrations: Uncorrected Momentum Spread.
Power Density to First Wall
Neutron Loss Through Beam Ports.

Some of these problems were seen to be serious, particularly those marked with an asterisk, but none was identified as being insuperable for beam energies of 3 MJ or above.

2. EMITTANCE MOMENTUM SPREAD BUNCH LENGTHS

2.1. Emittance at Injection

From the work of the RF Linac Group,[2] a value of emittance at the end of the injector was given:

$$\varepsilon_{lin} = 1.5 \times 10^{-6}/\beta\gamma(m). \qquad (3)$$

(All emittances here are quoted in their un-normalized form, and without the factor π).

After stacking $\sqrt{s}$ turns in each plane, the storage ring emittance may therefore be written as:

$$\varepsilon_{SR} = 1.5 \times 10^{-6} \cdot D_{\varepsilon}(s) \cdot \sqrt{s}\ /\beta\gamma \quad (m), \qquad (4)$$

where D_{ε} is a dilution factor depending on the number of stacked turns. At the workshop, it was judged that the minimum value for D_{ε} should be 1.4, and the criterion was adopted that for $\varepsilon_{SR} = 60 \times 10^{-6}$m,

$$D_{\varepsilon} = 40\beta\gamma/\sqrt{s} > 1.4 \qquad (5)$$

Further discussions of this topic will be found in References (4) and (5), and the final allowances arrived at during the Workshop are listed in Table VII.

2.2 Emittance in Final Beam

Turning to the far end of the system, emittance at the target is determined mainly by the target radius 'r', the reaction vessel radius 'R_v' and the beam port radius 'a'. That is, the final beam line emittance is given approximately by $\varepsilon_b \approx ar/R_v$.

However, it was felt that some allowance should be made for aberrations in the beam line. For example, if there were an effective uncorrected momentum spread $(\Delta p/p)_u$ in the beam, then since all of the beam should hit the target,

$$\varepsilon_b \simeq a[r - a(\Delta p/p)_u]/R_v = a\, r_{eff}/R_v \qquad (6)$$

That is, the on-momentum component of the beam should be focussed on to a smaller target and radius, r_{eff}, leaving $a(\Delta p/p)_u$ for the chromatic effect. The criterion adopted was that $(\Delta p/p)_u = 2 \times 10^{-3}$ was a reasonable assessment for a beam whose total $(\Delta p/p)$ was $\pm 10^{-2}$, so that with $a = 0.15$ m, $r_{eff} = r - 0.3$ mm.

On subsequent reflection, this may only be one of several allowance that should be made, and more work is required on the final focussing problem.

At one point in the study, limitations on the choice of 'R_v' and 'a' imposed by power density deposition at the first wall, and by constraints on the neutron flux through the beam ports, were considered. However, it was felt that insufficient information was available about future improvements in reaction vessel design, and that uncertainties about the degree of conservatism in the gain estimates made it difficult to form any worthwhile criteria on these topics. The final parameters adopted are summarized in Table II.

2.3 Emittance in Storage Rings

As will be seen from the last line of Table II, a factor 1.2 effective dilution was allowed between storage ring and beam line, to take account of mismatch due to non-linear effects after bunch compression.[13] This factor was chosen rather arbitrarily and more work is required to confirm or modify it. The resulting value of $\varepsilon_{SR} = 60 \times 10^{-6}$m, consistent with current ring design experience, was selected for all three cases.

2.4 Momentum Spread

The value of $(\Delta p/p)$ at injection, provided by the RF Linac Group,[2], was taken to be $\pm 2 \times 10^{-4}$. Similarly the Final Beam Transport Group[3] provided the value $(\Delta p/p)_b = \pm 10^{-2}$ as the likely spread that could be handled in the final beam line.

Starting from the above $(\Delta p/p)_{inj}$ value, the bunch compression studies[13] for a compression factor 7, led to the value $\pm 4 \times 10^{-3}$ at injection from the storage rings. This is not simply $7 \times (\Delta p/p)_{inj}$, due to the mechanism of phase space rotation during compression[13]. Summarizing:

TABLE II
FINAL BEAM EMITTANCE

CASE		A	B	C
Target Radius	r(mm)	2.0	2.5	4.0
Effective "	r_{eff}(mm)	1.7	2.2	3.7
Reaction Vessel Radius	R_v(m)	3.54	4.58	7.71
Beam Port Radius	a(m)	0.15	0.15	0.15
Beam Line Emittance	ε_b($\times 10^{-6}$m)	72	72	72
Storage Ring "	ε_{SR}($\times 10^{-6}$m)	60	60	60

It will be seen that the beam port radius was kept at what seemed to be a reasonable maximum value of 15 cm, consistent with attainable gradients in the final focussing quadrupoles, and that the beam emittance was kept at 72 x 10^{-6} m for all three cases.

$$(\Delta p/p)_{inj} = \pm 2 \times 10^{-4}$$
$$(\Delta p/p)_{ej} = \pm 4 \times 10^{-3}$$
$$\text{Max.}(\Delta p/p)_b = \pm 10^{-2}$$

As remarked in Section 2.2, an assumed effective uncorrected spread at the target was taken to be:

$$(\Delta p/p)_u = \pm 2 \times 10^{-3}$$

2.5 Bunch Lengths

Finally to set the scene for storage ring parameters, the bunch lengths at target (cf. Table I), combined with the selected compression factors in beam lines and storage rings, lead to the following values as shown in Table III.

3. CHOICE OF N_b, N_{SR}, S, AND STORAGE RING PARAMETERS

Following the argument of Section 1.3, embodied in eqn. (2), the first obvious constraints on the numbers N_b and N_{SR} to be considered involved the Courant-Maschke formula for space-charge-limited power in the beam lines, and the Laslett tune shift formula for space charge during accumulation in the rings.

3.1 Space Charge Limit in Beam Lines

The Courant-Maschke formula for a periodic focussing channel was used in the form:

$$P_b(TW) \leqslant 1687 \times (\beta\gamma)^{7/3} \cdot (\gamma - 1) \cdot (A/q)^{4/3} \cdot \varepsilon_b^{2/3} \cdot B_Q^{2/3} , \quad (7)$$

with A = 238, q = 1 for U^{+1} ions, and using B_Q = 4T for the field on the superconducting quadrupole poletips. The minimum tolerable number of beam lines $(N_b)_{min}$ is then given by

$$N_b > P_p/P_b , \quad (7a)$$

where P_p is the peak power in the total beam pulse, quoted in Table I. Results for the 3 sample cases are quoted in Table IV.

TABLE III
BUNCH LENGTHS

CASE		A	B	C
Bunch length at target	ℓ_b(m)	1.25	3.485	6.10
Bunch length at S.R. Exit	50 ℓ_b/7(m)	8.93	24.89	43.57
Bunch length in S.R.	50 ℓ_b(m)	62.5	174.25	305

TABLE IV
SPACE-CHARGE-LIMITED POWER IN BEAM LINES

CASE	A	B	C
P_b(TW)	5.9	26.9	26.9
P_p(TW)	100	150	300
$(N_b)_{min}$	17	6	12

Each of the N_b beam lines is derived from a compressed bunch in a storage ring.

3.2 Laslett Tune Shift During Accumulation

The usually-accepted limit $\Delta\nu \lesssim 0.25$ due to space charge during accumulation and storage in the rings was expressed in the simplified form:

$$\Delta\nu = \frac{q^2}{A} \cdot \frac{1.5347 \times 10^{-18}}{2\pi} \cdot \frac{n_{SR}}{\epsilon_{SR}} \cdot \frac{\beta}{(\beta\gamma)^3} \lesssim 0.25 \quad (8)$$

for the same ϵ_{SR} in both planes, and where n_{SR} is the number of ions in each storage ring. For A = 238 and q = 1, as before,

$$n_{SR} \lesssim 2.436 \times 10^{20} \cdot \epsilon_{SR} \cdot (\beta\gamma)^3/\beta, \quad (8a)$$

so that the minimum acceptable number of rings $(N_{SR})_{min}$ is given by N/n_{SR}, with N given in Table I. The resulting calculations give:

TABLE V

LASLETT TUNE SHIFT LIMIT IN RINGS

CASE	A	B	C
$(n_{SR})_{min} \times 10^{14}$	6.82	14.1	14.1
$(N_{SR})_{min}$	2	2	5

It should be remarked that a more accurate analysis shows a rather stricter constraint during the stacking process, when only one of the phase planes has been filled.

3.3 Longitudinal Microwave Instability

One of the most serious problems studied during the Workshop concerned the longitudinal microwave instability, which occurs due to coupling of the beam with its containing environment and manifests itself by a momentum spread blow-up. The problem is discussed in detail in References (9), (10), and (6).

The instability is characterized by a beam current threshold defined by the Keil-Schnell criterion:

$$I_{ks} \lesssim |n| \cdot \beta^2\gamma \cdot (\Delta p/p)^2 \cdot (AM_p/q) \cdot /(Z_n/n). \quad (9)$$

Taking $|n| \simeq 1$, $\Delta p/p = 2.8 \times 10^{-4}$ corresponding to full width at half maximum during bunch compression[13], A = 238, q = 1, and M_p = 938 MeV, the remaining difficulty is to estimate the effective coupling impedence (Z_n/N). Given this number, the average current per storage ring would be limited to

$$I_{av}/50\ N_{SR} \lesssim I_{ks} \quad (9a)$$

where I_{av} is taken from Table I; hence there is a lower limit on the number of rings N_{SR} if the instability threshold is not to be reached.

During the course of the study, the best estimate that could be made for (Z_n/n) was to say that it might not be too different from the PS and ISR value of 25Ω. Accordingly, this value was selected as a criterion, "faute de mieux", and led to the limits summarized in Table VI.

TABLE VI

KIEL-SCHNELL THRESHOLD FOR $(Z_n/n) = 25\Omega$

CASE	A	B	C
I_{ks}(Amp)	31.8	63.16	63.16
$(N_{SR})_{min}$	7	3	5

Hence, compared with the Laslett tune-shift limit, this criterion determined a rather stricter limit on the minimum number of rings.

Lively discussion of this topic was pursued throughout the Workhsop, and by the end of the second week it was agreed that the coupling impedance for heavy ion rings could be 40-100 times greater than the above value: in other words, the instability could not be avoided. Attention then shifted to the growth time for the instability, and it was argued that the effect might not be serious under 10 ms or more, (less than the required storage time). These arguments are considered in detail in References (9), (10), and (6): however, by the end of the Workshop, the limitation propounded in Table VI was the best that could be put forward, and was incorporated into the parameter framework.

Further exploration of this problem is required to determine the growth time in a likely heavy ion system, and further theoretical or experimental contributions would be extremely valuable.

3.4 Storage Ring Lattice Considerations

To determine the minimum framework for a storage ring driver system, two further criteria are required, referring to the ring lattice:

(i) Dipole Field: $B \simeq 10P/3\rho \leq 5T$ (superconducting), leading to $\rho(m) \simeq 2P/3$, (with P in GeV/c).

(ii) Circumference Ratio: $R/\rho \gtrsim 1.5$, leading to $C = 2\pi R \gtrsim 50 \cdot \ell_b N_{bunch}$

These assignments determine a minimum number of bunches, $N_{bunch} = N_b/N_{SR}$. Incorporating them into the range of constraints outlined above, the final assessment of minimum storage ring system was arrived at as follows:

TABLE VII
MINIMUM STORAGE RING SYSTEMS

CASE	A	B	C
$(N_{bunch})_{min}/SR$	5	3	2
$(N_{SR})_{min}$	7	3	6
$(N_b)_{min}$	35	9	12
$50\ell_b(m)$	62.5	174.25	305
C(m)	312.5	522.75	610
R(m)	49.74	83.20	97.08
$\rho(m)$	31.6	44.9	44.9
$R/\rho(m)$	1.57	1.85	2.16
B(T)	5	5	5
S	20	57	81
D_ε	1.91	1.61	1.35

It should be emphasized that these are 'minimum' systems, in the sense that the numbers of rings and beam lines are the minimum possible to avoid the various limitations. The space charge problems become less severe when larger values of N_{SR} and N_b are selected. This is already evident with Case C, where larger N_b is required in order to reduce S and raise D_ε above the minimum level 1.4 quoted at the Workshop. For example, the following choices for Cases B and C are possible, and would reduce the requirements on injected current, permit a larger dilution factor, and allow operation further from the space-charge limits in rings and beamlines.

CASE	N_{bunch}/SR	N_{SR}	N_b	S	D_ε	$I_{lin}(mA)$
B	3	6	18	36	2.02	231
C	3	10	30	36	2.02	265

4. FURTHER PROBLEMS

Most of the problems listed in Section 1.4 have already been discussed in the course of Sections 2 and 3, but four of them have not yet been referred to. They are as follows:

4.1 Beam Loss on Septa[8]

During the course of considering the injection process, the problem of beam loss on septa emerged as a severe constraint in high-intensity heavy ion machines. Due to their short range in material, even a small fraction of the heavy ions in the injected beam lost on a septum may vaporize the material, and the resulting 'black cloud' of vapor may destroy the following beam. The problem is described in detail in Reference (8), taking the 3MJ case B with $N_{SR} = 3$ as an example.

Expressed at its worst, the effect is that the tolerable fractional beam loss is of order 10^{-5}. Less dramatically, it may be said that the beam halo at the septum should be less dense than the central beam by a factor 1330; and this factor is reduced if the number of storage rings is increased.

This constraint was recognized as a particularly severe feature of heavy ion storage rings, and detailed numerical studies are needed to examine whether it may not be the determining factor in the choice of N_{SR}.

4.2 Beam Loss from Charge Exchange Scattering

Newly available data on the cross-section for charge-exchange scattering was used to assess the importance of this effect on determining the tolerable lifetime in heavy ion storage rings. The detailed analysis is described in References (11) and (6).

Taking a conservatively-large estimate of the cross-section for U^+ ions, beam loss for the cases listed in Table VII would be a few percent during the filling time. Although it is not clear what loss is tolerable around the ring, this effect also suggests that a larger value of N_{SR} is preferable. Again, more detailed numerical studies and more experimental evidence on cross-sections is desirable.

4.3 RF Stacking

As an alternative (or an addition) to multiturn stacking in transverse phase space, RF stacking was considered, and interesting schemes were described by the Japanese members of the Group[6], [7]. Although such schemes have considerable attraction, it was generally felt that the long filling times make them unsuitable for the HIF systems considered at the Workshop.

4.4 Ejection Studies

The ejection problem for heavy ion storage rings was examined in terms of normal fast ejection techniques. Apart from the stipulation that large full-aperture kickers would be required, no serious problems were identified: the septum-loss problem described in Section 4.1 is avoided.

5. CONCLUSIONS

The Workshop served to clarify the major constraints involved in designing a storage ring system for heavy ion fusion, and to identify several serious and fascinating problems.

It was generally agreed that longer-term studies of these interesting topics was very desirable, if resources could be made available at the different accelerator laboratories: theoretical, numerical, and experimental studies where appropriate could be identified over a wide range of topics.

Many of the problems are common to all modern high-intensity accelerator and storage ring designs, but a few are peculiar to or particularly serious in, heavy ion machines: for example, beam loss on septa, charge exchange scattering loss, high bunch compression. Although seen to be severe, none of these problems was identified to be insuperable.

REFERENCES

All of the following papers appear in these Proceedings.

(1) R.O. Bangerter. Sample Target Data

(2) RF Linac Group. Summary Report

(3) Final Beam Transport Group. Summary Report

(4) R.J. Burke. Storage Ring Injection

(5) N. Takeda and S. Fenster. Study of Inter-Beam interaction in Injection Processes at the Space Charge Limit.

(6) T. Katayama, A. Noda, N. Tokuda, Y. Hirao. Beam Injection and Accumulation Method for Heavy Ion Fusion Storage Rings.

(7) Same authors. Design Study of an Accelerator for Heavy Ion Fusion.

(8) L.W. Jones. Beam Scraping Problems in Storage Rings: The Black Cloud.

(9) D. Möhl. Longitudinal Beam Stability in Heavy Ion Storage Rings.

(10) S. Fenster. Longitudinal Microwave Instability.

(11) J.R. Le Duff and J.R. Maidment. Beam Loss in the Storage Ring Complex Due to Charge Exchange Scattering.

(12) T. Katayama, A. Noda and Y. Hirao. Numatron and TARN.

(13) M. Cornacchia and G.H. Rees. Bunch Compression in Heavy Ion Fusion Storage Rings.

(14) J.R. Le Duff. Integer Resonance Crossing in H.I. Accumulator Ring.

Beam Injection and Accumulation Method in Storage Rings for Heavy Ion Fusion

T. Katayama, A. Noda, N. Tokuda and Y. Hirao

Institute for Nuclear Study, University of Tokyo

Tokyo, JAPAN

ABSTRACT

A combination of multiturn injection and RF stacking is proposed as as efficient beam injection method in storage rings for heavy ion fusion. Five turn injection in each transverse phase space and four RF stackings give a total of 100 stacking turns. This represents a compromise between the tolerable emittances and momentum spread in the ring.

Space charge limitations and coherent beam instabilities are investigated. The most severe limit is found to be the transverse coherent instability, but this can be controlled by the use of sextupole and octupole magnetic fields.

Assuming a charge exchange cross section of 1×10^{-15} cm^2, the e-folding life time is estimated at 180 ms, while the stacking time is 40 ms.

1. INTRODUCTION.

The heavy-ion inertial fusion program has become more promising through intensive work[1 ~ 3] on high-energy heavy-ion accelerators during the past three years. The heavy ion method is superior to those of the other particle beams because of its drastic reduction in the peak current requirement to the order of 1 kiloampere (particle current). This reduction of current is allowed by the comparatively high energy per particle in relation to its range-energy behavior. At present it is a consensus among accelerator physicists that such high currents of heavy ions could be produced, handled, transported and focused on a pellet by the use of conventional high energy accelerator techniques, especially RF linacs with storage rings or induction linacs. It is also true, however, that many kinds of research and development should be pursued: for example it is a serious problem to accumulate heavy ion beams for ~ 100 turns in the limited emittances and momentum spread without any significant beam loss, and to compress them into small bunches in the storage rings.

In the present paper, the combination of multiturn injection in the two transverse phase spaces and RF stacking in the momentum space, is proposed as an efficient beam accumulation method which in principle brings about very small beam loss during the accumulation process. Details of the design of the accelerator are given for U^{+1} ions, as at the Workshop, but the proposed method takes a rather long time and might be generally favored for longer life ions such as Xe^{8+}.

2. REQUIREMENTS ON THE STORAGE RINGS

First we will start from R.O. Bangerter's three cases of target data at this workshop, listed in Table 1 for convenience. Emittance considerations in the beam lines give an upper limit of the allowable transverse emittances in the storage ring as 30 π mm.mrad (unnormalized). The momentum spread at ejection from the storage ring should be lower than $\pm$ 0.4 % because the momentum spread at the target is assumed to be $\pm$ 2 % and the bunch compression factor in the beam transport lines is designed to be 5.

TABLE 1 3 CASES OF TARGET DATA AND BEAM PARAMETERS.

E(MJ)	p_p(TW)	T(GeV)	r(mm)	t(ns)	t_p(ns)	g
1	100	5	2	20	6	8
3	150	10	2.5	40	16	30
10	300	10	4	70	20	120

CASE	A	B	C
E(MJ)	1	3	10
N($\times 10^{15}$)	1.25	1.875	6.25
T(GeV)	5	10	10
E_p(MJ)	0.6	2.4	6
N_p ($\times 10^{15}$)	0.75	1.5	3.75
I_p(A)	2×10^4	1.5×10^4	3×10^4
I_{av}(A)	10^4	0.75×10^4	1.43×10^4

Ions are U^{+1} and the following notation is used. E; Beam stored energy, P; Peak power, T; Kinetic energy, r; Target radius, t; Pulse width, g; gain of the pellet, N; No. of ions. Subcript p refers to peak value at the end of pulse.

Table 2 Ring parameters

Case	A	B	C	
Number of rings (N_{SR})	7	4	9	
Harmonic number	6	3	2	
Particles / ring	1.79	4.69	6.94	($\times 10^{14}$)
Particles / bunch	0.30	1.56	3.47	($\times 10^{14}$)
Emittance	30 π	30 π	30 π	($\times 10^{-6}$ m•rad)
Average radius	59.8	83.1	97.1	m
Radius of curvature (B = 5T)	31.6	44.9	44.9	m
Circumference	375.6	522	610	m

Other parameters of the storage rings are given in Table 2 which are determined by considerations of space charge power limit in beam lines (Courant-Maschke formula), limited tune shift in rings for accumulation ($\Delta\nu = 0.25$), and bunch lengths before and after compression.

Momentum spread of the beam from the injector linac is assumed to be $\pm 2 \times 10^{-4}$ after the debuncher, and the phase spread in the ring after the multiturn injection could be 2π, which means that the beam is completely debunched. The longitudinal emittance, ε_L, of the beam in the ring is

$$\varepsilon_L = \Delta\phi \cdot \Delta T = 105.6 \quad (\text{keV}\cdot\text{rad}) \tag{1}$$

where T denotes a kinetic energy of each nucleon in the ion. In the present paper numerical values are calculated for the case A, while the results for other two cases are also listed in Table 5.

3. MULTITURN INJECTION

Ions are first injected for 5 turns in the horizontal phase space of the injection ring, whose diameter is six times larger than that of the storage rings. The reason why 5 turns are used is given in the following paragraph. Beam is ejected from the injection ring by the fast ejection method and its transverse phase spaces are interchanged with each other in the beam transport lines from the injection ring to the storage rings. Then beam is injected for 2 turns in each horizontal space of three storage rings, whose tune values of betatron oscillation are adjusted to

a half integer at this time. This process is repeated two times and another four storage rings are filled with two-turn beams. After the two turn injection process, the tune value of betatron oscillation of each storage ring is adjusted to an integer plus three quarters, and beam is injected in each storage ring for three turns. The total lay-out of the injection ring and the storage rings is illustrated in Fig. 1.

In order to reduce the beam loss at the septum of the inflector during the beam injection process and to minimize the dilution factor in each phase space, five turn injection is applied for the injection ring and storage rings, by the following process:

1) The tune value of horizontal betatron oscillation is adjusted to half integer and the beam is injected in the ring during a time $2\,\tau_o$, where τ_o is one revolution period in the ring.

2) After two turn injection, the position of the septum of the inflector is moved a distance of ~ 10 mm in the transverse phase space within a time of $1/100\,\tau_o$ in order to reduce the beam loss at the septum to less than 1%. The horizontal tune value of the ring also should be changed from half integer to integer plus three quarters, when the tune shift due to the already injected two turn beams and one turn beam to be newly injected, is compensated.

3) Beam is subsequently injected in the horizontal phase space during the time $3\,\tau_o$ instead of $4\,\tau_o$, because the tune shift due to the space charge of successively injected beam is significantly large, and the phase advance of the betatron oscillation per revolution is varied well away from $\pi/2$.

Details of the multiturn injection method are given in the Appendix to the present paper.

The dilution factor of the emittance during the whole process of 5 turn injection is claculated to be 2.4 in each phase space. The emittance of the linac beam is given by

$$5 \times \pi\varepsilon_{linac} \times 2.4 = 30\ \pi \times 10^{-6} \quad (\text{m}\cdot\text{rad}) \ , \qquad (2)$$

$$\pi\varepsilon_{linac} = 2.5\ \pi \times 10^{-6} \quad (\text{m}\cdot\text{rad}) \ , \qquad (3)$$

and the normalized emittance is

$$\pi\varepsilon_{n} = \pi\varepsilon_{linac}\ \beta\gamma$$

$$= 0.534\ \pi \times 10^{-6} \quad (\text{m}\cdot\text{rad}) \ , \qquad (4)$$

which is smaller than the value estimated by the linac group at this workshop. But the peak current of the linac beam can be reduced to ~ 50 mA in our method, to allow such small emittance to be obtained.

4. RF STACKING

The injected beam in the storage ring by the five turn injection method is completely debunched. It is captured adiabatically by the RF separatrix and is accelerated to the stacking orbit, when the rate of change of momentum for the sychronous particle is given by

$$\frac{dp/dt}{p} = \frac{f_{rev}}{E_N \beta^2} \frac{q}{A} \cdot eV \cdot \Gamma \ , \qquad (5)$$

where f_{rev} is a revolution frequency around the ring, E_N is a total energy of each nucleon, $\beta = v/c$, q/A is a charge to mass ratio and

$\Gamma = \sin\phi_s$. The fractional momentum difference between the injected orbit and the bottom of the stacked region is designed at 1.5 %, the acceleration period is 5 ms, and the required RF voltage is 356 kV. The period of phase oscillation during the acceleration is 1.48 ms.

During a period of acceleration from the bottom to the top of the stacked region, the RF voltage should be reduced to avoid an undesirable energy spread of the stacked beam in the stacked region. Final RF voltage is determined, as the area of the separatrix is just equal to the longitudinal phase space area of the injected beam, 105.6 keV·rad. In order to cover the longitudinal phase space area, S, of the injected beam by the separatrix, the minimum RF voltage is given by the following relation.

$$S = \left(\frac{hqeV}{A}\right)^{1/2} \alpha(\Gamma)\, \frac{16\beta}{h} \left(\frac{E_N}{2\pi|\tilde{\eta}|}\right)^{1/2} , \qquad (6)$$

where h is a harmonic number and $\tilde{\eta}$ is defined as

$$\tilde{\eta} = \frac{1}{\gamma_{tr}^2} - \frac{1}{\gamma^2} . \qquad (7)$$

Other notations concerning the synchrotron oscillation can be found in Reference 4. Substituting numerical values in the relation, a minimum voltage 81.6 keV is obtained. The phase oscillation period at the final voltage is 3.09 ms, and the necessary time to change adiabatically from the initial bucket to the final one is given by

$$T = \frac{1 + \kappa}{2(1 - \kappa)} \left(\frac{1}{\omega_2} - \frac{1}{\omega_1}\right) , \qquad (8)$$

where ω_1 is an angular frequency of phase oscillations associated with the initial bucket, ω_2 is that of the final bucket and κ is a quantity related to the phase space efficiency of the process. Substituting numerical values, κ is assumed to be 0.9, and T is 2.43 ms. Thus the shape of the envelope of the RF voltage is that shown in Fig. 2.

Next we must consider the relation between the number of RF stackings, the compression voltage and the final momentum spread in the storage ring. For simplicity, we assume that the momentum spread after n times RF stacking is

$$n \times \left(\frac{\Delta p}{p}\right)_i \quad , \tag{9}$$

where $(\Delta p/p)_i$ represents an initial momentum spread of $\pm 2 \times 10^{-4}$. The compression voltage including the effect of space charge and momentum spread is given by[5)]

$$\frac{eV}{2\pi\gamma Amc^2} = \frac{3N_b q h^2 r_o g}{A\gamma^3 R \cdot \Delta\phi_o \cdot \Delta\phi_{MIN}\,(\Delta\phi_o + \Delta\phi_{MIN})} + \frac{1}{q \cdot \Delta\phi^2_{MIN}}\, h\,|\tilde{\eta}|\,\beta^2 \left(\frac{\Delta p}{p}\right)^2 \tag{10}$$

where

mc^2 = 931.5 MeV, $r_o = 1.547 \times 10^{-18}$ m

q = charge state (= 1)

g = geometrical factor (= 1.5)

N_b = number of particles/bunch

$\Delta\phi_o$ = initial phase spread (= 2 π)

$\Delta\phi_{MIN}$ = final phase spread (= 0.2 π) .

The final phase spread is determined so that the phase compression factor in the ring is 10, when the tune shift, $\Delta\nu$, during the compression is assumed to be 2.5. The compression voltage is

$$eV = 0.1424\ (n^2 + 0.1798) \quad \text{(MeV)} \tag{11}$$

Next we should calculate the separatrix height, H, related to the compression voltage and the final momentum spread, $\Delta p/p$, by using the following formulae,

$$H = \left(\frac{hqeV}{A}\right)^{1/2} Y \frac{\beta}{h} \left(\frac{E_N}{\pi|\tilde{\eta}|}\right)^{1/2} \text{(keV)} \quad , \tag{12}$$

$$\frac{\Delta p}{p} = \frac{1}{\beta^2} \frac{2H}{E_N} \quad . \tag{13}$$

Numerical results are given in Table 3.

TABLE 3

n	eV (MeV)	H (keV)	$\Delta p/p$ (%)
0	0.025	22.29	0.107
2	0.595	107.48	0.517
4	2.304	211.46	1.016
6	5.152	316.21	1.520
8	9.139	421.15	2.024
10	14.266	526.17	2.529

n: Number of RF stackings

eV: Compression voltage

H: Separatrix half height

$\Delta p/p$: Momentum spread (full width) after the compression

If we assume that the final momentum spread in the storage ring should be less than 1 %, the maximum number of RF stackings is 4.

As mentioned in preceding Sections, the number of multiturn injections is 5 in each transverse phase space. Then the required peak current, I_p, for the linac is given by

$$5^2 \times I_p \tau_o n = eN \qquad (14)$$

where N is a number of the particle in each storage ring, and

$$I_p = \frac{1.6 \times 10^{-19} \times 1.79 \times 10^{14}}{5^2 \times 4 \times 6 \times 10^{-6}} = 47.7 \quad \text{mA} . \qquad (15)$$

5. BEAM INSTABILITIES

5.1) Space charge limit

The space charge limit in a circular ring is given by

$$N = \frac{2\pi\Delta\nu}{B \cdot r_p} \left(\frac{A}{q^2}\right) \varepsilon\beta^2\gamma^3 \quad , \qquad (16)$$

where B is a bunching factor, r_p is a classical proton radius 1.547×10^{-18} m and ε is an unnormalized emittance. In the injection ring, emittance should be averaged over horizontal and vertical phase spaces, each of which has a numerical values of 30 π mm·mrad and 2.5 π mm·mrad. The averaged emittance is

$$\pi\varepsilon = \pi\sqrt{\varepsilon_x \cdot \varepsilon_y} = 8.66\,\pi \times 10^{-6} \quad (\text{m·rad}) . \qquad (17)$$

If we take a bunching factor 1.0, the space charge limit in the injection ring is 9.8×10^{13} particles. In the storage ring, emittance is 30 π mm·mrad both in the horizontal and vertical phase spaces and the space charge limit is 3.38×10^{14} particles. In both rings, space charge limit exceeds the designed circulating currents.

5.2) Resistive wall instability

Next we will consider the longitudinal and transverse coherent resistive wall instabilities. The longitudinal coherent limit is given by the Keil-Schnell criterion[6],

$$\left|\frac{Z_L}{n}\right| < F \frac{\beta^2 \gamma E_o}{e} \frac{|\tilde{\eta}|}{I} \left(\frac{\Delta p}{p}\right)^2 \qquad (18)$$

where Z_L/n is a longitudinal coupling impedance. Its numerical value should be examined further for heavy ion machines. However we will adopt here the value of 25 Ω which is scaled from the experimental values at ISR & CPS[7]. Thus the longitudinal coherent limit is 59 A for a momentum spread of $\pm 2 \times 10^{-4}$, and there would be no problem related to the longitudinal coherent instability in the injection ring and the storage rings.

On the other hand the transverse coherent instability limit is given by

$$\left|\frac{Z_\perp}{n}\right| < 4F \frac{AE_o}{qe} \frac{\nu\beta\gamma}{I_o R} \left(\left| (n - \nu)\tilde{\eta} + \xi \right| \frac{\Delta p}{p} + \frac{\partial \nu}{\partial a^2} \Delta a^2 \right) \qquad (19)$$

where $Z_\perp/n$ is a transverse coupling impedance and ξ is a chromaticity. The first term in the bracket shows the effects of sextupole fields, and the second term the octupole fields. In the storage ring the momentum spread is fairly large, ~ 1 %, and the correction due to the sextupole fields is much more efficient than that of octupole fields. When we introduce a chromaticity of -10, the intensity limit is 0.54 A or 2.0×10^{13} particles, which is much smaller than the space charge limit. The e-folding growth time of this instability is given by [8]

$$\tau = \frac{4\pi\nu\cdot\gamma AE_o/qe}{cI\ \mathrm{Re}(Z_\perp)} \simeq 46\ \mathrm{ms}\ , \qquad (20)$$

if we assume the radius of the vacuum chamber to be 5 cm and the stored current to be 4.78 A. This formula, however, holds under the condition that there is no sextupole and no octupole corrections. We expect that TCI can be controlled by their corrections during a total accumulation time of $\sim$ 40 ms.

6. LIFE TIME OF THE BEAM IN THE STORAGE RING.

In high-intensity heavy-ion storage rings, a beam loss due to an electron transfer process between ions in the beam, $A^{n+} + A^{n+} \rightarrow A^{(n+1)+} + A^{(n-1)+}$, may be a severe problem. The loss rate α is estimated as follows:

$$\alpha \equiv \frac{1}{N}\frac{dN}{dt} \qquad (21)$$

$$= n_{lab} v_{cm} \sigma_{cm}\ . \qquad (22)$$

The symbols are defined in Table 4, where machine parameters are also listed. The density of ions in the ring is

$$n_{lab} = \frac{N}{2\pi RS} \quad , \tag{23}$$

on the assumption that the beam is completely debunched. The beam is to be stored in the ring as shown in Fig. 3. Then the cross section of the beam is

$$S = \pi ab + b\Delta x_p \quad , \tag{24}$$

where a and b are obtained from the beam emittance ε and the average betatron amplitude function, $\bar{\beta}$,

$$a = \sqrt{\varepsilon_x \bar{\beta}} \quad , \tag{25}$$

$$b = \sqrt{\varepsilon_y \bar{\beta}} \quad , \tag{26}$$

The beam spread due to a momentum dispersion is

$$\Delta x_p = \eta \frac{\Delta p}{p} \quad . \tag{27}$$

The dispersion function is approximately

$$\eta = \bar{\beta}^2/R \quad . \tag{28}$$
$$= 1.81 \quad (m)$$

Then the beam cross section is numerically calculated with values listed in Table 4, and the density is

$$n_{lab} = 4.62 \times 10^{14} \quad (m^{-3}) \quad . \tag{29}$$

The speed of the ion in the center of mass frame is given by

$$\beta_{cm}{}^2 = \left(\frac{\beta}{2} \frac{\delta' p}{p} \right)^2 + \left(\beta\gamma \sin \frac{\theta}{2} \right)^2 \quad . \tag{30}$$

As the ion momenta are considered to be distributed as in Fig. 4, the typical momentum difference between the ions which will collide with each other, is

$$\frac{\delta' p}{p} = \frac{\Delta p}{p} \frac{2a}{2a + \Delta x_p} \quad , \tag{31}$$

where $\delta' p/p$ is determined so that the areas of the parallelogram and the rectangle are equal. Then the first term of eq.(30) is 1.65×10^{-4}. The maximum collision angle in the laboratory is evaluated by

$$\theta = 2\sqrt{\varepsilon_x / \bar{\beta}} \quad , \tag{32}$$

and the second term is numerically 3.61×10^{-4}. Then the velocity in the c.m. frame is

$$v_{cm} = 1.19 \times 10^5 \ (m/s) \quad . \tag{33}$$

which corresponds to a kinetic energy of 75 eV.

According to papers[9,10] the cross sections for the electron transfer process of various ions are estimated to be of the order of 10^{-15} cm^2. Therefore a value of 1×10^{-15} cm^2 is appropriately adopted here for U^{1+}.

Now the loss rate can be numerically calculated, and

$$\alpha = 5.50 \ (s^{-1}) \quad . \tag{34}$$

The life time, the inverse of the loss rate, is

$$\tau = 0.182 \quad (s). \tag{35}$$

which means that the beam will be lost by the amount of 20 % during stacking process of ~ 40 ms. Therefore if such an amount of beam loss is serious, even though it does not occur at localized positions such as the inflector septum, but could be uniformly lost around the ring, another kind of ion of low intrabeam charge exchange cross section such as Xe^{8+} should be used.

Table 4 List of symbols and machine parameters for case A

N	number of ions in the ring	1.79×10^{14}
n_{lab}	density of ions	
R	mean radius of the ring	59.8 m
S	cross section of the beam	
v_{cm}	velocity of ions in the center of mass frame	
α	loss rate	
β	ratio of ion velocity to that of light	0.208 (21 MeV/u)
$\bar{\beta}$	average betatron amplitude function	10.4 m
γ	$1/\sqrt{1 - \beta^2}$	1.0224
$\frac{\delta' p}{p}$	momentum difference between colliding ions	
$\frac{\Delta p}{p}$	total momentum spread	1.6×10^{3}
ε_x	emittance in the horizontal direction	30×10^{-6} m·rad
ε_y	emittance in the vertical direction	30×10^{-6} m·rad
η	dispersion function	
θ	collision angle in the laboratory frame	
σ_{cm}	cross section of the electron transfer process	1×10^{-19} m^2
τ	life time	

Table 5 Summary of the calculations for three cases.

Case	A	B	C
No of multiturn	5 × 5 = 25	25	25
Dilution factor for multiturn	2.4	2.4	2.4
Normalized emittance of the injected beam from the linac	$0.534\pi\times10^{-6}$ (m·rad)	$0.759\pi\times10^{-6}$ (m·rad)	$0.759\pi\times10^{-6}$ (m·rad)
LINAC peak current	48 mA	125 mA	158 mA
RF stacking number	4	4	4
Momentum spread after the compression in the ring	1 %	1 %	0.899 %
required period for one RF stacking	10 ms	28 ms	47 ms
Total injection period for each ring	40 ms	112 ms	188 ms
Total accumulation period for n_r rings	∿40 ms	∿112 ms	∿200 ms
Fusion repetition rate	20 Hz	8 Hz	5 Hz
Space charge limit in the stacking ring storage ring	8.6×10^{13} 3.3×10^{14}	1.8×10^{14} 8.7×10^{14}	5.7×10^{14} 1.4×10^{15}
Longitudinal coherent limit	300 A	more safe than in case A	more safe than in case A
Transverse coherent limit	0.54 A	"	"
Growth time of transverse instability	46 ms	"	"
Compression voltage	2.3 MV	2.2 MV	1.5 MV
Compression time	102.4 μs (17 turns)	∿100 μs	∿100 μs

APPENDIX

Scheme of multiturn injection into transverse phase space

For the purpose of reducing the beam loss due to the collision with an inflector septum, the following process was studied.

1st) Before the beam injection the tune value of the betatron oscillation should be adjusted to a half integer taking account of the space charge effect due to the intensity of a single turn.

2nd) The beam from the linac is injected by a two turn injection method during the time $2\,\tau_o$, where τ_o is the revolution time of the beam.

3rd) The position of the septum in the phase space should be moved in a time of $\frac{1}{100}\,\tau_o$ in order to reduce the beam loss to around 1 %.

4th) The horizontal tune value is shifted to an integer +3/4, taking account of the effect of the space charge force due to the two turn beam already stacked in the ring, and the first one turn beam to be injected in the next step.

5th) The beam from the linac should be three turn injected during the time interval $3\,\tau_o$, and just before the three turn the position of the septum is moved from x = 11 mm to x = 21 mm in a time of $\frac{1}{100}\,\tau_o$.

The acceptance of the ring and the emittance of the beam from the linac were assumed to be $30\,\pi \times 10^{-6}$ and $2.5\,\pi \times 10^{-6}$ m·rad (unnormalized), respectively.

In the second process the transfer matrix of one turn, M_o, can be written as

$$M_o = \begin{pmatrix} \cos\{2\pi(N + \frac{1}{2} + \Delta\nu)\}, & \beta\sin\{2\pi(N + \frac{1}{2} + \Delta\nu)\} \\ -\frac{1}{\beta}\sin\{2\pi(N + \frac{1}{2} + \Delta\nu)\}, & \cos\{2\pi(N + \frac{1}{2} + \Delta\nu)\} \end{pmatrix} , \quad (A\text{-}1)$$

where N is an integer, $\Delta\nu$ is the tune shift due to the space charge effect of the beam, and $\alpha \left(= -\frac{1}{2}\beta'\right)$ is assumed to be zero. We represent the beam ellipse in the phase space just one turn after injection as $(a\cos\theta + x_c,\ b\sin\theta)$, where a and b are the length of horizontal and vertical axes of the beam ellipse and x_c is the position of the center of the beam as shown in Fig. A-1. Using

$$M_o = \begin{pmatrix} -\cos\Delta\mu, & -\beta\sin\Delta\mu \\ \frac{1}{\beta}\sin\Delta\mu, & -\cos\Delta\mu \end{pmatrix} , \quad (A\text{-}1)'$$

where $\Delta\mu = 2\pi\cdot\Delta\nu$, the position of the beam with respect to the closed orbit after another revolution is given by

$$x = -\cos\Delta\mu(a\cos\theta + x_c) - \beta\, b\sin\theta\cdot\sin\Delta\mu \ . \quad (A\text{-}2)$$

The maximum value of x is obtained for the value of θ which satisfies

$$\frac{dx}{dx'} = 0 \quad (A\text{-}3)$$

and

$$\tan\theta = \frac{\beta b}{a}\tan\Delta\mu \ . \quad (A\text{-}4)$$

For such a value of θ,

$$x = -x_c\cos\Delta\mu \pm \sqrt{a^2\cos^2\Delta\mu + \beta^2 b^2\sin^2\Delta\mu} \ . \quad (A\text{-}5)$$

The maximum value of x in the equation (A-5) when $\Delta\mu$ is varied, is obtained as

$$x_{max} = \beta \cdot b \sqrt{\left| 1 - \frac{x_c^2}{a^2 - b^2\beta^2} \right|} \qquad (a \neq b\beta) \qquad \text{(A-6)}$$

$$= |x_c| + a \qquad (a = b\beta)$$

In our case the numerical values are as follows;

$$\begin{aligned} \beta &\simeq 15 \text{ m}, \\ a &= 4.0 \times 10^{-3} \text{ m} \\ b &= 6.25 \times 10^{-4} \\ x_c &= -4.5 \times 10^{-3} \text{ m} \quad . \end{aligned} \qquad \text{(A-7)}$$

and the maximum value is

$$x_{max} = 0.0106 \text{ m} \quad . \qquad \text{(A-8)}$$

Therefore when the position of the inflector septum is shifted outward as far as 11 mm after 2 turn injection in a time $\frac{1}{100}\tau_o$, no further beam collision with the septum is expected.

In the third process, it is necessary to estimate the required high voltage of the pulsing system for bump magnets. The bump magnets should be located 90° up and down stream of the inflector. In Case A, the required deflection angle of the bump magnet is estimated to be 6.733×10^{-4} rad in order to distort the closed orbit by 11 mm at the position of the inflector. If each bump magnet is divided into 6 units which are excited in parallel, then the necessary deflection angle for each unit is $\frac{1}{6} \times 6.733 \times 10^{-4} = 1.122 \times 10^{-4}$ rad. The field strength of the bump magnet is calculated at 177 G for case A, where the total momentum of U^{1+} is 47349 MeV. The required current for each bump magnet unit is calculated to be 704.8 A if a single turn coil is used.

If we assume a critical damping, the rise time t_r from 5 % to 95 % of the maximum value is given by

$$t_r = 1.14 \frac{L}{Z_o} \quad , \tag{A-9}$$

where L and Z_o are the inductance of the coil and the characteristic impedance of the circuit, respectively. The inductance of the magnet is given by the relation

$$L = N^2 \cdot \mu_o \frac{w \cdot \ell}{d} \cdot F \quad , \tag{A-10}$$

where μ_o is the permeability of air, w, ℓ, d are the width of the pole, the length of the magnet, and the gap height of the magnet, respectively, and F is the ratio of the leakage flux defined by

$$F = \frac{\phi}{\phi_1} \quad , \tag{A-11}$$

where ϕ and ϕ_1 are the total flux in the iron yoke and the total flux which goes through the pole face, respectively. Assuming the following values

$$\begin{aligned} w &\simeq 0.07 \text{ m} \\ \ell &\simeq 1.0 \text{ m} \\ d &= 0.05 \text{ m} \\ F &\simeq 2.0 \quad , \end{aligned} \tag{A-12}$$

L is 3.52 μH and the characteristic impedance Z_o should be 67 Ω so as to make the rise time t_r as short as 60 μs. The required high voltage V_o is given by

$$V_o = 2 Z_o \cdot I$$

and is 94.44 kV, which is a manageable value.

Then the horizontal tune of the betatron oscillation is moved to an integer +3/4, including the space charge effect due to the beam already injected into the ring and the beam which will be injected in the next turn.

After tuning, the beam from the linac is injected by three-turn injection as is illustrated in Fig. A-2 (a) ∿ (c). In the calculation, the additional effect of space charge due to beam newly injected into the ring is taken into account. The tune shift is given by the formula

$$\Delta\nu = \frac{-NB \cdot r_p \, q^2}{2\pi\varepsilon\beta^2\gamma^3 A} \quad , \tag{A-14}$$

where B, r_p and ε are the bunching factor, the classical proton radius and the unnormalized emittance of the beam. In case A, this effect is estimated to be $\Delta\nu_1 = -0.07$ and the transfer matrices of the 1st 2nd and 3rd turns, M_1, M_2 and M_3, are given by

$$M_i = \begin{pmatrix} \cos 2\pi\left(N + \frac{3}{4} + (i-1)\Delta\nu_1\right), & \beta \sin 2\pi\left(N + \frac{3}{4} + (i-1)\Delta\nu_1\right) \\ -\frac{1}{\beta}\sin 2\pi\left(N + \frac{3}{4} + (i-1)\Delta\nu_1\right), & \cos 2\pi\left(N + \frac{3}{4} + (i-1)\Delta\nu_1\right) \end{pmatrix} \tag{A-15}$$

$i = 1, 2, 3.$

Due to space charge tune shift, the beam will come back to the septum position after three turns, as is shown in Fig. A-2. Hence it is needed to shift the septum position to x = 21 mm in the time interval $(2 + \frac{99}{100})\,\tau_o < t < 3\tau_o$. The required current for the bump magnet is 576.7 A, and the high voltage is calculated at 77.3 kV.

During the multiturn injection process, beam with an emittance of $2.5\,\pi \times 10^{-6}$ m·rad (unnormalized) is injected into the ring with an

acceptance of $30\ \pi \times 10^{-6}$ m·rad during $\{ (2 + 3) - \frac{1}{100} \times 2 \}$ turns.

Then the dilution factor due to this multiturn injection is

$$D = \frac{30}{2.5 \times \{(2 + 3) - \frac{1}{100} \times 2\}} = 2.41 \quad . \qquad \text{(A-16)}$$

This factor is close to the value of the usual multiturn injection, but in this scheme beam loss due to collision with the inflector septum is reduced to 2 % of the total beam.

References

1) ERDA Summer Study of Heavy Ions for Inertial Fusion, 1976, LBL-5543.

2) Proceedings of the Heavy Ion Fusion Workshop, 1977, BNL-50769.

3) Proceedings of the Heavy Ion Fusion Workshop, 1978, ANL-79-41.

4) C. Bovet et al., A selection of formulae and data useful for the design of A. G. synchrotrons, CERN/MPS-SI/Int. DL/70/4, 1970.

5) T. K. Khoe, "Longitudinal Bunching:, Proc. of the Heavy Ion Fusion Workshop, 1977, BNL-50769.

6) W. Schnell, Coherent instabilities of proton beams in accelerators and storage rings-experimental results, diagnosis and cures CERN 77-13, 1977.

7) D. Möhl, Talk at this workshop.

8) B. Zotter and F. Sacherer, Transverse Instabilities of Relativistic Particle Beams in Accelerators and Storage Rings, CERN 77-13, 1977.

9) K. T. Cheng, G. Das, Y. K. Kim and R. C. Raffenetti, Proc. of the Heavy Ion Fusion Workshop, 1977, BNL-50769.

10) J. Macek, Proc. of the Heavy Ion Fusion Workshop, 1978, ANL-79-41.

Figure captions

Fig. A-1. Beam injection is carried out with the elliptically-shaped beam shown in the figure. The number of betatron oscillations per revolution is tuned to a half integral value, including the space charge effect due to the one-turn injected beam. During the first turn, the beam ellipse revolves by 180° in phase space, but during the second turn the beam ellipse rotates as illustrated in the figure due to the space charge effect of another one-turn beam. In order to avoid beam loss, the septum is shifted to x = 11 mm in the time interval $(1 + \frac{99}{100})\tau_o < t < 2\tau_o$, where τ_o is a revolution time of the beam.

Fig. A-2. In this process the tune value of betatron oscillation is adjusted to integer plus three quarters including the space charge effect due to the one-turn beam.

(a) In the first turn, the beam ellipse rotates in the phase space by 90°.

(b) In the second turn, the tune is shifted by the space charge force due to another one-turn beam and the beam ellipses rotate as is shown in the figure.

(c) After three turns, the first beam comes back to the septum position as is illustrated in the figure because of the tune shift due to additional space charge effect. In order to reduce beam loss, the septum is shifted from x = 11 mm to x = 21 mm in the time interval $(2 + \frac{99}{100})\ \tau_o < t < 3\ \tau_o$.

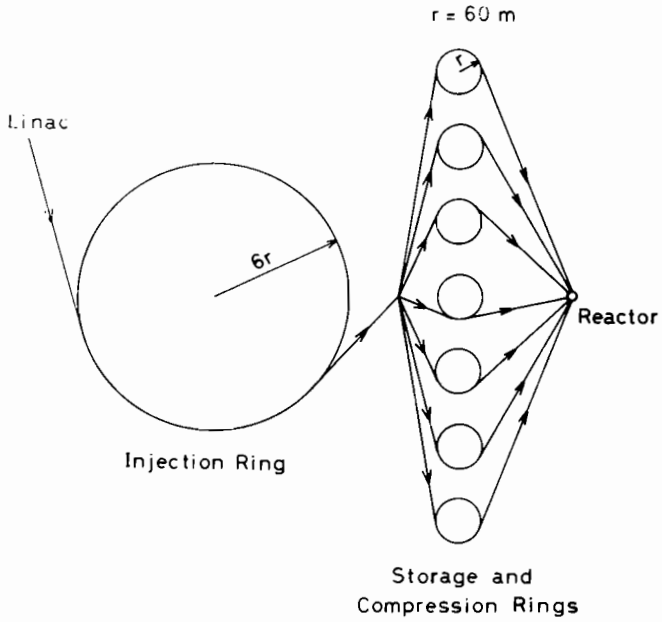

Fig.1 Schematic layout of the injection ring and storage rings for case A.

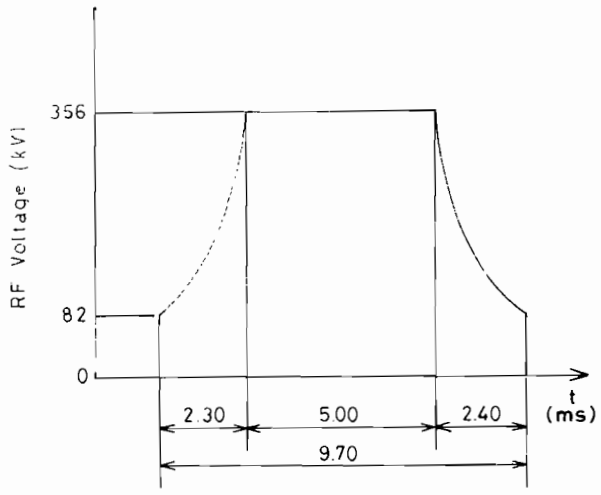

Fig.2 An envelope of the RF field for the momentum stacking.

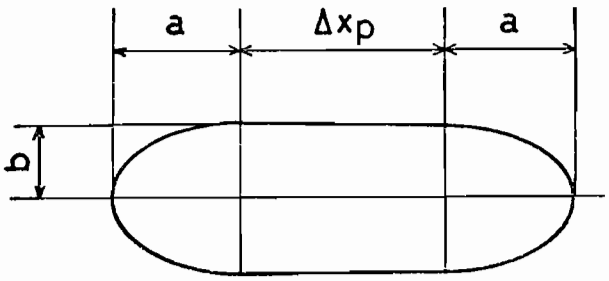

Fig. 3. The beam profile in the storage ring.

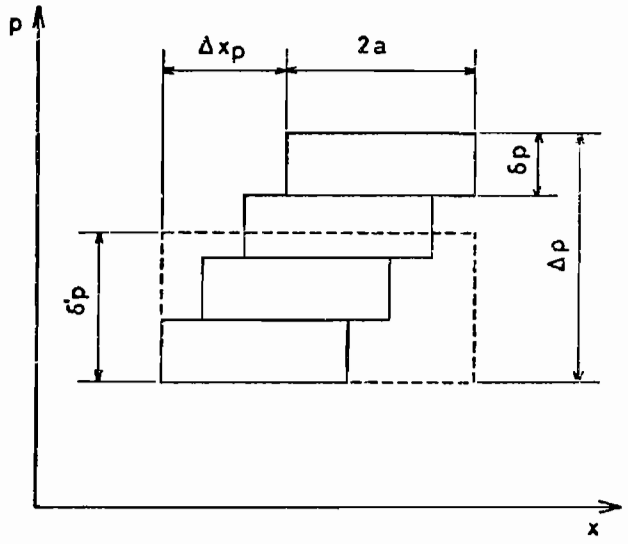

Fig. 4. Four beam pulses of different momenta are stacked in the storage ring. The typical momentum spread $\delta'p$ is determined so that the area of the ractangle (dashed line) and that of the four pulses are equal.

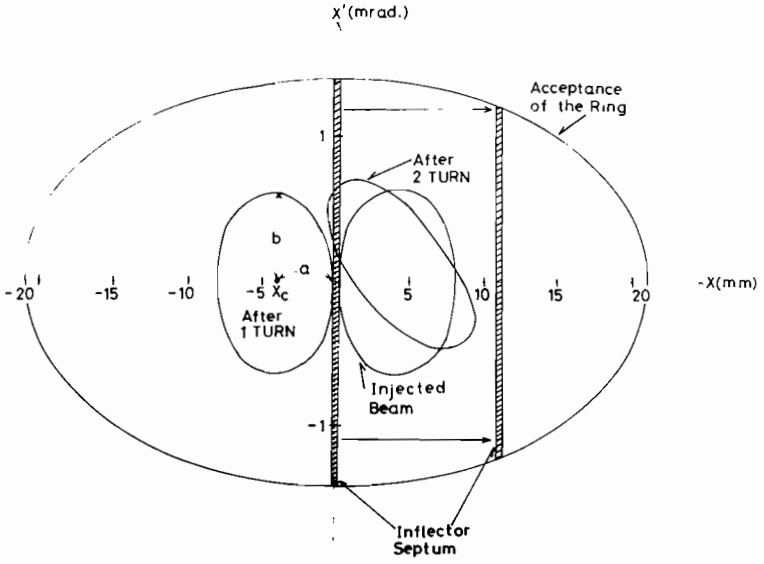

Fig. A-1 Schematic diagram of the first 2-turn-injection with the half integral tune value.

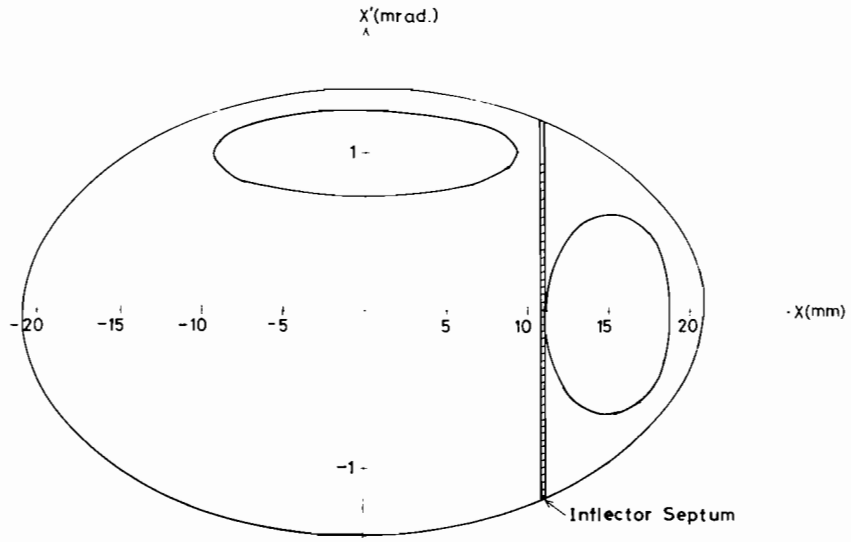

(a)

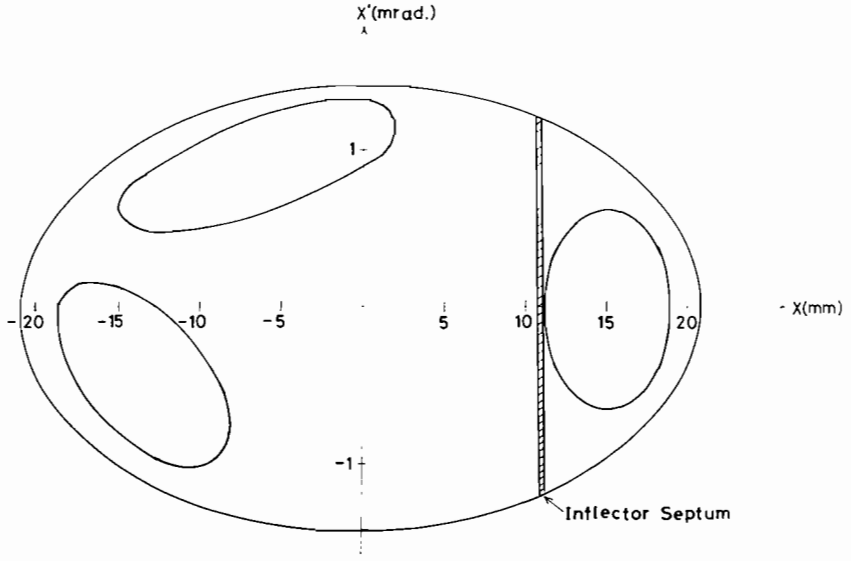

(b)

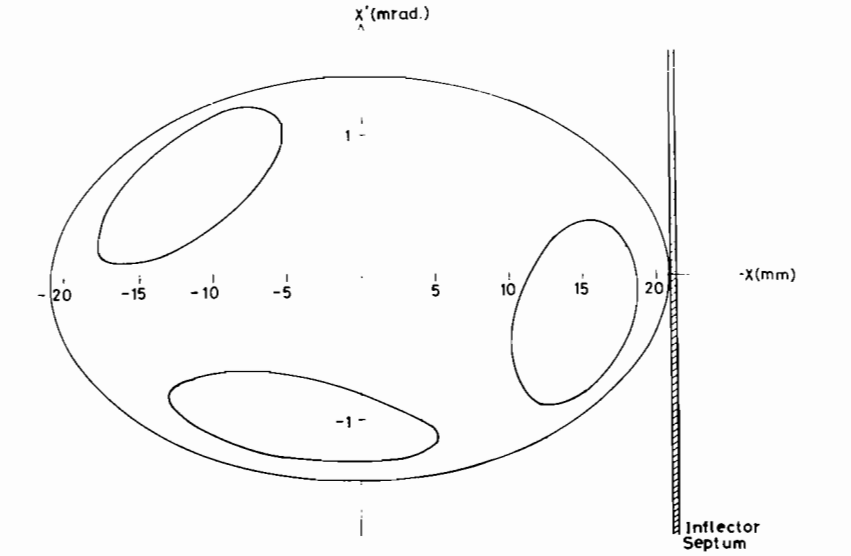

(c)

Fig. A-2. Schematic diagram of the second 3-turn-injection with the tune-value of integer plus three quarters.

BEAM LOSS IN THE STORAGE RING COMPLEX DUE TO CHARGE EXCHANGE SCATTERING

J.R. Le Duff & J.R. Maidment
Rutherford Laboratory

1. INTRODUCTION

We have estimated the beam loss due to charge exchange scattering for the three reference designs used during this study. The formula derived under simplifying assumptions is similar to that used previously by Mills[1]. Our results show that this effect is by no means negligible and indicate a need for both more complete calculations and further experimental data on charge exchange cross-sections for specific ions.

2. BEAM LIFETIME

In the lab. frame we have

$$d\dot{N} = v\sigma\rho^2 dV \quad , \tag{1}$$

where v = relative velocity, ρ = particle density, N = number of particles in a bunch of volume V and σ = event cross-section. All quantities are measured in the laboratory frame.

This leads to an e-folding time τ given by

$$\frac{1}{\tau} = \frac{1}{N}\int v\sigma\rho^2 dV \quad . \tag{2}$$

To evaluate the integral in equation (2) we make the following simplifying assumptions:

a) The relative velocity, v, is that due to betatron motion only and is an average relative velocity.

b) The cross-section, σ, is independent of the velocity.

c) The effect of storage ring dispersion on the particle density is neglected.

d) The particle density, ρ, is assumed to be uniform. However the maximum amplitude (which defines the beam emittance) is taken as twice the rms amplitude of a gaussian distribution.

The validity of these assumptions is commented upon later. Under these assumptions equation (2) may be written

$$\frac{1}{\tau} = \sigma v \frac{N}{V} \quad . \tag{3}$$

Now $V = 4\pi\langle x\rangle\langle y\rangle\ell$, and we take an average relative velocity $v = 2\beta c\langle x'\rangle$ where $\langle x\rangle$, $\langle y\rangle$ = rms transverse amplitudes, ℓ = bunch length and $\langle x'\rangle$ = rms angular spread, βc = particle longitudinal velocity.

We assume equal emittances in each transverse plane so that

$$\langle x\rangle = \langle y\rangle = \frac{1}{2}(\varepsilon\beta_x)^{1/2} \quad ,$$

where β_x = envelope function

and $\varepsilon = 4\langle x\rangle\langle x'\rangle$.

Substituting into equation (3) we obtain

$$\frac{1}{\tau} = \frac{N\sigma\beta c}{\pi\,\varepsilon^{1/2}\,\beta_x^{3/2}} \quad . \tag{4}$$

We assume a uniform longitudinal particle distribution $\frac{N\beta c}{\ell} = \frac{I}{Ze}$, and on transforming the cross-section to the center of mass frame obtain

$$\frac{1}{\tau} = \frac{1}{\pi}\frac{I}{Ze}\frac{\sigma_{cm}}{\varepsilon^{1/2}\,\beta^{3/2}\gamma} \quad , \tag{5}$$

where we have dropped the subscript from the envelope function β.

The loss rate will vary around the ring due

to the azimuthal variation of β. In evaluating equation (5) we therefore take an effective value of β defined by

$$\beta_{eff} = \left[1/2 \left(\frac{1}{\beta_{min}^{3/2}} + \frac{1}{\beta_{max}^{3/2}} \right) \right]^{-2/3} .$$

The resultant lifetimes, for a cross-section $\sigma_{cm} = 10^{-15} cm^2$, for each of the three reference cases are presented in Table 1. Values for β_{min} and β_{max} have been taken from Cornacchia and Rees[2].

TABLE 1

Case	A	B	C
β_{eff}(m)	6.2	6.2	6.2
ε(m.rad)	60×10^{-6}	60×10^{-6}	60×10^{-6}
$\sigma_{cm}(cm^2)$	10^{-15}	10^{-15}	10^{-15}
γ	1.0226	1.0451	1.0451
I(A)	6	17.1	24.3
τ(ms)	102	37	26

The present numbers assume a charge state 1.

3. COMMENTS AND CONCLUSIONS

Equation (5) shows that $\tau \sim \frac{\varepsilon^{1/2}}{I}$. We have used the final storage/compression ring parameters and these contain some allowance for emittance dilution. While the beam is being stacked in these or similar intermediate rings τ will be less than the quoted values by up to 40%. Since the minimum beam handling times between linac and final compression in the rings are respectively 0.7, 1.0 and 3.3 ms we would estimate the beam loss, using $\sigma_{cm} = 10^{-15}$ cm^2, to be at least 1/2%, 2.5%, and 12% respectively for cases A, B, and C.

We have used a somewhat arbitrary cross-section of $\sigma_{cm} = 10^{-15}$ cm^2 for the 'Uranium-like' ion. Recent measurement[3] on Cs^+ ions indicate that this may not be an unreasonble value. Clearly further measurements on other ion species are necessary. Intuitively it seems appropriate to select a closed-shell ion. However, if this leads to either a multiply charged ion of $A \geq 200$ or a singly charged ion of $A < 200$ problems of space charge in circular rings would become exacerbated.

We made several assumptions (a) and (c) above seem equation (5). Assmptions (a) and (c) above seem justifiable since, for the uncompressed beams, momentum spreads are of order 10^{-4} while angular spreads are of order 10^{-3}. We have not attempted to consider the situation during compression in the rings because of significant perturbations to the lattice parameters by space charge effects and because the compression stage occurs over a relatively short time scale (60-100 turns, 400-600 μs).

To obtain an accurate assessment of the problem, complete calculations (numerical simulation?) should be performed using realistic 6-D distributions, including space charge effects, combined with the cross-section for loss (ionization may leave one particle within the ring acceptance) as a function of relative ion velocity.

REFERENCES

1. F.E. Mills, ERDA Summer Study of Heavy Ions for Fusion, LBL 5543, p. 79, (1976).
2. M. Cornacchia, G.H. Rees. These proceedings.
3. K.F. Dunn et al, 1979 J. Phys. B: Atom. Molec. Phys., Vol. 12, L623, (1979).

BEAM SCRAPING PROBLEMS IN STORAGE RINGS; THE BLACK CLOUD

Lawrence W. Jones
University of Michigan

1. INTRODUCTION

The heavy ion, multi-GeV drivers for inertial confinement fusion are being designed to produce beams of an energy, power, and specific ionization sufficient to raise matter to thermonuclear temperatures. The magnitude of these parameters is so far beyond current experience that some problems raised warrant careful scrutiny. In particular, the consequence of some fraction of the beam lost on storage ring inflection septa, extraction channels, and beam-defining collimators seems potentially very serious. Unless carefully contained, a beam halo can easily vaporize the best refractory materials, and the resulting vapor cloud will interact destructively within microseconds with the following beam. The limits on beam flux which may be so lost for particular examples are orders of magnitude below current experience.

2. BEAM AND SEPTUM PROPERTIES

As examples of the problems in this area, consider the parameters of a 10 GeV, 3-MJ $^{238}U^{+1}$ linac-storage ring driver[1]. The critical quantities, referenced to the linac output, are:

T = 10 GeV
I_{inj} = 0.30 Amperes from linac injector
P_{inj} = 3.0 GW
E = 3MJ total beam energy
$N = 1.875 \times 10^{15}$ U^{+1} ions finally accumulated
$\frac{\varepsilon_{inj}}{\pi} = 1.5 \times 10^{-6}/\beta\gamma$ m linac injector emittance
$\frac{\varepsilon_{SR}}{\pi} = 60 \times 10^{-6}$ m storage ring emittance
τ = 5.9 μsec period of revolution in S.R.
n_t = 64 injected turns into each of 3 S.R.
t = 380 μsec total time of injection into each S.R.

We will assume that, where lost, the beam strikes a tungsten surface. The relevant properties of tungsten are:

density	$\rho \simeq 20$ g/cm^2
atomic mass number	A = 184
specific heat	$c \cong 0.145$ J/g
thermal conductivity	$1.50 \frac{W}{cm^\circ K}$
melting temperature	T = 3653°K
latent heat of fusion	ℓ = 190 J/g

From this may be derived several quantities of interest assuming that the boiling point is close to the melting point and the latent heat is small compared to the sensible heat.

Range of 10 GeV U^{+1} in W: $\delta x = 0.2$ g/cm^2 = 0.01 cm

Energy to melt W: $u = c\Delta T + \ell = 680$ J/g
$u\delta x = 140$ J/cm^2

Black body radiation of W at 4000°K: $p = \sigma T^4 = 1450$ W/cm^2

Thermal conductivity of W over ΔT = 3000°K, Δx = 0.1 cm: $p = k \frac{dT}{dx} = 45$ kW/cm^2

The handbook vaporization temperature and latent heat for tungsten are given at atmospheric pressure: it is my understanding that the vaporization temperature in vacuum is close to the melting temperature, and that the latent heat there is small. In what follows we will assume a vaporization temperature of 4000° K and a total heat required to raise room-temperature tungsten to vapor (in vacuum) at 4000°K as 750 J/g = 150 J/cm^2.

(1) N.M. King. These Proceedings.

3. ILLUSTRATION OF THE PROBLEM

The scope of the problem is recognized when these values are combined with the beam parameters. Thus, if all of the beam were dumped into tungsten the 3MJ is sufficient to vaporize 4 kg of W; the full beam rate would vaporize tungsten at a rate of 4 metric tons per second. In order to dissipate this energy by radiation, the full beam energy would need to be spread (uniformly) over an area of tungsten of 165 m^2. Since the beam is absorbed in a thin surface skin of thickness 100 sine microns (θ is the angle between the beam and the normal to the the surface), it seems improbable that this energy can be removed by conduction, e.g. by water cooling of septa or slits. The effect of thermal conductivity will be to increase the effective depth over which the ionization energy is deposited beyond the 0.01 cm nominal range. However the linac beam power is so high (3 GW) that thermal conductivity cannot dissipate the temperature build-up from even a small fraction of the beam. Thus the means for dissipating any beam energy lost are assumed to be: (a) the sensible heat to raise W to the boiling point (it could be cooled between pulses), (b) radiation from the hot tungsten, and (c) ablation or vaporization from the surface. In the case of this device, this ablation can cause immediate destruction of the beam. The following argument illustrates this concern.

4. EFFECTS OF SEPTUM VAPORIZATION

Consider that the full beam falls on a septum of vertical height y, and vaporizes tungsten at a rate of 4×10^6 g/sec. At T = 4000°K, the rms x-component of velocity of the tungsten ions will be 425 m/sec; the density of tungsten vapor atoms close to this septum will be

$$\rho = \frac{4 \times 10^6 \, n_a/A}{(2)y \langle v_x \rangle} = \frac{3.1 \times 10^{23}}{(2)y} \ \frac{\text{atoms}}{\text{cm}^2} ,$$

where y is the vertical height of the septum, n_a is Avogadro's number, A = 184 for W, and the factor of two is appropriate if the vapor can fly off to ± x, rather than in one direction only. The limited data available on charge exchange cross sections indicate $\sigma \sim 4 \times 10^{-16}$ cm^2 for $C_s^{+1} + C_s^{+1}$: singly charged ions of U, etc. probably have charge-changing cross sections on neutral, heavy atoms at high energy of at least 10^{-16} cm^2. This suggests that, for a 1 cm septum which may vaporize to both sides, the fraction of the incident beam which, when lost on a septum, will develop a vapor cloud equal to an ion interaction mean free path is:

$$f = \frac{2}{3.1 \times 10^{23} \times 10^{-16}} = 6.5 \times 10^{-8}$$

This vapor would propagate across the vacuum chamber at a rate $\langle v_x \rangle$, or 0.4 mm/μsec. In the time it takes to fill the storage ring (380 μsec) this cloud would propagate 16 cm. Of course the high-energy tail of the thermal distribution would propagate correspondingly faster. The conclusion I draw from this simple calculation is that one must so engineer the beam and the various septa so that any beam lost is absorbed by the heat capacity of the loss target and/or radiated as black body radiation. Even in the linac or transfer line, a vapor cloud will develop fast enough to destroy following beam in a 1 cm^2 aperture in several microseconds if $\gtrsim 10^{-6}$ of the beam scrapes and leads to ablation. If the loss results in sputtering of metal at epithermal velocities, the vapor density is correspondingly reduced. If a lighter element is considered (beryllium or titanium) the heat capacity per gram is greater, but the number of atoms vaporized per unit energy may also be greater. As $\langle v_x \rangle$ will also be greater the problem is qualitatively similar.

5. TOLERABLE BEAM LOSS

The problem of accommodating the energy of the scraped beam on a storage ring inflection

septum may be restated as follows (for the numerical case under discussion). The heat capacity of the tungsten surface area normal to the beam of 150 J/cm^2 while the total beam energy is 3 x 10^{6}J. There may be n_{sr} storage rings. The fraction of beam which may be lost in each ring, f, on a septum of projected area A cm^2 is given by

$$f \lesssim \frac{150 n_{sr}}{3 \times 10^6} A \cong 5 \times 10^{-5} n_{sr} A.$$

If there are 3 storage rings, and if the septum area is 1 cm x 1 mm, the maximum loss f = 1.6 x 10^{-5}.

It may be noted that this beam would fall onto the septum with a power of 50 kW; even with the septum inclined at 5° (so that the energy is spread over 1 cm^2) the beam power is still 30 times that which could be removed by radiation.

The energy per unit area on the septum may be related to the emittance of the linac and the betatron wavelength (or, more explicitly, β_x and β_y). For our example, the linac emittance at 10 GeV is 0.5 cm rad, so that the beam area would be 5 cm^2 for $\beta_x = \beta_y = 33$ m. Thus the beam energy density, for three storage rings, is 200 kJ/cm^2. As the septum can only tolerate $\lesssim$ 150 J/cm^2, the beam halo at the septum must be less dense than the central beam by a factor of 1330. This is a less frightening factor than 10^5 (cited above). The problem may be made to appear even less severe if a larger number of storage rings and larger β values are considered. Thus, if there are 10 storage rings and β = 50 m, the beam energy density in each ring is only 38 kJ/cm^2, so that the halo density need only be less than the central beam density by a factor of 250.

In conclusion, we believe that this problem merits serious study. This limitation will affect the choice of storage ring parameters and perhaps the number of storage rings.

The diffusion equation for the temperature vs. time and depth for the one dimensional problem should be explored with the proper parameters for tungsten and other candidate materials (Ta, Mo, Ti, Be) considering heat capacity, conduction, and radiation.

The targets of high-power klystrons and x-ray tubes surely are limited by these same considerations, and there is a body of engineering experience in this connection which would be instructive.

BUNCH COMPRESSION IN HEAVY ION FUSION STORAGE RINGS

M. Cornacchia (BNL) and G. H. Rees (Rutherford Laboratory)

1. INTRODUCTION

Bunch compression in the proposed heavy ion fusion storage rings results in large transverse and longitudinal space charge forces. In this note parameters are derived for the bunch compression in three reference designs and aspects of the transverse and longitudinal motion are discussed.

Transverse and longitudinal space charge forces on an ion depend on both the transverse and azimuthal co-ordinates of the ion in the bunch. It appears therefore to be insufficient to treat the transverse and longitudinal motions separately in the non-adiabatic compression and that a detailed evaluation of the problem requires elaborate numerical simulation or an experimental test facility.

2. REFERENCE STORAGAE RING DESIGNS

Parameters used for the three reference designs are:

	CASE A	CASE B	CASE C
Ion	U^+	U^+	U^+
Kinetic Energy	5 GeV	10 GeV	10 GeV
Target Bunch duration	20 ns	40 ns	70 ns
Initial Bunch duration	1 μs	2 μs	3.5 μs
Revolution period	6 μs	6 μs	7 μs
Bunches/ring	6	3	2
Bending radius (B = 5T)	31.6 m	44.9 m	44.9 m
Mean radius	59.8 m	83.1 m	97.1 m
Emittance/π	60×10^{-6} rad m	37.5×10^{-5} rad m	60.0×10^{-6} rad m
I_{DC} ($\Delta\nu$=1/4)	18 A	23.3 A	32 A
50 I_{DC}	900 A	1165 A	1600 A
Number of bunches	24 (or 42)	12	18
Number of rings	4 or 7 ($\Delta\nu$ = 1/7)	4	9
Particles/ bunch, N	1.12 or 0.64×10^{14}	2.91×10^{14}	7×10^{14}
Energy in target	> 1 MJ	> 3 MJ	> 10 MJ
P(TW)	100 TW	150 TW	300 TW

The total bunch compression of a factor 50 is assumed to consist of a factor 7 in the storage rings and a factor 50/7 in the transport line to the target. The maximum momentum spread allowed at the target has been specified as $\Delta p/p = \pm 1\%$ and this infers, in the absence of dilution, a momentum spread for the unbunched storage ring beam of $\Delta p/p = \pm 2B_f \times 10^{-4}$ where B_f is a final bunch shape factor (approximately 2/3).

3. TRANSVERSE MOTION DURING COMPRESSION

Reference design B will be used to indicate the scale of the effect of the transverse space charge forces on the betatron motion. Ring B has a mean radius of 83.1 m and the following lattice design was assumed:

Betatron tunes ν_x, ν_y	8.3, 8.3
Number of cells	28
Cell length	18.65 m
Integrated quadrupole strength $\int g d\ell$	41.5 T
Peak value of beta-function, $\hat{\beta}$	33.1 m
Peak value of dispersion function, $\hat{\eta}$	2.2 m
Gamma transition, γ_t	7.7
Minimum value of beta-function, $\check{\beta}$	4.0 m
Minimum value of dispersion function, $\check{\eta}$	1.0 m

At a bunch compression of 7 and an assumed bunch shape factor of 2/3 the resulting bunching factor B = 0.0952 = 1/10.5 for a uniform transverse density.

The parameters above have been used in a program of A. Garren that solves the equation of the betatron envelope in the presence of linear transverse space charge forces. The program calculates the equivalent modifications to the lattice functions, and for B = 1/10.5 the following results were found (when B = 1 corresponded to $\Delta\nu = 0.25$):

$\nu = 8.3 \rightarrow 6.05$
$\hat{\beta}_x = 33.1 \rightarrow 38.6$ m
$\check{\beta}_x = 4.0 \rightarrow 6.23$ m
$\hat{\eta} = 2.2 \rightarrow 4.0$ m
$\check{\eta} = 1.0 \rightarrow 1.85$
$\gamma_t = 7.7 \rightarrow 5.6$

Results for other values of $\overline{B}$ are given in Fig. 1.

The dependence of the lattice functions on the bunching factor, depicted in Fig. 1, results effectively in a spread of values of these functions along the bunch, due to the longitudinal variation of the space charge density. Since different particles have different optics, it is impossible to completely match the beam ejected from the storage ring into the transfer line. The result is a blow-up of emittances. For the case B under consideration the maximum increase in horizontal betatron amplitude due to the dispersion mismatch is, for a bunching factor

$\overline{B} = \frac{1}{10.5}$:

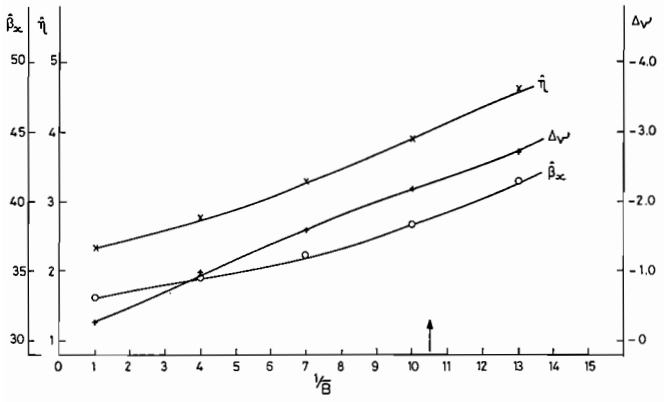

FIG.1. CHANGE IN LATTICE FUNCTIONS FOR CASE B (ν=8.3)

$$\Delta x_{disp} \simeq (\eta_1 - \eta_0) \cdot \frac{\Delta p}{p} = (4 - 2.2) \times 4 \times 10^{-3} = 7.2 \text{ mm},$$

where

η_0 = maximum value of the unperturbed dispersion function in the ring = 2.2 m

η_1 = dispersion in presence of space charge = 4 m

$\frac{\Delta p}{p}$ = maximum momentum deviation at the end of the compression = $\pm 4 \times 10^{-3}$. (This value is discussed in Section 4).

The mismatch of the β functions also introduces an increase in the horizontal and vertical betatron amplitudes of the order of

$$\Delta x_{bet} = \sqrt{\epsilon_0 \beta_1} - \sqrt{\epsilon_0 \beta_0} = \sqrt{37.5 \times 38.5} - \sqrt{37.5 \times 33} = 2.8 \text{ mm},$$

where

ϵ_0 = injected beam emittance = $37.5\pi \times 10^{-6}$ rad m

β_0 = unperturbed β function = 33 m

β_1 = β function in presence of space charge = 38.5 m.

It is debatable whether the blow-up of betatron amplitudes discussed above should be added linearly to the unperturbed amplitudes of the injected beam in order to estimate the resultant emittance blow-up. If we do so, we find, for the relative emittance increase,

$$\frac{\Delta\epsilon}{\epsilon_0} = \frac{x_1^2 - x_0^2}{x_0^2} = \frac{45.2^2 - 35.2^2}{35.2^2} = 0.65 ,$$

where x_1 and x_0 are the maximum perturbed and unperturbed betatron amplitudes.

If, instead, we add the amplitude increase quadratically, the relative emittance blow-up is only 4.8%. A statistically significant analysis of this effect would require further study; here, we shall arbitrarily settle for

approximately half the value calculated from the linear addition of betatron amplitudes, and assume:

$$(\Delta\epsilon/\epsilon_0)_{\text{mismatch}} = 30\% \ .$$

Figure 1 shows that a considerable fraction of particles (those in the higher charge density region) will cross two integer and four 1/2 integer resonances during the compression. We estimate first the blow-up in crossing the integer resonance.

For N random dipole errors in the ring, the oscillation amplitude increase is given by (r.m.s value):

$$\left\langle \frac{d\bar{x}}{d\theta} \right\rangle = \frac{\sqrt{N}\cdot \ell_{dip}\sqrt{\beta_{av}}}{2\sqrt{2}\pi\rho} \left\langle \frac{\Delta B}{B} \right\rangle \sin\phi = \frac{\sqrt{\beta_{av}}}{\sqrt{2N}} \left\langle \frac{\Delta B}{B} \right\rangle \sin\phi \ , \qquad (1)$$

where $\bar{x}$ = normalized maximum oscillation amplitude, horizontal or vertical (i.e. max. ampl. $\div \sqrt{\hat{\beta}}$).

θ = circumferential angle around the accelerator, in radians.

ℓ_{dip} = length of a single dipolar perturbation.

β_{av} = average value of horizontal or vertical β function at the peturbation location.

ϕ = betatron phase angle at a reference point in the ring.

ρ = bending radius.

$\left\langle \frac{\Delta B}{B} \right\rangle$ = r.m.s. value of random dipole errors.

In equation (1), we have made the simplifying assumption that the sources of errors come exclusively from the main dipoles. We assume that the tune change occurs linearly. Thus the non-integer part of the tune at the reference point in the ring is given by $\nu_f = \nu_{of} + A\theta$ and equation (1) becomes:

$$\left\langle \frac{d\bar{x}}{d\theta} \right\rangle = \frac{\sqrt{\beta_{av}}}{\sqrt{2N}} \left\langle \frac{\Delta B}{B} \right\rangle \sin\left(\nu_{of}\theta + \frac{A\theta^2}{2} + \phi_0\right) \ , \qquad (2)$$

where ϕ_0 is a constant.

The expectation value of the normalized betatron amplitude after crossing is:

$$\langle \bar{x} \rangle \text{ final} = \frac{\sqrt{\beta_{av}}}{\sqrt{2N}} \left\langle \frac{\Delta B}{B} \right\rangle \int_{\theta_c}^{\theta} \sin\left(\nu_{of}\theta + \frac{A\theta^2}{2} + \phi_0\right) d\theta \ . \qquad (3)$$

If the points θ_0 and θ are chosen well away from the resonance, the integral can be approximated by:

$$\sqrt{2\pi/A}\, \sin\left[\phi_0 - (\nu_{of}^2/2A) + (\pi/4)\right]$$

Thus, the final amplitude after crossing for the most unfavorable phase is:

$$\langle \bar{x} \rangle_{\text{final}} \simeq \frac{\sqrt{\beta_{av}}}{\sqrt{2N}} \left\langle \frac{\Delta B}{B} \right\rangle \sqrt{\frac{2\pi}{A}}$$

It is indicative to relate the residual dipole field perturbation $\langle \Delta B/B \rangle$ to a realistic value of the closed orbit distortions after correction for the unperturbed working point ν_0. The expectation value of the orbit distortion is given by, in normalized amplitude:

$$\left\langle \bar{x}_{co} \right\rangle = \frac{\sqrt{\beta_{av}}}{\sqrt{2}\ \sin \pi\nu_0} \frac{\pi}{\sqrt{N}} \left\langle \frac{\Delta B}{B} \right\rangle \ . \qquad (5)$$

Expressed in terms of the above closed orbit error, equation (4) becomes:

$$\langle \bar{x} \rangle \text{ final} = \left\langle \bar{x}_{co} \right\rangle \sin \pi\nu_0 \ \sqrt{2/\pi A} \ . \qquad (6)$$

Then, for $\left\langle \bar{x}_{co} \right\rangle$ assume 1 mm $\div \sqrt{\hat{\beta}}$.

In estimating the rate of tune change, we ignore the sinusoidal variation of the bunch length and take the average over the whole tune-span. This approximation is justified by the fact that the integer resonance is crossed twice and it is not possible to choose the fastest rate of tune change for both crossings. We choose, therefore $A = (8.3 - 6.1)/(2\pi \times 68) = 0.0051\ \text{rad}^{-1}$ where the number 68 is the number of bunch rotations during compression: see Section 4. Eqn. (6) gives the final normalized betatron amplitude after one crossing of the integer resonance. For two crossings, the value increases by $\sqrt{2}$, and we obtain:

x_{final} (not normalized) $= \sqrt{\hat{\beta}}\ \langle \bar{x} \rangle_{final} = 12.8$ mm

For the half-integer resonance we first calculate the stop-band half-width[1]:

$$\langle \delta\nu \rangle = \frac{1}{4\pi\ B\rho} \left[\sum_i \beta^2 x_i \right]^{1/2} \langle \Delta g \rangle\ \ell_q \ ,$$

where $\langle \Delta q \rangle$ is the r.m.s. of the gradient errors in the quadrupole of length ℓ_q. Assuming, for the lattice under consideration:

$$\left\langle \frac{\Delta g}{g} \right\rangle = 10^{-3} \ ; \ \frac{g\ell_q}{B\rho} = 0.18\ m^{-1}, \ g = \text{main quadrupole gradient},$$

$$\langle \delta\nu \rangle = \frac{0.18}{4\pi} \left[\sum_i \beta^2 x_i \right]^{1/2} \left\langle \frac{\Delta g}{g} \right\rangle \approx \frac{0.18}{4\pi} \sqrt{28} \times 33 \times 10^{-3} = 0.0025 \ .$$

The amplitude blow-up after crossing is given by:

$$\frac{x}{x_0} = \exp \left[\frac{2\pi\delta\nu}{(2\Delta\nu_r)^{1/2}} \right] \ ,$$

where x_0 = initial betatron amplitude

$\Delta\nu_r$ = average tune change per turn $= \frac{8.3 - 6.1}{68} = 0.032$.

From eqn. (6) we find the blow-up per crossing:

$$\frac{x}{x_0} = 1.06 \ .$$

For 4 crossings, the amplitude growth increases by $\sqrt{4}$:

$$\left(\frac{x}{x_0} \right)_{final} = 1.12 \ .$$

If we calculate the relative emittance blow-up, assuming that the betatron amplitudes are added linearly, we find:

For integer resonance: $\frac{\Delta\epsilon}{\epsilon_0} = 90\%$,

For $\frac{1}{2}$-integer resonance: $\frac{\Delta\epsilon}{\epsilon_0} = 26\%$.

(1) C. Bovet et al., A Selection of Formulae and Data Useful for the Design of AG Synchrotrons, CERN/MPS-SI/Int. DL 70/4, (1970).

For the integer resonance, the linear addition of amplitudes is justified by the fact that there is a coherent displacement of a cross-section slice of the beam: the 90% emittance blow-up concerns only that fraction of the beam which crosses the resonance twice, which is also, unfortunately the region with higher particle density. For the half-integer resonance, the blow-up is incoherent and a quadratic increase is probably more statistically realistic, which makes this resonance considerably less dangerous than the integer resonance. Finally, the magnetic field quality we have assumed for the dipole and quadrupole errors is, of course, subject to discussion.

The change in the bunching factor as the bunch compression proceeds is shown in Fig. 2 for the reference Case B.

The magnitude of the effects indicates that it may subsequently be necessary to reduce somewhat the number of particles per ring and increase the number of rings.

4. LONGITUDINAL MOTION DURING COMPRESSION

The reactive impedance due to the longitudinal space charge forces is:

$$\frac{Z}{n} = -\ jgZ_0/2\beta\gamma^2 \ . \qquad (9)$$

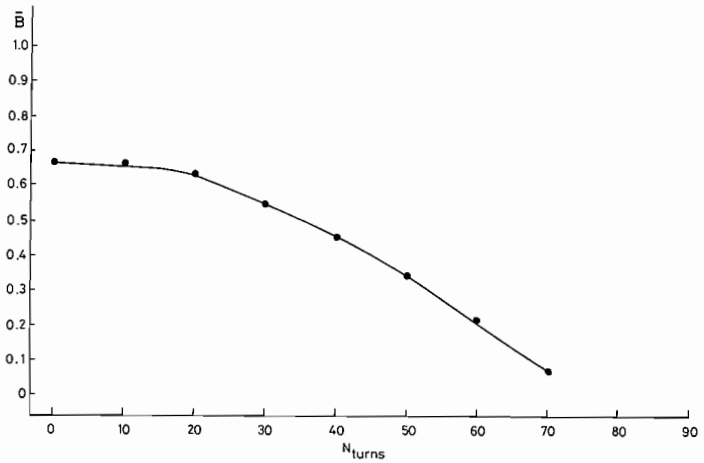

FIG.2. CASE B: BUNCHING FACTOR Vs NUMBER OF COMPLETED REVOLUTIONS

Assuming a value g = 2

$$\frac{Z}{n} \text{ (at 5 GeV)} = -j\,(1728)\Omega$$

$$\frac{Z}{n} \text{ (at 10 GeV)} = -j\,(1189)\Omega \quad .$$

The equivalent negative inductance values are:

	Case A	Case B	Case C
L =	−1.650 mH	−1.134 mH	−1.325mH .

The large values of Z/n and L are a consequence of the low β-values. To estimate the magnitudes of the longitudinal space charge forces, the storage ring bunches are assumed to have a parabolic form in the azimuthal direction so that the maximum energy gain or loss per turn is:

$$eV_{sc} = \pm\, 3\, NeL/2T^2, \qquad (10)$$

where T is half time duration of the bunch. The energy gains/losses per turn for the three reference designs are:

	Case A	Case B	Case C
−L	1.650 mH	1.134 mH	1.325 mH
N	0.64×10^{14}	2.91×10^{14}	7×10^{14}
T (min)	71.4 ns	142.8 ns	250 ns
eV_{sc}(max)	±4.98 MeV	±3.89 MeV	±3.57 MeV

The maximum levels are achieved just prior to ejection. The forces vary linearly along the extent of the bunch, being zero at the center. The energy gains will differ from the above values for bunch shapes other than parabolic and the variation with position will then become non-linear.

For rapid bunch compression it is necessary to compensate for the longitudinal space charge forces and to provide additional focusing fields. A closed curve in $(\Delta p/p, \phi)$ space containing all the beam particles may be made to rotate and reach a minimum phase extent after a quarter of a synchrotron period. For a linear rotation, the RF voltage waveform must be of a saw-tooth form and not sinusoidal. The bunch is extracted before reaching the quarter wavelength point to allow further rotation and compression in the external transfer line to the target.

When the RF waveform is of a saw-tooth form, the number of rotations of the bunch in the ring during a quarter of a synchrotron period is given by n_q:

$$n_q = \pi/[4(\gamma^{-2} - \gamma_t^{-2})\, h\, (\Delta p/p)]\ ,$$

where h is the harmonic number of the saw-tooth wave (= no of bunches),

γ_t is gamma transition, and

$(\Delta p/p)$ is the peak momentum spread at the quarter synchrotron point.

The peak voltage of the saw-tooth waveform for the rotation is given (when the space charge forces are compensated separately) by V:

$$eV = \pm\, 2E\pi^2\beta^2/(\gamma^{-2} - \gamma_t^{-2})\, h\, (4n_q)^2 \quad . \qquad (12)$$

E is γE_0 where E_0 is the rest energy of the ion.

V is proportional to $h\,\beta^2\,(\Delta p/p)^2\,(\gamma^{-2} - \gamma_t^{-2})$.

Parameters for the three reference cases are:

	Case A	Case B	Case C
h	6	3	2
f_o	166.7 kHz	166.7 kHz	142.8 kHz
hf_o	1 MHz	500 kHz	285.7 kHz
γ_t	5.54	7.7	9.0
$\Delta p/p$	$\pm4\times10^{-3}$	$\pm4\times10^{-3}$	$\pm4\times10^{-3}$
n_q	35.4	72.8	108.7
eV	±1.76 MeV	±1.69 MeV	±1.13 MeV
n	33	68	102

Here n is the actual number of bunch rotations in the storage ring and is given approximately by:

$$n = 2n_q \cos^{-1}(C^{-1} - D^{-1})/\pi$$

where C is the bunch compression factor 7, and D is the ratio of the peak $\Delta p/p$ after and before compression (a factor of 20 for $\Delta p/p = \pm 4 \times 10^{-3}$).

The value of $\Delta p/p = \pm 4 \times 10^{-3}$ has been assumed instead of the maximum allowed in the transfer line ($\pm 10^{-2}$) for two reasons:

a) to limit the amplitude of the saw-tooth RF waveform,
b) to limit one of the emittance blow-up effects discussed in Section 3.

The choice of $\Delta p/p = \pm 4 \times 10^{-3}$ infers that additional compression is undertaken in the transfer line to the target station. As an example parameters are given for Case B, assuming an external transfer line of length twice the circumference of ring B and the momentum spread increasing to $\pm 10^{-2}$.

T(1/2 bunch duration)	142.8 ns (initially)	20 ns (at target)
Space charge compensation	± 7.45 keV/m	± 380 keV/m
Additional compression	± 330 keV/m	± 46.2 keV/m,

where energy gains quoted correspond to the particles at the tail and head of the bunch.

At the end-point of compression in the storage ring the ratio of the saw-tooth compression forces to the space charge forces is:

	Case A	Case B	Case C
Ratio	5.0 %	6.2 %	4.5 %

Thus an error in the space charge compensation can readily lead to incorrect rotation of the bunch. Such an error may arise if the bunch shape is not of the assumed parabolic form, a probable event since the compression is non-adiabatic. For this reason it appears advantageous to compensate for the longitudinal space charge forces by including passive inductive cavities in the ring to cancel the equivalent negative inductance of the space charge forces. For Case B this would infer a total inductance of 1.134 mH.

A possible system for Case B would have 378 ferrite loaded cavities, each 3μH, with a maximum voltage per unit of ± 10 kV. The lowest cavity resonance would have to be > 15 MHz and all the resonances would have to be heavily damped. Ferrite Q values in the frequency range up to 15 MHz can be of the order 100 so that the total resistive component of $\frac{Z}{n}$ due to the inductive cavities may be approximately 10 Ω provided it proves possible to damp adequately the resonant modes.

The RF system to provide the saw-tooth waveform has received insufficient study. It may be adequate to approximate the saw-tooth by adding an appropriate number of harmonics, and if this is so, the later stages of the compression may be more readily controlled by switching to one of the higher harmonic RF systems at a lower peak voltage level. The effective $\frac{Z}{n}$ values for the individual cavities may be reduced by feed-forward techniques and by damping of higher modes. The limit to the reduction in $\frac{Z}{n}$ from a fed-forward system is set by the system-gain stability. Because of the peak beam current levels involved, the gain may have to be reduced as the compression proceeds. Without further sutdy of the RF systems and the storage rings it is not possible to say if there is adequate straight section space for the RF. There is probably not for the reference Case A which has the smallest ring circumference and largest RF requirements.

Longitudinal emittance dilution in the bunch compression is very important to evaluate since in the reference cases there is no allowance at all for any dilution. The most likely cause of emittance dilution is the effect of the variation of the longitudinal space charge forces across the transverse dimensions of the beam. In the derivation of the longitudinal space charge forces it has been assumed that the

parameter g, is a constant equal to 2. The exact expressions for g depend on the chamber dimensions and of the transverse density distribution in the beam.

For a circular beam centered in a circular chamber with a uniform transverse density distribution:

$$g = 1 + 2\,\ell n\left(\frac{b}{a}\right) - \left(\frac{r}{a}\right)^2 \qquad (14a)$$

where b is the chamber radius, a the beam radius and r the individual particle radius.

For a parabolic density distribution, the formula is modified to:

$$g = \left(\frac{3}{2}\right) + 2\,\ell n\left(\frac{b}{a}\right) - 2\left(\frac{r}{a}\right)^2 + \frac{1}{2}\left(\frac{r}{a}\right)^4 . \qquad (14b)$$

For an elliptical beam in an elliptical chamber, with the elliptical contours confocal, and for a uniform transverse density distribution:

$$g = \frac{2b_1b_2}{b_I^{\,2} + b_2^{\,2}} + 2\,\ell n\left(\frac{b_1 + b_2}{a_1 + a_2}\right) - G \ , \qquad (14c)$$

where $$G = 2\left(\frac{2b_1b_2}{b_1^{\,2} + b_2^{\,2}} - \frac{a_2}{a_1}\right)\left(\frac{x^2}{a_1^{\,2} - a_2^{\,2}}\right) + 2\left(\frac{a_1}{a_2} - \frac{2b_1b_2}{b_1^{\,2} + b_2^{\,2}}\right)\left(\frac{y^2}{a_1^{\,2} - a_2^{\,2}}\right) ,$$

(x,y) are particle transverse co-ordinates, (a_1, a_2) are semi-axes of the beam elliptical cross-section, and (b_1, b_2) are semi-axes of the chamber elliptical cross-section.

All three expressions for g indicate a large variation of the longitudinal space charge forces across a transverse section of beam. For example, in the first expression, eqn. (14a), g varies from

$$g = 1 + 2\,\ell n\,\frac{b}{a} \qquad \text{at } r = 0$$

to $$g = 2\,\ell n\,\frac{b}{a} \qquad \text{at } r = a$$

Since the space charge forces are larger than the saw-tooth compression forces there must be a pronounced effect on the bunch compression.

Numerical simulation is required to evaluate the problem. A realistic simulation must include both longitudinal and transverse motions, and at present it is unknown if realistic 3-D tracking programs can be developed.

5. CONCLUSIONS

1) Large transverse and longitudinal space charge forces are present in the beam during the bunch compression in the reference storage rings. Some dilution in the transverse and longitudinal emittances must therefore be expected.

2) For the transverse motion, dilution occurs due to crossing of betatron resonances and mismatch in transfer to the external beam line. For the Case B considered the transverse emittance/π was assumed to be 37.5×10^{-6} rad m and it is probable that a larger emittance could be tolerated in the target chamber for this case. Emittance dilution of the order 2 has been estimated but the estimates are crude and should be checked by numerical simulation.

3) Some dilution in the longitudinal emittance must be expected because of the variation of the longitudinal space charge forces across the transverse dimensions of the beam; thus it is not possible to have exact compensation of the longitudinal forces for all beam particles. It is important to evaluate the magnitude of the dilution because there are restrictions on: $\Delta p/p$ in the transfer line (transport difficulties for $\Delta p/p > \pm 1\%$) and $\Delta p/p$ at injection in the storage ring (longitudinal instability considerations). Longitudinal motion is dependent on the transverse and

longitudinal beam distributions and a realistic numerical simulation of bunch compression must include both longitudinal and transverse motions.

4) It is desirable to restrict the maximum momentum spread in the storage ring (to $\pm 4 \times 10^{-3}$ just prior to extraction) in order to limit the size of the RF system for bunch compression and to limit the transverse emittance dilution at transfer to the beam line.

5) It appears to be advantageous for the RF system design to have two RF systems, one to compensate for the longitudinal space charge forces and one to provide the bunch rotation/compression. The system suggested for space charge compensation is to use a large number of passive ferrite loaded cavities (whose resonant frequency is well above the harmonic components of interest in the beam current). The RF system for compression has ideally a saw-tooth waveform.

6) The effects of non-linear transverse density distributions have not been considered but could be important.

7) The compression leads to a large variation of the γ_t function along the bunch which will contribute to the dilution of the longitudinal emittance.

DESIGN STUDY OF AN ACCELERATOR FOR HEAVY ION FUSION

T. Katayama, A. Noda, N. Tokuda and Y. Hirao
Institute for Nuclear Study, University of Tokyo,
Tokyo, JAPAN

ABSTRACT

Design of a demonstration accelerator for heavy ion fusion based on a synchrotron system is briefly described. The proposed complex system of injector linac, rapid cycling synchrotron and five accumulation rings can produce a peak current 1.6 kA, peak power 32 TW and total energy 0.3 MJ. Investigations of the intrabeam scattering give a lifetime of the beam longer than the fusion cycle time of 1 sec.

1. INTRODUCTION

In recent years interest in high energy heavy ions has been growing in various fields of science and applications. In Japan an accelerator complex responding to these demands has been proposed at INS, University of Tokyo; this is called the NUMATRON[1, 2] and it should provide heavy ions up to uranium in an energy range of 0.1 ~ 1.3 GeV per nucleon. The main feature of the accelerator is to provide a high intensity heavy ion beam by the use of two synchrotrons and an injection method which combines the techniques of multiturn injection and RF stacking.

Here we will present the design of the demonstration synchrotron-based accelerator complex for fusion power generation: it is not directly aimed at producing practical fusion power plant, but is a first step to show the feasibility of heavy ion fusion.

General requirements for the accelerator are given in Table 1.

Table 1 General Requirements for the Demonstration Accelerator

Total energy	0.3 MJ
Peak Power	32 TW
Beam pulse width	10 ns
Number of particles	1×10^{14}
Peak Current	1.6 kA
Energy deposition	6.8 MJ/g
Repetition rate	1 Hz

2. OUTLINE OF THE ACCELERATOR

The accelerator consists of two ion sources followed by 1 MV Cockcroft-Walton generators, Wideröe linacs, Alvarez linacs, rapid cycling synchrotron and five accumulation/compression rings, from which 20 beam bunches are extracted simultaneously and are carried to a reactor chamber located at the center of the accumulators. Total beam intensity is 1×10^{14} within a time of 10 ns, which corresponds to 32 TW total peak power, 300 kJ total energy and 1.6 kA peak current. Throughout the design of the accelerator, xenon ions have been assumed because their intensity and characteristics at the ion source stage are well understood at present.

3. INJECTOR LINAC

From the point of view of acceleration efficiency, high charge state of the ion is preferable. However, since the available intensity of high charge state ions is low, in the present paper a Xe^{2+} beam is assumed at the ion source stage.

The Xe^{2+} beam is accelerated by the 1 MV Cockcroft-Walton and is injected into the first π-3π mode Wideröe linac. The expected intensity from this injector system is 5 particle mA[3], and two such systems are funneled to obtain an intensity of 10 particle mA. Kinetic energy and velocity at the input of the first Wideröe linac are T_i = 15.15 keV and β_i = 0.57%,

respectively, and the structure of the Wideröe linac is almost the same as the one designed for the NUMATRON project. After acceleration to 400 keV per nucleon by the two π-3π mode Wideröe linacs, the xenon beam is stripped by a gas stripper to the equilibrium charge state of q = 4. The fraction in the equilibrium charge state at this stripping energy is estimated to be 0.2[1]. The resulting 2 particle mA beam is accelerated to 20 MeV per nucleon by the π-3π and π-π mode Wideröe linacs and the Alvarez linac. The total length of linacs is about 250 m.

If the intensity of Xe^{4+} at the ion source stage were sufficiently high, say 2 particle mA, the injector system would be much simpler.

4. RAPID CYCLING SYNCHROTRON

Basic requirements for the synchrotron are as follows:

1. Xe^{4+} beam is injected at the energy of 20 MeV/u and should be accelerated up to around 150 MeV/u.

2. The output intensity of the synchrotron should amount to 1 x 10^{14} particles per second.

Linac beam is injected into the synchrotron by the multiturn injection method, 10 turns horizontally by 5 turns vertically. Assuming the dilution factor to be 2, the emittances after the multiturn injection are $100\pi \times 10^{-6}$ m rad in horizontal phase space and $50\pi \times 10^{-6}$ m rad in the vertical one.

The space charge limit in the ring is simply given by

$$N = \frac{2\pi\Delta\nu}{Br_p} \left(\frac{A}{q^2}\right) \varepsilon\beta^2\gamma^3 , \qquad (1)$$

where B is a bunching factor, r_p is the classical proton radius 1.533 x 10^{-18} m and ε is an emittance. If we take the bunching factor as 10, the space charge limit at injection energy is calculated to be 2 x 10^{12} particles/pulse. In order to attain the intensity required by the fusion program, say 1 x 10^{14} particles/s, the synchrotron should be a rapid cycling one with a repetition rate of 50 Hz.

The required peak current from the Alvarez linac is given by

$$I_{peak} = \frac{N \times e}{50 \times \tau_{rev}} = 0.89 \text{ mA}, \qquad (2)$$

which is obtained easily by the present technique of heavy ion linacs.

From considerations of magnetic rigidity and attainable maximum field in normal bending magnets, the parameters given in Table 2 are suitable for the present design.

The RF voltage required for the acceleration of the beam is given by

$$V \sin\phi_s = 2\pi\rho R\dot{B} . \qquad (3)$$

In the present design, the maximum $\dot{B}$ is 186 Webers/m^2·sec and the stable phase angle is 30°, so that V is 5.4 MV/turn. This enormous RF voltage is supplied by 50 cavities, each of which has 2 accelerating gaps with a gap voltage of 54 kV. The revolution frequency of the beam changes from 139.2 kHz at injection to 346.5 kHz at ejection, so that the RF frequency ratio is the moderate value 2.5.

The vacuum pressure required to assure 80 percent survival rate of the accelerated beam is 6.2 x 10^{-9} torr, taking the charge exchange cross section due to collisions of the Xe beam with N_2 gas to be 2.7 x 10^{-16} cm^2 at 150 MeV/u and 1.7 x 10^{-15} cm^2 at 20 MeV/u.[4] Using a bellows type vacuum chamber of 0.12 mm thick stainless steel, and a dry pumping system, this vacuum pressure is easily obtained without eddy current effects on the beam.

We will consider the transverse coherent resistive wall instability, TCI, which is most severe for the acceleration of high intensity heavy ion beams. The TCI limit is given by[5]

Table 2 Synchrotron Parameters

Design kinetic energy	
at injection	20 MeV/u
at ejection	150 MeV/u
Intensity (Space charge limit)	2×10^{12} ions/pulse
Repetition Rate	50 Hz
Radius of curvature	33 m
Average radius	70 m
Circumference	439.8 m
Focusing structure	$F\bar{U}D\bar{U}$
Number of betatron oscillations per turn	~ 6.25
Transition kinetic energy	5.8 GeV
Number of cells	64
Length of the unit cell	6.87 m
Length of the bending magnet	3.24 m
Magnetic field strength of the bending magnet	
at injection	5.93 kG
at ejection	18.32 kG
Maximum time derivative of the magnetic field	1863 kG/s
Momentum compaction factor	2.56×10^{-2}
Momentum spread of the beam	
at injection	5×10^{-4}
at ejection	1.25×10^{-4}
Revolution frequency	
at injection	139.2 kHz
at ejection	346.5 kHz
Required energy gain per turn	2.7 MV
Harmonic number	10
RF frequency	
at injection	2.78 MHz
at ejection	6.93 MHz
Number of accelerating stations	50
Number of RF cavities per station	2
Total number of accelerating gaps	100
Vacuum pressure	6×10^{-9} Torr

$$N \leqslant \frac{2A}{q^2} \quad \frac{F_\gamma}{\left|\frac{Z_T}{Z_o}\right| r_p} \quad \nu \left| (n-\nu)\hat{\eta} + \xi \right| \frac{\Delta p}{p} \qquad (4)$$

where Z_T is the transverse impedance of the ring and Z_o is the vacuum impedance $120\pi\Omega$, $\hat{\eta} = 1/\gamma_t^2 - 1/\gamma^2$, and ξ is a chromaticity. The momentum spread of the injected beam is assumed to be 5×10^{-4}. When we introduce a chromaticity of around $\xi = \left(\frac{\partial \nu}{\partial(\Delta p/p)}\right) = -6$, the intensity limit is 5.6×10^{10} particles, which is much smaller than the space charge limit. However, the growth time of this instability is about 10 ms even when 2×10^{12} particles are injected into the synchrotron. This growth time just equals the acceleration time, and so the TCI will be well corrected by suitable sextupole and octupole magnets.

Due to adiabatic damping during acceleration, the momentum spread and emittances at the final energy are 1.25×10^{-4}, $35\pi \times 10^{-6}$ m•rad (horizontal) and $18\pi \times 10^{-6}$ m•rad (vertical), respectively.

Most parameters of the synchrotron are given in Table 2.

5. ACCUMULATION AND COMPRESSION RINGS

Ten pulses of the synchrotron beam are stacked in each accumulation ring, whose diameter is twice as large as that of the injector synchrotron. Two pulses are injected in separate longitudinal spaces, and RF stacking is repeated five times. The space charge limit of each ring is calculated to be 6×10^{13} particles, assuming that bunching factor during a stacking process is 1.0 in the ring, and the emittance is $17.7\pi \times 10^{-6}$ m•rad. This limit is large enough compared with 10 pulses from the synchrotron, 2×10^{13} particles.

The RF stacking process in the accumulation ring is similar to that which is used for the ISR at CERN[6] and for TARN at INS.[7, 8] The outline of the RF stacking process is as follows.

The beam from the synchrotron bucket is transferred into the accumulation ring bucket with synchronization of the RF systems. After capture of the beam, the RF frequency is varied

for changing the equilibrium orbit. The rate of momentum change for the synchronous particle is given by:

$$\frac{dp/dt}{p} = \frac{1}{E_s \beta^2} f_{rev} \varepsilon eV \sin\phi_s \quad , \qquad (5)$$

where E_s is total energy per nucleon. Assuming the momentum difference between the injection orbit the top of the stacked orbit to be 2 , and the RF stacking time to be 5 ms, the required RF voltage is 400 kV. During this process the RF frequency must be changed at the rate:

$$\frac{df}{dt} = \frac{\varepsilon eV \cos\phi_s \cdot h \cdot f_s^2 \cdot \kappa}{E_s} \quad , \qquad (6)$$

where f_s is a revolution frequency and is η/β^2. Substituting numerical parameters, we obtain the sweep range of RF frequency as 52.5 kHz.

In the final bunch compression process, the required RF voltage is [9]:

$$eV = 2\pi\gamma A m_p c^2 \left[\frac{3Nqh\, r_p g}{A\gamma^3 R \Delta\phi_o\, \Delta\phi_{MIN}(\Delta\phi_o + \Delta\phi_{MIN})} + \frac{h \cdot \eta\beta^2}{q\Delta\phi^2_{MIN}} \left(\frac{\Delta p}{p}\right)^2 \right] \quad , \qquad (7)$$

where $\Delta\phi_{min}$ is given by the relation

$$\Delta\phi_{MIN} = \frac{h\beta c}{2R} \Delta t \quad .$$

For the purpose of reducing the RF voltage, the harmonic number of the accumulation ring is determined at 20. Substituting Δt = 10 ns, $\frac{\Delta p}{p} = 2.5 \times 10^{-3}$, $N = 2 \times 10^{13}$, $\Delta\phi_o = 2\pi$, we obtain V = 28.6 MV/turn, which will be supplied by 60 RF cavities with 240 accelerating gaps. Each gap produces a potential difference of 120 kV which is within present RF technique. The compression time is estimated to be 5.8 μs which corresponds to 2.9 revolutions in the ring.

In order to afford spaces for cavities and equipment for the extraction channels, the cell number of the magnetic focusing structure is chosen to be 128 and each cell has a long straight section.

The vacuum pressure required to assure 80 percent survival rate is 1.5×10^{-10} torr. On the other hand, the lifetime due to intrabeam scattering of the Xe^{4+} beam at the 2×10^{13} intensity is 1.52 sec in the designed accelerator.[10]

In Table 3, major parameters of the accumulation ring are given.

Table 3 Accumulation/Compression Ring Parameters

Kinetic energy of Xenon ion	150 MeV/u
Intensity	2×10^{13} ions/pulse
Repetition rate	1 Hz
Magnetic Field Bending Magnet	18.32 kG
Radius of Curvature	ρ = 33 m
Average radius	R = 140 m
Circumference	C = 879.65 m
Number of cells	128
Focusing structure	$F\bar{O}D\bar{O}$
Revolution frequency	173.25 kHz
Transition kinetic energy	9.61 GeV
Number of betatron oscillations per revolution	~ 10.25
Required energy gain per turn	28.6 MV/turn
Momentum compaction factor	9.52×10^{-3}
Momentum spread of the stacked beam	6.52×10^{-4}
Harmonic number	h = 20
R.F. frequency	3.465 MHz
Number of R.F. cavities	60
Total number of gaps	240
Final bunch length	20 ns
Bunching time	5.8 μs
	= 2.9 revolutions
Vacuum pressure	1.5×10^{-10} Torr
Number of extraction channels	20
Momentum Spread after compression (full width)	1.33%
Emittance after compression	
(Horizontal)	$35\pi \times 10^{-6}$ m rad
(Vertical)	$18\pi \times 10^{-6}$ m rad

The intensity limit due to the transverse coherent resistive wall instability is 5 x 10^{11} particle if we introduce a chromaticity of -6. The e-folding growth time of the instability for the intensity of 2 x 10^{13} is 1 ms, a factor 3 less than the accumulation time. From the point of view of TCI, the momentum spread of the stacked beam should be large to give larger tune spread for Landau damping. As is clear from equation (7), large momentum spread requires enormous RF voltage which is far beyond present RF techniques, so that other methods to cause Landau damping, for example creating an amplitude dependent tune shift by octupole magnets, will be useful.

6. CONCLUSION

The goal of our design for a heavy ion fusion accelerator is achieved by a massive system which consists of 5 acccumulation rings, each with 20 beam lines, and a rapid cycling synchrotron. For further progress of the design, detailed investigation of the techniques for surmounting the transverse resistive wall instability is necessary.

References

1) Y. Hirao et al., "NUMATRON, Part II", INS-NUMA-5, 1977.

2) Y. Hirao, "NUMATRON Project", Proc. of the Int. Conf. on Nuclear Structure, p. 594 (1977).

3) J.M. Watson, "ANL Experimental Program", Proceedings of the Heavy Ion Fusion Workshop, ANL, 1978, p. 17.

4) G.H. Gillespie, K. Cheng and Y.K. Kim, "Atomic Cross Sections for Fast Xe^{q+} and U^{q+} Ions Colliding with Atoms and Molecules", Ibid., p. 175.

5) B. Zötter and F. Sacherer, "Transverse Instabilities of Relativistic Particle Beams in Accelerators and Storage Rings", CERN-77-13 (1977), 175.

6) W. Schnell, Proc. of Conf. on High Energy Acc., Dubna (1963).

7) Y. Hirao et al., "Test Accumulation Ring for NUMATRON Project -- TARN --", INS-NUMA-10 (1979);
S. Yamada and T. Katayama, "Injection and Accumulation Method in the TARN", INS-NUMA-12 (1979).

8) Y. Hirao et al., "Test Accumulation Ring for NUMATRON Project", IEEE Trans. NS Vol. NS-26, No. 3, 3730 (1979).

9) T.K. Khoe, "Longitudinal Bunching", Proc. of the Heavy Ion Fusion Workshop at BNL (1977).

10) K. Katayama, A. Noda and N. Tokuda, "Lifetime of Ion Beam in an Accumulation Ring". These Proceedings.

INTEGER RESONANCE CROSSING IN H.I. ACCUMULATOR RING

J. Le Duff
Rutherford Laboratory

1. INTRODUCTION

The R.F. Linac scheme requires current multiplication in order to reach the necessary amount of peak power on the target. As part of this multiplication, a complementary accumulator ring is filled up to its current limitation within the usual Laslett tune-shift limit $\Delta\nu = 0.25$. However, during compression the tune can spread over, at least, one integer. The compression time is of the order of several tens of revolutions: (the revolution period is of the order of 5 μs).

Experimentally, on existing circular machines, relatively fast crossing of half-integer resonances has been achieved, which is not true for integer resonances. However, in the case of a heavy ion accumulator ring there is concern with relatively fast crossing of such resonances during the compression time (a fraction of a synchrotron oscillation period), the beam being ejected after this operation.

In what follows, two simple approaches are considered for the transient particle dynamics when the operating tune is very close to an integer resonance and assuming dipole defects are distributed around the ring.

2. INTEGER RESONANCE BEHAVIOR IN CASE OF STATIC TUNE ($\nu \simeq k$)

Let's assume a single defect corresponding to a field error $\frac{\delta B}{B} = 10^{-4}$ over a magnetic length of 6 meters. For $\nu = k$, a particle initially moving on the reference closed orbit (axis of the magnetic structure) will get, at each revolution, the same angular kick at a constant betatron phase. Obviously the amplitude of the induced betatron motion will increase linearly with the number of revolutions

$$\hat{x}_n = n \frac{\delta B \Delta s}{B\rho} \beta_x$$

where $\frac{\delta B}{B} \Delta s$ is the integrated field error, n the number of revolutions, β_x the envelope function $\left(\beta_x \approx \frac{R}{\nu_x}\right)$, ρ the bending radius.

Using previous numbers with, in addition, $\beta_x = 10$ meters and $\rho = 50$ meters, one gets

$$\hat{x}_n = \frac{n}{10} \text{ (mm)} .$$

An amplitude growth of 1 cm is then obtained after 100 revolutions.

Assume now that N dipole defects are randomly distributed around the circumference. Considering only the bending magnets as error sources, a realistic value is $N \simeq 50$. With no correllation between errors, this leads to:

$$\hat{x}_n = \frac{n\sqrt{N}}{10} \text{ (mm)}$$

which now corresponds to an amplitude growth of 7 cm after 100 turns.

This is certainly unacceptable. However, in the absence of non-linearities, the tune will vary across the integer during compression which increases the space charge forces progressively. This is the object of the next Section.

3. INTEGER RESONANCE CROSSING: VARIABLE TUNE

Using the smooth approximation for the optics, the particle motion in the transverse plane can be written as follows:

$$\frac{d^2x}{d\theta^2} + \nu^2(\theta)\cdot x = F(\theta) , \quad ds = Rd\theta ,$$

where $F(\theta)$ represents the dipole defects distributed along the circumference.

$$F(\theta) = R^2 \frac{\delta B(\theta)}{B\rho} .$$

As usual, let's take the main component of its Fourier expansion:

$$\frac{d^2x}{d\theta^2} + \nu^2(\theta)\cdot x = R^2 F_k \cos(k\theta + \alpha_k) \quad ,$$

where k is the integer close to the tune. One will assume that k is different from a multiple of $\frac{M}{2}$, where M is the periodicity of the magnetic structure. Then the envelope function β_x is not expected to change when ν varies.

Assuming also that ν varies slowly, one can get the adiabatic solution for the homogeneous equation (absence of defects), through the W.K.B. approximation:

$$x(\theta) = Ax_1(\theta) + Bx_2(\theta) \quad ,$$

where:

$$x_1(\theta) = \nu(\theta)^{-1/2} \cos\{\int^{\theta} \nu(\theta)\, d\theta\}$$

$$x_2(\theta) = \nu(\theta)^{-1/2} \sin\{\int^{\theta} \nu(\theta)\, d\theta\}$$

In the presence of defects, the general solution can be obtained by using the method of variation of parameters, which leads to:

$$\frac{dA}{d\theta} = - R^2 F_k\, x_2(\theta) \cos k\theta$$

$$\frac{dB}{d\theta} = R^2 F_k\, x_1(\theta) \cos k\theta$$

With the following assumptions in addition:

i) $x(0) = 0$

ii) $\nu = \nu_o + k - a\theta$ where ν_o is the non integer part of the tune at $\theta = 0$.

iii) $\Delta\nu \ll k$ total tune variation $(0 \leq \theta < \infty)$,

it comes out that:

$$A(\theta) = - \frac{R^2F_k}{\sqrt{k}} \int_o^{\theta} \sin\left\{(\nu_o + k)\theta - a\theta^2\right\} \cos k\theta . d\theta$$

$$B(\theta) = \frac{R^2F_k}{\sqrt{k}} \int_o^{\theta} \cos\left\{(\nu_o + k)\theta - a\theta^2\right\} \cos k\theta . d\theta \quad ,$$

and $x(\theta) = A(\theta).x_1(\theta) + B(\theta)\, x_2(\theta)$.

It looks realistic to integrate for A and B up to infinity, because as soon as the tune has moved away from the integer the amplitudes will stop growing.

The fast varying terms in the previous equations can be neglected, keeping in mind that half of the effect will happen before the integer is crossed:

$$A(\infty) \approx \frac{R^2F_k}{\sqrt{k}} \int_o^{\infty} \sin(a\theta^2) d\theta$$

$$B(\infty) \approx \frac{R^2F_k}{\sqrt{k}} \int_o^{\infty} \cos(a\theta^2) d\theta \quad .$$

According to the well known Fresnel's integrals, after a while the amplitude of the particle motion becomes:

$$\boxed{\hat{x}(\infty) = \frac{1}{2} \frac{R^2F_k}{k} \sqrt{\frac{\pi}{a}}}$$

which is inversely proportional to the square root of the crossing speed.

For comparison let's consider the case a = o and $\nu = k$. From previous equations one gets:

$$A(\theta) = 0$$

$$B(\theta) = \frac{R^2F_k}{2\sqrt{k}}\, \theta$$

$$\hat{x}(\theta) = \frac{1}{2} \frac{R^2F_k}{k}\, \theta$$

showing that the amplitude is now increasing linearly with θ.

From the first section, and assuming $R = 1.5 \times \rho$, one can roughly deduce:

$$F_k \approx 2.8 \times 10^{-7} (m^{-1})$$

The variable tune case then gives:

$$\hat{x}(\infty) \approx \frac{1.25 \times 10^{-6}}{\sqrt{a}} \quad (m)$$

For a total tune shift of 0.5 over 100 turns one gets:

$$\hat{x} = 4.5 \times 10^{-2} \text{ mm}$$

which looks quite reasonable.

However in practice, the non-linearities of the space charge forces may keep the tune on the integer, or very close, as soon as the amplitude starts to grow. The truth may be somewhere between the two approaches.

It will certainly be very interesting to study integer resonance crossing on an existing machine experimentally as a function of closed orbit correction. A crossing time less than 1 ms is required to answer our present worry.

I would like to thank G. Leleux, J.L. Laclare and M.P. Level for useful discussions.

LIFETIME OF ION BEAM IN AN ACCUMULATION RING

T. Katayama, A. Noda and N. Tokuda
University of Tokyo

Beam loss due to charge exchange processes such as

$$A^{n+} + A^{n+} \rightarrow A^{(n+1)+} + A^{(n-1)+}$$

may be a severe obstacle to accumulating intense ion beams in a storage ring. Here, the loss rate is estimated for a ring where Xe^{4+} ions are supposed to be accumulated.

The loss rate is given by

$$\alpha \equiv \frac{1}{N}\frac{dN}{dt} \qquad (1)$$

$$= n_{lab}{}^{v}\, cm^{\sigma}\, cm \ . \qquad (2)$$

The symbols are defined in Table 1, where machine parameters are also listed. The density of ions in the ring is

$$n_{lab} = \frac{N}{2\pi RS} \ , \qquad (3)$$

on the assumption that the beam is completely debunched. The beam is to be stored in the ring as shown in Fig. 1. Then the cross section of the beam is

$$S = \pi ab + b\Delta x_p \ , \qquad (4)$$

where a and b are obtained from the beam emittance ε and the average betatron amplitude function, $\bar{\beta}$,

$$a = \sqrt{\varepsilon_x \bar{\beta}} \ , \qquad (5)$$

$$a = \sqrt{\varepsilon_y \bar{\beta}} \ . \qquad (6)$$

The beam spread due to a momentum dispersion is

$$\Delta x_p = \eta \frac{\Delta p}{p} \qquad (7)$$

The dispersion function is approximately

$$\eta = \bar{\beta}^2/R \qquad (8)$$

Then the beam cross section is numerically calculated with values listed in Table 1, and the density is

Table 1 List of Symbols and Machine Parameters

N	number of ions in the ring	2×10^{13}
n_{lab}	density of ions	
R	mean radius of the ring	140 m
S	cross section of the beam	
V_{cm}	velocity of ions in the center of mass frame	
α	loss rate	
β	ratio of ion velocity to that of light	0.507 (150 MeV/u)(~ 19.5 GeV) 0.204 (20 MeV/u)(~ 2.6 GeV)
$\bar{\beta}$	average betatron amplitude function	13.7 m
γ	$1/\sqrt{1-\beta^2}$	
$\frac{\delta' p}{p}$	momentum difference between colliding ions	
$\frac{\Delta p}{p}$	total momentum spread	2.5×10^{-3}
ε_x	emittance in the horizontal direction	35×10^{-6} m-rad
ε_y	emittance in the vertical direction	18×10^{-6} m-rad
η	dispersion function	
θ	collision angle in the laboratory frame	
σ_{cm}	cross section of the electron transfer process	1×10^{-19} m^2
τ	life time	

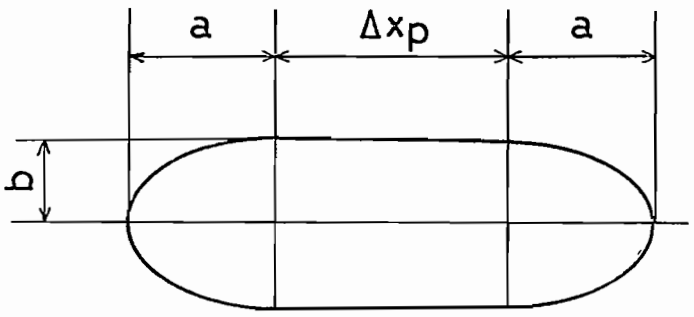

Fig. 1. The beam profile in the accumulation ring.

$$n_{lab} = 2.01 \times 10^{13} \ (m^{-1}) \ . \qquad (9)$$

The speed of the ion in the center of mass frame is given by

$$\beta_{cm}^{\ 2} = \left(\frac{\beta}{2}\frac{\delta' p}{p}\right)^2 + \left(\beta_\gamma \sin\frac{\theta}{2}\right)^2 \qquad (10)$$

As the momenta of ions are considered to be distributed as shown in Fig. 2, the typical momentum difference between the ions which will collide with each other, is

$$\frac{\delta' p}{p} = \frac{\Delta p}{p}\ \frac{2a}{2a + \Delta x_p} \ , \qquad (11)$$

where $\delta' p/p$ is determined so that the areas of the parallelogram and the rectangle are equal. Then the first term of eq. (10) is 1.59×10^{-3} for 150 MeV/u and 6.50×10^{-4} for 20 MeV/u. The maximum collision angle in the laboratory is evaluated by

$$\theta = 2\sqrt{\varepsilon_x/\beta} \ , \qquad (12)$$

and the second term is numerically 1.56×10^{-3} for 150 MeV/u and 5.63×10^{-4} for 20 MeV/u. Then the velocity in the cm frame is

$$v_{cm} = \begin{cases} 3.27 \times 10^5 \ (m/s) \ (150 \ MeV/u) & (13) \\ 1.24 \times 10^5 \ (m/s) \ (20 \ MeV/u) \ . & (14) \end{cases}$$

As experimental data of cross sections for the electron transfer processes are scarce and there are no data for $Xe^{4+} + Xe^{4+} \rightarrow Xe^{5+} + Xe^{3+}$, so a theoretically predicted value is adopted. Macek estimated the cross section for $Xe^{8+} + Xe^{8+} \rightarrow Xe^{9+} + Xe^{7+}$ at much smaller than $10^{-18} cm^2$.(1) It is supposed that such a small cross section is due to a $4d^{10}$ closed outer shell configuration of a Xe^{8+} ion. In our case of Xe^{4+}, however, four electrons remain in the outer shell, so the cross section should be larger. According to papers presented at previous Heavy Ion Fusion Workshops(2) the cross sections for the electron transfer process of various ions are estimated to be of the order of $10^{-15} cm^2$. Therefore, a value of $1 \times 10^{-15} cm^2$ is adopted here.

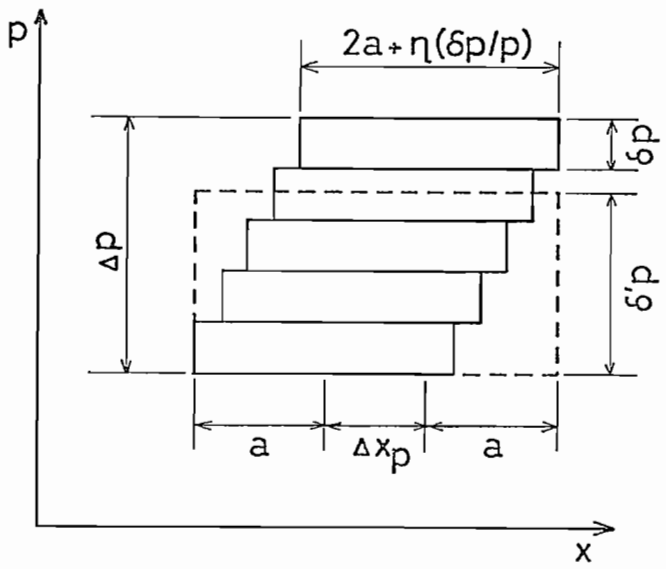

Fig. 2. Five beam pulses of different momenta are stacked in the accumulation ring. The typical momentum spread $\delta' p$ is determined so that the area of the rectangle (dashed line) and that of the five pulses are equal.

Now the loss rate can be numerically calculated, and

$$\alpha = \begin{cases} 0.657 \ s^{-1} & (150 \ MeV/u) \ , & (15) \\ 0.249 \ s^{-1} & (20 \ MeV/u) \ . & (16) \end{cases}$$

The life time, the inverse of the loss rate, is

$$\tau = \begin{cases} 1.52 \ s & (150 \ MeV/u) \ , & (17) \\ 4.02 \ s & (20 \ MeV/u) \ . & (18) \end{cases}$$

These lifetimes are long enough in a heavy ion fusion driver complex which includes an accumulation ring where about 10^{13} ions are stored.(3)

References:

(1) J. Macek, Proceedings of the Heavy Ion Fusion Workshop, Argonne, 1978, p. 183.

(2) Proceedings of the Heavy Ion Fusion Workshop, Berkeley, 1977, Proceedings of the Heavy ion Fusion Workshop, Argonne, 1978.

(3) T. Katayama and A. Noda. These Proceedings.

LONGITUDINAL BEAM STABILITY IN HEAVY ION STORAGE RINGS

D. Mohl
CERN

1. INTRODUCTION

This is an attempt to scale conditions for longitudinal beam stability to heavy ion storage rings (HIS) which have been proposed as part of some accelerator schemes to drive pellet fusion [1]. The instability considered has been observed in many high intensity proton machines. In the CERN 25 GeV Proton Synchrotron (PS), it can occur near transition energy [2] as well as during debunching at high energy [3]. In the 30 GeV intersecting storage rings (ISR) similar effects happen to the newly injected beam [4] when too dense bunches are transferred. In all these cases the instability manifests itself by a rapid blow-up of the beam momentum spread and this blow-up is accompanied by RF activity observed on beam current pick-up electrodes at frequencies in the, say, 0.3 - 2 GHz region. The picture is consistent with the assumption (first made in the classical paper by Nielsen, Symon and Sessler [5] and generalized by many subsequent workers) that a longitudinal density modulation $\lambda = \lambda_o e^{i n (s/R - \omega t)}$ develops on the beam and self-amplifies via the interaction with structures surrounding the beam.

2. ASSUMPTIONS FOR SCALING

For the present purpose I shall take three sets of observation as established:

i) The instability threshold is described by the "Keil-Schnell" selfbunching criterion [6] with local values for momentum spread and beam current [2,3,7] (although a rigorous derivation only exists for the coasting beam case). By the same token the growth rate is determined by the coasting beam selfbunching rate taking the local value for the current of a bunched beam.

ii) The impedance Z_n describing the coupling of the beam to its environment at a frequency near n times the particle revolution frequency is $|Z_n/n| \simeq 20\ \Omega$ with a real part $R_n/n \simeq 2 - 15\ \Omega$ both in ISR and PS for the 0.5 - 2 GHz region.

iii) Growth times can be as fast as 100 μs in the PS and probably also in the ISR.

As the real part R_n/n is of vital importance for our scaling two comments are in order : R_n has been estimated from measurements [8] of the growth rate of the transverse head tail instability using relations between transverse and longitudinal impedance. Clearly this is an indirect measurement which in addition gives lower limits on R_n to the extent that Landau damping tends to reduce transverse growth.

Values obtained in this way are R_n/n = 2 - 5 Ohm in PS and 2 - 15 Ω in ISR (f = 0.1 - 2 GHz). In the ISR, Z_n seems to be inductive rather than capacitive as expected for perfect walls. This permits some cross checks on R_n from the longitudinal growth rate (see following section). Further checks are possible observing that the "imperfect wall contribution" Z_w to Z_n is a physical impedance. Hence transformations[13] can be used which relate R_w, X_w and Z_w and permit e.g. to calculate $R_w(\omega)$ if $|Z_w(\omega)|$ is known over a large enough frequency range. From these checks one might speculate that R_n becomes comparable in magnitude to $|Z_n|$ at frequencies around a GHz.

3. SCALING RELATIONS

a) Threshold current [6] ("Keil-Schnell") :

$$I \lesssim F \left|\frac{\eta}{Z_n/n}\right| \left(\frac{\Delta p}{p}\right)^2_{FWHM} \beta^2 \gamma U_p \frac{A}{q} \qquad (1)$$

where :

F is a form factor depending on the nature of the impedance and the sign of η. As a rule of thumb $F \sim 1$;

$\eta = \gamma^{-2}_{transition} - \gamma^{-2}$ is the "off energy" function of the storage ring (machine constant at fixed energy depending on the distance from transition energy).

$Z_n = \int_0^{2\pi R} \frac{\langle E_{n,s} \rangle \, ds}{I_n}$ is the coupling impedance defined by the longitudinal electric field $E_{n,s} \exp\{in(s/R - \omega t)\}$ induced by a beam current $I_n \exp\{in(s/R - \omega t)\}$ and summed over one turn and averaged over the beam cross section.

$\left(\frac{\Delta p}{p}\right)_{FWHM}$ is the beam momentum spread (full width at half maximum)

$\beta = v/c$, $\gamma = (1-\beta^2)^{-\frac{1}{2}}$ are the usual relativistic factors

$U_p \simeq \frac{m_o c^2}{e} = 980$ MV is the "proton rest voltage" and

A, q are the mass number and the charge state of the ion (A = 238, q = 1 for U_{238}^{+1}).

If (1) is violated for any mode number n, the corresponding beam density modulation will self amplify. The e-folding time for conditions for above the threshold (1) is obtained [5,6,9], noting that $1/\tau = \mathrm{Im}(n.\omega)$ and solving

$$(n\omega - n\omega_{rev})^2 = n^2 \omega_{rev}^2 \frac{i\eta I Z_n/n}{2\pi \beta^2 \gamma U_p (A/q)} \qquad (2)$$

where $\omega_{rev} = \beta c/R$ is the (angular) particle revolution frequency. For protons conditions near threshold and more details are described, e.g. in ref. 9).

We shall be interested in cases where $Z_n = R_n + i X_n$ is such that $|X_n| >> R_n$. Then (see ref. 5) for the "good" sign of X_n and η (capacitive X_n below, inductive above transition*) we find from (2)

$$\frac{1}{\tau} \approx n\omega_{rev} \sqrt{\frac{|\eta| I}{2\pi\beta^2\gamma U_p (A/q)}} \frac{R_n/n}{2\sqrt{X_n/n}} \qquad (2a)$$

And for the "bad" sign ("negative mass region" [5])

$$\frac{1}{\tau} \approx n\omega_{rev} \sqrt{\frac{|\eta| I}{2\pi\beta^2\gamma U_p (A/q)}} \sqrt{\frac{|X_n|}{n}} \qquad (2b)$$

---

* Following bad tradition [5] we use the theorists ($e^{-i\omega t}$) rather than engineers ($e^{j\omega t}$) convention. Hence capacitive impedance means positive Im(Z) etc.

For coasting proton beams, the threshold and growth rate conditions are discussed in literature[9]. The generelization to bunched beams is done - somewhat in an ad hoc manner - in references 2, 3, 7 and this bunched beam theory seems to fit with observation [2,3,4]. The generalization to heavy ions can be readily done following e,g. Hereward's "old fashioned" derivation [10]. He observes that threshold corresponds to conditions where the RF potential ("self bucket") induced by the perturbed beam is just deep enough to hold the beam momentum spread. In a similar fashion the growth time is related to the period of synchrotron oscillation in the self bucket.

4. IMPEDANCES IN AN HIS

Relations to estimate Z_n/n for many structures are compiled in reference 11. Two things are important for our scaling, namely the γ dependence of the impedances and the cut off wave number beyond which the beam ceases to couple to the walls.

In the long wavelength limit (see below) the basic contribution to Z_n namely the impedance of a beam (radius b) in a perfectly conducting smooth chamber (radius h) is

$$\frac{Z_n}{n} = i \frac{377\ \Omega}{\beta\gamma^2} \{\frac{1}{2} + \ell n\ (\frac{h}{b})\} \qquad (3)$$

Note the difference between high energy protons ($\beta\gamma^2 >> 1$) and heavy ions ($\beta\gamma^2 < 1$).

Additional contributions to Z_n due imperfect walls (cavities, cross section variations, ferrite structures, etc.) are similar in proton and heavy ion storage rings up to the cut off wave number which can be shown to be of order (Appendix) $n_c \simeq \gamma \frac{\text{storage ring circumference}}{2\pi \times \text{chamber half height}}$

For above this cut off the beam fails to couple to the wall. In the cut off region (say, up to $2\ n_c$) the growth rate is roughly constant (Fig. 1) for constant wall impedance Z_n/n rather than to increase linearly with frequency as suggested by (2).

5. SCALING

We conclude from section 4 that the HIS will be dominated by the large capacitive impedance (3). [This was first pointed out to me by Graham Rees.] Since probably all HIS will work below transition, we take equation (2a) to work out the growth rate. Guided by experience from PS and ISR we take for the real part $R_n/n = 2\ \Omega$ (optimistic ?) or $R_n/n = 15\ \Omega$ (pessimistic ?). With the parameters of Table 1 we find

$$\tau \simeq 800\ \mu s \qquad \frac{R_n}{n} = 2\ \Omega$$

$$\tau \simeq 100\ \mu s \qquad \frac{R_n}{n} = 15\ \Omega$$

at the cut off $n_c = \frac{\gamma R}{h} = 2{,}5 \times 10^3$.

It is possible in principle to reduce $1/\tau \propto |X_n|^{-\frac{1}{2}}$ by increasing the capacitive space charge impedance (increase of h). This would however further complicate the RF manipulations required for controlled beam bunching because the external RF has to counteract space charge.

It might also be argued that Z/f rather than Z/n should be kept constant scaling wall imperfections between machines of similar size. This would improve the HIS growth times by 2 - 3.

6. HOW MANY E-FOLDINGS ARE TOLERABLE ?

For a perfect coasting beam the initial perturbation is the Schottky noise [12] due to the finite particle number. The corresponding current may be written in terms of the average beam current I_o as

$$I_n = \sqrt{2\ e\ q\ f_{rev}\ I_o}$$

where we assume high mode number such that $n\,|\eta|\,\frac{\Delta p}{p} \gtrsim 1$.
"Catastrophic" growth has occurred when this current becomes comparable to the DC component i.e. when

$$I_n\ e^{t/\tau} = I_o$$

From which one obtains:

$$t/\tau = \tfrac{1}{2}\, \ell n(I_o/2\ e\ q\ f_{rev}) \simeq 17 \text{ in HIS}$$

This would suggest that, say, 15 growth periods are acceptable.

On the other hand assume that a 1 per mille high frequency modulation remains as a memory of the linac bunch structure. Then, $\ell n\ 10^3 \approx 7$ e-foldings lead to large blow-up, $t/\tau \approx 5$ may be acceptable.

As a result with "pessimistic scaling" one expects deterioration of the HIS beam after, say, 1 ms. With "optimistic scaling" the corresponding time is $\approx$ 10 ms. Beam may be required in an HIS for several ms. Assume for instance $N_{SR} = 5$ rings with S = 60 turn injection in each ring from the same linac. Then, the first ring has to hold beam for at least $t_{rev} \times N_{SR} \times S \approx 2$ ms before all rings can simultaneously eject onto the pellet.

CONCLUSION

Longitudinal stability in a HIS is an important and challenging problem with possible repercussion on parameters like the number of rings, the aperture of the vacuum chamber (cost !) , the ion charge state, the storage time, etc.

A beam environment with a low resistance is important to permit safe beam storage for several milliseconds. Care has to be taken about cavities, ferrite structures, ceramics etc. to keep their coupling resistance R_n/n as low as a few Ohms even for singly charged ions. For higher charge states the tolerable impedances are lower (in proportion to the square of the ion charge if the same number of ions is used).

Impedance values of a few Ohms are at least as good as those obtained (after work !) in PS and in ISR where $|Z_n/n|$ is estimated to be about 20 Ω and R/n of the order of 2 - 15 Ω over the frequency range of concern.

There are interesting differences between the HIS and the proton case, amongst them :

The $1-\beta^2$ cancellation of space charge forces is ineffective in a HIS (typically $\beta \approx 0.3$). Hence the capacitive impedance due to

space charge (direct and images on perfect walls) is large, typically 1,5 kΩ compared to a few Ohms in ISR and PS at high energy .

To the extent that this impedance cannot be compensated by inductive walls (a difficult task for 1500 Ω) a "typical" HIS beam will always be unstable with growth proportional to the resistive "wall imperfection". What one can hope for then is slow enough growth within the required few milliseconds of storage time. On the positive side, the frequency band of importance, is, say, 1 GHz in a HIS rather than 20 GHz or more in PS and ISR, because due to Lorentz contraction the cut off wavelength is γ-times shorter in high energy proton machines. The smaller frequency band might make it easier to improve the effective coupling resistance and/or device feedback stabilization.

TABLE 1

Assumed Parameters

			PS (at high energy)	ISR (injected pulse)	HIS (typical)
Circumference/$2\pi R$		(m)	100	150	100
Relativistic factors	β		1	1	0.3
	γ		20	25	1
Beam Current	I	(A)	1	1	60
Revolution Frequency	f_{rev}	(kHz)	475	315	140
Energy parameter	$\frac{\beta^2\gamma\, U_p A}{q}$	(GeV)	20	25	20
Off energy function	$\eta = \gamma_t^{-2} - \gamma^{-2}$		1/38	1/100	- 1
Half height of beam chamber	h	(mm)	35	30	40
Cutt off mode number	$n_c = \gamma R/h$		6×10^4	$1{,}2 \times 10^5$	$2{,}5 \times 10^3$
Space charge impedance	$\frac{377\ \Omega}{\beta\,\gamma^2}(\frac{1}{2} + \ell n\, \frac{b}{h})$	(Ω)	1	0.6	1500
Wall impedance	$\frac{R_n}{n}$	(Ω)	2-15	2-15	2-15
	$\frac{X_n}{n}$	(Ω)	20	- 20	<< 1500

REFERENCES

1. See e.g. W. Hermannsfeldt, LBL report 9332 - 1979 as well as work reported in the Proc. of 1979 Workshop on Heavy Ion Driven Fusion, Oakland 1979 (to be published).

2. W. Hardt, in Proc. of IXth International Conference on High Energy Accelerators, Stanford 1974, p. 434.

3. D. Boussard, CERN report LAB.II/RF/Int. 75-2, (1975).

4. A. Hofmann, S. Hansen, CERN-ISR Performance reports, TH-RF AH/SH 25.6.1975, ISR-TH AH - 10.12 1975.
B. Brabham et al., IEEE Transact. NS 24, (1977) p. 1436

5. C. Nielsen, X. Symon, A. Sessler, Proc, Int. Conf. on High Energy Accelerators, Geneva 1959, p. 239.
V. Neil, A. Sessler, Rev. Sci. Instrum. 36, (1965) p. 429

6. A.M. Sessler, V. Vacarro, CERN report 67-2, (1967)
E. Keil, W. Schnell, CERN, ISR-TH 70-44, (1970)

7. H.G. Hereward, Proc. 1975 Isabelle Summer Study, BNL p. 555
F. Sacherer, IEEE Transact. NS-24 (1977), p. 1393
P. Channell, A. Sessler, Nucl. Instr. Math. 136, (1976), p. 473

8. J. Gareyte, in Proc. IX Internat. Conf. on High Energy Accelerators, Stanford 1974, p. 341
A. Hofmann, F. Sacherer, ISR Performance report ISR/TH/AH/28.2.1978

9. A. Hofmann in CERN report 77-13, (1977), p. 139.

10. H.G. Hereward, CERN/PS/DL 69-11, (1969).

11. G. Guignard, CERN report 77-10, (1977).

12. H.G. Hereward, in CERN report 77-13, (1977), p. 281.

13. See e.g. H.W. Bode : Network Analysis and Feedback Amplifier Design, Van Nostrand, N.Y. 1962.

14. B. Zotter, Part. Acc. 1, (1970), p. 311
E. Keil, B. Zotter, Part. Acc. 3, (1972), p. 11

A P P E N D I X

Coupling impedance of a beam in a circular tube

The fields can readily be obtained e.g. from the static field of a ring of charge in a perfect tube as given in text books. A Lorentz transformation yields the field of a moving ring. Integrating over a perturbed coasting beam, assuming uniform radial density and working out the average electric field yields the coupling impedance (in terms of modified Bessel functions I and K) as

$$\frac{Z_n}{n} = i \frac{2 \times 377\ \Omega}{\beta \gamma^2 x^2} \{ 1 - 2 I_1(x) [K_1(x) + \alpha I_1(x)] \} \qquad (A1)$$

where $$\alpha \approx \frac{K_o(x_w) - r K_1(x_w)}{I_o(x_w) + r I_1(x_w)}$$

$$r = \frac{\beta \gamma Z_s}{i\ 377\ \Omega}$$

$$Z_s = - \frac{E_z}{H_\phi} \Big/_{\text{wall}} \quad \text{(wall "surface impedance")}$$

$$x = \frac{n \text{ beam radius (b)}}{\text{orbit radius (R)}}$$

$$x_w = \frac{n \text{ chamber half height (h)}}{\text{orbit radius (R)}}$$

For low modes ($x_w < 1$) this yields

$$\frac{Z_n}{n} = \frac{i Z_o}{\beta \gamma^2} \left[\ln\left(\frac{h}{b}\right) + \frac{1}{4} \right] + \frac{Z_s R}{n h}$$

The factor ¼ rather than ½ as assumed above comes from the fact that we average over a uniform beam. For the central field in a uniform beam or the average over a Gaussian beam ½ is more realistic.
[If one wants to work in terms of the central field one can still use (A1) but replace the term $2I_1(x)$ in front of the innermost bracket by x]

Note that for $x_w << 1$ the wall impedance $Z_w = \frac{Z_s R}{h}$ simply adds to Z_n. The behaviour over a wider frequency range is illustrated in Fig. 1 where R_n/n and the "growth rate"

$$\left(\frac{R_n/n}{2\sqrt{X_n/n}} x \right)$$

are drawn from (A1) assuming parameters such that the wall imperfections give $Z_w/n = 15\ \Omega$ independent of frequency and space charge yields $Z_n/n = i\ 1.5\ k\Omega$ for low modes. Equation (A1) can also be used to calculate the surface impedance required for perfect compensation and the "residual" impedance Z_n (which can become resonant !) for non perfect compensation of the space charge terms. Note that (A1) is an approximation valid for small surface impedance. More general results are given by Keil and Zotter [14].

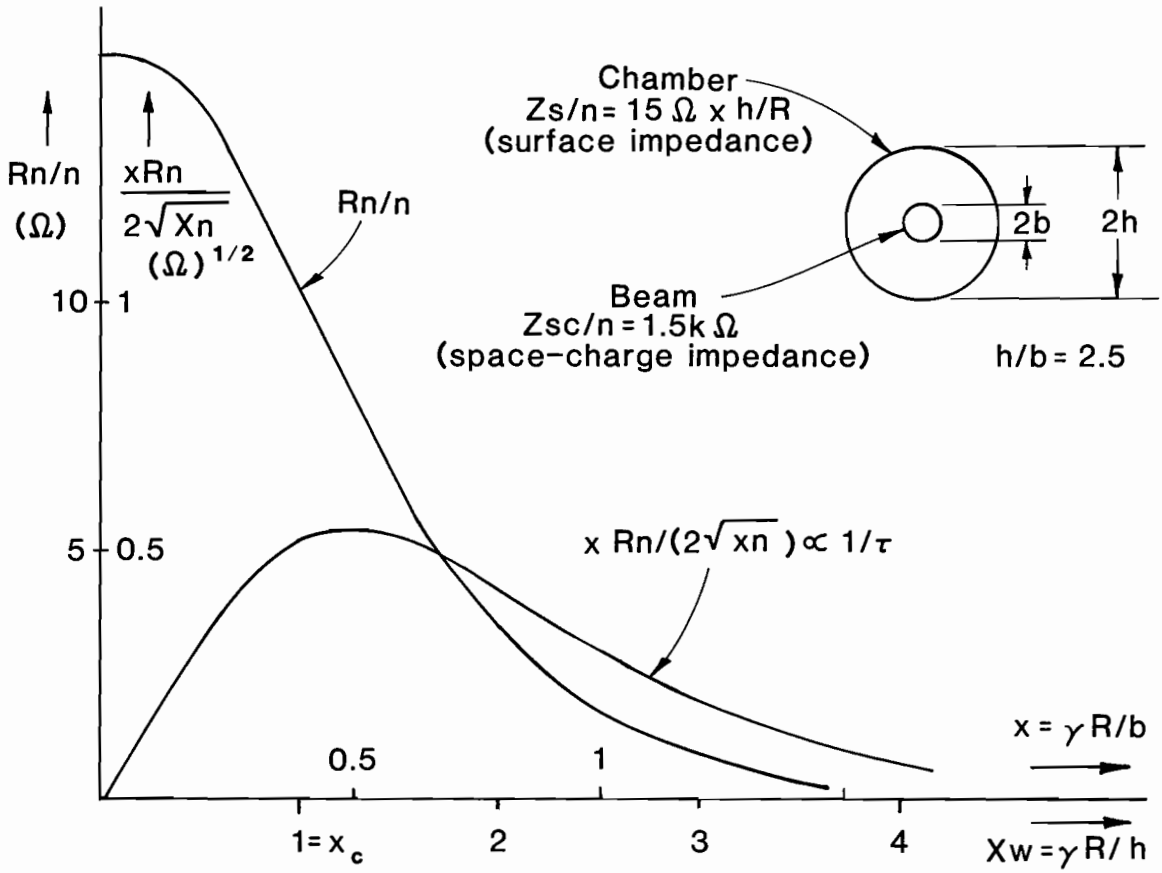
Rn/n
(Ω)
xRn / 2√Xn
(Ω)^1/2
10
1
5
0.5
Rn/n
Chamber
Zs/n = 15 Ω x h/R
(surface impedance)
Beam
Zsc/n = 1.5k Ω
(space-charge impedance)
2b
2h
h/b = 2.5
x Rn/(2√xn) ∝ 1/τ
x = γ R/b
0.5
1
1= x_c
2
3
4
Xw = γ R/ h

Fig. 1

LONGITUDINAL MICROWAVE INSTABILITY

S. Fenster
Argonne National Laboratory

A small deviation from the nominal distribution of particles in longitudinal position and momentum creates fields that may or may not increase this deviation; in the former case, a longitudinal instability occurs. They have been observed at microwave frequencies and their growth rate may be calculated in terms of the longitudinal impedance, which is the ratio of the negative of the voltage induced once around the ring to the perturbation current. This voltage is obtained by integrating the axial longitudinal electric field along the particle trajectory over one turn. The relevant frequencies are those above the cutoff for chamber propagation.

A derivation of the relationship between growth rate and impedance is given here, starting from a chosen point in Ref. 1. The only other instability considered here is the resonance effect produced by excessive tune shift due to space charge. We assume, without discussion, that $(\Delta\nu)_{max} = .25$; that is, this resonance growth is avoided (stability) by limiting the ring charge. On the other hand, the longitudinal microwave instability is assumed to be present (cannot be stabilized). Thus, the latter involves a limiting impedance to keep the growth rate low enough. The maximum allowed impedance for a maximum allowed growth rate is listed below.

Both instabilities are amenable to calculation only if quasistatic conditions obtain. Thus, the formulas below will be considered to apply during the following stages: post-injection debunching with BF = 1 and $\Delta\nu = 1/8$; and adiabatic rebunching with BF = 1/2 and $\Delta\nu = 1/4$.

We have altered the ring parameters from those of the workshop in accordance with these specifications.

Now, we will derive the relation between growth rate and resistive impedance.

Notation: MKSA units

q	= charge state	A	= atomic weight
m_p	= proton mass	e	= proton charge
c	= speed of light	β	= v/c
$\Delta p/p$	= momentum spread		
I	= electrical ring current		
Z_c	= capacitive longitudinal impedance		

N = no. particles on target

I_{av} = electrical current on target averaged over pulse shape

N_{bun} = number of bunches per ring

l_b = length of bunch on target

N_R = number of storage rings

C = ring circumference

E = energy on target

T = kinetic energy per beam ion

Z_r = resistive longitudinal impedance

Z_r' = resistive longitudinal impedance per meter

U' = normalized capacitive longitudinal impedance

V' = normalized resistive longitudinal impedance

n = number of instability density oscillations per turn

Z_o = 120 π

R = ring radius BF = bunching factor

ε_{sr} = transverse geometrical emittance (area/π) in ring

$\Delta\nu$ = allowed tune shift

ω_o = particle revolution frequency = BC/R

$\Delta\Omega_r$ = real frequency shift

$\Delta\Omega_i$ = instability growth rate

τ = instability rise time

$\Delta\Omega = \Delta\Omega_r + i\Delta\Omega_i$

z = x+iy = normalized $\Delta\Omega$

$f(z)$ = normalized longitudinal distribution function

$I_D'(z)$ = normalized dispersion integral

I_{sci} = space-charge limited ring instantaneous electrical current

n_{sc} = space-charge limit number of ions

f = frequency of the instability

$\omega = 2\pi f$

λ = wavelength of the instability

$\Delta\Omega_r = \omega - n\omega_o$

Normalization Definitions[1]

$$V' + iU' = \frac{2}{\pi} \cdot I \cdot \frac{q}{A} \cdot \frac{e}{m_p c} \cdot \frac{1}{c} \cdot \frac{1}{\beta^2} \frac{1}{(\Delta p/p)^2} \cdot \frac{1}{n} (Z_r + iZ_c)$$

$$z = \frac{2 \cdot \Delta\Omega}{n\omega_o (\Delta p/p)}$$

Relations

Space charge limit

$$n_{sc} = \frac{\pi}{15e} \cdot \Delta\nu \cdot \frac{A}{q^2} \cdot \frac{m_p c}{e} \cdot \varepsilon_{sr}\, \beta^2\gamma^3 \cdot BF$$

$$I_{sci} = \frac{\beta c q e}{2\pi R} \cdot n_{sc} \cdot \frac{1}{BF}$$

Mode number $\qquad n = 2\pi R \cdot f/c = 2\pi R/\lambda$

Ring and target energy balance

$$N_R \beta c q e n_{sc} = I_{av} l_b$$

Compression factor = 49

Note: $\frac{1}{30e} \cdot \frac{m_p c}{e} = \frac{1}{1.5347 \times 10^{-18}}$

$$C = 49\, l_b \times N_{bun}/BF$$

By Ref. 2,

$$Z_c/n \simeq Z_o/\beta$$

The dynamics of growth may be obtained from the dispersion relation. The time-dependent factor is exp $(-i \cdot \Delta\Omega \cdot t)$ and $\Delta\Omega$ is decomposed into its real and imaginary parts.

$$\Delta\Omega = \Delta\Omega_r + i\, \Delta\Omega_i$$

Two significant properties of the distribution function are:

a). $\int_{\text{real axis}} f(z)dz = \int_{-\infty}^{\infty} f(x) \cdot dx = 1$

b). f is nonzero on approximately $-\frac{1}{2} < x < \frac{1}{2}$.

The dynamical theory shows that the normalized dispersion integral

$$I_D'(z) = -i \int_{\text{real axis}} \frac{1}{u-z} \cdot \frac{df}{du} \cdot du$$

determines U', V' through the dispersion relation

$$(V' + iU') \cdot I_D' = 1.$$

and that x has the significance of normalized real frequency shift as defined above. This variable is eliminated in favor of the others below.

To find the relation among Z_r, $\Delta p/p$ and the growth rate $\Delta\Omega_i$, one must choose an f. Simplest is the step function:

$$f(x) = 1 \qquad -\frac{1}{2} \leq x \leq \frac{1}{2}$$

$$f(x) = 0 \qquad \text{elsewhere.}$$

The derivative of f is equal to ± the unit delta function at $x = \frac{-1}{+2}$ and we find

$$I_D' = \frac{-i}{z^2 - 1/4}$$

$$V' + iU' = -2xy + i\,(x^2 - y^2 - \frac{1}{4})$$

Assume, for the moment, that U' is a given number. Then,

$$x = \pm\sqrt{y^2 + \frac{1}{4} + U'}$$

$$V' = 2y\sqrt{y^2 + \frac{1}{4} + U'}$$

where we choose the sign to give growing waves. This expression may be substituted into the above normalization definition to express Z_r in terms of y and hence the growth rate. The value of U' is determined in terms of Z_c/n by the same definition. Numerical values below show $U >> \frac{1}{4}$, so $\frac{1}{4}$ can be dropped. Then, $\Delta p/p$ cancels out, and one finds a quadratic equation for $w \equiv y^2$ as:

$$w^2 + U'w - (\frac{V'}{2})^2 = 0$$

with roots

$$w_\pm = -\frac{1}{2}U' \pm \frac{1}{2}(U'^2 + V'^2)^{\frac{1}{2}}$$

Root w_- may be discarded as negative. One notes that $V'^2 << U'^2$ because $Z_r << Z_c$. The latter inequality is clearly true with the assumption $Z_c \simeq nZ_o/\beta \geq 10^6$. Thus, we find:[4]

$$y = \sqrt{w_+} = \frac{1}{2}\frac{V'}{\sqrt{U'}}$$

or

$$Z_r = (8\pi \cdot \frac{m_p c}{e} \cdot \frac{A}{q} \cdot \frac{1}{c} \cdot \frac{1}{I} \cdot \frac{Z_c}{n})^{\frac{1}{2}} \cdot R \cdot \Delta\Omega_i$$

This expression may be derived directly from a δ-function distribution taken for f. The result, in different notation, is:[1]

$$\Delta\Omega_i = \left[\frac{-e\eta\ \omega_o^2\ n\ I_o Z_i}{2\pi\beta^2 E}\right]^{\frac{1}{2}}$$

Put $\eta\to -1$, $E\to Am_pc^2$, $I_o\to I$, $e\to qe$, $Z_i\to Z_c+iZ_r$, $\omega_o\to\beta c/R$ to obtain

$$\Delta\Omega = \frac{nc}{2\pi R}\left[2\pi\cdot\frac{q}{A}\cdot\frac{e}{m_pc}\cdot\frac{I}{c}\cdot\left(\frac{Z_c}{n}+i\frac{Z_r}{n}\right)\right]^{\frac{1}{2}}$$

Assume $Z_r << Z_c$ and expand the sum in the root; the imaginary part is

$$\Delta\Omega_i = \frac{1}{2R}\left(\frac{1}{2\pi}\cdot\frac{q}{A}\cdot\frac{e}{m_pc}\cdot cI\cdot\frac{Z_c}{n}\right)^{\frac{1}{2}}\cdot\frac{Z_r}{(Z_c/n)}$$

which can be solved for Z_r as above. A useful form for systems work approximates:[2]

$$\frac{1}{n}Z_c \simeq \frac{1}{\beta}\gamma^2 Z_o, \qquad I \simeq I_{sc}$$

and reads:

$$\tau = \left(\frac{2R}{\Delta\nu\cdot\varepsilon_g\cdot}\right)^{\frac{1}{2}}\cdot\frac{R}{c}\cdot\frac{1}{\beta^2}\cdot\frac{Z_o}{Z_r}$$

In this estimate, the inductive effect of circular vacuum chamber, cross section variation and bellows, and plates formed by clearing electrodes or pick-up stations[2] have been neglected, as they can only improve the situation in a minor way.

Results are given in the following table, which differs from the Storage Ring Group Summary[3] because the charge balance equation is strictly kept at the sacrifice of a variation in ε_{sr}, and BF = .5 was chosen instead of BF = 1. The rise time τ has been taken as .01. Note that the factor γ^2 in the denominator of Z_c/n makes the crucial difference between Isabelle and the rings considered here.

Table of Heavy Ion Fusion Parameters, MKSA Units

Case	A	B	C
E	$1. \times 10^{6}$	$3. \times 10^{6}$	$1. \times 10^{7}$
N	1.25×10^{15}	1.875×10^{15}	$.625 \times 10^{16}$
T	0.5×10^{10}	$1. \times 10^{10}$	$1. \times 10^{10}$
I_{av}	$1. \times 10^{4}$	0.75×10^{4}	1.43×10^{4}
γ	1.0226	1.0451	1.0451
β	0.2089	0.2906	0.2906
$\beta\gamma$	0.2136	0.3037	0.3037
BF	.5	.5	.5
ℓ_b	1.25	3.485	6.10
$49\ell_b$	61.40	170.8	298.8
N_{sr}	4	3	9
N_{bun}	5	2	2
N_b	20	6	18
(N_b)min	17	6	12
$(\Delta p/p)$min	$\pm$ 2. $\times 10^{-4}$	$\pm$ 2. $\times 10^{-4}$	$\pm$ 2 $\times 10^{-4}$
ϵ_{sr}	5.478×10^{-5}	5.313×10^{-5}	5.911×10^{-5}
n_{sr}	3.1335×10^{14}	6.2386×10^{14}	6.9401×10^{14}
C	614.0	683.2	1195.2
R	97.72	108.73	190.2
(I_{sr})peak	10.25	25.51	16.22
U'	30.	28.	18.
n(2.5 GHz)	5117	5693	9960
Z_r	1024.7	612.7	1344.2
Z_r/n	0.2002	0.1076	0.1350
Z_r'	1.6688	0.8968	1.1247

CONCLUSION

Heavy ion beam fusion must operate at large U', far from the Keil-Schnell stability region, because a large $\Delta p/p$ (Landau damping) is prevented by limited ring bending magnet strength, injection problems, and economic need of a large BF. Also, one cannot increase the final $\Delta p/p$ by increasing the longitudinal emittance due to the final focussing limitations. Since Landau damping cannot be utilized, there is no point in placing $\Delta p/p$ at the high end of its allowed range. Here, upper limits have been obtained for the resistive impedance corresponding to an assumed upper limit on growth rate. At this point, the longitudinal resistive impedance Z_r needs to be determined for candidate rings via a theoretical and experimental program.

REFERENCES

1. A. Hofmann, CERN 77-13, p. 139 (1977).

2. G. Guignard, CERN 77-10, p. 87 (1977).

3. Heavy Ion Fusion Accelerator Study Storage Ring Group, 1979.

4. V. K. Neil and A. M. Sessler, Rev. Sci. Inst., 36, 429 (1965), Eq. (4.5)

NUMATRON and TARN

T. Katayama, A. Noda and Y. Hirao

Institute for Nuclear Study, University of Tokyo,
Tokyo, JAPAN

ABSTRACT

General descriptions of the NUMATRON design and related technical developments at INS, University of Tokyo, are reported. A test accumulation ring for NUMATRON project, TARN, was constructed for integrating various technical developments. Recent results of injection test using this ring are also described.

1. INTRODUCTION

In recent years, interests in high-energy heavy-ions have been growing up not only in the field of nuclear physics but also in the fields of atomic physics, solid-state physics, medical biology, fusion power generation engineering and many other sciences and applications. In Japan, an accelerator complex has been proposed at INS, University of Tokyo, which is named NUMATRON[1,2] and should provide heavy ions up to uranium in an energy range of 0.1 ∿ 1.3 GeV per nucleon. After completion of detailed design of the NUMATRON the major activity of the study group has been directed to the construction of the test accumulation ring for NUMATRON, TARN, which is a test facility not only for studying multiturn injection and RF stacking but also for integrating various technical developments.

In following sections, the outline of the NUMATRON is described as well as that of the TARN and preliminary results of the beam injection.

2. GENERAL DESIGN OF NUMATRON

The proposed accelerator consists of Cockcroft-Walton generators, three Wideröe linacs, two Alvarez linacs and two synchrotrons (Fig.1).

Two identical preaccelerators are arranged symmetrically in order to be able to operate in parallel. Each preaccelerator has a 500 kV high voltage generator and two ion source terminals. The acceleration voltage is adjustable in a wide range so that ions of various charge-to-mass ratios can be accelerated to a constant velocity. After passing through the buncher section, ions are injected into a row of three Wideröe linacs of a resonant frequency of 25 MHz. The first and the second are operated in π-3π mode and the third in π-π mode. The last Wideröe linac is followed by an Alvarez linac with a resonant frequency of 100 MHz at the energy of 1 MeV/u. Two stripper sections with achromatic charge analyzing systems are installed at the specific energies of 0.3 and 1.6 MeV/u in order to obtain an efficient acceleration. The injector linac specifications are shown in Table 1.

Table 1 The Injector Linac Specifications

	Wideröe 1	Wideröe 2	Wideröe 3	Alvarez 1	Alvarez 2
Operation Mode	π-3π, 38 gaps	π-3π, 20 gaps	π-π, 36 gaps	2π, 46 gaps	2π, 108 gaps
Synchrotron Phase (deg.)	-30.0	-30.0	-30.0	-25.84	-25.84
T/A (MeV/u)	0.015 - 0.146	0.146 - 0.305	0.305 - 1.102	1.120 - 1.603	1.600 - 10.023
v/c (%)	0.562 - 1.768	1.768 - 2.557	2.557 - 4.861	4.861 - 5.859	5.854 - 14.553
ε	0.0294 (U^{7+})	0.0294 (U^{7+})	0.0672 (U^{16+})	0.0672 (U^{16+})	0.193 (U^{46+})
L (m)	5.5	5.4	8.0	7.5	32.1
$\Delta T/(L\cdot\varepsilon)$ (MeV/m)	0.85	1.00	1.49	0.988	1.36
Z_{eff} (MΩ/m)	67.8	36.0	47.6	41.8 - 43.4	43.3 - 31.6
Power Loss (MW)	0.076	0.215	0.494	0.206	1.903
Q-magnet Sequence	FDFD	FDFD	FFDD	FFDD	FFDD
G (kG/cm)	10.0 - 3.18	3.18 - 2.20	3.50 - 1.83	4.00 - 3.30	3.30 - 1.33
cosμ	0.849	0.849	0.572	0.906	0.906
Aperture (mmϕ)	20, 25, 30	30	35	40	40
Admittance (mm mrad)	114 π	88.7 π	127 π	248 π	203 π

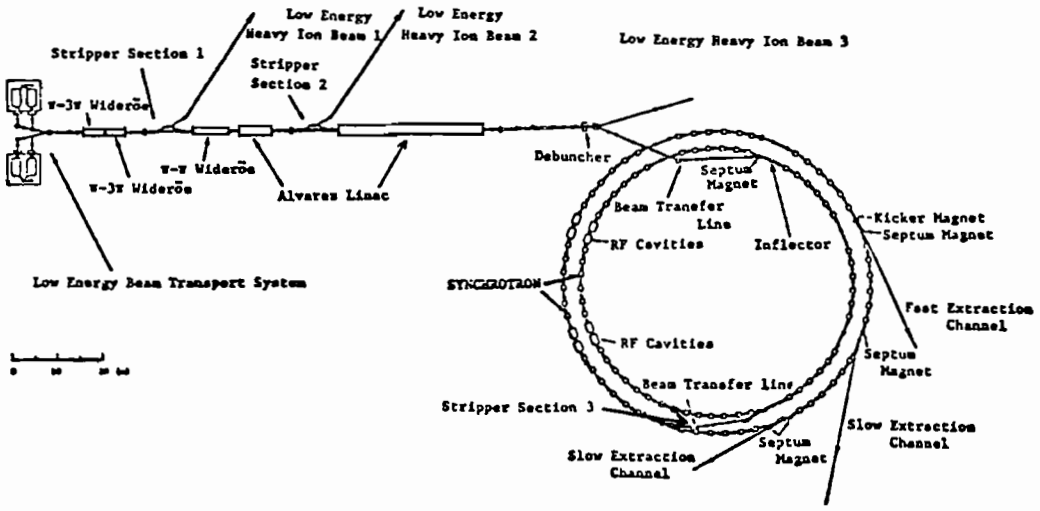

Fig. 1 Layout of NUMATRON

Final stage of the accelerator complex is composed of two synchrotrons. The first synchrotron has a capability of beam accumulation for obtaining heavy ions of high intensity. A combination of multiturn injection and RF stacking methods is applied to the injection scheme of the first ring.[3] The beam is accelerated up to the energy of 250 MeV/u and is extracted by a one turn ejection method. After passing through the final stripper section in the beam transport line between the first and the second synchrotrons, ions are completely stripped and injected into the second ring, where uranium ions are accelerated up to the maximum energy of 1270 MeV/u. The transition energy of the second synchrotron is 4.33 GeV and no ions are accelerated through the transition energy. The operation scheme of the linac and two synchrotrons is illustrated in Fig.2.

The RF systems in the rings are of two types, one of which is for RF stacking and the other is to accelerate the beams to the extraction energies. The former is described in the following Section on TARN.

The RF system for beam acceleration is designed so that the sweep range of frequency in the first ring is $1.65 \sim 6.97$ MHz, and in the second ring it is $3.6 \sim 11.2$ MHz for the various operation energies of the first and second synchrotrons. In the present design the magnetic fields of both synchrotrons vary linearly with time as $\dot{B} = 47.0$ kG. s^{-1}, and then the

required RF peak voltage is around 20 kV for the synchronous phase angle of 30°. On the other hand, the energy spread of the accumulated beam in the first ring is 200 keV for the stacked number of 50, and the required peak RF voltage is determined so that the separatrix well covers the energy spread of the beam, namely 80 kV.

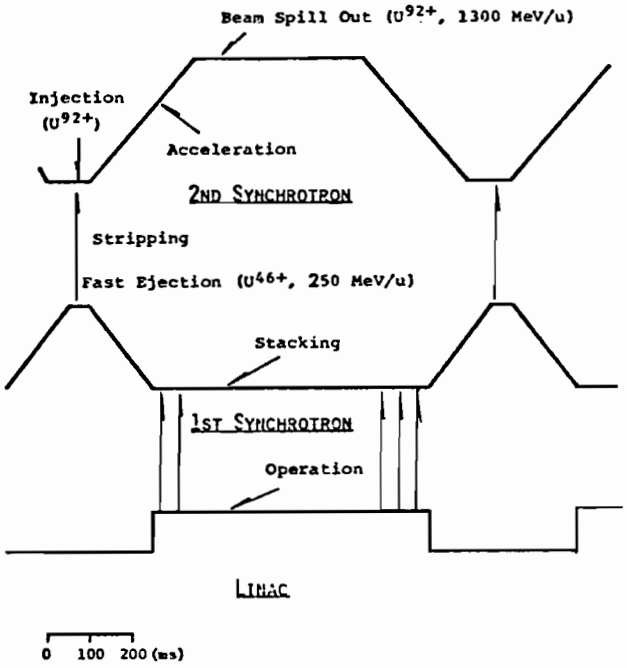

Fig.2 Operation Scheme of the Accelerator Complex

The required vacuum in the first ring is 2×10^{-11} torr for a survival rate of 90 % after an injection period of 1 sec, whereas in the second ring, 1×10^{-9} torr suffices to achieve the above survival rate because of its high energy operation. The output intensity of uranium is typically estimated at 10^9 particles per second, whereas for ions lighter than $Z \simeq 20$, it may be 10^{11} particles per second, limited by space charge effects.

In the present proposal, one fast ejection channel and two slow ejection channels are provided to answer the various needs for high energy heavy ion beams. Even at the final stage of the acceleration, the beam size is rather large and it is important that the ejection system is safe against beam blow up. From this point of view, we adopt the third integer resonance, although in this extraction mode, the arrangements of non-linear magnets will largely affect the emittance, spill time and the size of stable region.

The main parameters of the accelerator complex are given in Table 2.

Table 2 Numatron Parameters

A. Particle, Energy and Intensity

Particle	Max. Energy (GeV/u)	Intensity (pps)
U^{92+}	1.27	$\sim 10^{9}$
Kr^{36+}	1.47	$\sim 10^{11}$*
Ne^{10+}	1.81	$\sim 10^{11}$*

*Space Charge Limit

B. Injector	T/A(MeV)	Freq. (MHz)	β(v/c)	ε(q/A)
Cockcroft-Walton (500 KV)	0.0147	——	0.006	0.029(U^{7+})
Widerö (π-3π)	0.146	25	0.018	——
Widerö (π-3π)	0.305	25	0.026	——
Stripping	——	——	——	0.067(U^{16+})
Widerö (π)	1.10	25	0.048	——
Alvarez	1.60	100	0.059	——
Stripping	——	——	——	0.193(U^{46+})
Alvarez	10.0	100	0.146	——

C. 1st Synchrotron

Injection Energy		10 MeV/u
Maximum Energy		250 MeV/u
Repetition Rate of RF Stacking		100
Momentum Spread of Stacked Beam		± 0.7 %
Useful Aperture	radial	18 cm
	vertical	5 cm
Vacuum		2×10^{-11} torr
Space Charge Limit		
Number of Particles/sec		

D. 2nd Synchrotron

Guide Field (B_{max})		18.0 kG
Quadrupole Field $(dB/dr)_{max}$		1.38 kG/cm
Repetition Rate		1 Hz
Magnetic Radius		9.55 m
Average Radius		33.6 m
Circumference		211.2 m
Number of Normal Periods		24
Number of Long Straight Sections		8
Focusing Structure		FODO
Useful Aperture	radial	9 cm
	vertical	3.5 cm
Number of Betatron Oscillations		6.25
Phase Advance per Normal Period		70°
Vacuum		1×10^{-9} torr

3. TEST ACCUMULATION RING FOR NUMATRON PROJECT — TARN —

The test Accumulation Ring for NUMATRON, TARN, is constructed for developing technical subjects related to the heavy ion accelerator complex. The heavy ion beams, for example N^{5+} of 8.5 MeV/u, from the INS-SF Cyclotron[4] are injected and accumulated in the TARN, as shown in Fig.3.

The main parameters of the TARN are given in Table 3. The ring consists of eight bending magnets and sixteen quadrupole magnets with a lattice structure of FODO type. The mean radius is 5.06 m and the bending radius of the central orbit is 1.333 m. The overall ring view is shown in Fig.4. The heavy ion beam is accumulated in the ring by a combination of multiturn injection and RF stacking method. Expected intensity of accumulated ions such as N^{5+} is 10^{10} particles. The lifetime of the stacked beam is determined mainly by the charge exchange reactions between heavy ions and residual gas molecules. Assuming the cross section of these reactions to be $\sim 3\times10^{-17}$ cm^2, the required pressure in the ring is 1×10^{-10} torr for a survival rate of 90% during a stacking time of 1 sec. In following Sections, the design and performance of the ring are described.

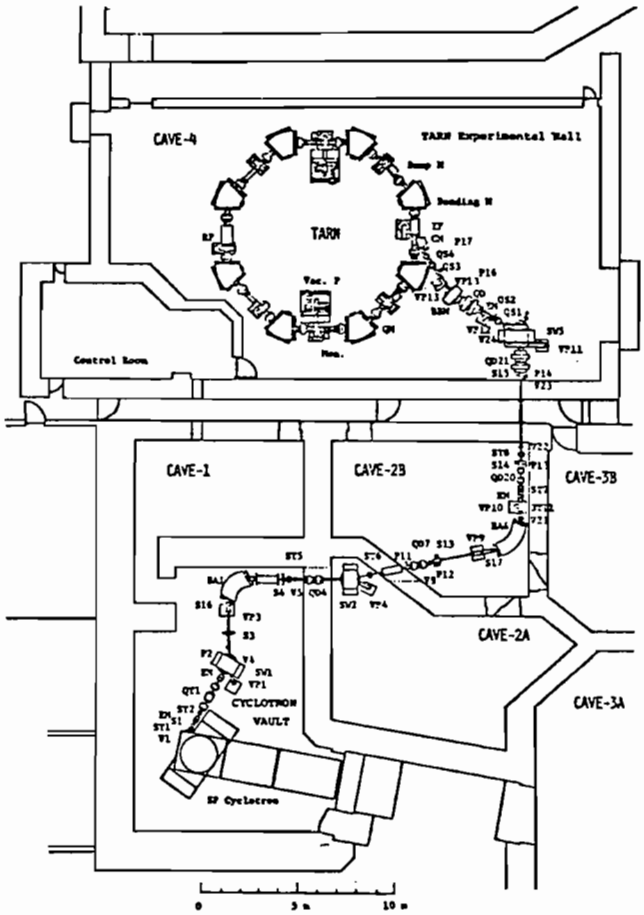

Fig.3 Layout of the TARN and the beam transport system from the SF Cyclotron. BA : Analyzer magnet. BBM : Bending magnet. SW : Switching magnet. Q : Quadrupole magnet. ST : Steering magnet. KM : Kicker magnet. S : Slit system. EM : Emittance monitor. P : Profile monitor. VP : Pumping system.

Table 3. Parameter List of the TARN

General		
Beam energy (for N^{5+})		8.56 MeV/u
Magnetic field		B = 8.574 kG
Bending radius		ρ = 1.333 m
Mean orbit radius		R = 5.06 m
Revolution frequency		f_o = 1.259 MHz
Betatron ν values		ν_x = 2.250
		ν_y = 2.200
Vacuum pressure		1×10^{-10} torr
Injection scheme		Multiturn injection
Magnet and Lattice		
Number of normal cells		8
Number of superperiods		8
Number of long straight sections		8
Periodic structure		Q_F B Q_D $\bar{O}$
Bending magnets		
Number		8
Gap		70 mm
Pole width		258 mm
Good field aperture		40 × 170 mm^2
Quadrupole magnets		
Number		16
Length		0.20 m
Field gradient		$k_F \simeq 0.240$ kG/cm
		$k_D \simeq 0.435$ kG/cm
Momentum compaction factor		Maximum = 1.70 m
		Minimum = 1.01 m
		Average = 1.41 m
Betatron amplitude function	(x)	(y)
	Maximum = 4.94 m	5.51 m
	Minimum = 1.08 m	1.18 m
RF Stacking System		
Frequency		8.81 MHz
Harmonic number		7
Maximum accelerating voltage		1.1 kV
Number of cavities		1
Total RF power		1.3 kW
Stacking parameter		
Momentum spread of the stacked beam		2.469 %
Momentum difference between the injection orbit and stack top		6.289 %
Repetition rate		50 Hz
Maximum RF stacking number		100

3.1 Magnetic Focusing System

The focusing structure of the TARN is a separated function FODO type, where both the superperiodicity and the number of normal cells are eight. The mean radius and the circumference of the ring are 5.06 m and 31.795 m, respectively, determined by considering the synchronization between the RF system of the TARN with a harmonic number of seven and that of the injector cyclotron. The number of betatron oscillations per revolution is around 2.25 both in horizontal and vertical directions. In Fig. 5, the working lines of the TARN for various sextupole corrections are shown.

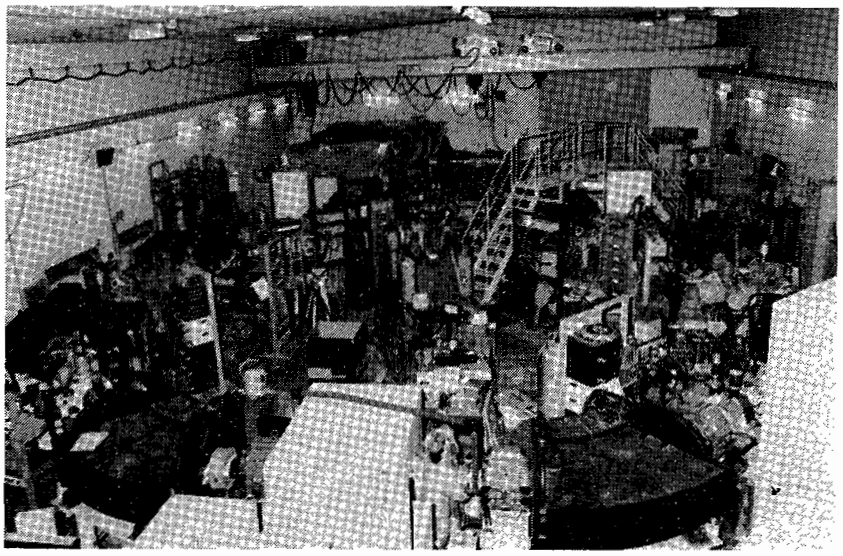

(a)

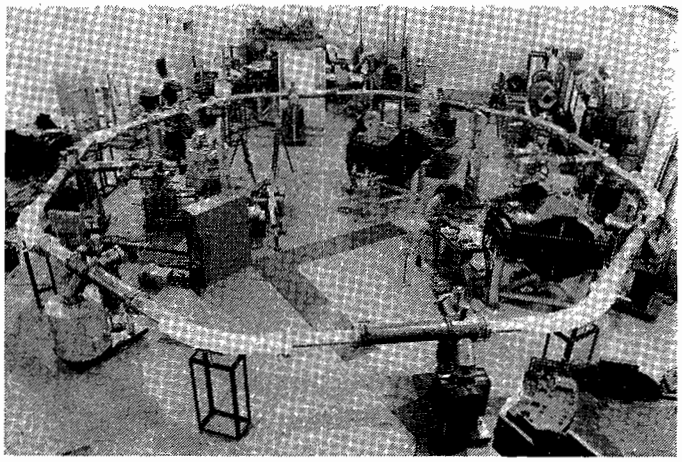

(b)

Fig. 4 a) Total view of the TARN. b) Vacuum system, arranged tentatively before the installation into the magnet gaps.

The useful aperture in the horizontal direction for the stacked beam is determined as 85 mm half width both in the bending magnet and qudrupole magnet, taking betatron oscillation amplitude, closed orbit displacement and the spread of closed orbit due to momentum spread of the stacked beam into account. The aperture of the bending magnet is 70 (height) x 258 (width) mm^2

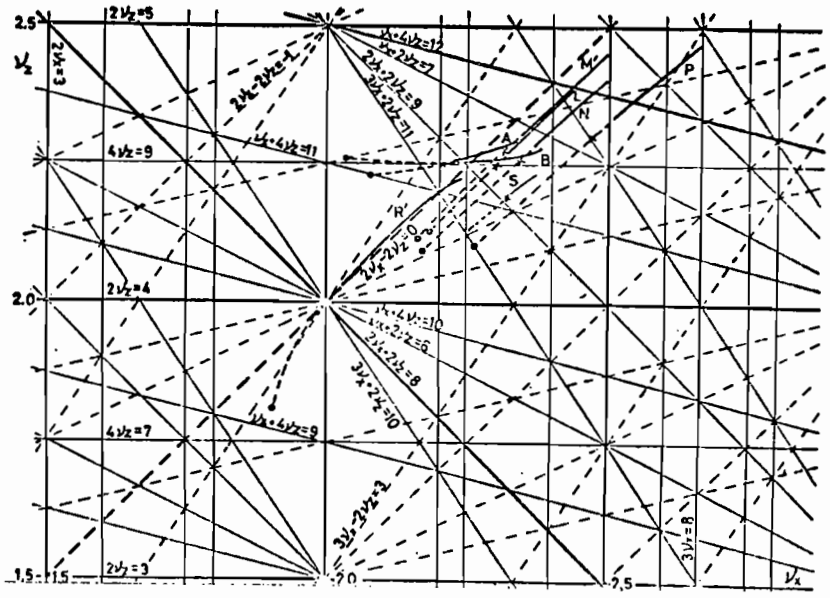

Fig.5 The work lines of the TARN. A and B represent the cases of the ideal and real magnets systems, respectively. Other lines (L ∿ R) represent the work lines with corrections.

including the thickness of the vacuum chamber wall, 4 mm, and spaces for heat insulation elements and distributed ion pumps. The radius of the inscribed circle of the quadrupole magnet is 65 mm.

The bending magnet is a window-frame type, which has merits of compactness of the structure and good field uniformity. In order to avoid the sagitta due to the small radius of curvature, 1.333 m, the magnet is fan-shaped. The edges of the magnet pole at both ends were designed to be normal to the central orbit. In order to reduce the flux density at the edge of the iron yoke, the pole edges were cut with four steps approximating Rogowski's curve. The shielding plates were attached at both ends considering the small distance between the bending magnet and quadrupole magnets. The shape of fringing field is shown in Fig.6.

The uniformity of the bending field along the radial direction was measured at the inner side of the magnet gap, sufficiently close to the edge, and was better than $\pm\ 2 \times 10^{-4}$ over the whole useful aperture.

The quadrupole magnet was designed to afford the possibility of AC operation to allow fast tuning of ν-values. The shape of the pole was determined using the computer program TRIM and is a hyperbola

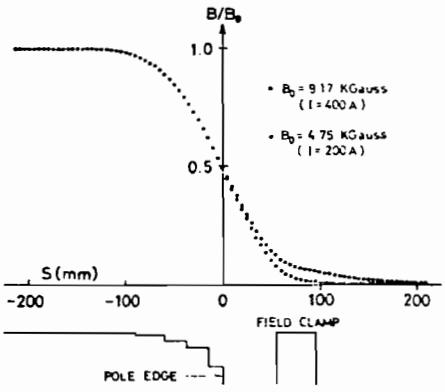

Fig.6 The distribution of the magnetic field along the beam orbit near the pole edge of the bending magnet. The effective edge was calculated according to these curves.

which extended to its tangential line at both sides. The mechanical pole edge was cut so as to enlarge the flat region of the effective focusing strength.[5)]

The field gradient of the quadrupole magnet was measured with twin coils translated horizontally and the induced voltage at each coil was fed into a VFC circuit of high sensitivity.[6)] The deviation of the field gradient along the radial direction was found to be less than 0.5 % in a whole region from x = - 85 to + 85 mm, where x denotes the distance from the central axis of the magnet as shown in Fig.7. The deviation of the effective length was also measured by the longer twin coils and was found to be less than 1% over the above region. The effective length was calculated to be 260 mm, while the geometrical one is 200 mm.

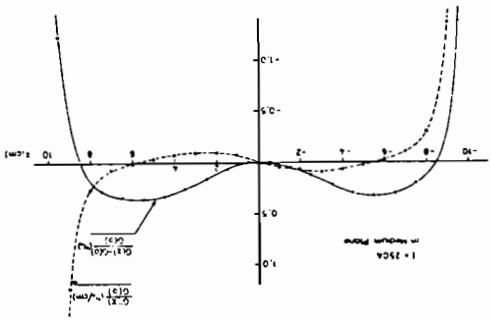

Fig.7 The field gradients of the quadrupole magnet (——), and the sextupole component (---) along the beam orbit. The value of G(0) is 0.44 kG/cm.

3.2. Multiturn Injection and RF Stacking

A combination of multiturn injection and RF stacking,[7,8)] is applied to the TARN. In this injection method, heavy ions from the cyclotron are injected into a transverse phase space via a magnetic and electrostatic inflectors while two bump magnets in the ring are excited, and then, are stacked into a longitudinal phase space by an RF field. This injection scheme is very efficient for obtaining higher beam intensity.

For the multiturn injection scheme, two bump magnets are located upstream and downstream from the injecting position. These magnets produce a distortion in the closed orbit between them and the distance between the magnets should be half a betatron wave-length in order to avoid any effect on other parts of the equilibrium orbit. The collapsing rate of the closed orbit distortion is determined so as to optimize the beam intensity stacked in the transverse phase space.

The procedure of RF stacking in the TARN is similar to the one which is used for the stacking of high energy proton beams at ISR, CERN.[9)]

The initial voltage of RF field is determined such that the separatrix well covers the phase space area of the injected beam, and is rather freely chosen within the limits of satisfying the above condition. Then the RF voltage for the capture process is determined at the same value as that during acceleration, 1100 V, at which the period of phase oscillation is 1.13 msec.

The rate of change of momentum for the synchronous particle, $\frac{dP/dt}{P}$, is designed at 1.52×10^{-2} (ms^{-1}) for the synchronous phase angle of 30° and RF voltage of 1100 V. The fractional momentum variation corresponding to the distance from the injection orbit to the bottom of the stacking orbit is 3.82 %. Then it takes 2.5 ms to change the momentum. The revolution-frequency difference between the injected beam and stacked one at the bottom is 32.6 kHz, and the corresponding RF frequency difference is 228 kHz.

During acceleration from the bottom to the top of the stacked region, the RF voltage is adiabatically reduced to the final voltage, 100 V. This reduction of RF voltage is necessary because the high RF voltage brings about undesirably large momentum spread of the stacked beam when the separatrix is moved to the top of the stacking orbit.

The momentum difference between the bottom and the top of the stacked beam is designed as 2.469 %, and hence the RF frequency must be changed by 149 kHz for this acceleration. In order to keep $\sin\phi_s = 0.5$ during the acceleration, the time derivative of the frequency must be 8.8 kHz/ms and the time required for the deposit is 17 ms.

Using the results of the above calculations, a total stacking number for both transverse and longitudinal phase spaces is obtained as a function of the half aperture offered for the multiturn injection. The total stacking number has the maximum value of about 1900 at $x_\beta = 20$ mm. The calculated envelopes of multiturn injected and RF stacked beams are shown in Fig. 8 as a function of length along the central orbit.

3.3 RF System, Beam Monitor and Control

The RF system is composed of a low level RF electronics system and high power parts including an accelerating cavity. The low level RF electronics plays an important role to obtain phase lock between

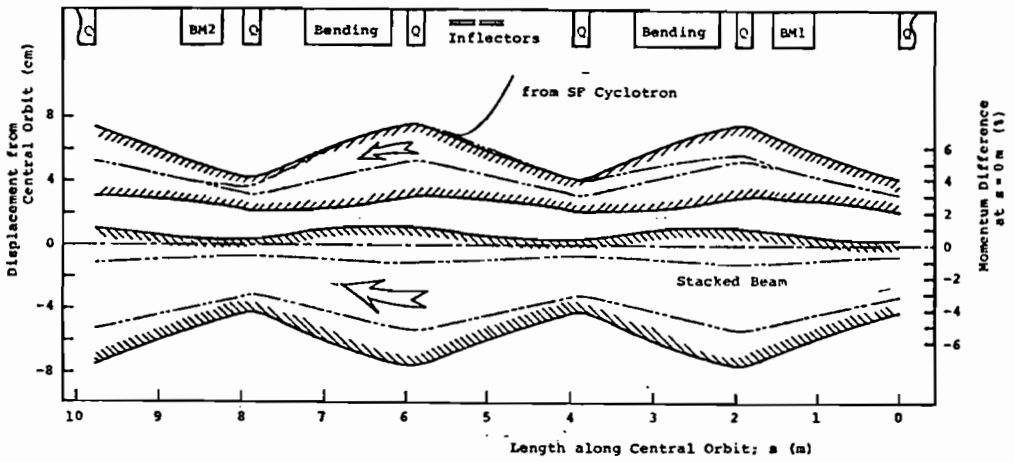

Fig.8 The envelopes of multiturn injected and RF stacked beams are shown by solid lines.

beam and RF accelerating field. Also it is used to control the accelerating voltage and frequency so as to obtain the optimum RF stacking condition. Programmed accelerating voltage and frequency are illustrated in Fig.9.

The amplitude of the RF field is modulated by a balanced modulator in accordance with the waveform from a function generator. The fast feedback voltage control function is given by an amplitude normalizer. It stabilizes the RF voltage against the variation of the cavity impedance due to the sweep of the frequency.

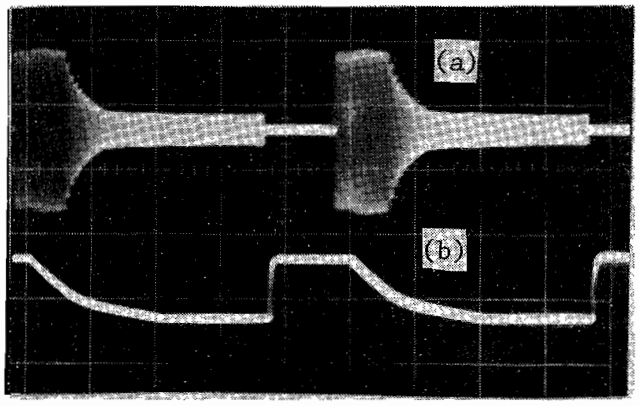

Fig.9 (a) Programmed accelerating voltage in the RF cavity. It rises from 0 V to 500 V and decreases to 100 V. (b) Accelerating frequency, which varies from the base frequency 8.00 MHz by 380 kHz. The time scale is 5 ms/div.

The phase difference between the accelerating field and the fundamental mode of the bunch signal is measured by a phase detector, where the beam phase information is derived from a core-type beam monitor with a resonator whose resonant frequency is adjusted at the RF frequency. The output signal of the phase detector is fed to a voltage controlled oscillator (VCO) through a summing amplifier. The

output frequency of the VCO is determined by the voltage on a varacter, which is composed of a program term from the function generator and a feedback one coming from the phase detector. The absolute value of the stable phase angle is determined by a phase shifter in the loop.

An accelerating structure is composed of two cavities with an electrical length of a quarter wave. In order to tune the cavity over an operating frequency and to reduce the size of the cavity, 24 ferrite rings, 328 mm O.D., 260 mm I.D. and 20 mm thick, are stacked in the cavity. Each ferrite ring is sandwiched by cooling copper discs. The resonant frequency of the cavity is varied by changing a capacitance between two inner conductors or by impressing the biasing magnetic field in the ferrite cores. The copper plate was wound around the ferrite rings by two-turns.

The RF power is fed to the cavity by a 5 kW RF power amplifier through a wide band transformer of a transmission type for matching their impedances. The transformer was also used to obtain two RF fields, whose phases are different by 180° from each other for the push-pull operation of the cavity.

Several kinds of beam monitors were prepared for efficient beam handling during injection and stacking. Electrostatic monitors with capacitive pickups and magnetic monitors using ferrite cores were used in a non-destructive manner, which is necessary for beam stacking. The former detects beam position by measuring asymmetry of induced charges on two electrodes. The magnetic monitor, where a coil picks up magnetic flux induced in the ferrite core, provides informations on beam intensity and phase. Output signals are converted into sine-wave through a tank circuit and fed to the RF control system. Four beam-dumping (Faraday-cup type) monitors are installed in the ring for studying the injection orbit of the beam in the ring. This detector, with sixteen strips of Be-Cu foil 500 μm in thickness and 2 mm in width, measures intensity and position simultaneously.

3.4. Vacuum System

On-beam pressure lower than 1×10^{-10} torr (1.33×10^{-8} Pa) is required to achieve 90 % survival probability of accumulated ions during a

period of 1 sec.[10] Since 1976, some preliminary tests on ultra-high vacuum (UHV) system have been carried out, two test stands for UHV studies being constructed. The vacuum chamber of test stand I is cylindrical, 30 cm in diameter and 200 cm in length, and is made of stainless steel 316L. The pumping system is composed of a 1500 ℓ/s titanium sublimation pump with liquid nitrogen shroud, and a 500 ℓ/s turbomolecular pump backed by a 400 ℓ/s oil diffusion pump. On the other hand, the vacuum chamber of test stand II is a prototype model of the bending section and the short straight section in the TARN. The pumping system is composed of a 400 ℓ/s sputter-ion pump and a 200 ℓ/s turbomolecular pump backed by a 100 ℓ/s turbomolecular pump. The baking and discharge cleaning effects were measured using test stands I and II, respectively.

Pumping characteristics have been studied to establish efficient procedures for baking out the vacuum chamber and glow discharge cleaning in Ar or Ar + O_2. It is found that the partial pressure of H_2O decreases significantly after glow discharge processing. In the typical spectrum, a peak at m/e = 16 was the highest one. It may be understood that this peak is not due to ions in gas-phase, but to O^+ ions emitted from the surface of the quadrupole mass-filter caused by electron impact desorption effect.[11] This peak is a very useful indicator of "cleanliness" of the surface in the system.

In November 1978, the whole vacuum system was assembled tentatively prior to installation into the magnet gaps. The system was baked at 250°C for 50 hours, and the average pressure of 2×10^{-11} torr was attained after 1,000 hour pumping down without glow discharge processing.

The system is illustrated in Fig. 10. The chamber has a circumferencial length of 31.8 m, and is divided into eight unit sections, each of which consists of one dipole magnet chamber of 45×234 mm^2 rectangular cross section, two quadrupole magnet chambers of 90×190 mm^2 diamond-shaped cross section, and a straight section chamber. These chambers are made of stainless steel 316L. Each pumping system is composed of a sputter-ion pump, a titanium sublimation pump, and a distributed pump, which is installed along the inside of the outer wall of the dipole magnet chamber and is also used as a high-voltage electrode for in situ glow discharge cleaning.[13]

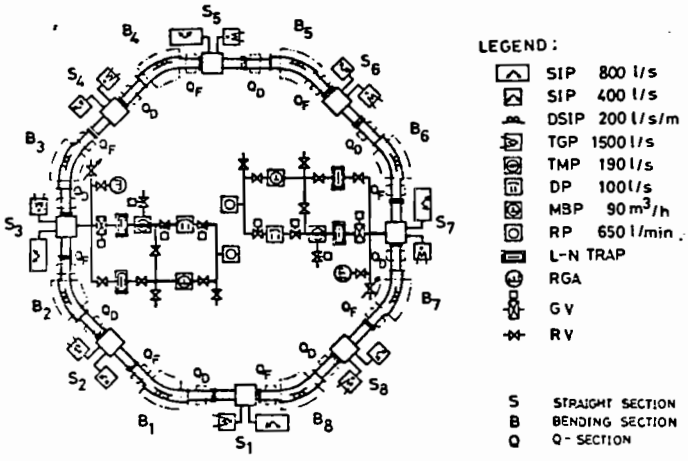

Fig.10 Vacuum System of the TARN

As shown in Fig.10, two roughing and auxiliary pumping systems are located at the straight sections S-3 and S-7, each of which comprises a turbomolecular pump backed by either an oil diffusion pump or a mechanical booster pump, and a rotary pump.

The straight section S-1 is connected to the injection beam transport line through three stages of differential pumping system.

3.5. Preliminary Results of Injection Test into TARN

The first trial of beam injection from the SF-Cyclotron to the TARN was performed successfully in August, 1979. The molecular hydrogen beam (H_2^+) of 14 MeV was used, because the dissociation cross section is similar to the charge exchange cross sections of heavy ions with residual gas molecules. In October, α particles (He^{2+}) of 28 MeV were also stacked in the ring.

Typical results of beam injection and accumulation using an electrostatic beam monitor are shown in the following figures. Figure 11 shows the 80μs long injected beams, which are pulse shaped from the C.W. cyclotron beam by a kicker magnet installed at an upstream position in the beam transport line. The upper picture shows the intensity of a single turn injected beam and the lower one shows the intensity of the beam four-turn injected when ν_x was adjusted to 2.25. According to the field decrease of the bump magnets, the beam is injected in multiturn fashion the intensity grows as illustrated in Fig. 12. The lower two curves show the current forms of the kicker and bump magnets. Accumulated intensity by multiturn injection is $\sim 10^8$ particles. The beam injected in multiturn is captured by the RF field. Fig.13 shows that the captured beam lasts till the next injection time after 25 ms. This

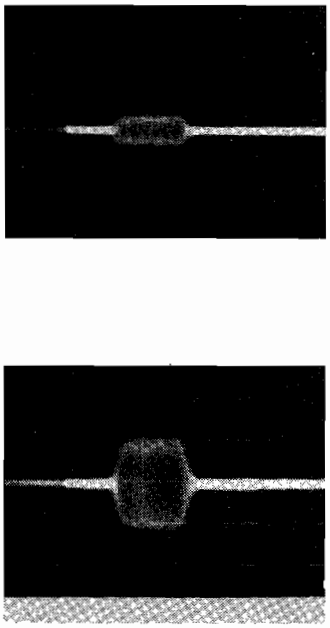

(b)

Fig.11 Shape of the injected beam with a length of 80 μs, a) single turn injection, b) four turn injection, observed by electrostatic beam monitor, 40 μs/div.

picture is taken by observing the 4th harmonics of the beam signals, avoiding severe noise from the RF source. Captured beam is moved to the stacking orbit by sweeping the RF frequency. The spectrum analyzer device is used for observing the beams, which have frequency components corresponding to the range of momentum spread of the beam. A typical result is shown in Fig.14. It is, however, difficult to estimate the intensity of stacked beam correctly at present. Further investigations for measuring the intensity of the stacked beam is needed. A sextupole magnet correction system for control of chromaticity is being designed in order to surmount the transverse coherent resistive wall instability. The intensity limit of the stable

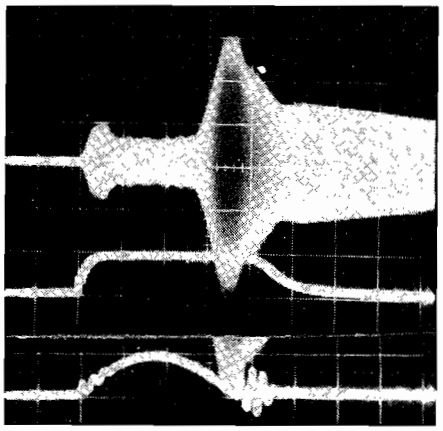

Fig.12 Injected beam in multi-turn (a), current form of kicker magnet (b), current form of bump magnets (c), 20 μs/div.

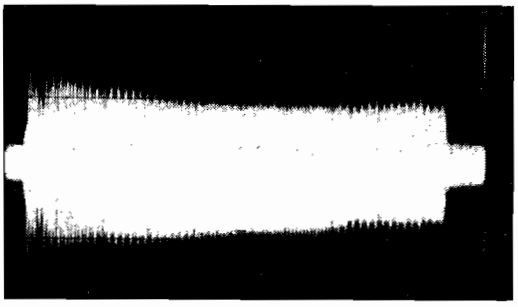

Fig.13 Captured beam by RF field, 2 ms/div, 4th harmonic observation of electrostatic monitor signal.

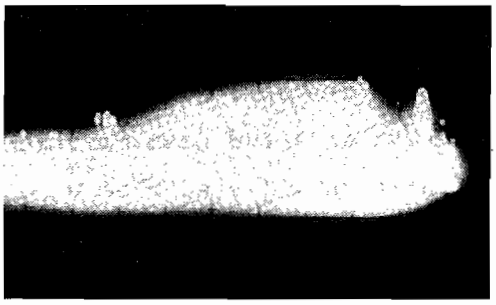

Fig.14 Display of spectrum analyser, illustrating the momentum spread of captured beam by the frequency sweep of 380 kHz.

beam is estimated at 6×10^8 without correction and 4×10^9 with correction for N^{5+}. The growth rate of the instability if we store 2×10^{10} N^{5+} into the ring is estimated at 0.2 sec.[13)]

ACKNOWLEDGMENT

The study of the project is advanced by the NUMATRON group at INS. The authors would like to express their thanks to the members of the group and also to the members of the SF-Cyclotron group. They are also grateful to Professor K. Sugimoto and M. Sakai for their continuous encouragement and to Dr. A. Garren for his calculations of the sextupole correction system.

REFERENCES

(1) Y. Hirao et al., "NUMATRON, Part II", INS-NUMA-5, 1977.

(2) Y. Hirao, "NUMATRON Project", Proc. of the Int. Conf. on Nuclear Structure, P.594 (1977).

(3) T. Katayama and S. Yamada, "Injection Method of the NUMATRON", Proc. of the 2nd Symp. on Acc. Sci. and Tech., p.151 (1978).

(4) Y. Hirao et al., "The INS 176 cm Sector Focusing Cyclotron", Proc. 7th Int. Conf. on Cyclotrons and Their Applications, p.103 (1975).

(5) M. Kumada et al., "Wide Aperture Q Magnet with End Cut Shaping", Proc. of 2nd Symp. on Acc. Sci. and Tech., p.75 (1978).

(6) M. Kumada et al., "Flux Meter for Field Gradient with Pendulum", Proc. of 2nd Symp. on Acc. Sci. and Tech., p.75 (1978).

(7) E. Keil, "Stacking in Betatron Phase Space for the ISR", ISR-TH/67-10.

(8) S. Yamada and T. Katayama, "Injection and Accumulation Method in the TARN", INS-NUMA-12 (1979).

(9) For example W. Schnell, Proc. of Conf. on High Energy Acc., Dubna (1963).

(10) K. Chida et al., "Vacuum System of the Test Ring for the NUMATRON", Proc. of the 2nd Symp. on Acc. Sci. and Tech., p.34 (1978).

(11) P. A. Redhead, "Ion Desorption by Electron Bombardment; Relation to Total and Partial Pressure Measurement", J. Vac. Sci. Technol. Vol.7, No.1, 182 (1970).

(12) A. G. Mathewson, J. Kouptsidis and L. Hipp, Proc. 7th Int. Vac. Congr. and 3rd Int. Conf. Solid Surfaces, Vienna, 1977.

(13) A. Garren and A. Noda, "A Sextupole Magnet Correction System for TARN", INS-NUMA-14, (1979).

STORAGE RING INJECTION

R. J. Burke
Argonne National Laboratory

Introduction

Multiturn injection is an essential step in generating high power beams for heavy ion fusion. Systems have been proposed that use a hundred turns of injection or more,[1,2,3] which must be done with minimal beam losses. To cause the stored beam to miss the back side of the inflector, adequate separation is required between the stored and incoming beams. This dilutes the phase space density, but the allowable dilution is also constrained by the limits on the brightness of the linac beam and the final focussing requirements set by the size of the fusion fuel pellet. The injection problem is thus bracketed by the constraints of beam loss on the one hand and phase space density on the other.

The most commonly proposed scheme to accomplish many turns of injection has been to inject N_1 turns into the horizontal plane of a ring used expressly for injection, transfer this accumulated beam to a storage ring after first interchanging the horizontal and vertical phase planes, and repeat the process N_2 times for a net multiplication of the linac current by $N_1 \times N_2$. For convenience, we assume $N_1 = N_2 = N$ and write $N^2 = S$, the total number of turns injected into the first ring and destined for any one final storage ring.

Investigation of injection schemes at ANL has begun to incorporate detailed space charge effects using numerical simulation.[4] The results so far confirm the expectation that space charge effects complicate the injection problem, and more dilution seems necessary to avoid excessive beam loss. The means to increase the dilution allowance are, however, very limited.

Allowed Dilution

The dilution allowance may be written

$$D = \frac{\varepsilon_{SR}}{\varepsilon_L (S)^{\frac{1}{2}}}$$

where ε_{SR} = the emittance of the stored beam and ε_L is the emittance of the linac beam. The total number of injected turns is also the ratio of the overall current of the beam stored in the ring (I_{SR}) to that out of the linac (I_L). The average stored current, based on the space charge limit, is

$$I_{SR} = K \cdot \Delta\nu \cdot \varepsilon_{SR} \cdot (\beta\gamma)^2 \cdot \overline{B} \cdot BF \quad ,$$

where the value of K is about 100 if the average magnetic field ($\overline{B}$) is expressed in Teslas and the emittance is expressed in mr-cm. The expression gives the same average current for a given fill and different azimuthal beam distributions (i.e., bunching factors, BF) as long as the corresponding value of the tune shift is used.

The dilution may now be written

$$D \sim \left(\frac{I_L}{\Delta\nu \cdot B \cdot BF}\right)^{\frac{1}{2}} \frac{\varepsilon_{SR}^{\frac{1}{2}}}{\beta\gamma\ \varepsilon_L} \quad .$$

The variables in this expression are subject to numerous constraints. As noted above, ε_{SR} is constrained by the final focussing requirements. Much consideration of the normalized linac emittance ($\beta\gamma\ \varepsilon_L$) has led to rough agreement about the minimum feasible; though reductions are not impossible, they are expected to be very difficult. Multiple front ends and other concepts have raised the linac current to the point where economics may be the limiting factor. The tune shift and bunching factor should not be too small to achieve cost effectiveness in the storage rings. Thus, a small average field, or large ring radius, may be the most useful possibility for increasing the dilution allowance.

If there were a more important reason for keeping the ring radius small, this means of providing a larger dilution allowance could not be used. From the results of the storage ring group at the workshop, it appears that such a reason could be avoidance of the longitudinal microwave instability. The potential conflict stems from the dependence of the Keil-Schnell threshold current[5] for this instability on the momentum spread of the stored beam, which is related to the ring radius in the following way.

As the ring circumference is increased, so tends to be the length of the beam contained in it. This requires increased longitudinal compression to reach the final beam length determined by the short pulse duration needed to drive fusion pellets to ignition. Additionally, efficient focussing constrains the momentum spread in the compressed beam to some upper limit; and for a given upper limit, conservation of phase space in the longitudinal plane requires that the momentum spread before the final compression must decrease as the amount of compression is increased. Thus, enlarging the circumference of a ring tends to require storing beam with smaller momentum spread, raising the concern that the stored beam will be unstable.

The storage ring parameters generated at the workshop use relatively high average magnetic fields, apparently to avoid the instability by maintaining adequate momentum spread in the ring. As shown in Table I, however, these designs may be easily adjusted to larger ring radius, lower magnetic field, fewer turns of injection, and larger allowed dilution without changing the momentum spread (or the final compression factor). The changes are made by adjusting the bunching factor, tune shift at the space charge limit, number of rings, and number of bunches per ring. As seen in Table I, all of the changes that have been made are non-controversial.

Discussion

The revised parameters show that phase space dilutions by more than a factor of 2.5 can be provided for the systems considered at the workshop. Initial studies of injection in the presence of strong space charge forces[4] permit optimism that the allowance of this much dilution will result in acceptably small beam loss. In fact, the ease of reducing the injected turn requirement to a relatively small number suggests that one or more of the other significant parameters of the systems are not optimal and invites consideration of further parameter changes. Alternatively, one could simply rejoice at the prospect of an easier injection task, and that it is not mandatory to employ schemes that call for additional rings for injection, multiple ring filling ejection, and transfer, etc. Nevertheless, these schemes appear to be technically realistic, if confined to reasonable limits, and the most immediate question may not be technical feasibility but cost. Thus, it could be profitable to return to a higher degree of difficulty for the injection problem, if this allows changes that significantly reduce the overall cost.

In the systems studied, the linear accelerator is the obvious subject for cost reduction attempts. Most obviously relevant to the injection problem is the beam current, which was taken to be 0.3 A. For cases B and C, the peak power needed to accelerate the beam is 3 GW. A reasonably optimistic unit cost for rf power is 0.1 $/W. The resultant $300 M price for the beam power component of the rf requirement suggests that it may be advisable to lower the current to cut the cost, and accept the corresponding increased difficulty in the injection problem.

Reducing the total accelerating voltage of the linac would not only reduce the rf costs, but all other linac costs as well. In the context of the fusion pellets considered at the workshop, one would keep the ion kinetic energy and shorten the linac by increasing the ion charge state.

Table II compares some parameters for a Case B system (3 MJ, 10 GeV) using U^{+2} with the previous U^{+} system. Halving the linac cost and increasing the cost for rings probably brings the total cost down.

In addition to the space charge effects or charge state that were regularly considered before the workshop, the effect of the charge state on the longitudinal instability must also be taken into account. The systems studies at the workshop were guided by the dependence of the Keil-Schnell threshold current, which varies inversely with the charge on the ions. It appears, however, that the Keil-Schnell threshold criterion is irrelevant for HIF storage rings because of the low velocity of the ions, which results in a large capacitive contribution to the complex inpedance. This makes the stored beams unstable with a modest resistive impedance component.[6] The amount of momentum spread required for stabilization would result in excessive chromatic aberration in final focussing and/or impractical ring parameters. Stabilization by providing compensating inductive impedance also appears inapplicable. Because the impedance provided by any physical feature of the ring will depend on the frequency, such compensation would not stabilize all of the relevant modes.[7] Therefore, the risetime of the instability rather than the threshold current appears to be the governing consideration.

Fenster[6] finds that the risetime may be expressed for the purposes of systems studies in the following convenient form

$$t_{rise} = \left(\frac{2R}{\Delta\nu\varepsilon_{SR}}\right)^{\frac{1}{2}} \frac{Z_o}{2\pi Z_r \beta^2 c} \quad \text{(sec)}$$

Z_r is the resistive contribution to the longitudinal impedance ($\Omega\ m^{-1}$) and $\Delta\nu$ is the tune shift at the space charge limit. In the examples given in Table I and Table II, the problem has been looked at in terms of the values of Z_r needed to achieve $t_{rise} = 0.01$ sec. Since the beam is accumulated in a fraction of this time (about 2 msec), the values of Z_r given in the tables should substantially overestimate the requirement.

Summary

Some basic issues involved in injecting the beam into storage rings with the principal parameters of those studied at the workshop have been considered. The main conclusion is that straightforward adjustments of the storage ring parameters makes injection easy. The largest number of injected turns is fourteen, and the phase space dilution allowance seems adequate to ensure very small beam loss during injection. The adjustments also result in lower bending magnet fields, and high field superconducting magnets (e.g., 5 Tesla) are not necessary. The design changes do not necessarily affect the Keil-Schnell criterion for stability of the longitudinal microwave instability, although that criterion appears to be irrelevant. Because the beams are expected to be unstable, but with slow growth rates, the vacuum chamber impedances required to give equal risetimes for the various designs are compared for systems posing various degrees of difficulty for injection.

Finally, the impact of the parameters on cost is noted, and a system is considered that cuts the length of the linac in half by using doubly charged ions. Aside from the possible net decrease in cost, the system using doubly charged ions required fewer injected turns (due to the same changes made for the other revised systems) and a slightly lower resistive impedance per unit of length than the comparison U^+ system.

TABLE I

Comparison of Revised Parameters (NEW) with Those Suggested at Conclusion of Workshop (WS)

$A = 238$, $q = +1$, $I_L \approx 300$ mA, $\beta\gamma\varepsilon_L = 1.5$ μm-rad, $\Delta p/p = 2.8 \times 10^{-4}$ (FWHM, beam stored in ring)

	CASE A		CASE B		CASE C	
	NEW	WS	NEW	WS	NEW	WS
E (MJ)	1		3		10	
T (GeV)	5		10		10	
Bρ (T-m)	158		224		224	
t_f (ns)	20		40		70	
I_{aV} (kA)	10		7.5		14.3	
l_b (m)	1.25		3.485		6.1	
Total Compression, LC	49		49		49	
Δν	0.25	.068	0.25	.115	0.25	0.19
BF	0.5	1.0	0.5	1.0	0.5	1.0
ε_{SR} (μm-rad)	57	60	55	60	61	60
N_{SR}	4	7	3	3	9	6
h	8	5	6	3	4	2
N_b	32	35	18	9	36	12
R (m)	156	49	326	81.6	382	95.1
t_{rise} (sec)	0.01		0.01		0.01	
Z_r ($\Omega\ m^{-1}$)	2.14	2.24	1.63	1.15	1.68	.968
$\overline{B}$ (T)	1.01	3.2	0.69	2.7	0.59	2.4
I_{SR} (S.C.L.) (A)	6.4	5.8	8.5	17	8.1	4
I_{SR} (avg) (A)	3.2	5.8	4.25	17	4.1	24.3
I_{SR} (exit) (A)	45	41	60	120	57	170
S	10	20	14	57	14	81
D	2.6	1.9	2.98	1.61	3.3	1.35

TABLE II

Comparison of 3 MJ System for U^{+2} with U^{+} System from the Workshop

q	+2	+1
E (MJ)	3	
T (GeV)	10	
Bρ (T-M)	112	224
$\overline{T}_f$ (nsec)	40	
I_{aV}(kA)	15	7.5
l_b (m)	3.485	
LC	50	49
Δν	0.25	.115
BF	0.5	1.0
ε_{SR} (μm-rad)	57	60
N_{SR}	12	3
h	2	3
N_b	24	9
$(N_b)_{min}$	15	6
R (m)	112	81.6
t_{rise} (sec)	0.01	
Z_r (Ωm^{-1})	.93	1.15
$\overline{B}$ (T)	1	2.7
I_{SR} (SCL) (T)	12.5	17
I_{SR} (avg) (A)	6.3	17
S	21	57
D	2.5	1.6

Definition of Symbols

$\bar{B}$	= average magnetic bending field = $\frac{B\rho}{R}$
BF	= bunching factor in storage ring
D	= maximum allowable dilution per 2-D phase plane during injection
h	= number of bunches from each storage ring
I_{aV}	= nominal beam current on target
I_L	= linac beam current
I_{SR} (S.C.L.)	= peak stored current at space charge limit
I_{SR} (avg)	= average current of stored beam
I_{SR} (exit)	= peak beam current at extraction
LC	= total compression of beam bunches beyond their length when stored at the space charge limit
l_b	= final length of each beam bunch
N_b	= total number of beams on target
$(N_b)_{min}$	= number of beams required by transport power limit
N_{SR}	= number of storage rings
S	= total injected turns per storage ring
R	= average radius of storage ring
t_f	= nominal duration of beam pulse on target
t_{rise}	= risetime of longitudinal microwave instability
Z_o	= 120 π
Z_r	= resistive impedance of storage ring vacuum chamber per unit of length
ε_L	= emittance of linac beam
ε_{SR}	= emittance of beam stored in ring
ν	= betatron tune of storage ring

References

1. ERDA Summer Study of Heavy Ions for Inertial Fusion, LBL-5543, (1976).

2. Proceedings of the Heavy Ion Fusion Workshop, BNL-50769, (1977).

3. Proceedings of the Heavy Ion Fusion Workshop, ANL-79-41, (1978).

4. H. Takeda and S. Fenster, "Study of Inter-Beam Interaction In Injection Processes at the Space Charge Limit, " proceedings of this workshop.

5. E. Keil and W. Schnell, CERN Report ISR-TH-RF 169-48, (1969).

6. S. Fenster, "Longitudinal Microwave Instability," proceedings of this workshop.

7. T. Khoe, private communication.

STUDY OF INTER-BEAM INTERACTION IN INJECTION PROCESSES AT THE SPACE CHARGE LIMIT

H. Takeda and S. Fenster
Argonne National Laboratory

1. INTRODUCTION

Augmenting a particle simulation program originally by I. Haber,[1] beam dynamics of the injection process into a storage ring is studied. Although a real storage ring recently designed employs various kinds of magnetic elements, the essential features of its beam dynamics are determined by the quadrupole doublets. The lattice structure of the storage ring consists of 20 FODO periods. Figure 1 shows the lattice, and Table 1 shows the storage ring parameters.

The quadrupoles are assumed to be thin. Thus, by obtaining an FODO transport matrix for one period starting from beam injection point I, acceptance ellipse parameters α_{Aj},β_{Aj}[2] are calculated at I for both x-x′ and y-y′ planes (j=x,y) for a given phase advance per period. In this paper, we discuss single plane (xx′) injection. We set the beam emittance ellipse parameters for the y-y′ plane (α_{By},β_{By}) equal to the acceptance ellipse (α_{Ay},β_{Ay}) and take the center of the beam ellipse in the y-y′ plane at the center of the beam transport system. Thus, the beam ellipse in the y-y′ plane is exactly matched, regardless of its emittance, so the beam ellipse in the y-y′ plane has the same periodicity as the storage ring elements. Thus, the four-dimensional efficiency and dilution of the injection process are equal to the two-dimensional ones in the x-x′ plane. We wish to check whether beam loss or phase space dilution can occur due to multibeam envelope oscillations dependent on the beam stacking method in injection.

The program keeps track of beam loss for a given aperture of a transport line; a special method accounts for septum losses. Chamber wall image force is not included in the calculation, and the septum has thickness equal to zero.

2. BEAM STUDY

We will briefly describe here the circle coordinate transformation[3] which is convenient for optimizing beam shape parameters. For a given injection point I in a storage ring, it is always possible to find a coordinate system so that the acceptance ellipse at I is a circle. The transformation from x-x′ coordinates to circle coordinates is a function of I.

They are given as:

$$T = \begin{pmatrix} \frac{1}{\sqrt{\beta_{AI}}} & 0 \\ \frac{\alpha_{AI}}{\sqrt{\beta_{AI}}} & \sqrt{\beta_{AI}} \end{pmatrix} \qquad \text{Physical} \longrightarrow \text{Circle}$$

$$T^{-1} = \begin{pmatrix} \sqrt{\beta_{AI}} & 0 \\ -\frac{\alpha_{AI}}{\sqrt{\beta_{AI}}} & \frac{1}{\sqrt{\beta_{AI}}} \end{pmatrix} \qquad \text{Circle} \longrightarrow \text{Physical}$$

where α_{AI}, β_{AI} are acceptance ellipse parameters at I.

The following results are obtained by varying mesh size, beam size, and time step length by factor of two. The result is independent of these factors. All calculations were done with 1024 macro particles for each injected turn. The time step for the particle pusher is 1/5 of each lattice period. Thus, 100 time steps make one turn around the ring. The initial particle distribution is chosen as K-V for each injected turn.

a). Four turn, tune $\nu_x = 5 + \frac{1}{4}$ injection

This tune gives a phase advance at injection point I after one turn of the storage ring of $(5\times360+90)^{\circ}$. Thus, in Fig. 2-1, we see the acceptance at point I of the ring filled with the incident beam at position 1; it is expected to come to position 2 after one turn. It clears the thin septum due to betatron oscillation with zero loss. The dilution of this complete injection is theoretically calculated to be 2.0 without loss. Figure 2-2 shows the result for zero current of this injection scheme. Figure 2-3 shows the result with 1. mA in each beam. A total of four turns reaches the space charge limit of 4. mA. The two figures correspond at time step 400.

b). Five turn, tune $\nu_x = 5 + \frac{1}{4}$ injection

As is seen in Fig. 2-1, there is a hole in the center of x-x' acceptance at point I in four turn injection. If we inject a beam in the center of the acceptance at the first turn followed by bumping of the equilibrium orbit, we

can inject five turns as seen in Fig. 3-1. Theoretically, the dilution of this injection is calculated to be 1.60 without septum loss. Figure 3-2 shows the result for five turns with zero current. Figure 3-3 shows the result with 0.8 mA each beam. A total of five turns reaches the space charge limit of 4 mA. The two figures correspond at time step 500.

c). Four turn, tune $\nu_x = 5$ injection

This tune gives a phase advance at injection point I after one turn of the storage ring as $(5\times360)^{o}$. Injection is performed as follows. First, the equilibrium orbit is bumped locally at I such that it is two beam widths to the right of the septum. Inject the first turn. Bump the equilibrium orbit at I toward the left of the septum by the full width of the beam. Inject the second turn. Subsequent turns are injected the same as the second turn. Figure 4-1 shows the acceptance and beams at I. Theoretically, the dilution of this injection is calculated to be 1.57 without septum loss. Figure 4-2 shows the result for four turns with zero current. Figure 4-3 shows the result with 1 mA in each beam. A total of four turns reaches the space charge limit of 4 mA. The two figures correspond at time step 400.

3. SUMMARY OF CONDITIONS AND RESULTS

Scheme	a	b	c
Phase Advance/Period	94.5^{o}	94.5^{o}	90^{o}
Quadrupole Thin Lens Power*	0.44776 1/m	0.44776 1/m	0.43116 1/m
No. of Injection Turns	4	5	4
Acceptance α_{Ax}	0.73661	0.73661	0.70711
β_{Ax}	4.67707 m	4.67707 m	4.920 m
Acceptance ε_{Ax}	25 mr cm	25 mr cm	25 mr cm
Beam α_{Bx}	0.36831	0.36831	0.20676
β_{Bx}	2.33854 m	2.33854 m	1.4386 m
Emittance ε_x	3.125 mr cm	3.125 mr cm	3.98 mr cm
No. of macro particles/turn	1024	1024	1024
Beam loss due to septum	30	203	403
Beam loss by wall**	105	75	0
Total loss/Total beam	3.30%	5.43%	9.84%

Acceptance	ε_{Ay}	3.125 mr cm	3.125 mr cm	3.125 mr cm
Beam	α_{By}	-0.73661	-0.73661	-0.70711
	β_{By}	4.67707 m	4.67707 m	4.920 m
Beam Emittance	ε_{By}	3.125 mr cm	3.125 mr cm	3.125 mr cm

*Lens power = 1/focal length.

**Vacuum chamber cross section is assumed as 14 cm × 8 cm.
The beam X_e^{+1} is assumed to have 8.5 MeV kinetic energy.

4. DISCUSSION

We notice that, for the beam at the space charge limit, although the turns are deformed in phase space due to mutual beam interaction, they can still be identified individually. A ring large enough to contain the beam with space charge artifically turned off suffers losses on the septum and on the walls at full current. The total magnitude of the loss and its partition among wall and septum both depend strongly on which injection scheme is used. The septum losses differ by a factor of 10, and the best scheme in that regard suffers from significant wall depletion. Scheme b illustrates a trade-off: the incoming current is 20% lower than that of Scheme a, but the septum losses are eight times greater.

The next step is to add wall image forces to the program to make it more accurate. The present results are probably accurate enough to prove that injection schemes cannot be ordered in efficiency and dilution or evaluated properly without this type of computation. The space charge effect is so significant in these high-efficiency, low-dilution injection processes that two-plane vs. one-plane injection schemes may exchange places in merit. We have considered only schemes that have 100% efficiency with zero space charge. Dilution can be improved by accepting losses, but quantitative determinations will require study of a wider class of schemes.

FIGURE CAPTIONS

Fig. 1 The storage ring is represented by a circle, with focusing and defocusing quads indicated. One period consists of two units drift space (2×1.64m) followed by a thin defocusing (x) quad, one unit drift space, thin focusing (x), and two units drift space.

Fig. 2-1 Injection scheme of four turn, $\nu_x = 5.25$ is shown in circle coordinates in x-x′ phase space. The acceptance is represented by a circle. Each beam is represented by an ellipse.

Fig. 2-2 x-x′ phase space at injection point I for four turn $\nu_x = 5.25$ injection with zero current. This figure shows beam phase space at time step 400.

Fig. 2-3 x-x′ phase space at injection point I for four turn $\nu_x = 5.25$ injection with a total current 4 mA. This figure shows beam phase space at time step 400.

Fig. 3-1 Injection scheme of five turn, $\nu_x = 5.25$ is shown in circle coordinates in x-x′ phase space. The acceptance is represented by a circle. Each beam is represented by an ellipse.

Fig. 3-2 x-x′ phase space at injection point I for five turn $\nu_x = 5.25$ injection with zero current. This figure shows beam phase space at time step 500.

Fig. 3-3 x-x′ phase space at injection point I for five turn $\nu_x = 5.25$ injection with a total current 4 mA. This figure shows beam phase space at time step 500.

Fig. 4-1 Injection scheme of four turn, $\nu_x = 5.0$ is shown in circle coordinates in x-x′ phase space. The acceptance is represented by a circle. Each beam is represented by an ellipse.

Fig. 4-2 x-x′ phase space at injection point I for four turn $\nu_x = 5.0$ injection with zero current. This figure shows beam phase space at time step 400.

Fig. 4-3 x-x′ phase space at injection point I for four turn $\nu_x = 5.0$ injection with a total 4 mA. This figure shows beam phase space at time step 400.

The code on the scatter plots in Figs. 2-2, 2-3, 3-2, 3-3, 4-2, and 4-3 indicates the number of macro particles per printing bin; we have not, as yet, used these details.

REFERENCES

1. I. Haber, NRL Memorandum Report 3705.

2. The acceptance ellipse is defined as:

$$x^2 + (\alpha_{Ax}x + \beta_{Ax}x')^2 = \beta_{Ax}\varepsilon_{Ax}$$

$$y^2 + (\alpha_{Ay}y + \beta_{Ay}y')^2 = \beta_{Ay}\varepsilon_{Ay}$$

where ε_{Ax}, ε_{Ay} are acceptances for x, y, respectively.

3. C. Bovet, R. Gouiran, I. Gumowski, and K. H. Reich, CERN/MPS-SI/Int. DL/70/4, p. 17.

ACKNOWLEDGMENT

We deeply appreciate I. Haber for his offer to use his computer program freely, and we thank him for the many discussions for the details of the program and the time he spent with us.

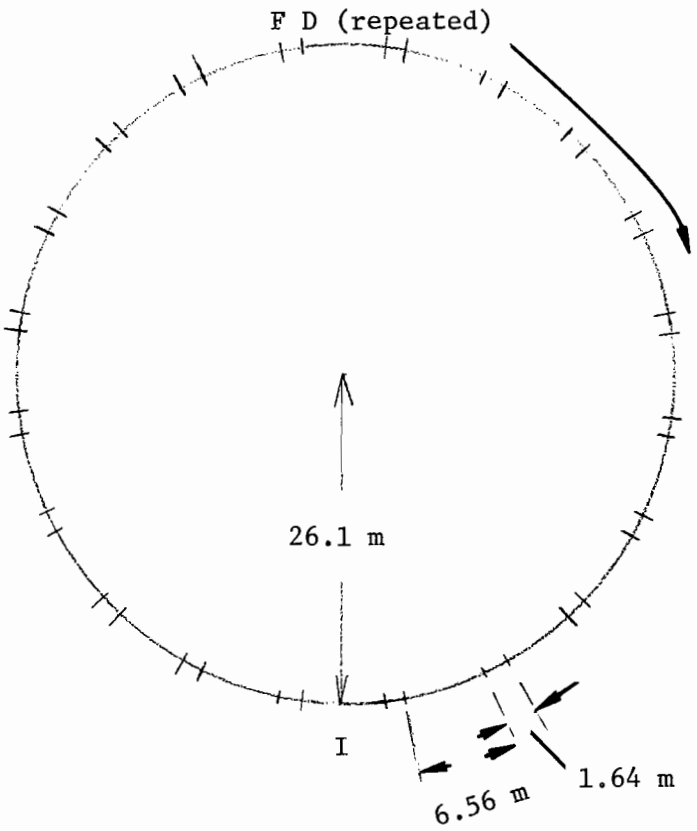

Fig. 1

Storage ring lattice D and F corresponds to defocusing and focusing quadrupoles.

Table 1. Storage Ring Parameters

Method	1	2	3
Quadrupole thin lens power	0.44776 1/m	0.44776 1/m	0.43116 1/m
Acceptance X	25 mr cm	25 mr cm	25 mr cm
α_{Ax}*	0.73661	0.73661	0.70711
β_{Ax}*	4.67707 m	4.67707 m	4.920 m
Acceptance Y	3.125 mr cm	3.125 mr cm	3.125 mr cm
α_{Ay}*	-0.73661	-0.73661	-0.70711
β_{Ay}*	4.67707 m	4.67707 m	4.920 m

*See Ref. 2.

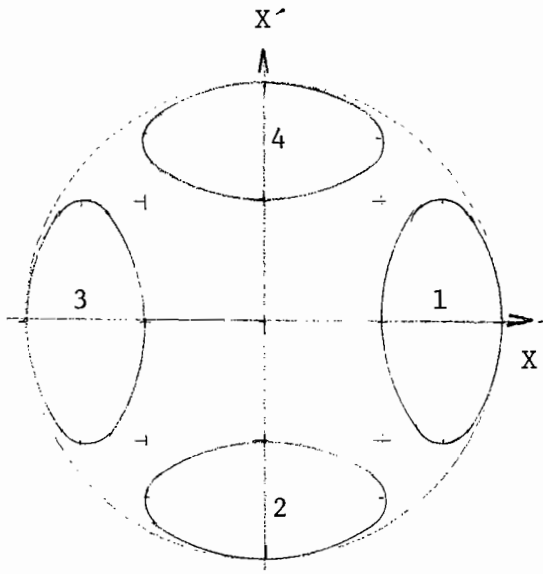

Fig. 2-1

Four turn injection, tune ν_x = 5 + 1/4, X-X´ phase space in circle coordinates. Outer circle is X acceptance. Inner ellipses are injected turns.
Dilution = 2.

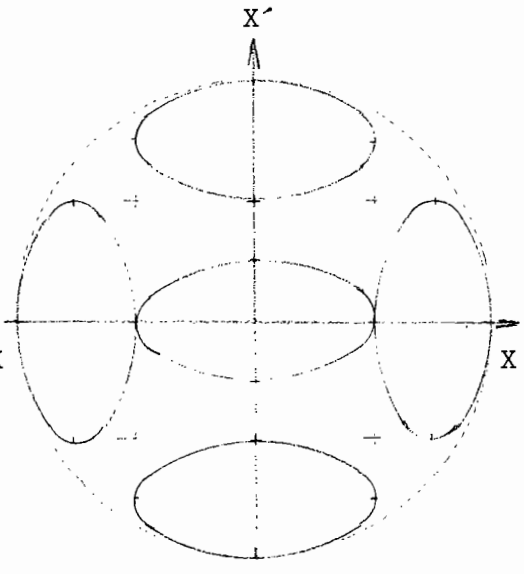

Fig. 3-1

Five turn injection, tune ν_x = 5 + 1/4, X-X´ phase space in circle coordinates. Outer circle is X acceptance. Inner ellipses are injected turns.
Dilution = 1.6

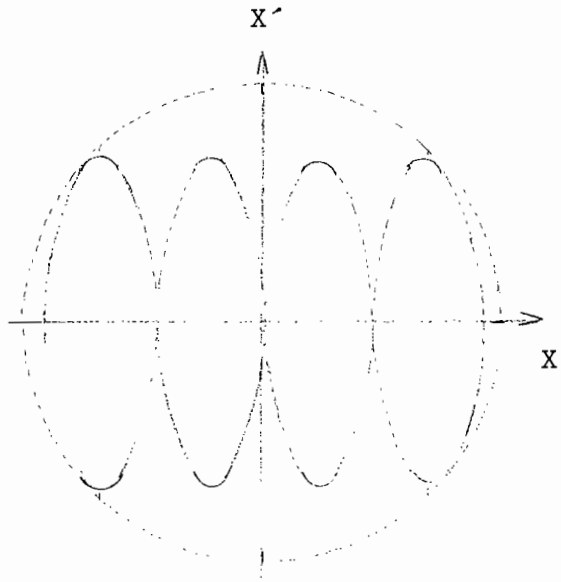

Fig. 4-1

Four turn injection, tune ν_x = 5.0, X-X´ phase space in circle coordinates. Outer circle is X acceptance. Inner ellipses are injected turns.
Dilution = 1.57

Fig. 2-3. x vs. x′ phase space plot for 4 turn injection, tune $\nu_x = 5 + 1/4$. Each beam current = 1 mA.

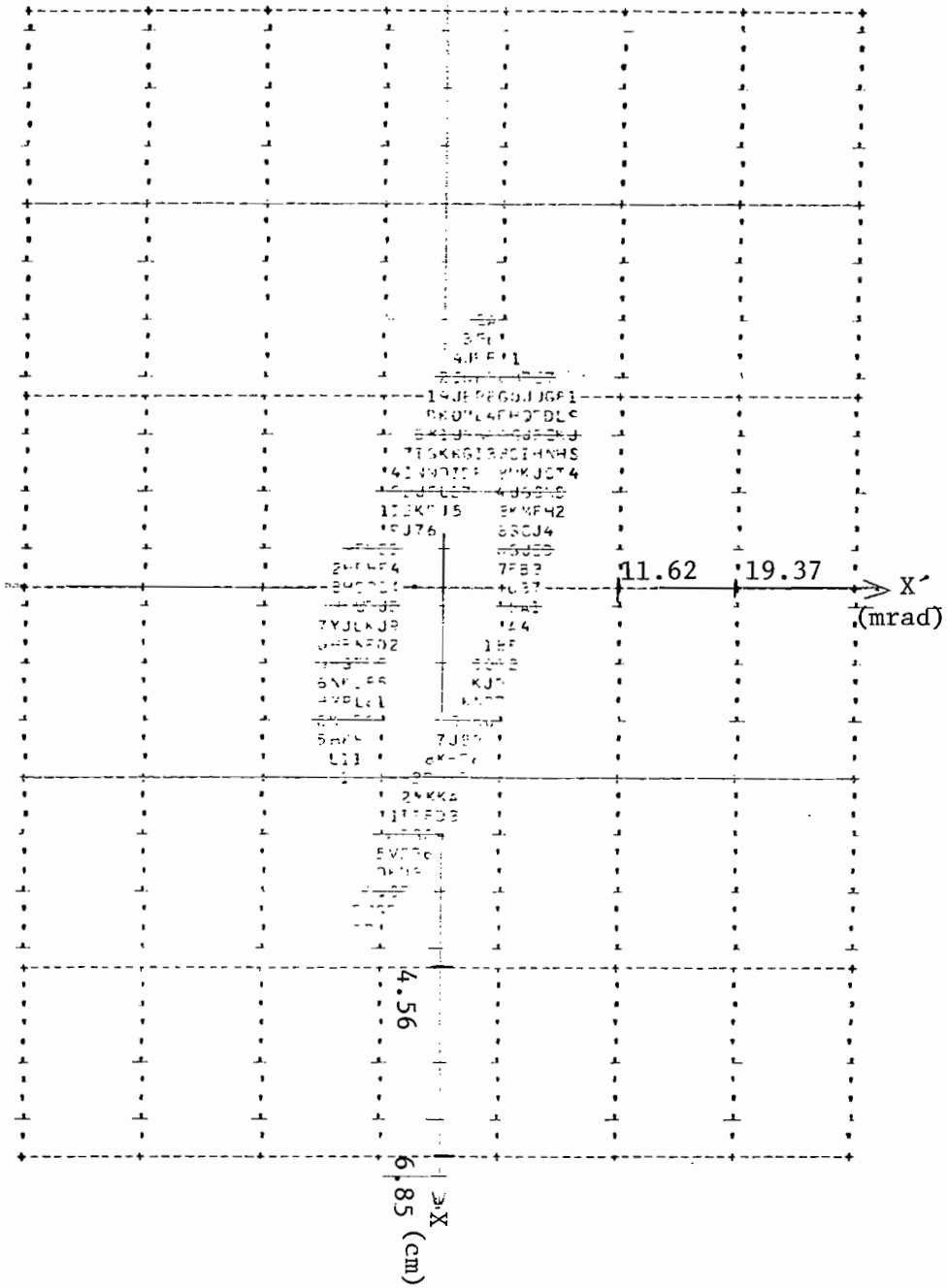

Fig. 2-2. x vs. x′ phase space plot for 4 turn injection, tune $\nu_x = 5 + 1/4$. Each beam current = 0 mA.

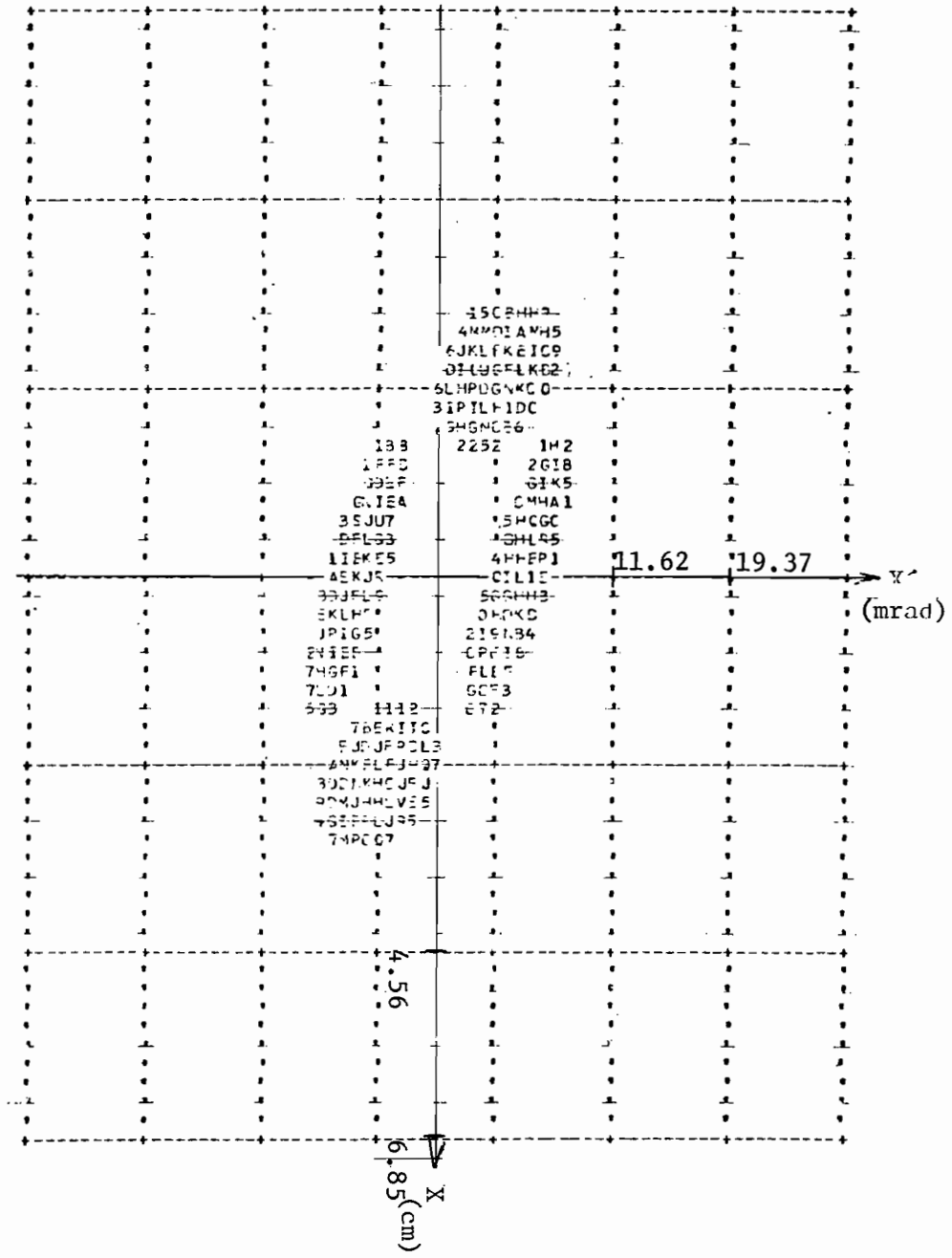

Fig. 3-2. x vs. x′ phase space plot for 5 turn injection, tune $\nu_x = 5 + 1/4$. Each beam current = 0 mA.

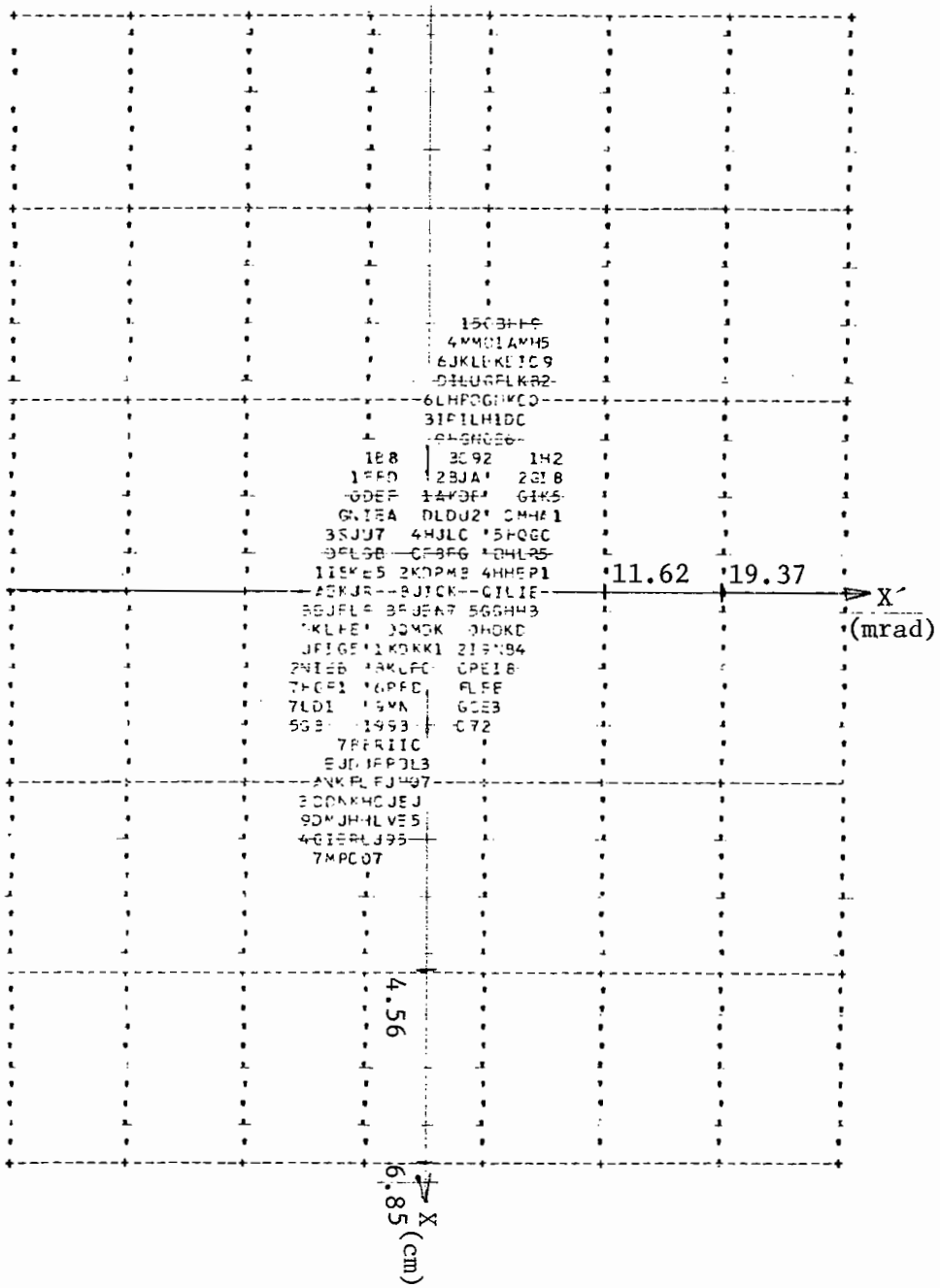

Fig. 3-3. x vs. x′ phase space plot for 5 turn injection, tune $\nu_x = 5 + 1/4$. Each beam current = 0.8 mA.

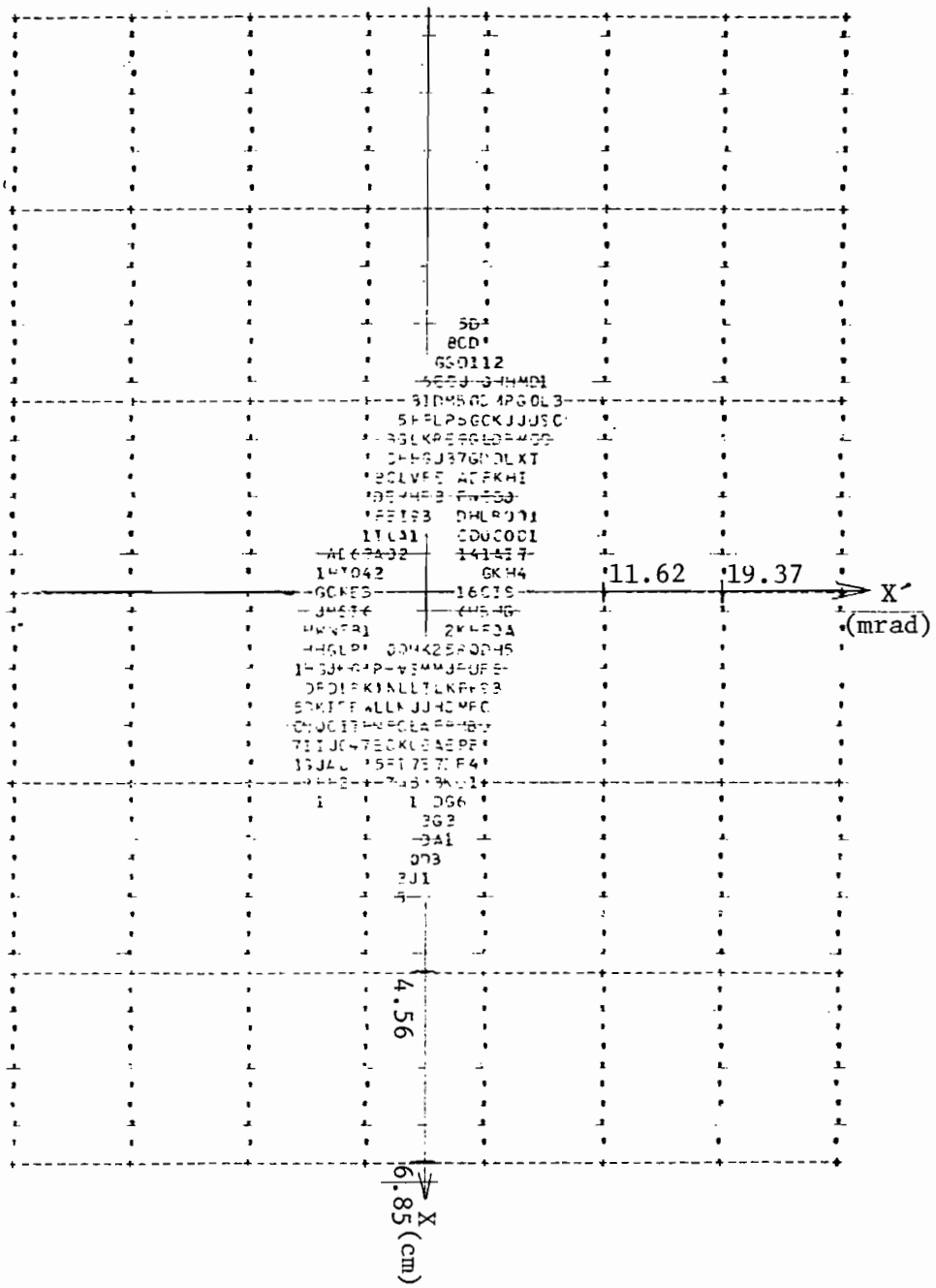

Fig. 4-2. x vs. x′ phase space plot for 4 turn injection, tune ν_x = 5.0. Each beam current = 0 mA.

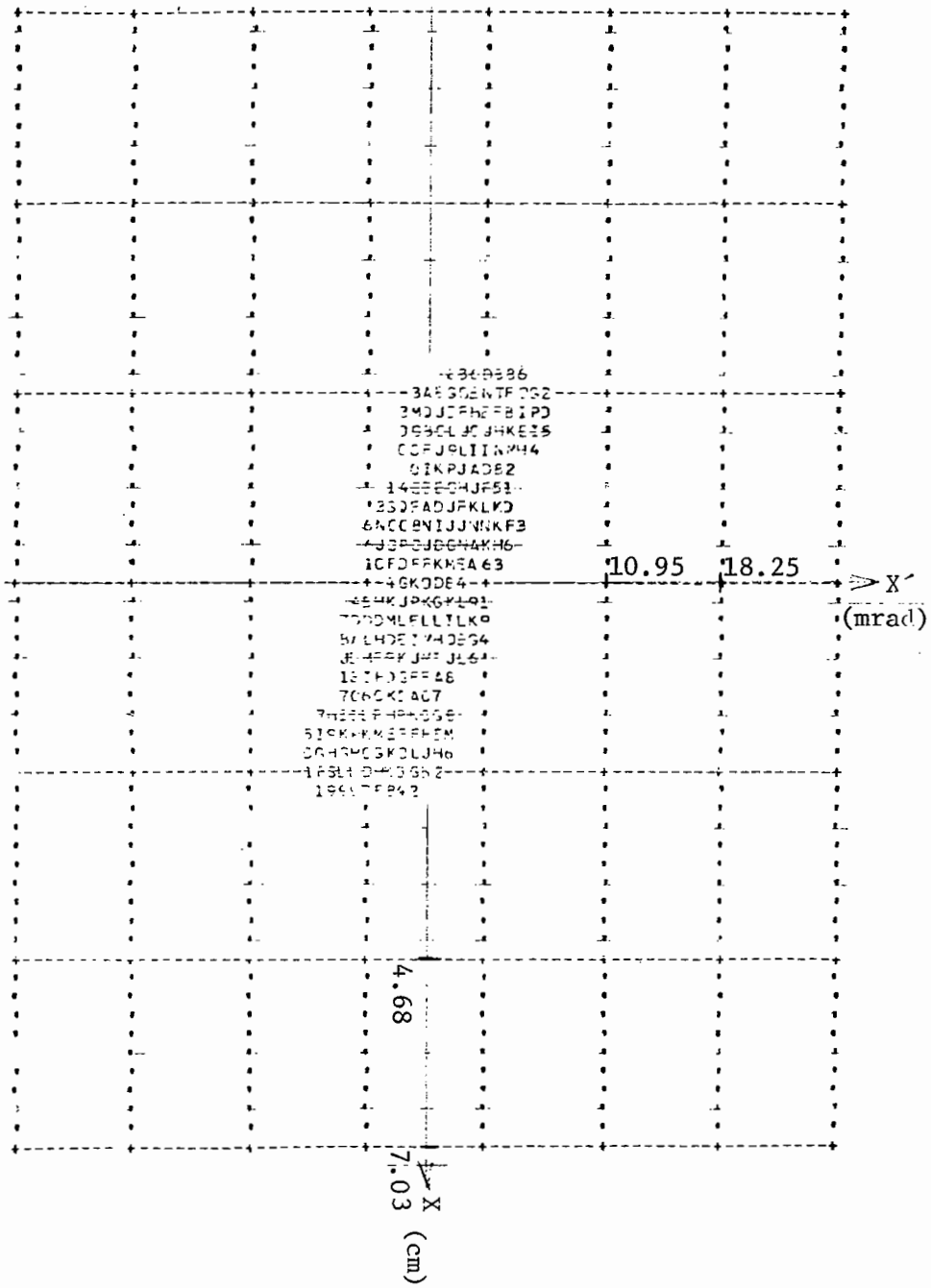

Fig. 4-3. x vs. x′ phase space plot for 4 turn injection, tune ν_x = 5.0. Each beam current = 1 mA.

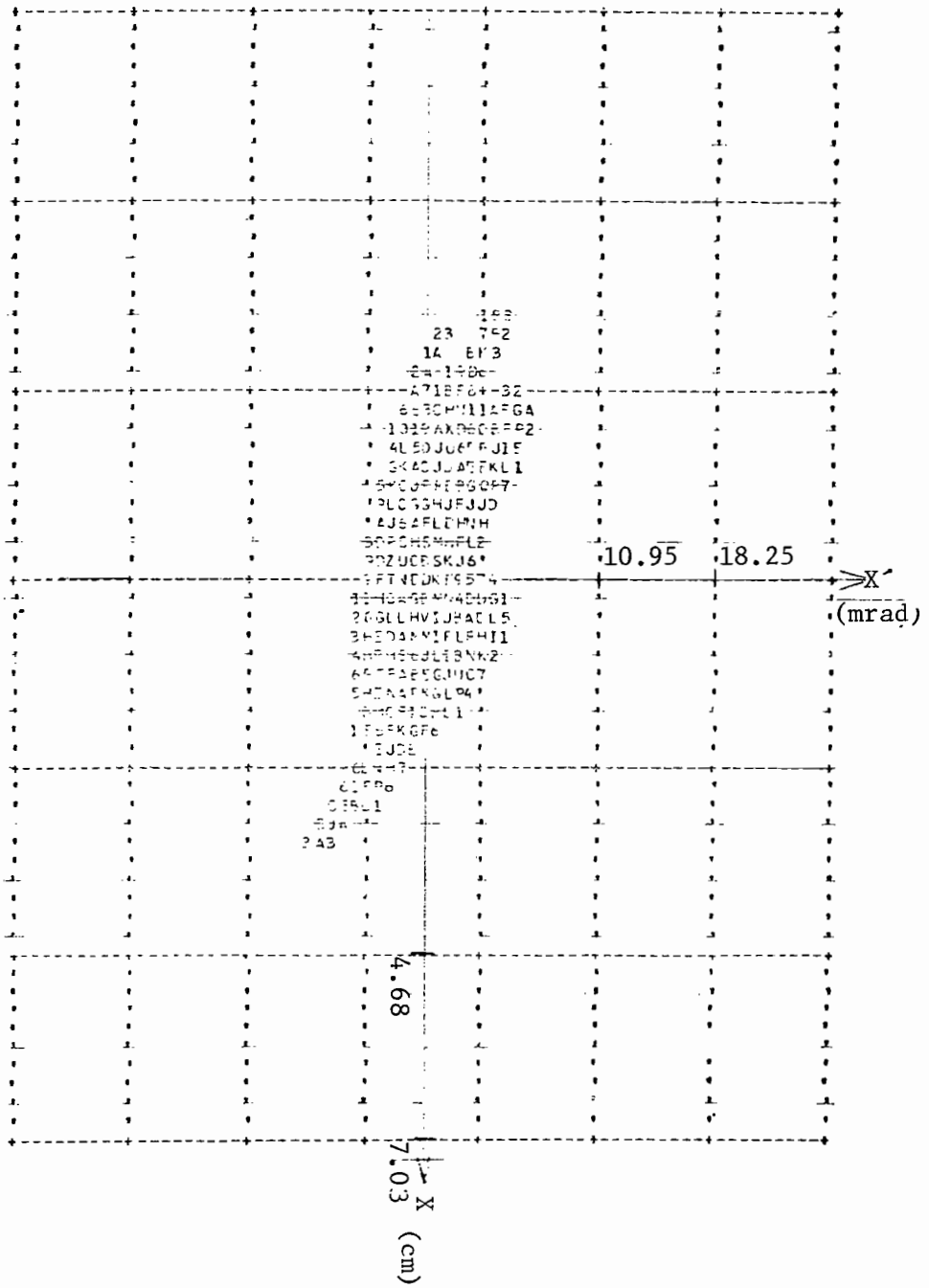

FINAL TRANSPORT IN VACUUM -- SUMMARY

K. Brown (SLAC), E. Colton (ANL), S. Fenster (ANL), A. Garren (LBL),
I. Haber (NRL), I. Hofmann (Garching), J. Lawson (Rutherford),
S. Penner (NBS), and J. Peterson (LBL)

INTRODUCTION

Those considering final transport in vacuum believe that the main problem is the effect of space charge on the final focussing design. It was thought best to approach this from two directions:

1. Assume uniform charge density in the axial and transverse directions in order to modify the zero space-charge designs.

2. Evaluate the designs taking account of non-uniform densities by simulation and other methods.

CONTRIBUTIONS

The participants carried out a number of relevant studies which are included in these proceedings, and which are briefly summarized here:

1. Design and chromatic correction of final focus beam-line at zero current, by K. Brown and J. Peterson. The beam line is made up of three half-wave sections that include dipoles and sextupoles in the first two. The sextupoles are arranged in pairs at betatron phase intervals of 180 degrees in order to suppress their contribution to geometric aberrations. If chromatic corrections are not needed, the third section can stand alone. The corrections increase the momentum acceptance by a factor of two, permitting a 3% spread onto a 4 mm target.

2. Effects of third order aberrations in the above beam line were evaluated by E. Colton, and found to be negligible.

3. Beam line with space charge. The same beam-line, without dipoles or sextupoles, was modified by A. Garren to take account of space charge. Also procedure was proposed for calculation of dispersion in the presence of space charge.

4. Spherical aberration from non-uniform space charge. If the space charge density is non-uniform, it causes a variation of the focal length of the final quadrupole multiplet between the center and edge of the beam. An estimate of this effect by J. D. Lawson shows that this effect could be serious.

5. Numerical simulation of final transport have been made by I. Haber. The first example replaced the final quadrupoles with a single thin lens, the second was that of paragraph 3. Use of K-V distributions confirmed the envelope integrations used in 3. Use of a non-uniform distribution showed some worsening of performance.

6. Coherent Space Charge Instability. Analytic calculations by I. Hoffman show that stability thresholds are considerably reduced when the horizontal and vertical emittances are unequal.

CONCLUSIONS

Problems remain in the design, evaluation, and optimization of final vacuum transport beam lines due to the combination of large values of current and momentum spread. At present a reasonably conservative estimate of allowable momentum spread is about $\pm$ 1% until a chromatic correction system with space charge is demonstrated.

CALCULATIONS OF MAJOR 3RD ORDER GEOMETRIC ABERRATIONS FOR FINAL TRANSPORT LINE

Eugene Colton
Argonne National Laboratory

Karl Brown and Jack Peterson have presented a Final Transport Line for 10 GeV U^{+4}. The system consists of three 1/2 wave quadrupole sections and three dipoles. Furthermore, the system has been chromatically corrected to second-order utilizing two families of sextupoles.

The system was designed to produce a final 4mm radius spot in the center of a 5m radius reaction chamber for a beam with a geometrical emittance of 60 x 10^{-6} π m-rad in both transverse phase planes; the starting ellipses in the phase planes are upright, viz

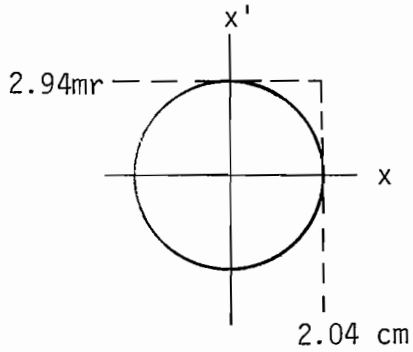

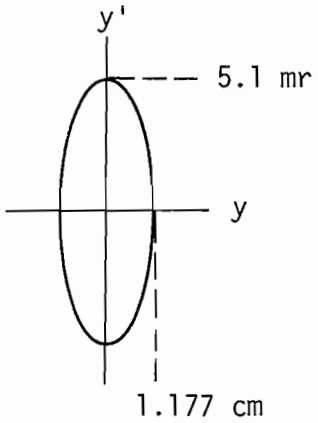

x_o = 2.04 cm

x'_o = 2.94 mr

y_o = 1.177 cm

y'_o = 5.1 mr

The final transfer matrices, e.g. $\begin{pmatrix} C & S \\ C' & S' \end{pmatrix}$

are $\begin{pmatrix} -0.197 & 1.11 \times 10^{-3} \\ 1.41 \times 10^{-2} & -5.07 \end{pmatrix}$ in the x plane (Horiz.)

and $\begin{pmatrix} -0.3413 & 1.6 \times 10^{-4} \\ 7 \times 10^{-3} & -2.93 \end{pmatrix}$ in the y plane (Vert.).

where the primes denote differentiation with respect to s. So the system is point to point and waist to waist ($S = C' = 0$).

The third-order aberration coefficients for the system can be calculated by integrating the first-order functions over the transport.

An aberration coefficient for a quadrupole system is given by (see Steffen p. 52)

$$q = S(s_e) \int_0^{s_e} C(s)\, f(s)\, ds - C(s_e) \int_0^{s_e} S(s)\, f(s)\, ds \qquad (1)$$

where s_e is the end of the beam (the central trajectory propagates in the +s direction), and f is the driving coefficient for the aberration . Since the system is point to point ($S(s_e) = 0$), we rewrite Eq. 1

$$q = -C(s_e) \int_0^{s_e} S(s)\, f(s)\, ds \qquad (1')$$

The Transport run indicates that the large beam envelopes occur at very large S values (i.e., are built up only by the initial angles), therefore, we only consider the aberrations due to the initial angles x_o' and y_o' and not those involving the initital beam sizes x_o and y_o. The problem is reduced to a modest exercise of evaluating four aberrations instead of twenty.

The terms are

$$(x|x_o'^3) = -C_x(s_e)\, \frac{3}{2} \int_0^{s_e} S_x^2 \left(KS_x'^2 - \frac{1}{18} K''\, S_x^2\right) ds$$

$$(x|x_o'\, y_o'^2) = -C_x(s_e) \int_0^{s_e} S_x \left[\frac{S_x}{2} \left(KS_y'^2 - \frac{1}{2} K''S_y^2\right) - S_y S_y' \left(KS_x' + K'S_x\right)\right] ds$$

$$(y|y_o'^3) = C_y(s_e)\, \frac{3}{2} \int_0^{s_e} S_y^2 \left(KS_y'^2 - \frac{1}{18}\, K''S_y^2\right) ds$$

$$(y|x_o'^2 y_o') = C_y(s_e) \int_0^{s_e} S_y \left[\frac{S_y}{2} \left(KS_x'^2 - \frac{1}{2} K''S_x^2\right) - S_x S_x' \left(KS_y' + K'S_y\right)\right] ds$$

where $K = 0$ in a field free region

and $K = \frac{g}{B\rho}$ in a quadrupole where g is the field gradient.

we integrate the terms involving K" <u>once</u> by parts and assume $K' = 0$ at $s = 0$ and at s_e

$$\int_0^{s_e} K''S_x^4\, ds = -4 \int_0^{s_e} K'S_x^3 S_x'\, ds$$

$$\int_0^{s_e} K''S_x^2 S_y^2\, ds = -2 \int_0^{s_e} K'(S_xS_x'S_y^2 + S_x^2S_yS_y')\, ds$$

The final expressions for the aberration coefficients

$$(x|x_o'^3) = -\frac{3}{2} C_x(s_e) \int_0^{s_e} [KS_x^2 S_x'^2 + \frac{2}{9} K'S_x^3 S_x']\, ds \tag{2}$$

$$(x|x_o' y_o'^2) = -\frac{1}{2} C_x(s_e) \int_0^{s_e} [K(S_x^2 S_y'^2 - 2S_xS_x'S_yS_y') + K'(S_xS_x' S_y^2 - S_x^2S_yS_y')]\, ds \tag{3}$$

$$(y|y_o'^3) = \frac{3}{2} C_y(s_e) \int_0^{s_e} (KS_y^2 S_y'^2 + \frac{2}{9} K'S_y^3 S_y')\, ds \tag{4}$$

$$(y|x_o'^2 y_o') = \frac{1}{2} C_y(s_e) \int_0^{s_e} [K(S_x'^2 S_y^2 - 2S_xS_x'S_yS_y') + K'(S_x^2 S_yS_y' - S_xS_x'S_y^2)]\, ds \tag{5}$$

Equations (2)-(5) are integrated to give the 3rd order aberrations - contributions are non-zero only within the magnetic elements. We ignore the three dipoles of the system and integrate over the twelve quadrupoles. For simplicity we approximate the fringe field behavior of a quadrupole by linear functions i.e., the K value is assumed to behave as shown

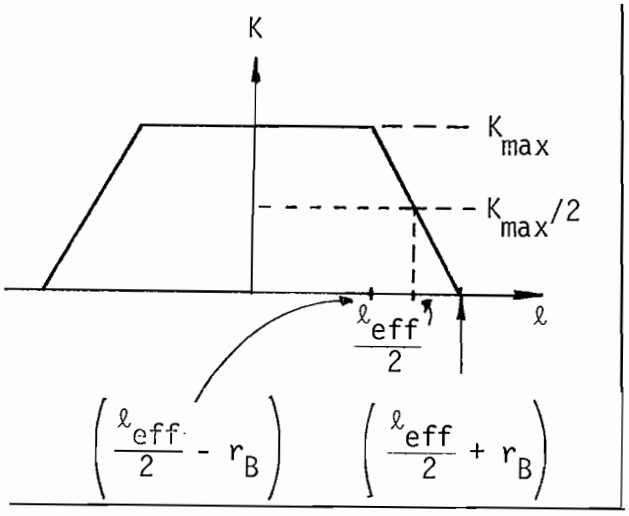

The gradient is constant with value

K_{max} for $|\ell| < \frac{\ell_{eff}}{2} - r_B$

where ℓ_{eff} = quadrupole effective length and r_B = bore radius

and the gradient changes linearly when

$$\frac{\ell_{eff}}{2} - r_B < |\ell| < \frac{\ell_{eff}}{2} + r_B$$

Of course we maintain the same integrated strength as for a square edge magnet:

$$\int_{-\infty}^{\infty} K d\ell = K_{max}\, \ell_{eff} = K_{max}\, [(\ell_{eff} - 2r_B) + \frac{1}{2}(2r_B + 2r_B)],$$

so in the central regions $K = K_{max}$, $K' = 0$ and in fringe regions

$$K' = -\frac{K_{max}}{2r_B} \frac{\ell}{|\ell|}$$

$$K = \frac{K_{max}}{2r_B}\left[\left(\frac{\ell_{eff}}{2} + r_B\right)\right] + \ell K'$$

Each quadrupole was subdivided into fifty intervals and Eqs. (2)-(5) were evaluated numerically for an interval

$$\Delta + (\ell_{eff} + 2r_B)/50 \qquad \text{and} \qquad \phi = \Delta\sqrt{K}$$

The S and S' functions were taken through each section of quadrupole by the standard transform

$$\begin{pmatrix} S \\ S' \end{pmatrix} = \begin{pmatrix} \cos\phi & \frac{\sin\phi}{\sqrt{K}} \\ -\sqrt{K}\sin\phi & \cos\phi \end{pmatrix} \begin{pmatrix} S_o \\ S'_o \end{pmatrix} \qquad \text{for a focussing quad}$$

$$\begin{pmatrix} S \\ S' \end{pmatrix} = \begin{pmatrix} \cosh\phi & \frac{\sinh\phi}{\sqrt{K}} \\ \sqrt{K}\sinh\phi & \cosh\phi \end{pmatrix} \begin{pmatrix} S_o \\ S'_o \end{pmatrix} \qquad \text{for a defocussing quad}$$

where the starting values of the S and S' functions were taken from the TRANSPORT output at $\ell = -\ell_{eff}/2$ and transformed back to $\ell = -(\ell_{eff}/2 + r_B)$.

Equations (2) to (5) reduce to a summation over the contributions from twelve quadrupoles

$$q = \sum_{i=1}^{12} \Delta q_i \qquad \text{for each aberration}$$

The contributions from each quadrupole to the four aberrations, as well as the final results are listed in Table II. The coefficients are small as calculated by this method - the major contributors to $(x|x_o'^3)$ are quadrupoles 3, 6 and 11 where the beam is 50 cm wide horizontally. For the extreme rays

$x_o' = 2.94$ mrad, $y_o' = 5.1$ mrad

$\Delta x_1 = (x|x_o'^3)\, x_o'^3 = 4.67$ mm

$\Delta x_2 = (x|x_o'y_o'^2)\, x_o' y_o'^2 = 1.59$ mm

$\Delta y_1 = (y|y_o'^3)\, y_o'^3 = 0.31$ mm

$\Delta y_2 = (y|x_o'^2 y_o')\, x_o'^2 y_o' = 1.58$ mm

In view of the expected distribution functions, most x_o', y_o' values will be small; since the aberration contributions are cubic in angle the geometric aberrations cause a negligible increase in final focus size. The results as found in this quick analysis should be verified with a ray tracing program.

TABLE I. QUADRUPOLE DATA

QUADRUPOLE	ACTION	g(T/m)	ℓ_{eff}(m)	r_b(m)
1	HF	1.8966	1.0	0.15
2	VF	-3.6847	1.0	0.15
3	HF	5.8519	2.0	0.3
4	VF	-7.1923	2.0	0.3
5	VF	-7.1923	2.0	0.3
6	HF	5.8519	2.0	0.3
7	VF	-3.6847	1.0	0.15
8	HF	1.8966	1.0	0.15
9	HF	1.8097	1.0	0.15
10	VF	-3.5971	1.0	0.15
11	HF	5.8879	2.0	0.30
12	VF	-7.8457	2.0	0.30

TABLE II. ABERRATION CONTRIBUTIONS

	ABERRATION (mm/(mr)^3)			
QUADRUPOLE	$(x\|x_o'^3)$	$(x\|x_o'y_o'^2)$	$(y\|y_o'^3)$	$(y\|x_o'^2y_o')$
1	2.08×10^{-8}	-0.73×10^{-8}	-3.33×10^{-8}	$+6.0\times10^{-8}$
2	1.414×10^{-4}	6.40×10^{-4}	$+4.73\times10^{-4}$	$+1.17\times10^{-3}$
3	5.88×10^{-2}	3.79×10^{-3}	4.59×10^{-5}	$+5.45\times10^{-3}$
4	-7.654×10^{-5}	2.20×10^{-3}	$+2.37\times10^{-4}$	$+4.78\times10^{-3}$
5	-0.30×10^{-3}	2.18×10^{-3}	$+2.36\times10^{-4}$	$+4.85\times10^{-3}$
6	5.82×10^{-2}	3.78×10^{-3}	$+4.63\times10^{-5}$	$+5.52\times10^{-3}$
7	1.428×10^{-4}	6.41×10^{-4}	$+4.73\times10^{-4}$	$+1.16\times10^{-3}$
8	2.099×10^{-8}	-0.73×10^{-8}	-3.31×10^{-8}	$+6.02\times10^{-8}$
9	1.976×10^{-8}	0.76×10^{-8}	-3.18×10^{-8}	$+5.61\times10^{-8}$
10	1.467×10^{-4}	6.54×10^{-4}	$+4.77\times10^{-4}$	$+1.19\times10^{-3}$
11	6.657×10^{-2}	4.16×10^{-3}	$+4.88\times10^{-5}$	$+5.94\times10^{-3}$
12	1.511×10^{-4}	2.73×10^{-3}	$+3.03\times10^{-4}$	$+5.79\times10^{-3}$
TOTAL	0.1839	2.078×10^{-2}	2.34×10^{-3}	3.585×10^{-2}

CHROMATIC CORRECTION FOR THE FINAL TRANSPORT SYSTEM

K. L. Brown (SLAC) and J. M. Peterson (LBL)

I. INTRODUCTION

The final transport and focusing of the heavy-ion beam onto the fusion pellet in vacuum is complicated by several non-linear effects -- namely, chromatic (momentum dependent) effects, geometric aberrations, and space-charge forces. This paper gives an example of how the chromatic effects can be nullified, at least to second order. Whether third- or higher-order terms are important is not yet clear. Space-charge effects are important but are not considered here.

II. THE NEED FOR A CHROMATIC CORRECTION SYSTEM

Consider the problem of bringing a 10 GeV U^{4+} beam from the end of a FODO-type transport lattice and focusing it onto a 4 mm radius pellet. Let the emittance in each transverse plane be 60 π mm-rad. We take for the values of the betatron functions at the end of the transport lattice β_x = 6.93 m and β_y = 2.31 m (corresponding to a 4-meter FODO period with 60 degrees phase shift per period). The matched beam spot at this point is 20.4 mm (horizontal radius) by 11.8 mm (vertical radius).

To match this beam to the 4 mm pellet ($\beta_x = \beta_y$ = 0.27 m) at the center of a 5-meter-radius reaction chamber, it is convenient to use a half-wave optical system consisting of four quadrupole magnets as shown in Figure 1. This focusing array was devised using the TRANSPORT program.[1]

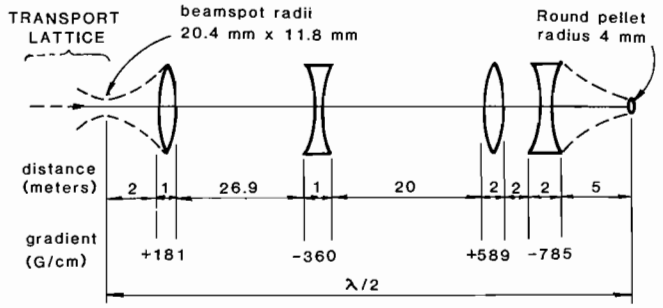

Figure 1. A Half-wave Section Matching the Beam from a 4-meter FODO Transport System to a Round, 4-mm-Radius Target Pellet

This half-wave matching section, although achromatic in first order, has significant second-order chromatic coefficients:

Coefficient	Contribution to Spot Radius for 1%Δp
(x:x'Δp) = 2.02 mm/(mrad-%)	5.9 mm
(y:y'Δp) = 0.369	1.9

where the symbol (x:x'Δp) represents the coefficient multiplying the input horizontal angular width x' and the momentum spread Δp of the beam in the second-order expansion for the horizontal radius x at the pellet, et cetera. These coefficients indicate that a momentum spread of more than 0.5 percent will seriously degrade the focal spot at the pellet. It would be advantageous for a high-current accelerator system to be allowed an energy spread of several percent. Thus we are led to consider a system for correcting the chromatic aberration in the final transport.

III. AN EXAMPLE OF A CHROMATIC-CORRECTION SYSTEM

It is common in synchrotron/storage ring technology to reduce chromatic effects by the use of sextupole magnets at points of relatively high dispersion. Such arrangements produce

---

[1] K. L. Brown, D. C. Carey, Ch. Iselin, and F. Rothacker, "TRANSPORT, a Computer Program for Designing Charged Particle Beam Transport Systems", SLAC 91, (1973 Rev.), NAL91, and CERN 73-16.

momentum-dependent focusing effects which can cancel, to first order, the chromatic effects of the basic lattice. The extent to which this technique is useful depends on the strength of the second and higher-order effects produced in the dipole and sextupole magnets.

Methods have been developed[2] for introducing the sextupole magnets in such a way that the net second-order geometrical aberrations are relatively small. The basic strategy is to use pairs of sextupoles with half-wavelength separations so that their higher-order effects tend to cancel. As an example of such a chromatic-correction system, consider the arrangement shown in Figure 2.

This system consists of three half-wave sections with each section being optically like that shown in Figure 1. The last half-wave section is exactly the one shown in Figure 1. The first half-wave section has the same quadrupole arrangement but has in addition two dipole magnets to create dispersion and two sextupole magnets to produce momentum-dependent focussing in the two transverse planes. The second half-wave section is a mirror image of the first -- i.e., it has identical elements but in the inverse order. With this symmetry the higher-order effects of the sextupoles tend to cancel. The amount of dispersion required is such that the beam width due to momentum spread is about the same as that due to the transverse emittance at the sextupole magnets. Note that the beam is focused to a 4-mm round spot at the end of the first half-wave section as well as at the pellet. This sharp secondary focus is convenient in that it allows the cancellation of the higher-order aberrations to be somewhat independent of the exact location of the sextupole magnets.

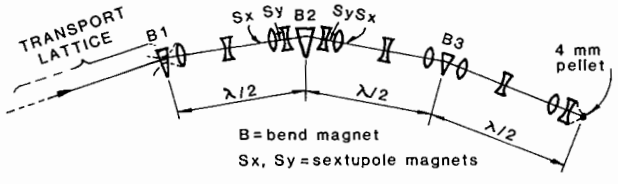

Figure 2. A 3λ/2 Chromatic-Correction and Matching Section

The TRANSPORT program was used to find magnet parameters such that the coefficients (x:x'Δp) and (y:y'Δp) became negligibly small (on the order 10^{-5} mm per mrad-percent). The most important remaining second-order coefficients that affect the beam size at the pellet are:

Coefficients	Contribution to Spot Radius (Δp = 1%)
$(x:x\Delta p) = 1.24 \times 10^{-2}$	0.25 mm
$(x:\Delta p^2) = 2.86 \times 10^{-2}$	0.03
$(x:xx') = 2.75 \times 10^{-2}$	1.65
$(x:yy') = 2.46 \times 10^{-2}$	1.48
$(y:x'y) = 4.26 \times 10^{-2}$	1.47
$(y:xy') = 0.99 \times 10^{-2}$	1.03
$(y:y\Delta p) = 0.84 \times 10^{-2}$	0.10

These coefficients were evaluated under the approximation of "square-edge" magnetic fields -- i.e., negligible fringe fields at the ends of the magnets.

This chromatic-correction system was evaluated using the TURTLE[3] program, in which individual rays are traced using matrix elements good to second order for each component of the transport line. The results are shown in Figure 3, in which the rms horizontal and vertical widths and the fraction of the particles striking the 4 mm-radius pellet are plotted as a function of the momentum half width. In transverse phase space, the particle densities used in these calculations were uniform in x-y

[2]K. L. Brown, "A Second-Order Magnetic Optical Achromat", SLAC-PUB-2257, 1979.

[3]K. L. Brown and Ch. Iselin, CERN 74-2, "Decay Turtle", 1974.

and in x'-y' spaces out to the the elliptical boundaries $(x/a)^2 + (y/b)^2 = 1$ and $(x'/e_x)^2 + (y'/e_y)^2 = 1$.

The plots in Figure 3 show that the chromatic effects in this corrected system are relatively small for a momentum spread of less than ± 2 or 3 percent. That there is some spreading of the beam with no momentum spread and consequent loss at the 4 mm radius target is attributable mostly to the second-order geometric aberrations produced by the sextupoles. The question of how much these second-order geometric terms can be reduced by alternative arrangements of the lattice has not been pursued.

To illustrate the efficacy of this chromatic-correction system, similar ray-tracing calculations were made for the simple one-half-wave matching section without chromatic correction (Figure 1) between the end of the transport lattice and the 4 mm pellet. The results are plotted in Figure 4. Comparison with Figure 3 shows that this chromatic-correction system improves the momentum acceptance of the final transport by about a factor of 2. It shows also that for a momentum spread of less than one percent the chromatic correction is probably unnecessary.

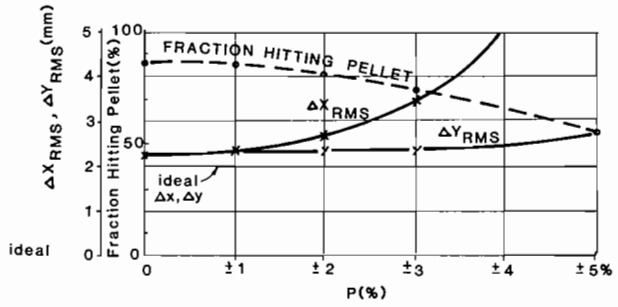

Figure 3. The Momentum Sensitivity of the 3λ/2 Chromatic-Correction System

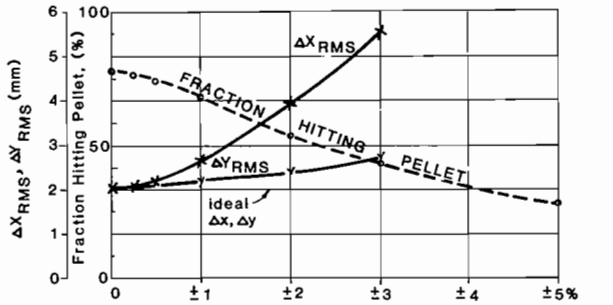

Figure 4. The Momentum Sensitivity of the λ/2 Matching System (without Chromatic Correction)

IV. SUMMARY

We have illustrated by means of an example that the inherent momentum sensitivity of a simple, four-quadrupole-magnet final transport for focusing a heavy-ion beam on to a small pellet can be improved through the use of a particular arrangement of sextupole magnets.

The relative importance of third- and higher order terms in such a chromatic-correction system is not yet clear. Preliminary estimates[4,5] have given inconsistent results; further analysis is in progress.

One of the weaknesses of this chromatic correction system is that it does not easily lend itself to the inclusion of space-charge effects. Subsequent to this work, new optical arrangments have been developed which appear to be more amenable to the inclusion of both chromatic and space-charge corrections in the same system. However, no significant results in this regard are now available.

---

[4] E. Colton, private communication.

[5] J. Spencer, private communication.

Coherent Space Charge Instability of a Two-Dimensional Beam

Ingo Hofmann
Max-Planck-Institut für Plasmaphysik

Space charge induced coupling between different degrees of freedom can be responsible for emittance growth or transfer of emittance from one phase plane to another. The underlying instability mechanism is coherent if it depends primarily on the electric field due to the collective motion, in contrast with an incoherent growth that can be described as a single particle effect. Such coherent phenomena become increasingly important if one studies beams where the space charge force is no longer negligible compared with the external focusing force, as in Heavy Ion Fusion applications.

In this note we present results of analytic calculations on the coherent space charge instabilities of a beam with initial Kapchinskij-Vladimirskij distribution and unequal emittances, rsp. average energy in the two transverse phase planes $x\text{-}p_x$ and $y\text{-}p_y$. We note that in computer simulation calculations evidence has been given for rapid emittance transfer to occur if the initial emittances ε_x, ε_y are noticeably different [1,2]. We have not attempted to make a quantitative comparison of our results with those from computer simulation. The main purpose of this study is to give some insight into the instability mechanism, the dimensionless parameters that characterize the situation and the growth rates one may expect to find.

Dimensionless Parameters

For the round beam case with equal emittances, which was studied by Gluckstern [3], stability is described by one single parameter, the space charge depressed tune ν/ν_o. For the anisotropic beam three parameters are required, instead, which we have chosen to be

---

1 P. Lapostolle, this workshop
2 R. Chasman, IEEE Trans.Nucl.Sci., NS-16, 202 (1969)
3 R.L. Gluckstern, Proc.of the 1970 Proton Lin.Acc.Conf., Batavia, p.811

$\alpha \equiv \frac{\nu_y}{\nu_x}$ tune ratio; $I \equiv \frac{\omega_p^2}{\nu_x^2}$ intensity; $\eta \equiv \frac{a}{b}$ excentricity

with $\omega_p^2 = 4q^2N/(\nu^2 ab)$ the "plasma frequency" and a, b the x, y semi axi of the elliptic cross section uniformly charged unperturbed beam. The tune depressions are found as

$$\frac{\nu_x^2}{\nu_{ox}^2} = \frac{1+\eta}{1+\eta+I}, \quad \frac{\nu_y^2}{\nu_{oy}^2} = \frac{1+\eta}{1+\eta+I\eta/\alpha^2}$$

with ν_{ox}, ν_{oy} the zero intensity tunes.

Results

The dispersion relation has been calculated by integrating the Vlasov equation along unperturbed orbits (details see elsewhere[4]). Eigenmodes of the perturbed electrostatic potential V can be written as finite order polynomials in x, y with a distinction between "even" and "odd" (as describing the symmetry in the angle if elliptic coordinates are introduced):

even	odd	mode
x	y	dipole
$x^2+A_2y^2$	xy	quadrupole (envelope)
$x^3+A_3xy^2$	$y^3+B_3x^2y$	sextupole
$x^4+A_4x^2y^2+C_4y^4$	$x^3y+B_4xy^3$	octupole

etc.

Anisotropy lowers the stability threshold considerably. Instability occurs as a result of (linear) mode coupling or depression of ω^2 to zero and negative values. Modes that are stable in a round beam for arbitrary tune depression, like the sextupole mode (Fig.1a), can become unstable with anisotropy. A general rule of stability in terms of η, α has not been found. It may be of interest to note that we have calculated a number of cases and found that imbalance in energy as well as in emittance can give rise to instability. As a general feature, however, instabilities with noticeable growth rates were found only if the tune in one of the directions is sufficiently much depressed. A lower bound of .75 for the two depressed tunes seems to be quite safe from this point of view. Future work should consider non-KV distributions and r-z ellipsoidal geometry.

---

4 I. Hofmann, to be published

Figures:

The normalized mode frequency $\sigma \equiv \omega/\nu_x$ is plotted against intensity I. In case of complex solutions Re σ is shown by a dashed line and Im σ (instability growth rate) by a dotted line. Examples are given for even modes and for different sets of α, η, which are readily converted into the ratio of emittances, $\varepsilon_x/\varepsilon_y = \eta^2/\alpha$, and the ratio of single particle energies $E_x/E_y = \eta^2/\alpha^2$.

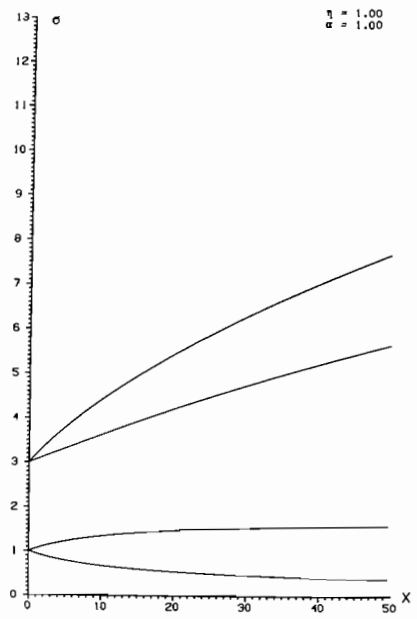

a) sextupole (round beam)

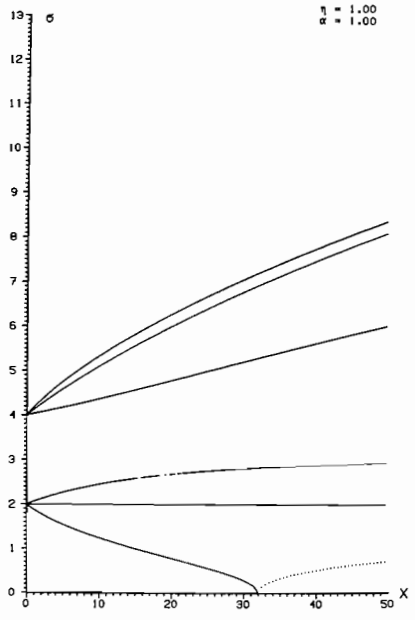

b) octupole (round beam)

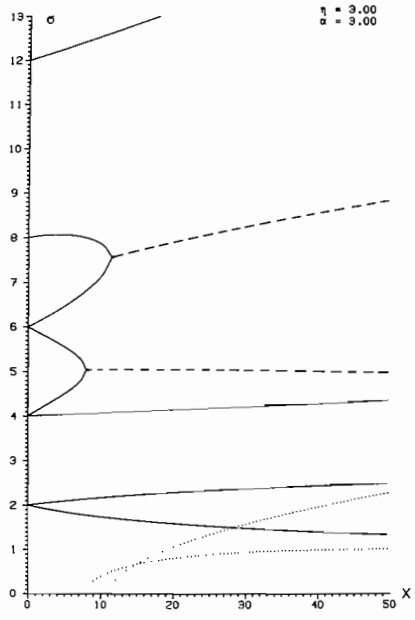

c) octupole

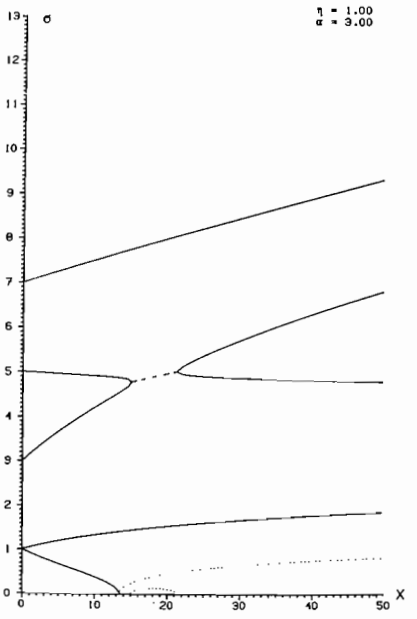

d) sextupole

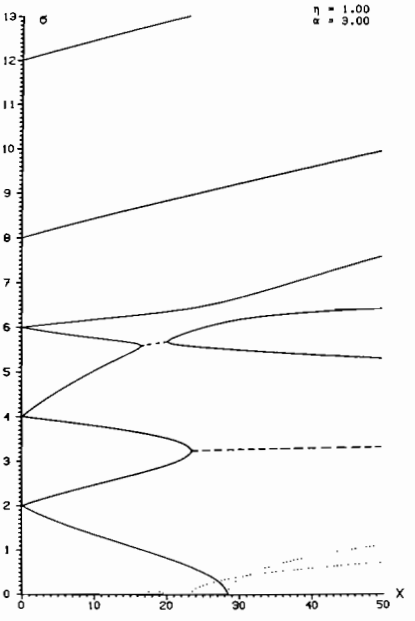

e) octupole

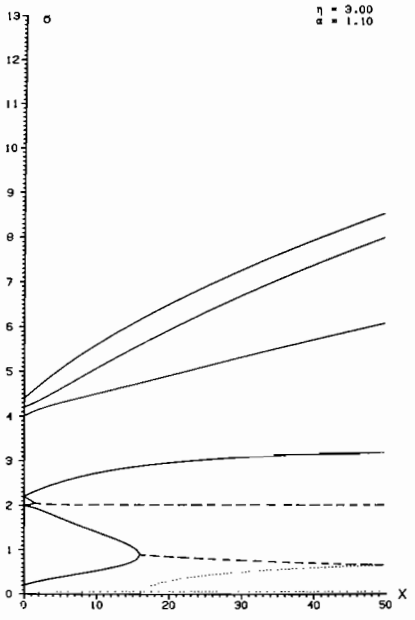

f) octupole

Numerical Simulation of Space Charge Aberrations in Final Focusing*

I. Haber
Naval Research Laboratory

For a sufficiently intense beam, the size of the final spot will depend not only on the design of the final focussing system but also on the detailed distribution of the beam entering that system. In particular, any deviations from a uniform beam cross section give rise to non-linear space charge forces which can defocus the beam. Because space charge forces increase in relative importance as the beam expands, aberrations become most significant when a beam, already near the space charge limit, is propagated at an expanded size in the final lens system.

Actual quantitative calculations of the importance of space charge aberrations can be a difficult task since the very nature of the phenomenon involves the self-consistent evolution of the beam in its own non-linear space charge forces. The behavior of the system can therefore be quite sensitive to the details of the distribution of the entering beam. In addition, the number of possible lens designs is quite large. Accordingly, a few sample simulations have been performed with the intent of discovering the likely importance of space charge aberrations. Preliminary results indicate that these space charge non-linearities can significantly affect final spot characteristics.

In order to examine system scaling and to test the limitations imposed by the numerics, a series of simulations was run using a simple idealized focusing system. This system was formed by allowing a symmetric beam to expand in its own space charge forces and then passing the beam through a lens system which is focussing in both planes. The entering symmetric beam was obtained by placing an appropriate strength quadruple at the mid plane between an F and D lens of the thin lens AG transport system in which the beam was propagating. While a strong thin final lens, focusing in both planes, does not exist in practice, such an idealized lens was assumed for the simulation.

Computer simulations performed previously[1], have shown that intense beams with non K-V distributions can propagate down an alternate gradient channel with little emittance growth. Figure 1 is a contour plot of the vertical phase space at the spot when the self-consistent non K-V distribution obtained from one of these simulations was used as the input distribution. While the simulation was run in normalized units, for 10 GeV singly ionized uranium ions transported through an alternate gradient system with 50 percent lens fill and a 1 T pole tip strength, the simulation corresponds to an approximately 1 kA beam at an rms emittance of 7.5 cm-mrad. The final lens focal length, chosen to be the same as the focal length of the lenses in the AG system, is then 6.4 m, and the 90 percent spot size is 1.6 mm. By comparison, Fig. 2 is a similar plot of the spot resulting when a K-V beam, with the same initial rms emittance and radius, is focused in the same way. The 90 percent spot size in this case is 0.7 mm.

A more realistic focusing system, consisting of six thin lens quadruples, was provided by A. Garren. The design was generated by altering the one described elswhere in these proceedings so as to consist of thin lenses and thereby simplify the simulation. The lens system is designed to bring a beam of U+4 ions from the output of a 60-24 AG system with an emittance of 6 cm-mrad and a current of 0.78 kA (electrical) down to a 4 mm radius spot 60 m away. The transport line period is 4 meters and the lenses are placed at 2.5, 16.5, 29, 40, 50, and 54 meters from the center of the last lens which has half the strength of the others in the transport system. The quadrupole gradients relative to the gradients in the transport system are -0.412, 0.330, -0.2434, 0.1667, 0.3334 and -0.5177 respectively.

Figure 3 shows the vertical phase space at the spot. Since the starting beam distribution was K-V, the non elliptical shape of the spot phase space distribution indicates that small imperfections in the initial distribution have grown as a result of traversing the focusing system. Since any actual beam entering a final lens system will likely have much larger deviatons from a K-V form than the simulation, significant deviations from the calculated spot characteristics are possible. Simulations have in fact been run which seem to verify the possibility of major aberration generated spot growth.

Since only a small number of simulations have been run thus far, the systematic sensitivity of lens design to space charge aberrations has not been explored. However, significant effects have been observed. It may therefore be necessary to preceed any extensive design of final lens systems with a program of simulations coupled to some actual measurements of beam characteristics.

* Work supported by the U. S. Department of Energy

References

1. I. Haber, IEEE Trans. Nucl. Sci., NS26, p3090 (Jun 1979)

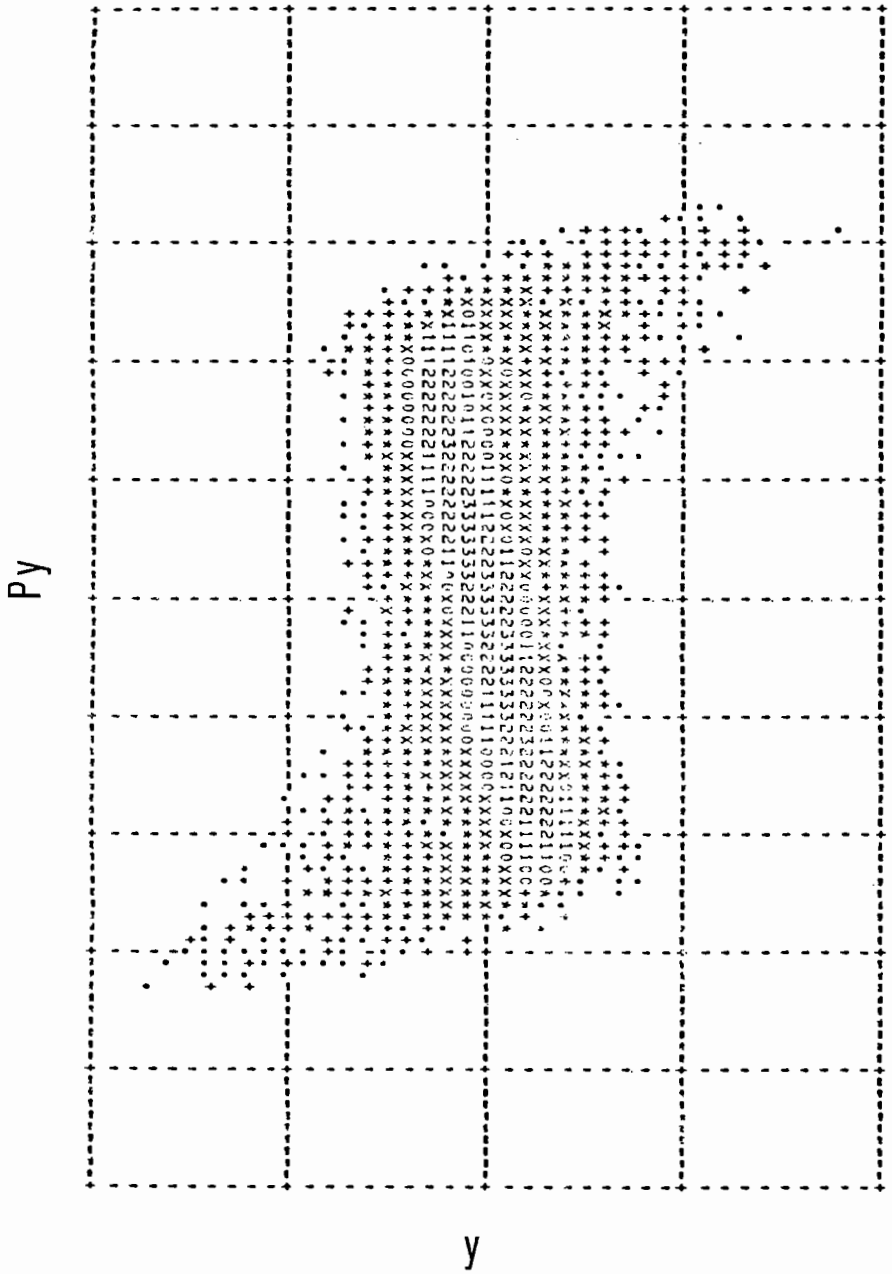

Figure 1 - Vertical phase space plot, at the spot, of a non K-V beam focused by a simple lens system.

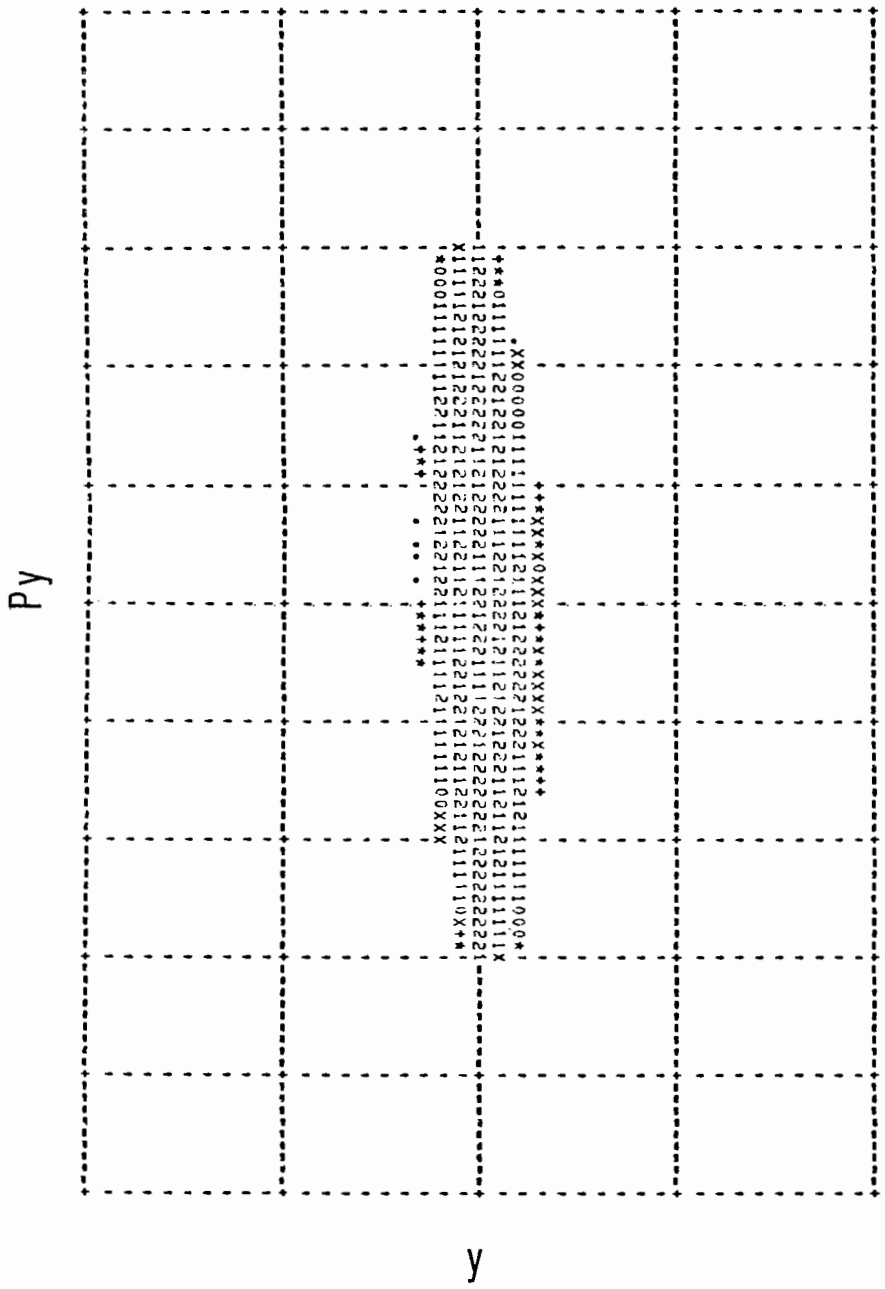

Figure 2 - Vertical phase space plot of a K-V beam with the same rms emittance and rms size and focused in the same way as in fig. 1.

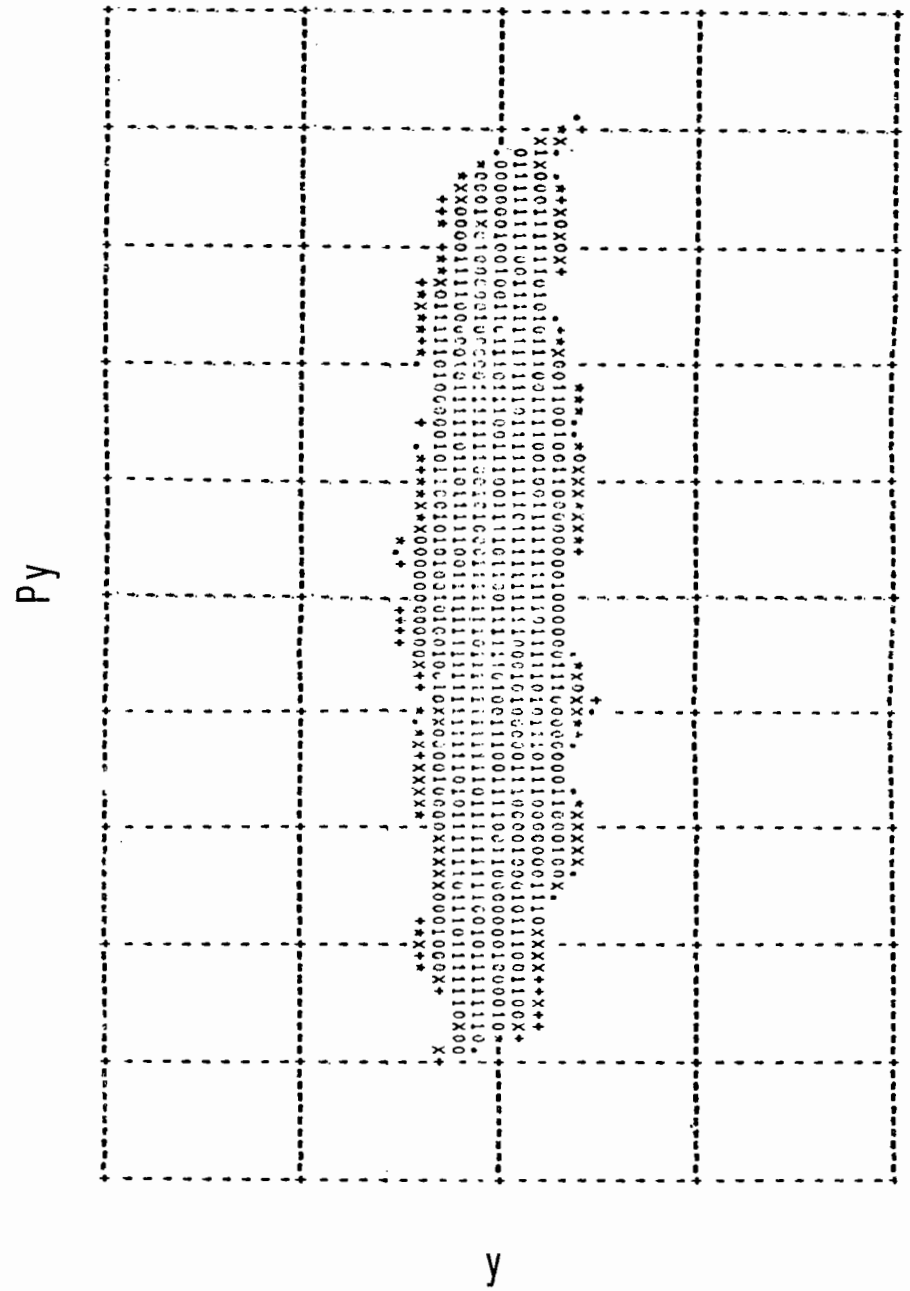

Figure 3 - Vertical phase space plot of a K-V beam after traversing a 60 m focussing system.

SPHERICAL ABERRATION FROM NON-UNIFORM SPACE-CHARGE

J. D. Lawson
Rutherford Laboratory

As an illustrative example of the effect of non-uniform space-charge, we calculate the spherical aberration coefficient of a lens, which has its focusing power reduced by a space-charge distribution that is slightly non-uniform,

$$n = n_0 - \Delta n \frac{x^2}{a^2}, \quad x < a \qquad (1)$$

$$= 0, \quad x > a$$

where n is the density and a is the beam radius.

For a density distribution of the form given in equation (1), the outer rays will be brought to a focus before the inner rays, since the defocusing effect of the space-charge will be less than it would be if Δn were zero. We consider a system such that, when $\Delta n = 0$, the space-charge just doubles the focal length of the lens. This represents a "tune depression" factor of 1/2. The space charge is assumed localized at the lens.

If the lens focal length is f_0, then the "focal length" of the space-charge contribution is $-2f_0$ when $\Delta n = 0$, and for a parallel beam of radius a incident on the lens, all rays will meet that axis at a distance $2f_0$ from the lens at an angle $a/2f_0$. For finite Δn, the outer rays will travel at an increased angle, $(a/2f_0)(1 + \Delta n/2n)$. At the focus for rays near the axis, the spot size will be $a\Delta n/2n$. Setting this equal to $C_s\theta^3$, where C_s is the spherical aberration coefficient of the combined lens and space-charge, we get

$$C_s = \frac{(2f_0)^3}{a^2} \frac{\Delta n}{2n} . \qquad (2)$$

The figure below illustrates the argument.

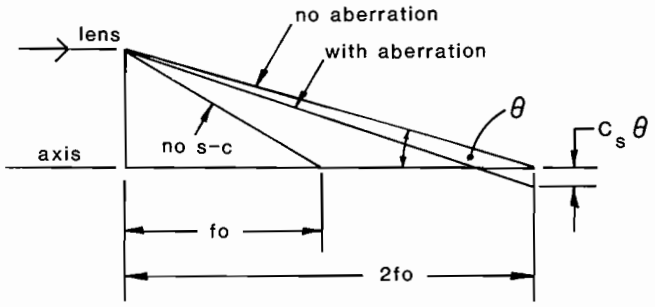

We estimate this effect first for a periodic FODO lattice. For thin lenses with spacing L and tune 60° without space charge, f = L, and the maximum β function value is 3.46L. If space charge depresses the tune to 24° then β = 8.2L, and $a = \sqrt{\beta\epsilon}$ where ε is the emittance/π. From equation (2) we then have

$$C_s = \frac{L^2}{2\epsilon} \frac{\Delta n}{n} \qquad (3)$$

Taking L = 5m, $\epsilon = 6 \times 10^{-5}$ mrad and $\Delta n/n = 0.1$, we get $C_s = 2 \times 10^4$ m/rad^3 $= 2 \times 10^{-2}$ mm/mr^3. Since a ≈ 50 mm and $\theta = a/\beta \approx 1$ mr, the effect here is negligable.

Secondly, for the final focus case the circle of least confusion is $1/4\ C_s\theta^3 = 1/4\ a(\Delta n/n)$. This suggests a serious effect, (several mm even for $\Delta n/n = 0.1$). This conclusion is pessimistic, however, since the space-charge is not concentrated at the lens; it becomes most effective only near the focus, where small angular deflections have relatively little effect. Nevertheless, it is clear that future consideration is needed.

Studies of a Beam Line for Transport to a Target

A. Garren
Lawrence Berkeley Laboratory

Introduction

An example beam line for transport of a 10 GeV U^{+4} beam from a periodic lattice to a 4 mm target has been designed by K. Brown and J. Peterson for the zero space charge case.[1] Two variants of this line exist: a straight 60 m four quadrupole module without chromatic corrections, and a line with three of these modules including dipoles and sextupoles for chromatic correction.

As an approach to some of the problems of final vacuum transport of intense beams, this note describes calculations to modify the beam line of Brown and Peterson to take account of space charge, and to assess its performance with respect to momentum spread and intensity variation along the bunch.

Secondly a computational program is outlined for design of the sextupole chromatic correction system of beams with space charge, including a way to obtain their dispersion.

Beam Line Without Sextupole Corrections

The beam line to be considered is exhibited in Fig. 1 and Table I. On the left is a periodic FODO cell lattice, to the right a transport channel that focusses the beam onto the target. The cells are 4 m long, with 1 m long quadrupoles and 1 m long drifts. The gradients are such as to produce $\mu_o = 60$ degrees betatron phase advance at zero current.

The system is intended for the 10 MJ case: U^{+4} K.E. = 10 GeV, target radius a = 4 mm. The current I is 780 A (electrical), which depresses the phase advance to $\mu = 24°$. (Many such beams are required to deliver the needed total energy).

Table 1 Lengths and quadrupole gradients of the last half cell and final focus transport line for 10 GeV, U^{+4} beams at three current levels.

Element	Length (m)	Gradient (T/m) I = 0A	390A	780
		Q = 0	3.194×10^{-4}	6.387×10^{-4}
QD/2	0.5	-34.44	-34.44	-34.44
L	1.0			
QF/2	0.5	34.44	34.44	34.44
L1	2.0			
Q1	1.0	1.84	-5.55	-14.86
L2	13.0			
Q2	1.0	0.0	5.33	9.53
L3	11.5			
Q3	1.0	-3.64	-5.50	-7.16
L4	10.0			
Q4	1.0	0.0	7.39	4.95
L5	8.5			
Q5	2.0	5.91	5.96	5.14
L6	2.0			
Q6	2.0	-7.88	-7.58	-8.53
L7	5.0			

The following calculations were performed, using the SYNCH computer program:

1. Periodic solutions to the equations for the beam envelope radii a_x, a_y

$$\frac{d^2 a_{x,y}}{ds^2} + K a_{x,y} - \frac{E^2_{x,y}}{a^3_{x,y}} - \frac{Q}{a_x + a_y} = 0 \quad (1)$$

were obtained for the cells. Here $K = (dB/dx)/B\rho$, $E_{x,y}$ are the emittance areas divided by π,

$$Q = \frac{4 r_p q^2 N}{A \beta^2 \gamma^3} = 1.288 \times 10^{-7} \frac{qI}{A(\beta\gamma)^3} \quad (2)$$

where N is the number of ions per unit length and I is the current in amperes.

2. The tune depression is calculated as follows. Single particle rays are integrated using

$$\frac{d^2(x,y)}{ds^2} + \left(\pm K - \frac{Q}{A_{x,y}(A_x + A_y)} \right) (x,y) = 0,$$

cell transfer matrices are obtained from the final values of rays with initial values (1,0) or (0,1), and then the tunes are obtained from the matrix traces.

3. The envelope equations (1) are tracked through the channel to the target, using the cell periodic solutions as starting conditions. An optimizing routine adjusts the gradients to obtain the desired conditions at the target:

$$a_x = a_y = 4 \text{ mm}, \quad a'_x = a'_y = 0$$

Additional constraints were added to limit the maximum beam radii. Two quadrupoles were added, so that the maximum radius along the channel increased only from 25 cm in the zero-current line to 35 cm in the modified line with 780 A.

The principal results are shown in Table II.

Chromatic Behavior of the Example System

An approximate estimate of the increase in spot size to be expected from the final doublet

Table II Properties of 10 GeV, U^{+4} beams in FODO cells and final transport channel at three current levels

Current (electrical)	I	0	390	780	Amp.
Space charge parameter	Q	0	3.19×10^{-4}	6.39×10^{-4}	
Cell phase advance	μ	60	36.7	24.4	deg.
Cell beam radius max.	a_{max}	1.99	2.51	3.06	cm.
Cell beam radius min.	a_{min}	1.20	1.55	1.91	cm.
Channel phase hor.	μ_x	180	115	91	deg.
Channel phase vert.	μ_y	180	152	156	deg.
Channel radius max.	a_x	24.8	28.7	35.5	cm.
Channel radius max.	a_y	16.1	30.0	30.4	cm.
Target beam radius	a*	0.40	0.40	0.40	cm.
Relative velocity	β		0.291		
Relative momentum	$\beta\gamma$		0.304		
Magnetic rigidity	$B\rho$		56		T-m
Emittance/π	E		60		mm-mrad

ignoring space charge may be obtained using the thin lens approximation. If the beam has a waist at the target and is nearly parallel at the doublet entrance, it can then be shown* that the β-function at the target depends on momentum deviation $\delta = \Delta p/p$ as

$$\beta_o(\delta) \simeq \beta_o \left[1 - 4\delta + (2M_{12}\,\delta/\beta_o)^2 \right] \qquad (5)$$

where M is the transfer matrix from doublet entrance to target, $\beta_o = r_o^2/\varepsilon$, and

$$M_{12} = L + \ell + \sqrt{\ell\,(L + \ell)} \qquad (6)$$

Here L is the distance from the final lens to the target, and ℓ is the doublet separation. If the maximum δ is taken to be that which doubles β (40% increase in r_o), and we take the mean of the horizontal and vertical values of M_{12}^2 we get

$$\left(\frac{\Delta p}{p}\right)_{max} = \pm \frac{r_o^2}{2\varepsilon\sqrt{(L + \ell)(L + 2\ell)}} \qquad (7)$$

For the example beam line L = 6 m, ℓ = 2 m and $(\Delta p/p)_{max} = +0.011\%$

To estimate the chromatic effect of the example beam line more accurately, beam envelopes were tracked through the system for off-momentum particles. In this calculation K in Eq. (1) is made proportional to $(1 + \delta)^{-1}$ and Q to $(1 + \delta)^{-2}$. The calculation is inexact in that the denominator of the space charge term should contain the effective size of the beam due to superposition of the different momentum components. However the space-charge term is more important than the emittance term at places where the beam sizes are large, and there the dependence of a_x and a_y on momentum is relatively small. Hence the results, shown in Table III, may not be too inaccurate.

*Specifically one sets $M_{11} = 0$ in both planes. The δ^2 term is larger than the δ term if $\delta > (\beta_o/L)^2 \sim 10^{-3}$ for the example beam line.

Table III Effect of Momentum Error on Channel Performance

Momentum deviation	$\Delta p/p$	-0.01	0	0.01	
Q = 0:					
Radii at channel entrance ($a_x' = a_y' = 0$)	a_x	.020	.020	.012	m
	a_y	.012	.0120	.012	m
Radii at target position:	a_x	.0072	.0040	.0073	m
	a_y	.0044	.0040	.0043	m
Waist position (from target)	S_x	-0.04	0	+0.04	m
	S_y	-0.1	0	+0.1	m
Radii at waist	a_x	.0038	.0040	.0043	
	a_y	.0041	.0040	.0040	
Q = .0000639:					
Radii at entrance	a_x	.0307	.0306	.0306	
	a_y	.0190	.0191	.0192	
Radii at target	a_x	.0235	.0040	.0199	
	a_y	.0054	.0040	.0037	
Waist position	S_x	-1.0	0		
	S_y	-0.1	0	+0.1	
Radii at waist	a_x	.003	.004		
	a_y	.005	.004	.003	

It was assumed that each momentum constituent was matched in the cells -- this accounts for the variation of radii a_x, a_y at the channel entrance. For the zero space charge case the horizontal beam size has increased from 4 to 7 mm at the target for ± 1% momentum error, the vertical size hardly at all. The spot area $a_x\, a_y$ increases by a factor of 2, while from Eq. (5) one predicts a factor 1.4. For 780A the area at the target is increased by a factor of six.

Thus the theoretical momentum acceptance for zero current is about ± 1% , for the channel example 0.7% at zero current and about 0.2 at 780A. The increased sensitivity at 780A may not be directly due to space charge, but rather to increased chromaticity, which varies as $\sum K_i\beta_i$. It may be possible to reduce this effect by more careful design of the channel.

Sensitivity to Current Level

The change of the beam radii at the target as a function of current was calculated by tracking envelopes through the channel whose quadrupole gradients were fixed at values to focus the 780A beam to 4 mm radii at the target. As with the momentum dependence calculations, matched envelopes in the periodic lattice were taken as initial values in the channel. The results, Table IV, show higher tolerance to current than to momentum variation. For example the current must be depressed about 20% to produce a 50% growth of spot-radius.

Evaluation of Example Beam-Line

The resulting beam-line appears satisfactory in that it produces the desired spot size, the beam dimensions are reasonable, and it is not too sensitive to current variations. However its momentum acceptance is very small and it may behave badly with more realistic distributions. Work is now in progress to produce a superior channel. The main ideas are to increase the density of quadrupoles so that their focussing effect will dominate the space-charge effect, to produce beam envelopes that are on the average more symmetrical, and to avoid very small intermediate waists, such as that near Q3.

Dispersion in Beam with Space Charge

A beam line with sextupole corrections was also calculated by Brown and Peterson.[1] It

Table IV Dependence of Spot-Size at Target on Current
$Q_o = 6.387 \times 10^{-5}$ (I_o = 780A)

Q/Q_o	a_x(mm)	a_y(mm)
0	64.1	26.0
0.1	51.5	27.1
0.2	40.1	27.7
0.3	30.2	24.8
0.4	22.5	19.0
0.5	16.9	14.0
0.6	12.6	10.3
0.7	9.12	7.69
0.8	6.42	5.88
0.9	4.62	4.66
0.925	4.35	4.45
0.95	4.16	4.26
0.975	4.05	4.12
1.0	4.02	4.00
1.025	4.06	3.92
1.05	4.17	3.87
1.075	4.33	3.85
1.10	4.53	3.86

consists of three modules like the channel shown in Fig. 1 with the center one reflected. Dipoles and sextupoles are placed in the first two modules for chromaticity correction. In this section an approximate method to calculate dispersion in beams with space charge will be outlined, which should be useful in calculating sextupole corrections.

Suppose each momentum component of the beam has a K-V distribution with ellipse axes a_x, a_y. Let there be a rectangular distribution in momentum deviation $\delta = \Delta p/p$, $-\Delta < \delta < \Delta$. If the dispersion (to be calculated) is η, then the horizontal beam dimension will be

$$A_x = a_x + \eta \cdot \Delta \tag{8}$$

We treat the resulting beam as a uniform-density ellipse with axes A_x, a_y. Single particles will then follow the equations

$$\frac{d^2X}{ds^2} + \left(K - \frac{Q}{A_x(A_x + a_y)} \right) X = \frac{\delta}{\rho} \tag{9}$$

$$\frac{d^2Y}{ds^2} + \left(-K - \frac{Q}{a_y(A_x + a_y)} \right) Y = 0 \tag{10}$$

where ρ is the local radius of curvature and X, Y are taken relative to the center of the beam. Decomposing the horizontal motion relative to the center of each momentum constituent,

$$X = x + \eta\,\delta, \tag{11}$$

gives the following equations in place of Eq. (9);

$$\frac{d^2x}{ds^2} + \left(K - \frac{Q}{A_x(A_x + a_y)} \right) x = 0 \tag{12}$$

$$\frac{d^2\eta}{ds^2} + \left(K - \frac{Q}{A_x(A_x + a_y)} \right) \eta = \frac{1}{\rho} \tag{13}$$

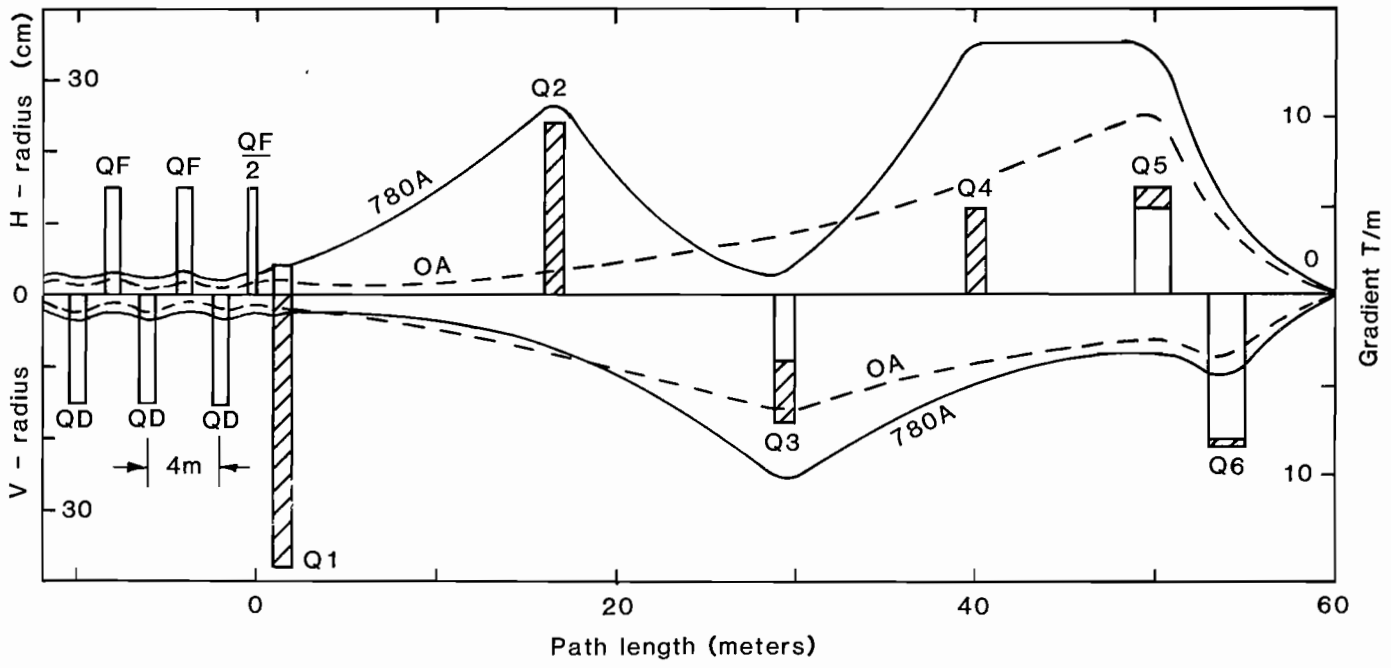

Fig. 1 Final Transport System for 10 GeV, U^{+4} Beams. Beam envelopes and quadrupole gradients designed for zero currents (dashed curves, open bars) and for 780A (solid curves, cross hatched bars). Beam is focussed to 4mm radius waist at 60m, the target position.

Equations (10), (12) lead to the envelope equations

$$\frac{d^2a_x}{ds^2} + Ka_x - \frac{Qa_x}{A_x(A_x + a_y)} - \frac{\epsilon_x^2}{a_x^3} = 0 \qquad (14)$$

$$\frac{d^2a_y}{ds^2} - Ka_y - \frac{Q}{A_x + a_y} - \frac{\epsilon_y^2}{a_y^3} = 0 \qquad (15)$$

The beam evolution is traced by simultaneously integrating Eqs. (13), (14), (15) with A_x given by (8). Single particle behavior can be obtained by also integrating Eqs. (10) and (12). For a periodic lattice one must find periodic solutions in a_x, a_y, and η.

It is assumed in the above derivation that the momentum of individual particles does not change significantly and that particles do not move longitudinally to parts of the bunch with very different momentum spread Δ during the period of interest.

After carrying out the integrations, one should estimate the true charge distribution resulting from superposition of the beamlets and estimate the non-linear forces arising from this distribution. If these do not seem serious, it may be possible to apply sextupole chromatic corrections. To calculate these, appropriate non-linear kicks can be applied at the sextupole locations and a set of single rays traced through the system corresponding to a small δ value together with a non-zero initial value of either x, x', y, or y'. The initial and final values of these rays give the second order transport coefficients T_{ij6}, where i and j = 1, 2, 3, 4. The correction consists of reducing the largest of these coefficients to zero.

Acknowledgment

The author wishes to thank Dr. Lloyd Smith and Dr. Sam Penner for their helpful suggestions.

Reference

1. K.L. Brown and J.M. Peterson, "Chromatic Correction for the Final Transport System", these proceedings.

FINAL TRANSPORT IN GAS AND PLASMA*

C. L. Olson
Sandia National Laboratories
Albuquerque, New Mexico 87185

I. Introduction

There exist several possible schemes for final transport of the heavy ion beam through the reactor chamber in the presence of a background gas or plasma. The optimization of the transport process depends significantly on the heavy ion beam parameters. Since the first HIF workshop,[1] the desired HIF parameters have changed considerably.[2-4] It was the purpose of the working group on final transport in gas and plasma† to examine and assess the various transport schemes in view of the new HIF parameters and other recent developments.

At the first HIF workshop in 1976, parameters for several HIF targets were given.[1] One target used a 40 GeV U beam at 100 TW, and the other three used a 100 GeV U beam at 600 TW. Since that first workshop, the desired HIF parameters have changed due to an improved understanding of deposition physics and the natural evolution of target designs.[2-4] The trend has been toward lower ion energies and higher ion currents. At this workshop,[4] three new pellet parameter sets were proposed: the desired HIF beam parameters were 5 GeV U at 100 TW, 10 GeV U at 150 TW, and 10 GeV U at 300 TW. This evolution of HIF parameters is summarized in Fig. 1.

*Work supported by U. S. Department of Energy

†Members of the working group on final transport in gas and plasma: K. A. Brueckner (LJI), H. L. Buchanan (LLNL), Z. G. T. Guiragossian (TRW), R. F. Hubbard (Jaycor), J. D. Lawson (Rutherford), E. P. Lee (LLNL), D. S. Lemons (LASNL), C. L. Olson, Chairman (SNL), W. B. Thompson (UCSD), D. A. Tidman (Jaycor), and S. S. Yu (LLNL).

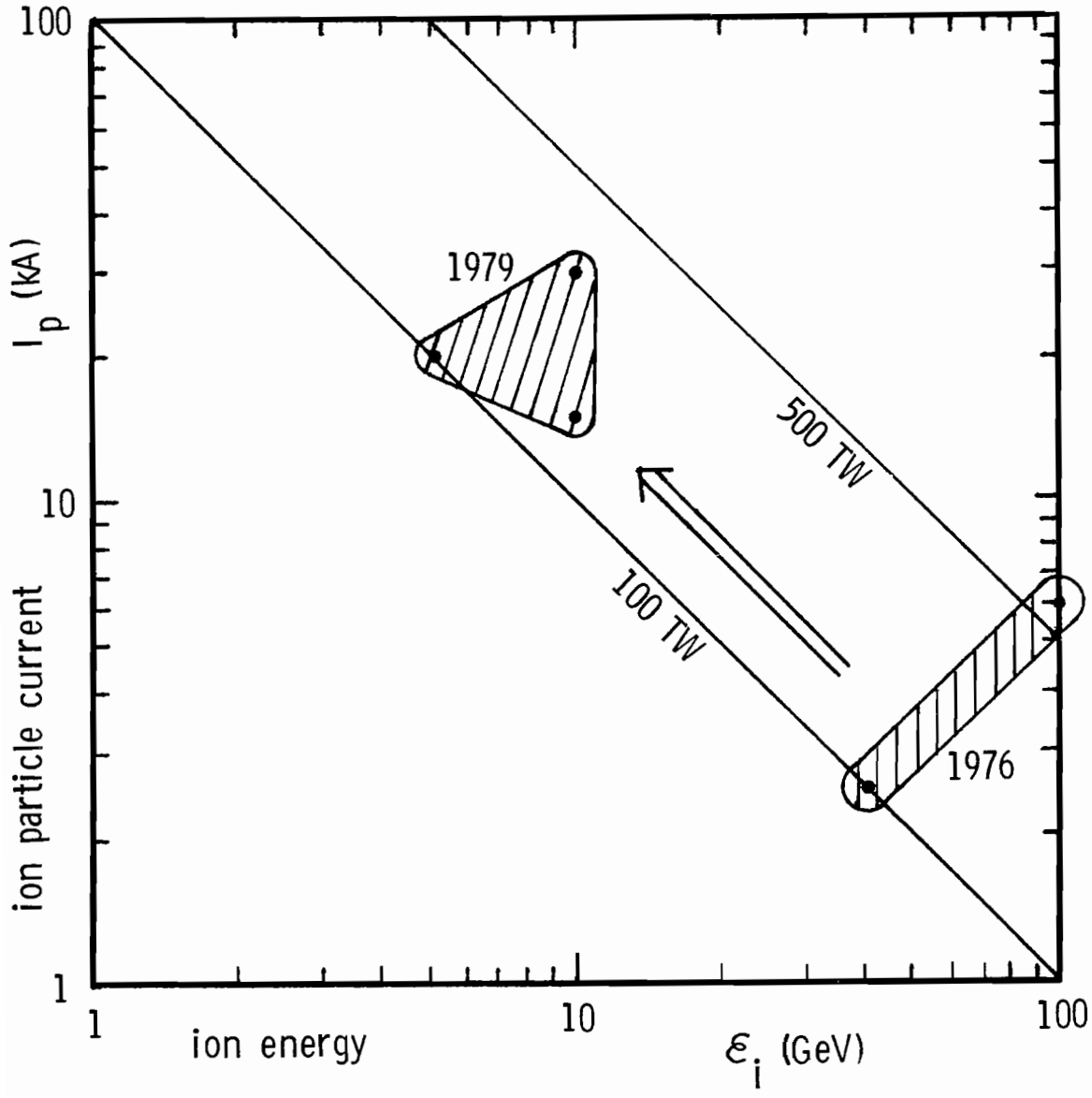

Fig. 1. Evolution of HIF parameters (for uranium ion beams).

Because of these parameter changes, and based on our investigation of the transport regimes, several new conclusions have resulted. The main conclusions, as substantiated in this paper, are as follows:

1. The "1 Torr window" is essentially closed for 5 GeV U. For 10 GeV U, use of this window may be considered; for higher energies ($\gtrsim$ 15 GeV), prospects for the use of this window improve substantially.
2. A new optimum transport regime lies in the 10^{-4} Torr - 10^{-3} Torr lithium pressure regime. In this regime, which is consistent with the HYLIFE lithium waterfall reactor concept,[5] the HIF beam(s) propagate in an essentially unneutralized state, and plasma and gas effects are just beginning to be important.
3. If the ion energy decreases any further ($<$ 5 GeV), or if the charge state increases much above unity ($\bar{z} >> 1$), or if the ion atomic mass number decreases significantly ($A << 238$), then it rapidly becomes necessary to provide neutralization by some means (e.g., co-moving electrons, gas or plasma background, etc.).

In the following, we will discuss the basic transport effects, and the basic transport pressure regimes that have led to these conclusions.

2. Basic Transport Effects

The basic transport effects associated with HIF beams as a function of pressure are summarized in Fig. 2. The pressures considered vary from 10^{-6} Torr to 10^{3} Torr, and the effects listed cover the fundamental areas of concern for HIF transport. The effects are conveniently grouped as space charge effects, atomic physics effects, zero-order plasma effects, and plasma instabilities. Each of these effects will now be briefly discussed.

Space charge effects include space charge spreading, charge buildup at the pellet, and the effects of space charge electric fields at the walls.

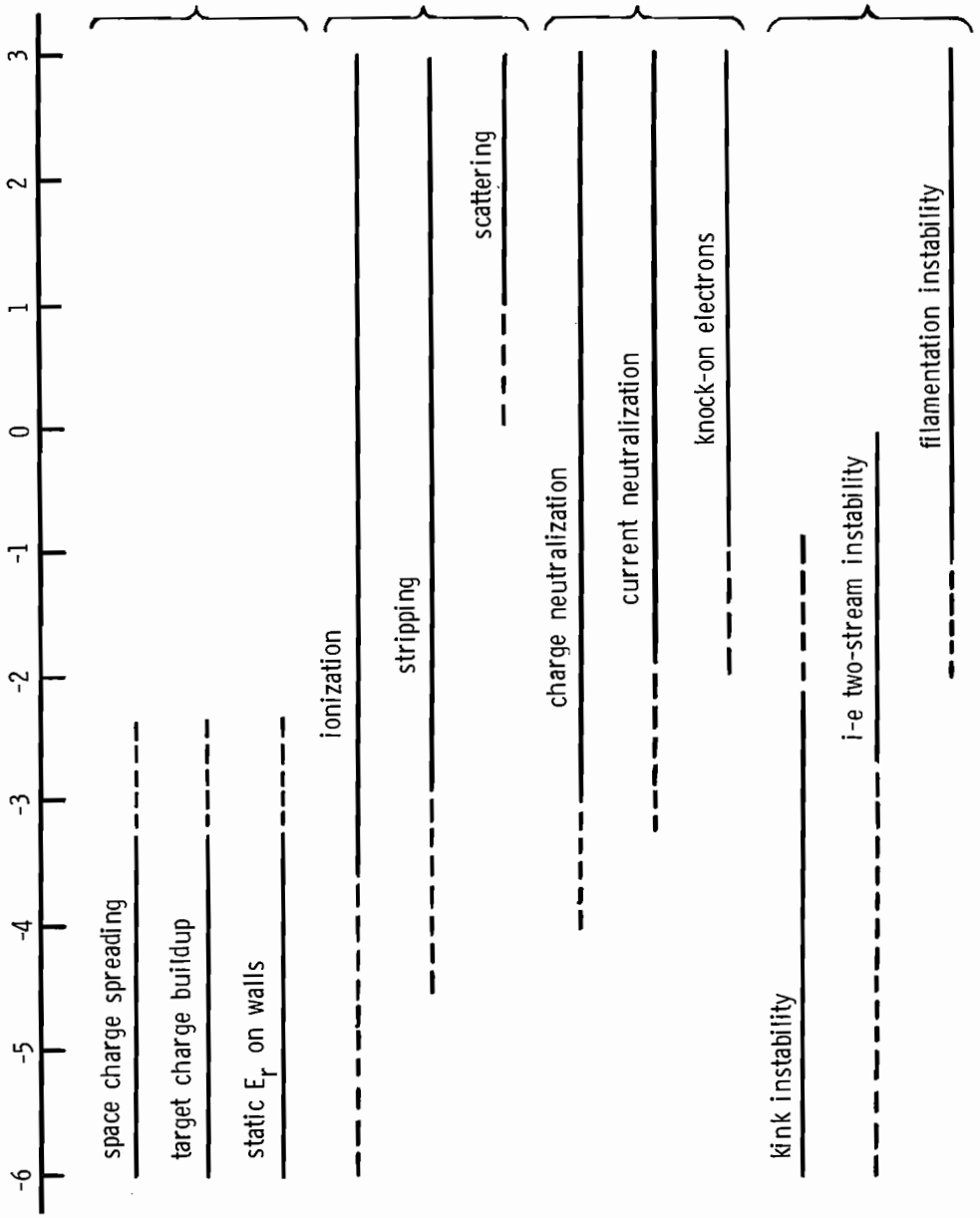

Fig. 2. Transport effects as a function of gas pressure.

Space charge spreading effects may be envisioned by considering the case of a paraxial, zero emittance beam that is focused in the axial (z) direction from an injection radius R at z = 0 to a point at z = L. Due to radial space charge spreading, the beam radius at z = L will not be zero, but will have a finite value r_{min}. The radial equation of motion for an ion at the beam edge is relativistically (in CGS units)

$$\gamma M\ddot{r} = 2e\mathcal{Z}I/(\beta cr) \tag{1}$$

where M is the ion mass, e is the magnitude of the charge of an electron, $\mathcal{Z}$ is the ion charge state, I is the (unneutralized) ion current, $v_z = \beta c$ is the ion axial velocity, c is the speed of light, $\gamma = (1 - \beta^2)^{-1/2}$, and a dot ($\dot{}$) denotes d/dt. Rewriting (1) as

$$\int_o^t [d/dt(dr/dt)]\ (dr/dt)dt = \int_R^{r_{min}} (K/r)dr \tag{2}$$

where $K = 2e\mathcal{Z}I/(\beta c\gamma M)$, and noting that $(dr/dt)/(dz/dt) = -R/L$ at z = 0, and dr/dt = 0 at z = L, we find that the particle current I_p ($I_p = I/\mathcal{Z}$) is given by

$$I_p = \frac{\beta^3 \gamma}{4\mathcal{Z}^2} \frac{Mc^3}{e} \frac{R^2}{L^2} \frac{1}{\ell n(R/r_{min})} \tag{3}$$

If r_{min} is set equal to the pellet radius, then I_p represents that current at which space charge spreading effects will just begin to cause the beam to miss (spread larger than) the pellet. If we consider beams composed of ions with energy $\mathcal{E}_i$ and particle current I_p given by (3), then the number of beams N required to achieve a power P at the pellet is $N = Pe/(I_p\mathcal{E}_i)$, or

$$N = \frac{4Pc}{\beta^3(\gamma-1)(\gamma)} \frac{\mathcal{Z}^2}{A^2} \frac{L^2}{R^2} \frac{\ell n(R/r_{min})}{(M_p c^3/e)^2} \tag{4}$$

where A is the atomic number and M_p is the mass of the proton ($M = AM_p$). In practical units, this is

$$N = (1.36\times10^{-4}) \frac{P(TW)}{\beta^3(\gamma-1)(\gamma)} \frac{\mathcal{Z}^2}{A^2} \frac{L^2}{R^2} \ell n\ (R/r_{min}) \tag{5}$$

The non-relativistic results analagous to (1)-(5) are obtained in the limit $\gamma \to 1$, $(\gamma-1) \to \beta^2/2$; these results have been frequently discussed in the literature, and at past workshops.[1-3] Note that for the non-relativistic case, N scales as $(\mathcal{Z}/A)^2\ (L/R)^2\ (1/\mathcal{E}_i^{5/2})$ and that there is only a weak logarithmic dependence on r_{min}.

Result (5) is plotted in Fig. 3 for uranium (A = 238) for the case of P = 100 TW, R = 10 cm, r_{min} = 0.2 cm, and L = 10 m. Note that for 30 GeV U^{+1}, N = 1 is sufficient. For 10 GeV U^{+1}, N ≈ 10. For $\mathcal{E}_i \lesssim 5$ GeV or $\mathcal{Z} \gtrsim 4$, then $N \gtrsim 100$. Note however, that by changing parameters to R = 20 cm and L = 5 m, N decreases by a factor of 16. In any event, the trend is clear that for low energies ($\mathcal{E}_i < 5$ GeV) and high charge states ($\mathcal{Z} \gtrsim 4$), a substantial number of beams is required.

It should be noted that the radial equation of motion (1) omits the effects of beam pinching (which reduces radial spreading) and the effects of finite emittance (which increases radial spreading).. Beam pinching due to the self-magnetic field of the beam reduces the radial force in (1) by a factor $1/\gamma^2$. For 10 GeV U, $\gamma = 1.045$ and $1/\gamma^2 = 0.916$, so pinching effects would reduce the beam spreading force by only ~8%. Finite emittance effects have been considered in conjunction with space charge spreading effects by Garren[6] and Lawson.[7] For this case, the beam envelope equation analagous to (1) is

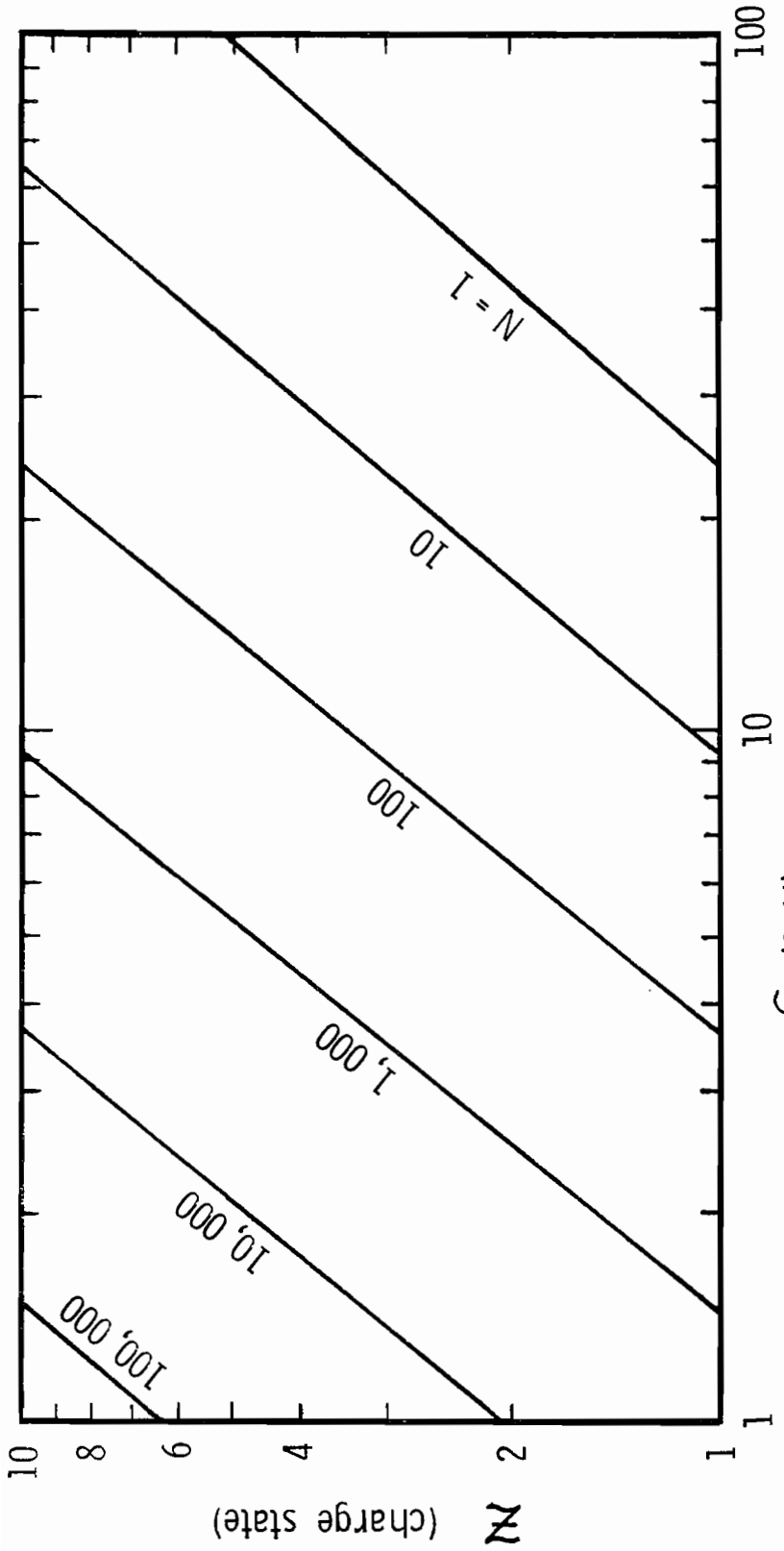

Fig. 3. Number of uranium beams (N) required for $\mathcal{P}$ = 100 TW, R = 10 cm, r = 0.2 cm, L = 10 m, A = 238. The initial emittance was taken to be zero. For non-zero emittance, N will be larger than that shown.

$$d^2r/dz^2 = [K/(\beta c)^2]/r + \varepsilon^2/r^3 \tag{6}$$

where ε is the (unnormalized) transverse phase space emittance. Equation (6) readily integrates to give

$$2[K/(\beta c)^2] \ln (R/r_{min}) = (R^2/L^2) - \varepsilon^2/r_{min}^2 \tag{7}$$

Result (7) is the same as result (3), but with the R^2/L^2 replaced by $(R^2/L^2)C$, where the correction factor C is

$$C = 1 - (L^2/R^2)(\varepsilon^2/r_{min}^2) \tag{8}$$

It follows that in (5), N increases by the factor C^{-1}. The limit C = 0 means that the beam radius at z = L equals r_{min} due to finite emittance effects alone, and any space charge spreading will cause the beam to spread more and miss the pellet. The limit C = 1 means emittance effects are negligible, which requires $\varepsilon \ll (r_{min})(R/L)$. For R = 10 cm, r_{min} = 0.2 cm, and L = 10 m, $\varepsilon \ll$ 2 cm mrad is required to make emittance effects negligible; if ε = 1 cm mrad, then N in Fig. 3 should be increased by 33%. We conclude that finite emittance effects may increase N significantly above that given in Fig. 3.

Other space charge effects include charge buildup at the pellet, and possible field emission from the transport tube walls due to the large space charge fields. Charge buildup effects may be roughly evaluated by assuming all of the beam charge is deposited on a sphere of radius r_{min}. The resulting potential ϕ is

$$\phi = I_p \mathcal{Z} t_b / r_{min} \tag{9}$$

where t_b is the beam pulse length. $e\phi$ may be compared with $\mathcal{E}_i$ to estimate the importance of charge buildup. The radial space charge field E_r at a wall of radius R_w for an unneutralized beam (of radius $R < R_w$) is

$$E_r = 2I_p\mathcal{Z}/(\beta c R_w) \qquad (10)$$

Field emission from the wall may become a problem for $E_r \gtrsim 200$ kV/cm. If there is a single beam inside the accelerator, then this can be a real problem.[8] On the other hand, for final transport, if the number of beams N is greater than or equal to that given by (5), then E_r as given by (10) is typically too small to cause field emission problems.

Space charge effects for various HIF parameters are given in Table 1 for the case of P = 100 TW and a total energy $\mathcal{E}_t$ = 1 MJ. Case 1 (100 GeV U^{+1}) is typical of the parameters suggested for HIF at the first workshop.[1] For this case, only 1 beam is needed and space charge effects are almost negligible. Case 2 (10 GeV U^{+1}) is typical of the parameters suggested at this workshop. Note that space charge effects are now important, several beams are needed, E_r is large (if only 1 beam is used), and $e\phi$ is significant. Case 3 (1 GeV U^{+1}) represents parameters for pellets similar to those optimized for light ion fusion (LIF). Here we see that space charge effects are dominant, field emission would definitely occur for 1 beam, $e\phi >> \mathcal{E}_i$, and conventional accelerator technology could not be employed. A reasonable conclusion, as was the consensus at the end of this workshop, is that the ion energy should be about 10 GeV U^{+1}, and no lower. This energy permits conventional accelerator technologies to be exploited, but at the limit where space charge effects are significant.

Returning to Fig. 2, we now comment briefly on other transport effects. Atomic physics effects relevant to HIF transport include ionization of the background gas by processes induced by the beam ions, stripping of the beam ions to higher charge states by the background gas, and scattering of the beam ions by the background gas. Upper bound estimates for the ionization and stripping cross sections of relevant ions (Xe,U) in various gases

Table 1. Space charge effects for various HIF accelerator parameters.

	CASE 1	CASE 2	CASE 3
ION	U^{+1}	U^{+1}	U^{+1}
ENERGY	100 GEV	10 GEV	1 GEV
β	0.723	0.290	0.0943
RANGE IN Au (COLD)*	5069 MG/CM^2	212 MG/CM^2	36 MG/CM^2
RANGE IN Au (HOT)*	4235 MG/CM^2	154 MG/CM^2	16 MG/CM^2
PARTICLE CURRENT (FOR 100 TW)	1 KA	10 KA	100 KA
CONVENTIONAL ACCELERATOR	APPEARS POSSIBLE (SPACE CHARGE EFFECTS SMALL)	MAY BE POSSIBLE (SPACE CHARGE EFFECTS IMPORTANT)	NOT POSSIBLE (SPACE CHARGE EFFECTS DOMINATE)
N (NUMBER OF BEAMS) (R =10 CM, r=0.2 CM, L=10 M)	1	10	~2,000
E_r AT ACCELERATOR DRIFT TUBE WALL (R = 10 CM)†	8 KV/CM	206 KV/CM	6.4 MV/ CM
$e\phi$ CREATED BY SPACE CHARGE AT PELLET (ϵ = 1 MJ, r = 0.2 CM)	0.045 GEV	0.45 GEV	4.5 GEV

*MEHLHORN RESULTS: COLD: ρ = 19.3 G/CM^3

HOT: ρ = 0.193 G/CM^3, 200 EV

† FOR TOTAL CURRENT IN 1 BEAM

(H_2, N_2, Li, Ne) were given by Gillespie et al. at the third workshop;[9] those results were used in the estimates in Section 3. A summary of atomic physics needs for HIF transport was given by Yu at the second workshop,[10] where the importance of knowing the effective charge state of the ion was noted. It should be emphasized that more exact calculations, and data, are still needed to make accurate estimates of the relevant ionization and stripping cross sections.

Zero-order plasma effects include charge neutralization, current neutralization, and more recently, the knock-on electron effect of Hubbard et al.[11] It is usually assumed that charge neutralization occurs on the time scale of the plasma frequency ω_{pe} of the background plasma [$\omega_{pe} = (4\pi n_e e^2/m)^{1/2}$ where n_e is the electron density and m is the mass of an electron]. While this is roughly true locally inside the beam, a consistent overall picture of charge neutrality for an isolated HIF ion pulse drifting in a gas has not been established. Similarly, complete current neutralization is typically assumed (at higher pressures) and this has been used as an initial assumption for investigating, e.g., the filamentation instability. More recently, it has been found that the decay of the return current toward the end of the pulse leads to a sizable net current with significant pinch forces that can result in anharmonic emittance growth. These effects have been studied by Yu et al.,[12] and Brueckner,[13] who have found them to seriously affect the focussing of HIF beams. The knock-on electron problem arises from beam ion collisions with the gas that produce a flux of forward-directed electrons with velocities higher than those of the ions. If a sufficiently large current of knock-on electrons is created ahead of the beam, this current will ionize the gas ahead of the beam, and eventually result in a field frozen current that can subsequently defocus the ions. These effects will be discussed further in Section 3.

There is a constant concern that plasma instabilities may ultimately prevent HIF transport. To date, the most important instabilities appear to be the "wriggle" instability, the ion-electron two-stream instability (beam ions/plasma electrons), and the filamentation instability (for a current neutralized beam). As noted by Thompson,[14] the "wriggle" instability is an electrostatic kink instability with a growth rate of the order of the beam ion plasma frequency ω_B [$\omega_B = (4\pi n_b \bar{Z}^2 e^2/M)^{1/2}$]. For very low pressures, where $\bar{Z} \approx 1$, the growth rate is very low, and this instability should not be a problem. At higher pressures, $\bar{Z}$ increases quickly, but so does the plasma background density which tends to inhibit growth of this instability. The two instabilities that persist, and are important in determining the "1 Torr window" are the ion electron two-stream instability and the filamentation instability; these will be discussed further in Section 3.

In summary, Fig. 2 presents an overview of basic HIF transport effects as a function of pressure. Note that at low pressures relatively few effects exist, while at high pressures a large variety of phenomena come into play.

3. Transport Regimes

A summary of reactor schemes and HIF transport regimes is given in Fig. 4. In the center of the figure, we have plotted particle current vs. $\log_{10}$[p(Torr)] and show the operating regimes relevant to 5 GeV U^{+1} (as will be discussed below).

Reactor schemes split into four categories with somewhat arbitrary pressure limits as follows. For very low pressures ($p < 10^{-4}$ Torr), dry wall reactor schemes must be employed and the required standoff distance is relatively large. For moderately low pressures (10^{-4} Torr $< p < 10^{-3}$ Torr), the HYLIFE liquid lithium waterfall reactor scheme[5] is applicable (since the vapor pressure of lithium is 10^{-4} Torr at ~400°C and 10^{-3} Torr at ~450°C).

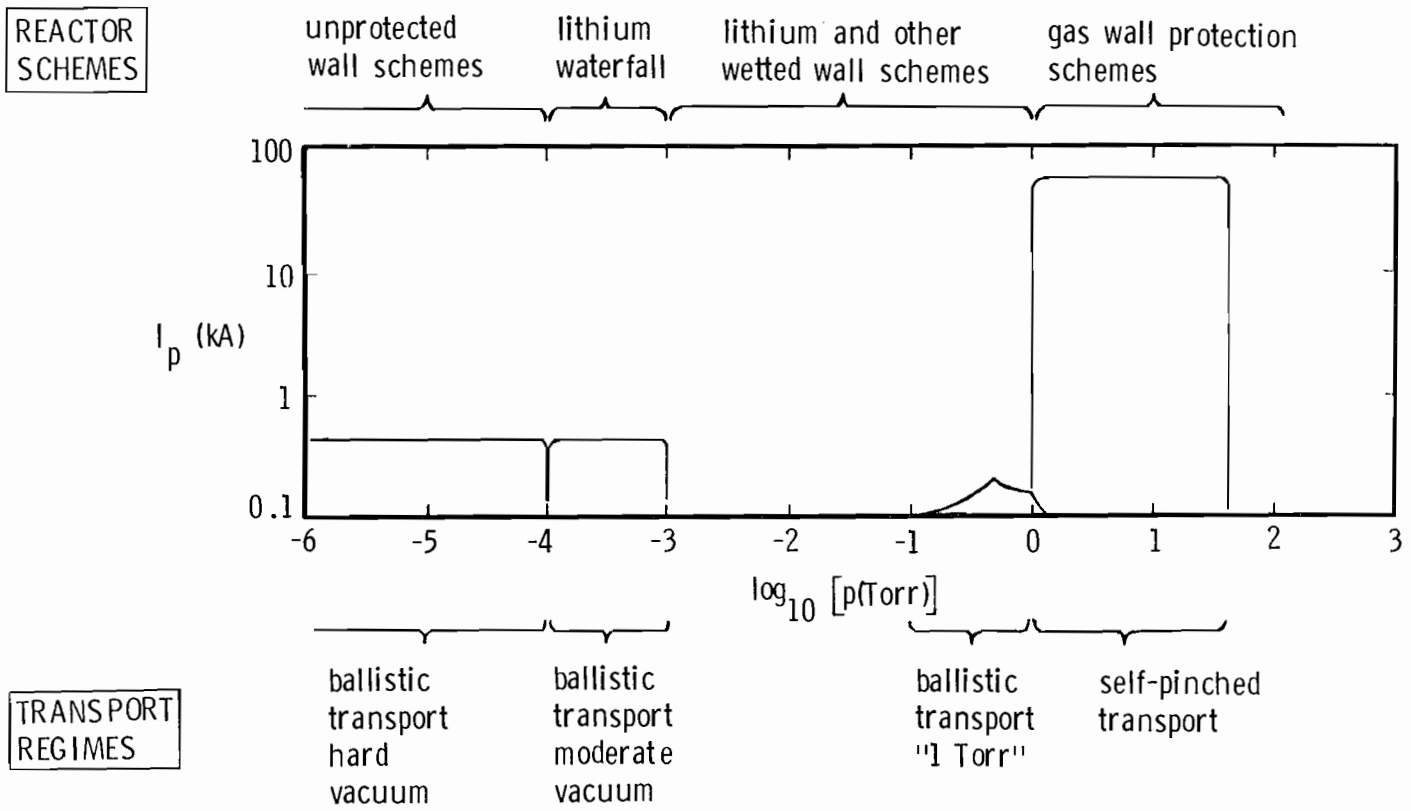

Fig. 4. Operating regimes for HIF (results shown for 5 GeV U^{+1}).

For pressures from 10^{-3} Torr to ~1 Torr, there exist several wetted wall reactor scenarios. For $p > 1$ Torr, the gas density begins to be high enough to offer some wall protection by the absorption of radiation and alpha particles from the pellet blast.

Four HIF transport regimes are also identifiable, as indicated in Fig. 4. These regimes are:

1. Ballistic transport in hard vacuum ($p < 10^{-4}$ Torr)
2. Ballistic transport in moderate vacuum (10^{-4} Torr $< p < 10^{-3}$ Torr)
3. Ballistic transport at "1 Torr"
4. Self-pinched transport at 1-50 Torr

Each of these regimes will now be briefly discussed.

Ballistic transport in hard vacuum ($p < 10^{-4}$ Torr) - By ballistic transport is meant that after the final focusing magnet, the beam ions are directed toward and simply drift to the target. Ballistic transport in hard vacuum is characterized by $n_p << n_b$ where n_p is the plasma density and n_b is the beam density. The advantages of this regime are that the transport calculations are straightforward (space charge and magnetic field forces must be included), there is essentially no beam stripping, and there is essentially no plasma physics involved (as compared to the other transport regimes). The disadvantages of this regime are that it requires a dry wall reactor with a large cavity, pump down of the reactor between shots may be difficult, space charge beam spreading effects limit the current per beam (as in Fig. 3), and charge buildup at the pellet may have significant consequences. Alternative neutralization schemes (such as comoving electrons) might help to alleviate the last two disadvantages.

Ballistic transport in moderate vacuum (10^{-4} Torr $< p < 10^{-3}$ Torr) - Ballistic transport in moderate vacuum is the new "first choice" for HIF transport because for this regime most plasma complications are avoided and yet

a favorable reactor scenario exists. This regime is characterized by $n_p \lesssim n_b$. The advantages of this regime are that it is compatible with a compact reactor scenario (the HYLIFE lithium waterfall reactor concept[5]), charge neutralization is just beginning, beam stripping effects are just beginning, differential pumping in the magnetic lens port should be relatively easy, and most plasma complications (knock-on electrons, anharmonic emittance growth, filamentation, etc.) are avoided. The uncertainties for this regime are that classical transport for $n_p \lesssim n_b$ has not been studied in detail yet, the ion-electron two-stream instability is present but estimates of its saturation effects indicate that they should be small, and there may not be sufficient charge neutralization at the pellet. Further study is needed to clarify these questions.

Several relevant pressures for this regime are indicated in Fig. 5 for the case of 5 GeV U^{+1} in lithium. Without assuming any neutralization, the current remains limited by the space charge result (3). Stripping is just starting, and only a fraction of the beam will go from U^{+1} to U^{+2}. As the beam passes, collisional ionization will create a plasma with density $n_p \approx n_b$ at a pressure near the middle of this regime. Scattering is negligible. We conclude that plasma effects should be small, but that the regime $n_p \approx n_b$ merits more detailed investigation.

Ballistic transport at "1 Torr" - This regime is named in reference to a search for a propagation window near 1 Torr. This regime is characterized by $n_p >> n_b$, and plasma effects play a dominant role in determining the transport properties. The advantages of this regime are that it offers some wall protection and that the pump down of the reactor chamber between shots is less severe than for the vacuum regimes. The disadvantages are numerous. Stripping is severe, anharmonic emittance growth can be serious, and the transport properties are sensitive to the distribution of beam charge states. To permit

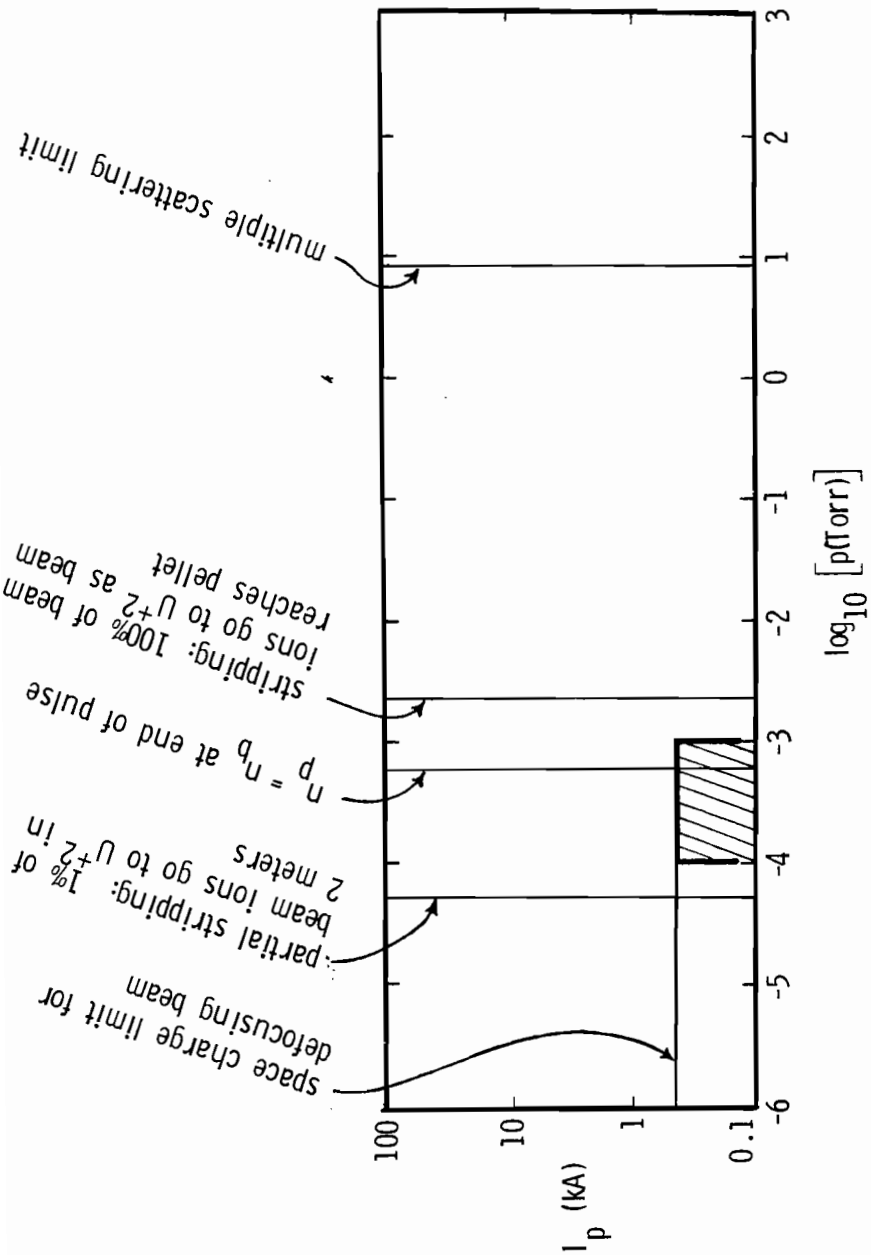

Fig. 5. Ballistic transport in moderate vacuum [$10^{-4} \lesssim$ p(Torr) $\lesssim 10^{-3}$] for 5 GeV U^{+1} in lithium. L = 5 m (corresponding to distance from reactor wall to pellet) was used in all calculations, except L = 10 m (corresponding to distance from center of final focusing magnet to pellet) was used to calculate the space charge limit. (R = 10 cm, r = 0.2 cm, beam pulse length = 10 nsec)

propagation, the parameters must be chosen to simultaneously avoid the ion-electron two-stream instability, the filamentation instability, the knock-on electron problem, and multiple scattering effects. Also, differential pumping in the final magnetic lens may be difficult.

The "1 Torr window" is shown in Fig. 6a for the case of 5 GeV U injected into neon, and in Fig. 6b for the case of 10 GeV U injected into neon. These results were calculated by Hubbard[15] for R = 10 cm, r_{min} = 0.2 cm, L = 5 m, plasma electron temperature $T_e(r_{min})$ = 100 eV, Z_{gas} = 10, and a beam longitudinal velocity spread $\Delta v_z/(\beta c)$ = 0.005. The loci shown have the following meanings. The two-stream instability is collisionally quenched to the right of the two-stream locus. The filamentation instability will grow less than 5 e-folds for parameter values below the filamentation locus. For currents below the knock-on electron locus, the beam will not spread by more than r_{min}. Similarly, for pressures below the scattering limit, the beam will not spread by more than r_{min}. It should be noted that many approximations must be made in deriving such loci (such as the effective ion charge state, the fraction of knock-on electrons inside the beam channel, etc.). However, these loci do represent the best current estimates for the various effects considered.

Note that in Fig. 6, for 5 GeV U, the window is effectively closed. For 10 GeV U, the window is enlarged; for higher energies ($\gtrsim$ 15 GeV),[15] the window is enlarged even more. Since the total current required to achieve a given beam power decreases as the energy increases, and since the maximum current per beam in the 1 Torr window increases as the energy increases, this means that the number of beams required to achieve a given power decreases quickly as the energy increases. We conclude that for 5 GeV U, the window is effectively closed; for 10 GeV U, use of this window may be considered; for $\gtrsim$ 15 GeV U, prospects for the use of this window improve substantially.

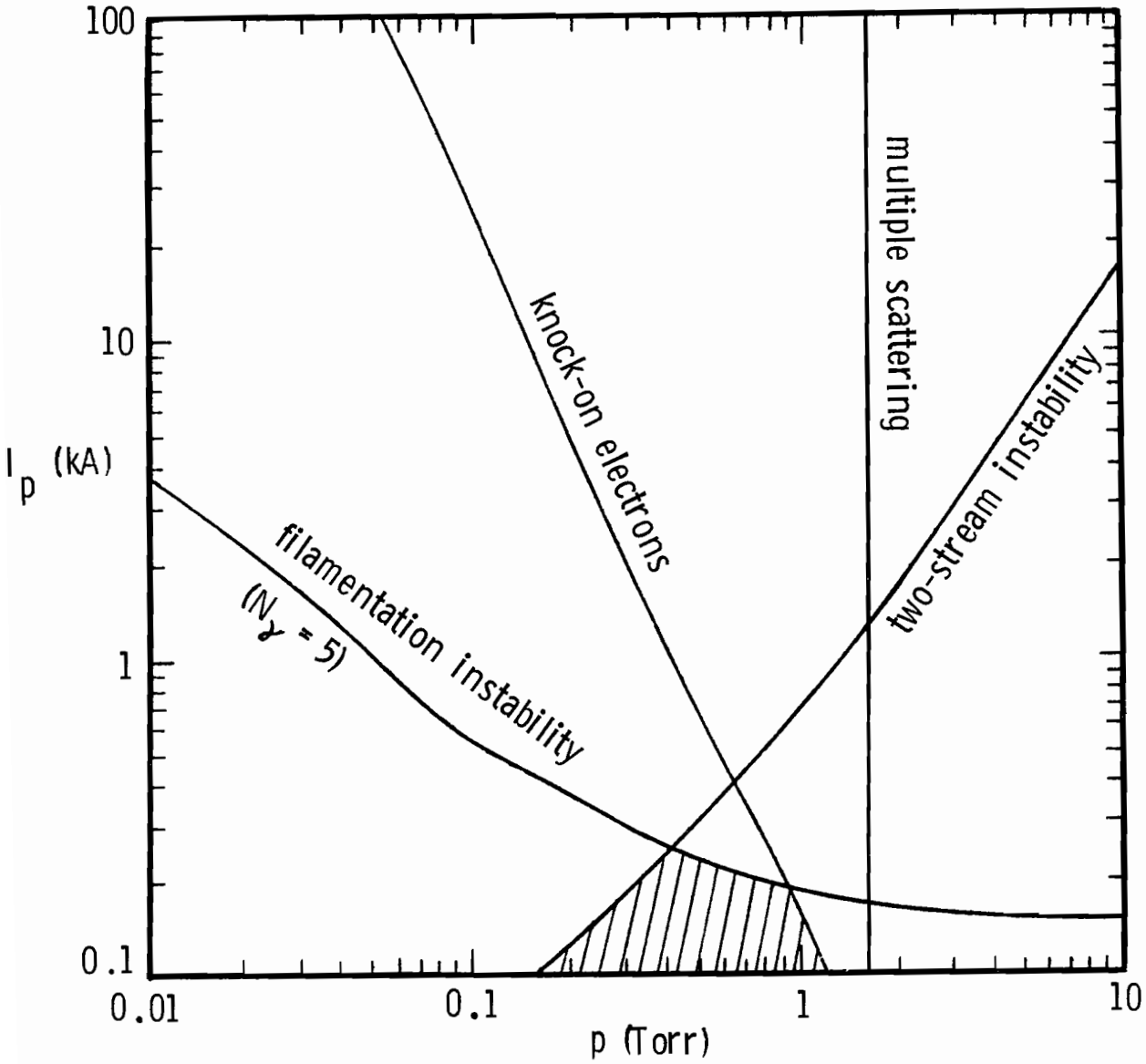

Fig. 6a. The "1 Torr window" (shown hatched) for 5 GeV uranium beam propagation in neon gas. R = 10 cm, r = 0.2 cm, L = 5 m, T_e(r=0.2 cm) = 100 eV, Z_{gas} = 10, $\Delta v_z/v_z$ = 0.005.

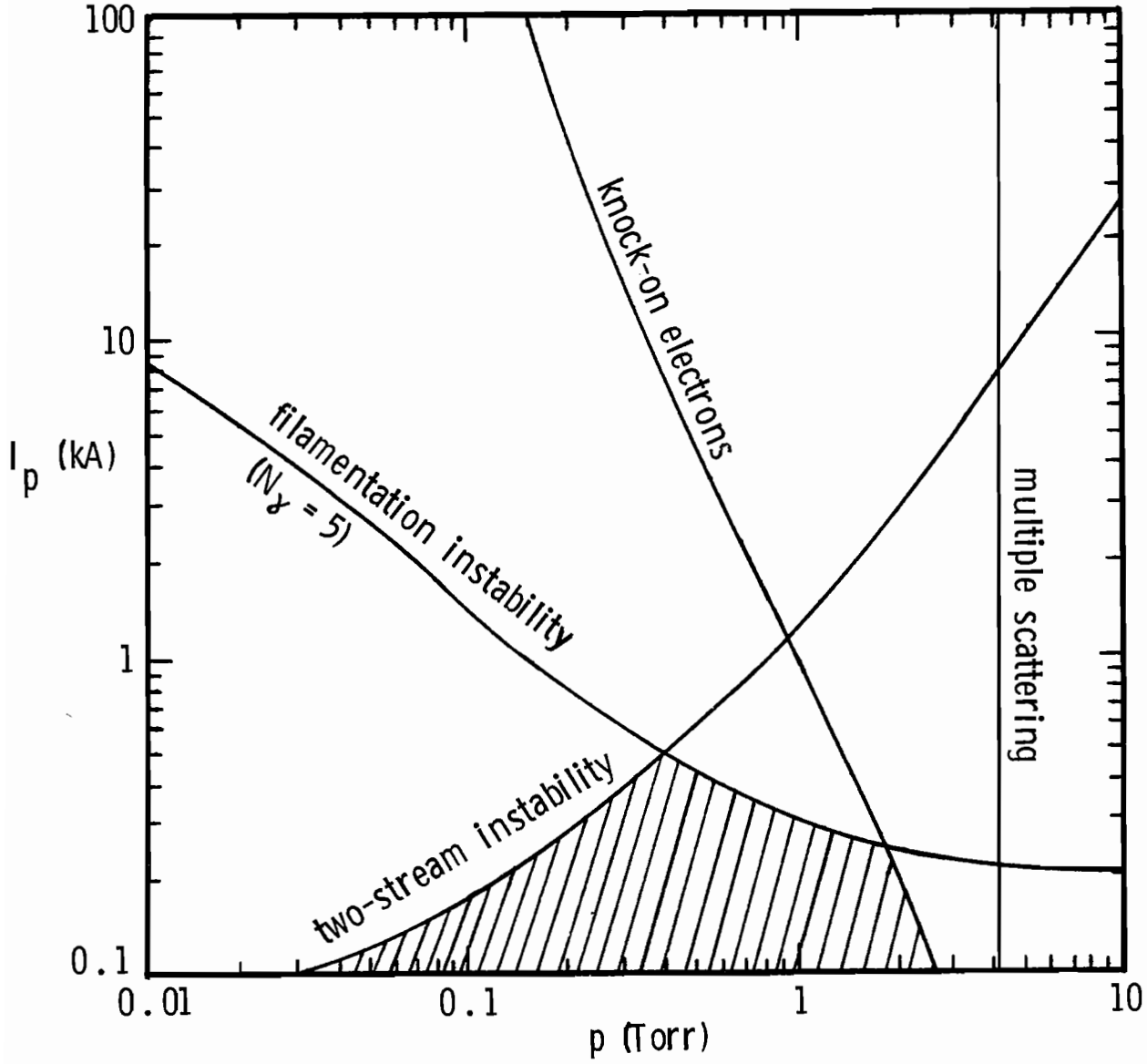

Fig. 6b. The "1 Torr window" (shown hatched) for 10 GeV uranium beam propagation in neon gas. R = 10 cm, r = 0.2 cm, L = 5 cm, T_e(r=0.2 cm) = 100 eV, Z_{gas} = 10, $\Delta v_z / v_z$ = 0.005.

Self-pinched transport at 1-50 Torr - For self-pinched transport, the HIF beam(s) would be focused to about the pellet radius at the input to the reactor chamber. The beam would ionize the gas and propagate in a self-pinched mode through the reactor chamber to the pellet. This regime is characterized by $n_p >> n_b$. The advantages of this regime are that substantial gas protection of the wall is possible; the mode is insensitive to scattering, filamentation, and the two-stream instability; and small reactor beam ports would simplify the differential pumping. The disadvantages are that knock-on electrons may be a problem, a counter-streaming electron beam may be needed, and the concept has not been tested experimentally. Nonetheless, this concept is interesting, and recent work on it is reported by Yu et al.[16]

4. Recommended HIF Transport Research Areas

Based on the above conclusions, highest priority is recommended for studies that would insure the success of ballistic transport in the moderate vacuum regime (10^{-4} Torr - 10^{-3} Torr). This includes detailed studies of the stripping and ionization cross-sections for this regime, basic HIF transport studies (onset of charge and current neutralization) for the case $n_p \lesssim n_b$, and studies of the saturation of the ion/electron two steam instability for the case $n_p \lesssim n_b$ (to insure that the effects are negligibly small on the HIF beam). Experiments to specifically investigate these effects are highly recommended.

If the final acceleration parameters dictate that neutralization must be used, then other areas of study that should be investigated include neutralization by use of co-moving electrons, self-pinched mode propagation, and further work on the "1 Torr window."

5. Conclusions

The main conclusions of this study are as follows:

1. The "1 Torr window" is essentially closed for 5 GeV U. For 10 GeV U, use of this window may be considered; for higher energies ($\gtrsim$ 15 GeV), prospects for the use of this window improve substantially.
2. The new first choice for HIF transport is to use ballistic transport in moderate vacuum (10^{-4} Torr - 10^{-3} Torr). This regime is consistent with the HYLIFE reactor scenario, and plasma and gas effects are just beginning to be important. Further research on this regime is highly recommended.
3. The use of essentially unneutralized beams for HIF transport is a great simplification that should not be abandoned if at all possible. This means that to minimize the number of beams according to (5), it is desirable to keep γ high, $\mathcal{Z}$ low, and A high. For $\mathcal{E}_i$ < 5 GeV, $\mathcal{Z} \gg 1$, or A $\ll$ 238, it rapidly becomes necessary to provide neutralization by some means (e.g., co-moving electrons, or a gas background such as occurs in the "1 Torr window").

We conclude that a reasonable HIF baseline transport scenario would be to use 10 GeV U^{+1} in the moderate vacuum regime (10^{-4} Torr - 10^{-3} Torr lithium). This scenario is relatively simple, it is consistent with a realistic reactor scheme, and it can be recommended with a relatively high confidence level.

Acknowledgements

While all members of the working group on final transport in gas and plasma contributed to this study, special thanks are due to R. Hubbard, Z. Guiragossian, and S. Yu. The contributions of M. Monzler and D. Cook on reactor scenarios are also gratefully acknowledged.

References

1. Proc. ERDA Summer Study of Heavy Ions for Inertial Fusion, Berkeley, California, July 19-30, 1976 (LBL Report LBL-5543).
2. Proc. Heavy Ion Fusion Workshop, Brookhaven National Laboratory, October 17-21, 1977 (BNL Report BNL 50769).
3. Proc. Heavy Ion Fusion Workshop, Argonne National Laboratory, September 19-26, 1978 (ANL Report ANL-79-41).
4. R. Bangerter, this workshop.
5. M. Monzler, J. Blink, J. Hovingh, W. Meier, and P. Walker, Reference 3, p. 225.
6. A. A. Garren, Reference 1, p. 102.
7. J. D. Lawson, private communication, this workshop.
8. S. A. Goldstein, private communication.
9. G. Gillespie, K-T. Cheng, and Y-K. Kim, Reference 3, p. 175.
10. S. S. Yu, Reference 2, p. 50.
11. R. F. Hubbard, S. A. Goldstein, and D. A. Tidman, this workshop, Appendix 5.
12. S. S. Yu, private communication, this workshop.
13. K. A. Brueckner, private communication, this workshop.
14. W. B. Thompson, Reference 3, p. 147.
15. R. F. Hubbard, private communication, this workshop.
16. S. S. Yu, E. P. Lee, and H. L. Buchanan, this workshop, Appendix 6.

THE LIGHT ION FUSION EXPERIMENT (LIFE) ACCELERATOR SYSTEM FOR ICF*

Zaven G.T. Guiragossian
TRW Defense and Space Systems Group, Redondo Beach, CA 90278

ABSTRACT

A Light Ion Fusion Experiment (LIFE) accelerator system is under study as a driver for ICF. The system consists of separate functional elements. Light ions are extracted from a pulsed cold plasma source and accelerated in multi-grid and multi-aperture accelerator structures, with provision for strong compression of beam pulses. D or He ion beams, 20 kA, 1-10 MeV, will be made to ballistically propagate in 10^{-4} torr gas by externally generated co-moving electrons which provide space-charge and current neutralization. The propagation method is relevant to the Heavy Ion Fusion program and helps to reduce the large number of heavy ion beams entering a reactor to a manageable few. The system is also a useful test bed to perform several propagation experiments in the near term. The reactor requirements in Heavy Ion Fusion and LIFE are identical.

* Work performed under the auspices of U.S. DOE, contract No. DE-AC08-79DP40109

INTRODUCTION

A novel light ion-accelerator system was conceived[1] at TRW to serve as a driver in ICF, and a study is now in progress to validate some of the key concepts in the system. The LIFE accelerator system is different in many respects from the mainline light ion driver approach at Sandia Laboratories[2] which consists of magnetically insulated diodes to produce MA level beam currents and propagate in preformed plasma channels, typically in a 50 torr ambient gas pressure. Because of the differences to be described, the LIFE system can best be viewed as an alternate-back up to the light ion mainline system and also as a useful test bed, to perform several propagation experiments in the near term which are relevant to the Heavy Ion Fusion program. Such propagation experiments appear to be critically needed to provide the experimental feedback on detailed "particle-in-cell" simulations such as the one presented by D.S. Lemons[3] for the LASL-TRW collaborative effort.

CONCEPT DESCRIPTION

The LIFE accelerator is based on the use of separate function hardware elements and the system is optimized to fulfill the requirements of an ICF ion beam driver. Considerations of potential ICF reactor scenarios and the state-of-the-art in pulse power technologies have also been made in the conception of the LIFE system. Separate hardware provisions are made to provide the following functional elements:

1. Generation of Intense Cold Ions: A pulsed intense cold plasma ion source is under development in which plasma induction occurs by pulsed RF power coupling in a large area. Ion extraction is timed to occur in the near afterglow regime of the plasma, about 2 μs after RF power is terminated. In this regime, ion density is high but ion temperature has cooled by ion-neutral atomic collisions. Light ions, D or He at densities of $n_i = 5 \times 10^{12} cm^{-3}$, and temperatures of $T_i \approx 0.1$ eV can be obtained over a 2 m diameter area by 1 MW, 1 ms, RF power at 300 kHz.

2. Intense Beam Acceleration: The LIFE accelerator concept is based on beam stacking by a multi-aperture multi-grid accelerator structure in which each beamlet is channel focused by shaped electrostatic fields. A different example of this principle is the recent MEQALAC accelerator system by A.W. Maschke.[4] Current densities of $J_b \simeq 1$ A/cm^2 are extracted and accelerated in a multi-grid sector with constant applied voltage, V_1, over a pulse duration of $t_p \sim 1$ μs. Beamlets are further accelerated in a following sector with time dependent applied voltage, $V_2 + V(t)$, such that $V_o = V_1 + V_2$ is the final energy of particles in the beam front. $V(t) = V_o [(t_o/t_o - t)^2 - 1]$, for $t < t_o$ where t_o is the flight time of the slowest particles at the beam front, in post-acceleration ballistic drift. Typically, a total current of $I_{acc} \simeq 20$ kA, constant to within a few percent will be accelerated with $V_o \sim 1$ MV and $V(t)_{max} \sim 10$ MV, for $0 < t < t_p$. Beamlet extraction and initial acceleration must be performed with constant applied voltages to preserve a well defined perveance condition and Child's law at the level of the plasma sheath. In this sector with $V_1 \sim 0.3$ MV, beamlet optics are designed to focus extracted beams of $r_b \sim 6$ mm down to a few mm, so that paraxial optics will apply in the subsequent time dependent acceleration. An example of the multi-aperture electrostatic focusing accelerator structure is shown in Figure 1. The optics of radial apertures as the one shown or hole geometries are under investigation with use of the codes[5] EGUN and EBQ. Figure 2 presents the manner whereby the accelator structure is energized.

3. Strong Time Compression: Provisions are made to program strong time compression of beam pulses at the level of 100:1 or 50:1, to deliver 1-2 MA beam currents at a target as 1 μs, 20 kA beam pulses from the accelerator are compressed to 10 ns in a ballistic transport distance of 10-15 m. Strong pulse compression is not feasible in single gap diode accelerators without introducing also strong beam defocusing effects; for these, pulse compression is confined to the level of 3:1 to 5:1 and MA currents need to be accelerated in order to deliver MA beams at targets. Accordingly, one of the main advantage in the LIFE system will be the use of relatively low power technology to energize the multi-grid accelerator structures. A flexible, programmable and highly efficient pulse power method[6]

is conceived by I. Smith for this project whereby the desired V(t) waveform can be tuned with a few tenth of a percent regularity.

4. Focusing: In addition to beamlet channel electrostatic focusing, the accelerator grid planes are spherically shaped with a radius of 10-15 m to provide the radial focusing of the entire beam. Provisions are made independently to apply systematic corrections of trajectories by shaped electrodes, both as a function of beam pulse time and overall beam radius.

5. Current Neutralization: The provision of current neutralization of intense light ion beamlets will be made at the exit end of the accelerator structure. It is required to produce co-moving and co-located electron-ion beams in order to have space-charge and current neutralized ballistic propagation over distances of 10-15 m in an ambient gas pressure of 10^{-4} torr. A detailed calculation[7] of the single and multiple scattering of ions off the nuclear coulomb field and ion energy straggling due to atomic ionization of a medium produced the 10^{-4} torr requirement, so that 1-10 MeV D or He ions will not spread more than $\pm$ 2 mm in 10 m of transport in N_2 gas. Therefore, beam neutralization by the ionization of ambient gas at 0.1 - 1 torr pressures is not acceptable and externally prepared co-moving electrons must be provided to the ion beam. The alternate propagation scheme is through pre-formed high return current plasma channels which are not considered here. A method of generating co-moving electrons is sketched in Figure 3. These electrons must become co-located with the ions within 20-50 cm of travel, otherwise the electrostatic field among electron and ion beamlets will raise the temperature of electrons causing a pressure which limits the amount of ballistic focusing of ions. Co-location is made possible by cusp magnetic fields which fan out co-moving electrons to quickly mingle with the ion beamlets and become trapped in their potential wells. A special test bed is being prepared at TRW to address experimentally the issues of current neutralization of intense and energetic ion beams.

6. Beam Power Profile Shaping: The flexibility in the LIFE accelerator concept in principle makes it possible to deliver a desired beam pulse profile from each beamline while providing also a strong beam

pulse compression at the target focus. Ordinarily, in a multi-beam target compression arrangement each beam would be programmed to fill a specified portion of the power profile, so that the totality of beams but no each beamline provide the power shape desired by target designers. Starting with one of the target design cases presented by R.O. Bangerter,[8] a smooth power raise from ~ 10% to 100% in 14 ns and flat top for 6 ns (see Figure 4), the time varying acceleration voltage waveform in the LIFE system can be programmed[9] according to the shape displayed in Figure 5 to deliver also a current amplified beam of 66:1 at the target focus, as shown in Figure 6. The accelerator will produce a nearly constant current source of 20 kA and in the above case, each beamline will impart 60 kJ energy at the target. A configuration of 34 beamlines is envisaged for a 150 TW, 2 MJ, 300 TW/cm^2 LIFE driver.

STRONG BEAM PULSE COMPRESSION TEST

Since strong beam pulse compression is one of the key features of the LIFE system, a small scale experiment was performed at TRW using most of the ingredients in the concept, to explore some of the issues of technical feasibility and hardware requirements. The experimental setup is given in Figure 7 and details are reported elsewhere.[10] The time varying acceleration voltage waveform was shaped by a 20 channel circuit, to accelerate and pulse compress He^+ ions up to 7 keV. A beam current of 0.6 mA was extracted at constant voltage and subsequently, a 1 μs duration pulse compressing voltage was applied in the following accelerator grids. The pulse compression time focus was located 66 cm downstream from the end of the accelerator. After careful shaping of the time varying voltage waveform, the 1 μs beam pulse was compressed to 8 ns at the time focus. Figures 8 and 9 show a collection of measurements in the temporal behavior of the detected beam current as a function of axial position from the accelerator. Voltage waveform tuning was accomplished by a variety of diagnostic techniques including the behavior of the beam itself. Once the desired waveform was tuned, highly reproducible results were obtained over long periods in time. No attempts were made to provide externally

current neutralization electrons or to design a good spatially focusing accelerator structure. The achieved beam pulse time compression is 125:1 in 66 cm of travel.

A test facility is being upgraded at TRW to scale up these measurements to the 500 keV level with 500 A, 1 μs, He^+ beams produced in a pre-prototype LIFE accelerator system.

REFERENCES

1. Z.G.T. Guiragossian, "Light Ion Fusion Experiment (LIFE), Key Concept Validation Study," TRW Document No. 33876.000, September, 1978; "Novel Light Ion Inertial Confinement Fusion Accelerator," Patent Disclosure TRW No. 11-170, June, 1979; and Bull. Amer. Phys. Soc. 24, 1033 (1979).

2. P.A. Miller et.al. Comments on Plasma Physics and Controlled Fusion, 5 (1979); D.J. Johnson et.al. Phys. Rev. Lett. 42, 610 (1979); G. Yonas, IEEE Trans. Nucl. Sci. NS-26, 4160 (1979).

3. D.S. Lemons, "Ion Beam Propagation Simulations," in this proceedings.

4. A. W. Maschke; R. Adams, et.al. "Description of the Ml MEQALAC and Operating Results," in this proceedings.

5. W.B. Herrmannsfeldt, EGUN, SLAC-166 (1973); A.C. Paul, EBQ, UCID-8005 (1978).

6. I. Smith (private communication).

7. J.L. Orthel and Z.G.T. Guiragossian, "Scattering and Straggling of the LIFE Beam," LIFE-TN-001.

8. R.O. Bangerter, in this proceedings (and private communication).

9. J.L. Orthel, "LIFE Beam Pulse Profile," LIFE-TN-003.

10. B.H. Quon, W.F. DiVergilio, W. Gekelman, Z.G.T. Guiragossian and R.L. Stenzel, "Generation of Strong Time Compressed Light Ion Beams," (submitted to Jour. Appl. Phys.); and Bull. Amer. Phys. Soc. 24, 1033 (1979).

L.I.F. E

MULTI-GRID, MULTI-APERTURE ACCELERATOR STRUCTURE

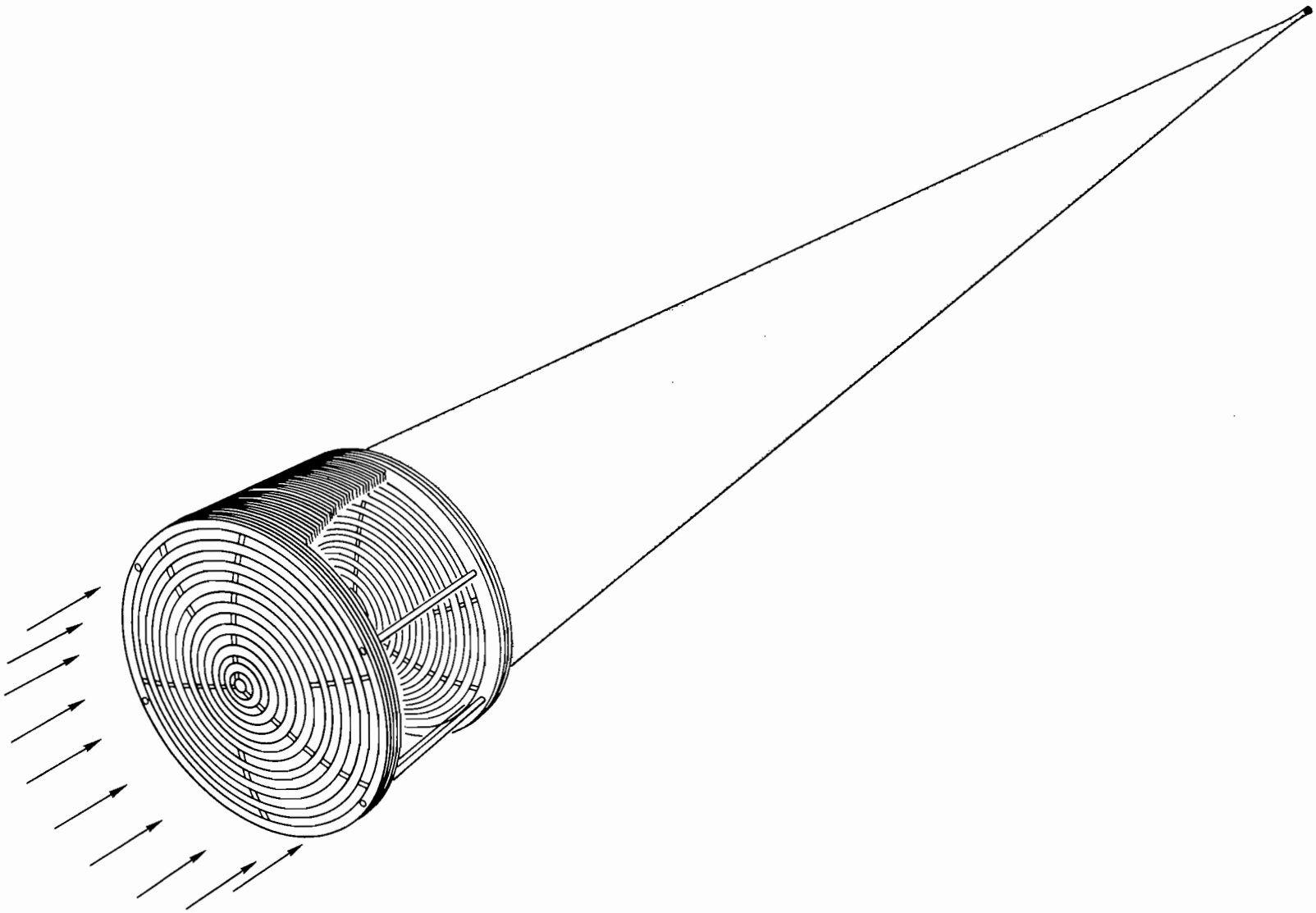

FIGURE 1

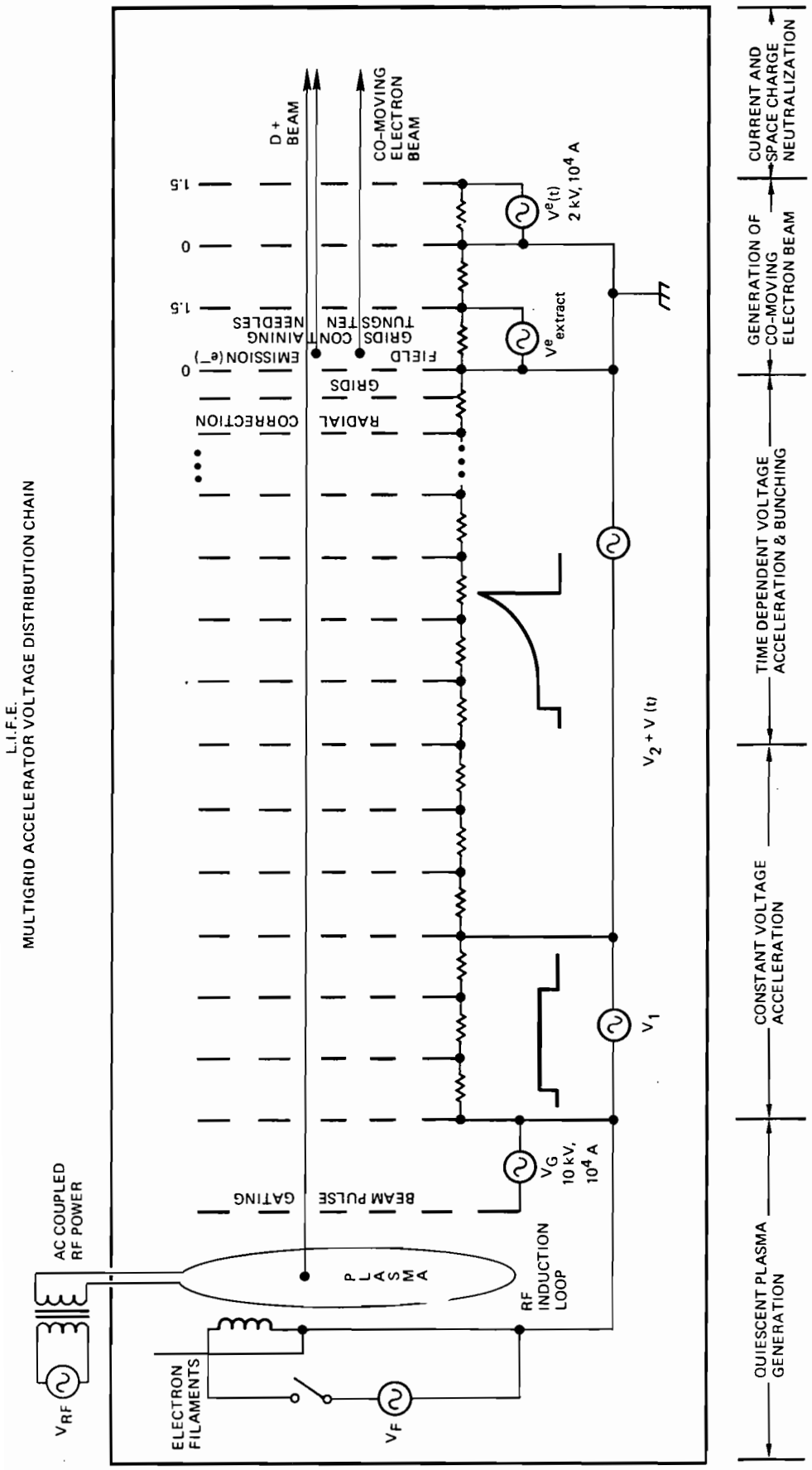
L.I.F.E.
MULTIGRID ACCELERATOR VOLTAGE DISTRIBUTION CHAIN
AC COUPLED RF POWER
V_{RF}
ELECTRON FILAMENTS
V_F
RF INDUCTION LOOP
PLASMA
BEAM PULSE GATING
V_G 10 kV, 10^4 A
V_1
$V_2 + V(t)$
D+ BEAM
CO-MOVING ELECTRON BEAM
1.5
0
1.5
0
EMISSION (e^-)
CONTAINING NEEDLES
TUNGSTEN GRIDS
FIELD GRIDS
RADIAL CORRECTION
$V^e(t)$ 2 kV, 10^4 A
V^e extract
QUIESCENT PLASMA GENERATION
CONSTANT VOLTAGE ACCELERATION
TIME DEPENDENT VOLTAGE ACCELERATION & BUNCHING
GENERATION OF CO-MOVING ELECTRON BEAM
CURRENT AND SPACE CHARGE NEUTRALIZATION

FIGURE 2

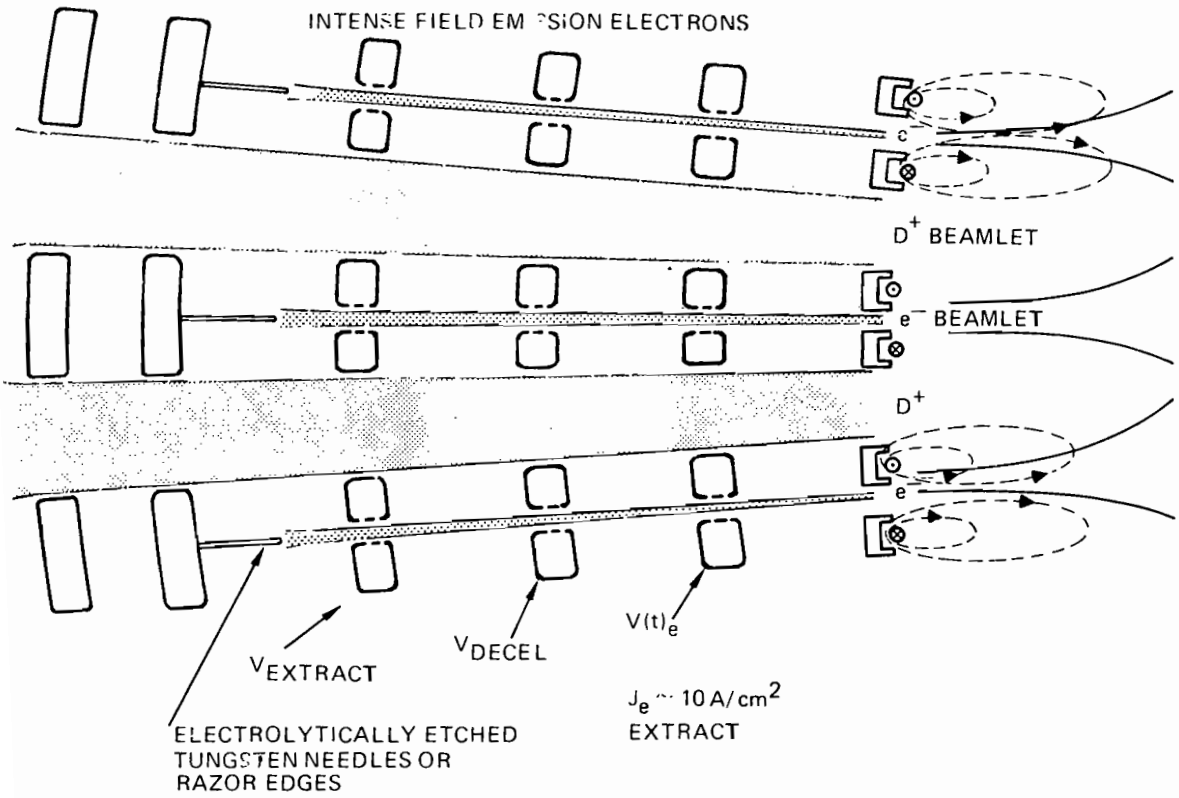

$v_e(t) = v_i(t)$ CURRENT
$n_e = n_D$ CHARGE
} NEUTRALIZATION

$$E_e(t) = \frac{m_e}{M_D} E_b(t)$$

$E_e MAX = 1.32$ (keV)

GENERATION OF CO-MOVING ELECTRON BEAM
FOR CURRENT & CHARGE NEUTRALIZATION
OF ACCELERATED DEUTERONS

FIGURE 3

FIGURE 4

L.I.F.E

SINGLE BEAM POWER PROFILE AT TARGET

$\int P(t)dt = 60$ kJ

POWER RISE TO 4.4 TW IN 14 ns (50%), FLAT FOR 6 ns (50%). POWER PROFILE ACCORDING TO R.O. BANGERTER (LLL) TARGET CALCULATIONS.

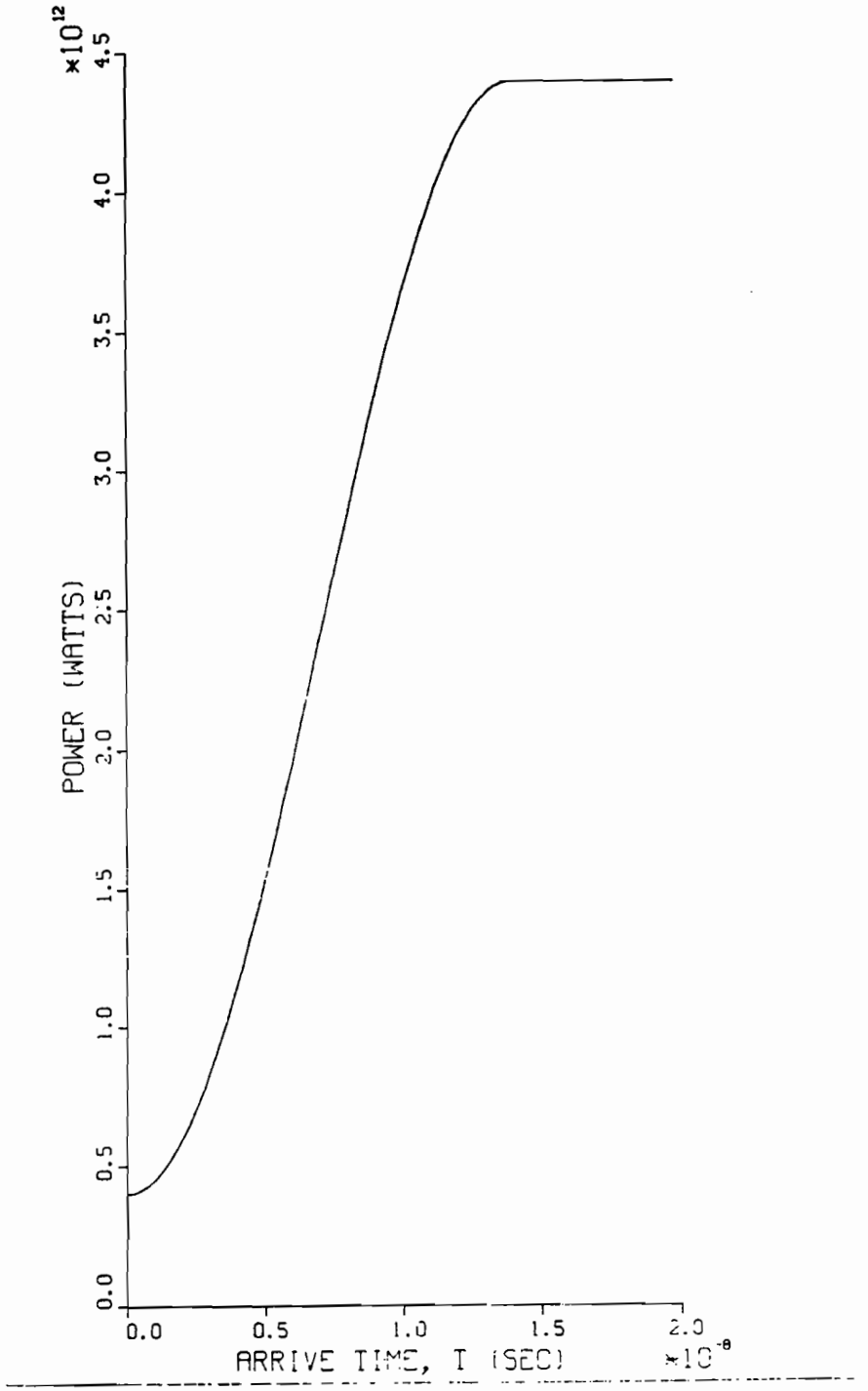

FIGURE 5

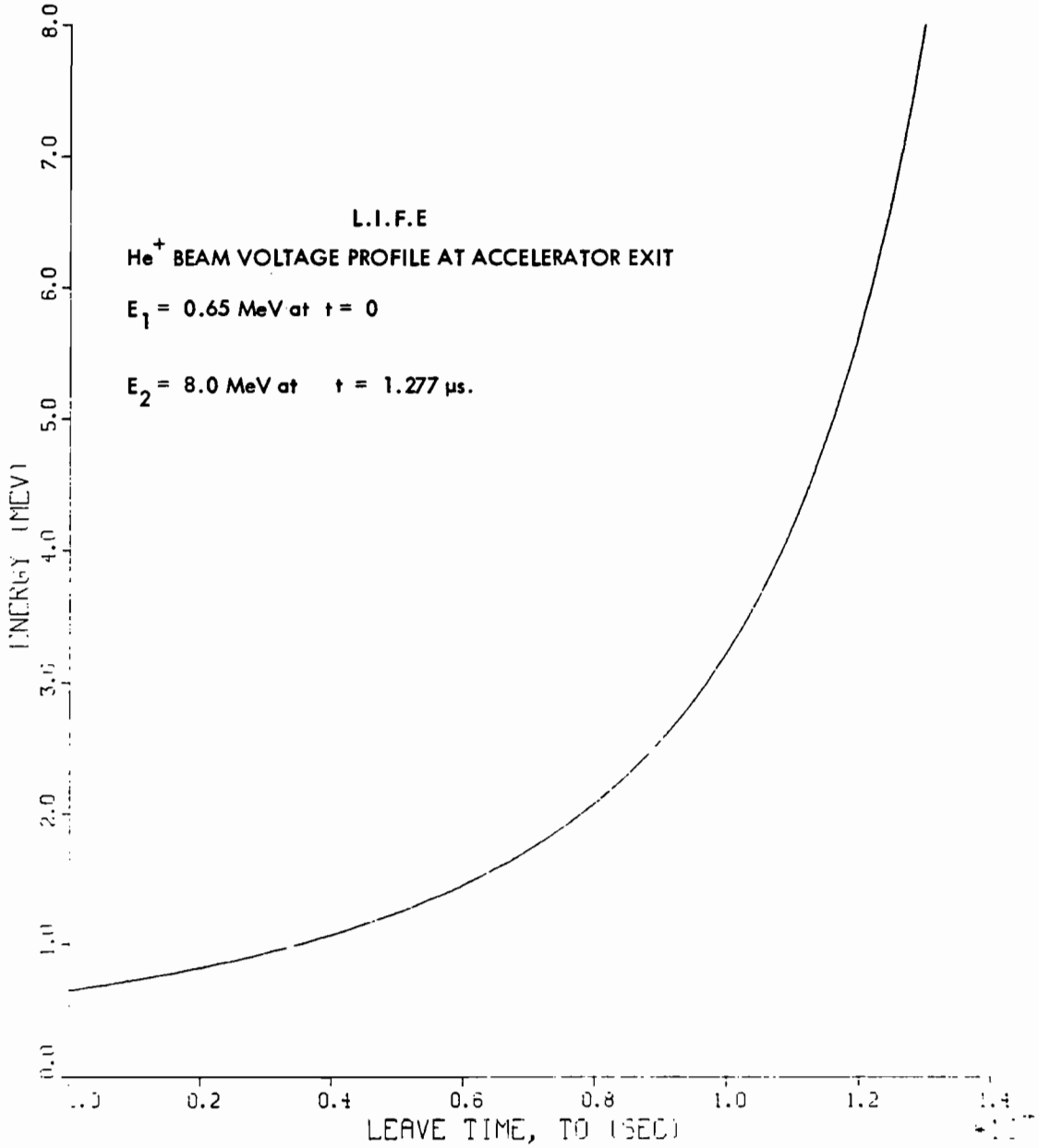
L.I.F.E
He+ BEAM VOLTAGE PROFILE AT ACCELERATOR EXIT
E1 = 0.65 MeV at t = 0
E2 = 8.0 MeV at t = 1.277 μs.
8.0
7.0
6.0
5.0
4.0
2.0
0.2
0.4
0.6
0.8
1.0
1.2
LEAVE TIME, TO (SEC)

FIGURE 6

L.I.F.E

Ho^+ BEAM VOLTAGE PROFILE AT TARGET

I_{accel} = 20 kA, t_{accel} = 1.28 μs, CA = 65.6

I_{target} = 1.3 MA, E_{target} = 60 kJ, T_{ave} = 3 MeV

R_{accel} = 1 m, A = 10 m, R_{focus} = 4 mm, A_{focus} = 0.5 cm^2

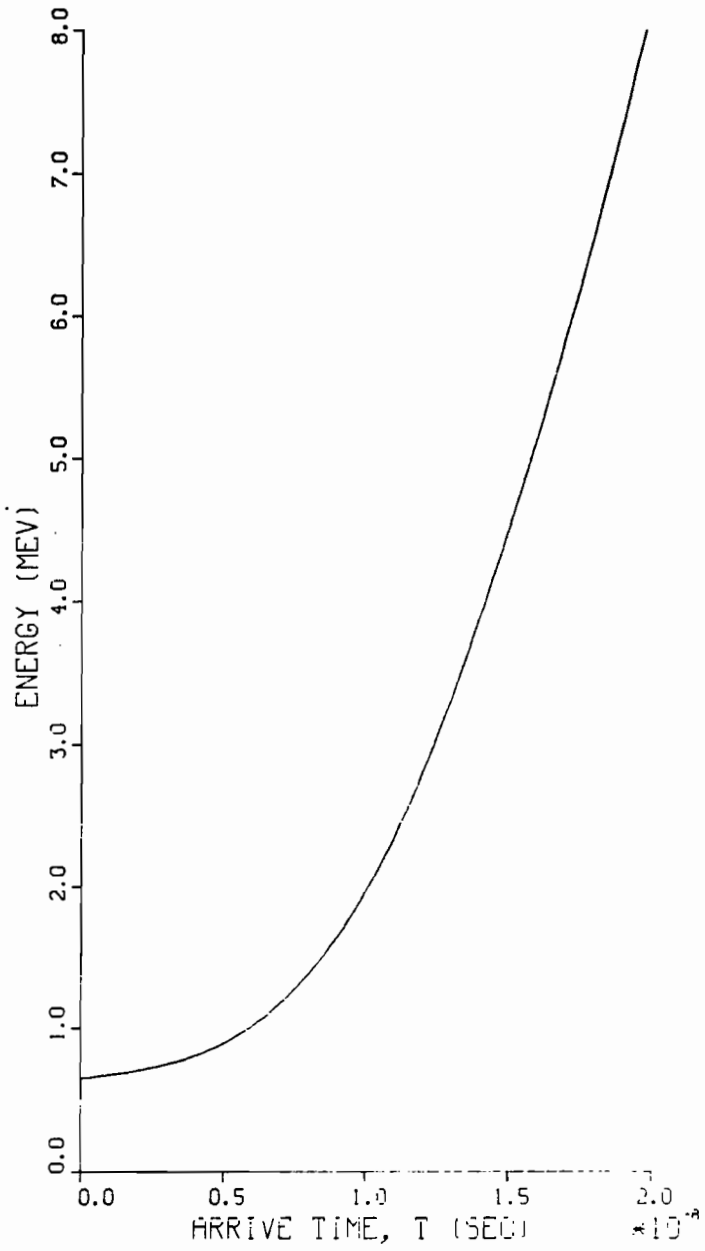

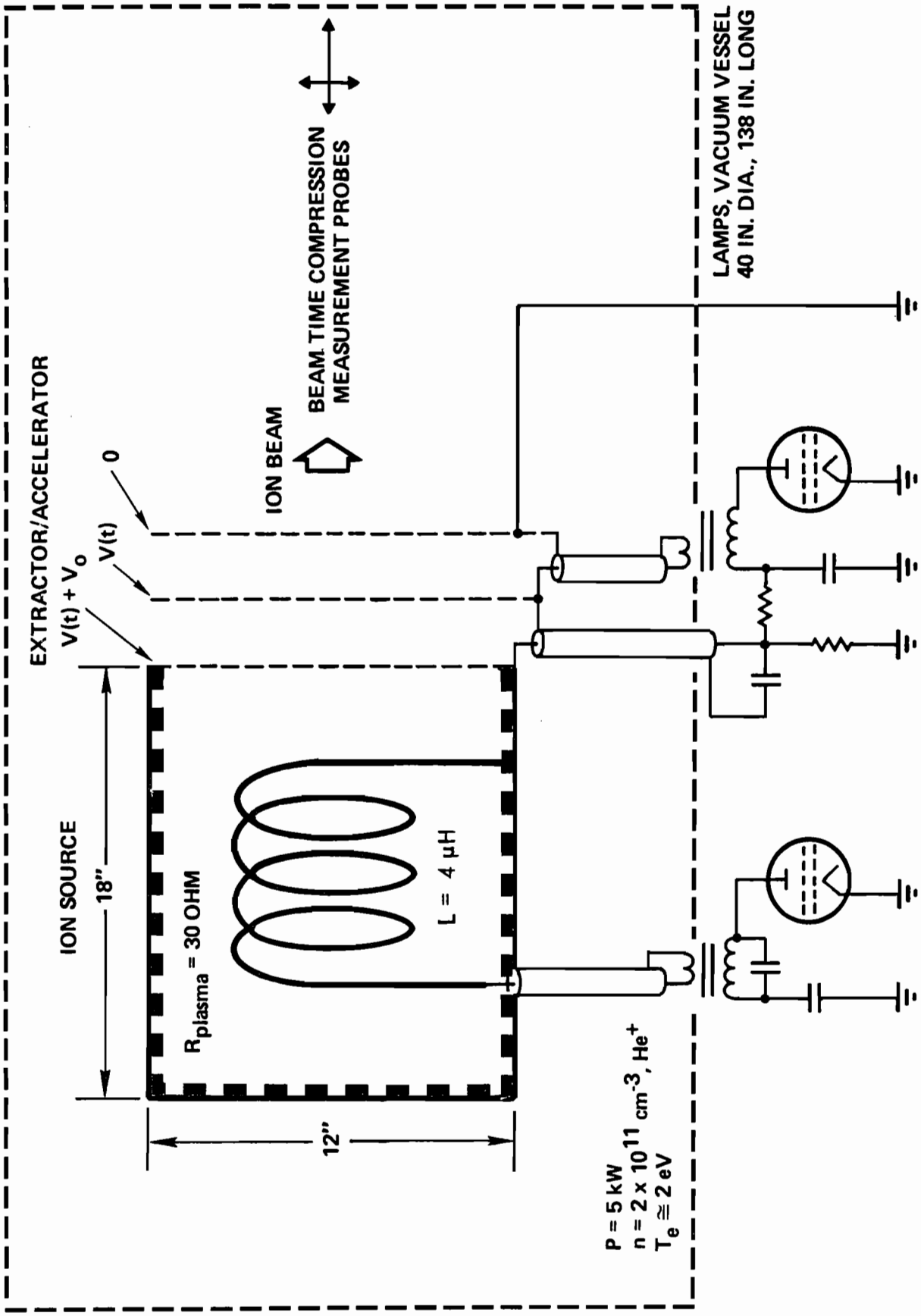
LIGHT ION BEAM COMPRESSION EXPERIMENT
EXTRACTOR/ACCELERATOR
V(t) + V_o
V(t)
0
ION BEAM
BEAM TIME COMPRESSION MEASUREMENT PROBES
LAMPS, VACUUM VESSEL 40 IN. DIA., 138 IN. LONG
ION SOURCE
18"
R_plasma = 30 OHM
L = 4 μH
12"
P = 5 kW
n = 2 x 10^11 cm^-3, He+
T_e ≅ 2 eV

FIGURE 7

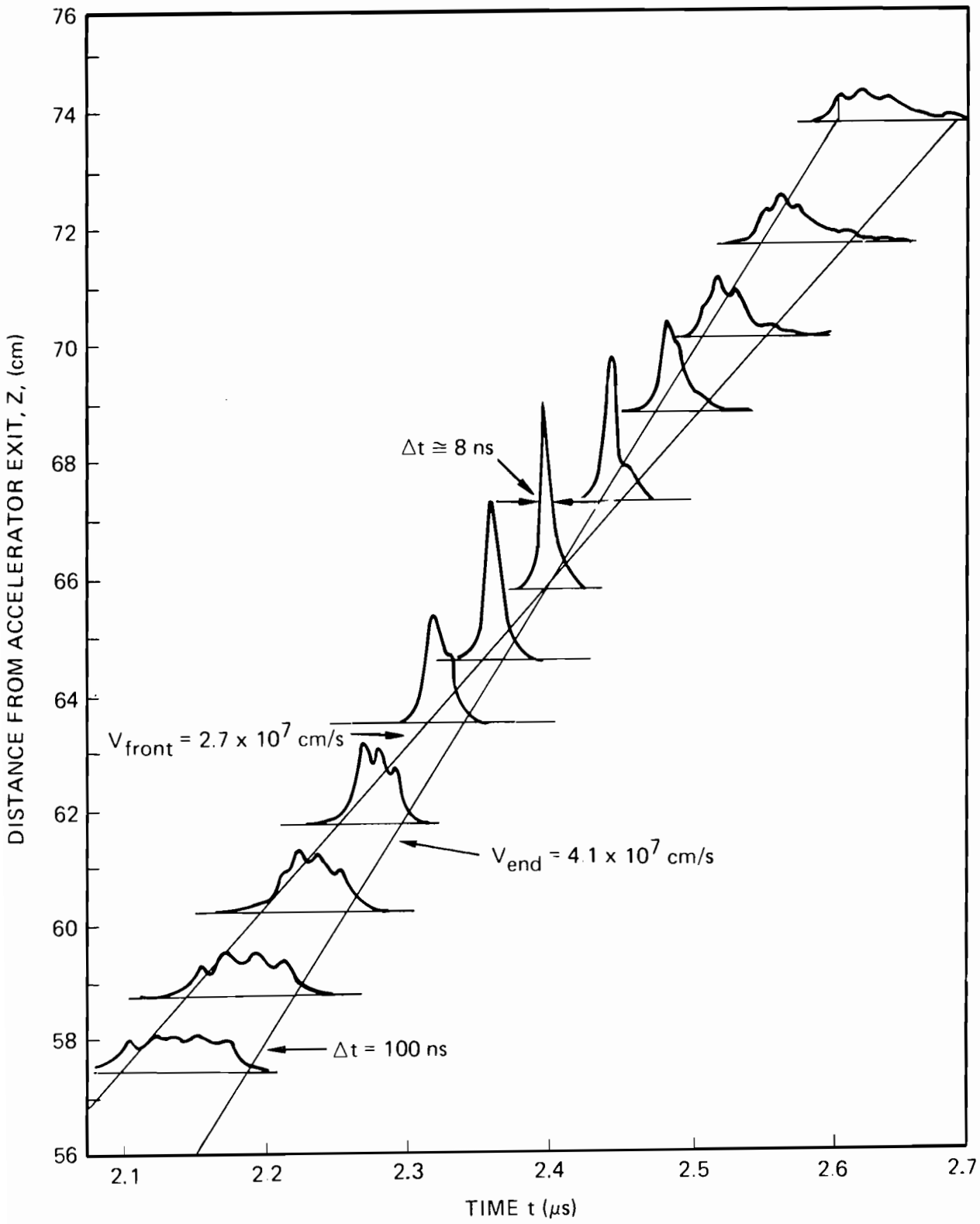
76
74
72
70
68
66
64
62
60
58
56
DISTANCE FROM ACCELERATOR EXIT, Z, (cm)
2.1
2.2
2.3
2.4
2.5
2.6
2.7
TIME t (μs)
Δt ≅ 8 ns
V_front = 2.7 x 10^7 cm/s
V_end = 4.1 x 10^7 cm/s
Δt = 100 ns

FIGURE 8

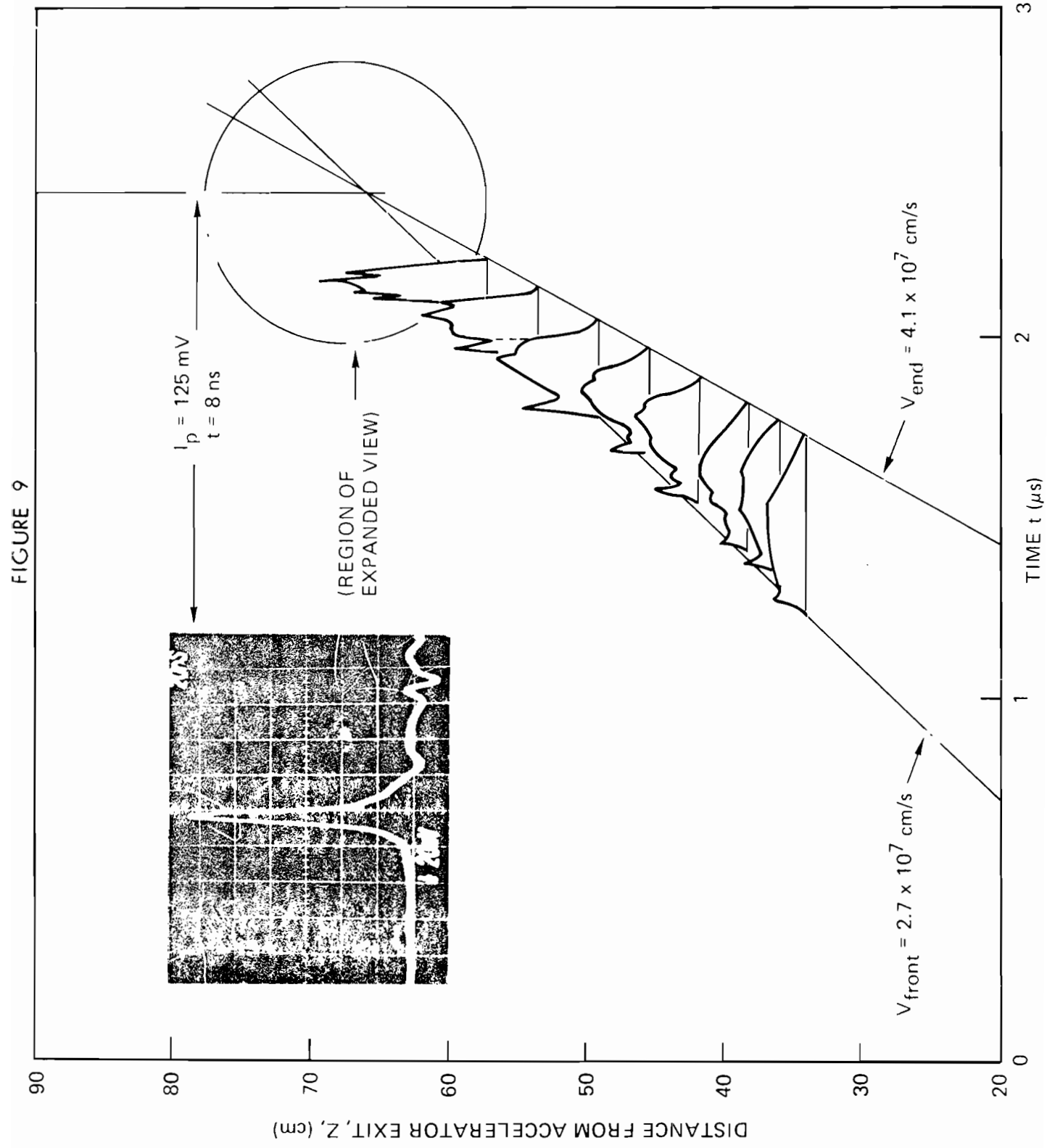
DISTANCE FROM ACCELERATOR EXIT, Z, (cm)
90
80
70
60
50
40
30
20
0
1
2
3
TIME t (μs)
V_{front} = 2.7 x 10^7 cm/s
V_{end} = 4.1 x 10^7 cm/s
I_p = 125 mV
t = 8 ns
(REGION OF EXPANDED VIEW)

FIGURE 9

ION BEAM PROPAGATION SIMULATIONS

Don S. Lemons
Los Alamos Scientific Laboratory

INTRODUCTION

A series of numerical particle-in-cell simulations of ion beam propagation have been performed with the LASL two-dimensional electromagnetic code, CCUBE.[1] A few results for each of two different simulations are presented. They are intended to illustrate plasma effects relevant to 1) ion propagation in a relatively dense plasma background, and 2) ion vacuum propagation with co-moving electrons.

PROPAGATION IN PLASMA BACKGROUND

Ion propagation through a background gas sufficiently dense to result in plasma production necessary to charge and current neutralize the beam but tenuous enough to avoid serious degradation of beam quality is a possible propagation mode for inertial confinement. In this mode ballistic ion beam propagation and focusing is a possibility provided the beam ion-background electron two-stream instability remains harmless. This issue along with the effects of incomplete current neutralization is investigated in the first simulation.

The simulation was performed in r,z cylindrical spatial coordinates which were divided respectively into 50 and 150 grid points. Spatial dimensions of the simulation grid and the unperturbed ion beam envelope are shown in Fig. 1(a).

The ion beam is injected at $t = 0$, from the LHS of the simulation grid. Beam ion speed is given by $\beta = 0.548$, beam ion to electron mass by $m_b/m_e = 50$, and beam-to-background plasma density by $n_b/n_e = 10^{-1}$. These and other dimensionless simulation parameters are listed in the Fig. 1 caption where V_{th} denotes thermal speed, and the subscripts "b", "i", and "e" denote beam ion, background ion, and background electron parameters.

Work supported by U.S. Dept. of Energy under Contract W-7405-ENG-36

The beam rises to full strength and propagates across the simulation in about 200 plasma periods, ω_{pe}^{-1}. During this time the beam first becomes charge and current neutralized (0-10 ω_{pe}^{-1}), begins to lose current neutralization and, consequently, magnetically pinch (~ 100 ω_{pe}^{-1}), and develop axial modulations in the beam density and velocity, a result of the nonlinear development of the ion-electron two-stream instability (100 ~ 150 ω_{pe}^{-1}).

Figures 1(a)-1(b) are respectively r - z and v_z - z phase plots of the beam ions after the beam has propagated across the simulation grid, the two stream instability has saturated and magnetic pinching is active. Spatial dimensions are in units of c/ω_{pe}, time in units of ω_{pe}^{-1}, and velocity in terms of $\beta_z\gamma$ where $\beta_z = V_z/c$ and $\gamma = (1 - \beta_z^2)^{-\frac{1}{2}}$.

For the initial beam and background plasma parameters, the ion electron two-stream growth rate (ω_I) and group velocity (V_{gr}) are given by $\omega_I = 0.0695\ \omega_{pe}$ and $V_{gr} = 0.643\ \beta C$. These parameters correspond to a factor of 10 growth in wave amplitude at the point $10\ V_{gr}/\omega_I$ or $50.6\ c/\omega_{pe}$, a distance which according to Figs. 1a-1b is associated with large one-dimensional beam density and velocity modulations. Wave saturation by trapping of the beam ions occurs at about this point. After saturation the background plasma is observed to heat at a rate consistent with a transfer of beam energy to plasma energy of 17%. This transfer is in line with the prediction of a single wave two-stream heating model,[2]

$$2\left(\frac{n_b}{2n_p}\ \frac{m_e}{m_i}\right)^{1/3} ,$$

which given the present simulation parameters is 20%. No instability produced deflection of beam particles in the radial direction is observed.

Magnetic pinching of the beam occurs in part because the neutralizing background electron stream depletes the electron population in the region of beam injection and electrons initially outside the beam cannot efficiently current neutralize the beam. This boundary effect was not anticipated but nonetheless results in a gross distortion of

the beam. The resulting beam envelope is in general consistent with the ion beam envelope equations derived by Wright.[3]

VACUUM PROPAGATION WITH CO-MOVING ELECTRONS

Vacuum or near vacuum ion beam propagation is also an attractive mode since uncertainties involved in beam plasma production and instabilities are avoided. In this case, active current and charge neutralization are necessary for ballistic propagation. This may be achieved either by beam electron pickup or the injection of comoving electrons as proposed in TRW's light ion driver.[4] The ion electron charge separation at injection which is a feature of the latter scheme provides considerable electrostatic energy which initially goes into the electrons. How and whether this energy is transferred to the ions in amounts which can inhibit ballistic focusing is a subject of continuing investigation.

It is, however, easy to estimate the electrostatic energy involved for a typical parameter. Assume an infinite sheet of ions and an infinite sheet of electrons both with thickness δ and density n separated by a distance Δ. The electrostatic energy per electron (W) due to the charge separation is then given by $W = 2\pi e^2 n\delta(\Delta + 2/3\ \delta)$. For $n = 10^{10}/cm^3$, $\delta = 5$ mm and $\Delta = 3$ mm, W = 2.86 keV, a significant amount of transverse energy is equally partitioned with the ions.

Electron motion within self-electrostatic fields is illustrated by the numerical simulation of the simultaneous injection into a vacuum of three pairs of cylindrical concentric hollow ion and electron beamlets. The simulation was performed in r,z coordinates on a grid of 80 by 100 grid points. Figures 2(a) and 2(b) are respectively ion and electron r,z phase plots 24.5 ω_{pe}^{-1} after injection. Spatial dimensions are in units of c/ω_{pe}. Initial beam velocities are given by $\beta = 0.0728$, $m_b/m_e = 3670$, and beamlet charge densities were initialized to provide for zero net charge within each beamlet pair. Other parameters are listed in the Fig. 2(a)-2(b) caption.

The ion time scale, ω_{pi}^{-1}, is too long in this simulation to observe ion motion. In contrast, the electrons are propelled into large excursions from the ions both axially and radially by electrostatic forces. The heads of the electron beamlets remain intact because beam charge

densities are initially zero and rise exponentially to their full value in about 20 ω_{pe}^{-1}.

ACKNOWLEDGEMENTS

This work was supported by the Department of Energy. Assistance from Lester Thode of Los Alamos Scientific Laboratory in setting up and interpreting results from the code CCUBE has been invaluable. Helpful discussions and guidance from Zaven Guiragossian are also acknowledged.

REFERENCES

1. CCUBE is a family of electromagnetic and electrostatic one- and two-dimensional particle-in-cell simulation codes developed by Brendan Godfrey, presently of Mission Research, Albuquerque, New Mexico.

2. L. E. Thode and R. W. Sudan, "Two-Stream Instability Heating of Plasmas by Relativistic Electron Beams," Phys. Rev. Lett. 30, 732 (1973).

3. T. P. Wright, "Analytic Ion Self-Pinch Formulae," Phys. Fluids 22, 1831 (1979).

4. TRW Proposal No. 33876.000, "L.I.F.E., Light Ion Fusion Experiment," September 1978.

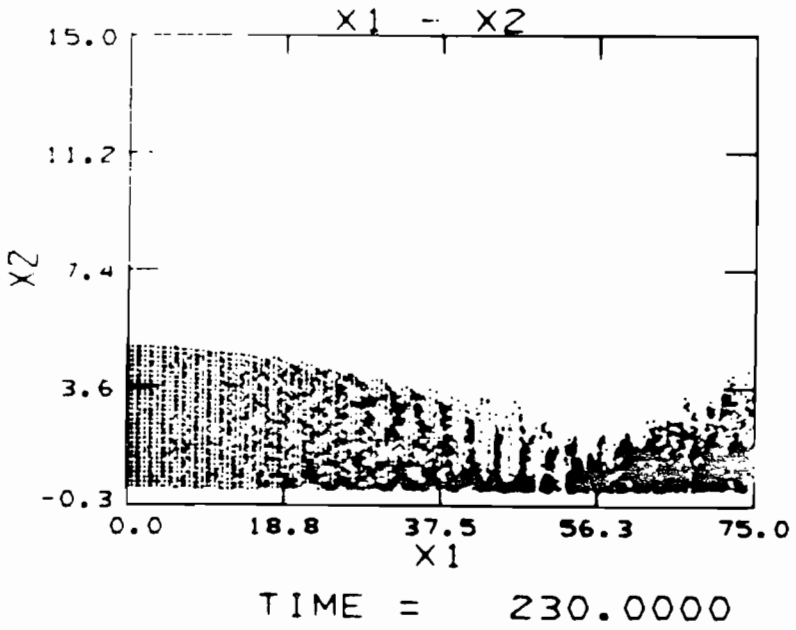

Fig. 1(a)

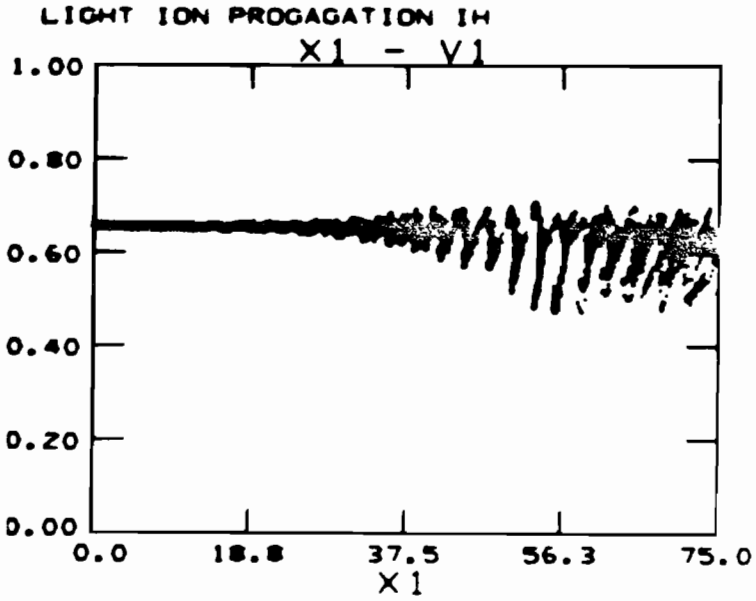

Fig. 1(b)

Figs. 1(a)-1(b). Ion beam particle plots in X2-X1 (i.e., r-z) space 1(a) and V1-X1 (i.e., V_z-z) space 1(b). Simulation parameters are $\beta = 0.548$, $m_b/m_e = 50$, $m_i/m_e = 100$, $n_b/n_e = 10^{-1}$, $V_{thb}/c = 10^{-3}$, $V_{thi}/c = 10^{-4}$, and $V_{the}/c = 10^{-2}$. Distances and times are in units of c/ω_{pe} and ω_{pe}^{-1} respectively.

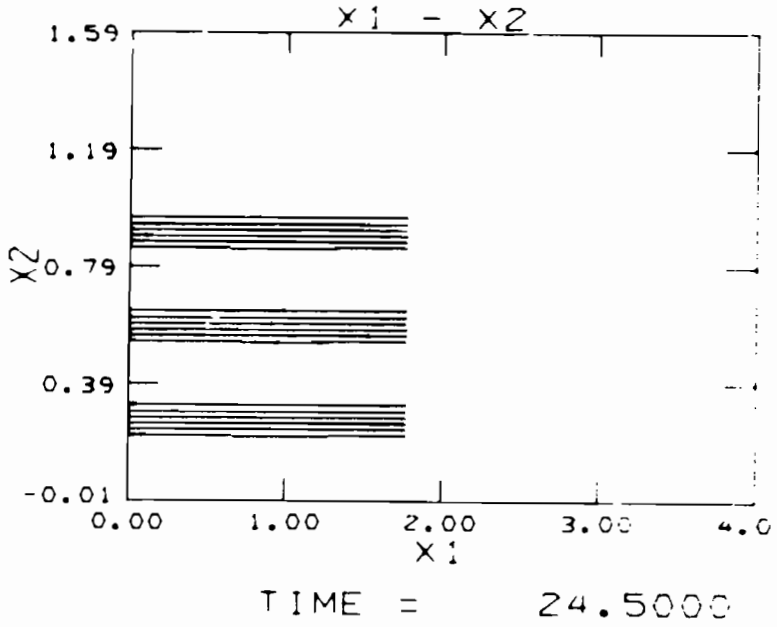

Fig. 2(a)

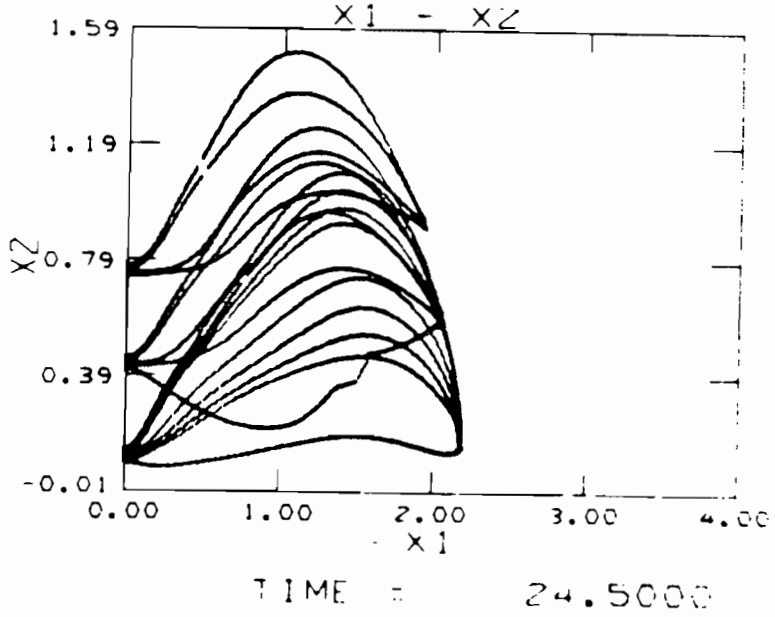

Fig. 2(b)

Figs. 2(a)-2(b). Ion beam 2(a) and co-moving electron 2(b) particle plots in X2-X1 (i.e., r-z) space. Simulation parameters are $\beta = 0.0728$ and $m_b/m_e = 3670.5$. Particles are completely cold. Distances and times are in units of c/ω_{pe} and ω_{pe}^{-1} respectively.

CONVECTIVE AND NONCONVECTIVE ION BEAM FILAMENTATION INSTABILITIES

Richard F. Hubbard
Jaycor

ABSTRACT

The electromagnetic filamentation instability is expected to occur in heavy ion beam fusion target chambers. For a converging beam, the instability is expected to be convective with group velocity v_g approaching the beam velocity V_b until the beam is ~10-50 cm from the target. The number of e-foldings N_γ is estimated by integrating the local growth rate along the beam trajectory. For a cold beam, the result agrees with the initial value problem solution of Lee, et al. Detailed numerical solutions to the full dispersion region predict somewhat lower values for N_γ. Close to the target, $v_g \rightarrow 0$, and the instability is effectively nonconvective, with N_γ proportional to the pulse length. If a realistic conductivity model is used ($\sigma \sim (Z_b/R)^2$), the number of e-foldings in the nonconvective region is generally smaller than N_γ in the convective region. Thus, any appreciable deterioration in beam quality is more likely to occur while the beam is in the convective region.

I. INTRODUCTION

The electromagnetic filamentation instability may play an important role in determining allowable operating parameters for heavy ion fusion (HIF) systems. If allowed to grow to large amplitudes in the target chamber, self-magnetic fields arising from this instability would cause the ion beam to break into several self-pinched filaments or beamlets, possibly resulting in an unacceptable deterioration in beam focussing quality.

Theoretical analyses of this effect have attempted to predict the number of e-foldings N_γ of the electromagnetic field amplitudes using linear stability theory. Hubbard and Tidman[1] and Hubbard, et al[2] estimated N_γ based on a local dispersion relation (hereafter referred to as the "local approximation") which showed that for ballistic focussing systems, transverse beam heating reduced N_γ to acceptable levels ($N_\gamma \lesssim 5$) in most cases appropriate to HIF reactors. However, calculations by Lee, and his co-workers[3,4,5] which treated perturbations as an initial value problem gave somewhat higher estimates of N_γ and led them to the conclusion that filamentation instability defocussing may not be easy to avoid.

Previous calculations with the local approximation centered on the regime where the axial group velocity v_g (measured in the <u>laboratory</u> frame) is much less than the beam velocity V_b. In this nonconvective regime, N_γ is proportional to the pulse length, and the perturbations do not propagate in the laboratory frame. In this note, we examine the convective instability ($v_g \approx V_b$) in more detail. Our conclusions can be stated as follows:

1. The local approximation predicts that $v_g \approx V_b$ when the conductivity is low. N_γ can then be estimated by integrating the growth rate $\gamma(z)$ along the beam trajectory. For a ballistically focussed beam, the resulting N_γ <u>agrees</u>

with the initial value method for a cold beam and is smaller by a constant factor 0.31 for a sufficiently warm beam. Detailed numerical solutions to the dispersion relation tend to lie midway between the warm and cold beam results.

2. The instability is almost always nonconvective when the beam is near the pellet for HIF systems with ballistic focussing. The group velocity increases monotonically with distance z' from the pellet.

3. The lower N_γ and the claim of nonconvective instability predicted by the local approximation[1,2] was due in a large part to assuming a constant σ throughout the target chamber. If a more realistic conductivity model is assumed, ($\sigma \sim R^{-2}$ where R is the beam radius), maximum nonconvective growth occurs at ~10-50 cm from the pellet, and the values of N_γ are comparable with (but usually somewhat smaller than) those occurring in the convective regime.

4. Both the local approximation and the initial value method thus predict $N_\gamma \gtrsim 5$ for highly stripped high current beams (e.g., charge state $Z_b \gtrsim 70$, beam particle current $\tilde{I}_b \gtrsim 2$ kA). However, we believe that macroscopic self-magnetic fields arising from the ion beam or from "knock-on" electrons are likely to lead to unacceptable ion orbit deflections in this regime. In particular, we recommend using H_2 or He at ~1 torr to reduce Z_b to ~20. In this regime, N_γ can be $\lesssim 2$ and filamentation can be avoided.

II. REVIEW OF FILAMENTATION MODELS

The local approximation[1,2] is based on the dispersion relation for electromagnetic waves generated by a shifted Maxwellian ($f \sim \exp(-(v_z - V_b)^2/2\Delta v_z^2 - v_\perp^2/2\Delta v_\perp^2)$) ion beam with beam plasma frequency ω_b, average velocity $V_b = \beta c$ and thermal velocity $\Delta v_\perp$ propagating in a resistive medium with scalar conductivity σ.

$$H(\vec{k};\omega) = 0 = k^2c^2 - \omega^2 + \omega_b^2 \left\{1 - \frac{V_b^2}{\Delta v_\perp^2}(1 + \xi_b Z(\xi_b))\right\} - 4\pi i\omega\sigma \ . \qquad (1)$$

Here $\xi_b = (\omega - k_{//} V_b)/\sqrt{2}\ k_\perp \Delta v_\perp$, and $Z(\xi_b)$ is the plasma dispersion function. Except for the conductivity term, Eq. (1) agrees with Davidson, et al[6] in the $k_{//} = 0$ limit. An additional term proportional to $k_{//}$ is negligible in the regime we are examining. The unstable mode is purely growing ($\omega_r = 0$) for $k_{//} = 0$. Approximate solutions in the hot beam regime ($|\xi_b| << 1$) and cold beam regime ($|\xi_b| >> 1$) for $k_{//} = 0$ are

$$\gamma = \mathrm{Im}(\omega) \underset{|\xi_b| << 1}{=} \frac{c^2(k_0^2 - k_\perp^2)}{-i\eta + 4\pi\sigma} \ , \qquad (2a)$$

and

$$\gamma = \beta\omega_b \underset{|\xi_b| >> 1}{} \ . \qquad (2b)$$

Here,

$$k_0 = \omega_b V_b/\Delta v_\perp c \qquad (3)$$

is the maximum unstable wave number, and

$$\eta = \frac{k_0^2 c^2}{\sqrt{2}\, k_\perp \Delta v_\perp} \left(Z(\xi_b) + \xi_b\, Z'(\xi_b) \right) \tag{4a}$$

$$\eta = i\sqrt{\frac{\pi}{2}}\, k_0^2 c^2 / k_\perp \Delta v_\perp \qquad |\xi_b| \ll 1 \tag{4b}$$

$$\eta = 2i\, \omega_b \beta\, (k_\perp c / k_0 \Delta v_\perp)^2 \quad . \qquad |\xi_b| \gg 1 \tag{4c}$$

Eq. (2b) is valid only when $\beta\omega_b \gg 4\pi\sigma\ \Delta v_\perp / c)^2$.

The axial group velocity for $k_{//} = 0$ is

$$v_g = \frac{\partial \omega_r}{\partial k_{//}} = -\frac{\partial H}{\partial k_{//}} \Big/ \frac{\partial H}{\partial \omega_r} = \frac{\eta\, V_b}{\eta + 4\pi i \sigma} \tag{5}$$

Clearly, $v_g \approx V_b$ for $-i\eta \gg 4\pi\sigma$, leading to convective instability, while for $-i\eta \ll 4\pi\sigma$, $v_g \to 0$, and the instability is effectively nonconvective. In the nonconvective regime, $N_{\gamma,\ hot}^{nc} = \bar{\gamma}(z')\ \tau_p$ where $\bar{\gamma}$ is the average growth rate at position z' (with respect to the pellet) and τ_p is the pulse length. Close to the pellet, $\Delta v_\perp$ and σ are both large, and $v_g \to 0$ over a wide range of system parameters.[2]

The initial value method[3,4,5] predicts that for ballistic focussing, field amplitude $A \approx (L/(L-z))^\alpha$ where L is the chamber radius, and

$$\alpha = 2Z_b \left(\frac{L}{R_0}\right) \left\{ \frac{1}{\beta\gamma_r} \left(\frac{\tilde{I}_b}{m_e c^3/e} \right) \frac{m_e}{m_b} \right\}^{1/2} \quad . \tag{6}$$

Here R_0 is the beam radius at entry (z = 0). The number of e-folding is thus

$$N_\gamma = 2Z_b \left(\frac{L}{R_0}\right) \left\{ \frac{1}{\beta\gamma_r} \left(\frac{I_b}{(m_e c^3/e)} \right) \frac{m_e}{m_b} \right\}^{1/2} \ell n \left(\frac{L}{L-z} \right) \tag{7a}$$

$$= \left(\frac{\omega_{bo} L}{c}\right) \ln\left(\frac{L}{L-z}\right) \qquad (7b)$$

Here ω_{bo} is the beam plasma frequency at $z = 0$, and $\gamma_r = (1 - \beta^2)^{-\frac{1}{2}}$.

III. LOCAL APPROXIMATION IN THE CONVECTIVE REGIME

We can recover the Lee, et al result (Eq. (7)) to within a numerical factor if $v_g \to V_b$ and Z_b is constant. For $|\eta| >> 4\pi\sigma$, Eq. (2a) for a hot beam can be integrated to give

$$N^c_{\gamma,hot} \approx \frac{1}{V_b} \int_0^{z^*} dz' \gamma(z') = \sqrt{\frac{2}{\pi}} \frac{k_\perp}{V_b} \left(1 - \frac{k_\perp^2}{k_0^2}\right) \int_0^{z^*} dx \Delta v_\perp(z') \ , \tag{8}$$

where z* is the approximate position at which the instability becomes nonconvective. In the absence of scattering, the thermal spread $\Delta v_\perp(z')$ increases from its value $\Delta v_{\perp o} = \Delta v_\perp(z = 0)$ according to[1]

$$\Delta v_\perp(z) = \Delta v_{\perp o}(R_o/R(z)) = \Delta v_{\perp o} \, L/(L-z) \tag{9}$$

Noting that maximum growth occurs at $k_\perp = k_o/\sqrt{3}$, Eq. (8) can be integrated to give

$$N^c_{\gamma,hot} = \frac{2}{3} \sqrt{\frac{2}{3\pi}} \frac{k_o \Delta v_{\perp o}}{V_b} L \, \ell n \, (L/(L-z)$$

$$= 0.31 \, \frac{\omega_{bo} L}{c} \, \ell n \, \left(\frac{L}{L-z^*}\right) \tag{10}$$

Eq. (10) therefore reduces to the Lee, et al result (Eq. (7)) in the nonrelativistic limit except for the numerical factor 0.31.

In the cold beam limit, the same procedure gives exact agreement with the initial value method. Noting that for Z_b constant, $\gamma(z) = \beta\omega_{bo}(R_o/R)$ $= \beta\omega_{bo}(L/L-z)$, the growth rate is integrated as before to give

$$N^c_{\gamma,cold} = \frac{\omega_{bo} L}{c} \, \ell n \left(\frac{L}{L-z^*}\right) . \tag{11}$$

IV. CONVECTIVE VS. NONCONVECTIVE INSTABILITY FOR $\sigma \sim R^{-2}$

We have previously claimed[2] that even though Eq. (6) allows v_g to vary from 0 to V_b, typical HIF parameters give $-i\eta \ll 4\pi\sigma$, and $v_g \ll V_b$. This led us to conclude that nonconvective instability was the more important, and that N_γ^{nc} given by Eq. (10) was a reasonable estimate for the number of e-foldings. However, the calculations in Refs. 1 and 2 assumed that conductivity σ was constant everywhere in the target chamber. When values of σ appropriate near the pellet are used, $v_g \ll V_b$ almost everywhere in the chamber. However, for typical ballistic focussing systems, we expect from classical transport models[7,8] that σ is several orders of magnitude lower near the chamber wall than at the pellet. We expect the instability to be convective in this regime with $v_g \approx V_b$.

In the region where R(z) exceeds a few centimeters, σ is approximately linear with density n_e. Direct ionization by the beam probably predominates, so $\sigma \sim n_e \sim R^{-2}(z)$. If $\sigma = \sigma_o(R_o/R)^2 = \sigma_o(L/(L-z))^2$ is assumed everywhere, the position z^* where the instability changes from convective to nonconvective is given by $\eta(z^*) \approx 4\pi\sigma(z^*)$, or

$$\sqrt{\frac{\pi}{2}}\ \frac{k_o^2 c^2}{\alpha\, k_o (\Delta v_{\perp o} L/(L-z^*)}} = 4\pi\ \sigma_o \left(\frac{L}{L-z^*}\right) \tag{12}$$

Here $\alpha \simeq 0.5 = k_\perp/k_o$. The boundary z^* is thus

$$z^* = \left[1 - \left(\frac{4\sqrt{2\pi}\ \ \alpha\beta\sigma_o \Delta v_{\perp o}}{V_b k_o c}\right)^{1/3}\right] L \quad . \tag{13}$$

The situation is illustrated in Figure 1 which shows typical regions of convective and nonconvective instability. Since $\eta \sim R$ and $\sigma \sim R^{-2}$, the transition region where $v_g \sim \frac{1}{2} V_b$ is quite small. Eq. (13) predicts $(1 - z^*/L) \sim 0.05 - 0.1$ in most cases. For $\sigma \sim R^{-2}$ maximum growth actually occurs in the convective

regime where $\eta = 8\pi\sigma$ and $v_g = \frac{2}{3} V_b$. However, we expect that detailed beam transport code results to show that $\sigma(z)$ will probably increase faster than R^{-2} in the $z \simeq z^*$ region due to avalanching and then increase more slowly with R as the plasma becomes fully ionized near the pellet. Thus, maximum growth may well occur in the nonconvective regime.

The following scenario can therefore be constructed. In the convective regime, perturbations are carried along with the beam until they arrive at $z \simeq z^*$. The number of e-foldings N_γ^c accumulates according to Eq. (10) or (11). As the beam continues to propagate, perturbations are rapidly left behind as v_g becomes small. The number of e-foldings is then obtained by calculating $\gamma(z')$ from Eq. (2) and taking $N_\gamma^{nc} \simeq \gamma(z')\tau_p$. Filamentation defocussing will be determined by the larger of the two N_γ's.

As an example, consider a 2 kA, 20 GeV, 10 nsec Uranium beam with $Z_b = 20$, $\Delta v_{\perp o}/V_b = 10^{-4}$, R_o - 10 cm, $\sigma_o = 10^{12}$ s^{-1}, and L = 500 cm. Then $z^* \simeq 470$ cm, and $N_{\gamma,hot}^c = 1.4$. Note that $N_{\gamma,cold}^c = 3\ N_{\gamma,hot}^c$. The calculation of N_γ^{nc} is somewhat arbitrary since maximum growth does not occur in the nonconvective regime. If we choose $z = z^* + 0.2\ (L-z^*)$, then $v_g \sim 0.25\ V_b$, and $N_\gamma^{nc} \simeq 0.85$. $N_{\gamma,hot}^c > N_\gamma^{nc}$ in this example, but the difference is less than a factor of 2. If $Z_b = 70$ (which is typical of Ne at 1 torr instead of H_2 or He at 1 torr) then $z^* = 480$ cm, $N_{\gamma,hot}^c = 5.8$, and $N_\gamma^{nc} = 4.5$. We have calculated N_γ^c and N_γ^{nc} for a variety of HIF parameters; in most cases, $N_{\gamma,hot}^c > N_{\gamma,hot}^{nc}$ but the disagreement is usually less than a factor of 2. In general, $N_\gamma^{nc} > N_{\gamma,hot}^c$ can be obtained by increasing the ratio of the pulse length τ_p to the beam transit time $\tau_L = L/V_b$ or by changing the details of the conductivity model. The most dangerous nonconvective instability occurs at some tens of centimeters from the pellet where σ^{-1} (and hence N_γ^{nc}) may be an order of magnitude higher than the value near the pellet used by Hubbard, et al.[1,2]

Beam convergence does not play a role in the nonconvective regime, so one might expect approximate agreement with Lee's calculations for a non-converging finite-pulse beam.[3] For a warm beam of length τ_p, the number of e-foldings predicted by Lee is

$$N_{\gamma,hot} \lesssim (\xi_L^{-2} - 1) \frac{\tau_p}{\tau_m} , \tag{14}$$

where $\tau_m = k^2c^2/4\pi\sigma$, and $\xi_L^2 = k^2\Delta v_\perp^2 / \beta^2\omega_b^2$. (Note that he defines $\Delta v_\perp$ to be $\sqrt{2}$ larger than our value.) Substituting the definitions of τ_m and ξ_L gives

$$N_{\gamma,hot} \leq \left\{ \frac{\omega_b^2 \beta^2 c^2}{4\pi\sigma\Delta v_\perp^2} - \frac{k^2c^2}{4\pi\sigma} \right\} \tau_p \quad . \tag{15}$$

This upper limit agrees <u>exactly</u> with Eq. (2a) in the nonconvective limit ($4\pi\sigma >> - i\eta$).

V. NUMERICAL SOLUTIONS TO FILAMENTATION DISPERSION RELATION

Since the local approximation predicts that $N^c_{\gamma,hot}/N^c_{\gamma,cold} = 0.31$, independent of model parameters, we expect that numerical solutions to the full dispersion relation (Eq. (1)) will lie between the limits given by Eqs. (10) and (11). We have carried out such a calculation, numerically integrating solutions to Eq. (1) from z = 0 to z = z* as given in Eq. (13).

Figure 2 summarizes the results of such a calculation for a 1 kA Uranium beam with $Z_b = 18.1$ (He at 1 torr), $\beta = 0.4$, $\Delta v_\perp/V_b = 2 \times 10^{-4}$, L = 5 m, $R_o = 10$ cm, and $\sigma_o = 10^{11}$ s^{-1}. The figure plots the "exact" growth rate $\gamma_{ex}(z)$, accumulated e-foldings $N^c_{\gamma,ex}(z) \equiv \int_o^z dx\ \gamma_{ex}(x)/V_b$, and plasma dispersion function argument $|\xi_b(z)|$ verses distance z from the chamber wall. The value $k_\perp = 2.5$ $cm^{-1} \approx 2.5\ k_o$ was chosen to maximize $N^c_{\gamma,ex}(L-z^*) \equiv N^c_{\gamma,ex}$. Since $|\xi_b| \sim 1$, it is not surprising that $N^c_{\gamma,ex} = 2.0$ lies near the average of $N^c_{\gamma,hot} = 1.0$ and $N^c_{\gamma,cold} = 3.3$. Eq. (13) is usually adequate for estimating z* since $|\xi_b(z = z^*)|$ is almost always less than 0.5; z* =480 cm for the above example. The rapid drop in γ and $|\xi_b|$ as $z \to L$ is seen in all ballistic mode propagation examples we have investigated.

Figure 3 plots $N^c_{\gamma,hot}$, $N^c_{\gamma,cold}$, and $N^c_{\gamma,ex}$ verses $k_\perp$ for the example in Figure 2. The variations in the analytical estimates of $N^c_{\gamma,cold}$ is entirely due to small changes in z* as $k_\perp$ is changed. The peak in $N^c_{\gamma,ex}(k_\perp)$ is quite broad, and in all cases, $N^c_{\gamma,ex} \lesssim 0.6\ N^c_{\gamma,cold}$.

Figure 4 plots the three estimates of N^c_γ, the beam change state Z_b, and the convective - nonconvective boundary z* verses pressure in torr assuming Helium in the target chamber. Z_b was estimated using a variation of the Yu, et al model,[7] and the calculation will be described in more detail elsewhere. We assume $\sigma_o = 3 \times 10^9\ Z_b^2$, which again comes from assuming that direct

ionization by the beam is the dominant process, and other parameters are as in Figure 2. $N_{\gamma,ex}^{c}$ is maximum for $k_{\perp} \sim 0.25\ k_o$ in all cases, and begins to look dangerous ($N_{\gamma,ex}^{c} \sim 5$) for $Z_b \gtrsim 50$. This high charge state is reached at much lower pressures (below 1 torr) for heavier gases such as Neon. Again, $N_{\gamma,ex}^{c}$ is almost a factor of two lower than $N_{\gamma,cold}^{c}$ in all cases.

Two factors which have been omitted from our analysis may further reduce $N_{\gamma,ex}^{c}$. First, the constant Z_b assumed was the upper limit calculated at $z = L$. Using a variable $Z_b(a) \leq Z_b(L)$ in the numerical integration would obviously reduce $N_{\gamma,ex}^{c}$ somewhat. Also, filamentation growth ceases for modes with $k_{\perp} \lesssim \pi/R(z)$ as the beam approaches the pellet since the unstable wavelength exceeds the beam diameter. At pressures below a few torr, this effect probably causes convective growth to cease before the beam reaches the convective/nonconvective boundary at $z = z^*$. For example, in the 1 torr case, the condition $R = \pi/k_{\perp}$ is reached at a distance $z = 450$ cm from the wall for $k_{\perp} = 3$ cm which is smaller than $z^* = 479$cm. $N_{\gamma,ex}^{c}(z = 450\ \text{cm})$ is only 1.8 instead of our earlier estimate of 2.0. The two effects cited here may reduce N_{γ}^{c} by as much as a factor of two at low pressures; the reduction is much smaller for $Z_b \gtrsim 50$ or higher beam currents. The dotted line in Figure 4 shows the effect of cutting off $N_{\gamma,ex}^{c}$ when the unstable wavelength exceeds $R(z)$. The dashed line gives an estimate of the nonconvective number of e-foldings N_{γ}^{nc}, which is always less than $N_{\gamma,ex}^{c}$ for a 10 nsec pulse.

V. CONCLUSIONS

The local dispersion relation for the electromagnetic filamentation instability predicted to occur in heavy ion fusion target chambers will be convective until the beam is a few tens of centimeters from the target. Upper and lower limits on the number of e-foldings of the field amplitudes (N_γ^c) in the convective regime are given by Eqs. (10) and (11) for ballistically focussed beams. Numerical integration along the beam trajectory of the full dispersion relation solutions (Eq. (1)) give estimates of $N_{\gamma,ex}^c$ which are near the average of the upper and lower limits. Close to the pellet, the instability is effectively nonconvective, and the results of Hubbard and Tidman[1] generally apply. However, N_γ^{nc} is usually lower than N_γ^c, and hence the most serious deterioration of beam quality will usually occur in the convective regime.

The calculation by Lee for ballistic mode filamentation is assumed $|\xi_b| >> 1$, and the local approximation agrees <u>exactly</u> with Lee's result in this cold beam limit. However, numerical solutions to Eq. (1) indicate that $|\xi_b| \sim 1$ in most cases, leading to estimates of $N_{\gamma,ex}^c$ which are somewhat lower. The inclusion of a variable beam charge state will further reduce $N_{\gamma,ex}^c$, as will cutting off N_γ at the point where the beam radius becomes less than the unstable wavelength. Thus, the local approximation leads to the same scaling as the method of Lee, et al[3,4,5], but our detailed numerical estimates of the number of e-foldings are typically a factor of two lower. Also, the local approximation agrees with Lee's method in the high conductivity (nonconvective) limit in which N_γ is proportional to the pulse length.

Fig. 4 indicates that the most promising way of controlling filamentation growth is to minimize the beam charge state Z_b. For a variety of reasons, recent reactor scenarios have involved somewhat lower beam energies ($\sim$10 GeV), higher currents, and heavier gases (e.g., Neon). This will make it difficult, if not impossible, to keep Z_b low unless the chamber pressure is lowered significantly . The higher beam densities associated with these scenarios further increase filamentation growth rates for the ballistic propagation mode in $\sim$1 torr gas-filled reactors. However, both pinched-mode propagation in gas-filled reactors and ballistic mode propagation in low density ($< 10^{-3}$ torr) Lithium waterfall reactors are much less susceptible to filamentation instability and may have other important advantages as well.

ACKNOWLEDGEMENTS

Conversations with Drs. Derek Tidman, John Guillory, Paul Ottinger, and E. Lee are gratefully acknowledged. This work was supported by the Department of Energy under contract DE-AC08-79-DP40101.

REFERENCES

1. R. F. Hubbard and D. A. Tidman, Phys. Rev. Lett. 41, 866 (1978).

2. R. F. Hubbard, D. S. Spicer, and D. A. Tidman, in Proceedings of the Heavy Ion Fusion Workshop, Argonne National Laboratory, p. 379 (1978).

3. E. P. Lee, in Ref. 2, p. 393; E. P. Lee, Bull. Am. Phys. Soc. 23, 888 (1978).

4. F. W. Chambers, E. P. Lee, and S. S. Yu, Bull. Am. Phys. Soc. 23, 770 (1978).

5. H. L. Buchanan, F. W. Chambers, E. P. Lee, S. S. Yu, R. J. Briggs, and M. N. Rosenbluth, Lawrence Livermore Laboratory, UCRL Report 82586, 1979.

6. R. C. Davidson, D. A. Hammer, I. Haber, and C. E. Wagner, Phys. Fluids 15, 317 (1972).

7. D. S. Spicer, R. F. Hubbard, and D. A. Tidman, Bull. Am. Phys. Soc. 23, 770 (1978).

8. S. S. Yu, H. L. Buchanan, E. P. Lee, and F. W. Chambers, Ref. 2, p. 403.

LIST OF SYMBOLS

$H(\vec{k};\omega)$	Plasma dielectric function
$k_\perp$, $k_{//}$	Perpendicular and Parallel wavenumbers
$\omega = \omega_r + i\gamma$	Frequency
V_b	Beam velocity
$\Delta v_\perp$	Transverse beam thermal velocity
$Z(\xi_b)$	Plasma dispersion function with argument $\xi_b = (\omega - k_{//} V_b)/\sqrt{2}\, k_\perp \Delta v_\perp$
σ	Electrical conductivity
ω_b	Beam plasma frequency
$Z'(\xi_b)$	$dZ(\xi_b)/d\xi_b$
η	See Equation (4)
v_g	Parallel group velocity
τ_p	Pulse length (temporal)
Z_b	Beam charge state
L	Chamber radius
z	Distance from the chamber wall
N_γ	Number of e-foldings of e-m field
N_γ^{nc}	Nonconvective number of e-folds
$N_{\gamma,hot}^{c}$	Convective number of e-folds, $\lvert\xi_b\rvert \ll \lvert$
$N_{\gamma,cold}^{c}$	Convective number of e-folds, $\lvert\xi_b\rvert \gg \lvert$
$N_{\gamma,ex}^{c}$	Convective number of e-folds, numerical solution to full plasma disp. relation

R	Beam radius
R_o, ω_{bo}	Values at injection
z^*	Location of transition between convective and nonconvective regions ($v_g = \frac{1}{2} V_b$)
$\tilde{I}_b$	Beam <u>particle</u> current

FIGURE CAPTIONS

Figure 1. Approximate locations of the convective and nonconvective regions of filamentation instability for a ballistically focussed heavy ion beam. For most of the beam trajectory, the group velocity $v_g \approx V_b$, the beam velocity, so perturbations are convected with the beam. However, close to the target, v_g decreases rapidly due to an increase in conductivity and transverse beam temperature. Perturbations pile up locally, and the instability is effectively nonconvective. The transition between the two regions is defined by the position z* at which $v_g = \frac{1}{2} V_b$.

Figure 2. Filamentation growth rate γ, number of e-foldings $N^c_{\gamma,ex}(z)$, and plasma dispersion function argument $|\xi_b| = \gamma/\sqrt{2}\, k_\perp \Delta v_\perp$, plotted verses distance z from the chamber wall. We assume a 20 GeV Uranium beam with charge $Z_b = 18$, $\tilde{I}_b = 1$ kA, initial radius $R_o = 10$ cm, $\Delta v_{\perp o}/V_b = 2 \times 10^{-4}$, L = 5 meters, $k_\perp = 0.25\, k_o = 2.5\ \text{cm}^{-1}$, and $\sigma = 10^{11} (R_o/R)^2\ \text{sec}^{-1}$. The growth rate is calculated numerically using the full dispersion relation (Eq. (1)), and $N^c_{\gamma,ex}(z) = V_b^{-1} \int_o^z \gamma(z')\, dz'$ is integrated only up to the transition point z* defined by Eq. (13). Since $|\xi_b| < 2.6$ everywhere, $N^c_{\gamma,ex}$ is substantially below the $|\xi_b| \gg 1$ cold beam limit.

Figure 3. Variation of the three estimates of N^c_γ based on Equations (1), (8), and (11), verses $k_\perp/k_o$, where $k_o = \omega_b V_b/\Delta v_\perp c$ is independent of z if Z_b is constant. All other parameters are as in Figure 2. The small variation in $N^c_{\gamma,cold}$ is entirely due to changes in z* with $k_\perp$. The exact numerical solution $N^c_{\gamma,ex}$ has a broad peak centered on $k_\perp = 0.25\, k_o$ which lies near the average of the cold and hot beam

analytical estimates. The cold beam estimate agrees with the Lee, et al results for a converging beam.

Figure 4. Beam charge state Z_b, location z* of the convective-nonconvective transition region, and the three estimates of N_γ^c as functions of the chamber pressure in torr, assuming Helium. The increase in the number of e-foldings with pressure is due entirely to the increased beam charge state, which increases both ω_b and σ. The dotted line shows the effect of cutting off the integration of N_γ^{ex} at the point where the unstable wavelength exceeds the beam radius. The dashed line is an estimate of N_γ^{nc} taken slightly into the nonconvective regime. The variation of N_γ^{nc} with pressure is reduced considerably by assuming $\sigma \sim Z_b^2$. Note that $N_\gamma \gtrsim 5$ is considered dangerous.

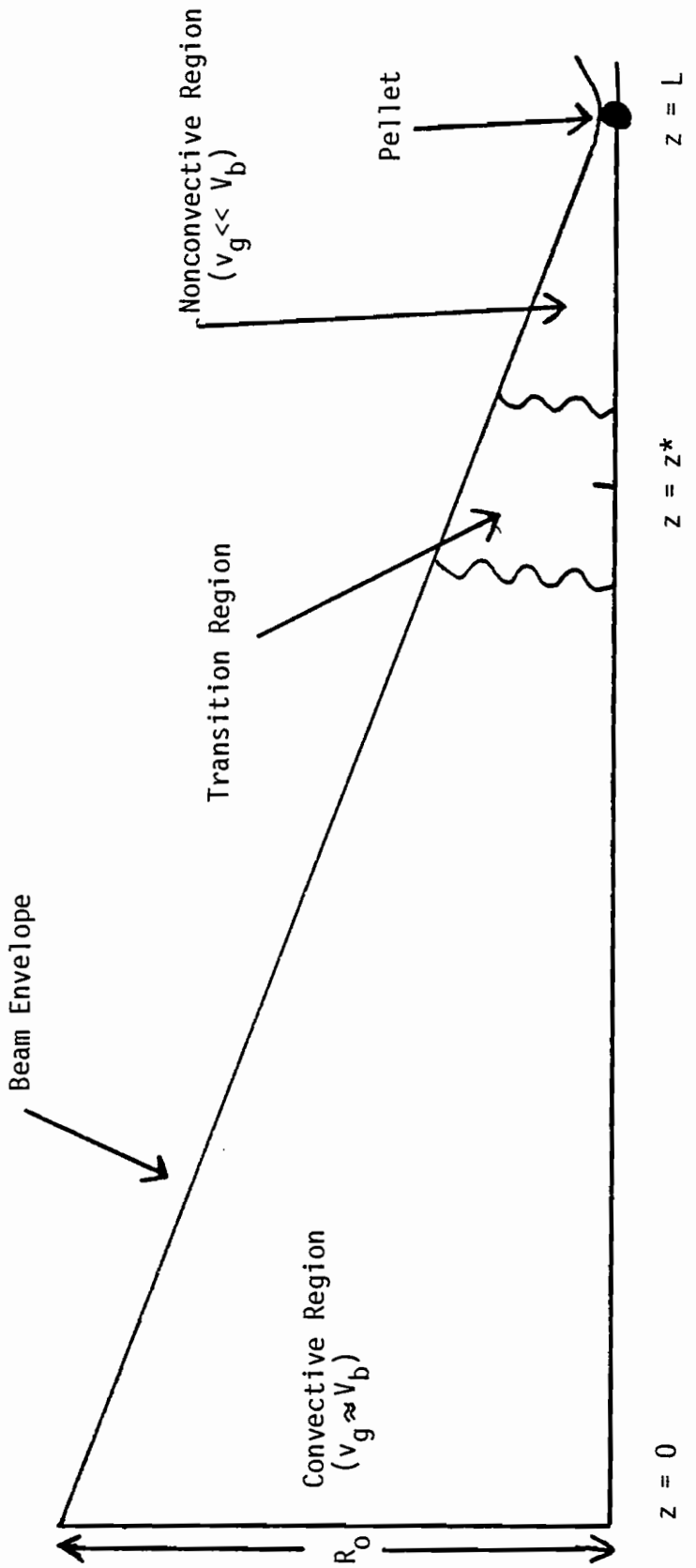
Nonconvective Region
($v_g << V_b$)
Pellet
z = L
Transition Region
z = z*
Beam Envelope
Convective Region
($v_g \approx V_b$)
z = 0
R_o

Figure 1

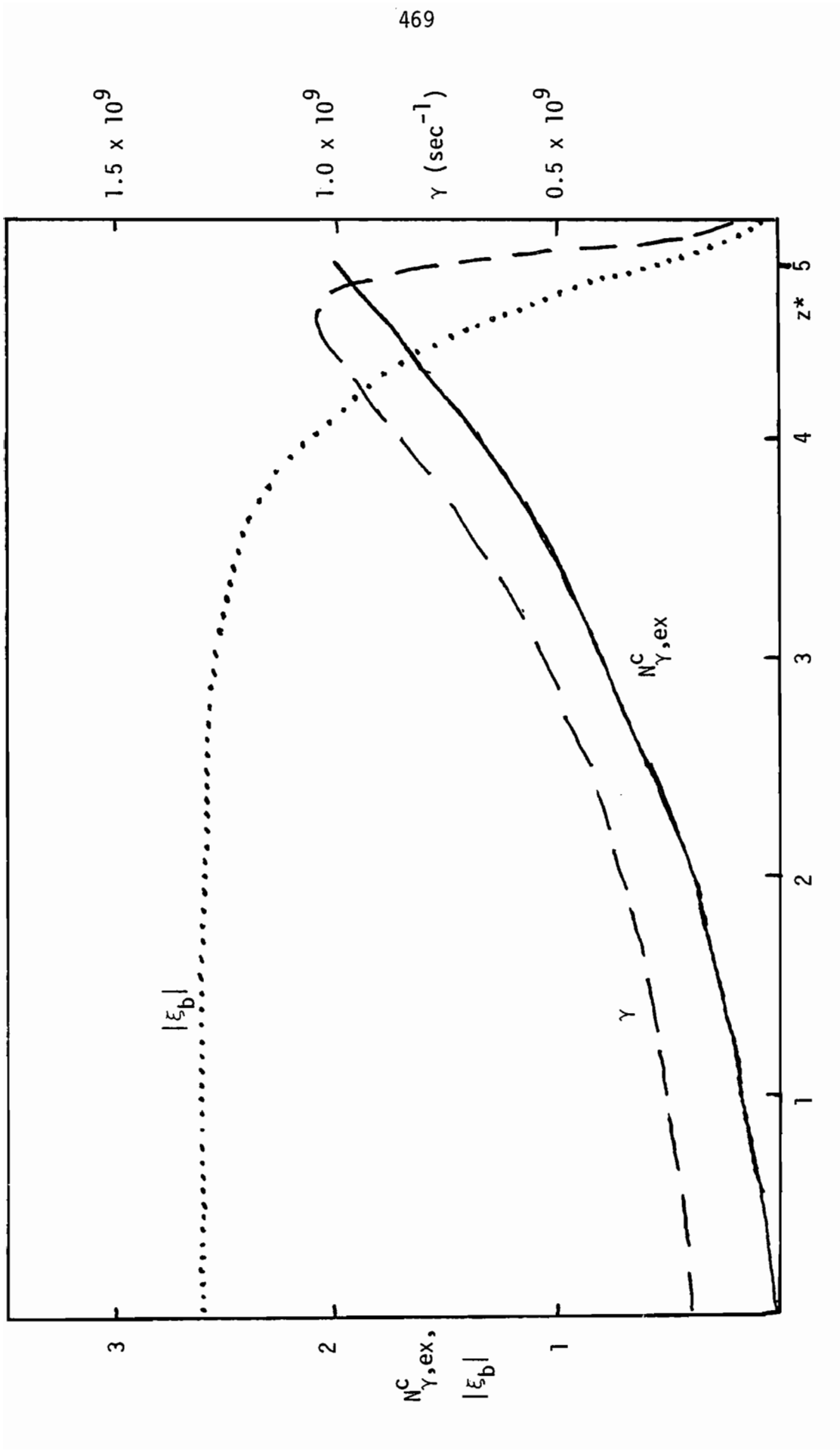
1.5 x 10^9
1.0 x 10^9
0.5 x 10^9
γ (sec^-1)
|ξb|
γ
N^c γ,ex
N^c γ,ex, |ξb|
3
2
1
1
2
3
4
5
z*
Distance from Chamber Wall (meters)

Figure 2

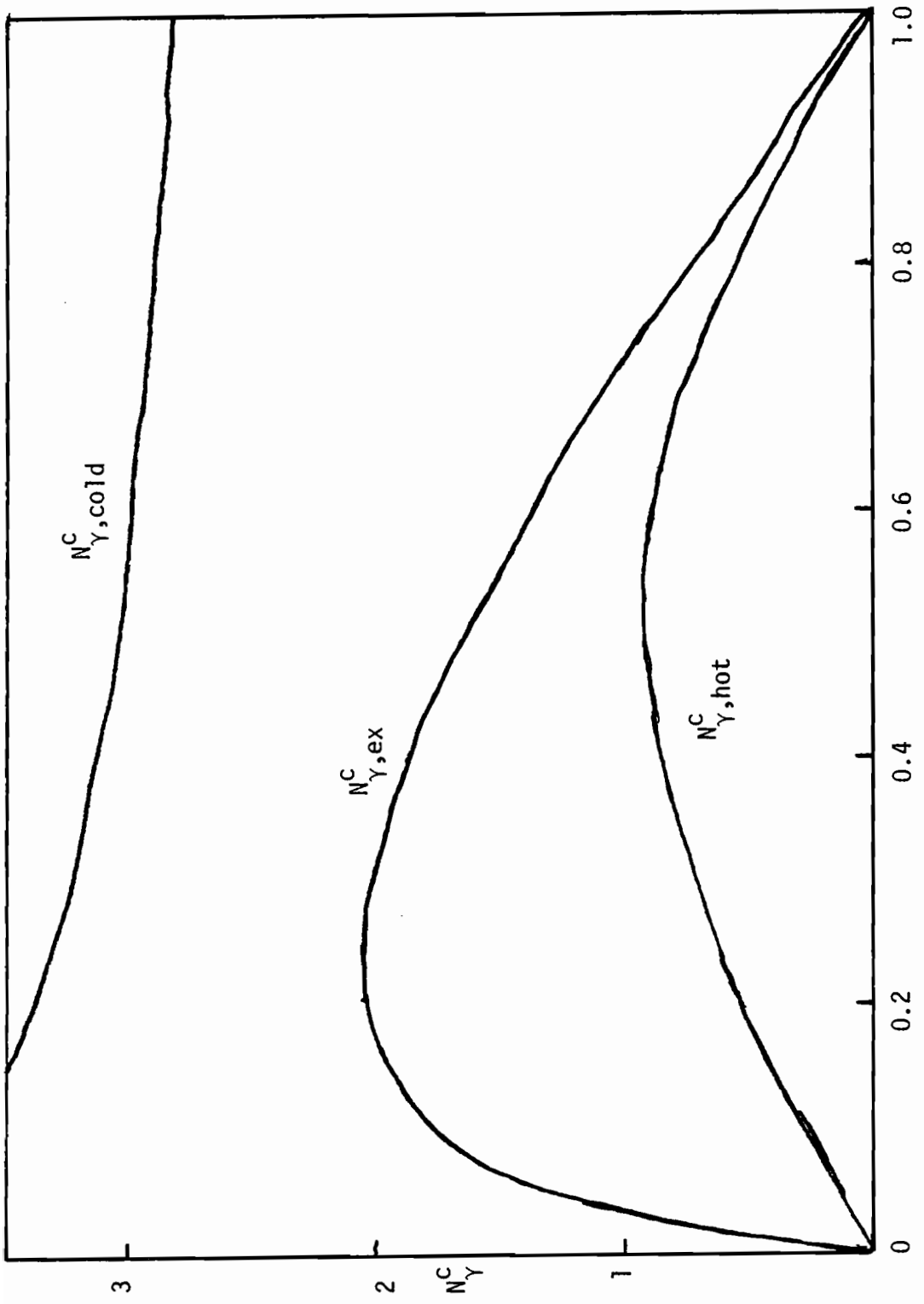
$N^c_{\gamma,cold}$
$N^c_{\gamma,ex}$
$N^c_{\gamma,hot}$
N^c_γ
3
2
1
0
0.2
0.4
0.6
0.8
1.0
k/k_o

Figure 3

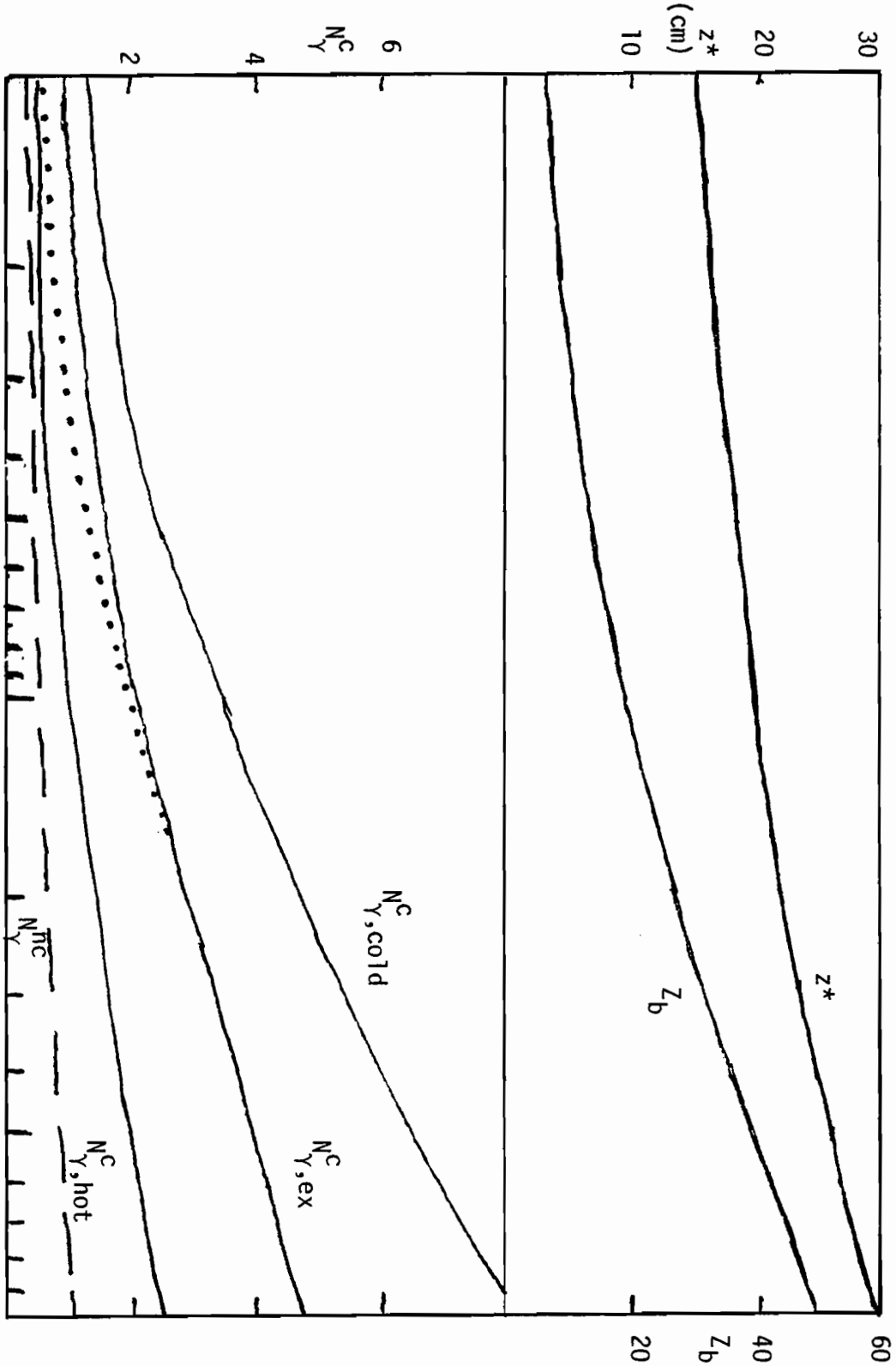
30
20
10
z*
(cm)
6
4
2
N_γ^c
0.1
1.0
10
pressure
(torr)
60
40
20
Z_b
z*
Z_b
$N_{\gamma,cold}^c$
$N_{\gamma,ex}^c$
N_γ^{mc}
$N_{\gamma,hot}^c$

Figure 4

FILAMENTATION OF A CONVERGING HEAVY ION BEAM*

E. P. Lee and H. L. Buchanan

Lawrence Livermore Laboratory

and

Marshall N. Rosenbluth

Institute for Advanced Study,
Princeton, New Jersey 08540

*Work performed by LLL for U.S. DOE under contract No. W-7405-Eng-48

Abstract

A major concern in the use of heavy ion beams as igniters in pellet fusion systems is the vulnerability of the beam to the transverse flamentation instability. The undesirable consequence of this mode is the transverse heating of the beam to the extent that convergence on the pellet becomes impossible. This work considers the case of a beam injected into a gas filled reactor vessel, where finite pulse length and propagation distance play an important role in limiting growth. Two geometries are analyzed: a non-converging case where the radius at injection is nearly equal to the desired radius at the pellet, and a converging case in which the injection radius is large and the beam is pre-focused to converge at the target. It is found that a cold beam will be severely disrupted if the product of the magnetic plasma frequency and the propagation distance is much larger than unity. This product may be lowered by dividing the energy of the original beam into many ($\approx$50) individual beams arranged to converge simultaneously at the pellet, however this represents a significant engineering complication. Even if this product is large, growth may be limited to about six e-foldings if enough transverse velocity spread is added that the latter half of the pulse propagates in pinched equilibrium. The disadvantage of this mode is, however, that much of the pulse is lost to thermal expansion.

Introduction

Among the critical issues confronting the use of heavy ion beams as pellet igniters is whether such a beam can propagate through the reactor vessel to finally achieve a spot size of the order of 1 mm on the pellet. Assuming the beam can be directed to strike the target, this final spot

size will not be obtainable if the beam has been subjected to any of various instabilities which transversely heat it at the expense of its longitudinal energy. The most serious of these appears to be the filamentation instability, in which modes of transverse wave number k can grow with characteristic times $\tau_m = 4\pi\sigma/c^2k^2$, where σ denotes the conductivity of the background plasma. The use of a low pressure ($n_g \approx 10^{12}$) vessel environment and/or many (~ 50), simultaneous, low current beams would allow each beam to be magnetically stiff and hence stable over the entire distance of flight. This approach, however, places constraints on the reactor system and suggests the examination of unstable growth in the high pressure ($n_g \approx 10^{16}$) regime. This report is a summary of the results of a more comprehensive treatment given elsewhere[1,2] of filamentation growth in converging and non-converging beams of heavy ions in a background plasma of finite conductivity.

The basic mechanism of the filamentation instability is that a beam which is given small transverse mode structure will separate into small beamlets as the result of the attraction of parallel currents. If the beam is moving in a background plasma such that charge neutralization can occur, each beamlet will continue to self-pinch until its magnetic pressure $B^2/8\pi$ becomes equal to the transverse thermal pressure $\gamma n\ (1/2\ mv_{th}^2)$. If we define η to be the ratio of thermal pressure to pinch pressure for a filament in the instant just after the perturbation, we conclude that $\eta \approx 1$ should be required for successful propagation. For $\eta < 1$ the filament will pinch at a rate, (Ω) proportional to the square root of the ratio of the magnetic force per unit length to the mass per unit length. A maximum growth rate occurs for a filament whose radius is less than or equal to the magnetic skin depth of the pulse and takes the value $\Omega_{max} = \Omega_b = (4\pi q^2 n/\gamma mc^2)^{1/2}$

where Ω_b is just the magnetic plasma frequency divided by γc. If the beam is to propagate a distance L, then the total number of e-foldings of growth is $\alpha = \Omega_b L$. In light of these observations, we can take α and η as two dimensionless characterizations of the beam and its filamentary tendencies.

Non-Converging Case

In the previous treatment of the non-converging beam[1] the equilibrium distribution function $f_0 = n_0 F(\underset{\sim}{v})\, H(\tau)\, H(\tau_p - \tau)$ and the equilibrium vector potential A_0 are perturbed by the form

$$(f_1,\ A_1) \propto \exp\,[i(\underset{\sim}{k}\cdot\underset{\sim}{r} - \Omega z - \omega\tau] = \exp\,[i(\underset{\sim}{k}\cdot\underset{\sim}{r}) + g], \qquad (1)$$

where z is the longitudinal variable measured from the reactor wall into the chamber and $\tau = t - z/\beta c$ is a convenient transformed time such that $\beta c\tau$ is a longitudinal distance into a pulse of duration τ_p as measured from the head. We have assumed $\underset{\sim}{\nabla} A_0 = 0$ and have let $H(\tau)$ represent the step function. The resulting dispersion relation is

$$\bullet\, i\omega\tau_m = 1 + \Gamma(k,\Omega) \qquad (2)$$

where
$$\Gamma(k,\Omega) = \Omega_b^2 \int d^2\underset{\sim}{v}\ \frac{F(\underset{\sim}{v})}{(\Omega - \underset{\sim}{k}\cdot\underset{\sim}{v}/\beta c)^2}\ , \qquad (3)$$

giving a growth exponent of

$$g(\Omega,\tau,z) = i\Omega z - (\tau/\tau_m)\ (1 + \Gamma) \qquad (4)$$

Several velocity distributions have been studied, the most convenient being the single pole approximation to the Maxwellian:

$$\Gamma_s \equiv \left(\frac{\Omega}{\Omega_b} + i\delta\right)^{-2} \tag{5}$$

where $\delta(k) = kv_{th}/(\sqrt{2}\,\Omega_b\beta c)$. The dispersion relation becomes

$$i\omega\tau_m = 1 + \left(\frac{\Omega}{\Omega_b} + i\delta\right)^{-2} \tag{6}$$

If τ is held fixed and the growth factor g, given by Eq. 4, is maximized with respect to z we obtain

$$g_{max} = \left(\frac{1}{\delta^2} - 1\right)\frac{\tau}{\tau_m} \leq \frac{\tau_p}{\delta^2\tau_m} \tag{7}$$

It is interesting to note here that the mode number dependencies of τ_m and δ leave g_{max} independent of k at fixed τ. Further, if we assume a parabolic profile for the beam current density J_b and a conductivity independent of r and arrange the thermal velocity so that the beam pinches half-way back from the head (specifically we require that $\eta = 1$ at $\tau = \tau_p/2$), then

$$g_{max} \leq \frac{\tau_p}{\delta^2\tau_m} = \frac{6}{\eta} \tag{8}$$

If $\eta = 1$ we obtain marginally severe growth but have sacrificed the first half of the pulse to rapid expansion.

Converging Beam

We consider next a geometry in which the pulse converges from a large radius at z = 0 to the chosen target radius at z = L. We perturb away from straight line converging particle orbits. The unperturbed system

is characterized by $\nabla A_0 = 0$ and distribution function f_0 which is of finite extent and uniform in the tranverse plane, f_0 is normalized to density n_w at Z = o. The problem of characterizing f_0 is simplified by noting that

$$\underset{\sim}{V} = \underset{\sim}{v}\,(1 - z/L) + \frac{\beta c}{L}\ \underset{\sim}{r} \tag{9}$$

is an integral of the unperturbed motion which displays the assumed convergence at z = L; thus we consider $f_0 = n_w F(\underset{\sim}{V})$. The density at arbitrary z is then

$$n_0(z) = \int d^2\underset{\sim}{v}\ f_0 = \int d^2\underset{\sim}{V}\ n_w F(\underset{\sim}{V}) = \frac{n_w}{(1-\frac{z}{L})^2}\int d^2\underset{\sim}{V}\ F(\underset{\sim}{V}) = \frac{n_w}{(1-\frac{z}{L})^2}. \tag{10}$$

The mean squared thermal velocity is then

$$v_{th}^2(z) = |\underset{\sim}{v} - <\underset{\sim}{v}>|^2 = \frac{1}{(1-\frac{z}{L})^2}\int d^2\underset{\sim}{V}\ V^2 F(\underset{\sim}{V}) = \frac{v_{th}(0)}{(1-\frac{z}{L})^2}\ , \tag{11}$$

where $v_{th}^2(0)$ is the initial mean squared thermal velocity assumed independent of $\underset{\sim}{r}$.

To parallel previous work we have

$$\beta c\frac{\partial f_1}{\partial z} + \underset{\sim}{v}\cdot\underset{\sim}{\nabla} f_1 = -\frac{q\beta}{\gamma M}\underset{\sim}{\nabla} A_1 \cdot \underset{\sim}{\nabla}_v f_0\ , \tag{12}$$

$$\nabla^2 A_1 - \frac{4\pi\sigma}{c^2}\frac{\partial A_1}{\partial \tau} = -\frac{4\pi J_{b1}}{c} = -4\pi q\beta\int d^2\underset{\sim}{v} f_1\ . \tag{13}$$

We proceed in the conventional way by formally solving Eq. (12) for f_1:

$$f_1 = f_{10} - \frac{q\beta}{\gamma M} \int_o^z \frac{dz'}{\beta c} \left(\nabla_{\sim} A_1 \cdot \nabla_{\sim v} f_o\right) \Big|_{z'} \tag{14}$$

where f_{10} is the initial disturbance carried along the unperturbed orbits. Recall that both $\underset{\sim}{V}$ and $\underset{\sim}{v}$ were constants of the motion; hence if we introduce $u(z) = (1 - \frac{z}{L})^{-1}$ we can write Eq. (9) as

$$\underset{\sim}{V} = \underset{\sim}{v}/u(z) + \frac{\beta c}{L} \underset{\sim}{r} = \text{constant} \tag{15}$$

Then any point along an unperturbed orbit can be described by

$$\underset{\sim}{r}(z')\, u(z') = \underset{\sim}{r}\,(z)\, u(z) + \frac{L}{\beta c} \underset{\sim}{V} [u(z') - u(z)] \tag{16}$$

We then select a perturbation with $\underset{\sim}{r}$ dependence of the form

$$(A_1, J_{b_1}) \propto \exp(i\underset{\sim}{k} \cdot \underset{\sim}{r} u) = \exp\left[i\underset{\sim}{k} \cdot \underset{\sim}{r}_o u + \frac{i\underset{\sim}{k} \cdot \underset{\sim}{V} L}{c} (u' - u)\right] \tag{17}$$

to obtain the perturbed distribution function with proportionality constants $\overline{A_1}$ and $\overline{J_{b_1}}$:

$$f_1 - f_{10} = -\left(\frac{q n_w L}{\gamma M c}\, i\underset{\sim}{k} \cdot \frac{\partial F}{\partial \underset{\sim}{V}}\right) \int_1^u \frac{du'}{(u')^2}\, \overline{A}_1' \exp\left[iu\underset{\sim}{k} \cdot \underset{\sim}{r} + \frac{i\underset{\sim}{k} \cdot \underset{\sim}{V} L}{\beta c} (u' - u)\right] . \tag{18}$$

The perturbed current is then

$$J_{b_1} - J_{b_{10}} = q\beta c \int d^2\underset{\sim}{v}\ (f_1 - f_{10})$$

$$= - \left(\frac{q^2 \beta n_w L u^2}{\gamma m}\right) \int d^2\underset{\sim}{V}\ i\underset{\sim}{k}\cdot \frac{\partial F}{\partial \underset{\sim}{V}} \int_1^u \frac{du'}{(u')^2}\ \overline{A}_1'\ \exp\left[iu\underset{\sim}{k}\cdot\underset{\sim}{r} + \frac{i\underset{\sim}{k}\cdot\underset{\sim}{V}L}{c\beta}\ (u'-u)\right] \quad (19)$$

We may reverse the order of integration and integrate by parts on $\underset{\sim}{V}$ to get

$$\frac{4\pi}{ck^2u^2}\ (\overline{J}_{b_1} - \overline{J}_{b_{10}}) = \alpha^2 \int_1^u du'\ A'(u-u')\ \hat{F}, \quad (20)$$

where $\alpha^2 = (4\pi q^2 n_w/\gamma M c^2)\ L^2 = \Omega_w^{\ 2} L^2$,

$$A = \overline{A}_1/u^2 ,$$

$$\underset{\sim}{\lambda} = (u-u')\ \frac{L\underset{\sim}{k}}{\beta c}$$

$$\hat{F} = \int d^2\underset{\sim}{V}\ F(\underset{\sim}{V})\ \exp(-i\underset{\sim}{\lambda}\cdot\underset{\sim}{V}) .$$

If we now apply the assumed form of Eq. (17) and the definitions above to Eq. (13) we obtain for the perturbed field

$$u^2 A + \tau_m \frac{\partial}{\partial \tau}\ A = \frac{4\pi}{ck^2u^2}\ \overline{J}_{b_1} \quad . \quad (21)$$

Finally if we define an amplitude χ proportional to the perturbed density, and a source S as

$$\chi = \frac{4\pi}{ck^2u^2}\,\bar{J}_{b_1} \quad \text{and} \quad S = \frac{4\pi}{ck^2u^2}\,\bar{J}_{b_{10}} \ ,$$

then Eqs. (20) and (21) can be written as

$$\chi = S + \alpha^2 \int_1^u du'\, A'\,(u-u')\,\hat{F} \quad , \tag{22}$$

$$u^2 A + \tau_m \frac{\partial}{\partial \tau} A = \chi \tag{23}$$

Cold Converging Beam

We first solve Eqs. (22) and (23) for the cold limit, where $F(\underset{\sim}{V}) = \delta(\underset{\sim}{V})$ gives $\hat{F}(\underset{\sim}{\lambda}) = 1$. Then differentiation of Eq. (22) twice gives

$$\frac{\partial^2}{\partial u^2}\,\chi = \alpha^2 A \quad . \tag{24}$$

If we further let $\tau_m \to 0$ either because $\sigma \to 0$ or $k \to \infty$ then Eq. (23) becomes

$$u^2 A = \chi \quad . \tag{25}$$

The solution is $\chi_{\pm} = u^{\ell}$ where

$$\ell = \frac{1}{2} \pm \left(\frac{1}{4} + \alpha^2\right)^{1/2} = \frac{1}{2} \pm \left(\frac{1}{4} + (\Omega_w L)^2\right)^{1/2} \quad . \tag{26}$$

The cold converging beam thus displays algebraic growth with distance rather than the exponential growth found for the straight beam. The magnitudes of growth, however, are quite similar over the distances of interest.

When τ_m is finite growth is reduced. This can be seen by application of the Laplace transform in the variable :

$$\tilde{X} = \int_0^\infty X \, d\tau \, e^{-p\tau}$$

and similarly for A. The system (22) and (23) combine to give

$$\frac{\partial^2}{\partial u^2} \tilde{X} = \frac{\alpha^2}{u^2 + p\tau_m} \tilde{X} \quad .$$

The WKB solutions, good for large α, are

$$\tilde{X}_{\pm} = \exp\left(\pm \alpha \int_1^u \frac{du'}{(u'^2 + p\tau_m)^{1/2}} \right) = \left[\frac{u + (u^2 + p\tau_m)^{1/2}}{1 + (1 + p\tau_m)^{1/2}} \right]^{\pm\alpha} \quad . (28)$$

We take the initial conditions to be

$$X(u=1) = \left\{ \begin{array}{ll} 0 & \tau < 0 \\ \\ 1 & \tau > 0 \end{array} \right\} \quad \text{and} \quad \frac{\partial}{\partial u} X(u=1) = 0 \quad .$$

We can approximate the inversion integral in the limit of $\frac{u^2\tau}{\tau_m} \gg 1$ and $\frac{\tau}{\tau_m} \ll 1$ with a saddle analysis to obtain $X \propto \exp[g]$ where

$$g \approx \frac{\alpha}{2}\left[1 + \ln\left(\frac{8}{\alpha}\right)\right] + \alpha \ln\left[u\left(\frac{\tau}{\tau_m}\right)^{1/2}\right] \quad . \tag{29}$$

The gross consequences of a non-constant background conductivity may be obtained by using a model in which conductivity rises as the inverse square of beam radius

$$\tau_m = \tau_m(u=1)\, u^2 = \tau_w\, u^2 \quad . \tag{30}$$

This is viewed as an attempt to model generation of conductivity proportional to beam intensity. Eq. (27) becomes

$$\frac{\partial^2}{\partial u^2}\,\tilde{\chi} = \frac{\alpha^2}{u^2(1 + p\tau_w)}\,\tilde{\chi} \quad , \tag{31}$$

with WKB solutions

$$\chi_{\pm} \approx \exp\left[\pm \frac{\alpha \ln u}{(1 + p\tau_m)^{1/2}}\right] \tag{32}$$

A saddle analysis of inversion integral yields $\chi \propto \exp(g)$ where

$$g \approx 3\left[\frac{\alpha}{2}\left(\frac{\tau}{\tau_w}\right)^{\frac{1}{2}} \ln u\right]^{2/3} - \frac{\tau}{\tau_w} \tag{33}$$

which is exactly the cold non-converging result with $\Omega_b z \rightarrow \alpha \ln u$.

Warm Converging Beam

Solution of Eqs. (22) and (23) for arbitrary choices of $F(\underset{\sim}{V})$ is in general quite tedious, but we may obtain the overall features by the use of a single pole form of $F(\underset{\sim}{V})$. This procedure yields

$$\hat{F}_L = \exp\,[\,-\,K(u-u')] \tag{34}$$

where K is a constant proportional to the thermal velocity. It may be shown that an arbitrary $F(\underset{\sim}{V})$ can be approximated in single pole form with

$$-\frac{1}{K^2} = \frac{\beta^2 c^2}{k^2 L^2}\int d^2\underset{\sim}{V}\,\frac{\underset{\sim}{k}\cdot\frac{\partial F}{\partial \underset{\sim}{V}}}{\underset{\sim}{k}\cdot\underset{\sim}{V}} \tag{35}$$

It is this fact that lends wide applicability to this somewhat unphysical form, for now Eq. (22) can be written as

$$\chi = S + \alpha^2\int_1^u du'\,A'(u-u')e^{\,-K(u-u')} \quad . \tag{36}$$

When the factor exp [K(u-1)] is absorbed into χ, S, and A, the equation returns to its cold form (already solved.) We can write the solutions

$$\chi = \chi_{cold}\, e^{-K(u-1)} \quad . \tag{37}$$

For a Maxwellian profile $K = \alpha\delta$.

In the limit of low conductivity ($\tau_m \to o$), we use the results of Eq. (26) with α large to get:

$$\chi \simeq u^{\alpha}\, e^{-\alpha\delta(u-1)} \tag{38}$$

Note that, in contrast to the straight beam case in this limit, the growth here reaches a maximum at $u = \frac{1}{\delta}$. This feature appears consistently in the warm beam analysis and is due to transverse phase mixing of beam

particles. As a result we should expect total growth of a warm beam to be somewhat less than the growth of the corresponding cold beam case. For instance, if we consider the case of τ_m finite we can proceed as before with the exception that, following the saddle point evaluation, we maximize the warm growth rate

$$g_{warm} = g_{cold} - \alpha\delta(u-1) \tag{39}$$

with respect to u, k, and τ. We find that growth is a maximum for k=o, u=∞, $\tau=\tau_p$ but with the product uk finite. Defining the quantity $Q = \alpha\eta/24$, we find

$$g_{max} = \frac{6}{\eta} 2Q \left[Q - (Q^2+1)^{1/2} + \ln\left(\frac{(Q^2+1)^{1/2}+1}{Q}\right)\right]$$

$$= \frac{6}{\eta} \begin{cases} 1 - \frac{1}{12}Q^2 \text{ for } Q \gg 1 \\ 2Q[\ln(\frac{2}{Q}) - 1] \text{ for } Q \ll 1 \ . \end{cases} \tag{40}$$

Observe that growth is less than the cold beam value of $6/\eta$ for all values of α and η.

Finally, for $\tau_m \propto u^2$ we proceed as before, but find that g_{max} can be written only as an implicit function of Q. Maximum growth still occurs at $\tau = \tau_p$ however, and is found to be everywhere less than that for the converging, constant conductivity case treated above. In particular, for $Q \ll 1$ we can approximate

$$g_{max} \approx \frac{6}{\eta} 2Q \ln(Q^{-1}) \left[1 - \frac{2}{\ln(Q^{-1})} - \frac{\ln\ln(Q^{-1})}{\ln(Q^{-1})}\right] . \tag{41}$$

It is obvious that the last two expressions are similar, at least in leading approximation, hence we adopt the general form

$$g_{max} = \frac{6}{\eta} f\ (\alpha\eta/24) \tag{42}$$

where the specific form of f depends on the precise situation. With the above results of Eqs. (40) and (41) we can characterize f in two limits

$$\begin{aligned} f\ (\ \alpha\eta \rightarrow \infty) &= 1 \\ f\ (\ \alpha\eta \rightarrow\ 0) &= \frac{\alpha\eta}{12}\left\{\ln\frac{1}{\alpha\eta} + C\right\} \quad . \end{aligned} \tag{43}$$

The constant C depends on the specific model but can be taken as approximately 2.2. Clearly, a non-converging beam must have $\eta \approx 1$ in order to propagate in equilibrium, giving only a few e-folds of growth during transit. For a converging beam, however, η increases proportional to σ/q^2 where q is the effective ion charge. For the beam to pinch at the pellet, η must be unity there. At the wall then, η must be much smaller and bounded by

$$\eta_w \leq \eta_{pinch} = (\sigma/q^2)_{min}/(\sigma/q^2)_{pellet} \tag{44}$$

where the minimum is taken over the converging profile. There is considerable growth, then, early in transit and it can be approximated when the conductivity ratio is high from Eq. (43):

$$g_{max} = \frac{\alpha}{2}\left\{\ln\left[\frac{(\sigma/q^2)_{pellet}}{(\sigma/q^2)_{min}}\right] + 2.2\right\} \tag{45}$$

Values of α less than unity could not yield large effects under extreme assumptions on conductivity development. Conversely it seems unlikely that $\alpha > 5$ could be tolerated even if σ/q^2 varied by only a factor of 10. One suspects that $\alpha \approx 3$ represents an effective bound for the converging beam. From our definition of $\alpha = \Omega_b L$ we should expect, then, a maximum transported energy of

$$W \leq (49\ \text{MJ}) \left(\frac{A}{Z}\right)^2 \beta^3 \left(\frac{\tau_p}{1\ \text{ns}}\right) \left(\frac{R_o}{L}\right)^2 , \qquad (46)$$

where A and Z are the atomic mass number and stripped charge for the beam particles, R_o is the rms radius of the beam at z=o and L is the chamber radius. The beam is assumed to have a parabolic profile with edge $a_o = \sqrt{3}\, R_o$ and central density $n = 2I_b/q\beta c\pi a^2$. If we take $\tau_p = 10$ ns, $A/Z = 4$, $R_o/L = 10^{-2}$, and $\beta = 0.3$ we find

$$W \leq 0.021\ \text{MJ} .$$

A total of 50 beams would be required to put 1 MJ on the target placing formidable complications in the way of reactor system design.

References

1. E. P. Lee "Filamentation During Final Transport in a High Pressure Gas," Proceedings of the Heavy Ion Fusion Workshop, Argonne National Laboratory, Argonne, Ill., September 19-26, 1978.

2. E. P. Lee, Simon Yu, H. L. Buchanan, F. W. Chambers, and Marshall N. Rosenbluth, "Filamentation of a Heavy Ion Beam in a Reactor Vessel," submitted for publication in Physics of Fluids.

KNOCK-ON ELECTRONS IN THE TARGET CHAMBER

R. F. Hubbard, S. A. Goldstein, and D. A. Tidman

Jaycor

Macroscopic magnetic fields arising from currents carried by the beam ions or by secondary electrons play a major role in determining the ion beam spot size. In a gas-filled target chamber, it has been generally assumed that the bare ion beam current I_b is almost balanced by a return current I_p which is carried by low energy secondary electrons. The resulting net current I_{net} is thus positive, leading to a magnetic field $B_\theta > 0$ which either weakly deflects the ions inward (ballistic or converging mode propagation) or pinches them more strongly into a thin, pencil-shaped beam (pinch mode propagation),[1,2]

However, we have pointed out recently that fast secondary electron may alter this picture considerably.[3] Particularly dangerous are those knock-on electrons with axial velocity $v_z > \beta_b c$, the beam velocity, since they may outrun the beam and set up a defocussing channel ahead of the beam. These electrons, which are produced by nearly head-on collisions between beam ions and both free and bound background electrons, are sufficiently numerous to alter the magnetic field substantially, and in many cases will probably reverse its direction.

Although some knock-on electrons are produced in all beam-plasma systems, they normally play a very small role. However, several unusual features make it possible for the knock-on electrons to exert a large influence on heavy ion beam transport. First, the cross section for producing these electrons scales as the square of $\hat{Z}_b$, the beam atomic number, so the knock-on current produced by a Uranium beam is almost four orders of magnitude larger than that produced by a proton beam moving at the same speed. Second, the relatively high knock-on electron energy (> 45 keV for $\beta_b = 0.4$) allows these

electrons to propagate as a nearly collisionless "beam", even in the presence of moderately high self-fields. In addition, if a substantial fraction of the knock-on current does get out ahead of the ion beam and can be charge neutralized by collisional ionization, the resulting field B_θ will usually be sufficient to pinch the electrons to a radius comparable with the ion beam radius. This means that the front portion of the ion beam will encounter a pre-existing $B_\theta < 0$ magnetic field which deflects the ions outward. Finally, because of the rapid rise in conductivity produced by the arrival of the ion beam, this field may persist throughout the beam pulse. The total scenario is illustrated in Figure 1, which shows knock-on electron orbits and the pinching magnetic field.

It is not yet clear whether knock-on electrons will lead to a deterioration in beam spot size for a given set of system parameters. The problem involves complicated spatial and temporal dependences plus self-fields whose sign may not be known. However, in this paper, we will use some simple analytical models developed in our previous work, and will defer until later a more detailed description of this complex phenomenon.

ESTIMATES OF KNOCK-ON CURRENT

A crude estimate of the knock-on current $I_k(> \beta_b)$ carried by electrons with axial velocities greater than the beam velocity $\beta_b c$ can be made from the total coulomb cross section for scattering by $> \frac{\pi}{2}$ in the beam frame.[3] This cross section is given by

$$\sigma_{\pi/2} = \frac{\pi r_e^2 \hat{Z}_b^2}{\beta_b^4} \quad , \tag{1}$$

where r_e and $\hat{Z}_b$ are the classical electron radius and beam atomic number, respectively. Note that electrons scattered through an angle greater than

$\pi/2$ in the beam frame are knocked forward with axial velocities which exceed the beam velocity. The total number of knock-on electrons $\hat{N}_k^{\pi/2}$ produced after the beam propagates a distance z is $\hat{N}_b\, n_e z \sigma_{\pi/2}$, where $\hat{N}_b = N_b L_b$ is the total number of beam ions, L_b is the beam pulse length and n_e is the density of background electrons. If $\beta_k \sim 1.3\beta_b$ and L_k are the characteristic velocity and length of the knock-on "beam", then $\hat{N}_k^{\pi/2} = N_k L_k \approx N_k(L_b + (\beta_k/\beta_b - 1)z)$. The total current carried by these electrons is $I_k = -\beta_k\, ec\, N_k$ and can be written

$$I_k(> \tfrac{\pi}{2}) = \frac{-\beta_k \tilde{I}_b n_e z \sigma_{\pi/2}}{\beta_b + (\beta_k - \beta_b)z/L_b} \quad , \tag{2}$$

where $\tilde{I}_b$ is the beam particle current. The second term in the denominator is a correction for the finite beam pulse length and becomes important when $z \gtrsim L_b$.

At pressures of 1 torr or greater, the current predicted by Eq. (2) can be quite large in some cases. Neglecting the finite pulse length correction, and setting $\beta_k/\beta_b = 1.3$, the ratio of the knock-on current to the beam particle current for a Uranium beam can be rewritten as

$$\frac{I_k(> \tfrac{\pi}{2})}{\tilde{I}_b} = \frac{9.7 \times 10^{-5}\ pz\ \hat{Z}_g}{\beta_b^4} \quad . \tag{3}$$

Here p is the pressure in torr and $\hat{Z}_g$ is the number of electrons per background gas atom (or molecule). For a 20 GeV Uranium beam propataing 1 m in 1 torr of He, $I_k(> \frac{\pi}{2}) \approx I_b$. However, for a 10 GeV beam propagating in 1 torr of Ne (which is typical of most recent reactor scenarios), $I_k(> \frac{\pi}{2})$ is increased by a factor of 20. Since $\tilde{I}_b$ is typically 1 kA, it is clear that

the knock-on current will often approach or exceed the Alfven current $I_A = 17\ \beta_k\gamma_k$ (kA) after propagating less than 1 m. If a substantial fraction of this current can get out ahead of the beam and become charge neutralized, it will tend to be strongly pinched by its own magnetic field even if the radius of this knock-on beam is initially large.

KNOCK-ON BEAM RADIUS AND ION ORBIT DEFLECTIONS

As a result of the collisional ionization process, knock-on electrons acquire a transverse velocity $v_{\perp k}$ which is comparable in magnitude with the axial velocity v_{zk}. Thus, the knock-ons would quickly fly out to a large radius R_k in the absence of self fields. However, as soon as the knock-on beam is charge neutralized, the self magnetic field will tend to pinch the beam to a smaller radius. If $I_k(> \frac{\pi}{2})$ is less than the Alfven current, the knock-on beam radius can be estimated by assuming that beam to be in a quasi-static Bennett equilibrium.[3] If the knock-on beam emittance is constant,[4] $R_k\Delta v_{\perp k}$ is constant, where $\Delta v_{\perp k}$ is the transverse thermal velocity of the knock-on beam. In a Bennett equilibrium,[4] $(\Delta v_{\perp k}^2/\beta_k^2 c^2) = -\alpha\, I_k(z)/I_A$. Here $I_k(z)$ is calculated from Eq. (2), and α is the fraction of that current which gets out ahead of the ion beam. For a converging beam in a chamber of radius L, one can eliminate $\Delta v_{\perp k}$ to get

$$R_k(z) = \frac{\Delta v_{\perp k}(0)}{c\beta_k}\ \frac{R_b(0)}{2}\ \left(2 - \frac{z}{L}\right)\left\{\frac{-\,I_A}{\alpha I_k(z)}\right\}^{\frac{1}{2}} . \qquad (4)$$

This expression is valid only for $|\alpha\, I_k| < I_A$. If the knock-on beam current exceeds I_A, $\nabla \vec{B}$ drifts tend to focus the beam to a radius smaller than the ion beam radius. Otherwise, the knock-on radius is usually a few times the ion beam radius.

Only that fraction of the knock-on beam current which lies inside the ion beam radius can contribute to the defocussing magnetic field. For a radially uniform knock-on beam, this effective current is

$$I_k^{eff}(z) = \alpha\, I_k(z) \left(\frac{R_b(z)}{R_k(z)}\right)^2 \quad . \tag{5}$$

It is important to note that for ballistic focussing, it is possible to have $I_{net} < 0$ through the entire ion beam pulse so long as the resulting ion orbit deflections are sufficiently small. In our previous work[3], we numerically integrated the standard paraxial envelope equation for the ion beam using $I_{net}=I_k^{eff}< 0$ to estimate the ion beam spot size. That study demonstrated that for propagation in He at 20 GeV, there could be a severe deterioration in spot size for a 1 kA ion beam at pressures above a few torr.

If the defocussing magnetic field present at the front of the ion beam pulse is frozen in by the high conductivity, it is possible to make a simple analytical estimate of the attainable spot size. If the ion beam is assumed to be cold, the minimum spot size for a constant I_k^{eff} is[5]

$$R_{min} = R_o \exp\left(-\frac{(R_o/L)^2}{2K}\right) \quad . \tag{6}$$

R_o is the initial beam radius, and K is the generalized perveance[5], which for a charge neutralized heavy ion beam in the field produced by I_k^{eff} is

$$K = -\frac{6.41 \times 10^{-8}\, Z_b\, I_k^{eff}}{A\,(\gamma_b^2 - 1)^{1/2}} \quad . \tag{7}$$

Here I_k^{eff} is measured in amps, and A = 238 for Uranium. Note that $\gamma^2 - 1 \simeq \beta^2$ for the mildly relativistic ion beam. Equations (6) and (7)

can be combined to give an estimate for the maximum allowable effective knock-on current in order to reach a given spot size R_{min}.

$$\left|I_{k,max}^{eff}\right| = \frac{7.8 \times 10^6 \, R_o^2 \, A\beta_b}{L^2 Z_b \ell n(R_o/R_{min})} \quad . \tag{8}$$

Note that this current is determined primarily by the focussing angle $R_o/L \sim 10^{-2}$ and is only weakly dependent on R_{min}. For typical parameters, $\left|I_{k,max}^{eff}\right|$ is less than 1 kA. For purposes of making simple estimates, I_k^{eff} can be taken to be the value at the midpoint of the trajectory ($z = \frac{1}{2}L$).

As an example, consider a 10 GeV, 1 kA Uranium beam propagating a distance L = 5 m in 1 torr of Ne, and assume R_o = 10 cm and L_b = 100 cm. Eq. (2) predicts that $I_k(> \frac{\pi}{2}$, z = 2.5 m) is - 22 kA. Assume that 10% of this amount produces a charge-neutralized knock-on beam ahead of the ion beam (i.e., $\alpha = 0.1$). For $\beta_k/\beta_b = 1.3$, I_A = 6.7 kA, and thus Eq. (4) predicts R_k = 7.2 cm at $z = \frac{1}{2}L$ (assuming $\Delta v_{\perp k}(0) = 0.55 \, \beta_k c$). Since R_b = 5 cm at this point, $I_k^{eff} = (-2.2)\,(5/7.2)^2 = -1.1$ kA. However, the allowable $I_{k,max}^{eff}$ predicted by Eq. (8) for R_{min} = 0.2 cm and Z_b = 70 is only - 760 A. Thus, the desired spot size could not be attained if the defocussing field is frozen in. It is clear that since both α and R_k cannot be estimated accurately, changes in their assumed values could easily reverse this conclusion. If αI_k is reduced from 2.2 kA to 0.22 kA (which could be produced by lowering the pressure or reducing the assumed value of α), then I_k^{eff} would be reduced to only 11 A, and the effect of the knock-ons would be negligible.

NET CURRENT REVERSAL BY THE ION BEAM

According to the model we have been developing, the front end of the ion beam pulse experiences an effective net current I_k^{eff} (< 0) determined by

the total knock-on current and beam radius. It is of critical importance to determine how quickly (if at all) this net current can be reversed by the positive ion current. We define ξ as the distance from the ion beam head back into the pulse, and ξ_{cr} as the distance from the beam head at which the net current is reversed (i.e., $I_{net}(\xi_{cr}) = 0$). For $\xi_{cr} << L_b$, only the front portion of the beam experiences the defocussing field, and the knock-on electrons will probably have only a minimal effect. For $\xi_{cr} \sim L_b$, most or all of the ion beam pulse experiences an outward deflection. For ballistic propagation, this can be tolerated so long as the effective knock-on current lies below the critical value given in Eq. (8). However, pinched mode propagation obviously requires a small value of ξ_{cr} since the pinch requires $B_\theta > 0$.

The net current can be estimated from a circuit equation of the form

$$\frac{\partial}{\partial \xi}\left(\tilde{L}\, I_{net}\right) = \frac{c}{2\beta_b \pi R^2 \sigma}\left[- I_{net} + Z_b\, \tilde{I}_b + I_k^{eff}\right], \tag{9}$$

with all quantities functions of ξ. The exact form of the inductance term $\tilde{L}$ depends on the details of the circuit model. We take R as constant and $\tilde{L} \sim 1$. An upper limit to ξ_{cr} can be found by retaining only the $Z_b\, \tilde{I}_b$ term on the right hand side of Eq. (9) and assuming the following forms for $\tilde{I}_b$ and σ:

$$\tilde{I}_b(\xi) = \tilde{I}_b'\, \xi\ ,$$

$$\sigma(\xi) = \sigma_o + \Lambda\, I_b'\, \xi^2\ . \tag{10}$$

This corresponds to direct ionization by a linear ramped pulse. With the initial condition $I_k^{eff}(\xi = 0) = I_k^{eff}(0)$, Eq. (9) can be integrated and

solved for $I_{net} = 0$ to give

$$\xi_{cr}^2 = \frac{\sigma_o}{\Lambda I_b'} \left\{ \exp\left[\frac{-4\pi\beta_b \tilde{L} R^2 \Lambda I_k^{eff}(0)}{Z_b c} \right] - 1 \right\} \tag{11}$$

In order to make numerical estimates, we assume that the ionization cross section $\sigma_+ = 10^{-18} Z_b^2 \beta^{-2}$ cm^2 (based on Gillespie, et al[6]), and that the conductivity is given by[7] $\sigma = 1.8 \times 10^{-4} n_e T_e^{-\frac{1}{2}}$. The resulting nominal value for Λ is

$$\Lambda_o = \frac{3.2 \times 10^5 Z_b^2}{T_e^{\frac{1}{2}} R_b^2 \beta^3} \quad (\text{Amp-cm-sec})^{-1} . \tag{12}$$

Note that $\Lambda = \frac{1}{2} \frac{d^2\sigma}{d\tilde{I}_b d\xi}$.

Figure 2a plots ξ_{cr} versus $I_k^{eff}(0)$ for a typical converging beam with $\beta_b = 0.2$ (5 GeV), $Z_b = 70$, $R_b = 5$ cm, $\tilde{L} = 1$, $T_e = 4$ eV, and $\sigma_o = 10^{10}$ s^{-1}. Curves are plotted for $\Lambda = 0.3$, 1, and $3\Lambda_o$, allowing for an order of magnitude variation in conductivity. Figure 2b contains similar plots for $\beta = 0.4$ ($\sim$20 GeV). It is clear that ξ_{cr} is extremely sensitive to small variations in conductivity (or Λ) and I_k^{eff} . Unfortunately, neither quantity can be estimated with great precision. Figure 2 also indicates that in most cases, the current will be reversed close to the ion beam head ($\xi_{cr} \lesssim 10$ cm), or else the defocussing field will persist throughout the pulse ($\xi_{cr} \gtrsim L_b \sim 100$ cm). Since the minimum effective knock-on current necessary to prevent field reversal by the ion beam is typically 10^2 A for these parameters, we expect the defocussing field to persist throughout the beam pulse at sufficiently high pressures if even a modest amount of self-pinching occurs.

For pinched mode propagation, the background gas may be completely stripped and conductivity may exceed 10^{15} s^{-1}. For illustrative purposes, we consider a pinched beam with R_b = 0.2 cm, β = 0.3, I_b' = 20 A/cm, Z_b = 70, and σ_o = 10^{10} s^{-1}. Assuming that $\sigma(\xi$ = 20 cm) is 10^{15} s^{-1}, the resulting Λ is 1.25 x 10^{11} $(A\text{-cm-sec})^{-1}$. For $\tilde{L}$ = 1, Eq. (11) predicts that the defocussing field will destroy the pinch if I_k^{eff} > 1.5 kA. However, since R_b is so small, the inductance term $\tilde{L}$ should probably be increased by at least a factor of 2, thereby proportionally reducing the allowable I_k^{eff}. One can be cautiously optimistic that at pressures below 1 torr in Ne the defocussing field can be reversed near the head of the beam, but this field reversal becomes much more uncertain at higher pressures.

DISCUSSION AND CONCLUSIONS

It is virtually certain that heavy ion beams will produce massive quantities of knock-on electrons for target chamber pressures above 1 torr. We have shown that the magnitude of the resulting current is more than sufficient to pinch the knock-on beam in most cases, assuming that a substantial fraction of this beam actually gets out ahead of the ion beam pulse. Although at least some of the ion beam experiences this defocussing, the overall effect on beam propagation is minimal if field reversal induced by the ion beam occurs near the beam head. Our simple model for studying this field reversal process has not been conclusive owing to uncertainties in conductivity and in the radius of the knock-on beam. For ballistic mode propagation, ion beam induced field reversal is not necessary so long as the net knock-on current lying inside R_b does not exceed the limit given crudely in Eq. (8). However, field reversal <u>must</u> occur quickly for pinched-mode propagation to be viable.

There are several factors which we have not yet discussed which could modify the model we have presented considerably. First, electric fields present inside the ion beam may prevent knock-on electrons from getting out ahead of the beam. As long as the stripped ion beam current is not exceeded by the current carried by fast electrons, the inductive field E_z will be negative. Hence, knock-ons inside the ion beam will actually be accelerated forward to higher energies. This will tend to neutralize quickly the space charge at the head of the ion beam (especially for a ramped pulse), so any electrostatic fields near the head of the ion pulse will probably be greatly reduced.

Yu[8] has pointed out that the self pinching of knock-ons cannot occur until the knock-ons in the channel ahead of the beam become space charge neutralized. The distance for achieving neutralization must be longer than the mean free path for ionization given by

$$\lambda_i = \frac{1}{\sigma_i n_g} \quad . \tag{13}$$

Here σ_i is the ionization cross section and is typically (1-5) x 10^{-18} cm^2, depending on the gas specie and knock-on energy (20-100 keV). For $\lambda_i \gtrsim 20$ cm (as is typical of Ne at 1 torr), the beam will travel a considerable distance into the chamber before self-pinching begins, and I_k^{eff} will be substantially reduced. However, by raising the pressure or using a more readily ionized gas, λ_i can be reduced to a few cm or less, and self-pinching is more likely to occur. In addition, for self-pinched ion beams propagating in > 10 torr of Ne, knock-on current densities will be sufficiently large to induce breakdown or avalanching even if the beam is not initially pinched.

An additional feature which we have not discussed is the possible enhancement of conductivity by energetic secondary electrons at energies above the 1 eV bulk plasma produced by a large radius ballistically focussed beam. Such an enhancement would probably prevent the ion beam from reversing the knock-on field under any circumstances. However, if the resulting frozen net current lies well below the limit set by Eq. (8), field induced ion orbit deflections and anharmonic emittance growth[2] might actually be reduced below what has been calculated in the past. Since the estimated temperature inside a pinched beam is expected to be 100 eV, one would not expect substantial conductivity enhancement by energetic secondary electrons.

ACKNOWLEDGEMENTS

Conversations with Drs. John Guillory, Paul Ottinger, C. L. Olson, E. P. Lee, and S. S. Yu are gratefully acknowledged. This work was supported by the Department of Energy under contract DE-AC08-79-DP40101.

REFERENCES

1. S. S. Yu, H. L. Buchanan, F. W. Chambers, and E. P. Lee, Argonne National Laboratory Report No. ANL-79-41, 1979, edited by R. Martin. (Proceedings of 3d Workshop and Heavy Ion Beam Fusion), p. 403.

2. H. L. Buchanan, F. W. Chambers, E. P. Lee, S. S. Yu, R. J. Briggs, and M. N. Rosenbluth, Lawrence Livermore Laboratory, UCRL Report 82586, 1979.

3. R. F. Hubbard, S. A. Goldstein, and D. A. Tidman, JAYCOR Tech Note 350-79-005, 1979.

4. E. P. Lee and R. K. Cooper, Part. Accel. 7, 83 (1976).

5. J. D. Lawson, The Physics of Charged-Particle Beams (Clerendon Press, Oxford, 1977), p. 136.

6. G. Gillespie, K-T. Cheng, and Y-K. Kim, Ref. 1, p. 175.

7. K. A. Brueckner and R. C. Vik, Physical Dynamics Report PD-77-138, 1977.

8. S. S. Yu, private communication.

FIGURE CAPTIONS

Fig. 1 - Knock-on electron orbits as seen in the laboratory frame. Electrons which outrun the beam produce plasma channel ahead of the beam with a magnetic field $B_\theta < 0$ which pinches the electrons and causes them to execute sinusoidal betatron orbits. This field will persist at least part of the way into the ion beam pulse (shaded area), thereby deflecting ions outward. In many cases, the ion beam will reverse the magnetic field at some point, leading to a region where electrons are magnetically expelled. The case illustrated is somewhat unusual in that field reversal, if it occurs at all, will usually occur within a few centimeters of the beam head.

Fig. 2 - Critical distance from the beam head ξ_{cr} verses effective knock-on current $I_k^{eff}(0)$, lying inside the ion beam at $\xi = 0$. Parameters assumed in Fig. 2a are for a converging beam with $\beta_b = 0.2$ (5 GeV), $Z_b = 70$, $R_b = 5$ cm, $\tilde{L} = 1$, $T_e = 4$ eV, $I_b' = 20$ A/cm and $\sigma_o = 10^{10}$ s^{-1}. The nominal value Λ_o is based on the estimate in Eq. (12) and is a measure of how fast the conductivity builds up as a result of the rising beam. If $I_k^{eff}(0)$ is sufficiently small, ξ_{cr} is a few centimeters or less, and knock-on defocussing will not effect most of the ion beam pulse. Equation (11) is used to estimate ξ_{cr}. Figure 2b is a similar calculation for $\beta_b = 0.4$.

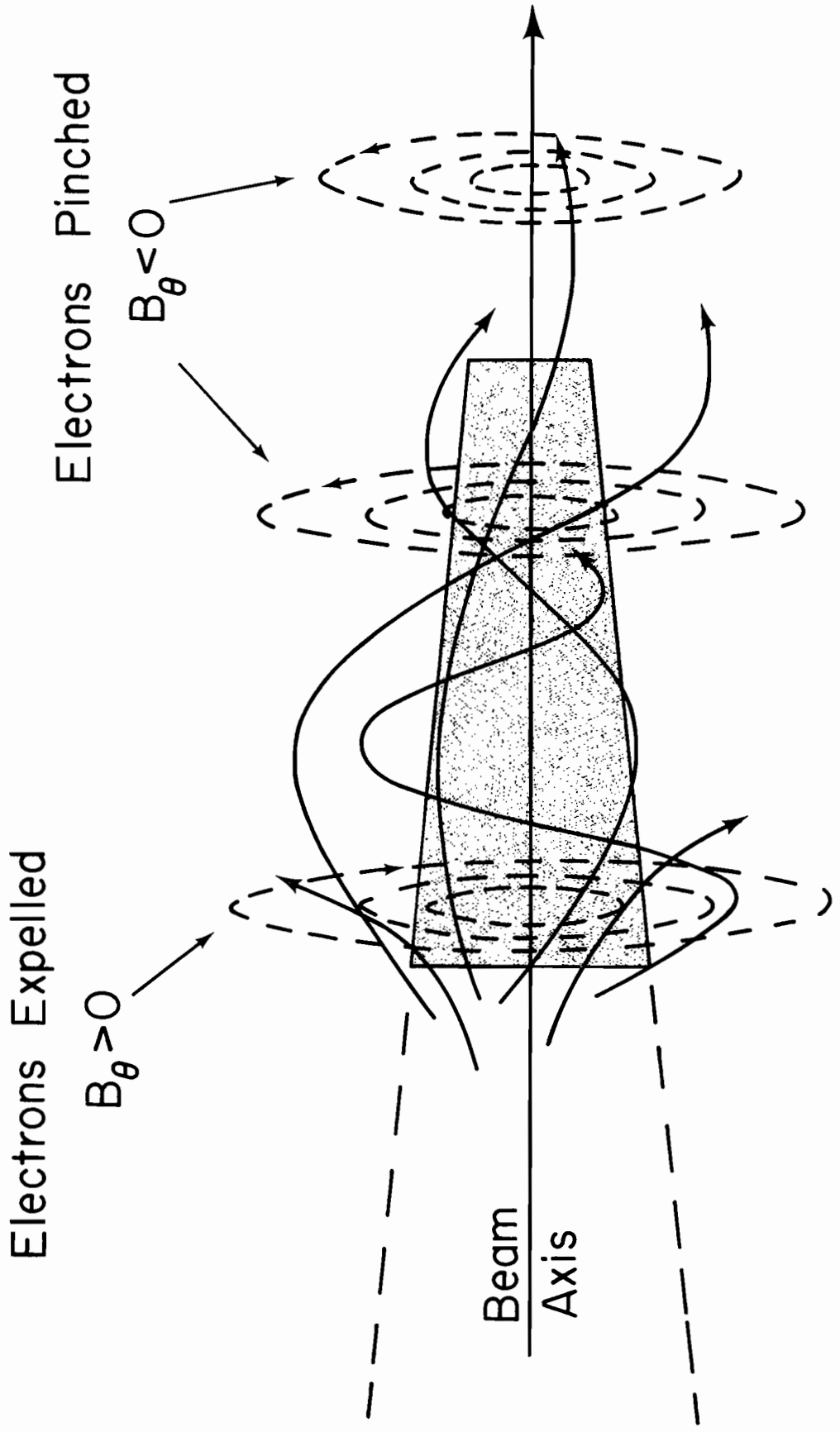
Electrons Pinched
$B_\theta < 0$
Electrons Expelled
$B_\theta > 0$
Beam
Axis

Figure 1.

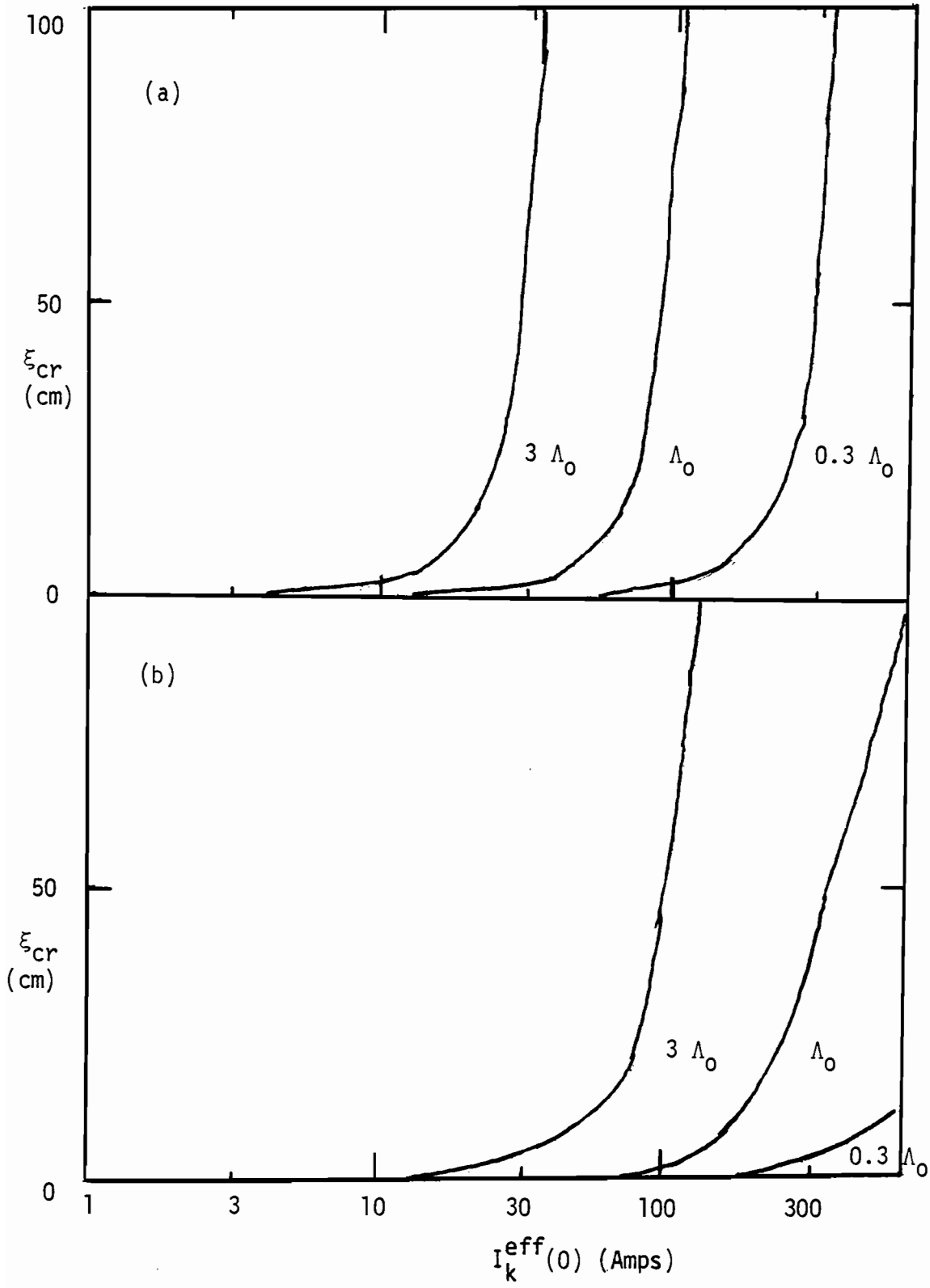
100
(a)
50
ξ_{cr} (cm)
3 Λ_o
Λ_o
0.3 Λ_o
0
(b)
50
ξ_{cr} (cm)
3 Λ_o
Λ_o
0.3 Λ_o
0
1
3
10
30
100
300
$I_k^{eff}(0)$ (Amps)

Figure 2

FOCAL SPOT SIZE PREDICTIONS FOR BEAM TRANSPORT THROUGH A GAS-FILLED REACTOR

S. S. Yu, E. P. Lee, and H. L. Buchanan

Lawrence Livermore Laboratory

ABSTRACT

Results from calculations of focal spot size for beam transport through a gas-filled reactor are summarized. In the converging beam mode, we find an enlargement of the focal spot due to multiple scattering and zeroth order self-field effects. This enlargement can be minimized by maintaining small reactors together with a careful choice of the gaseous medium. The self-focused mode, on the other hand, is relatively insensitive to the reactor environment, but is critically dependent upon initial beam quality. This requirement on beam quality can be significantly eased by the injection of an electron beam of modest current from the opposite wall.

Work performed by LLL for U. S. DOE under Contract No. W-7405-Eng-48

I. SUMMARY OF RESULTS

Results from calculations of focal spot size for heavy ion beams transported through a gas-filled reactor are summarized below. Three transport modes have been studied. The first is the ballistic mode where beams are injected through large portholes (∿15 cm radius) to converge at the target. The second is the self-focused mode where beams are injected through small portholes (sub-cm), and propagate in their self-generated pinch field. The third mode is a variant of the second: an electron beam of modest current is injected from the opposite wall to aid the ion beam pinching.

The basic tools for our analyses are a set of 1-D codes which calculate the r.m.s. radius of a beam during its passage through the reactor. Analytic formulae for the r.m.s. radius of the beam in the target region were derived on the basis of several approximations which were shown by the 1-D codes to be reasonable in the range of parameters of interest for HIF. We have also checked 1-D code results against simulations and 2-D codes. These codes include only classical effects (no instabilities), and the predicted focal spot size represent the minimum disruption the beam is expected to experience.

Ballistic Mode

We find an enlargement of the focal spot size due to multiple scattering and classical self-field effects. The magnitude of these effects seem large enough to be of concern for target requirements. However, there is still sufficient uncertainty in the theory, particularly in connection with the calculation of beam-generated electrical conductivity, that firm predictions are not yet possible. Detailed calculations of the electrical conductivity with Boltzmann codes are in progress. Calculations up to this point indicate the sensitivity of final focal spot size to various beam and reactor parameters, and suggest several ways for minimizing the spot size enlargement:

1. Small reactors. The neck radius of the beam is a very sensitive function of the reactor size. To keep the neck radius small, the

total path of propagation in gas should be kept to a minimum ($z_o \leq 5$ meters). In addition, the neck radius is reduced by maintaining large portholes. The geometric factor R_w/z_o should be maximized, where R_w is the beam radius at reactor wall.

2. Proper choice of gas medium. To minimize multiple scattering effects, one is restricted to a low-Z material below a few torr. Self-field effects could be significantly reduced by choosing a good conducting gas, e.g., Ne and N_2 are better conductors than He or Li. One might also consider mixtures involving more complex gases, e.g., H_2O. Self-field effects are relatively insensitive to gas pressure.

3. Some pulse shaping in the radial direction would be helpful. Emittance growth is minimized by having a nearly square current profile. The magnitude of the current in a given beamlet has relatively little effect on the emittance increase in the classical calculations. Since the change in beam emittance in the reactor is independent of its initial value, little is gained by improving beam quality at entrance. Overall, the effects of initial beam parameters on focal spot size enlargement due to classical phenomena are secondary. One should note, however, that the beam energy cannot be lowered much below 10 Gev, since multiple scattering, which is proportional to β^{-4}, would become intolerable.

Pinched Modes

Whereas the reactor geometry and reactor environment are constrained in the ballistic mode of propagation, the self-focused mode is insensitive to the reactor size, and can accommodate a large range of gas types and pressure ($\sim$1 to 50 torr). In addition, the small portholes associated with the self-focused mode ease pumping requirements. The constraint for this mode is on beam quality. The self-focused beam characteristically expands at the beam head, and is pinched at the tail. The amount of beam head lost, and the final pinch radius at the tail are both sensitive to the initial beam emittance. Our code indicates that with initial emittance of 1 mrad-cm, the beam is pinched to a radius of $\sim$1 mm with only a small portion of the beam head lost. But the ion beam pinching rapidly degrades as the initial emittance is increased. Beam radius at injection is also an important

parameter. The optimal beam size at entrance is a few millimeters. Generally, the more current there is in a given beamlet, the tighter is the final pinch. However, beam current is not as critical a parameter as the beam quality in determining the final beam radius.

The requirement on beam quality could be significantly eased by the injection of an electron beam from the opposite wall simultaneously with or prior to the injection of the heavy ion beam. Our code indicates that vast improvements in the ion beam pinching is achieved with a modest electron beam current. With a 3 kA/cm^2 e-beam, a 3 mrad-cm ion beam is pinched to slightly larger than 1 mm at the beam tail with little loss of the beam head. The stable propagation of such a e-beam has been demonstrated experimentally.[1]

II. THEORY

The basic ansatz for our beam transport studies is the envelope equation[2] which describes the evolution of the r.m.s. radius R of a beam segment (characterized by $x = \beta c\tau$, the distance from the beam head) as a function of z, the distance from the reactor wall:

$$\frac{\partial^2 R}{\partial z^2} = \frac{E^2}{R^3} - \frac{\overline{k_\beta^2 r^2}}{R} \tag{1}$$

The envelope equation is quite general, and is derived by taking appropriate moments of the particle equations of motion. The complications lie in evaluating the evolving emittance E, and the pinch force, characterized by the average betatron oscillation $\overline{k_\beta^2 r^2} = I_{net}/I_A$, where I_{net} and I_A are the net current and Alfven current, respectively. Since the physics of the ballistic mode and the pinched modes are quite different, they will be discussed separately.

Ballistic Mode

Only the effects of multiple scattering and classical pinch fields are included in the present study. The classical field effects arise from incomplete current neutralization, which results in self-magnetic fields that deflect beam particles.[3] Degradation of the focal spot size happens

in two ways. First, when particles at different radial positions of a given beam segment experience different focusing forces (due to anharmonic pinch fields), there is a net increase in the emittance of that disc, which leads in turn to an enlarged neck radius. Secondly, the average pinch force experienced by various beam segments are different. The resulting variable focal lengths imply that as the beam impinges upon a target placed at any point in the reactor, most of the beam discs will be slightly out of focus.

For the converging beam, it is possible to derive an approximate solution for the neck radius of a beam segment from Eq. (1). It is given by

$$R_n = E_f \left(\frac{z_o}{R_w}\right) / \left[1+\delta\right]^{1/2} \tag{2}$$

where the final emittance is the initial emittance enhanced by multiple scattering and self-field effects

$$E_f^2 = E_0^2 + (\Delta E^2)_{scatt} + (\Delta E^2)_{field} \tag{3}$$

The geometric factor (z_o/R_w) in Eq. (2) determines the amount of emittance growth that can be tolerated to achieve a given neck radius. The parameter δ represents a correction due to gross pinching effects, given by

$$\delta = 2\left(\frac{z_o}{R_w}\right)^2 \overline{k_\beta^2 r^2}\ \ell n\left(\frac{R_w^2}{E_f\, z_o}\right) \tag{4}$$

Emittance increase due to multiple scattering is well known, and is given by

$$(\Delta E^2)_{scatt} = \sigma_{scatt}\, n_g\, R_w^2\, z_o/3 \tag{5}$$

where n_g is the gas density, and the factor of 1/3 results from the converging beam geometry. σ_{scatt} is an effective cross section for multiple scattering, given by

$$\sigma_{scatt} = \frac{8\pi e^4 Z_i^2 Z_g^2}{M^2 c^4 \beta^4 \gamma^2}\ \ell n\tau \tag{6}$$

where Z_i and Z_g are the atomic number of the heavy ion and the gas, respectively, and M is the mass of the ion. $\ell n\tau$ provides the cutoff in momentum transfer.

To calculate the emittance growth due to self-fields requires detailed knowledge of the evolving velocity distribution of the beam particles. Explicit evaluation of this effect is not known in general. However, for the converging beam, it is possible to employ a perturbative approach upon the assumption that deviations from ballistic trajectories are slight. A simple formula then emerges:[4]

$$(\Delta E^2)_{field} = s\ (\overline{k_\beta^2 r^2})\ z_o^2 \tag{7}$$

where s is a radial shape factor, given by

$$s = \left(\frac{\overline{k_\beta^4 r^2}\ R^2}{(\overline{k_\beta^2 r^2})^2} - 1 \right) \tag{8}$$

s = 0 if the net current profile is square, and is 1/45 for a parabolic profile and 0.15 for a Gaussian profile.

To complete the derivation of the neck radius, $\overline{k_\beta^2 r^2}$ must be evaluated. The pinch force results from the aggregate effect of the beam current and the plasma current. Initially, one might expect $\overline{k_\beta^2 r^2}$ to be a very sensitive function of the beam current and the degree of stripping of the heavy ion. However, in the highly current neutralized regime relevant for heavy ion fusion, the plasma current varies in such a way as to cancel both the beam current and the effective ion charge state dependence to leading order. The resultant $\overline{k_\beta^2 r^2}$ is sensitive only to atomic properties of the gas. It is given approximately by

$$\overline{k_\beta^2 r^2} = \frac{1}{4} \left(\frac{m}{M}\right)\left(\frac{\beta}{\gamma}\right)\left(\frac{\nu_m}{c\,\sigma_{ie}}\right) \ell n\, \kappa \tag{9}$$

where ν_m is the momentum transfer rate, and σ_{ie} is the relativistic limit of the non-relativistic ionization cross section for the gas by electron impact. The dependence on beam particle current I_{bo}/e, the effective charge state of the ion Z, and the beam segment position x are contained in the single parameter κ. κ = 1 at beam head, and away from the beam head, ($x >> x_r = \beta c \tau_r$, where τ_r is the rise time), we have

$$\kappa = \left(\frac{2eZ^2\ \sigma_{ie}\ I_{bo}}{m\ \nu_m\ \beta^2\ c^2} \right) \left(\frac{x}{x_r} - \frac{1}{2} \right) \qquad x >> x_r \tag{10}$$

The size of the neck radius of a beam segment is given by Eqs. (2) to (10). The position of the neck z_n can also be obtained from Eq. (1):

$$z_n = z_o - \overline{k_\beta^2 r^2}\left(\frac{z_o^3}{R_w^2}\right) \tag{11}$$

where z_o is the geometric focal point for a ballistic beam. Variations of the focal length with x comes through the factor $\overline{k_\beta^2 r^2}$.

Finally, the r.m.s. radius of the beam in the region around the neck is given by

$$R^2 = R_n^2 + \frac{E_f^2}{R_n^2}(z_n - z)^2 \tag{12}$$

Pinched Modes

The physics of the pinched mode is more complicated, and we do not have simple analytic solutions in this case. Detailed 1-D and 2-D codes are required to calculate the beam envelope and results of these calculations have been reported previously.[5] However, we will attempt to give a heuristic description of the underlying physics.

As a self-pinched beam moves towards the target away from the porthole, the main body of the pulse eventually settles into an equilibrium. The equilibrium radius is obtained by setting $\partial^2 R/\partial z^2 = 0$ in Eq. (1):

$$R_{eq} = \frac{E_f}{\sqrt{\overline{k_\beta^2 r^2}}} \tag{13}$$

The final emittance E_f is again the initial emittance enhanced by multiple scattering and self-field effects. However, emittance growth due to multiple scattering for a self-focused beam is small because $(\Delta E^2)_{scatt}$ is proportional to R^2. Hence, the self-focused mode is not confined to low-Z material and/or low pressure as is the converging beam mode.

Emittance growth due to self-fields can be minimized by injecting the beam at nearly the matched radius. Emittance growth due to mismatch has been studied with simulation codes,[6] and a phenomenological model which reproduces the observed effects was constructed. It is given by[4]

$$\frac{\partial E^2}{\partial z} = -\left[\frac{\overline{k_\beta^2 r^2}\ R^2}{\frac{1}{A}\left(\frac{E}{R}\right) + \frac{1}{B}\left(\frac{\overline{k_\beta^2 r^2}\ R}{E}\right)}\right]\frac{\partial^2 R}{\partial z^2} \tag{14}$$

where A and B are numerical constants. For a slightly mismatched beam, the net emittance gain is predicted to be[4]

$$(\Delta E^2)_{field} = 2\ \overline{k_\beta^2 r^2}\left(R_{eq} - R_w\right)^2 \tag{15}$$

The calculation of $\overline{k_\beta^2 r^2}$ has been performed with detailed numerical codes.[5] To obtain a physical feel for the requirements for pinching, one could invert Eq. (13) to derive the required net current to attain a given target size

$$I_{net} = \frac{\beta\gamma Mc^3}{e\ Z}\ \overline{k_\beta^2 r^2} = \frac{\beta\gamma Mc^3}{e\ Z}\left(\frac{E_f}{R_{eq}}\right)^2 \tag{16}$$

As a numerical example, we consider a 10 Gev uranium beam with 1 kA particle current. Assuming Z = 80, the beam current is 80 kA, while the net current required to pinch a 1 mrad-cm beam to 1 mm [Eq. (16)] is only 3 kA. Hence, more than 95% current neutralization can be tolerated.

The amount of current neutralization is controlled by the magnetic decay time τ_m

$$\frac{I_{net}}{I_{beam}} \sim \frac{\tau}{\tau_m} \tag{17}$$

where τ_m is proportional to the electrical conductivity

$$\tau_m = \frac{4\ \pi\sigma\ R^2}{c^2} \tag{18}$$

The electrical conductivity σ is proportional to $Te^{3/2}/Z_g^{eff}$ where Z_g^{eff} is the effective charge state of the gas, while Te is the electron

temperature. The electron temperature is determined by direct heating by ions and Joule heating, combined with thermal cooling in the radial direction. The general trend is for the conductivity, and therefore the magnetic decay time to increase with beam current. However, the increase is less than linear. Eq. (17) therefore predicts an increase in I_{net} with I_{beam} which is also less than linear. Hence, from Eq. (13), we have a decrease in R_{eq} with increased beam current at a rate which is slower than a square root. Thus, independent of the details of the fields and plasma channel, the strong dependence of the pinch radius on beam quality and its weak dependence on beam current can be qualitatively understood.

The theory of electron beam aided pinched propagation, together with numerical results from a parameter search, have been reported.[7] Calculations involving an e-beam current are quite similar to the pure self-focused mode calculations except that there is an additional contribution to $\overline{k_\beta^2 r^2}$ due to the external current. We would stress that the external current of the order of 3 kA/cm^2 is in itself far too weak to pinch the beam. The external current merely serves to hold together the ion beam head loosely. This leads in turn to rapid generation of self-fields.

REFERENCES

1. R. J. Briggs, J. C. Clark, T. J. Fessenden, R. E. Herter, and E. J. Lauer, "Transport of Self-focused Relativistic Electron Beams," Proceedings of the 2nd International Topical Conference on High Power Electron and Ion Beam Research and Technology (Cornell, 1977).

2. E. P. Lee and R. K. Cooper, Particle Accelerators 7, 83 (1976).

3. See also D. Mosher and S. Goldstein, "Disruption of Geometric Focus by Self-Magnetic Fields," Proceedings of Heavy Ion Fusion Workshop (Argonne, 1978).

4. E. P. Lee and S. S. Yu, "Model of Emittance Growth in a Self-Pinched Beam," UCID-18330 (1979).

5. S. S. Yu, H. L. Buchanan, E. P. Lee, and F. W. Chambers, "Beam Propagation Through a Gaseous Reactor-Classical Transport," Proceedings of Heavy Ion Fusion Workshop (Argonne, 1978).

6. Unpublished work of E. P. Lee and H. L. Buchanan.

   W. A. Barletta, "Computational Models of Beam Emittance Growth" (to be published).

7. H. L. Buchanan, F. W. Chambers, E. P. Lee, S. S. Yu, R. J. Briggs, and M. N. Rosenbluth, "Transport of Intense Particle Beams with Application of Heavy Ion Fusion," submitted to Third International Topical Conference on High Power Electron and Ion Beam Research and Technology (Novosibirsk, USSR, 1979).

LIST OF PARTICIPANTS

ATTENDEES
WORKSHOP ON HEAVY ION FUSION
October 29, 1979
Lawrence Berkeley Laboratory

Name	Affiliation
Bangerter, R.	Lawrence Livermore Laboratory
Billman, K.	Electric Power Research Inst.
Boehne, D.	GSI
Brueckner, K.	University of California - San Diego
Brown, K.	Stanford Linear Accelerator Center
Burke, R.	Argonne National Laboratory
Channell, P.	Los Alamos Scientific Laboratory
Cho, Y.	Argonne National Laboratory
Chupp, W.	Lawrence Berkeley Laboratory
Cline, D.	Fermi National Accelerator Laboratory
Colton, E.	Argonne National Laboratory
Cornacchia, M	Brookhaven National Laboratory
Courant, E.	Brookhaven National Laboratory
Faltens, A.	Lawrence Berkeley Laboratory
Fenster, S.	Argonne National Laboratory
Foss, M.	Argonne National Laboratory
Gammel, G.	Brookhaven National Laboratory
Garren, A.	Lawrence Berkeley Laboratory
Godlove,T.	U.S. Department of Energy
Guiragossian, Z.	TRW Systems and Energy
Haber, I.	Naval Research Laboratory
Halbach, K.	Lawrence Berkeley Laboratory
Herrmannsfeldt, W.	Stanford Linear Accelerator Center
Hofmann, I.	Max-Planck Institute for Plasmaphysik
Hoyer, E.	Lawrence Berkeley Laboratory
Hubbard, R.	Jaycor
Humphries, S.	Sandia Laboratories
Irani, A.	Brookhaven National Laboratories
Jameson, R.	Los Alamos Scientific Laboratories
Johnsen, K.	Brookhaven National Laboratory
Jones, L.	University of Michigan
Jorna, S.	Physical Dynamics, Inc.
Judd, D.	Lawrence Berkeley Laboratory
Katayama, T.	University of Tokyo
Kawasaki, S.	Kanazawa University
Keane, J.	Brookhaven National Laboratory
Keefe, D.	Lawrence Berkeley Laboratory
Khoe, T.	Argonne National Laboratory
Kim, C.	Lawrence Berkeley Laboratory
Kim, K.	Lawrence Berkeley Laboratory
King, M.	Rutherford Laboratory
Knapp, E.	Los Alamos Scientific Laboratory
Lambertson, G.	Lawrence Berkeley Laboratory
Lapostolle, P.	GANIL

Laslett, L.J.	Lawrence Berkeley Laboratory
Lawson, J.	Rutherford Laboratory
LeDuff, J.	ORSAY
Lemons, D.	Los Alamos Scientific Laboratory
Lofgren, E.	Lawrence Berkeley Laboratory
Maidment, J.	Rutherford Laboratory
Martin, R.	Argonne National Laboratory
Maschke, A.	Brookhaven National Laboratory
Mirk, K.	Lawrence Berkeley Laboratory
Mobley, R.	Brookhaven National Laboratory
Mohl, D.	CERN
Morton, P.	Stanford Linear Accelerator Center
Neuffer, D.	Fermi National Accelerator Laboratory
Noda, A.	University of Tokyo
Ohnuma, S.	Fermi National Accelerator Laboratory
Olson, C.	Sandia Laboratories
Osher, J.	Lawrence Livermore Laboratories
Penner, S.	National Bureau of Standards
Peterson, J.	Lawrence Berkeley Laboratory
Plass, G.	CERN
Pusterla, M.	University of Padova
Rees, G.	Rutherford Laboratory
Richter, B.	Stanford Linear Accelerator Center
Rosenblum, S.	Lawrence Berkeley Laboratory
Sawyer, G.	Los Alamos Scientific Laboratory
Sessler, A.	Lawrence Berkeley Laboratory
Shiloh, J.	Lawrence Berkeley Laboratory
Smith, L.	Lawrence Berkeley Laboratory
Staples, J.	Lawrence Berkeley Laboratory
Stokes, R.	Los Alamos Scientific Laboratory
Swenson, D.	Los Alamos Scientific Laboratory
Talbert, W.	Los Alamos Scientific Laboratory
Teng, L.	Fermi National Accelerator Laboratory
Terwilliger, K.	University of Michigan
Thompson, W.	University of California - San Diego
Tidman, D.	Jaycor
Wangler, T.	Los Alamos Scientific Laboratory
Watson, J.	Argonne National Laboratory
Wilson, M.	National Bureau of Standards
Wilson, P.	Stanford Linear Accelerator Center
Yu, S.	Lawrence Livermore Laboratory

TECHNICAL INFORMATION DEPARTMENT
LAWRENCE BERKELEY LABORATORY
UNIVERSITY OF CALIFORNIA
BERKELEY, CALIFORNIA 94720